Proceedings of the XX International Congress of the Mexican Hydrogen Society

[Online]

Sociedad Mexicana del Hidrógeno A.C.

CONACYT

"Proyecto apoyado por el CONACYT"

Oaxaca, México on September 23th to 25th, 2020

In honor of

Professor Perla B. Balbuena

Texas A&M University

ISSN-2448-7120 Año 7 Número 7, 2020

Edition led by Dra. Claudia Lopez Sánchez, Instituto Tecnológico de Oaxaca

Topics

This conference will address important aspects of the hydrogen technologies, from fundamentals to applications, policies and environmental aspects.

Topics are broadly divided into the following topics.

1. Hydrogen production, storage and applications.

2. Fuel Cells components and stacks.

3. Nanostructured materials.

4. Bioelectrochemical cells.

5. Renewable energy systems.

Committee

SMH Commitee

Dra. Beatriz Ruiz Camacho –Presidente.

Dr. Guadalupe Ramos-Sánchez-Vicepresidente.

Dr. Gliserio Romeli Barbosa Pool-Tesorero.

Ing. Juan Antonio Gutiérrez Rodríguez-Secretario.

Organizing Committee – Oaxaca Institute of Technology

General Coordinador M.I. Marco Antonio Maldonado Núñez.

Dra. Claudia López Sánchez

MC. Jorge Miguel Martínez Canseco.

MC. Aymara Judith Diaz Barrita.

Dr. Emilio Hernández Bautista.

MI. Marco Antonio Sánchez Medina.

Dra. María De Jesús Ramírez Altamirano.

MC. Mario Diaz González.

MC. Minerva Donaji Méndez López.

Dra. Marisol Altamirano Cabrera

MC. Maricela Morales Hernandez

C. Emmanuel Daniel Sosa Cruz

C. Diego Bolaños Miguel

Proceedings Editors

Dra. Claudia López Sánchez

MC. I.Q Eminele Reyes Rodriguez

Q.F.B Jeimy Magdala López Torres

I.Q Alma Lilia Antonio Cruz

General Program Congress

Time		September 23			September 24	September 25
09:00	09:20	Pre-congress courses			Opening (09:00-09:30)	Connection to the platform
09:20	09:40	Introduction to Computational Materials Science by Fernando A. Soto, PhD. Texas A&M University	Nuclear Magnetic Resonance for Solid Materials and Electrocatalyst by Marco A. Vera, MsC. Universidad Autónoma Metropolitana [UAM-I]	Simulation by Finite Volume Method (FVM). Electrical/thermal conductivity by Jorge Andaverde Arredondo, PhD. Universidad Veracruzana [UV]	Plenary Perla Balbuena, PhD Texas A&M University	Plenary Emilio Nieto, PhD National Hydrogen Center [NHC]
09:40	10:00					
10:00	10:20					
10:20	10:40					088
10:40	10:45				Free time + coffee	Free time + coffee
10:45	11:05				046	014
11:05	11:25				023	080
11:25	11:45				030	021
11:45	12:05				091	055
12:05	12:25				039	069
12:25	13:00				Free time + LUNCH	Free time + LUNCH
13:00	13:20				Plenary Gerardo Arriaga, PhD [CIDETEQ]	Best PhD Thesis plenary conference
13:20	13:40					
13:40	14:00				006	057
14:00	14:20	Free time			054	038
14:20	14:40				050	079
14:40	15:00				062	Poster session
15:00	15:20				073	
15:20	15:40				004	
15:40	16:00				036	
16:00	16:20				029	
16:20	16:40				059	
16:40	17:00				035	
17:00	17:20				034	
17:20	18:00				1st day activities closure	SMH Assembly Posters awards Congress closure

- Hydrogen Production, Storage and Applications
- Fuel Cells Components & Stacks
- Nanostructured materials
- Bioelectrochemical cells
- Renewable energy systems

Daily Program

September 23rd

Time	Pre-congress courses		
9:00-14:00	Molecular Modelling	Nuclear Magnetic Resonance for Solid Materials and Electrocatalyst	Simulation by Finite Volume Method (FVM) Electrical/termal conductivity

September 24th

Time	ID	
9:00-9:30		Opening.
9:30-10:40		Plenary: **Advances in the Understanding of Catalytic and Electrocatalytic Processes by Integration of Theory aand Experiments** Prof. Perla Balbuena Texas A&M University
10:40-10:45		Free time + coffee
10:45-11:05	**046**	A method for Oxyhydrogen purification and cleaning.
11:05-11:25	**023**	Mixed iron oxides as materials for hydrogen production: thermochemical cycles studies.
11:25-11:45	**030**	Kinetic Study of Methane Partial Oxidation by Chemical Looping Process using $NiWO_4$ as an Oxygen.
11:45-12:05	**091**	Photocatalytic H_2 production using exfoliated Cd-$ZnS(EN)_{0.5}$ hybrid sheets.
12:05-12:25	**039**	Effect of H_2 generated by ethanol steam reforming in scr of NOx from emissions of diesel engines with Pt-Ag/Al_2O_3-WOx/cordierita.

12:25-13:00		Free time + Lunch.
13:00-13:40		Plenary: **Electrochemical Hydrogen Compression Systems** Dr. Gerardo Arriaga CIDETEQ
13:40-14:00	**006**	Seaweed-derived KOH activated biocarbon for electrocatalytic oxygen reduction and supercapacitor applications.
14:00-14:20	**054**	High-performance Pd nanocatalyst supported on Vulcan XC-72 functionalized with Cu organometallic compounds for the Ethanol Oxidation Reaction in alkaline media.
14:20-14:40	**050**	Effect of capping agents' ratio in the synthesis of Pt_3Fe polyhedral nanoparticles and their catalytic activity for RRO.
14:40-15:00	**062**	Doped carbon nanostructures in fuel cells.
15:00-15:20	**073**	Pt catalysts supported on mesoporous carbons synthesized using inorganic templates, and evaluation of their activity for the oxygen reduction reaction.
15:20-15:40	**004**	Au@Pd/C core shell structures for enhance the oxygen reduction reaction at PEM-FC.
15:40-16:00	**036**	CFD PEMFC simulation with different levels of enriched air.
16:00-16:20	**029**	Study of water management in solid styrene electrolytes.
16:20-16:40	**059**	Theoretical Aspects of Precursor Fibers to Activated Carbon Fibers to Store Hydrogen.
16:40-17:00	**035**	Human Urine Role as Water, Nutrients, and Energy Source in Bioelectrochemical Systems Based on the Circular Economy Concept: A Review.
17:00-17:20	**034**	Preparation of Sulfonated PEEK and Graphene Oxide Materials for Proton Exchange Membranes.
17:00-18:00		1st Day of Activities Clossure Closure.

September 25th

Time	ID	
9:00-9:40		Connection to the platform.
9:40-10:20		Plenary Emilio Nieto, PhD National Hydrogen Center [NHC]
10:20-10:40	**088**	Global Overview of Hydrogen Tecnologies Development
10:40-10:45		Free time + coffee.
10:45-11:05	**014**	Hydrogen synthesis from seawater by means of solar energy.
11:05-11:25	**080**	Sustainability Criteria for Systems with Hydrogen Energy Storage Devices located in Mexico.
11:25-11:45	**021**	Synthesis of Mo_2C-Ni_2Mo_3N nanocomposites as a catalyst for bio jet fuel production.
11:45-12:05	**055**	Optimization of $BioH_2$ production by consolidated bioprocessing of corncob pretreated with diluted acid
12:05-12:25	**069**	Stem of faba bean as potential source for fermentative biohydrogen production
12:25-13:00		Free time + Lunch
13:00-13:40		Best PhD Thesis Conference: **Diseño de Catalizadores trimetálicos con bajo contenido de Pt para la Reacción de Reducción de Oxígeno: Estudio Teórico-Experimental** Dr. Heriberto Cruz Martínez
13:40-14:00	**057**	Effect of catalysts supported on a zeolite in the production of H_2 from the gasification of palm kernel shell
14:00-14:20	**038**	Hydrogen production by methanol conversion on Pd and Ni base catalysts supported ZnO-rod

14:20-14:40	**079**	Experimental characterization of the clamping and pressure distribution in a PEM electrolyzer: gasket materials and bolt torques
14:40-17:00		Poster Session
17:00-18:00		SMH Assembly Poster Awards Congress closure

Invited speakers

Professor Perla B. Balbuena
Texas A&M University

Perla Balbuena obtained in 1973 a BSC in Chemical Engineering from Universidad Tecnológica Nacional in Argentina, she then obtained a MSC from the University of Pennsylvania in 1983 and a Ph. D. from University of Texas at Austin in 1996. Her research interests and investigation are devoted to Catalysis on metal nanoparticles for fuel cell electrocatalysts, Catalyzed growth of single-walled carbon nanotubes, Gas separation and storage in metal organic frameworks, Solid-electrolyte interphase layer nucleation and growth in Si and carbon anodes of Li-ion batteries, Materials for photocatalysis: Oxygen evolution in doped oxides , Materials for solar cells and hydrogen production: Hydrogen evolution on coated semiconductors covered by co-catalysts, and Shale gas thermodynamics: Phase behavior of hydrocarbon + water mixtures in confined media. She is author of more than 230 scientific publications with more than 15000 citations and an h-index: 63. She has received multiple important awards such as NSF/POWRE award, 1997, NSF/CAREER award, 1999, GPSA Professorship, 2005, AAAS Fellow, 2013, TEES Senior Fellow, 2013 and active member of multiple scientific communities.

Dr. Emilio Nieto Gallego
National Hydrogen Center, Spain

From September 2014 – June 2017 Emilio Nieto Gallego was in charge of the management and coordination of the whole activities of the National Hydrogen Center. The National Hydrogen Center is a 50% consortium between the Ministry of Economy, Innovation and Competitiveness and the Junta de Castilla La Mancha. The main goals achieved during his administrations were: 6 new European projects (FCH JU, H2020) and 16 National sponsored projects (CDTI, MINECO, Extremadura, JCCM, CORFO, FEDER), as well as 8 new developed industrial projects, 4 peer review articles and three book chapters. He has been Author of various research articles and two patents of high impact on materials science. Member of European and National Technology Platforms. EOI professor staff for a Master on "Eco-innovation on industrial processes". Advisory Board member for two European Projects (ChemWater and CRM_InnoNet CSA projects). Member of Experts Operational Groups on EIP Raw Materials by the European Commission. Member of Industry Expert Group on Industrial Water Management: Barriers and Bottlenecks on EIP on Water by the European Commission. International Advisory Board member of the European Fuel Cell Congress EFC19 December 2019, Naples. Expert Evaluator for the European Commission on Horizon 2020 (SPIRE 2014-2017). Expert Evaluator for the KIC Raw Materials KAVA proposals (2017-20). Expert Evaluator for the ERAMIN 2 proposals (2017). Monitor/Reviewer/Project Technical Advisor (PTA) for the European Commission on FPVII (MINERALS4EU, EURARE).and H2020 (PRODIAS, REE4EU, ADIR).

Dr. Gerardo Arriaga Hurtado

CIDETEQ

Luis Gerardo Arriaga Hurtado has been a member of the National System of Researchers since 2003. He is the leader and technical manager of the National Micro and Nanofluidic Laboratory (LABMyN) located in CIDETEQ SC since 2016, and was in charge of the sub-direction of energy generation by road electrochemistry where he is a senior researcher C. He has published more than 170 scientific articles in international journals indexed in the JCR, among which Applied Catalysis B stands out: Environmental, Biosensors and Bioelectronics, Chemical Communications, Lab on a Chip, Journal of Power Sources, Journal of Materials Chemistry A, Electrochimica Acta and several popular articles. It has an H index of 31 and more than 2500 citations. He has supervised 15 doctoral theses (100% of the doctors belong to the SNI). He has been the inventor of 2 granted patents and 2 patents registered with the IMPI. He has been technical manager in various international projects such as: FONCICYT (250203); CONACYT INNOVATE UK 2015; ANR-CONACYT bilateral with France 2009-2011 (163114); UNESCO Chair in Materials and Technologies for Energy Conversion, Saving and Storage (MATECSS) with Canada and developing countries 2014-2016; CNRCONACYT Bilateral Project (J000.382 / 2009) with Italy and with the CNM National Microelectronics Center in Spain GICSERV Project (150111) among others. He is part of various evaluating committees at CONACYT such as: CONACYT Chairs Program (Energy), SENER Energy Sustainability, SEMARNAT, National and International Sabbatical Program, National Quality Postgraduate Program, Basic Science, FOMIX, SNI Area VII Review Committee.

Sponsors

Index

Hydrogen production, storage and applications

	for the Hydrogen Production under Visible Light.	Meléndez-Zaragoza, J. M. Salinas-Gutiérrez, A. López-Ortiz, V. H. Collins-Martínez.*		
086-A 086-F	Study of the synthesis temperature effect on the photocatalytic properties of the spinel-type $MnCo_2O_4$ towards the production of hydrogen from the water splitting under visible light.	J. A. Jiménez-Miramontes, J. L. Domínguez-Arvizu, B. C. Hernández-Majalca, J. C. Pantoja-Espinoza, J. M. Meléndez-Zaragoza, J. M. Salinas-Gutiérrez, A. López-Ortiz, V. Collins-Martínez.	30	178
087-A 087-F	Study of $CoFe_2O_3/Cu_2O$ heterojunction as photocatalyst for hydrogen production under visible light.	J. L. Domínguez-Arvizu, J. A. Jiménez-Miramontes, B. C. Hernández-Majalca, J. C. Pantoja-Espinoza, J. M. Meléndez-Zaragoza, J. M. Salinas-Gutiérrez, A. López-Ortiz, V. Collins-Martínez*.	31	196
091-A	Photocatalytic H_2 production using exfoliated Cd-$ZnS(EN)_{0.5}$ hybrid sheets.	D. Ramírez-Ortega, A.B. Ramos, A. Hernández-Gordillo, R. Zanella, S.E. Rodil.	32	

Fuel Cells Components and Stacks

ID	Title	Autor(s)	Abstract page	Full paper page
001-A 001-F	Improved preparation of the membrane-electrode assembly for PEM electrolysis through an automatic catalytic ink application system.	A. Martínez-Septimo; M. A. Valenzuela-Zapata; R. G. González-Huerta.	34	212
011-A 011-F	Analysis of ordered and disordered conductive phases in a PEMFC synthetic catalyst laye.	C. Pacheco, B. Escobar, A. Rodriguez, R. Barbosa.	35	220

074-A	Development of a test PEM electrolyzer based on advanced manufacturing techniques.	C.Y. Montalvo-Fernández, J.M. Sandoval-Pineda, R. de G. González-Huerta.	50	
079-A 079-F	Experimental characterization of the clamping and pressure distribution in a PEM electrolyzer: gasket materials and bolt torques.	R. Moreno Soriano, N. Rojas, E. Nieto, R. González-Huerta, J. Sandoval-Pineda.	51	324

Nanostructured materials

ID	Title	Autor(s)	Abstract page	Full paper page
003-A	Effect of epitaxial growth of bimetallic nanocrystals on the electrocatalytic activity of ORR.	Francisco F. Tello Casas; Rosa de Guadalupe González Huerta; Martha L. Hérnandez Pichardo; Paz del Ángel.	53	
004-A 004-A	Au@Pd/C core shell structures for enhance the oxygen reduction reaction at PEM-FC.	Eduardo Y. Cervantes-Aspeitia; Martha L. Hernández-Pichardo; Paz del Ángel.	54	336
008-A	Electrospun N-doped carbon nanofibers as metal-free electrocatalysts for the oxygen reduction reaction in alkaline medium.	M.G. Ayala-Sánchez; B. Escobar-Morales; J. Escorcia-García; I.L. Alonso-Lemus.	55	
009-A	Electrospun Ce: $CoFe_2O_4$ nanofibers as bifunctional nanocatalysts for Oxygen Evolution and Oxygen Reduction Reactions.	P.C. Cintrón-Núñez, B. Escobar-Morales, J. Escorcia-García, I.L. Alonso-Lemus, F.J. Rodríguez-Varela.	56	

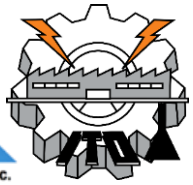

	evaluation of their activity for the oxygen reduction reaction.			
083-A 083-F	Kinetics of the Oxygen Reduction Reaction for Pt nanoparticles supported on novel reduced graphene oxide-polyindole.	N.M. Sánchez-Padilla, J. Manríquez, L. Da Silva, R. Benavides, D. Morales-Acosta.	72	372
092-A 092-F	Novel and cheaper process for the development of carbon nanoestructures by using Orange peel waste for the generation of carbons applied to supercapacitors.	G.G. Suárez-Velázquez, J. A. Ramírez de León, J.F. Castañón-Rodríguez, W. J. Pech-Rodríguez.	73	379

Bioelectrochemical cells

ID	Title	Autor(s)	Abstract page	Full paper page
010-A 010-F	Use microbial fuel cells for degradation of Used Lubricating Oils (ULO) and production of energy.	Esther Ibarra Altamirano; Miguel Mauricio Aguilera Flores; Verónica Ávila Vázquez.	75	386
021-A	Synthesis of Mo_2C-Ni_2Mo_3N nanocomposites as a catalyst for bio jet fuel production.	Jonathan Jesús Malpica Maldonado, Ana Lidia Martínez Salazar, José Aarón Melo Banda, Benjamín Portales Martínez, Sebastián Pacheco Buendía.	76	
035-A 035-F	Human Urine Role as Water, Nutrients, and Energy Source in Bioelectrochemical Systems Based on the Circular Economy Concept: A Review.	Mariana Martínez-Castrejón, Giovanni Hernández-Flores, Omar Solorza-Feria, Oscar Talavera-Mendoza, Osbelia Alcaráz-Morales, América Libertad-Rodríguez Herrera.	77	394

090-A	Study of separators in electrochemical assisted constructed wetlands.	M.G. Salinas-Juárez, S.I. Ortíz Zamora, M.C. Durán Domínguez.	83

Renewable energy systems

ID	Title	Autor(s)	Abstract page	Full paper page
006-A	Seaweed-derived KOH activated biocarbon for electrocatalytic oxygen reduction and supercapacitor applications.	Perez-Salcedo, K.Y; Shi, X; Kannan, A. M; Vayssieres, L; Escobar, B.	85	
007-A 007-F	Electrolyte flow influence analysis in the behaviour of 15 kW alkaline water electrolysis stack.	Valeria Juárez Casildo; Mónica Sánchez Delgado; Rosa de Guadalupe González Huerta	86	418
014-A	Hydrogen synthesis from seawater by means of solar energy.	Rafael García Gutiérrez, Rafael Cabanillas López, Ricardo Rodriguez Carbajal, Ricardo Rangel Segura	87	
031-A	Review of environmental policy instruments for the management of hydrogen from community forestry in Mexico.	María Liliana Ávalos Rodríguez, José Juan Alvarado Flores, Jorge Víctor Alcaraz Vera, José Guadalupe Rutiaga Quiñones	88	
032-A	Synthesis of non-stoichiometric copper sulfides Cu2-xS (1 ≤ x ≤ 2) under ambient conditions: mechanochemical reactions in the CuS-Cu2S system.	E.A. Badillo Arroyo, K.P. Padmasree, A.F. Fuentes	89	

Abstracts

Hydrogen production, storage and applications

ID 002

Offshore Wind Power For Hydrogen Production, General Status

Malinalli Pérez-Vigueras[1*], Rosa González-Huerta[1], Rogelio Sotelo-Boyas[2.]

[1]Instituto Politécnico Nacional-ESFM. Departamento de Energía. UPALM, CP 07738, Ciudad de México.

[2]Instituto Politécnico Nacional-ESIQIE. Laboratorio de Electroquímica. UPALM, CP 07738, Ciudad de México

[2]Instituto Politécnico Nacional-ESIQIE. Departamento de Ingeniería Química Petrolera. UPALM, CP 07738, Ciudad de México

* Corresponding author: malinallipv@gmail.com

ABSTRACT

World energy consumption is forecast to increase exponentially in the coming decades, driven by rising living standards and population growth worldwide. Therefore, the growing need for more energy will require enormous development in the generation of energy and more secure and diversified energy sources. Because of the distance between the parks and the coast (> 10 km), most of the time a cable is expensive and generates ecological damage, this project proposes the use of offshore wind energy for hydrogen production used electrolysis.

A review of the general state was carried out of offshore wind energy considering the technological factors, supply and characteristics of the best offshore wind farms. A description of the situation in Mexico is presented in terms of offshore electricity, areas of opportunity and technological, environmental, social and regulatory gaps are analyzed.

Keywords: Offshore; wind energy; hydrogen; renewable energies.

ID 005

Ni electrodeposites on 304 steel electrodes in a hydrogen generator reactor

Flores Melo Luis Manuel[1], González Huerta Rosa de Guadalupe[2], Arce Estrada Elsa Miriam[1*]

[1]Instituto Politécnico Nacional, ESIQIE, Departamento de Ingeniería en Metalúrgica y Materiales, UPALM, Ed. 7. Zacatenco. Ciudad de México, C.P. 07738. México.

[2]Instituto Politécnico Nacional, ESIQIE, Laboratorio de Investigación de Electroquímica, UPALM, Ed. 7. Zacatenco. Ciudad de México, C.P. 07738. México.

* Corresponding author: 4427791760 and melomano182.mm@gmail.com

---

ABSTRACT

The hydrogen production as an energy alternative plays a significant role. Therefore the water electrolysis has gained relevance as a method of hydrogen generation. There are different methods for the generation of hydrogen, and a very effective option is the alkaline electrolyzer, as it is an economical device, due to the simplicity of its components and its operating conditions. However, to make it economically attractive, low-cost electrodes must be designed that support the conditions and be efficient. For this research work, 304 steel was used as an electrocatalyst; however, when operating the system above 2V, corroded steel generating Cr (VI), which is harmful to humans. In order to reduce this process and maintain low-cost materials, we chose to coat the steel with a nickel monolayer by electrodeposition, because the nickel has high chemical stability in alkaline media. The efficiency of the electrocatalyst and its resistance to corrosion were analyzed by linear polarization techniques and electrochemical impedance spectroscopy. As well as the characterization of the electrodes by scanning microscopy and X-ray diffraction before and after the corrosive evaluation.

Keywords: Electrodeposition, electrode, reactor, hydrogen

ID 023

Mixed iron oxides as materials for hydrogen production: thermochemical cycles studies

Lorenzo Antonio Cruz Santiago[1*], Ana Lidia Martínez Salazar[1], Benjamín Portales Martínez[2], Ana Adela Lemus Santana[2], Edilso Francisco Reguera Ruíz[2]

[1] Centro de Investigación en Petroquímica, Instituto Tecnológico de Ciudad Madero, Tamaulipas, México.

[2] Laboratorio Nacional de Conversión y Almacenamiento de Energía, Centro de Investigación en Ciencia Aplicada y Tecnología Avanzada - Unidad Legaría, IPN, CDMX, México

* lacrus8@gmail.com

ABSTRACT

Mixed iron oxides are materials with great potential for two-step thermochemical cycles since these oxides contain divalent cations that confer the possibility of reducing the working temperatures of cycles. Two-step thermochemical processes are promising technologies for hydrogen production. In these processes, the first step is the endothermic reduction of a metal oxide at elevated temperatures by oxygen release, the second step corresponds to exothermic oxidation of reduced metal oxide at lower temperatures by taking oxygen from water and producing hydrogen via water-splitting reaction. In this work, $[Zn_xMg_zFe(III)_{1-x-z}]_{tet}[Mg_yFe(II)_{1-x-y-z}Fe(III)_{1+x+z}]_{oct}O42-$ systems were synthesized through coprecipitation route. The $Zn(NO_3)_2$, $MgCl_2$, $Fe(NH_4)_2(SO4)_2$ and $FeCl_3$ precursors at several ratios were mixed with constant stirring until homogenization was achieved. NaOH was used as a precipitating agent. The samples were characterized by infrared spectroscopy, Mössbauer spectroscopy, X-ray diffraction, and thermogravimetric analysis. Infrared spectroscopy confirmed the occurrence of ferrites, with bands in the range of 300–650 cm−1 that are characteristic for Fe-O bond in Fe_3O_4. Through Mössbauer spectroscopy, the iron sites and relative amounts of each contribution were assigned. X-ray patterns, reveal incremented zinc ion insertion into magnetite structure as zinc relative concentration increases, particularly in the plane (311). Powder patterns refinements were performed to evaluate the experimental lattice parameter and crystallite size. From both techniques results, it was possible to calculate and fit the theoretical lattice parameter to obtain the structural composition. Thermochemical studies were performed by thermogravimetry from room temperature to 1000 °C. Magnesium ferrite presented the highest loss mass (approximately 15%). The characterization of these materials provides relevant information for its possible application in two-step thermochemical cycles in order to hydrogen production.

Keywords: mixed iron oxides; coprecipitation; two-step thermochemical cycles; Mössbauer spectroscopy.

ID 025

Raman study of ammonia borane at high temperatura

R. Hinojosa N.[1, 2, 3]*, E.V. Mejía-Uriarte[1], R Y. Sato-Berrú[1]

[1] Programa de Maestría y Doctorado en Ingeniería, Universidad Nacional Autónoma de México, Edificio Bernardo Quintana Piso 1, C.U., 04510 Coyoacán, CDMX, México.

[2] Instituto de Ciencias Aplicadas y Tecnología, Universidad Nacional Autónoma de México, Circuito Exterior S/N, Ciudad Universitaria, A.P. 70-186, Delegación Coyoacán, C.P. 04510 CDMX, México.

[3] Facultad de Ciencias, Universidad Nacional Autónoma de México, Av. Universidad 3000, Circuito Exterior S/N Delegación Coyoacán, C.P. 04510 Ciudad Universitaria, D.F. México

** hinro36@ciencias.unam.mx*

ABSTRACT

Ammonia borane (NH_3BH_3, AB) is a compound of great importance due to its high hydrogen content (19.6% wt) [1], Also, it is a solid and stable material at room temperature. Due to these characteristics, this compound gets a lot of attention and has been proposed as a material that can store hydrogen to be used in fuel cells [2]. The study of this compound in the hydrogen release process is of great importance for its handling and application conditions. It is known that in the process of releasing hydrogen by thermolysis for AB, occurs in three steps; first a 6.5 % wt is released between 85 and 130 ^{0}C, second step 6.9% wt is released around 130 to 200 ^{0}C, the third release step occurs at high temperature (> de 1170 ^{0}C), in general the study of this compound focuses on the first two release steps [3]. Release temperature may depend of heating ramp and material purity. In this work, we follow the process of hydrogen release from AB by thermolysis, with Raman spectroscopy, recording the changes in intensity and shifts of the bands associated with the NH and BH bonds showed in figure 1.

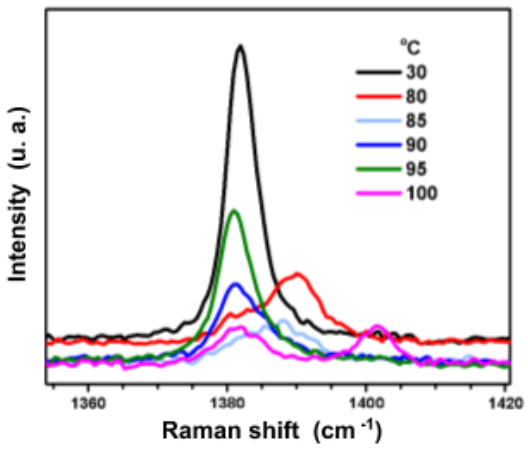

Figure 1. Bands sensitive to hydrogen release in 1385 (cm-1) NH3du (du, umbrella).

ID 030

Kinetic study of methane partial oxidation by chemical looping process using $NiWo_4$ as an oxygen carrier for syngas production

P.E. González-Vargas, J.M. Salinas-Gutiérrez, M.J. Meléndez-Zaragoza, V. Collins-Martínez, A. López-Ortiz *

Centro de Investigación en Materiales Avanzados, S.C., Miguel de Cervantes 120, Complejo Industrial Chihuahua

Chihuahua, Chih. México. C.P. 31136

** Tel: +52 6144394815; e-mail: alejandro.lopez@cimav.edu.mx*

ABSTRACT

Partial oxidation of methane (POX) by chemical looping process (CLPO) using metal oxides (MeO) as the only source of oxygen (oxygen carrier) to produce syngas ($MeO + CH_4 = Me + H_2 + CO$) and regenerating the metal oxide by the oxidation of reduced metal with a steam oxidizing atmosphere for the hydrogen release ($Me + H_2O = MeO + H_2$) has been proposed. It was previously proved the potential capacity of nickel tungstate ($NiWO_4$) as an oxygen carrier to be used on CLPO process, to confirm this a kinetic study was performed on the involved redox reactions and their kinetic parameters are determined. In order to evaluate the $NiWO_4$ oxidation and reduction kinetics, thermogravimetric analyses (TGA) were performed in three redox cycles in a temperature range of 850 to 950°C and reducing atmosphere from ca. 5 to 9 v% of CH_4/Ar, while oxidation employed concentrations from ca. 0.8 to 2.2 v% H_2O/Ar. For the kinetic study, the data corresponded to the second cycle reduction or oxidation period for each experimental condition. Results indicate a global reaction order n=1.47 for the methane reduction of the material, while a reaction order of n = 0.94 for the oxidation step. These global reaction orders indicate that there are several reaction steps involved, which are described. Activation energies of 27.7 kcal/mol and 17.7 kcal/mol for the reduction and oxidation reactions were found, respectively, which involve global phenomena, including the chemical reactions and other physical phenomena.

Keywords: $NiWO_4$; kinetics; syngas; chemical looping.

ID 038

Hydrogen production by methanol conversion on Pt and Ni base catalysts supported ZnO-rod

Ventura Rodríguez Lugo[1], Gilberto Mondragón-Galicia[2], Albina Gutiérrez-Martínez[2], Claudia Gutiérrez-Wing[2], Omar Rosales González[1], Pavel López[2], Pastora Salinas-Hernández[3], Fernando Morales Anzúrez[3] Francisco Tzompantzi[4], María I. Reyes Valderrama[1] and, Raúl Pérez Hernández[2, *]

[1]Universidad Autónoma del Estado de Hidalgo. Ciencias de la Tierra y Materiales. C.P. 42184 Pachuca, Hidalgo. México.
[2]Instituto Nacional de Investigaciones Nucleares, Carr. México-Toluca S/N, La Marquesa, Ocoyoacac, Edo. de México C. P. 52750.
[3]Universidad del Istmo-Campus Tehuantepec, Santo Domingo Tehuantepec, Oaxaca, C.P. 70760, Mexico.
[4]Depto. de Química, Area de Catalisis, Universidad Autonoma Metropolitana-Iztapalapa, Iztapalapa, CDMX, 09340, Mexico.
* Corresponding author: 5553297200 ext. 12534, raul.perez@inin.gob.mx

---

ABSTRACT

PtNi/ZnO-rod catalysts were evaluated on autothermal steam reforming of methanol (ASRM) for hydrogen production as a function of the reaction temperature. Catalytic materials were characterized by SEM-EDS, XRD, TEM, HRTEM, TPR and BET. Analysis by SEM and TEM showed structural modifications on the surface of the ZnO rods after Ni impregnation. Catalysts activation at 500°C in H_2 stream yielded different phases on each system, NiZn from the Ni/ZnO rod sample, a PtZn phase on the Pt/ZnO-rod catalyst, and a mixture of Ni-Zn phases, PtZn and PtNi structures in the PtNi/ZnO sample were observed. The reactivity of the catalytic materials in the range of 200-400°C range showed that the bimetallic sample had the highest catalytic activity among all the catalysts studied. This finding could be associated to PtZn and NiZn alloys present in the catalysts, which were identified by XRD and HRTEM analyses. These NiZn and PtZn alloys were formed on the surfaces of the ZnO-rods through a hydrogen reduction treatment in the catalysts. These intermetallic alloys can modify the CO selectivity in the ASRM reaction. The characterization of catalysts by XRD after the catalytic testing showed that the intermetallic PtZn structure was stable during the reaction in the Pt/Zn-rod sample. The cubic Ni0.75-Zn0.25 structure identified in the Ni/ZnO-rod sample was transformed to Zn0.1-Ni0.9-O and metallic Ni. When Pt and Ni are together in the bimetallic PtNi/ZnO-rod sample, the tetragonal NiZn structure is unstable and was destroyed during the ASRM reaction, although the cubic Ni0.75-Zn0.25 structure remained, emerging then a new phase of Ni0.7Pt0.3. The promotion effect of Pt and/or Ni on the ZnO-rod was clearly showed.

Keywords: ZnO rod; PdNi/ZnO catalyst; H2 production; ASRM.

ID 039

Effect of H_2 generated by ethanol steam reforming in SCR of NOx from emissions of diesel engines with Pt-Ag/Al_2O_3-WOx/cordierita

Naomi N. González [*1], José Luis Contreras[1], Beatriz Zeifert[2], Gustavo A. Fuentes[3], Tamara Vázquez[2] and Ricardo López M.[1]

[1] *Departamento de Energía, Universidad Autónoma Metropolitana Azcapotzalco, Av. Sn. Pablo 180, Col. Reynosa Tamaulipas, Ciudad de México, Código Postal 02200, México*
[2]*ESIQIE, Instituto Politécnico Nacional. UPALM. Zacatenco, Ciudad de México, México.*
[3] *Departamento de IPH, CBI Universidad Autónoma Metropolitana Iztapalapa.*
* iq_naomi@hotmail.com

ABSTRACT

Diesel vehicles constitute an important component within mobile sources, they are known to have superior thermal efficiency compared to stoichiometric engines, that is, they reduce CO_2, CO and HC emissions [1-2], however, emit a series of pollutants including particulates (PM) and nitrogen oxides (NOx). These emissions are the main precursors of tropospheric ozone (O_3) and secondary particulate matter (PM) [3-4]. Selective Hydrocarbon Catalytic Reduction (HC-SCR) is an effective technology that is widely used today to reduce NOx emissions from mobile sources, such as Diesel vehicles. The HC-SCR of NOx emitted by Diesel engines with Pt-Ag/γ-Al_2O_3-WOx/Cordierite using H_2 generated by ESR with Ni-Co/Hydrotalcite-WOx is a promising alternative.

The catalytic materials were characterized by: N_2 Physisorption, MEB/EDS, DRX, UV-vis spectroscopy and RAMAN spectroscopy. The effect of the presence of C_3H_8 and H_2 on the reduction of NOx was studied using a mixture of synthetic gas similar to that emitted by a Diesel engine, as well as the longevity of the Pt-Ag/γ-Al_2O_3-WOx/Cordierite catalyst at different velocity space (GHSV of 30,000, 70,000 and 10,000 h-1). The Ni-Co/Hydrotalcite-WOx catalysts evaluated in the ESR reaction confirmed the presence of H_2, CO_2, CH_4, CO in the reaction products. The evaluation of the Pt-Ag/γ-Al_2O_3-WOx/Cordierite catalyst showed a wide temperature range, with two maxima at 150 and 350°C, in the first maximum 94% NO conversion was obtained, but between 180 and 250°C exhibit minimal reduction. Again between 300 and 400°C the conversion increases again, reaching 96% conversion, it being evident that the presence of more than one reducing gas in the reaction considerably improves the activity of the catalysts, widening the evaluation temperature range.

Keywords:

ID 040

Energía los Cabos

Cristina Martín González

HDF Energy
20 Rue Jean Jaurès
33310 Lormont (France)

+33 06 22 53 59 54
* Cristina.martin@hdf-energy.com

ABSTRACT

The power grid of Baja California Sur is isolated from the national grid, operating as an island. Due to its geography, power generation needs to be carried out locally to meet the increasing demand, which limits the energy mix. Since the intermittency of renewable power sources creates instability in the grid, leading in certain cases to blackouts, the state relies on thermal power plants for its electrical requirements.

Energía Los Cabos is a Project developed by HDF Energy to address the challenges of Baja California Sur's power grid. It consists on a Renewstable® power plant that produces stable electricity from intermittent energy sources by combining a photovoltaic park with a hydrogen-based energy storage, coupled with battery backup storage. An oversized photovoltaic park delivers power to the grid while the sun is shining and produces green hydrogen through the water electrolysis. The hydrogen is stored in specialized tanks and reconverted into electricity at night or on cloudy days. Thus, the plant's service will be equivalent to that provided by diesel or gas-fired power plants, but without the downside of pollution or fuel supply logistics.

The project is sized to produce 22 MW during the day and 6 MW at night, which equals the electrical consumption of over 60,000 people, and reduces local CO_2 emissions by 90,000 tons per year. Moreover, the fixed rate energy tariff over 25 years and its production dependent uniquely on local resources increases the energy security of the state.

Keywords: power plant; renewable; green hydrogen; energy security.

ID 042

Modeling and simulation of the adsorption and storage of Hydrogen in calcite stone oil fields

Ernesto López-Chávez[1,*], Alberto García-Quiroz[1], Yesica A. Peña-Castañeda[1], José A. I. Díaz-Góngora[2] , Fray de Landa Castillo-Alvarado[2], Williams Ramìrez Carbellido[3]

[1]Autonomous University of Mexico City. Fray Servando Teresa de Mier 92, Col. Obrera, Cuauhtémoc, México, City, C.P. 06080.
[2]Centro de Investigación en Ciencia Aplicada y Tecnología Avanzada del Instituto Politécnico Nacional, Unidad Legaria. Calzada Legaria No. 694 Col. Irrigación, Del. Miguel Hidalgo, Mexico City, C.P. 11500.
[3]Escuela Superior de Física y Matemáticas del Instituto Politécnico Nacional. Edificio 9 de la Unidad Profesional Adolfo López Mateos. Colonia Lindavista. Del. Gustavo A. Madero. México City, C.P 07030.
* Corresponding author: (52)55 51349804 Ext 11110, elopezc_h@hotmail.com

---

ABSTRACT

Due to the thermodynamic conditions prevailing at very shallow depths of calcite stone oil fields, molecular hydrogen has been reported to be released from hydrocarbon or heavy oil located on the surface of the calcite stone. Since this region is physically inaccessible, there is a need to realize modeling and simulation of the hydrogen adsorption and storage process under reservoir conditions.

Motivated by the previous problem, in this work, first principles studies and molecular dynamics calculations were realized in order to have a better understanding of the adsorption mechanisms and quantify the adsorption capacity of hydrogen in calcite stone ($CaCO_3$). Firstly, a characterization of $CaCO_3$ was made obtaining for it its structural, electronic, vibrational, thermodynamic properties, and Mulliken population analysis. Subsequently, Molecular Dynamics simulations were performed in order to obtain adsorption energies of the H_2 molecules on the surface (110) of the 2x2 supercell of calcium carbonate for N=3,5 and10 hydrogen molecules. The results of the molecular dynamics simulations show that only 0.42% by weight of the H_2 molecules could be adsorbed and stored by the $CaCO_3$ surface in oil field.

Keywords: Hydrogen adsorption, storage of hydrogen, oil reservoir, atomic simulations, calcite stone.

ID 043

Hydrogen production from oil fields through zwitterionic liquids: A computational simulation

Ernesto López-Chávez[1], Alberto García-Quiroz[1,*], Yesica A. Peña-Castañeda[1], José A. I. Díaz-Góngora[2], Fray de Landa Castillo-Alvarado[3]

[1]Autonomous University of Mexico City. Fray Servando Teresa de Mier 92, Col. Obrera, Cuauhtémoc, México, City, C.P. 06080.

[2]Centro de Investigación en Ciencia Aplicada y Tecnología Avanzada del Instituto Politécnico Nacional, Unidad Legaria. Calzada Legaria No. 694 Col. Irrigación, Del. Miguel Hidalgo, Mexico City, C.P. 11500.

[3]Escuela Superior de Física y Matemáticas del Instituto Politécnico Nacional. Edificio 9 de la Unidad Profesional Adolfo López Mateos. Colonia Lindavista. Del. Gustavo A. Madero. México City, C.P 07030.

* Corresponding author: (52)55 5134-9804 ext 11109 and alberto.garcia@uacm.edu.mx

---

ABSTRACT

One of the key stages for the development of hydrogen science and technology is the methods for the production of hydrogen and the understanding from the atomic and molecular levels of the physicochemical processes that are carried out. Currently, hydrogen production methods are mainly based on the electrolysis of water and on hydrocarbons reforming and non-hydrocarbons reforming technology. Since, hydrogen fuel is believed that it will be a promising candidate to lead a new hydrogen economy, the need to research new hydrogen production methods that reinforce existing ones becomes important. In this sense, in this work we present a computational simulation based on molecular dynamics that it demonstrates the possibility of extracting hydrogen from the limestone rock of oil fields by using zwitterionic liquids (ZL) in the processes of enhanced recovery of crude oil. In our model, molecular dynamics simulations were started from rest in a simulation cell containing: limestone rock surface, molecule of asphaltene, molecule of geminal zwitterionic, and H_2 molecules. The dielectric constant of water was used to represent the effect of the aqueous medium. This simulation cell was previously optimized using a forcefield approximation. All of the chemical species were optimized by DFT methods. The results indicate that, before applying the ZL, the hydrogen molecules and the asphaltene molecule (which represents the crude oil) are strongly adhered to the rock surface; but when the ZL is applied, it begins to interact with the other species, so, both oil and hydrogen molecules are released from the rock, thus starting the production process.

Keywords: Hydrogen production, molecular simulation, forcefields, DFT methods, limestone rock.

ID 044

High Activity and Stability of the NiCu@Pt catalyst supported in RGO

Padilla-Islas Miguel Adrian[1], Tellez-Cruz Miriam Marisol[1], Solorza-Feria Omar[1]

[1] CHEMISTRY DEPARMENT, CINVESTAV, México CDMX. *
*adrianmapi@gmail.com cel: 5535784453

ABSTRACT

The catalyst of octahedral shaped NiCu cores were prepared through chemical reduction method by a modified polyol process with the right amount of oleylamine, oleic acid and precursor salts of non-noble metals, $Cu(acac)_2$ and $Ni(acac)_2$, using morpholine borane as reducing agent, while the shell of Pt was deposited by galvanic displacement on the Ni-Cu nanoparticles. The presence of alloy Ni-Cu in the core and Pt in the shell

To measure the catalytic activity and stability of the alloy catalyst (electrodes containing Pt loading of 0.02 mg/cm2, 20 wt.% Pt/C, E-TEK), the polarization curves were obtained. The alloy catalyst showed higher catalytic activities and stability than Pt/C. It can be concluded that in platinum formed alloy with transition metals, the electronic state of Pt and the nearest neighbor Pt–Pt distance changes, which significantly influence the electrocatalytic activity for oxygen reduction.

The aforementioned catalyst was shown to possess improved resistance to electrochemical surface area (ECSA) loss during accelerated aging tests relative to commercially available pure Pt electrocatalysts.

Keywords: alloy, stability, RGO

ID 045

Hydrogen adsorption on Single Wall Carbon Nanotubes doped with Nitrogen using DFT theory.

O. Ramírez-Rodríguez[1*]; G. Ramírez-Dámaso[1]; A. Pineda-Jiménez[1]; E. Rojas-Hernández[1] and F. Caballero [2].

[1]Escuela Superior de Ingeniería y Arquitectura "Unidad Ticomán" del Instituto Politécnico Nacional (SEPI), Av. Ticomán No. 600, Col. San José Ticomán, C. P. 07340, Alcaldía Gustavo A. Madero, CDMX, México.

[2]Carrera de Ingeniería Química, Facultad de Estudios Superiores Zaragoza C. II UNAM, Batalla 5 de Mayo s/n, Col. Ejército de Oriente, C.P. 09320, Alcaldía Iztapalapa CDMX, México.

* Corresponding author: phone number 55-65-04-97-85 and e-mail omarod672@gmail.com

---

ABSTRACT

In this work, we present results of the energies of hydrogen adsorption on a single wall carbon nanotube (SWCNT) of dimensions mxn (3x6) and carbon nanotube doped with nitrogen (SWCNT-N) with the same dimensions (3x6). We began with the build of a nanotube with and without Nitrogen, optimizing their structures and obtaining their states of minimum energy. Then we added hydrogen molecules on the external surface of nanotube and optimized his structure, obtaining one more time his state of minimum energy. We repeated this procedure for the nanotubes doped with nitrogen and compared the states of minimum energy of both nanotubes.

We reported the variation in the diameter of nanotubes and the difference in energies of nanotubes with and without hydrogen. We have obtained that our SWCNT with 84 carbon atoms increases their energy linearly with the increase of the number of nitrogen and hydrogen molecules; this SWCNT can accept 8 nitrogen atoms and 8 hydrogen molecules. In our calculations, we have used the module Dmol3 of the molecular simulation program Materials Studio.

Keywords: Carbon nanotubes, hydrogen storage, DFT theory.

ID 046

A method for Oxyhydrogen purification and cleaning

Alejandro Wintergerst-Felipe[1*], Rosa de Guadalupe González-Huerta R de G.[2], Juan Manuel Sandoval-Pineda[1], Luis Ricardo Vega Ventura[1]

[1]Instituto Politécnico Nacional, Sección de Estudios de Posgrado e Investigación, Escuela Superior de Ingeniería Mecánica y Eléctrica-U. Azcapotzalco., Av. de las Granjas 682, Col. Santa Catarina, CP 02250, Ciudad de México

[2]Instituto Politécnico Nacional, Escuela Superior de Ingeniería Química e Industrias Extractivas, Laboratorio de Electroquímica y Corrosión. UPALM, CP 07738, Ciudad de México.

*wintergerst.af09@gmail.com

ABSTRACT

The use of hydrogen as a source of clean energy is increasing, however, until now, it has not been possible to scale it up to mass production, such as that existing with petroleum-derived fuels. This research is focused to be implemented in dual combustion processes, either with diesel (internal engine combustion) or with LP gas (open or external combustion), and shows the development of an oxyhydrogen gas (OH_2G) purification system, obtained by the alkaline electrolysis process. Previously, when producing oxyhydrogen gas, it had some electrolyte residues (NaOH); this is because the maximum working temperature of the electrolyser rises to 90 ° C; at this temperature, the electrolyte in liquid phase tends to evaporate, the salts of the NaOH contained in the water are transported in gaseous form through water vapor, which can damage the combustion engine chamber. To prevent this phenomenon from occurring, a purification system is designed, which includes the phase separator and some devices with a heat exchange cooling method, recirculating both the Oxyhydrogen gas and the electrolyte, maintaining the electrolysis process at an optimal operating temperature of 60 ° C and thus avoiding drag of the electrolyte.

Keywords: *Hydrogen purification, Alkaline electrolysis, Dual Combustion*

ID 057

Effect of catalysts supported on a zeolite in the production of H_2 from the gasification of palm kernel Shell

Juan C. Acevedo-Páez[1,2*]; Erika Arenas[2]; Zulamita Zapata-Benabithe[2]; Jessica M. Durán[1]; Fausto R. Posso[3]

[1]Universidad de Santander, Facultad de Ingenierías, Avenida 4 #10N-61 Cúcuta, Colombia
[2]Universidad Pontificia Bolivariana, Facultad de Ingeniería Química, Circular 1 #70-01 Medellín, Colombia
[3]Universidad de Santander, Facultad de Ingenierías, Calle 70 #55-210 Bucaramanga, Colombia
* Corresponding author: +57 313-8290852; jua.acevedo@mail.udes.edu.co

ABSTRACT

The research in progress aims to determine the effect of a new catalyst configuration (Support: natural or modified clinoptilolite, active phase: Ni, promoters: Ca, K) on the yield of hydrogen production present in the syngas, by palm kernel shell gasification using TGA-MS. Clinoptilolite from the province of Guayas (Ecuador), is treated with an acid leaching using 2M HCl solution, and it is mixed with metal salts ($Ni(NO_3)_2*6H_2O$, $Ca(NO_3)_2*4H_2O$, KNO_3) to incorporate Ni, Ca, and K via ion exchange, respectively. Four catalyst configurations are synthesized (CLxNi, CLxNiyCa, CLxNiyK, CLxNiyCayK), where CL corresponds to clinoptilolite, x is 10, and y is 5 w/wt. The same process is replicated with natural clinoptilolite. Different techniques are applied to evaluate the physicochemical and structural properties of the catalysts such as BET, XRF, FESEM, TPD-CO_2, XPS, DRX.

For the gasification process, the palm kernel shell from Norte de Santander (Colombia) is subjected to a pyrolysis process at 800 °C for 30 minutes at a heating rate of 30 °C/min using TGA. Subsequently, the biochar obtained is mixed with each supported catalyst (10 w/wt) and introduced into a TGA, then the temperature is increased to 950 °C, at a heating rate of 30 °C/min with a N_2 flow of 50 ml/min. When this temperature is reached, the gasifying agent (steam) is introduced into a mixture of H_2O/N_2 gas (50% v/v) for 60 minutes. The process is repeated using a gas mixture (H_2O/CO_2), eliminating the entry of N_2 and replacing it with CO_2, maintaining the initial process flow of 50 ml/min. The gases produced are analyzed on a mass spectrometer. This research is expected to contribute to the development of catalysts supported on clinoptilolite, to improve the yield of hydrogen production from biomass.

Keywords: hydrogen; catalyst; palm kernel shell; gasification

ID 058

Hydrogen-dechlorination of persistent organic compounds, insights from first principles modelling

I. Leal VIllanueva[1], J.C. Pacheco-Kato[1], G. Ramos-Sánchez[2,*]

[1]Universidad de Guadalajara, Enrique Díaz de León 1144, Lagos de Moreno, Jalisco, México.
[2]Departamento de Química, Departamento de IPH, CONACYT, Universidad Autónoma Metropolitana – Iztapalapa.
* gramos@xanum.uam.mx

ABSTRACT

Organochlorines are a special type of compounds commonly found in pesticides which are persistent to almost any type of decomposing treatment. Their toxicological effects are still unclear; however, they are related to neurological and endocrine disorders. The chemical stability in this kind of compounds leads to chlorine contamination, mainly by the accumulation of these compounds either in living tissues and soils (ref). The process of removing chlorine-carbon bonds by the effect of **Hydrogen** (Hydrodechlorination) has been the only method capable to reduce the concentration of such contaminants in liquid phase, thus giving extra application to the electrochemical processes to produce Hydrogen. However, the utilization of noble metals as catalysts, the fast poisoning of the catalysts and the overall price of the process has limited their large scale utilization. The development of alternative catalysts and processes is mandatory but many fundamental questions remain still elusive. In this work we propose a combined study to determine the main steps of the mechanism and the effect of the catalysts surface and hydrogen coverage to determine the hydrodechlorination mechanism. In the first part of the work the possible dechlorination of these compounds (specifically chlorometane) is revised within Density Functional Theory with the Kohn-Sham scheme. Geometry optimizations for reactants and products were carried with several methods and basis sets to propose a typical SN2 type reaction with the main idea of removing the chlorine atom to understand how the carbon-chlorine bond can be broken. In the second part, Pd, Pt, Cu (111) and Os and Mg (1000) surfaces were analyzed as possible metal centers for CH_3Cl Hydrodechlorination. H and CH_3Cl adsorption was investigated as function of position, orientation and coverage. Although the hydrogen atoms change drastically their properties upon adsorption on the metallic surfaces none of them seems to affect the interaction with CH_3Cl. Thus, the co-adsorption of species seems the only viable option to carry the hydrodechlorination reaction.

This work was supported by Conacyt CB A1-S-15770-0096

Keywords: organochlorides; DFT; water treatments using hydrogen; hydrogen coverage effects

ID 059

Theoretical Aspects of Precursor Fibers to Activated Carbon Fibers to Store Hydrogen

Omar Rodríguez-Rivero[1], Fray de Landa Castillo-Alvarado[1], Teresa Ramírez-Rodríguez[2,*]

[1]Escuela Superior de Física y Matemáticas-Instituto Politécnico Nacional
[2]Escuela Superior de Ingeniería Textil-Instituto Politécnico Nacional
* Corresponding author: 43520891, teresa.ramirez7715@gmail.com

ABSTRACT

Among various precursors for producing carbon fibers, naturally occurring fibers such as lignocelluloses can adsorb hydrogen. In this study, we will focus on showing that cotton fibers that contain cellulose and lignin as main chemical compounds are a good precursor to obtain activated carbon fibers. Cotton cellulose is highly crystalline and oriented. For native crystalline cellulose (Cellulose I), this model assumes a monoclinic unit cell with space group P21 and two anti-parallel cellobiose chain segments occurring in opposite directions to along the fiber axis. Type II cellulose can be prepared by precipitating cellulose dissolved in an aqueous medium or also in mercerization. Preliminary work on moving type II cellulose, a two-cell unit cell; a = 8.14Å, b = 9.14Å, c = 10.3Å and γ = 62 °. Through molecular modeling and using the theory of the functional of the density based on local and semi-local approaches to the energy of electronic exchange-correlation (LDA and GGA) for which the Materials Studio software was used, taking as a point starting point that Generalized gradient approximations (GGA) seek to improve the precision of the local gyro density approximation (LSD) in electronic structure calculations and that, on the other hand, Perdew and Wang have developed a GGA based on the cut in space The actual long-range spurious components of the second-order gradient expansion for the exchange-correlation gap were chosen to perform these functional molecular modeling. The results of thermodynamic properties were obtained, which helped us to have an approximation of the behavior in the experimentation. The mercerization process is an important treatment given to the cotton fiber, which allows the alkali to penetrate not only in the amorphous regions but also in the crystalline regions, achieving that the structure is accompanied by loss of resistance between the cellulose chains resulting in temporary weakening while the fiber remains swollen, the flattened shape of the fiber changes its characteristics to a rounded shape.

According to the visual analysis of each temperature, the alkali concentration, the temperature and their interaction had a significant effect on the secondary cell wall of the cotton, this due to the oxidation effect.

Keywords: activated carbon fibers; cotton fibers; mercerized

ID 063

Comparision between principal parameters use in Dielectric Barrier Discharge Plasma for hydrogen production from hydrocarbons

Miguel Angel Segura[1], Martin Nieto Perez[2], Rosa de Guadalupe González Huerta[3*]

[1]Centro Mexicano para la Producción más Limpia, IPN, Av. Acueducto S/N, Ticoman, Gustavo A. Madero, 07340, México
[2]Centro de Investigación en Ciencia Aplicada y Tecnología Avanzada unidad Querétaro, IPN, Cerro Blanco 141, Colinas del Cimatario, 76090, México
[3]Escuela Superior de Ingeniería Química e Industrias Extractivas, IPN, Av. Luis Enrique Erro S/N, unidad profesional Adolfo Lopez Mateos, Zacatenco, Gustavo A. Madero, 07738, México
* Corresponding author: 442-487-8322, msegurar99@gmail.com

ABSTRACT

This brief review compare the different parameters use in dielectric barrier discharge plasma for hydrogen production from hydrocarbons. Dielectric barrier discharge is mainly the most used non-thermal plasma (NTP) for hydrocarbon reforming. Their low cost and continuous process arise as an advantage over other reforming methods. Plasma promotes the creation of exited species that could begin a variety of chemical processes.

This different chemical processes dependent upon operation parameters, feedstock, initial concentration, pressure, temperature, voltage, frequency, etc. Know how these parameters affect final output is very important. Although, optimize these parameters could lead us to higher purity and higher hydrogen yield.

NTP technique have encountered applications not only in hydrogen production, but also in destruction of organic volatile compounds (VOCs), recent work show how different hydrocarbon can be reform or destroyed, so is worthy study that too. Among these parameters four are compared: applied voltage, gas carrier, initial feedstock and number of reactors. Taking these parameters as benchmark different hydrogen yields are compared. This lead to reactor efficiency and destruction rates. Also, non-thermal plasma could be escalate for other applications. Not pretending been a exhaustive review, data taking from different scientific publications are compared. Finally, these work could be use as a starting point to a deeper study in hydrogen production with this technique, and the parameters, if found, could easily that can be taken to the laboratory.

Keywords: *Non-thermal plasma, plasma parameters, hydrocarbon reforming, hydrogen production.*

ID 065

Corrosion Process Analysis on Anode of Nickel-plated Stainless Steel

J. A. Melo-Máximo[1*], E. M. Arce-Estrada[1], R. G. González-Huerta[2]

[1]Instituto Politécnico Nacional ESIQIE, Dep. de Ingeniería en Metalurgia y Materiales, UPALM, CP. 07738, CDMX.

[2]Instituto Politécnico Nacional ESIQIE, Laboratorio de Electroquímica, UPALM CP. 07738, CDMX.

* 5531321110 - jorgemelomaximo@hotmail.com

ABSTRACT

Alkaline electrolysis provides a sustainable solution to produce hydrogen replacing or enrichment conventional energy production ways, for example, internal combustion engines, atmospheric burners, etc. Unfortunately, secondary water electrolysis reactions lead to the formation of undesirable compounds, such as iron or nickel oxides, as well as ions in solution, among which hexavalent chromium (Cr (VI)) stands out for its high degree of toxicity. Alkaline electrolysis involves a series of electrochemical reactions that are carried out in an aggressive medium, with highly alkaline pH conditions (> 12) and oxidation potentials (E > 1.5 V) that accelerate the degradation of the material.

In this study, is boarded the main fundaments of the alkaline electrolysis, just as the electrochemical reactions generated into the alkaline media. A method is proposed to reduce the generation of Cr (VI) through the application of Ni films of 10 um thick obtained by electrodeposition techniques. It is taking as evidence that Ni is an excellent material for its alkali resistance and electrocatalytic activity. Together with an austenitic steel-based system, the production of undesirable components in the system can be reduced or eliminated. in this step first, the characterization techniques used was cyclic voltammetry to detect Ni coating. As well as a microstructural test using Scanning Electron Microscopy (SEM) whit elemental analysis (EDS); before and after every electrochemical characterization to find the best structural characteristics of the coating. In the microstructural results, is observed that the coatings growth is in flakes form, and these form islands of around 10 um high and 2 um wide, they coalesce as the deposit grows. Furthermore, the results of the first electrochemical tests show the evolution of oxygen in the sample starting at 1.58V and there is the presence of Ni $(OH)_2$ at a potential of 1.4 V/RHE.

Keywords: Hydrogen; Electroplating; Stainless Steel; Nickel.

ID 066

Bioetanol steam reforming of Co-Ni/like-Hydrotalcites Catalysts to produce H_2

(The promoting effect of WOx and the long-term stability)

Jose L. Contreras [a*], Naomi N.González [a], Ricardo López M[a], Beatriz Zeifert[b], José Salmones[b], Tamara Vázquez[b], Gustavo A. Fuentes[c], Deyanira Angeles[a]

[a] Universidad Autónoma Metropolitana-Azcapotzalco, CBI-Energía, Ciudad de México, 02200, México.
[b] Instituto Politécnico Nacional, ESIQIE, UPALM, Zacatenco, Ciudad de México, 07738, México.
[c] Universidad Autónoma Metropolitana-Iztapalapa,CBI-IPH, Ciudad de México, 09340, México.
*Corresponding author: jlcl@correo.azc.uam.mx

ABSTRACT

For the production of H_2 by ethanol steam reforming (ESR), the calcined hydrotalcite-WOx-supported Ni-Co catalysts have been studied investigating the effect of the Ni / Co atomic ratio from 2.2 to 0.139 and the results were promising for the catalyst with ratio 2.2 in terms of selectivity to H_2. However, it was not known whether the addition of WOx to hydrotalcite could stabilize its structure thermally, preventing the reduction of the area of the support and of the Ni and Co crystallites and with it the deactivation by sintering. For this study, 6 catalysts were prepared varying the W concentration from 0.5wt% to 16wt%, maintaining the concentration of 10wt% Ni and 4.5wt% Co using the coprecipitation method. The ethanol conversion was total at 600 ° C and the selectivities were: 76% H_2, 21% CO_2, 1% CO, 2% CH_4, in N_2 stream using a H_2O / ethanol ratio 4 at atmospheric pressure.

Continuous evaluation showed that the catalyst with WOx was less deactivated than the catalyst without WOx. In our case we are still evaluating the catalysts in inert atmosphere or with a small amount of O_2 in the feed stream. Ni / Co catalysts showed carbon (coke) levels less than 4.9wt% for a 1440 min evaluation. By XRD the chemical species observed were: periclase MgO, alumina Al_2O_3, spinels of Co, Co_2O_3, bunsenite NiO, spinels of $MgAl_2O_4$. When we calcined the sample with 16 wt%W up to 800°C we observed a total transformation of the previous species by others with greater crystallinity. The graph of BET area versus W concentration (WOx) showed that effectively at low W contents (0.1 to 1wt%) the catalyst area was greater for the samples with W than the area for the sample without W at 450, 600 and 800 ° C.

Keywords: Ni-Co-Hydrotalcite-WOx ; catalysts, ESR of Ethanol, H_2 production.

ID 068

Graphene and graphene-N-doped for hydrogen storage, a DFT study

C. F. Trejo-Beltrán [1], G. Ramírez-Dámaso[1*], J. Roberge[1], E. Rojas-Hernández[1], O. Ramírez-Rodríguez[1], O. K. Díaz-Mejía[1] and M. R. Lorenzana-Jiménez[1].

[1] Escuela Superior de Ingeniería y Arquitectura Unidad Ticomán del Instituto Politécnico Nacional, Av. Ticomán No. 600, Col. San José Ticomán, C. P. 07340, Alcaldía Gustavo A. Madero, CDMX, México.

* Corresponding author: 5537013733, gramirezdpn.mx

ABSTRACT

The study of new materials and its applications in the generation of clean energies is one of the most important topic of science and technology. In particular the use of hydrogen, as a source of energy, needs solve the problem of hydrogen storage, because hydrogen is the lightest gas, whose transport in gaseous state present several problems. In this work we use the unit cell of crystal structure of graphite in order to build a 5x5 supercell of graphene, with 50 C atoms, and with the objective of study his capability of trapping hydrogen molecules on his surface. Also we doped with nitrogen atoms at different positions of graphene sheet. We allow hydrogen molecules to interact over the surface of graphene and near the region were is placed nitrogen atom. We use Castep of the molecular simulation program Materials Studio, to optimize the geometry of these crystal structures and we obtain his state of minimum energy. We report the variation in the geometry of the hexagons that form graphene, we compare the changes in the values of their enthalpies with and without hydrogen molecules and present their Raman spectrum.

Keywords: graphene; graphene doped with nitrogen; hydrogen storage; DFT study.

ID 071

The feasibility of seasonal hydrogen energy storage in a stand-alone solar system

Jorge Olmedo-González[1]*, Guadalupe Ramos-Sánchez[2], Rosa de Guadalupe González-Huerta[1]

[1]Instituto Politécnico Nacional-ESIQIE, Electrochemistry Research Lab, UPALM, 07738, Mexico City
[2]Universidad Autónoma Metropolitana- Iztapalapa, Chemistry Department, 09340, Mexico City
* Corresponding author: 5527092864 and jorgeolmedog@outlook.com

---

ABSTRACT

Energy storage technologies (EST) have a crucial role in variable renewable energies, due to their natural intermittence or irregularity, therefore it is necessary to control in indirect way electrical energy production. EST selection is mainly based on opting for the technology with the best capacity to compensate the fluctuations of the renewable energy, where parameters such as response time, storage duration and power rating are considered. Batteries have been the best option in stand-alone power systems due to these systems are focused on compensating daily fluctuations where the renewable system is dimensioned with respect to seasonal insolation minimums. However, seasonal fluctuations are not regulated, which results in energy losses.

In this work is studied the feasibility of seasonal hydrogen energy storage in a stand-alone solar system, where is analyzed 1-year insolation data in México City and the consumption profile is considered constant in all days. The results indicate that months with higher insolation 12% to 40% solar energy can be lost and can be achieved 25% annual loses, where the 84% of the days exceed the average minimum insolation. Considering a hydrogen system efficiency of 45%, it is possible to reduce photovoltaic system installed power by up to 21.5%. The feasibility of storing 25% of losses will depend on the power capacity of the system and the hydrogen storage technology. On the other hand, in small systems the installed power reduction obtained may not be relevant and profitable.

Keywords: Seasonal energy storage, Hydrogen energy, Stand-alone power system, Solar energy

ID 075

Electrocatalytic materials for electrolysis in acid medium

A.M Fernandez[*,1] and J. Gutierrez-Castañeda[1].

[1]Instituto de Energias Renovables, Universidad Nacional Autonoma de Mexico,

Av. Xochicalco s/n, Col Ruben Jaramillo, 62580, Temixco, Mor. Mexico

* Corresponding author: afm@ier.unam.mx

ABSTRACT

The accelerated consumption of fossil fuels and their high greenhouse gases emissions have motivated the investigation of alternative fuels. Renewable energy has proven to be a promising option to replace fossil fuels since it is environmentally friendly and sustainable, and its sources such as solar, wind, maritime and geothermal energy are abundant on earth [1].

Hydrogen is often considered the best media for storing energy that comes from renewable and intermittent energy sources. With the increasing capacity of renewable energies that reach gigawatts, a storage system of equal magnitude is required. However, due to the low demand for electrolytic hydrogen in the last century, research on membrane water electrolysis (PEM) has been neglected [2].

The catalysts for the hydrogen evolution reaction are necessary for a hydrogen economy to be sustained since they are the best proposal to replace fossil fuels, in this work three Pt, Ru and Ir alloys were synthesized for use as catalysts in The production of hydrogen by electrolysis in an acid medium, the samples were characterized physicochemical and it was found that the best proportion of these metals is $Pt_{2.5}Ru_{0.5}Ir_{4.5}$ which presented characteristic kinetic parameters of Platinum without being pure Platinum, physical tests such as EDS and X-rays showed the appearance of the Ir-Pt phase and presence of very discrete ruthenium.

It is important to mention that water electrolysis has been recognized as the only current practical method for the production of hydrogen from renewable energy sources [3].

Keywords: water electrolysis, electrocatalitic materials, PEM-Electrolyzer component

ID 076

ADSORBED METHANE MOLECULES AS A PART OF AN SMART GATING SYSTEM.

J. Galicia[1], A. A. Lemus-Santana[1], B. Portales-Martínez[1], F. Echevarría[1], N. Torres[1], E. A. Juárez-Arellano[2], E. Reguera[1,*].

[1]Centro de Investigación en Ciencia Aplicada y Tecnología Avanzada (CICATA), Instituto Politécnico Nacional, Calzada Legaria No. 694, Col, Irrigación, Del. Miguel Hidalgo, Ciudad de México, C. P. 11500, México.

[2]Universidad del Papaloapan, Circuito Central 200, Parque Industrial, Tuxtepec, C. P. 68301, México.

* Corresponding author: 5511959921 and edilso.reguera@gmail.com

---

ABSTRACT

This contribution reports the preparation of a composite material formed by functionalized single walled carbon nanotubes (SWCNT) and Zn(II) methylimidazolate (ZIF-8). When characterized by nitrogen isotherms, these new system mimics parent SWCNT isothermal curve, but with a notorious increment of adsorbed amount of N_2. The observed increased of storage capacity and the adsorption enthalpy suggest that, upon the composite formation a new system of pores results. When tested for methane storage application, the recorded CH_4 isotherms show pronounced kinetic effects that progressively decrease on repeated cycles of adsorption- desorption. Evaluation suggests that the guest molecules became part of the system and simplify the pass of CH_4 through the channels and pores. Facilitated transport of methane molecules could be explained by the rotation of the methyl group (Gate Opening phenom) at the access window of the ZIF-8 framework pores when a small number of methane molecules are confined within the composite material.

Keywords: Composite Materials; SWCNT; ZIF-8; CH_4 Storage; Adsorption Isotherms, Molecular Gating System.

ID 077

Comparison between post-combustion carbon capture technology and the use of blue and green hydrogen in natural gas combined cycles as CO_2 mitigation strategies: a study under the context of Mexico's clean energy market

Pablo Rene Díaz-Herrera[1*], Gabriel Ascanio[2], Agustín M. Alcaraz-Calderón[3], Ascención Romero-Martínez[4]

[1] Facultad de Ingeniería, Universidad Nacional Autónoma de México (UNAM), 04510, México City, Mexico.
[2] Instituto de Ciencias Aplicadas y Tecnología, Universidad Nacional Autónoma de Mexico (UNAM), 04510, Mexico City, Mexico.
[3] Instituto Nacional de Electricidad y Energías Limpias, Reforma 113, 62490, Cuernavaca, Morelos, Mexico.
[4] Instituto Mexicano del Petróleo, Dirección de Investigación en Exploración y Producción, Gerencia de Herramientas para Pozos e Instalaciones. Eje Central Lázaro Cárdenas 152, 07730, Mexico City, México.
* Corresponding author: 7771862239, pablor.diazh@gmail.com

ABSTRACT

This work aims to compare three strategies for reducing CO2 emissions from natural gas combined cycles (NGCC): a) NGCC with post-combustion carbon capture (PCC) plant; b) NGCC operating with blue hydrogen (bH2) produced via SMR plus carbon capture, utilization and storage (CCUS) project; c) NGCC operating with a blend of green hydrogen (gH2) and natural gas. These mitigation strategies were analyzed from the point of view of energy producers under the context of Mexico's clean energy market. Sensitivity analysis has been carried out varying fuel and clean energy certificate (CEC) prices. Results show that to meet the carbon emission factor mandatory by the law, fuels with high H2 content are required. In general, the incorporation of a PCC plant offers better economic performance than the other carbon mitigation alternatives studied. Although gH2, at current fuel prices, utilization in NGCC is more expensive than installing a PCC facility, it can be competitive in a scenario of high prices of imported natural gas ($9/MMBTU) and very low renewable electricity prices ($20/MWh).

Keywords: green hydrogen, blue hydrogen, carbon capture, hydrogen-powered gas turbines.

ID 078

Layered Double Hydroxides as an electrocatalyst for oxygen production in alkaline media

Miguel Oliver-Tolentino[1*], Ariel Guzmán-Vargas[2], Enrique Lima[3], María De J. Martínez-Ortiz[2]

[1] CONACYT – Universidad Autónoma Metropolitana – Iztapalapa, 09340 Ciudad de México, Mexico.
[2]Instituto Politécnico Nacional, ESIQIE-SEPI-DIQI, Laboratorio de Investigación en Materiales Porosos, catálisis Ambiental y Química Fina, UPALM, Zacatenco, GAM, 07738, CDMX, México.
[3]Instituto de Investigaciones en Materiales, Universidad Nacional Autónoma de México, Circuito Exterior s/n Ciudad Uiversitaria, Coyoacán, México, DF 04510, Mexico
* Corresponding author: miguel.oliver@conacyt.mx

ABSTRACT

Water splitting represents an attractive option for chemical energy storage. In this process, oxygen evolution reaction is the limiting step because it has slow kinetics related to its multistep proton-coupled electron transfer phenomenon. Therefore, development of alternative catalysts appropriate for large-scale application and high efficiency in water splitting is attractive area of research and innovation. In particular, oxides containing 3d transition metals, among them Ni, Co and Fe have been used as electrocatalyst on OER in alkaline media. In this context, layered mixed hydroxides commonly called layered double hydroxides (LDHs) or hydrotalcite-like materials (HTs) containing 3d metals are the most promising candidates as OER electrocatalysts, and their performance is mainly related to important surface area and large availability of M–OH groups.

In this work, different LDH are synthesized by co-precipitation method, using 3d metal (Mn, Ni, Fe, Co); the electrocatalytic activity is related with the electronic properties, basicity and acidity on the surface, and cation distribution on the layer. Also, the incorporation of Flourine in the layer was evaluated. The oxygen evolution capacity and stability indicate that these materials are a promising electrocatalyst for water splitting.

Keywords: component; formatting; style; styling

ID 082

Study on redox properties of the NiO-CeO_2/Al_2O_3 catalytic system by X-ray photoelectronic spectroscopy (XPS)

Josué Yamin Sánchez Sánchez[1], Ignacio René Galindo Esquivel[1,*], Hugo Pérez Pastenes[2], Sara Núñez Correa[2]

[1]Departamento de Ingeniería Química, Universidad de Guanajuato, Noria Alta s/n Guanajuato, Gto., 36050, México

[2]Facultad de Ciencias Químicas, Universidad Veracruzana, Av. Universidad s/n Coatzacoalcos, Ver., 96539, México

* igalindo@ugto.mx

ABSTRACT

The surface physicochemical properties play an important role in the development of catalysts. Knowing the chemical composition, electronic structure, as well as the metal-support interactions help determine the activity and selectivity of the catalyst. In this study, the surface properties were analyzed by x-ray photoelectron spectroscopy (XPS) of the NiO-CeO_2/Al_2O_3 catalytic system synthesized by the sol-gel method. First, nickel catalysts supported on alumina were characterized with variations of 10 and 30% by weight of nickel, observing the presence of both hydroxides and oxides corresponding to Ni^{2+} oxidation states, as well as certain proportions of non-stoichiometric nickel (N^{3+}). Subsequently, a CeO_2/Al_2O_3 catalyst was analyzed under conditions without and with reduction, demonstrating the presence of different oxidation states in the Cerium spectra (Ce^{3+} and Ce^{4+}). Finally, the NiO-CeO_2/Al_2O_3 catalytic system was characterized, handling percentage variations of 3, 5, 6 by weight of nickel and cerium. The deconvolved peaks demonstrate the presence of the different expected oxides (NiO, CeO_2 and Al_2O_3). At the same time, the analysis of the binding energies of the different peaks obtained indicate the intervention of solid solutions (Ni-O-Ce) caused by the different interactions of electronegativity and oxidation states that promote the formation of vacancies in the crystalline structures, promoting the formation of new species observed in deconvolved spectra such as $NiAl_2O_4$, $Ni(OH)_2$, $CeAlO_4$. The metal-support interactions cause the formation of intermediate compounds which can affect the physicochemical properties of our catalyst, resulting in a benefit to be subjected to different processes such as dehydrogenation, oxidation, reforming, among others.

Keywords: XPS; Superficial analysis; Solid solutions; Catalysis

ID 084

Effect of Piranha solution as oxidant in graphene oxide synthesis and in its behavior as photocatalyst for the hydrogen evolution

B. C. Hernández-Majalca, J. L. Dominguez-Arvizu, J. Jiménez-Miramontes, J. C. Pantoja-Espinoza, M.J. Melendez-Zaragoza, J.M. Salinas-Gutiérrez, A. López-Ortiz, V. Collins-Martínez*.

Departamento de Ingeniería y Química de Materiales, Centro de Investigación en Materiales Avanzados, S.C.,

Miguel de Cervantes 120, Chihuahua, Chih., 31136, México.

* Corresponding author: virginia.collins@cimav.edu.mx

ABSTRACT

Due to the two-dimensional nature of GO, a small superposition of the conduction and valence bands, can be presented in this material, which is responsible for its semimetal character, compared to a semiconductor whose bands must be separated. Depending on the GO oxidation level, the value of this separation, known as bandgap energy, can vary from 0 to 3.7 eV. The main aim of this study is to propose a fast and simple synthesis method for GO, which present self-tuning optoelectronic properties, advantageous features, for their application towards the photocatalytic hydrogen production. Graphene oxides (GO) were prepared through a modification of the Tour method from graphite powder by applying a microwave pretreatment. One GO sample was obtained by the oxidation using a mixture of H_2SO_4 and H_3PO_4 as main oxidants (T-GO). Another GO sample (P-GO) was oxidized employing a Piranha solution (H_2SO_4/H_2O_2). The study of morphology, crystalline structure, size, surface area and optical characterization of the material was carried out by SEM, XRD, TEM, BET and UV-Vis spectroscopy, respectively. Photocatalytic activity evaluation of the GOs towards hydrogen production through the water splitting reaction under visible light was followed by gas chromatography. Results indicate sample P-GO achieved a production of 8000 nmolH_2/g, while T-GO presented a negligible photocatalytic activity, under the same time and irradiation conditions. The difference of photocatalytic activity between these two GOs can be explained in terms of the oxidation degree of each material, so that the piranha solution was able to intercalate molecular oxygen allowing a controlled oxidation of graphite particles assisted by microwave heating.

Keywords: Piranha solution; Water splitting; Graphene oxide; Hydrogen production

ID 085

Synthesis, Characterization and Photocatalytic Evaluation of g-C_3N_4/Ag/Zn_2TiO_4 Heterojunction for the Hydrogen Production under Visible Light

J. C. Pantoja-Espinoza, J. L. Domínguez-Arvizu, J. A. Jimenez-Miramontes, B. C. Hernández-Majalca, M. J. Meléndez-Zaragoza, J. M. Salinas-Gutiérrez, A. López-Ortiz, V. H. Collins-Martínez*

Departamento de Ingeniería y Química de Materiales, Centro de Investigación en Materiales Avanzados, S.C., Miguel de Cervantes 120, Chihuahua, Chih., 31136, México.

* Corresponding author: virginia.collins@cimav.edu.mx

ABSTRACT

In recent years, the exploration of clean energy has been growing due to the increase of industrial development. Current research for the production of hydrogen through photocatalysis aims to take advantage of the use of solar energy. Although this photocatalytic process has already been reported in the literature one remaining challenge is to find highly efficient photocatalysts to make it economically viable for larger scale hydrogen production. The objective of the present study is to synthesize, characterize and photocatalytically evaluate the g-C_3N_4/Ag/Zn_2TiO_4 heterojunction towards the hydrogen production under visible light. In order to prepare the hetero-linked photocatalyst, individual materials were first synthesized. g-C_3N_4 was obtained by urea pyrolysis at 325 °C during 1 hour followed by an additional 1 hour at 450 °C under air and nitrogen atmospheres, respectively. Zn_2TiO_4 powders were prepared by the modified Pechini method obtaining the crystal structure by calcination at 450 and 550 ° C for 2 and 1 hours, respectively. Ag/Zn_2TiO_4 and g-C_3N_4/Ag/Zn_2TiO_4 materials were prepared by photo-anchoring and impregnation, respectively. TGA was used to obtain urea pyrolysis and Zn_2TiO_4 calcination temperatures. Characterization of the materials was carried out using XRD, FT-IR, UV-Vis, BET and SEM, for the study of crystallinity, spectroscopic analysis, specific surface area and morphology, respectively. Photocatalytic evaluation of the materials was performed using triethanolamine as a sacrificial agent in aqueous solution employing a batch reactor irradiated with visible light. Results indicate that the greatest hydrogen production was achieved by g-C_3N_4/Ag/Zn_2TiO_4 heterojunction with 848 mmol $H_2/h \cdot g_{cat}$ after 8 h. This heterojunction was composed of 20% g-C_3N_4 and 80% of Ag/Zn_2TiO_4 and 1% Ag. This heterojunction can be considered as a high potential photocatalyst in the field of green hydrogen production.

Keywords: hydrogen production, photocatalysis, heterojunction, g-C_3N_4.

ID 086

Study of synthesis temperature effect on the photocatalytic properties of $MnCo_2O_4$ spinel towards the production of hydrogen by water splitting under visible light

J. A. Jiménez-Miramontes, J. L. Domínguez-Arvizu, B. C. Hernández-Majalca, J. C. Pantoja-Espinoza, J. M. Meléndez-Zaragoza, J. M. Salinas-Gutiérrez, A. López-Ortiz, V. Collins-Martínez*

Departamento de Ingeniería y Química de Materiales, Centro de Investigación en Materiales Avanzados, S.C., Miguel de Cervantes 120, Chihuahua, Chih., 31136, México

* Corresponding author: virginia.collins@cimav.edu.mx

ABSTRACT

Hydrogen generation through the photocatalytic separation of the water molecule has become a promising energy alternative with greater attention in recent years. One of the main reasons of this is due to the possibility of using sunlight as an energy source to carry out this process. However, this reaction is not thermodynamically feasible to proceed. Since, semiconductors with suitable optical properties to provide an overpotential of 1.23 eV to dissociate the water molecule are needed. For this reason, the search for materials that are photoactive under visible light, inexpensive, eco-friendly and having a band gap energy to overcome the water dissociation potential is essential. In this work, the calcination temperature effect on the photocatalytic performance of $MnCo_2O_4$ (MCO) was carried out, since the metallic cobaltite system theoretically presents adequate optical properties to be used in this type of process, while the information of these type of materials for this application is scarce. Cobaltites were synthesized by the Pechini method at temperatures of 350, 600, 900°C by four hours to obtain three MCO samples. Characterization of these materials consisted in X-Ray Diffraction (XRD), BET surface area by N_2 physisorption, Scanning Electron Microscopy (SEM) and UV-Vis spectroscopy. The diffractograms indicate the presence of $MnCo_2O_4$ in pure phase, with an increased crystallinity as temperature was raised. However, BET areas exhibited the opposite behavior, decreasing from 84 m^2/g to 1 m^2/g. Morphology of the obtained particles changed from irregular polygons to sintered polygons along with increasing temperature, with sizes ranging from ~50 nm to ~500 nm due to sintering. These MCOs presented a band gap of ~1.3 eV. The photocatalytic evaluation was performed by monitoring the hydrogen evolution by gas chromatography. MCO at 900°C presented the best photocatalytic performance achieving a production of 1152 nmol $H_2/g{\cdot}h$.

Keywords: water splitting; Spinel; Manganese cobaltite; hydrogen production.

ID 087

$CoFe_2O_4/Cu_2O$ heterojunction study as photocatalyst for visible light hydrogen production

J. L. Domínguez-Arvizu, J. A. Jiménez-Miramontes, B. C. Hernández-Majalca, J. C. Pantoja-Espinoza, J. M. Meléndez-Zaragoza, J. M. Salinas-Gutiérrez, A. López-Ortiz, V. Collins-Martínez*

Departamento de Ingeniería y Química de Materiales, Centro de Investigación en Materiales Avanzados, S.C., Miguel de Cervantes 120, Chihuahua, Chih., 31136, Mexico

* Corresponding author: virginia.collins@cimav.edu.mx

ABSTRACT

In recent years, research related to visible light-driven photocatalysts has attracted a lot of attention towards hydrogen production using solar energy. However, single phase photocatalysts studies have suggested that their optoelectronic properties can be improved by means of heterojunction generation with other semiconductors, turning this into a higher visible light absorption and quantum yield bringing a superior hydrogen production. In this research we study the $CoFe_2O_4/Cu_2O$ heterojunction by comparing their photocatalytic activity with the individual materials synthesized by Pechini´s method and Benedict reaction respectively. Hydrogen content was measured by gas chromatography observing a significant ten times higher activity in heterojunction than the individual oxides. Synthesized materials were characterized through XRD, SEM, TGA, UV-Vis and BET surface area techniques whilst their electrochemical properties by means of cyclic voltammetry and electrochemical impedance spectroscopy were employed to elaborate the Mott-Schottky plots and calculate band gap edge positions of individual materials.

Keywords: Hydrogen production, photocatalysis, heterojunctions, visible light photocatalyst

ID 091

Photocatalytic H_2 production using exfoliated Cd-$ZnS(EN)_{0.5}$ hybrid sheets

D. Ramírez-Ortega[1], A.B. Ramos[1], A. Hernández-Gordillo[1]*, R. Zanella[2] and S.E. Rodil[1]

[1]Instituto de Investigaciones en Materiales, Universidad Nacional Autónoma de México. Circuito Exterior SN, Ciudad Universitaria, C.P. 04510, México D.F., Coyoacán, México.
[2]Instituto de Ciencia Aplicadas y Tecnología, Universidad Nacional Autónoma de México. Circuito Exterior SN, Ciudad Universitaria, C.P. 04510, Mexico City, México.
* agileohg@iim.unam.mx.

ABSTRACT

Solar-driven photocatalytic water splitting is one of the most promising processes to address the severe situation of global energy supply and associated environmental issues because it converts the abundant solar energy into hydrogen-fuel from the water by using semiconductor systems as photocatalysts. For this purpose ultrathin sheets of $ZnS(EN)_{0.5}$ hybrid and the one modified with Cd^{2+} ions were exfoliated "*in situ*" during the photocatalytic test in H_2 production. The samples were prepared by chemical precipitation in a mixture of butanol-ethylenediamine-water solution, varying the Cd^{2+} contents of 0.1 to 0.6 molar ratio. The formation of Cd-$ZnS(EN)_{0.5}$ hybrid compounds and its physicochemical properties were investigated by diverse techniques: X-ray Diffraction, Thermogravimetric, Textural analysis, Infrared, Diffuse Reflectance and X-ray Photoelectron Spectroscopies, Scanning Electron and High-Resolution Transmission Electron Microscopy. The photocatalytic test showed that the unmodified $ZnS(EN)_{0.5}$ hybrid presented high H_2 production rate (23 molh^{-1}) when methanol was used as sacrificial electron donors reagents (SEDr). The results showed that the orthorhombic $ZnS(EN)_{0.5}$ structure was stable at 6 cycles of reaction but suffer exfoliation of the lamellar structure during the photocatalytic cycles in methanol- water solution under UV irradiation. The doped Cd-$ZnS(EN)_{0.5}$ hybrid presented an enhanced H_2 production rate (32 µmolh^{1}) for low Cd^{2+} doping, showing minor exfoliation of the lamellar structure, preserving the high photoactivity after 6 cycles of irradiation. The degree of exfoliation contributed to increasing the surface area and shorten the distance from the interior toward the crystal hybrid composite surface, which promoted the charge separation and improved the photocatalytic activity.

This work was supported by CONACYT-Fronteras 1740 and CONACYT Research Fellow /1169 project.

Keywords: H2 evolution; sheets ZnS, doped Cd ions, exfoliation process.

Fuel Cells components and stacks

ID 001

Improved preparation of membrane-electrode assembly for PEM electrolysis through automatic catalytic ink application system

A. Martínez-Septimo[1,2], M. A. Valenzuela-Zapata[2], R. G. González-Huerta[3]*

[1]Instituto Politécnico Nacional-ESIQIE, Lab. Catálisis y Materiales, Zacatenco, C.P. 07738, CDMX, México
[2]Instituto Politecnico Nacional ESIQIE, Laboratorio de Electroquímica, UPALM, C.P. 07738, CDMX, México
*Corresponding author: rosgonzalez_h@yahoo.com.mx

ABSTRACT

Currently, hydrogen has been proposed as a viable energy vector. One of the most efficient and cleanest method for the hydrogen production is proton exchange membrane water electrolysis (PEMWE) [1]. Therefore, the efficiency and stability in PEMWE has to be improved based on the design of gas diffusion layer, bipolar plates and membrane-electrodes assembly (MEA). For this propose, a MEA was made through an innovate method based in an automatic catalytic ink application system additionally, a new PEMWE was designed and made in-home. The new PEMWE designed, was integrated with the improved MEA, which was feed with deionized water (≥18 MΩcm) @25°C and tested using a DC power source. The experiments were recorded in the current range from 0.1 to 0.6 A cm^{-2} at 300 s. At the same current density (0.2 A cm^{-2}) the potential of the new PEMWE design with the improved MEA was lower (3 V) than the potential measured in a older made in-home design (5 V) with a MEA made through a manual spraying catalytic ink application. These better results are attributed to an improvement in water distribution into gas diffuser (porous titanium) and a better dispersion and adhesion of the catalytic layer on the membrane.

Keywords: PEM water electrolysis; Supported catalyst; TiO_2; Ir-Ru based anode; iridium oxide; ruthenium oxide.

ID 011

Analysis of ordered and disordered conductive phases in a PEMFC synthetic catalyst layer

C.Pacheco[1], B. Escobar[1, *], A. Rodriguez[2], R. Barbosa[2, *]

[1] Centro de Investigación Científica de Yucatán, A.C. Carretera Sierra Papacal Chuburna Puerto Km 5, C.P. 97302, Sierra Papacal, Yucatán, México.

[2]Universidad de Quintana Roo, Boulevard Bahía s/n, C.P 77019, Chetumal, Q. Roo, México.

* Tel: +52 9999300205; e-mail: beatriz.escobar@cicy.mx

* Tel: +52 9831566032; e-mail: romelix1@gmail.com

ABSTRACT

The current research analyzes the behavior of effective transport coefficient (ETC) through the disorder process of real and simulated micrographs of a polymeric electrolyte fuel cell (PEFC) electrode. The suggested methodology examines an ordered bar system that evolves into a heterogeneous stochastic system, which uses simulated images generated by computational algorithms and experimental images from the scanning electron microscope (SEM). The behavior of the electrode microstructure was studied through images with different surface fractions of the conductive phase. Microstructural variation is imposed by statistical moments of reconstruction by simulated annealing (SA). The ETC was determined numerically by the finite volume method (FVM) and generalized by a conduction efficiency (ek). The case studies showed that the microstructure ordered in bars has a load transport equal to the surface fraction of the study phase, and through the disorder process, the value of ek (%) decreases until it reaches a stable value of ek (%). For example, for the 70% surface fraction, the initial ek is 70.55 ± 0.05%, after 100 iterations of the disorder process the new ek is 21.28 ± 0.26%, and after 1000 iterations, the value of ek gets steady at 20.56% with a standard deviation of 0.20%. The trend of the ek results was similar in systems with different surface fractions. Then, our research proposes an innovative methodology, as a design tool, to improve the load transport in fuel cell electrodes.

Keywords: Effective transport coefficient; PEFC; Aligned composites; Catalyst layer

ID 012

Nitrogen and Sulphur co-doped Ordered Mesoporous Carbon Hollow Spheres with High Catalytic Activity and Exceptional Electrochemical Stability for the Oxygen Reduction Reaction

J.C. Carrillo-Rodriguez[1], B. Escobar-Morеales[2], A.M. Garay-Tapia[3], F.J. Rodríguez-Varela[1] and I.L. Alonso-Lemus[4*]

[1]Sustentabilidad de los Recursos Naturales y Energía, Cinvestav Unidad Saltillo, Av. Industria Metalúrgica, 1062, C.P. 25900, Ramos Arizpe, Coahuila, México

[2]CONACYT, Centro de Investigación Científica de Yucatán, Calle 43 No. 130, Col. Chuburná de Hidalgo, Mérida, Yucatán, C.P. 97200, México

[3]Centro de Investigación en Materiales Avanzados S.C., Unidad Monterrey, Alianza Norte 202, Autopista Monterrey-Aeropuerto km 10, Parque PIIT, Apodaca, Nuevo León, C.P. 66628, México

[4]CONACYT, Cinvestav Unidad Saltillo, Sustentabilidad de los Recursos Naturales y Energía, México

* Corresponding author: phone +52-01-844-4389626, e-mail: ivalemus@gmail.com

---

ABSTRACT

In this work, Novel Nitrogen and Sulphur co-doped Ordered Mesoporous Carbon Hollow Spheres (N-S-OMCHS) has been synthetized by the hard-template method, using resorcinol and formaldehyde as carbon source, while 2-pyridinecarboxialdehyde and 2-thiophenemethanol has been used as nitrogen and sulphur sources, respectively. A non-doped Ordered Mesoporous Carbon Hollow Spheres (OMCHS) has also been synthetized for comparation purposes.

The morphology of N-S-OMCHS has been analyzed in a Transmission Electron Microscope (TEM), resulting in a highly rough irregular hollow spheres, while the elemental mapping shows the well-dispersed nitrogen and sulphur on the shell of the spheres. Characterization by X-Ray Photoelectron Spectroscopy (XPS) shows the formation of N-pyridinic and N-quaternary nitrogen species and thiophene sulphur species.The catalytic activity of the electrocatalysts for the ORR have been evaluated by the Rotating-Ring Disk Electrode (RRDE) technique. N-S-OMCHS shows a higher performance than non-doped OMCHS, with an onset potential (E_{Onset}) of 0.88 V, half-wave potential (E½) of 0.78 V and a current density (j) of -0.73 mA cm^{-2} at 0.8 V (all potentials vs. RHE). Moreover, the electron transfer number denotes a four-electron pathway (n=3.96), while the H_2O_2 yield ($\%H_2O_2$= 1.2) is lower than non-doped OMCHS. Nevertheless, after accelerated degradation tests (3000 cycles, between 0.6 and 1.0 V), N-S-OMCHS shows a high stability and improvement in catalytic activity compared to OMCHS and Pt/C, with E_{Onset}= 0.88 V, E½= 0.78 V and j= -0.60 mA cm^{-2} at 0.8 V. Moreover n= 3.99 and $\%H_2O_2$ = 0.5. The catalytic activity and the electrochemical stability for the ORR of N-S-OMCHS electrocatalyst indicates that it is a potential candidate for Anion Exchange Membrane Fuel Cells (AEMFC) cathode applications.

Keywords: Ordered Mesoporous Carbon Hollow Spheres; co-doping; Oxygen Reduction Reaction; electrocatalysts

ID 017

Diagnosis and evaluation of an open cathode fuel cell stack

O. Aguayo[1], C. Pacheco[1], B. Escobar[1], J. Hernández[2], R. Barbosa[2,*]

[1] Centro de Investigación Científica de Yucatán, Calle 43 No 130, Col. Chuburná de Hidalgo, C.P.97200, Mérida, Yucatán, México.

[2] Universidad de Quintana Roo, Boulevard Bahía s/n esq. Ignacio Comonfort Col. Del Bosque. C.P. 77019 Chetumal, Quintana Roo, México.

* romelix1@gmail.com

ABSTRACT

Increasing demand for portability and mobility of electronic devices arises to develop smaller and lighter portable electronic devices, which involves meeting the power requirements of these devices. Over time, devices have decreased in size, but their demand for power increases day by day. One of the most available technologies that represent significant potential and lower environmental impact is fuel cells, which use hydrogen as an energy vector, and they are considered an efficient and clean source of energy. The objective of this work is to develop an open cathode PEM fuel cell (OC-PEMFC) for portable applications, as well as its diagnosis and evaluation in real operation. The manufacturing process consisted of depositing the components in layers: 1) endplate, 2) flow channel with gas diffuser layer, 3) silicone seals, 4) MEA, 5) gas diffusion layer. The OC-PEMFC operating conditions were ambient temperature and relatively low hydrogen pressure, to achieve maximum power with minimum size and weight. The characterization of the electrical response in steady-state and dynamic was performed using electrochemical polarization curves and as chronoamperometry. A more compact device (5.43 mm per cell) and lighter compared to conventional designs were obtained. The best electrical performance was achieved with the conditions of forced convection and hydrogen flow of 0.03 L min^{-1}, obtaining at maximum power (575 mW), a current of 586 mA, the potential of the stack was 0.98 V, and its efficiency 26.83%. These results indicate that the proposed design is promising for portable applications and represents an essential step for future OC-PEMFC developments.

Keywords: fuel cell; open cathode; stack; hydrogen.

ID 019

Influence of sulfonation time on thermal properties and solubility of poly (styrene-co-butyl acrylate) membranes

L. Francisco-Vieira, L. Da Silva, D. Morales-Acosta*, R. Benavides*

Centro de Investigación de Química Aplicada, Blvd Enrique Reyna No. 140, Col. San José de los Cerritos, 25290. Saltillo, Coahuila, México

*Tel: +52844-4389830 E-mail: roberto.benavides@ciqa.edu.mx; diana.morales@ciqa.edu.mx

---

ABSTRACT

Sulfonation is a powerful strategy for the modification of hydrocarbon polymers used for the preparation of membranes for fuel cell technologies and involves the substitution of hydrogen atoms (H) by sulfonic acid (-SO_3H) groups in the polymer chain, enabling its ion exchange capacity (IEC). The sulfonation degree (DS) can be controlled through time and temperature during the reaction with different sulfonation agents. In this context, the sulfonation of poly (styrene – co – butyl acrylate) (StBuA) was carried out with sulfuric acid at a molar ratio of 150% relative to the theoretical molar amount of benzene rings and a temperature of 40 ºC. Reaction times of 2, 3, 4 and 5h were tested and even longer periods of 7, 9 and 12h were also evaluated. The sulfonated copolymers were dissolved in polar aprotic solvents and membranes prepared by casting and differences followed by characterization techniques as FTIR and TGA. It was observed, through FTIR, that as the reaction time increases, a widening of the absorption bands characteristic of the SO_3H groups occurs. Thermal gravimetric analysis (TGA) confirmed the successful sulfonation through the weight loss due to sulfonic groups, as well as a good thermal stability over 380 °C for the longest reaction time of 12h. sStBuA membranes exhibited color changes through the sulfonation time, starting with yellowness and ending with brownish for 12h.

Keywords: membranes; styrene-co-butyl acrylate; sulfonated copolymers; fuel cells.

ID 024

Study of the integration of a System PEMFC (580W) – Charger – Li-Ion Battery Module for an Electric Vehicle

J.L. Díaz-Bernabé[1], A. Rodríguez-Castellanos[1], S. Citalán-Cigarroa[1], O. Solorza-Feria[1*]

[1] Departamento de Química, Centro de Investigación y de Estudios Avanzados del IPN, Av. Instituto Politécnico Nacional No. 2508, Sn. Pedro Zacatenco, Ciudad de México, México.

* Corresponding author: osolorza@cinvestav.mx

ABSTRACT

In this communication the behavior of an integrated system consisting of 580W Proton Exchange Membrane Fuel Cell (PEMFC) stack - battery charger - Li-Ion battery module, for its use in a hybrid electric vehicle will be presented. A Buck-Boost converter was designed to regulate the current and voltage of the battery module in Charging-Mode. The ideal behavior of the whole system is estimated by modeling the main components and the responses of PEMFC stack, charger, and battery module are followed by means of simulation results, performed in SPICE. Results show that the PEMFC device is sensitive to changes of the load requirements (battery charging-current), so an oversize of its power level is necessary in a practical implementation. The followed methodology will be presented and discussed in this presentation which can be easily adapted to higher power levels in electric vehicular applications.

Keywords: PEMFC systems, Li-Ion Battery, DC-DC Simulation;

ID 026

Influence of resorcinol-formaldehyde molar ratio in the properties of Mesoporous Carbon Supports for PEMFC Catalysts

E.T. Zanoni, R. Benavides, L. Da Silva, D. Morales-Acosta*

Centro de Investigación de Química Aplicada, Blvd Enrique Reyna No. 140, Col. San José de los Cerritos, 25290. Saltillo, Coahuila, México

* Corresponding author: diana.morales@ciqa.edu.mx

ABSTRACT

Carbon materials from mesoporous phenolic resins are considered an advanced class of high-stable mesoporous materials with potential application as fuel cell support electrodes. The performance of these carbons depends greatly of the structure and purity of polymeric precursors, and could be easily controlled to get the final properties required. Resorcinol-formaldehyde (RF) resins, with 1:2 and 1:3 molar ratios, were synthesized using Pluronic ® F127 as structure director. Synthesized RF resins were subsequently carbonized at 700 °C to obtain mesoporous carbon (MC). RF resins and their corresponding MC were characterized by FT-IR, TGA, RAMAN, TEM, BET and SAXS techniques. The obtained results indicate that resin with R/F=1:3 shows a greater thermal stability near to 300 °C and a higher percentage of residues, which in turn suggests an enhanced crosslinking mechanism. For the MC obtained from this resin (R/F= 1:3) a disordered structure and a low specific surface area value (S_{BET} = 35.9 m^2/g) was observed. In contrast, a highly ordered mesostructure was obtained for the MC from the resin R/F=1:2, with larger pore size (7 nm) and the highest specific surface area (S_{BET} = 107 m^2/g); a partial crystalline mesostructure was confirmed by SAXS. In the RAMAN spectrum for the carbonized samples, two peaks were observed, corresponding to amorphous carbon (peak D at 1333 cm^{-1}) and crystalline graphite (peak G at 1598 cm^{-1}), with an intensity ratio (I_D / I_G) of 0.86 for both MC, indicating a high order of crystalline graphite regardless of the R/F molar ratio. The results suggest that a low content of formaldehyde in the resin promotes the formation of a mesophase during the polycondensation reaction, generating a carbon material with better textural properties for their application as electrodes in fuel cells.

Keywords: *Resin, Resorcinol-Formaldehyde, Mesopores, Carbon*

ID 027

Synthesis of Random Polystyrene-co-Acrylonitrile-co-Butyl Acrylate Terpolymers as potential solid electrolytes for fuel cells

L.G. Delgado Interial, R. Benavides*, L. Da silva*, D. Morales-Acosta, L. Francisco-Vieira

Centro de Investigación en Química Aplicada, Blvd. Enrique Reyna H. 140, Saltillo Coah. 25294

* E-mail: roberto.benavides@ciqa.edu.mx, luciano.dasilva@ciqa.edu.mx

---

ABSTRACT

Nafion® electrolytes in fuel cells have been the most commercialized polymeric membranes; even though it has some drawbacks such as high cost and limited operating temperature (<100°C). Styrenic sulfonated membranes are an alternative to Nafion®, since polystyrene is a low-cost material with processing feasibility and high mechanical properties. However, it has also some drawbacks, like a low flexibility and a poor chemical resistance. Copolymerization techniques have been implemented to enhance mechanical and chemical properties of polystyrene. Terpolymers containing styrene (St) as a molecular base, butyl acrylate (BuA) as flexible component and acrylonitrile (ACN) to enhance chemical stability, were prepared by free radical polymerization. Several molar composition ratios of the St:ACN:BuA were prepared: 70:10:20, 70:15:15, 70:20:10, 80:05:15, 80:10:10 and 80:15:05. FTIR vibrational bands indicate the formation of terpolymers and ^{1}H and ^{13}C NMR chemical shifts from the corresponding functional groups associated with the comonomers confirmed the proposed structure, even though some differences in comonomer composition. The terpolymers exhibited the ability of forming a flexible film and showed variations in solubility with respect to pure polystyrene. According to GPC, terpolymers showed MW values up to 150,000 g/mol. DSC thermal analysis indicated Tg values from 64 to 80ºC, depending on the content of comonomers, while TGA showed decomposition temperatures over 350°C. Complex modulus values obtained from TMA flexure experiments decrease along the content of BuA (~3600 to 1500 MPa); on the contrary, when ACN content is increased, modulus goes from ~3600 to 4500 MPa.

Keywords: Polystyrene membranes; terpolymers; solid electrolytes; fuel cells

ID 028

Solid Oxide Fuel Cell: Metallic Interconnectors Analysis

José Juan Alvarado Flores[1,*], María Liliana Ávalos Rodríguez[2], José Guadalupe Rutiaga Quiñones[1], Jaime Espino Valencia[3] and Jorge Víctor Alcaraz Vera[4]

[1]Facultad de Ingeniería en Tecnología de la Madera, Universidad Michoacana de San Nicolás de Hidalgo. Santiago Tapia 403, CP 58000, Morelia, Michoacán, México.

[2]Centro de Investigación en Geografía Ambiental, Universidad Nacional Autónoma de México. Antigua Carretera a Pátzcuaro No. 8701, C.P. 58190, Morelia, Michoacán, México.

[3]Facultad de Ingeniería Química, Universidad Michoacana de San Nicolás de Hidalgo. Francisco J. Mújica S/N, Col. Felicitas del Rio, C.P. 58000, Morelia, Michoacán, México.

[4]Instituto de Investigaciones Económicas y Empresariales, Universidad Michoacana de San Nicolás de Hidalgo. Francisco J. Mújica S/N, Col. Felicitas del Rio, C.P. 58000, Morelia, Michoacán, México.

* Corresponding author: doctor.ambientalista@gmail.com

ABSTRACT

Today, alternative sources of energy have been considered as an option to reduce the cost of oil, because they are environmentally friendly and do not generate pollution as high as that derived from fossil fuels. In large-scale electricity generation systems, solid oxide fuel cells (SOFCs) offer several advances over other fuel cell technologies, because they can have a very high conversion efficiency (35-55%) and also have the ability to be used with a wide variety of fuels. Interest in SOFC stems from their higher efficiencies and lower levels of emitted pollutants, compared to traditional power production methods. Interconnects are a critical part in SOFC stacks, which connect cells in series electrically, and also separate air or oxygen at the cathode side from fuel at the anode side. Therefore, the requirements of interconnects are the most demanding, i.e., to maintain high electrical conductivity, good stability in both reducing and oxidizing atmospheres, and close thermal expansion coefficient (TEC) match and good compatibility with other SOFC ceramic components. This paper reviewed the interconnect materials, and coatings for metallic interconnect materials in a SOFC cell.

Keywords: solid oxide fuel cells (SOFC); interconnect; spinel; coating

ID 029

STUDY OF WATER MANAGEMENT IN SOLID STYRENE ELECTROLYTES

L. Da Silva*, M.M. Salas, L. F. Vieira, L.G. D. Interial, D. Morales-Acosta, A. de León Santillán, R. Benavides

Centro de Investigación en Química Aplicada, Blvd. Enrique Reyna H. 140, Saltillo, Coah. 25294, Mexico.
* Corresponding author E-mail: luciano.dasilva@ciqa.edu.mx

ABSTRACT

The variety of polymeric materials with distinct chemical structures that precisely control the molecular architecture underlies the numerous industrial uses of polymers over the past few decades. Polymer electrolytes or gel-type polymer electrolytes, for example, are interesting alternatives to substitute liquid electrolytes in different systems such as fuel cells (FC) and dye-sensitized solar cells (DSSC). For application in FC, the Nafion electrolyte is the most widely studied. However, this material is highly dependent on hydration and operating temperature. To a certain extent, concepts and models of proton conductivity in bulk water carry over to proton conductivity in Nafion and other polymer electrolyte membranes. To understand how water acts on these systems, in this work we conducted a study to identify the kind of interaction between the adsorbed water and the electrolyte structure of membrane. Differents copolymers were synthesized from styrene as the main comonomer and characterized chemically and thermally. Membranes were prepared by casting, hydrated and the Water Uptake (WU) and Water Content (WC) were determined. Differential Scaning Calorimetry (DSC) was used to determine the kinds of present water. We observed that several compositions absorb a lot of water and do not showed conductivity because it is basically free water and does not interact with the copolymer. For other side, when the copolymer structure allows strong interaction with water, the kind of water present also changes and this is reflected in the ionic properties of the membrane.

Keywords: Polystyrene membranes; water management; solid electrolyte; Fuel cells

ID 034

Preparation of Sulfonated PEEK and Graphene Oxide Materials for Proton Exchange Membranes

A. Saldívar-Martínez, D. Morales-Acosta*, P.C. Flores-Escareño, R. Benavides*, L. Da Silva.

Centro de Investigación de Química Aplicada, Blvd Enrique Reyna No. 140, Col. San José de los Cerritos, 25290. Saltillo, Coahuila, México

* E-mail: roberto.benavides@ciqa.edu.mx; diana.morales@ciqa.edu.mx

---

ABSTRACT

Sulfonated polyether ether ketone (sPEEK) and their composites are considered one of the most promising alternative polymeric materials for the development of proton exchange membranes (PEM) due to good mechanical properties, resistance to high temperatures and excellent chemical resistance. The degree of sulfonation (DS) of PEEK can be controlled by reaction time and temperature, as well as the sulfonating agent. This study reports the preparation of sPEEK with varying DS and sulfonated reduced graphene oxide (srGO) for their potential application as composite proton exchange membranes for fuel cells. The sulfonation of PEEK was carried out using concentrated sulfuric acid (H_2SO_4) at 70 ºC and several reaction times (3-5h). GO synthesized by Tour's method was further reduced and chemically modified using the same sulfonating agent at 70 ºC. The sulfonation of PEEK and rGO was characterized by 1H NMR, FT-IR, and TGA-DSC techniques. FT-IR and 1H NMR confirmed the successful sulfonation of sPEEK and it was observed through TGA and 1H NMR that long reaction time increases the DS from 50 to 76% while maintaining good thermal stability over 300 °C for all reaction times. On the other hand, the sulfonation of rGO and its effects were characterized by FT-IR and TGA to evaluate its potential of becoming a prospect for application in PEMFC.

Keywords: PEEK; sulfonated PEEK; sulfonated reduced graphene oxide; PEM fuel cells

ID 036

CFD PEMFC simulation with different levels of enriched air

Eduardo A. Rosado Vázquez[1], Humberto J. Mandujano Ramírez[1], Sandra J. Figueroa Ramírez[1], Juan M. Sierra Grajeda[1*]

[1]Universidad Autónoma del Carmen, Facultad de Ingeniería, zip code 24180. Cd del Carmen Campeche, México

* Corresponding author: 7771843585; jsierra@pampano.unacar.mx

---

ABSTRACT

The present work, is about the simulation and analysis using computational fluid dynamic (CFD) on a proton exchange membrane fuel cell (PEMFC) considering steady state and non-isothermal conditions, different scenarios were evaluated varying oxygen concentration for enriched air at the cathode entrance. The model consists of a 3D mono-cell with a channel in each plate that meanders in a squared shape eight times in order to cover its area. The model includes a membrane, catalytic layers, diffusion layers, monopolar plates. The mesh is a hexahedral type with 569,088 elements. The operation conditions were 1 atm and 300 K considering one phase. Properties as pressure, temperature, current density, species concentration are obtained at different components of the membrane-electrodes ensemble. Analyzing the processed results, one can observe, when the oxygen arrives to the catalytic layer is enough and approximately homogeneous, the grater the oxygen concentration at the cathode entrance the more is the generated current density at the catalytic layer. The protonic conductivity and the ionic current density have a similar behavior. Moreover, the obtained properties distribution at the diffusion layer, catalytic layer and the membrane, the heterogeneity at these components is very similar for different oxygen concentration at the cathode entrance but with ranges of values that depends on this parameter. This way, the ranges' upper limit on current density, relative humidity, oxygen concentration, protonic conductivity, and temperature, increase with increasing oxygen concentration at the cathode entrance. Besides, it is observed that at very high rates the polarization curves separation is less compared with an optimal rates range. Also, at very low rates, this sensibility to oxygen concentration is low because the oxygen is not enough at the catalytic layer. It was observed an optimal range of rates where sensibility to oxygen concentration at the cathode entrance is noticeable and important due to enriched air adds to the system´s electric power in an appreciable way.

Keywords: PEMFC; enriched air; CFD;

Effect of Polymer Sulfonation on the thermal and Ion Exchange Capacity Properties of SPEEK Membranes for PEMFC

P.C. Flores Escareño, R. Benavides*, L. Da Silva, D. Morales Acosta*

Centro de Investigación en Química Aplicada, Blvd. Enrique Reyna No. 140, Col. San José de los Cerritos, 25290. Saltillo, Coahuila, México.

*Corresponding author: +52844-4389830 E-mail: roberto.benavides@ciqa.edu.mx; diana.morales@ciqa.edu.mx

---

ABSTRACT

Poly(ether-ether-ketone) is an alternative polymeric material for the development of proton exchange membrane for fuel cell application. In this work, the chemical modification of poly(ether-ether-ketone) by electrophilic sulfonation was carried out using sulfuric acid at several temperatures 70 y 80°C and several reaction times (1-5 h). SPEEK membranes were obtained by casting. The physicochemical, thermal, mechanical, and ionic conductive properties of sulfonated PEEK and membranes were evaluated. The sulfonation of PEEK was confirmed for all conditions established. The sulfonated PEEK long times (SPEEK 804 y SPEEK 805), the low solubility and/or high hydrophilicity affect their processing confirmed by FTIR and ^{1} HNMR, while the sulfonation degree (DS) was calculated by ^{1}H NMR, and the results were similar than those reported in the literature (48 to 68 %). Thermal stability as well as the glass transition varied with respect to the DS. SAXS results show the increasing amorphous nature of the membranes with increase DS value. Depending on the degree of sulfonation, the water uptake (WU) and ion exchange capacity (IEC) of the membranes varied from 4%-112% and 0.78-2.28 meq g^{-1}, respectively, which in some cases were higher than those obtained for commercial NAFION® membrane (WU=13% and IEC= 0.91 meq g^{-1}). Results regarding proton conductivity from the latter will be presented as well.

Keywords: PEEK; Sulfonation; membranes; Fuel Cells.

Análisis numérico tridimensional de una celda de combustible tipo PEM con canales de flujo de tipo espiral

Tonatiuh A. Rodríguez[1*], Juan M. Sandoval-Pineda[1], Rosa de G. González-Huerta[2]

[1]Instituto Politécnico Nacional, ESIME-Unidad Azcapotzalco., SEPI, Av. de las Granjas 682, Col. Santa Catarina, CP 02250, Ciudad de México

[2]Instituto Politécnico Nacional, ESIQIE, Laboratorio de Electroquímica y Corrosión, UPALM, CP 07738, Ciudad de México

*Corresponding author: ale_tona@icloud.co

ABSTRACT

Se ha reconocido que tanto el rendimiento como la estabilidad operativa de las celdas de combustible de membrana de intercambio de protones (PEMFC) están estrechamente relacionadas con el transporte de agua y los comportamientos de acumulación en el Ensamble Membrana-Electrodos (MEA por sus siglas en inglés). Por lo tanto, una gestión óptima del agua es altamente deseada. La placa bipolar es un componente clave en este dispositivo, ya que conecta cada celda eléctricamente, suministra gases reactivos al ánodo y al cátodo, y elimina los productos de reacción de la celda. En este trabajo se realiza la modelación tridimensional y estacionaria de una celda de combustible tipo PEM con canales en espiral empleando técnicas de modelación de dinámica de fluidos computacional, específicamente el software ANSYS FLUENT. Se optimiza el diseño tomando en cuenta el ancho del canal, ancho de la costilla, altura del canal, longitud de los canales y orientación de los canales de flujo. Se analizan los parámetros de operación del dispositivo, presión, temperatura, distribución de gases reactivos y velocidad de flujo dentro de los canales. Se realiza una comparación entre los canales de tipo espiral y los de tipo serpentín y paralelo y los resultados se comparan con datos experimentales. El radio y el área de la zona activa son 2 cm y 12.566 cm^2, respectivamente. Como resultado, se obtuvo un análisis comparativo de esta configuración en espiral evaluando la dispersión de los gases en toda el área activa. Este diseño de campo de flujo permite que los gases se mezclen en cada giro para minimizar el efecto del bloqueo del canal evitando la acumulación de agua. Esto garantiza la distribución uniforme de los gases reactivos y el control de la pérdida de agua de la celda de combustible. Se ha encontrado que la uniformidad de la dispersión de los gases depende en gran medida del diseño de los canales de flujo.

Keywords: *Fuel cell PEM; CFD; Canales de flujo.*

ID 067

SOFC solid electrolytes based on the CeO_2-Ln_2O_3 system; effect of sintering aids on their electrical properties

D.E. Puente-Martínez[1], K.A. González-García[1], J.A. Díaz-Guillén[1*], S. Martínez-Montemayor[2], J.C. Díaz-Guillén[3], G. Ochoa-Hernández[4], M.E. Bazaldúa-Medellín[5], K.P. Padmasree[5], A. F. Fuentes[5].

[1]Tecnológico Nacional de México- IT de Saltillo, 25280-Saltillo, Coahuila México.
[2]Centro de Investigación en Química Aplicada, 25294-Saltillo, Coahuila México
[3]COMIMSA-CONACYT, 25290- Saltillo, Coahuila México
[4]Universidad Virtual del Estado de Michoacán, 58147-Morelia, Michoacán México
[5]Cinvestav Unidad Saltillo, 25900-Ramos Arizpe, Coahuila México.
l*Corresponding author e-mail: jadiaz@itsaltillo.edu.mx (José Alonso Díaz-Guillén)

ABSTRACT

Ceramic materials based on cerium oxide CeO_2 (ceria) are known by their interesting ionic conduction properties at intermediate temperatures, which make them interesting candidates to be used as solid electrolytes in Solid Oxide Fuel Cells (SOFC). These electrical properties can be improved with the incorporation of different elements (in solid solution) in the cubic structure of ceria, due mainly to the increase of the number of oxygen vacancies in the unit cell or the modification of the lattice parameter. This project evaluates the viability of mechanical milling (mechanochemistry) to generate a composition of the system CeO_2-Er_2O_3 ($Er_{0.1}Ce_{0.9}O_{1.95}$). This powder processing method allows obtaining metastable phases at room temperature, which include a large number of structural defects, which will have an interesting effect on their electrical properties. XRD analysis revealed that this system can be synthesized after 20 hours of milling, by using a planetary mill and ZrO_2 containers and balls. Post-milling thermal treatments at 1500°C promotes the cubic structure of this fluorite-type composition. Their electrical properties were analyzed (in sintered pellets) by impedance spectroscopy for pure $Er_{0.1}Ce_{0.9}O_{1.95}$ and the same system mixed with 2 wt. % of CaO, ZnO, MgO and TiO_2 as sintering aids. Results reveal that these materials show high ionic conductivities at temperatures of 650°C. These properties are improved with the incorporation of sintering aids and are comparable with such reported by different reports on ceria-based materials. These results corroborate the viability of these materials to be used as solid electrolytes in SOFC.

***Keywords*:** SOFC; Doped ceria; Solid electrolytes; Mechanochemistry

ID 072

Direct alcohol fuel cell with anode fuel supplied via capillary channels and a self-breathable open cathode

M. Paredes, E. Escobedo, L.C. Ordóñez*

[1]Unidad de Energía Renovable, Centro de Investigación Científica de Yucatá.Parque Científico Tecnológico de Yucatán. Carretera Sierra Papacal – Chuburná Puerto, km 5.

Sierra Papacal, Yucatán, México. C.P: 97302. E-mail: lcol@cicy.mx

---

ABSTRACT

In the present work, we design and manufacture a passive direct alcohol fuel cell (DAFC) with a 9 cm^2 active area of the electrode. The anode-side flow field architecture consisted of conical capillary channels with the ability to self-pump fuel to the catalytic layer. At the cathode, the flow field had a rhomboidal pin matrix configuration that allowed the diffusion of oxygen from the air to the catalytic layer and proper evacuation of the water resulting from the reaction. We study the reactants' fluid regimens in both electrodes by using computational fluid dynamics (CFD). The different parts of the prototype were manufactured employing CNC machining. Nafion-117® membrane was used as the electrolyte, carbon cloth as diffusers and PtSn/C and Pt/C as catalysts at the anode and cathode, respectively, with a metal loading of 1 mg Pt/cm^2. Cell performance was determined using 1, 2, 3 M ethanol solutions as fuel. The DAFC was operated with passively and actively approaches. Similarly, crossover tests were performed at different flowrates and in passive modality. It was observed that 2M ethanol solution is adequate to obtain a stable performance of the self-supply of fuel inside the DAFC. The characterization results showed that it is possible to work without forced flows and it is possible to eliminate the peripheral systems of the fuel cell.

Keywords: Direct alcohol fuel cell; self-breathing; self-pumping, CFD

Development of a test PEM Electrolyzer based on Advanced Manufacturing Techniques.

C.Y. Montalvo-Fernández[1,*], J.M. Sandoval-Pineda[1], R. de G. González-Huerta[2]

[1]Instituto Politécnico Nacional, ESIME SEPI, Unidad Azcapotzalco, Av. de las Granjas 682, Col. Santa Catarina, CP 02250, CDMX, Mexico.
[2]Instituto Politécnico Nacional, ESIQIE Laboratorio de Electroquímica y Corrosión. UPALM, CP 07738, CDMX, Mexico.

*Corresponding author: ingmontalvo_ipn@hotmail.com, Phone: +52 5578008959

ABSTRACT

PEM Electrolyzers to produce high purity hydrogen, typically use Pt, Ir, Ru and Rh for electrode catalysts and a Nafion membrane which not only separates the electrodes, but also acts as a gas separator. Various factors affect the efficiency of the electrolyzer, such the correct distribution of the Ir-Ru in catalysts layer or the all stack assembled to a proper tightening pressure; but this is not enough if a correct manufacturing design is not applied.

This paper shows the result of a simulation performed by ANSYS®, about a flow study inside an PEM electrolyzer in order to reduce the ohmic resistance derived from a new distribution of channels for evacuate gases and liquids of the electrolyzer, all based on a refining and advanced manufacturing procedure called V engineering model supported on GAMP methodology. The improving results are shown and applied in a real manufactured PEM electrolyzer. In addition, with some Ir-Ru electrocatalyst layers, this new design is critical to allow an increasing efficiency of the electrolyzer in terms to achieve a similar performance than a commercial device.

Keywords: GAMP methodology; PEM Electrolyzer; flow study; advanced manufacturing.

ID 079

Experimental characterization of the clamping and pressure distribution in a PEM electrolyzer: gasket materials and bolt torques.

R. Moreno Soriano[1], N. Rojas [2], E. Nieto[2], R. González-Huerta[1*], J. Sandoval-Pineda[1*]

[1]Instituto Politécnico Nacional – ESIME – Azc, SEPI, Av. De las Granjas, No 682, Azcapotzalco, CP 02250, México

[2]Centro Nacional del Hidrógeno, Prolongación Fernando el Santo s/n, CP 13500 Puertollano, Spain.

* Corresponding author: beto.mec@outlook.es

ABSTRACT

To keep all elements of an electrolysis cell optimally connected is one of the most important criteria in its design. The main parameters affected by the clamping force are: compression pressure distribution, water/gas handling, contact resistance and mass transfer limitations in the cell. The homogeneous distribution of the compression pressure over the cell active area ensures a greater number of contact points between components. More contact points, means a better electric current distribution, decreasing the contact resistance and increasing cell performance. The optimal distribution and value of the clamping points is crucial for increasing the cell performance.

In this work, the compression pressure distribution inside a PEM electrolysis cell with an active area of 25 cm^2 is experimentally evaluated, using different materials (Teflon®, Viton®, Ethylene and Nitrile) with different thicknesses. The evaluation of the sealing material is performed taking as performance indicators: total compressed area (%) and compression pressure on the area active, for different torques applied. The experimental values obtained were compared with theoretical ones. Pressure distribution was obtained by using pressure-sensitive films, analyzing the distribution of pressure points from 3D graphics, and quantifying the intensities of the images obtained. The results obtained showed that the distribution of the pressure points depends on the stiffness and thickness of the gasket materials. For a tightening torque of 3.70 Nm, a pressure of 2.23 Mpa is obtained with 85 % of the compressed active area using Nitrile-Ethylene gaskets. Finally, the electrochemical characterization of the cell was performed through IV curves, the cell performance for a current density of 2.0 A/cm^2, is 2.40 V with an overall efficiency of 58.78 % and electrical consumption of 6.07 kWh/Nm^3.

Keywords: Proton exchange membrane electrolysis; Gasket materials; Bolt torque; Clamping pressure.

Nanostructured materials

ID 003

EFFECT OF EPITAXIAL GROWTH OF BIMETALLIC NANOCRYSTALS ON THE ELECTROCATALYTIC ACTIVITY OF ORR

Francisco F. Tello Casas[1], Rosa de Guadalupe González Huerta[1], Martha L. Hérnandez Pichardo[2], Paz del Ángel[3]

[1] Instituto Politécnico Nacional ESIQIE, Lab. de Electroquímica, Ed. Z-5, 3er piso, C.P. 07738, CDMX
[2] Instituto Politécnico Nacional ESIQIE, Lab.de Nanomateriales, Ed. Z-5, 2 piso, C.P. 07738, CDMX
[3] Instituto Mexicano del Petróleo, Lab. Microscopia Electrónica de transmisión, C.P. 07730, CDMX

*Corresponding author: f.tello_99@hotmail.com

ABSTRACT

Pt-Pd/C bimetallic catalysts were synthesized by surface redox reactions. The parent metal catalyst (10%Pd/C) was modified by the addition of Pt by using the "refilling" method. This method consisted adsorbing hydrogen first on the parent metal (Pd) and subsequently reducing the $PtCl_6^-$ species by contact with the Pd-H interface. At the time of depositing the salt of the second metal (H_2PtCl_6), there is a reduction only where it was adsorbed the hydrogen, which led to selective deposition of Pt over Pd. Favorable results were obtained towards the oxygen reduction reaction (ORR) with 1%Pt-Pd synthesis, since a higher current density was obtained with the CV technique. Using RDE technique, the half-wave fall was 0.85 V, which indicates an improved catalytic activity towards the ORR. It was possible to reduce the amount of Pt and it was shown that with 1% nominal, certain facets are covered and better interaction of the two materials is achieved having favorable results. This synthesis technique has not been reported in the literature for the electrochemical study of ORR.

ID 004

Au@Pd/C core shell structures for enhance the oxygen reduction reaction at PEM-FC

E. Y. Cervantes-Aspeitia[1,2], M. L. Hernández-Pichardo[1,*], P. Del Angel[3,*],

[1] Instituto Politécnico Nacional-ESIQIE, Laboratorio de Nanomateriales Sustentables, México City, 07738, México.
[2] Instituto Politécnico Nacional-ESIQIE, Laboratorio de Electroquímica, México City, 07738, México.
[3] Instituto Mexicano del Petróleo, Caracterización de Materiales Naturales y Sintéticos, México City, 07730, México.
* Corresponding author e-mail: pangel@imp.mx, mhernandezp@ipn.mx

---

ABSTRACT

Many electrochemical properties of metallic and bimetallic nanoparticles (NPs) are highly dependent on their morphology and size. In this work, a seed-growth method was used to synthesize dendritic core-shell Au@Pd nanoparticles supported on carbon (Au@Pd/C). The composition, morphology, and particle size of these catalysts were analyzed by HRTEM, HAADF-STEM, EDS mapping, XRD, and XPS. The Pd growth mechanism over the Au surface generated by this synthesis method drives to the formation of a dendritic-type porous Pd shell covering the Au core. This result was attributed to a poor capping ability of cetyltrimethylammonium chloride (CTAC), along with a sluggish reduction of Pd by ascorbic acid. The dendrite formation on the Au surface was attributed to the nucleation and epitaxial growth of Pd atoms on some facets of the Au NP, in the presence of adsorbed CTAC. Meanwhile, anisotropic growth occurred at all the other uncapped planes of the gold core. The electrocatalytic activity of the as-prepared catalysts was assessed through the oxygen reduction reaction (ORR), and it was compared to the activity of a commercial Pd/C catalyst. The Au@Pd/C catalyst exhibited a superior electrocatalytic activity due to the formation of a non-homogeneous Pd shell, as well as to the synergistic effects at the Au-Pd interfaces. The dendritic structure allowed for an increased number of exposed active sites, and the interplay between both metals favored the suppression of the adsorption of hydroxyl and super hydroxyl groups on the active sites, enhancing the oxygen reduction reaction kinetics of the Pd shell in acidic media.

Keywords: Au@Pd Nanoparticles; Carbon, Oxygen Reduction Reaction, Electrocatalysis.

ID 008

Sb_2S_3/ carbono nanofibers nanocomposite as a novel anode material for sodium ion batteries.

M.G. Ayala-Sánchez[1]; B. Escobar-Morales[2]; J. Escorcia-García[3]; I.L. Alonso-Lemus[4]

[1]Sustentabilidad de los Recursos Naturales y Energía, Cinvestav Unidad Saltillo, Av. Industria Metalúrgica, 1062, C.P. 25900, Ramos Arizpe, Coahuila, México.
[2]CONACYT, Centro de Investigación Científica de Yucatán, Calle 43 No. 130, Col. Chuburná de Hidalgo, Mérida, Yucatán, C.P. 97200, México.
[3]CONACyT, Cinvestav Unidad Saltillo, Av. Industria Metalúrgica, 1062, C.P. 25900, Ramos Arizpe, Coahuila, México.
[4]CONACyT, Cinvestav Unidad Saltillo, Av. Industria Metalúrgica, 1062, C.P. 25900, Ramos Arizpe, Coahuila, México.
*Corresponding author: ivonne.alonso@cinvestav.edu.mx

ABSTRACT

Sodium ion batteries (SIB) are promising candidates for application in electrical energy storage. Some advantages of sodium are its abundance, low cost, low toxicity and electrochemical performance similar to Lithium (Li). However, one of the main issues is that the ionic radius Na+ is greater than of Li + which causes a volumetric expansion in host materials causing the decreased performance. Therefore, is a key challenge to develop high performance SIB materials. In this work, nanocomposites of Sb_2S_3 / carbon nanofibers (CNF) were synthesized by electrospinning and SILAR methods. The effect of the calcination temperature of the CNF (800, 900 and 1000 °C) and the immersion cycles number (5 and 10) during the SILAR composites preparation were investigated and correlated with their physicochemical properties. The physicochemical properties of the nanocomposites were characterized by Raman spectroscopy, XRD, nitrogen adsorption-desorption and electron microscopy and the electrochemical properties were characterized by cyclic voltammetry and electrochemical impedance.

Keywords: SIB; CNF; SILAR; electrospinning.

Electrospun Ce:$CoFe_2O_4$ nanofibers as bifunctional nanocatalysts for Oxygen Evolution and Oxygen Reduction Reactions

P.C. Cintrón-Núñez[1,*], B. Escobar-Morales[2], J. Escorcia-García[3], I.L. Alonso-Lemus[4,*], F.J. Rodríguez-Varela[1].

[1]Sustentabilidad de los Recursos Naturales y Energía, Cinvestav Unidad Saltillo, Av. Industria Metalúrgica, 1062, C.P. 25900, Ramos Arizpe, Coahuila, México.
[2]CONACYT, Centro de Investigación Científica de Yucatán, Calle 43 No. 130, Col. Chuburná de Hidalgo, C.P. 97200, Mérida, Yucatán, México.
[3]CONACYT, Cinvestav Unidad Saltillo, Ingeniería en Cerámica, México.
[4]CONACYT, Cinvestav Unidad Saltillo, Sustentabilidad de los Recursos Naturales y Energía, México.
*Corresponding author: 8444389626 Email: ivonne.alonso@cinvestav.edu.mx

---

ABSTRACT

The interest in the development of novel and clean energy conversion systems has increased due to the shortage of fossil fuels. Electrolyzers and Fuel Cells are electrochemical devices for clean energy generation with low/zero emissions and high efficiencies. However, the sluggish kinetics of both the ORR and the OER limits the large-scale commercialization of these devices. In this regard, the development of bifunctional nanocatalysts with high activity towards the ORR and OER is a key challenge. Non-noble metal nanocatalysts, such as metal oxides are a promising alternative for these applications. In this work, Ce:$CoFe_2O_4$/C nanofibers have been synthetized and evaluated as bifunctional nanocatalysts for the OER and the ORR. Ce:$CoFe_2O_4$ nanofibers has been synthetized by electrospinning method and evaluated for both the Oxygen Evolution Reaction (OER) and the Oxygen Reduction Reaction (ORR). The effect of annealing treatment (T=300, 600 and 900°C) and Ce incorporating (0.01, 0.05 and 0.1 at. %) on their morphological and structural features has been characterized by FESEM, HRTEM, XRD, XPS, BET, Raman and element mapping. The catalytic activity for both ORR and OER nanocatalysts will be evaluated by Rotating-Ring Disk Electrode (RRDE) technique.

Keywords: bifunctional electrocatalyst; Oxygen Reduction Reaction; Oxygen Evolution Reaction; $CoFe_2O_4$ spinel.

ID 016

Pt and Pt-Sn nanoparticles supported on zeolite-carbon for oxygen reduction reaction in acid medium

P.J. Pérez-Díaz[1, *], B. Ruiz-Camacho[1], A. Medina-Ramírez[1]

[1]Department of Chemical Engineering, University of Guanajuato, DCNE, Col. Noria Alta s/n, C.P. 36050, Guanajuato, Gto., Mexico

* Corresponding author: +52 1 2282515360 Email: pperezdiaz01@gmail.com

ABSTRACT

Fuel cells are devices capable of generating electric power in a direct and clean way, capable of substituting the conventional batteries even the engines. It has been demonstrated that the proton exchange membrane fuel cells (PEMFCs) are the most promising devices, one of them are the direct methanol fuel cells (DMFC) that use methanol as fuel. The methanol is a good option as fuel due to it is found naturally in the liquid form, this makes the methanol easy to manage and store. The oxygen reduction reaction (ORR) is the cathodic reaction and it is the limiting reaction of the process due to its low kinetics of electron transfer compared to anodic reaction. In other hand, zeolites as the second catalyst can give stability and can improve the ORR. The zeolites are compounds of crystalline aluminosilicate of Si, Al y O with a tetrahedral structure; this property will allow enhancing the Pt dispersion and nucleation. Moreover, a bimetallic catalyst of Pt-Sn was proposed with the aim to increase the methanol tolerance. In this work three different electrocatalyst for ORR were evaluated in acid medium in presence and absence of methanol. For the preparation of the electrocatalysts, a X zeolite-carbon with a wt. % ratio 3:1 was synthesized by sol-gel method as substrate of Pt and Pt:Sn with a wt. % ratio 1:1. Additionally, Pt/C was tested at same conditions, with the objective of analyze the effect of the support in the ORR. It was demonstrated that the presence of Sn in the catalysts increases the methanol tolerance, and it allows to diminish the Pt load reducing the final cost of the electrocatalyst. XRD results showed the crystalline structure of the materials synthesized, and TEM images demonstrated the nanoparticles size and the metals dispersion onto the support material.

Keywords: oxygen reduction reaction; fuel cell; X zeolite; methanol tolerance

ID 018

Synthesis and Characterization of PtPd Bimetallic Nanoparticles as Efficient Electrocatalyst for Alcohol Oxidation

América Libertad Higareda Alvear[1], Ramiro Pérez Campos[2], Gerardo Antonio Rosas Trejo[3], Rodrigo Esparza[1,*]

[1]Centro de Física Aplicada y Tecnología Avanzada, Universidad Nacional Autónoma de México, Boulevard Juriquilla 3001, Santiago de Querétaro, Qro., 76230, México.

[2]Instituto de Ciencias Físicas, Universidad Nacional Autónoma de México, Av. Universidad s/n, Col. Chamilpa, Cuernavaca, Mor., 62210, México.

[3]Universidad Michoacana de San Nicolás de Hidalgo, Avenida Francisco J. Múgica S/N Ciudad Universitaria, Morelia, Michoacán, 58030, México.

* Corresponding author: Tel.: +52-442-192-6128 (ext. 136); resparza@fata.unam.mx

---

ABSTRACT

Power generation is an essential necessity that has generated concern worldwide due to high demands and decrease in fossil fuel reserves. Therefore, great efforts are required to develop alternative energy sources with greater efficiency and that are environmentally friendly. The most promising technologies to address these challenges are polymeric electrolyte membrane fuel cells (PEMFCs) and one area that has received much attention is the development of new electrocatalysts with greater catalytic efficiency than Pt/C. Bimetallic nanoparticles (BNPs) present better and even unique properties than monometallic nanoparticles and the bulk material but to really know their potential, we need to have control in their size, morphology, structure and composition. This work shows the synthesis of PtPd BNPs with different composition Pt:Pd, which were synthesized by chemical reduction in organic medium. BNPs showed controlled characteristics, which were verified by different characterization techniques such as scanning electron microscopy (SEM), transmission electron microscopy (TEM), X-ray diffraction (DRX) and X-ray photoelectron spectroscopy (XPS) to know their size, size distribution, composition, structure and information crystallographic. Then, the electrochemical activity of PtPd BNPs supported on XC-72 Vulcan carbon were investigated to methanol and ethanol oxidation reaction in alkaline medium by cyclic voltammetry, also the stability and durability was analyzed by chronoamperometry and accelerated electrochemical degradation test. These PtPd/C electrocatalysts exhibit high activity to alcohol oxidation and their performance is dependent with Pd amount showing the optimum activity and stability to PtPd (1:0.5)/C than commercial Pt/C.

Keywords: PtPd nanoparticles; electrocatalysts; alcohol oxidation; electrochemical characterization

ID 020

Cost effective synthesis of NiCu electrocatalyst as anode for direct ethanol fuel cell in alkaline media

Gladys Gallardo-Espinoza[1], José G. Becerra-Salais[1], Enrique Rocha-Rangel[1], José A. Rodriguez-Garcia[1], P. C. Melendez-Gonzalez[2], W. J. Pech-Rodríguez [1*].

[1]Universidad Politécnica de Victoria, Parque Científico y Tecnológico de Tamaulipas, Ciudad Victoria, Tamaulipas 87138, México

[2]Cinvestav Unidad Saltillo, Av. Industria Metalúrgica 1062, Parque Industrial Ramos Arizpe, 25900 Ramos Arizpe, Coahuila, México

* Corresponding author: wpechr@upv.edu.mx

ABSTRACT

Herein, we report a facile and cheap process to synthetize NiCu nanoparticles to be used as electrocatalyst for the Ethanol Oxidation Reaction (EOR). For that, an intermittent microwave assisted polyol process was used to synthetize NiCu in two steps. The, obtained material was characterized by FTIR measurements to determine the existing bonding between O, Ni and Cu. Also, to determine the capacity to oxidize ethanol in alkaline media a set of electrochemical experiments were performed. From the FTIR results it is demonstrated the presence of Cu-O bindings and also Ni-Cu binding. The results from CVs suggest that Cu great improve the performance of Ni to achieve the ethanol oxidation. The enhancing in current density for EOR in NiCu electrocatalysts can be explained by the well-known bifunctional theory that state that a second metal can provides OH groups at low potential that facilitate the rapid oxidation of ethanol onto the active metal, in this case Ni. Therefore, with this investigation we demonstrate a cost effective process to obtain active electrocatlysts for EOR and also this open the doors to further investigation of non-noble metals as electrocatalysts for this relevant electrochemical reaction.

Keywords: Synthesis, nanoparticles, electrocatalysts, oxidation.

Synthesis and characterization of MoP nanoparticles

Jonathan Jesús Malpica Maldonado[1*], Ana Lidia Martínez Salazar[1], José Aarón Melo Banda[1], Óscar Fernández Jonguitud[1], Mayra Elizabeth Juárez Méndez[1], Sebastián Pacheco Buendía[2].

[1]Tecnológico Nacional de México – Instituto Tecnológico de Ciudad Madero, Centro de Investigación en Petroquímica, Prolongación Bahía Aldair, Blvd. De las Bahías, Parque Industrial Tecnía, Altamira, Tamaulipas, 89603, México.
[2]Instituto Politécnico Nacional-Centro de Investigación en Ciencias Aplicada y Tecnología Avanzada, Unidad Altamira, Carretera Tampico-Puerto Industrial Altamira Km 14.5, Industrial Altamira, 89600 Altamira, Tamaulipas.
* Corresponding author: 833-337-29-21 Email: jjmm15.inq@gmail.com

---

ABSTRACT

Nowadays, the disproportionate use of fossil fuels has brought serious problems to the environment. However, many of the alternative energies under research have not been able to replace the fossil fuels that are used in the aviation sector. Therefore, governmental and non-governmental organizations have allocated funds for research on a possible alternative fuel that meets the requirements to be used by airlines on their commercial aircraft. In the present work, molybdenum phosphide synthesis was carried out through a new and alternative process to the conventional one. The formation of MoP was achieved under the programmed reaction temperature method, varying the synthesis temperature from 550 ° C to 800 ° C. MoP nanoparticles synthetized were analyzed using techniques as: X-ray Diffraction (XRD), Textural analysis (BET-BHJ), Scanning Electron Microscopy-X-Ray - Energy Dispersion Spectroscopy (SEM-EDS).
The characterization of these materials provided relevant information for it possible application as catalysts in hydroprocessing of α-cellulose in order to bio jet fuel production.

Keywords: Molybdenum Phosphide; nanoparticles; Bio-Jet fuel; Cellulose conversion.

ID 041

Hydrothermal green synthesis of Pt-Ni nanoparticles using *Sargassum sp*. extract

A. Gamboa[1], D. Rosas[1], B. Escobar[1,*]

[1] Centro de Investigación Científica de Yucatán, Calle 43 No 130, Col. Chuburná de Hidalgo, C.P.97200, Mérida, Yucatán, México.

*Corresponding author: beatriz.escobar@cicy.mx

ABSTRACT

The use of the marine macroalgae *Sargassum sp.* has taken importance in the last years because is a waste product on the beaches of the Caribbean, and their use can be economically attractive as potential reducing agents for metallic salt in the synthesis of Pt and Ni nanoparticles (Pt-Ni NPs). Using a hydrothemal method to realize a green synthesis of Pt-Ni NPs is an eco-friendly and low cost alternative to obtain NPs with more benefits over the traditional synthesis methods. The extract was prepared dissolving 50 g of dry seaweed powder in 500 mL of desionized water. The mixture was in a double termic hydrolyst and the extract was filtered by filter paper. Then Pt-Ni NPs were synthesized using 200 µL, 400 µL, 600 µL, 800 µL and 1000 µL of the extract, which were added to 5 mL of 1 mM salt of nickel chloride solution. Lattice parameters of the Ni-NPs were calculated from the electron diffraction pattern to identify the preferential planes and the physicochemical characteristics to have a good performance like NP to use in oxygen-reduction reaction (ORR). Their use as an electrocatalyst for fuel cell electrode is discussed.

Keywords: nickel nanoparticles; *Sargassum sp*.; green synthesis.

Effect of capping agents' ratio in the synthesis of Pt_3Fe polyhedral nanoparticles and their catalytic activity for RRO

Miriam Marisol Tellez Cruz[1*], Miguel Adrian Padilla Islas[1], Heriberto Cruz Martínez[2], Oscar Eduardo Cigarroa Mayorga[3], Omar Solorza[1]

[1]Cinvestav Zacatenco, Chemistry, Mexico
[2] Tecnologico de Monterrey, School of Engineering and Sciences, Mexico
[3] Dept. Advanced Technologies, UPIITA-Instituto Politécnico Nacional, México.

* Corresponding author: +52 (55) 57473800 ext. 4473 Email: mtellez@cinvestav.mx

ABSTRACT

Synthesis of Pt_3Fe polyhedral nanocatalysts for oxygen reduction reaction (ORR) in acid media is presented. Six systems of Pt_3Fe catalysts were prepared through chemical reduction with a variable amount of oleylamine and oleic acid and 3:1 precursor salt atomic ratio $Pt(acac)_2$: $Fe(acac)_3$. Subsequently, the catalyst was dispersed in a carbon matrix (Vulcan Carbon) previously thermally treated. XRD proved the presence of the Pt_3Fe alloy in the six systems without the presence of any iron oxide. STEM micrographs showed the nanoparticle´s morphology and how the ratio of oleic acid and oleylamine modify the particle size. The electrochemical performance of the Pt_3Fe/C six systems was evaluated by cyclic voltammetry, CO stripping, and rotating disk electrode in $HClO_4$ as the electrolyte showing four of the catalysts best catalytic activity (mass activity and specific activity) than commercially available 20-wt% Pt/C-Etek® catalyst. The stability of the best four catalysts was evaluated, showing good resistance to corrosion.

Keywords: Pt_3Fe intermetallic; polyhedral nanocatalysts; ORR.

ID 051

CuPt supported on Alumina as cathodic catalyst for PEM fuel cell.

E. Flores-Rojas[1,*], O. Solorza-Feria[2]

[1]Universidad del Valle de México, Campus San Rafael, Sadi Carnot No. 57, San Rafael, Cuauhtémoc, C. P. 06470, Ciudad de México, Mexico

[2] Departamento de Química, CINVESTAV, Av Instituto Politécnico Nacional 2508, Col. San Pedro Zacatenco, Delegación Gustavo A. Madero, C.P. 07360 Ciudad de México, Mexico

* Corresponding author: 5574842961 Email: erefrojas@gmail.com

---

ABSTRACT

The present work comprises a study about the synthesis, characterization, and performance evaluation of a CuPt/Al2O3 electrocatalyst with potential catalytic activity towards ORR. The electrocatalyst was prepared through a two-stage process, combining the versatile high-energy ball milling synthesis and the galvanic displacement method. On a first stage, high-energy ball milling was used to produce nanoparticles of Cu and obtaining alumina as support coming from wear of the vials milling. On a second stage, a galvanic displacement reaction via chemical reflux treatment was employed to promote an alloy between nanoparticles of Cu and Pt. A CuPt:Alumina (wt.%) ratio of ~50:50 was obtained. Physical characterization of the synthesized electrocatalysts involved XRD, STEM, AAS-ICP-MS and EDX-SEM studies confirming the formation of homogeneously-distributed metallic nanoparticles on the Alumina. The electrochemical evaluation, through cyclic voltammetry and steady-state polarization curves using rotating disk electrode technique, was performed for the synthesized electrocatalyst and for a commercial platinum-loaded carbon black (Pt Etek 20 wt%) catalyst. The synthesized electrocatalyst was electroactive for ORR and presented a higher mass activity than the commercial Pt catalyst and showed major stability after 3000 cycles of accelerated degradation test as well. Two membrane electrode assemblies (MEAs) for PEM fuel cell were fabricated. A MEA with the synthesized electrocatalyst and other with the commercial catalyst, both used as cathodes. Results under single-fuel cell operation showed the same performance trend for those materials that observed under electrochemical glass cell conditions.

Keywords: High Energy Milling; Oxygen Reduction Reaction; performance on cell; Galvanic Displacement

ID 052

Evaluation of biocarbons from sewage sludge of the Saltillo treatment plant in clean energy storage and generation applications: supercapacitors and fuel cells

J.J. Bárcenas-Esqueda[1], J.A. Díaz-Guillén[1], B. Escobar-Morales[2], F. Fernández-Luqueño[3], I.L. Alonso-Lemus[4], F.J. Rodríguez-Varela[3,*]

[1]Instituto Tecnológico de Saltillo, V. Carranza No. 2400, Col. Tecnológico, Saltillo, Coahuila, C.P. 25280, México.
[2]CONACYT, Centro de Investigación Científica de Yucatán, Calle 43 No. 130, Col. Chuburná de Hidalgo, Mérida, Yucatán, C.P. 97200, México.
[3]Sustentabilidad de los Recursos Naturales y Energía, Cinvestav Unidad Saltillo, Av. Industria Metalúrgica 1062, Ramos Arizpe, Coahuila, C.P. 25900, México.
[4]CONACYT, Sustentabilidad de los Recursos Naturales y Energía, Cinvestav Unidad Saltillo, Av. Industria Metalúrgica 1062, Ramos Arizpe, Coahuila, C.P. 25900, México.
[4]Sustentabilidad de los Recursos Naturales y Energía, Cinvestav Unidad Saltillo, México.
[*]Corresponding author: javier.varela@cinvestav.edu.mx

ABSTRACT

In this project, the use of residual sludge from the Saltillo water treatment plant as raw material to obtain activated biocarbons was investigated. The biomass was subjected to several treatments: carbonization, chemical activation and microwave-assisted functionalization with methanol (MeOH) and acetic acid (AAc). The physicochemical characteristics of the electrocatalysts were evaluated by Fourier Transform Infrared (FTIR) and Raman spectroscopy, X-ray diffraction (XRD), Scanning Electron Microscopy (SEM), Nitrogen adsorption/desorption analysis. Their catalytic activity for the Oxygen Reduction Reaction (ORR) in alkaline media was studied by Rotating-Ring Disk Electrode measurements. Moreover, Accelerated Degradation Tests (ADT) were performed on the electrocatalysts. The electrocatalyst obtained after functionalization with AAc (labeled as CA_{AAc}) showed slightly higher catalytic activity for the ORR compared to those before activation and functionalized with MeOH (CA and CA_{MeOH}, respectively). The percentage of peroxide generated, and the number of electrons transferred were also evaluated, indicating a trend towards a four electrons path. The biocarbons demonstrated competitive electrochemical parameters compared to more expensive carbon allotropes. Such characteristics indicate that these biocarbons are promising electrocatalysts for Anion Exchange Membrane Fuel Cells (AEMFCs).

Keywords: sewage sludge; biomass; Oxygen Reduction Reaction.

ID 053

Oxygen Evolution Reaction at novel low Pt content electrocatalysts supported on Ordered Mesoporous Hollow Carbon Spheres functionalized with Ru organometallic compounds

J.C. Martínez-Loyola[1,*], I.L. Alonso-Lemus[2], M.E. Sánchez-Castro[1], B. Escobar-Morales[3], F.J. Rodríguez-Varela[1,*]

[1]Sustentabilidad de los Recursos Naturales y Energía, Cinvestav Unidad Saltillo, Cinvestav Unidad Saltillo, Av. Industria Metalúrgica 1062, Parque Industrial Ramos Arizpe. Ramos Arizpe, Coahuila, C.P 25900, México.
[2]CONACYT, Sustentabilidad de los Recursos Naturales y Energía, Cinvestav Unidad Saltillo.
[3]CONACYT, Centro de Investigación Científica de Yucatán, Calle 43 No. 130, Col. Chuburná de Hidalgo, Mérida, Yucatán, C.P. 97200, México.
[*]Corresponding authors: josue.martínez@cinvestav.edu.mx, javier.varela@cinvestav.edu.mx

ABSTRACT

Nowadays, the Oxygen Evolution Reaction (OER) is regarded as one of the most important reactions in the generation of sustainable energy. Electrolyzers are electrochemical devices at which the splitting of water molecules takes place. One of the reactions during the splitting is the OER at the anode. Nevertheless, the development and commercialization of electrolyzers is limited, in part due to issues associated to the electrocatalysts, including poor stability and high costs. Herein, we report the characterization of novel electrocatalysts for the OER. Low Pt-content electrocatalysts (5 wt. %) are synthesized in a two-steps procedure: i) Ordered Mesoporous Hollow Carbon Spheres (OMHCS) are functionalized with the $[(\eta^6\text{-}C_6H_5OCH_2CH_2OH)RuCl_2]_2$ (*Ru-dim*) and $[(\eta^6\text{-}C_6H_4CH(CH_3)_2CH_3)RuCl_2]_2$ (*Ru-cym*) Ru organometallic compounds to obtain $OMHCS_{Ru\text{-}dim}$ and $OMHCS_{Ru\text{-}cym}$; and ii) Pt nanoparticles are dispersed by the microwave assisted polyol method over the functionalized spheres and non-functionalized OMHCS to develop the $Pt/OMHCS_{Ru\text{-}dim}$, $Pt/OMHCS_{Ru\text{-}cym}$ and Pt/OMHCS electrocatalysts. The functionalization of the OMHCS support promotes the formation of surface functional groups. Moreover, Pt-Ru alloyed phases are developed. $Pt/OMHCS_{Ru\text{-}dim}$ and $Pt/OMHCS_{Ru\text{-}cym}$ exhibit higher catalytic activity for the OER in terms of onset potential and current density, compared to the benchmark 20 wt. % Pt/C and Pt/OMHCS. The results show that the development of functionalized carbon supports with organometallic compounds is opening new horizons for the synthesis of high performance electrocatalysts for energy conversion reactions.

Keywords: functionalization of OMHCS; organometallic compounds; Oxygen Evolution Reaction

ID 054

High-performance Pd nanocatalyst supported on Vulcan XC-72 functionalized with Cu organometallic compounds for the Ethanol Oxidation Reaction in alkaline media

P.C. Meléndez González[1], M.E. Sánchez-Castro[1,2], I.L. Alonso-Lemus[3], B. Escobar-Morales[4], W.J. Pech-Rodríguez[5], Teko W. Napporn[6], F.J. Rodríguez-Varela[1,2*].

[1]Programa de Nanociencias y Nanotecnología, Cinvestav Unidad Saltillo, Av. Industria Metalúrgica 1062, Parque Industrial Ramos Arizpe. Ramos Arizpe, Coahuila, C.P 25900, México.
[2]Programa de Sustentabilidad de los Recursos Naturales y Energía, Cinvestav Unidad Saltillo.
[3]CONACYT, Sustentabilidad de los Recursos Naturales y Energía, Cinvestav Unidad Saltillo.
[4]CONACYT. CICY. Calle 43 No. 130 Col. Chuburná de Hidalgo, Mérida, Yucatán, C.P. 97200, México.
[5]Universidad Politécnica de Victoria, Av. Nuevas Tecnologías 5902, Parque Científico y Tecnológico de Tamaulipas, Cd Victoria, Tamps., C.P.87138, México
[6]Université de Poitiers, IC2MP UMR 7285 CNRS, «Equipe SAMCat», 4, rue Michel Brunet, B27, TSA 51106, 86073 Poitiers Cedex 09, France.

ABSTRACT

The most widely used support of metal nanoparticles in fuel cells applications is the commercially available Vulcan XC-72. Herein, we report its functionalization XC-72 with home-obtained mesityl copper (Cu-mes) and Cu coordinate (Cu(dmpz)L2) organometallic compounds. Pd nanoparticles are dispersed on the novel supports by the polyol method, obtaining Pd/$C_{Cu\text{-}mes}$ and Pd/$C_{Cu(dmpz)L2}$. The aim of the surface modification of the support is to promote the formation of functional groups and alloyed phases between Cu from the compounds and the Pd nanoparticles being dispersed on it. The catalytic activity of the nanocatalysts for the Ethanol Oxidation Reaction (EOR) in 0.5 mol L^{-1} KOH was evaluated. Characterization of the functionalized Vulcan by FTIR analysis shows the successful incorporation of the organometallic compounds. The XRD patterns demonstrate a shift towards higher 2θ angles at Pd/$C_{Cu\text{-}mes}$ and Pd/$C_{Cu(dmpz)L2}$, compared to conventional Pd/C, indicating the formation of alloyed Pd-Cu phases. Analysis by EDS shows that the organometallic compounds are chemically stable, maintaining a high Cu concentration after the synthesis of the nanocatalysts. In electrochemical characterization, the polarization curves of the EOR at the nanocatalysts show that Pd/$C_{Cu\text{-}mes}$ promotes the reaction at a more negative onset potential, i.e., E_{onset} = 0.38 V/RHE, compared to 0.41 V/RHE of Pd/C and Pd/$C_{Cu(dmpz)L2}$. The current density j delivered by Pd/$_{CCu\text{-}mes}$ is considerable higher (119.11 mA cm^{-2}), followed by Pd/$C_{Cu(dmpz)L2}$ and Pd/C (73.63 and 54.57 mA cm^{-2}, respectively). In AEM-DEFC tests, the cell equipped with a Pd/$C_{Cu\text{-}mes}$ anode nanocatalyst demonstrated the highest open circuit voltage (OCV, 0.60 V) followed by 0.50 and 0.38 V at the cells having Pd/C and Pd/$C_{Cu(dmpz)L2}$ anodes, respectively. The maximum cell power density of 0.14 W cm^{-2} at 0.5 A cm^{-2} has been generated by Pd/$C_{Cu\text{-}mes}$. Due to its high catalytic activity, Pd/$C_{Cu\text{-}mes}$ can find application in AEM-DEFCs.

Keywords: Pd nanocatalysts; organometallic; EOR; Vulcan XC-72.

ELECTROCHEMICAL EVALUATION OF PtNi BIMETALLIC NANOPARTICLES SUPPORTED ON DIFFERENT CARBON MATERIALS

J.C. Ortiz-Herrera[a,*], H. Cruz-Martínez[a]; M.M. Tellez-Cruz[b]; O. Solorza-Feria[b] and D.I. Medina[a]

[a]Escuela de Ingeniería y Ciencias, Instituto Tecnológico y de estudios Superiores de Monterrey, Carretera Lago de Guadalupe Km. 3.5, Colonia Margarita Maza; Atizapán de Zaragoza, Estado de México, C.P. 52926. México
[b]Departamento de Química, CINVESTAV, Av. Instituto Politécnico Nacional 2508, San Pedro Zacatenco, Gustavo A. Madero, Ciudad de México, C.P. 52926, México
* Corresponding author: 55-1265-2820 Email: devox@live.com.mx

---

ABSTRACT

Pt alloys with transition metals and other metals have generated great attention to be investigated. Some Pt-based alloy materials with transition metals such as Fe, Co, and Ni are considered good catalysts since some of these have good performance and durability PtNi bimetallic nanoparticles are one of the most promising electrocatalysts for the oxygen reduction reaction (ORR) in polymeric electrolyte membrane fuel cells (PEMFCs) due to their high catalytic activity and efficient utilization of Pt. Furthermore, improvising the stability remains a significant challenge. Due to this, it is very important to increase the stability of these electrocatalysts. In this sense, the support materials are fundamental to improve the durability of the electrocatalysts for the ORR. One of the most promising alternatives is to replace carbon black as support with novel carbon materials, such as carbon Nanotubes (CNT). Some studies have shown that CNTs can be a great support material due to their high electrical conductivity, thermal and chemical stability, and good mass transfer capacity. Therefore, in this work, the synthesis, physical characterization, and electrochemical evaluation of PtNi nanoparticles supported on CNT are analyzed for the ORR in an acid electrolyte. The physical characterization of the PtNi nanoparticles physical were investigated using X-ray diffraction (XRD), energy-dispersive X-ray spectroscopy (EDXS-SEM), and transmission electron microscopy (TEM), while the evaluation of the catalytic properties were determined through cyclic voltammetry (CV), CO-stripping, and a rotating disk electrode (RDE) electrochemical techniques.

Keywords: oxygen reduction reaction; polymeric electrolyte membrane fuel cells; carbon nanotubes.

Role of the LTL-Zeolite in the Pt/C-(zeolite) Electrocatalyst for Ethanol Electrooxidation in Acid Media

Miguel Villicaña Aguilera[1*], Adriana Medina Ramírez[1], Beatriz Ruíz Camacho[1]

[1]Departamento de Ingeniería Química, Universidad de Guanajuato, Campus Guanajuato, División de Ciencias Naturales y Exactas, Noria Alta, C.P. 36050. Mexico

* Corresponding author: +524737320006 Email: m.villicanaaguilera@ugto.mx , adriana.medina@ugto.mx , beatriz.ruiz@ugto.mx

---

ABSTRACT

The Pt/C is considered a great material used as anode electrocatalyst due to Pt ability for break C-C molecular bond. However, the electrocatalyst based in Pt have several problems related with poisoning by CO_{ads} which is produced due the ethanol partial oxidation. Based on the forgoing work, an alternative to reduce the poisoning effect and enhance the electrochemical is the use of zeolites, these materials poses high surface area, porous structure, thermal and chemical stability, these properties can improve the performance of the electrocatalyst activity for ethanol oxidation reaction (ROE).

In the present work was evaluated the effect of LTL zeolite on the electrochemical activity of Pt nanoparticles supported for ethanol oxidation in acid media. The LTL zeolite was synthesized by hydrothermal method, while the Carbon into LTL zeolite support was prepared by sol-gel technique.

The incorporation of Pt (10% wt.) on the support was carried by reduction method. The electrochemical evaluation was carried out to cycling voltammetry and chronoamperometric in acid media at a sweep rate of 50 mVs^{-1} in 0.5 M H_2SO_4 + 0.5 M CH_3-CH_2-OH. All measurements were performed in a conventional three electrodes cell. The LTL zeolite support and the correspond electrocatalyst Pt/C-(LTL zeolite) were characterized by X-ray diffraction (XRD), Transmission microscopy electronic (TEM), Scanning microscopy electronic (TEM) and nitrogen physisorption. The results indicated that LTL zeolite is highly crystalline, mesoporous and nanosize crystals of prismatic morphology.

The cycling voltammetry results exhibits a good rate of ethanol oxidation (current density 5.24 mA/cm^2) at 25°C due to a well dispersion of the Pt nanoparticles depositing in LTL zeolite. Likewise exist a positive synergic effect between LTL zeolite support with Pt NPs. Regarding chronoamperometric results corroborate that zeolite have important role in contact with the poisoners species due to oxophilic property.

Keywords: LTL Zeolite; Electrooxidation; Acid Media; Fuel cell

Doped carbon nanostructures in fuel cells.

Y. Ogarte[1], I. Zeferino-González[1], A. M. Valenzuela Muñiz[1] , Y. Verde-Gómez*[1]

[1]Tecnológico Nacional de México / IT de Cancún, Av. Kabah, Km. 3, Col. Centro, Cancún, Quintana Roo, C.P. 77515, México.

* Corresponding author: phone number, +52 998 8807432 and e-mail: verde@yahoo.com

ABSTRACT

Carbon nanotubes, graphene and graphene oxides have been under development due to their suitable properties to be applied in electrochemical energy devices such as supercapacitors, batteries and fuel cells. Recently, carbon nanostructures doped with heteroatoms have demonstrated to play an important role to improve the activity in electrocatalyst. This work presents the synthesis and characterization of the carbon nanostructures doped (CND) with nitrogen, sulfur, silicon and boron. The CND were synthesized by a modified chemical vapor deposition technique using ferrocene as catalytic agent and toluene as carbon source. Pyridine, thiophene, triphenylsilane and phenylboronic acid were used to dope the carbon during the synthesis, respectively. Results show that the morphologies and chemical properties were influenced by the type of heteroatom used. In order to compare these type of nanocarbons, the electrochemical properties and their as fuel cells electrocatalyst also will be analyzed.

This research was supported by “CONACyT-SENER-Sustentabilidad Energética” under grant No. 254667.

Keywords: Doped carbon nanotubes; heteroatoms; .

ID 064

Synthesis of Low Pt Loading Electrocatalysts using Doped Carbon Nanotubes as Support

M. Zi-Chi[1], L. C. Ordóñez[2], Y. Verde-Gómez[1], A. M. Valenzuela-Muñiz[1,*]

[1]Tecnológico Nacional de México/I.T. Cancún, Av. Kabah Km. 3, Cancún, Q. Roo, México C.P. 75000.
[2]Unidad de Energía Renovable, Centro de Investigación Científica de Yucatán A. C., Parque Científico Tecnológico de Yucatán, Yucatán, México. C. P. 97302
*Corresponding author: +52 998 880 74 32 ext. 2018 Email: ana.vm@cancun.tecnm.mx

---

ABSTRACT

The development of highly efficient electrocatalysts with low platinum loading is crucial in order to achieve the massive application of PEM fuel cells. Diverse studies have used Multi-walled carbon nanotubes (MWCNT) as support of Pt to improve the metal particles dispersion, as well as to provide a higher mechanical and electrochemical stability. However, it is well known that the electronic properties of MWCNT can still be improved, since the play an important role in the electrochemical performance.

The incorporation of heteroatoms to the MWCNT structure, can change positively the properties. Also, it is expected to have an effect on the Pt nanoparticles dispersion, affecting then, the electrochemical activity. Hence, in this research work low-Pt over doped MWCNT systems were obtained and evaluated.

The doped MWCNT were synthesized using a modified chemical vapor deposition method, using a previously reported procedure. Toluene was used as carbon source, ferrocene as metal catalyst and different precursors of doping agents (i.e. N, B, S, and Si). Low Pt loadings were deposited over pristine and doped MWCNT using the colloidal methodology.

The structure of the obtained materials was analyzed by X-ray diffraction and Raman spectroscopy. Also, energy dispersive X-ray spectroscopy and scanning electron microscopy studies were done in order to obtain the chemical content and the morphology. Finally, the electrochemical performance was evaluated by cyclic and lineal voltammetry in a normal three electrode cell. The results of the extensive physical and chemical characterization confirmed the growth of MWCNT doped with the different heteroatoms (N, B, S, Si). It was possible to establish that the morphological characteristics of the obtained doped carbon nanotubes varied, depending on the dopant.

Differences on the diameter, length, as well as the graphitization degree of the structure were found. It was expected then, to have an effect on the electrochemical performance associated to the dopant. Also, it was possible to confirm the low Pt loading over the supports. The interesting results that were obtained for the low-Pt loading over doped MWCNT electrochemical systems, will be presented and discussed at the conference.

Keywords: Low Pt loading; doped MWCNT; electrocatalysts.

ID 073

Pt catalysts supported on mesoporous carbons synthesized using inorganic templates, and evaluation of their activity for the oxygen reduction reaction

J. Mustieles, D. Pacheco-Catalán, E. Escobedo, M. Baas-López, L.C. Ordóñez*

[1]Unidad de Energía Renovable, Centro de Investigación Científica de Yucatá.Parque Científico Tecnológico de Yucatán.
Carretera Sierra Papacal – Chuburná Puerto, km 5.
Sierra Papacal, Yucatán, México. C.P: 97302.
*Corresponding author: lcol@cicy.mx

ABSTRACT

For the manufacturing of the electrodes of a fuel cell, usually are used Pt catalysts supported on Vulcan® carbon. However, the membrane electrode assembly (MEA) is manufactured using a compression-temperature process, which causes a collapse of part of the support matrix, and some active sites of the catalyst are submerged within it. Thus, part of these sites are not available to catalyze the reactions that occur at the electrode by a reduction in the mass transport process. To address this problem, we prepared carbon supports by using an inorganic template to favor an ordered structure and with better textural properties than Vulcan®. We used as an inorganic template the mesoporous material SBA-15, as well as, two treated versions of this material. Polypyrrole, polyaniline, and D-glucose were used as carbon precursors to determine the effect of the carbon precursor on the distribution of active sites, as well as on the textural properties. The obtained materials were used as Pt support, and the activity of the catalysts was evaluated for the oxygen reduction reaction.

Keywords: mesoporous carbon; SBA-15; inorganic templates; RRO.

Kinetics of the Oxygen Reduction Reaction for Pt nanoparticles supported on novel reduced graphene oxide-polyindole

N.M. Sánchez-Padilla[1,2], J. Manríquez[2], L. Da Silva[1], R. Benavides[1]*, D. Morales-Acosta[1]*

[1]Centro de Investigación en Química Aplicada, Blvd Enrique Reyna No. 140, Col. San José de los Cerritos, Saltillo, 25294; Coahuila, México.

[2]Centro de Investigación y Desarrollo Tecnológico en Electroquímica S.C., Parque Tecnológico Querétaro s/n, Sanfandila, 76703, Pedro Escobedo, Querétaro, México.

*Corresponding author: diana.morales@ciqa.edu.mx

ABSTRACT

Electrochemical study of the electron-transfer pathways associated with the O_2 reduction reaction (ORR) is typically carried out by linear-sweep voltammetry using a rotating disk electrode (LSV-RDE). In this investigation, ORR was studied using the Koutecký-Levich and the Andrieux-Savéant approaches on Pt nanoparticles (prepared by means of the polyol process) supported on reduced graphene oxide (rGO)-polyindole (PIN) hybrids (rGO_x-PIN_y, where x and y subfixes denote the fractions of rGO and PIN, respectively). Three types of Pt-modified rGO_x-PIN_y materials (Pt/rGO_x-PIN_y) were electrochemically tested by means of LSV-RDE deposited on glassy carbon electrode: Pt/rGO_{90}-PIN_{10}, Pt/rGO_{50}-PIN_{50}, Pt/rGO_{10}-PIN_{90}. For comparison purposes, analysis of the electrochemical responses was carried out by employing the theoretical models described by Andrieux-Savéant (AS) and Koutecky-Levich (KL) looking for understanding the effect of the PIN on the ORR kinetics. To achieve this, O_2-transfer ($k°_{O2}$, from the electrolyte to the electrocatalytic sites) and electron-transfer ($k°_{et}$, from the O_2 molecules to the electrode surface) constants were estimated by means of the AS and KL approaches, respectively. Both types of kinetic constants were compilation as follows: system **Pt/rGO** ($k°_{O2,AS}$ = 3.8×10^{-2} cm s^{-1}, $k°_{et,AS}$ = 1.1×10^{-6} cm s^{-1}; $k°_{et,KL}$ = 1.13×10^{-6} cm s^{-1}), system **Pt/rGO$_{90}$-PIN$_{10}$** ($k°_{O2,AS}$ = 2.2×10^{-2} cm s^{-1}, $k°_{et,AS}$ = 0.69×10^{-6} cm s^{-1}; $k°_{et,KL}$ = 1.9×10^{-6} cm s^{-1}, system **Pt/rGO$_{50}$-PIN$_{50}$** ($k°_{O2,AS}$ = 4.0×10^{-2} cm s^{-1}, $k°_{et,AS}$ = 1.4×10^{-5} cm s^{-1}; $k°_{et,KL}$ = 1.5×10^{-5} cm s^{-1}), and system **Pt/rGO$_{10}$-PIN$_{90}$** ($k°_{O2,AS}$ = 1.6×10^{-2} cm s^{-1}, $k°_{et,AS}$ = 0.97×10^{-5} cm s^{-1}; $k°_{et,KL}$ = 1.18×10^{-5} cm s^{-1} $k°_{O2}$ was the same magnitude order, at all the electrocatalytic systems, thus indicating that O_2 was firstly adsorbed at the junction **Pt|rGO.** Thereafter, the values of $k°_{et}$ were increased at the same time the content of PIN according to the next order **Pt|rGO < Pt/rGO$_{90}$-PIN$_{10}$ < Pt/rGO$_{50}$-PIN$_{50}$ ≈ Pt/rGO$_{10}$-PIN$_{90}$**, thus indicating that the activation energy of the ORR (G^0_{ORR}) was strongly decreased in the presence of the junction **PIN$_y$|Pt|rGO$_x$**. Consequently, K-L and AS provide a reliable and facile approach for evaluating the performance fuel cell electrocatalysts systems.

Keywords: Pt/rGO_x-PIN_y hybrids*; ORR;* electrocatalysis; activation energy.

ID 092

Novel and cheaper process for the development of carbon nanoestructures by using Orange peel waste for the generation of carbons applied to supercapacitors

Gladis G. Suárez-Velázquez[a,b*], José A. Ramírez de León[a], Juan F. Castañón-Rodríguez J.F.[a]

Wilian J. Pech-Rodríguez[b]

[a] Unidad académica de Trabajo Social y Ciencias para las humanidades. Universidad Autónoma de Tamaulipas, Centro universitario, 87120 Cd. Victoria, Tamaulipas, México.

[b] Ingeniería Mecatrónica, Universidad Politécnica de Victoria, Av. Nuevas tecnologías 5902, parque científico y Tecnológico de Tamaulipas, 87138 Cd. Victoria, Tamaulipas, México.

*Corresponding author: gsuarezv@upv.edu.mx

ABSTRACT

Today, human kind is facing energy and environmental issues due to the increasing demand for electrical energy. In this regard, extensive investigation has been carried out to develop efficient technologies to generate and storage electrical energy. One alternative to face these problems is by using raw or waste biomass such as orange skin, coconut shell and others.

In this work, it is presented a novel and effective thermal process for the development of conductive carbon nanostructures by using orange peel waste for energy storage applications. The Orange peel waste sample was first cleaned and treated under an ultrasonic bath then, was summited at thermal treatment by using high-temperature alumina crucibles while the atmospheric air was limited by covering the sample with fine-grain silica sand. The obtained carbonaceous material was physical and chemically characterized by XRD, FTIR, and SEM-EDS measurements. Cyclic voltammetry measurement was conducted in order to study the electric-double layer capacitance. The XRD analysis shows that the obtained sample was composed of a graphitized carbon phase and also CaO and $CaCO_3$ phases were observed with high crystalline quality. On the other hand, from FTIR spectrogram was observed in the presence of C-O, C=O and also Ca-O species on the surface of the obtained carbon nanostructure.

The CV's curves were analyzed and the electrical double layer capacitance was estimated for the sample the results were compared with the non-modified glassy carbon electrode. The electrochemical results reveal that the as-synthesized carbonaceous material under a controlled air atmosphere has prominent capacitance and thus can be used for energy storage applications. Therefore, herein is demonstrated that by the proposed novel thermal process is possible to obtain graphitized carbon nanostructure with good electrochemical properties at low cost.

Keywords: orange peel; supercapacitors; cyclic voltammetry.

Bioelectrochemical cells

ID 010

Use microbial fuel cells for degradation of Used Lubricating Oils (ULO) and production of energy

Esther Ibarra Altamirano[1]; Miguel Mauricio Aguilera Flores[1]; Verónica Ávila Vázquez[1]*

[1]Instituto Politécnico Nacional – Unidad Profesional Interdisciplinaria de Ingeniería Campus Zacatecas. Blvd. del Bote 202 Cerro del Gato Ejido La Escondida, Col. Ciudad Administrativa 98160 Zacatecas, Zac. Phone. 01-492-92-42-419, 01-492-92-55-998

* Corresponding author: vav_taba@hotmail.com

ABSTRACT

Microbial fuel cells (MFC) have gained great interest as an alternative energy conversion system for generating bioenergy. MFC technology is a promising sustainable energy alternative to combat problems related to non-renewable energy consumption, climate change and environmental pollution. Used Lubricating Oils (ULO) are defined as hazardous waste and their generation is increasing every year. In this work, a discontinuous cycle of 55 days was performed in a MFC, using ULO as substrate and potting soil as inoculum. Physicochemical and electrochemical tests were carried out to validate the degradation of ULO. Results show a MFC stabilization between day 9 and day 11, obtaining an open-circuit voltage up to 553 mV, DP_{max} of 0.24 mWm^{-2} and i_{max} of 2.35 mAm^{-2} from an initial potential of 223 mV. Turbidity reduction efficiency of 88% was found, and total and volatile solids reduction efficiencies of 40% and 10%, respectively, were found. These results demonstrate that MFC allows energy generation from the degradation of ULO, so it is presented as an alternative to the treatment of water contaminated with this type of hydrocarbons and as an alternative energy option.

Keywords: Environmental pollution; MFC; ULO.

Synthesis of Mo_2C-Ni_2Mo_3N nanocomposites as a catalyst for bio jet fuel production

Jonathan Jesús Malpica Maldonado[1], Ana Lidia Martínez Salazar[1], José Aarón Melo Banda[1], Benjamín Portales Martínez[2], Sebastián Pacheco Buendía[3]

[1]Tecnológico Nacional de México – Instituto Tecnológico de Ciudad Madero, Centro de Investigación en Petroquímica, Prolongación Bahía Aldair, Blvd. De las Bahías, Parque Industrial Tecnía, Altamira, Tamaulipas, 89603, México.
[2]Instituto Politécnico Nacional-Centro de Investigación en Ciencias Aplicadas y Tecnología Avanzada, Unidad Legaria, Calz Legaria 694, Col. Irrigación, Miguel Hidalgo, 11500 Ciudad de México, CDMX
[2]Instituto Politécnico Nacional-Centro de Investigación en Ciencias Aplicada y Tecnología Avanzada, Unidad Altamira, Carretera Tampico-Puerto Industrial Altamira Km 14.5, Industrial Altamira, 89600 Altamira, Tamaulipas.
* Corresponding author: 833-337-29-21 Email: jjmm15.inq@gmail.com

---

ABSTRACT

Recent years, aviation sector has been growing exponentially with the growth of the population worldwide. In the year 2012, this commercial sector represented 2% of greenhouse gas emission around the word. Recently, a growth of 4.5 to 4.8 in this sector has been estimated which could provoke an increase in the dumped pollutants in the air, producing serious problems in the environmental. Therefore, several organizations have focused their research on the bio jet fuel production through renewable source such as biomass.

The present research shows the synthesis and characterization of Mo_2C-Ni_2Mo_3N nanocomposites by ammonolysis in-situ via temperature programmed reaction method. Sucrose and ammonia released from ammonium heptamolybdate were employed as nitrogen and carbon sources. Synthesis process of nanocomposites consists of two stages. The first is the formation of carbon sphere by hydrothermal treatment through a 0.5 M aqueous sucrose solution and aqueous solution of precursor salts of Ni and Mo [$Ni(NO_3)_2$ and $(NH_4)_6Mo_7O_{24}{\cdot}4H_2O$] into Teflon-lined stainless steel autoclave at 200 °C during 24 h. Finally, in the second stage, the process of reducing metallic oxides and the formation of Mo_2C and Ni_2Mo_3 are carried out at 800 °C under a hydrogen atmosphere. Nanocomposites synthetized were analyzed using techniques as: X-ray Diffraction (XRD), Textural analysis (BET-BHJ), Scanning Electron Microscopy-X-Ray - Energy Dispersion Spectroscopy (SEM-EDS).

The characterization of these materials provided relevant information for it possible application as catalysts in hydroprocessing of α-cellulose in order to bio jet fuel production.

Keywords: Mo_2C-Ni_2Mo_3N; Nanocomposites; Bio jet fuel; biomass

ID 035

Human Urine Role as Water, Nutrients, and Energy Source in Bioelectrochemical Systems Based on the Circular Economy Concept: A Review

M. Martínez-Castrejón[a], J.A. López-Díaz[b], Z.S. Galarza-Brito[c], J. Ramirez-Nava[d], J.M. Bravo-Ramos[a], O. Solorza-Feria[e], O. Talavera-Mendoza[b], A.L. Rodríguez-Herrera[a], O. Alcaraz-Morales[f], G. Hernández-Flores[g,*]

[a] Centro de Ciencias de Desarrollo Regional, Universidad Autónoma de Guerrero, Privada de Laurel No. 13, Col. El Roble, Acapulco, Guerrero. C.P. 39640, Mexico
[b] Universidad Autónoma de Guerrero, Escuela Superior de Ciencias de la Tierra, Ex Hacienda San Juan Bautista S/n, Taxco el Viejo, Guerrero, C.P. 40323, Mexico
[c] Ingeniería en Tecnología Ambiental, Universidad Politécnica del Estado de Guerrero. Carretera Federal Iguala-Taxco, km 105, Puente Campuzano, Taxco de Alarcón, Guerrero, C.P. 40321, Mexico.
[d] Facultad de Ecología Marina, Universidad Autónoma de Guerrero, Gran vía tropical No 20, Fracc. Las playas, C.P. 39390, Acapulco, Guerrero, Mexico
[e] Centro de Investigación y de Estudios Avanzados del Instituto Politécnico Nacional, Dept. of Chemistry, Av. Instituto Politécnico Nacional 2508, Col. San Pedro Zacatenco, Delegación, Gustavo A. Madero, C. P. 07360, Mexico
[f] Facultad de Arquitectura y Urbanismo, Universidad Autónoma de Guerrero, Av. Juárez No.38 interior. C.U. Zona Norte, Chilpancingo, Guerrero, C.P. 39000, Mexico
[g] CONACyT - Universidad Autónoma de Guerrero, Escuela Superior de Ciencias de la Tierra, Ex Hacienda San Juan Bautista S/n, Taxco el Viejo, Guerrero, C.P. 40323, Mexico
* Corresponding author: ghernandez@conacyt.mx

ABSTRACT

The uncontrolled population growth increases the challenge of meeting human necessities. The consumption habits have compromised natural resources to unsustainable levels. Water and energy represent two basic requirements for each human being, and both are limited resources. Nowadays, sustainable practices for effluents treatment such as decentralized systems focused on recovering energy, nutrients, and water have drawn attention. Human urine (*HU*) is a physiological liquid waste where the principal component is water (~95%) and 5% are dissolved solids. The main components in this low percentage are nitrogen, phosphorous, and potassium. Also, a relatively high organic matter content is part of this effluent. From these characteristics, the *HU* is an effluent with the potential to recover nutrients, water, and energy from, through bioelectrochemical systems (*BS*). Thus, the aim of this work was to review the *HU* potential as water, nutrients, and energy source when used in bioelectrochemical devices based on the circular economy concept.In *BS*, the *HU* is an organic matter source that can be used as a substrate and converted to electrical energy by bacteria. Some anaerobic bacteria use the chemical energy of organic and inorganic compounds to grow and to deliver as electricity through a biochemical oxidation process. On the other hand, the microbial electrolysis cells (*MEC*s) need an external electrical current to convert the organic compounds into other products, *e.g*., nitrogen to ammonia sulfate or bicarbonate. The *HU* is an effluent that typically does not contain fecal coliforms. A person (age>15) produces *ca*. 2 L per day, *i.e*., this effluent can be used in sustainable practices to harvest energy and produce water. The proposal to use *HU* in electrochemical or *BS* is a novel way to treat and to take advantage of this physiological effluents. All the efforts done and developed in this field must be discussed and analyzed to improve the efficiency of systems.

Keywords: bioelectrochemical systems; circular economy; electrochemical systems; human urine

Hydrogen production by microbial co-cultures from agave biomass pretreated using microwave and ultrasound

Thelma K. Morales-Martínez, Angelica L. Ortíz-Cruz, Luis E. de la Cruz-Andrade, Gustavo A. Neyra-Escobedo, Myriam L. Guzmán Chávez, Josué González-Olvera, Miguel A. Medina-Morales, José A. Rodríguez-De la Garza, Mayela MorenoDávila, Leopoldo J. Ríos-González*

Departamento de Biotecnología Facultad de Ciencias Químicas, Universidad Autónoma de Coahuila, México
* Corresponding author: 8444155752; leopoldo.rios@uadec.edu.mx

---

ABSTRACT

Hydrogen represents an eco-friendly energy alternative that can be produced from renewable feedstocks, such as lignocellulosic materials. Recent studies carried out by our research group have demonstrated the potential of *Agave lechuguilla* as feedstock for biofuels production. Hydrogen production from lignocellulose involves a high energy consumption during the pretreatment, followed by the use of expensive enzymatic complexes in the saccharification stage. However, the Consolidated Bioprocessing -CBP (using microorganisms capable of carrying out both steps) and the use of more efficient heating systems such as microwaves or irradiation methods such as ultrasound can be an alternative to these inconvenient.

In the present work, an orthogonal design ($L9(3^4)$) was applied to optimize the acid pretreatment assisted by microwave and ultrasound to enhance the hydrogen production via Consolidated Processing (CBP). The effect of four factors on the hemicellulose removal was assessed, concentration of H_2SO_4 solution (0.5%, 1% and 1.5% v/v), pretreatment time (5 min, 10 min and 15 min), biomass/H_2SO_4 ratio (1:12, 1:24 and 1:36 and temperature in the pretreatment assisted by microwave (60 °C, 100 °C and 140 °C) and amplitude for the case of ultrasound (40, 60 and 100%). In the acid pretreatment assisted by ultrasound the temperature was maintained at 60 °C for all experiments. The results showed a higher hemicellulose removal during the pretreatment assisted by microwave (77%) compared to the assisted by ultrasound (28%). The optimal condition obtained using microwave were as follows: H_2SO_4 concentration of 1.5%, at 140 °C, with a ratio of biomass to liquid of 1:36 (w/v) during 10 min.

Comparing the results with previous studies carried out in a high-pressure reactor with heating using electric resistance, the pretreatment assisted by microwave reduced the pretreatment time by 75%. Finally, the pretreated biomass could be efficiently transformed into hydrogen using a co-culture of *Clostridium acetobutylicum, Clostridium cellulolyticum* and *Clostridium thermocellum* under anaerobic conditions.

Keywords: agave; hydrogen; microwave pretreatment; Consolidated Bioprocessing

Optimization of $BioH_2$ production by consolidated bioprocessing of corncob pretreated with diluted acid

LE De la Cruz-Andrade[a]; AS Flores-Morales[a]; JG Moreno-Cedillos[a]; LJ Rios-González[a] TK Morales-Martínez[a]; IMM Moreno-Dávila[a]; JA Rodríguez-De la Garza[a]; MA Medina-Morales[a,*]

[a]Departamento de Biotecnología Ambiental. Facultad de Ciencias Químicas. Universidad Autónoma de Coahuila. Blvd. Venustiano Carranza s/n, Col. República Oriente 25280. Saltillo Coahuila. México.

*Corresponding author: 52 (844) 4155752 Ext. 5. Email: miguel.medina@uadec.edu.mx

ABSTRACT

Biofuel production such as hydrogen has a process that has been studied up to a point that it may considered as a conventional processing compared to other approaches, being those, the consolidated bioprocesses. This type of work configuration allows the decrease of unitary operations in bioprocesses in a way that the hydrolytic enzyme producers and the bioH2 producer are present in the same reactor, thus making the process time and more cost effective, compared to other bioprocesses. As corn is an important crop in Mexico, being cobs the subproduct, it is an interesting subject of study to increase its added value under this line of research. For this study, corncobs were processed as fermentable sugars source for $bioH_2$ production by biotechnological means. Firstly, pretreatments using NaOCl, diluted acid and autohydrolysis were evaluated to improve corncob biodegradation. It was notorious that diluted acid pretreatment favored the accumulation of 135 g/L of glucose by enzymatic degradation and along with these results, FTIR, CrI analysis were added and SEM photographs as well. In the consolidated bioprocessing, bovine ruminal fluid and *Clostridium acetobutylicum* were put to interact which allowed us to apply a Taguchi experimental array to identify the most adequate operating conditions for bioH2 production. In the consolidated bioprocessing an amount of 575 mL of $bioH_2$ was obtained at 264 hours. The conditions obtained were 35 °C, solids loading of 5%, 1:2 inoculum ratio (BRF:*Clostridium*) and pH of 6.5. These results allow us to recommend corncobs as a suitable resource for bioH2 production under a consolidated bioprocess.

Keywords: *bovine* rumen; cellulases; lignocellulose; Clostridia

ID 056

Autohydrolysis and alcaline pretreatments evaluation to increase biodigestibility of corncobs under a consolidated bioprocessing for bioH_2 production

LA Paredes-Peña[a]; MA Medina-Morales[a]; AL Ortíz-Cruz[a]; HG Sifuentes-Sánchez[a]; LJ Rios-González[a]; IMM Moreno-Dávila[a]; JA Rodríguez-De la Garza[a]; TK Morales-Martínez[a,*]

[a]Departamento de Biotecnología Ambiental. Facultad de Ciencias Químicas. Universidad Autónoma de Coahuila. Blvd. Venustiano Carranza s/n, Col. República Oriente 25280. Saltillo Coahuila. México.

*Corresponding author: 52 (844) 4155752 Ext. 5. Email: thelma.morales@uadec.edu.mx

ABSTRACT

Biological production of H_2 from renewable energy source represents a feasible and environmental-friendly alternative compared to fossil fuels production. However, its conventional production from lignocellulose requires expensive enzymatic complexes which increases the cost of the process. To reduce costs and operational units in bioH2 production, the work configuration of consolidated bioprocessing allows a simultaneous production of hydrolytic enzymes and bioH_2 by the respective microorganisms in a single reactor. In this work, corncobs were used as they are an easy-to-obtain and high-occurrence byproduct in our country. The consolidated bioprocess strategy was carried out by the interaction between bovine ruminal fluid, which contains cellulose-hydrolytic microbial consortia and *Clostridium acetobutylicum*, which produces bioH_2. The combined microbial efforts were evaluated by using a Taguchi experimental array. Before bioH2 production, alkaline and autohydrolysis pretreatments were evaluated increase degradability of the material, which resulted in a glucose release of 123 g/L from the autohydrolysis pretreatment and a lower amount of 89.8 g/L from the NaOH pretreatment. In bioH_2 production results under the experimental array, the highest yield obtained was 220 L of bioH_2 per kilogram of biomass under the most adequate conditions from the experimental array which were 5% of solids loading, pH of 5.5 and temperature of 35 °C. These results show that the Taguchi experimental array is useful for the process and the analysis. Also, the results help establish corncob as a suitable resource for bioH_2 production for its degradability and its obtainability along with the successful production of H_2 in the evaluated conditions.

Keywords: pretreatments; microbial consortium; hydrolysis; biohydrogen

ID 069

Stem of faba bean as potential source for fermentative biohydrogen production

J. C. Gómora-Hernández[1,2], M. del C. Carreño-de-León[1], S. M. Fernández-Valverde[2*]

[1]División de Estudios de Posgrado e Investigación, Tecnológico Nacional de México/Instituto Tecnológico de Toluca, Av. Tecnológico s/n. Colonia Agrícola Bellavista, Metepec, Estado de México, C.P. 52149, México.

[2]bDepartamento de Química, Gerencia de Ciencias Básicas, Instituto Nacional de Investigaciones Nucleares, Carretera México-Toluca S/N, La Marquesa, Ocoyoacac, Estado de México, 52750, México.

ABSTRACT

Faba bean is a legume cultivated and consumed worldwide with a high content of proteins, carbohydrates, fiber and other trace elements such as calcium, iron and phosphorus. At the end of the faba bean harvest different residues are produced being stems the most rigid and recalcitrant fraction, which due to their high polysaccharides content are possible sources for value-add products production. Acid hydrolysis is a chemical method capable to disrupt the complex lignocellulosic matrix of stems and to produce monomeric sugars from cellulose and hemicellulose; these sugars are used for fermentative purposes. In this work, biohydrogen production was evaluated in mesophilic regime using 2 pure strains; *Clostridium butyricum* and *Enterobacter cloacae,* and stem of faba bean acid hydrolysates as the only carbon source. The concentration of the total reducing sugars and furfural obtained by hydrolysis with phosphoric acid were 11.82 g/L and 0.36 g/L respectively. Fermentation tests were performed in 20 mL vials prepared inside an anaerobic box, in which acid hydrolysate and minimum culture medium were mixed at different ratios. Microbial growth, biohydrogen production and pH were monitored throughout the experiment, while temperature and incubation time were set at 37 ± 1 ºC and 20 hours respectively. Microbial growth does not reached the stability phase since an increase in sugar loading rise the bacteria concentration, similar behavior was observed for volumetric biohydrogen production reaching a maximum of 3 mL with an initial sugar mass of 0.030 g. With 0.02 g of sugars, the volume of biohydrogen produced was lower; 2.23 mL, however at this sugar loading the maximum biohydrogen yield as function of either initial sugar mass or metabolized sugars was achieved; 111.05 mL H_2 / g initial sugar and 138.16 mL H_2 / g metabolized sugar respectively. Experimental results suggest that hydrogen yield can improve in a biorreactor increasing initial sugar loading since sugar bacterial degradation efficiency was around 80% in all experiments Stem of faba bean acid hydrolysates is a substrate with high potential to produce biohydrogen by dark fermentation.

Keywords: biohydrogen; stem of faba bean; lignocelluloses; dark fermentation

ID 070

Study of factors involved in the behavior of biofilms formed by biohydrogen-producing microflora identified by molecular biology using dairy wastewater.

I.M.M. Moreno-Dávila[1*], M.C. Tamayo-Ordoñez, A.I. Soria-Ortiz, B. Gutiérrez-Rodríguez, S.Y. Silva-Belmares, T.K. Morales-Martinez, J.A. Rodríguez de la Garza, L.J. Ríos González, G.J. Sosa Santillán.

[1]Autonomous University of Coahuila. Blvd V Carranza s/n, Colonia República, C.P. 25280, Saltillo, Coahuila, México
*corresponding author: I.M.M. Moreno-Dávila, phone number: 8444921088,
*Corresponding author: imayelamorenod@hotmail.com; mayela.morenodavila@uadec.edu.mx

---

ABSTRACT

Anaerobic digestion has proven to be an effective technology for the degradation of various components as well as the use of pretreated microorganisms to form biofilms, which can increase the efficiency of this process for the additional production of a biofuel such as biohydrogen.
This study investigated the effect of factors that influenced the performance of biofilms: pH (initial = 11.32, final = 4.5-4.7), HRT (0.5 and 1 h) and two types of support (natural and synthetic) for the maintenance of biofilms. The maximum results after 72 h of fermentation with *Opuntia imbricata* as natural support at TRH of 0.5 h obtained a specific production of 2.04 mmol H_2/gCOD removed, and a reduction in the COD of 64.7%, compared to the synthetic support that also operated at a 0.5 h HRT, a specific production of 1.31 mmol H_2/gCOD removed was obtained, and a COD reduction of 51.20%. The reactor is tested at a TRH of 1 h feeding the diary wastewater, using natural support and a specific production of 0.64 mmol H_2/gCOD removed was obtained, and a reduction in the COD of 51.20%; The reactor was tested at TRH of 1 h, with the synthetic support and a specific production of 0.59 mmol H_2/gCOD removed was obtained, and a COD reduction of 48.42%. The diary wastewater from the reactor outlet that used natural support at a TRH of 0.5 h, was recirculated, achieving an additional reduction in the COD of 17.01%, resulting in a total COD reduction of 81.7% and a specific production of 3.34 mmol of H_2/g COD removed. The microbial community detected in the biofilm by 16rRNA sequencing was formed by lactic acid bacteria of the *phylum Firmicutes.*

Keywords: biohydrogen; *Opuntia imbricata*; 16rRNA, chemical oxygen demand.

ID 090

Study of separators in electrochemical assisted constructed wetlands

M.G. Salinas-Juárez [1,*], S.I. Ortíz Zamora[2], M.C. Durán Domínguez[2]

[1]Facultad de Estudios Superiores Zaragoza. Universidad Nacional Autónoma de México. Batalla 5 de mayo S/N Esquina Fuerte de Loreto, Col. Ejército de Oriente, Iztapalapa C.P. 09230, Ciudad de México, México.
[2] Departamento de Ingeniería Química. Facultad de Química. Universidad Nacional Autónoma de México. Laboratorios 301, 302 y 303 de Ingeniería Química Ambiental y de Química Ambiental, Conjunto E, Edificio E-3 Alimentos y Química Ambiental, Circuito de la Investigación Científica s/n, Ciudad Universitaria, Alcaldía Coyoacán, 04510 Ciudad de México, México.
* Corresponding author: +52 55 45402421, e-mail: maria.salinas@outlook.com

ABSTRACT

In microbial fuel cells (MFC), power is generated from electron donors thar are present in wastewater. The MFC technology can be implemented in constructed wetlands to obtain power, and to improve the treatment efficiency, these systems are called constructed wetlands-microbial fuel cell (CW-MFC). An important factor affecting the electrical performance in CW-MFC is the separator material between electrodes.

The present study explored the use of clay, earthen and a non-woven cloth (NWC) in CW-MFC, as inexpensive alternatives to be used as separator between electrodes. Five CW-MFC were installed and planted with *Typha latifolia*. Each CW-MFC was fed with synthetic wastewater (5.30 L). Electrodes were made of graphite and materials for separators were non-woven cloth, earthen and clay were placed between the anode and the cathode. Treatment performance was measured by the removal of chemical oxygen demand, ammonia nitrogen, nitrates, nitrites and sulfates. The electrical performance of the CW-MFC was evaluated by measuring the current and voltage from the bioreactors which were connected to different values of external resistor (of 20000, 18000, 15000, 10000, 5600, 1000, 560, 100 and 10 ohms).

The highest organic matter removals correspond to the period in which the 18000 Ω resistor was connected to the circuit. Statistical analysis showed a significant difference among the experimental stages stablished by the resistor change for each reactor, but not among the reactors for parameters of contaminants removal. This means that the change of electric charge has a major influence in the removals than the materials used in the reactors.

The voltages output of the CW-MFC decreased when decreasing the resistor loads following the typical trend. However, the highest values for power density correspond to Reactor 3 on the 10000 Ω stage, showing that the reactor with plant and earthen separator provided a remarkable production of electricity (22,6 mW/m^2).

Keywords: microbial fuel cell; constructed wetland; external resistor; separator

Renewable energy systems

ID 006

Seaweed-derived KOH activated biocarbon for electrocatalytic oxygen reduction and supercapacitor applications

Perez-Salcedo, K.Y.[1]; Shi, X.[2]; Kannan, A. M.[2]; Vayssieres, L.[3]; Escobar, B.[1]*

[1] Centro de Investigación Científica de Yucatán. Carretera Sierra Papacal– Chuburná Puerto, Km. 5, Sierra Papacal, Mérida, 97302, México.

[2] Fuel Cell Laboratory, Arizona State University, Mesa, Arizona, 85212, USA

[3] International Research Center for Renewal Energy, Xi'an Jiaotong University. Xi'an, 710049, China.

ABSTRACT

Seaweed blooms have become a serious worldwide environmental, economic and social problem. Reducing the cost of electrodes for electrochemical generation/storage systems is crucial for its commercialization. *Ascophyllum nodosum* grows abundantly in northern oceans, in this study, we evaluate *Ascophyllum nodosum* derived chemically activated biocarbon (AKPH) with potassium hydroxide (KOH) as electrode material for oxygen reduction reaction and supercapacitors. Physical-chemical, morphological and electrochemical characterizations were performed. SEM micrographs revealed the morphology changes in AKPH due to KOH activation. AKPH nitrogen and sulfur contents were 0.80 and 5.62 (wt. %), respectively and it exhibited 1493 $m^2 g^{-1}$ surface area with an I_D/I_G intensity ratio of 1.34 ± 0.01. The electrochemical performance indicates a good performance when compared to commercial platinum, with an onset and half-wave potential of 0.878 and 0.75 V vs. RHE, respectively; and a current density of 5.2 mA cm^{-2}. AKPH exhibited a capacitance of 207.3 F g^{-1} at 0.5 A g^{-1} and good stability after 2,500 cycles at 5 A g^{-1} with a retention capability of 92.3%. This performance turns seaweed in a promising way to synthesize materials for applications in energy conversion and storage field.

Keywords: activated carbon; *Ascophyllum nodosum*; oxygen reduction reaction; capacitance.

ID 007

Electrolyte flow influence analysis in the behaviour of 15 kW alkaline water electrolysis stack

Valeria Juárez Casildo[1,2], Mónica Sánchez Delgado[2*], Rosa de Guadalupe González Huerta[1*]

[1]ESIQIE-IPN, Lab. Electroquímica y Corrosión, UPALM, CP 07738, Ciudad de México

[2]Centro Nacional del Hidrogeno (CNH2), Prolongación Fernando El Santo s/n, 13500 Puertollano, Ciudad Real, España

*Corresponding author: monica.sanchez@cnh2.es; rosgonzalez_h@yahoo.com.mx

---

ABSTRACT

It is well known that a really important problem in electrochemical proceses is the bifasic mixtures generation; when a electric potenitial is induced to an alkaline electrolyzer, the water molecule is broken producing H_2 and O_2, in consequense the electrolyte (KOH) starts moving by natural convection (NC) [1],[2] to a separator vessels where the electrolyte is desgasified.

The gas bubbles act as electrical insulatings, therfore the electrolyte conductivity becomes low and the ohmic resistances increases and a high electric consum. There are diferent ways to eliminate gas bubbles between electrodes, the easier one is pumping the electrolyte. Many estudies has been done in laboratory scale, they found that increasing de recycling flow (forced convection (FC)) improve the electrical eficiency by reducing the voltage consumption. On the other hand, diferent studies has been indicated that increasing flow has a negative efect in the gases purity [3],[4].

In this work, two flow profiles (NC and FC) has been evaluated in a 15 kW alkaline electrolyzer, wich has an active area of 1000 cm^2. In this complex system the CN is equal to 1.7 L/min and it was found that a low current densities becomes unestable increasing the void fraction. Also it has been demostrated that diferent flow values do not has influence in the V-i curve, but it has an impact in the gases difusion wich is stronger at low current densities; HTO (Hydrogen to oxygen) increased from 2.3% to 2.6 % vol and OTH (oxygen to hydrogen) from 0.14% to 0.34%vol. In addition, it has been found that system thermal management was improved by increasing the reciclying flow.

Keywords: Electrolyte flow rate; Energy consumption; Gas purity.

Hydrogen Synthesis from Seawater by Means of Solar Energy

Rafael Garcia Gutierrez[1], Rafael Cabanillas Lopez[2], Ricardo Rodriguez Carbajal[3], Ricardo Rangel Segura[4]

[1]Departamento de Investigación en Física, Universidad de Sonora, Hermosillo, Sonora, 83000, México
[2]Departamento e Ingeniería Química, Universidad de Sonora, Hermosillo, Sonora, 83000, México
[3]Departamento de Ingeniería Química, Universidad de Guanajuato, Guanajuato, Gto., 36000, México
[4]Departamento de Ingeniería Química, UMSNH, Morelia, Mich., 58030, México
*Corresponding author: rgarcia@cifus.uson.mx

ABSTRACT

In the electrolysis of seawater as a source of hydrogen, two options exist for the performance of the electrolysis process. The first option is the total desalination of the sea water and then add alkalis for the process of electrolysis to produce hydrogen in the cathode and oxygen in the anode. The disadvantages of this approach are the high cost of desalination and the water treatment to make it alkaline. The main advantage is the ability to use developed technology for the direct electrolysis of fresh water. The second option is to design an electrolyze system capable of utilizing sea water for direct electrolysis at a low power density and electrolyze only a small portion of the water in contact with the electrodes. The advantage of this method is the lower capital required for the system and natural elimination of the waste brine which is only slightly enriched with salts. Also using this technic is possible to produce important amounts of chlorine as a sub-product and also magnesium and sodium as hydroxides that have many uses in the chemical industry. In this research we produced hydrogen via electrolysis from simply natural resources, seawater and solar energy. In order to carry out this experiment we used water from Bahia of Kino Sonora, a place no too far from the University of Sonora, only 100 kilometers away, and a 100-W solar panel that generate DC electricity using directly sunlight that is an abundant resource in the coasts of Sonora. In this work we have been able to produce about 2 liters of hydrogen per hour and nearly 1.2 liters of chlorine per hour with a normal direct radiation of 900 W/m^2. This technique could be the solution to the fuels problematic of the ethnicities that inhabit the shores of Sonora and other states of México.

Key words: Hydrolysis; Hydrogen; seawater; Solar Energy.

ID 031

Review of environmental policy instruments for the management of hydrogen from community forestry in Mexico

María Liliana Ávalos Rodríguez[1]*, José Juan Alvarado Flores[2], Jorge Víctor Alcaraz Vera[3] and José Guadalupe Rutiaga Quiñones[2]

[1]Center for Research in Environmental Geography, National Autonomous University of Mexico. Former Highway to Pátzcuaro No. 8701, C.P. 58190, Morelia, Michoacán, México. Mail: lic.ambientalista@gmail.com

[2] Faculty of Engineering in Wood Technology, University Michoacana of San Nicolás of Hidalgo. Santiago Tapia 403, CP 58000, Morelia, Michoacán, México.

[3] Institute of Economic and Business Research, University Michoacana of San Nicolás of Hidalgo. Francisco J. Mújica S/N, Col. Felicitas del Rio, C.P. 58000, Morelia, Michoacán, México.

* Corresponding author: lic.ambientalista@gmail

ABSTRACT

The objective of this work is to review the environmental public policy instruments that can allow the management of hydrogen in Mexico, under a community forest management. The literature suggests that the instruments that link this premise can be environmentally planned, economic instruments, self-regulation and environmental audits, environmental impact assessment, Mexican Official Standards (NOM's, by its Spanish acronym), ecological planning of land use, environmental regulation of human settlements, among others. It has been observed that Mexico's energy regulations present great opportunities that can be addressed by a community organization. In the case of Mexico's forests can be through the activities developed from the energy use of forest, agricultural and livestock waste through the use of hydrogen, which would initially meet the energy demand of rural communities. The main findings of this study suggest that, in Mexico, there are environmental and ecological policy instruments that propose corrective rather than preventive actions for environmental balance. In the case of the energy use of waste, great challenges have been observed that are centered on the lack of normative regulation (mainly the lack of a NOM's in the matter of hydrogen and laws of the federal order that promote and sustain it). In addition, there is community resistance to include innovative processes in their organization, despite the existence of environmental policy instruments such as Clean Development Mechanisms (CDM), climate change strategies and environmental self-regulation that may include the use of hydrogen from forest, agricultural and livestock residues. One of the conclusions of this work is the possibility of promoting energy mechanisms in the forest communities of Mexico and proposing the necessary reforms to adjust any economic instrument to the hydrogen economy scheme.

Keywords: Policy instruments; waste; development mechanisms; community organization; forest management.

ID 032

Synthesis of non-stoichiometric copper sulfides $Cu_{2-x}S$ ($1 \leq x \leq 2$) under ambient conditions: mechanochemical reactions in the CuS-Cu_2S system

E.A. Badillo Arroyo, K.P. Padmasree, A.F. Fuentes*

Cinvestav Unidad Saltillo, Parque Industrial Saltillo-Ramos Arizpe, Ramos Arizpe, Coahuila 25900, México

* Corresponding author: 8444389600 antonio.fernandez@cinvestav.edu.mx

---

ABSTRACT

Thermoelectric power generation is considered a clean energy conversion technology for harvesting waste heat into useful electricity. State-of-the-art thermoelectric materials are currently based on different combinations of chemical elements such as Bi, Pb, Te or Se, to mention some; unfortunately, most of these elements are scarce in nature and/or considered harmful to the environment and to human life. Recently, copper sulfide-based materials have been considered like promising thermoelectric materials, because of their physicochemical properties, high abundance and low toxicity. However, solid-state strategies to synthesize these materials are complex because of the difficulties in controlling the oxidations state of copper. In order to explore the possibility of obtaining non-stoichiometric copper sulfides $Cu_{2-x}S$ ($1 \leq x \leq 2$) by using mechanical milling under ambient conditions, we have investigated mechanochemical reactions in the Cu_2S-CuS system. Commercially available chalcocite (Cu_2S) and covellite (CuS) powders as well as different stoichiometric mixtures of both chemicals, were subjected to mechanical milling. The evolution of the starting powders and mixtures with milling time and the final products, were examined by using X-ray diffraction (XRD), chemical and thermal analysis and X-ray photoelectron spectroscopy (XPS). The results showed that milling Cu_2S produced a polymorphic transformation to metastable chalcocite-Q; whereas, no changes were evident in the XRD pattern of CuS. As for the mixtures, those rich in chalcocite (more than 50 wt%) yielded mostly a crystalline product with an XRD pattern similar to that reported in the literature for digenite (Cu_9S_5), admixed with a small fraction of amorphous material; by contrast, mixtures rich in covellite yield a mixture of different non-stoichiometric sulfides and excess CuS. Thermal analysis results showed that on heating in air, these reacted powders are stable only up to 250°C and either decompose or react with atmospheric oxygen, at higher temperatures. XPS analysis showed that milling in air does not introduce new chemical species in the surface of the particles, but for those already present in the starting chemicals or the reaction products. Therefore, we believe that the proposed methodology might be a useful powder processing method, to obtain non-stoichiometric sulfides, with mixed oxidation states Cu^+/Cu^{2+}.

Keywords: copper sulfide; mechanical milling; thermoelectric material; thermoelectric power generation.

ID 033

Dye-Sensitized Solar Cells - Comparative Study of Sensitizers and Co-Sensitizer Effects of a New Tetrazole Derivative

L. da Silva[1*], R. Benavides[1], D. Morales-Acosta[1], H. S. Freeman[2]

[1]Centro de Investigacion en Quımica Aplicada, Blvd. Enrique Reyna H. 140, Saltillo, 25294, Mexico.

[2]Fiber and Polymer Science Program, North Carolina State University, USA

*Corresponding author: luciano.dasilva@ciqa.edu.mx

ABSTRACT

Dye-sensitized solar cell (DSSC) is a semiconductor photovoltaic device that directly converts solar radiation into electric current. A typical DSSC consists of a mesoporous photoanode with a dye-sensitized titanium dioxide (TiO_2) film, an electrolyte containing iodide/triiodide (I^{-1}/I_3^{-1}) redox couple, and a counter electrode with platinum (Pt) catalyst. Upon the absorption of light energy, a photo-excited electron is injected from the excited state of the dye (Dye*) into the conduction band of the TiO_2. However, the immobilization of the adsorbing dye molecules onto the surface of semiconducting metal oxide nanoparticles is crucial for initiating an electrical current, via the injection of electrons, which collectively act as the working electrode of a DSSC. Herein we report the synthesis, characterization and evaluation of the compound N,N-diethyl-4-{[(4'-nitro-2'-tetrazoyl)phenyl] diazenyl}aniline (**SD-1**). This dye was incorporated into DSSCs as sensitizer and a co-sensitizer with **HD-2** dye, to prepare the photoanode for a dye-sensitized solar cell (DSSC). **HD-2** is a dye described by H. Chemma et al. and is considered as an efficient sensitizer based on benzodioxan-stilbazole ancillary ligand. The photovoltaic performance was evaluated and compared with the co-sensitizer deoxycholic acid (**DCA**). The energy conversion efficiency of the DSSC was 8.38 % from **HD-2 – DCA**, 7.81% from **HD-2 – SD-1**, and 1.32% from **SD-1 – DCA**. The latter results suggest that steric effects restrict the anchoring ability of the tetrazole groups, by hindering their approach to TiO_2 surface and by restricting the coplanarity of the system. However, this effect is not significantly important when the **SD-1** is used as co-sensitizer for **HD-2**, which showed similar conversion efficiency as the **DCA**.

***Keywords*:** Tetrazole; solid electrolytes; sensitizers; co-sensitizer; dye-sensitized solar cell.

ID 048

Genetic mutations in the hydrogenase gene, cause differential regulation and variations in the production of molecular hydrogen in *Scenedesmus obliquus* and *Chlorella vulgaris*

Tamayo-Ordoñez Y.J.[1], Ayíl-Gutierrez B.A.[2], Ruiz-Marin A.[3], Tamayo-Ordoñez F.A.[3], Moreno-Davila I.M.M.[1], Rios-Gonzalez L.J.[1], De la Cruz-Arguijo E.A.[4], Tamayo-Ordoñez M.C.[1*]

[1]Facultad de Química de la Universidad Autónoma de Coahuila. Saltillo, Coah. México
[2]CONACYT- Centro de Biotecnología Genómica-IPN, Reynosa, México.
[3]Facultad de Química, Dependencia Académica de Ciencias Química y Petrolera, UNACAR, Carmen, México
[4]Centro de Biotecnología Genómica-IPN, Reynosa, México
*Corresponding author: mtamayo@uadec.edu.mx

ABSTRACT

Research related to the production of molecular hydrogen is a reality today, and algae have proven to be good biological models to produce different compounds of interest. In this project, we analyze how genetic variations in hydrogenase genes can affect the production of molecular hydrogen in two algae (*C. vulgaris* and *S. obliquuos*). The results obtained indicated that light quality is an important factor in achieving better levels of molecular hydrogen. The microalgae were immobilized and cultivated in urban wastewater to produce biohydrogen by deprivation of sulfur and two light qualities. The results indicated that blue light helps better algae growth compared to purple light. A maximum hydrogen production of 119 ml H2 L^{-1} and 55 ml H2 L^{-1} was reached for *S. obliquus* and *C. vulgaris*, respectively. The isolation and characterization of the *S. obliquus* and *C. vulgaris* hydrogenase gene, by means of PCR, allowed the in-silico 3D modeling of the hydrogenase proteins and their comparison with other algae genera. The 3D structure of hydrogenases indicated structural differences. The accessions of *Thalassiosira*, *Monoraphidium*, *Cocomyxa*, *Volvox* and *Nanochloropsis* indicated differences in 3D structure, when compared with the three-dimensional conformation of *S. obliquus* and *C. vulgaris*. For its part, the phylogenetic analysis indicated that it is not genetically related to *Coccomyxa* and N*anochloropsis*. These genetic differences can affect the levels of hydrogen production in the algae studied.

Keywords: microalgae; hydrogenase gene; molecular hydrogen; mutation

ID 080

Sustainability Criteria for Systems with Hydrogen Energy Storage Devices located in Mexico

Paola Andrea Urbano Arcila[1]*, Orlando Lastres Danguillecourt[2], Geovanni Hernández Galvez[3], Guillermo Rogelio Ibáñez Duharte[2], Jesús Antonio Enríquez Santiago[1]

[1]PhD. Candidate in the Universidad de Ciencias y Artes de Chiapas (UNICACH). Libramiento Norte Poniente 1150, Colonia Lajas Maciel C.P. 29039 Tuxtla Gutiérrez, Chiapas, México.
[2] PhD. Professor and researcher in the Universidad de Ciencias y Artes de Chiapas (UNICACH). Libramiento Norte Poniente 1150, Colonia Lajas Maciel C.P. 29039 Tuxtla Gutiérrez, Chiapas, México.
[3]PhD. Professor and researcher in the Universidad Popular de la Chontalpa. Carretera Cárdenas-Huimanguillo. Ranchería Paso y Playa, C. P. 86500 Heroica Cárdenas, Tabasco, México.
*Corresponding author: rosgonzalez_h@yahoo.com.mx; paolaurbano@hotmail.com

---

ABSTRACT

Sustainable development is one of the common objectives of almost all Nations, as well as the energy security and the access to this basic service for everyone. Renewable energy systems have different characteristics which put them closer to the sustainability objectives than the traditional energy generation systems, mainly in remote areas far from the national electric energy network. Isolated systems require a storage component. Battery banks have been mainly used, and less frequently the hydrogen storage systems (HSS). Most of the literature and researches have been developed in Europe, Asia, and North America. Every single location has different social, economic, and environmental characteristics, among others. That is why it is important to analyze those conditions for a Latin-American project site. Taking in account the criteria used in similar studies in other latitudes as well as the sustainable development criteria formulated for Latin America, particularly in Mexico; the analysis, selection and estimation of the sustainable criteria was carried out; This in order to include sustainability criteria in the traditional economic optimizations of isolated systems with a HSS.

This paper presents a comparison between the most common used values for some sustainable criteria for both energy storage technologies: Battery banks and HSS; which would be used later for a multicriteria analysis process to design and optimize a sustainable and renewable energy system with a storage component, principally for the electrification of remote communities. The obtained results allow to obtain solid and sufficient arguments to promote the hydrogen storage technologies application, highlighting its economic, operational and environmental advantages, mainly for the isolated systems.

Keywords: Hydrogen storage; sustainability criteria; renewable energy systems.

ID 081

Influence on the Performance of the Counter Electrode by Varying the Deposit Materials in the Application of Sensitized Solar Cells

J.R. Ramos Nava[1]*; W.J. Pech Rodríguez[1]; E.N. Armendáriz Mireles[1].

[1]1 Universidad Politécnica de Victoria, Parque Científico y Tecnológico de Tamaulipas, Ciudad Victoria, Tamaulipas 87138, México.

*Corresponding author: 831-113-9630 Email: 1430543@upv.edu.mx

---

ABSTRACT

In the present research work, the optimization of the counter electrode of the solar cell sensitized by dye was carried out by varying the electrocatalyst by depositing it by the screen-printing method. The electrodes obtained were characterized by means of electrochemical tests. Electrochemical studies showed that the electrodes composed of carbon and silver have a favorable reaction mechanism to carry out the ion collection and ion reduction processes of Iodo. From the VI curves, it was possible to demonstrate that the current density and the open circuit potential depend to a great extent on the material deposited on the conductive glasses. It is concluded that carbon and silver composite counter electrodes are a viable option since the production cost of the cell can be reduced without compromising its efficiency.

Keywords: DSSC; Curve V-I; screen-printing.

ID 089

Economic and Technological Strategy of the Dual Combustion of Hydrogen and Gas L.P in Steam Generators

Guadalupe Juliana Gutiérrez- Paredes [1*], Juan Manuel Sandoval-Pineda[1], Mariana Amador-Contreras[1], Froylán Soriano- Moranchel[1], Artemio García -Flores[2]

[1]Instituto Politécnico Nacional, Sección de Estudios de Posgrado e Investigación, ESIME Azcapotzalco, Av. de las Granjas 682, Col. Santa Catarina, C.P. 02250, CDMX, [2] Energika Group S.A. de C.V.

*Corresponding author: julygp04@yahoo.com.mx

ABSTRACT

The energy needs of our country have prompted the creation of new technological and economic strategies, especially in competitive industrial sectors, such as the steam generation, which daily demands high amounts of fóssil fuel for its production. This work presents a market study carried out on 255 companies, from which derived an economic and technological strategy for the dual combustion of hydrogen and gas L.P. The economic results obtained from the companies surveyed have shown that this technology considerably reduces annual costs, in addition to other relevant benefits such as greater energy potential and less emissions to the atmosphere, compared to conventional technologies.

Keywords: *Dual combustion; Hydrogen; Gas L.P; Steam generator; Economical; Technological*

Full Papers

Hydrogen production, storage and applications

Offshore Wind Power for Hydrogen Production, General Status

Malinalli Pérez-Vigueras[1*], Rosa Gonález-Huerta[1], Rogelio Sotelo-Boyas[2.]

[1]Instituto Politécnico Nacional-ESFM. Departamento de Energía. UPALM, CP 07738, Ciudad de México.
[2]Instituto Politécnico Nacional-ESIQIE. Laboratorio de Electroquímica. UPALM, CP 07738, Ciudad de México
[2]Instituto Politécnico Nacional-ESIQIE. Departamento de Ingeniería Química Petrolera. UPALM, CP 07738, Ciudad de México
* Corresponding author: malinallipv@gmail.com

ABSTRACT

World energy consumption is forecast to increase exponentially in the coming decades, driven by rising living standards and population growth worldwide. Therefore, the growing need for more energy will require enormous development in the generation of energy and more secure and diversified energy sources. Because of the distance between the parks and the coast (> 10 km), most of the time a cable is expensive and generates ecological damage, this project proposes the use of offshore wind energy for hydrogen production used electrolysis.
A review of the general state was carried out of offshore wind energy considering the technological factors, supply and characteristics of the best offshore wind farms. A description of the situation in Mexico is presented in terms of offshore electricity, areas of opportunity and technological, environmental, social and regulatory gaps are analyzed.

Keywords: Offshore; wind energy; hydrogen; renewable energies.

1. Introduction

The need for a sustainable energy supply is becoming increasingly important in view of declining fossil energy resources, environmental pollution, climate change and dependence of fossil fuel exporting countries. In this context, the development of renewable energies, especially those dedicated to electricity generation, has been extensive in recent years. Similarly, developing countries such as Mexico face difficulties with respect to climate conditions induced by climate change [1]. The results of floods and drought have affected economic growth and agricultural production. With regard to the energy crisis, hydrogen can play a vital role in the future and also minimize the effect of greenhouse gases (GHG) that generally affect the entire planet. Hydrogen as a fuel has great potential to significantly reduce GHG emissions and urban pollution, as well as being used in conjunction with natural

gas in private homes and is also a key industrial raw material. It can be used as a CO_2 neutral reducing agent to replace coke in steel production, which is more sustainable and advanced than conventional models [2].

Fuel cells are currently an expensive technology, but with the advancement of research and development they are expected to become affordable. Hydrogen fuel cells are expected to gradually replace fossil fuel vehicles as hydrocarbons reach a depletion stage.

Hydrogen production can be achieved using different renewable energy sources, including wind energy, solar energy, geothermal energy, and biomass. Above all other renewable energy sources, the production of hydrogen through electricity generated by wind is considered the simplest and cleanest approach. Hydrogen production through the use of wind energy in the electrolysis process is currently considered to produce the lowest GHG emissions of all hydrogen production sources. Furthermore, wind-generated electricity has the lowest cost per kWh of all renewable resources electricity generation [3]. Numerous studies have been conducted in the literature on hydrogen production using wind-generated electricity in different countries.

Different authors have identified that wind, solar energy and biomass [4,5] are the three most important renewable sources for the production of hydrogen. H_2 production systems based on terrestrial wind energy as the main source have been evaluated in the literature [6].

The performance of a wind turbine, and consequently the economic profitability of the investment project in which it is applied, largely depends on the proper selection of the technical characteristics of the machine according to the wind regime of the site where it is applied, as established by the IEC 61400-1 standard. Poor selection results in lower yields, higher maintenance costs, and a shorter lifespan. This points to the need to know very well the characteristics of the wind at the site of interest, which requires measurements of basic parameters such as wind speed and direction, as well as ambient temperature and atmospheric pressure [8]. On the other hand, offshore wind energy has great advantages in terms of speed compared to onshore wind, in onshore wind farms the speed at the tip of the blade is limited to 65 m / s, while in offshore it can go up to 90 m / s in the two blades and 75 m / s in the three blades, so the productivity of the turbine is higher. The global capacity of offshore wind energy is shown in Figure 1, the three countries with the most generated capacity are: the United Kingdom with a capacity of (8300 MW), then Germany (6417 MW) and China (4588 MW), for the year 2018. In figure (b), it can be seen that the trend of offshore wind generation is increasing rapidly with the contribution of generous amounts of MW in the coming years.

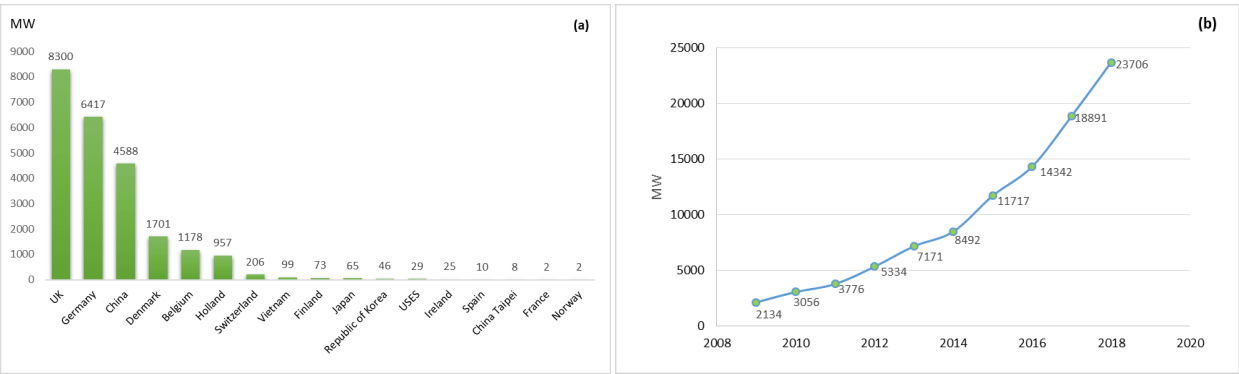

Fig. 1. Global capacity for offshore wind energy. (a) Capacity of the countries that develop offshore wind energy in 2018; (b) Global offshore wind power capacity trend.

The following sections explain why installing offshore wind farms is feasible:

- Wind speed is higher in the open sea than on land at the same height. Due to the smoothness of the ocean surface, low surface roughness and low turbulence intensity are generated. Therefore, higher wind speeds (80 to 90 m/s) are achieved at a lower height than on land (65 m/s).
- The reduction in tower height significantly reduces costs, on the other hand, the installation costs at sea are higher, although these expenses can be offset due to the increase in energy during the useful life of the park and the profits generated.
- Extensive turbine life and minimal damage from exhaustion. As a consequence of the low surface roughness and the lower vertical temperature gradient that is generated in the sea.
- Less environmental impact than onshore wind, offshore wind energy reduces the visual and acoustic impact compared to onshore wind farms.
- There is no need for land tenure or space limitations.
- Higher plant factor, this means longer operating hours than onshore wind.

In reality, the offshore wind field model is very similar to the onshore one, what essentially differentiates them is the material used for the offshore, since it requires anti-corrosive equipment and the nacelle is hermetic, unlike the onshore one that interacts with the environment, and finally the power line that would reach the earthly area.

The objective of this study is to focus on describing the general state of renewable hydrogen generation through the use of offshore wind energy. A review of the general state was carried out of offshore wind energy considering the technological factors, supply and characteristics of the best offshore wind farms. A description of the situation in Mexico is presented in terms of offshore electricity, areas of opportunity and technological, environmental, social and regulatory gaps are analyzed. The study provides valuable information for policy and decision-makers.

2. Materials and Methods

To meet the stated objective, the present study is an inductive method investigation, the method is a documentary investigation. The information necessary to carry out the research is from printed and electronic bibliographic sources (articles, research, publications, databases, etc.), as well as consultations with experts on the subject.

3. Results and Discussion

Table 1 below shows the largest wind farms in the world (from highest to lowest capacity), as well as their location and main characteristics in 2018 [9]. This table highlights the offshore wind farms in the United Kingdom and Germany. The capacity of the largest current commercial turbines is 7 MW (154 m in diameter), the maximum existing turbine capacity is 8.8 MW (164 m in diameter) and it is expected that concepts of 10, 12 and 15 MW will be further developed. . The table does not show the depth distances of the facilities, they can be in shallow water (from 1 to 10m) or with a depth of up to 45m.

Table 1. The world's largest offshore wind farms today.

Offshore wind farm	Country	Year opened	Total capacity	No. Of turbines	Capacity of each turbine	Technology	Distance from the coast	Area occupied by the park
Walney Extension	UK	2018	659 MW	87	40 of 8.25MW & 47 of 7MW	MHI-Vestas de Siemens Gamesa	14 km	73 km²
London Array	UK	2013	630 MW	175	3.6 MW	Siemens	20 km	100 km²
Gemini Wind Farm.	Holland	2017	600 MW	150	4 MW	Siemens SWT-4.0		
Gode Wind 1&2	Germany		582 MW	154	6 MW	Siemens	12 km	
Gwynt y Môr	UK		576 MW	160	3.6 MW			80 km²
Race Bank	UK	2018	573 MW	91	6 MW	Siemens	28 km	
Greater Gabbard	UK		504 MW	140	3.6 MW	Siemens	25 km	

Currently, offshore wind farm projects are being developed and are planned to be inaugurated in the coming years. The size of the capacity they will generate consists of 1,386 MW in the United Kingdom and in other European countries such as Germany and Denmark, between 100 to 800 MW, in total there are 16 projects that will be developed in Europe using offshore wind energy [10]. The average development time of an offshore wind farm ranges

from 3 to 10 years. And the process that takes the longest is the foundation for each offshore wind turbine.

According to the information consulted, the following Table 2 shows the commercial supply chain by different sector used in offshore wind farm facilities.

Table 2. Supply chain for offshore wind energy.

Supply chain	Company	Supply chain	Company
Developers	Orsted (antes Dong Energy) E.ON Vattenfall, Suecia Innogy (antes RWE), Alemania Iberdrola/ScotishPower Inversores	Foundations and substations	Astilleros
Turbine manufacturers	Siemens-Gamesa MHI Vestas GE (Alstom) Senvion Ming Yang Sewind	Installation Boat Owners	SeaJacks SeaFox Fred Olsen MPI
Cable manufacturers	Prysmain Nexans JDR NKT	Wind energy equipment maintenance suppliers	GE Power & Water Renewable Energy Wind farm maintenance services ExxonMobil Fuels & Lubricants The Energy Research Center of the Netherlands Renewable Energy Solutions AEROGIDS. Predictive maintenance in wind turbines Global Energy Services - SIEMSA Offshore wind minivets Resanic solutions at height Availon United Wind Service Gamesa SIEMENS SURESPAN wind energy services
Offshore installers	DEME Van Oord Boskalis Jan de Nul SHL Heerema		

Regarding the technological situation, some factors such as transmission, foundations, park installation devices and operation and maintenance are presented in Table 3 as the best available options and future developments. In the foundations section, the percentages are

presented in terms of the foundations most used in offshore wind farms. It should be noted that currently the installation boats are subject to the availability of other energy sectors such as the oil industry.

Table 3. Technology situation in offshore wind farms

	Technology
Transmission	Alternating current mainly Direct current developing
Foundations	Mono-polites, 82% Jackets, 7% Base Gravity, 6% Floating: not yet large-scale, but potentially future
Installation Boat Fleet	Jack-ups with cranes of more than 1500t specialized DP2 floats, versatile with O&G and begin to have specialized for the industry CTVs (Crew Transfer Vessels), specific for the industry
Operation and maintenance	Mainly with daily CTVs Flotels begin to develop

3.1 Offshore Wind Energy In Mexico

Mexico does not have its own technology in terms of wind energy. Only some links in the value chain have been established in the country, such as those for civil and electrical works, logistics for the transportation of components, and the manufacture of some components such as metal towers, electrical transformers for export, and assembly of blades and electric generators of permanent magnets. The wind power plants built so far, as well as those that are in different stages of development in this country, use imported wind turbines. These elements represent about 75% of the cost of a plant of this type, and manufacturing in its place of origin represents the creation of a large number of jobs [11]. However, Mexico has the potential to include offshore wind energy in its energy matrix.

The two marine regions that guard the Mexican country are: that of the Mexican Pacific, including the gulfs of California and Tehuantepec, and that of the Atlantic, with the Gulf of Mexico and the Caribbean Sea. Mexico has 11,122 km of coastline. Less than half the length of the coast is suitable for installing wind farms, according to the National Atlas of Areas with High Potential for Clean Energies (AZEL) and the World High Wind Power [12,13]. Without considering the environmental interest, marine transit, or areas of fishing use. The locations with high potential are the Yucatan peninsula, the coast of Tamaulipas, Baja California with average wind speeds of 8 m/s and Oaxaca up to 10 m/s based on information from the World Bank Group [14].

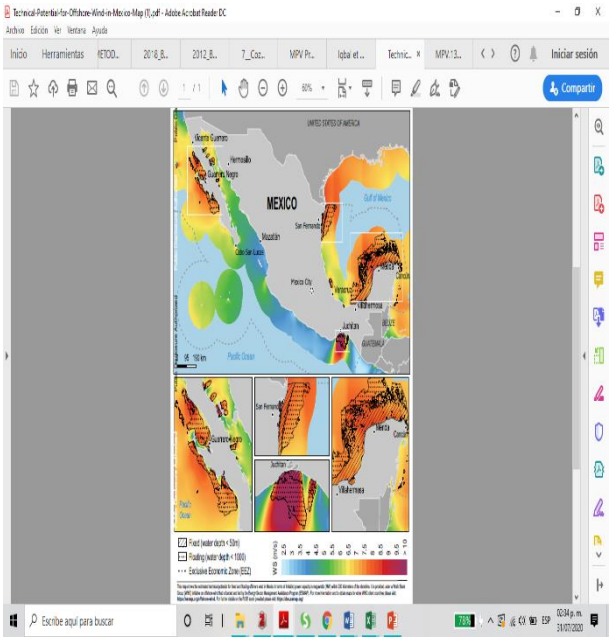

Fig. 2. Offshore wind technical potencial in Mexico.

In Mexico there are no regulations for the generation of offshore wind energy, therefore it is necessary to develop laws and regulations as the main basis for the development of offshore wind farms. Having the right legislature is the beginning of any energy development, since it controls and prevents abuses and economic, social and environmental damages. The challenges that Mexico presents are based on technological gaps, since it is necessary to have turbines designed for the specific weather conditions either on the coast of Tamaulipas, Oaxaca, Baja California or on the Yucatan peninsula, in addition to conditioning them for extreme circumstances in the event of hurricanes.

It should be noted that conducting social and environmental impact studies are of utmost importance to avoid affecting marine fauna and thereby make appropriate decisions.

On the other hand, transmission to the electrical network is another important factor, due to the intermittent energy and the distance from transmission to the electrical network. A good option would be energy storage. An advantage is that Mexico has ports along the Gulf of Mexico, there are also ships used in the oil industry, which would facilitate operation and maintenance. Also the oil industry has experience in platforms.

3.2 Platforms or artificial islands to produce hydrogen near offshore wind farms

The development of this concept could produce quantities of hydrogen on an industrial scale from the electricity available at the site. It also provides alternatives to contentious or overloaded cable lines, at sea or on land. Furthermore, gas could easily be stored and transported by ship or pipeline to where it is needed. H_2 as an efficient means of energy storage can balance seasonal fluctuations in renewable energy sources. Regardless of whether electrolyzers are installed on reused oil rigs, new hydrogen rigs or artificial islands are highly dependent on site conditions.

An increasing number of organizations have announced that they intend to turn this vision into action such as Engineering firm Tractebel introduced a new offshore platform design to produce hydrogen in the ocean in January 2020. Which plans to be implemented in 2025 and will have a capacity of 400 MW, H_2 production: 80,000 m^3/h and water will be supplied from a desalination plant: 125 m^3 every hour. Figure 3 shows the design of an offshore platform presented by Tractebel Overdick and Tractebel Engineering, two engineering and service firms owned by French energy provider ENGIE.

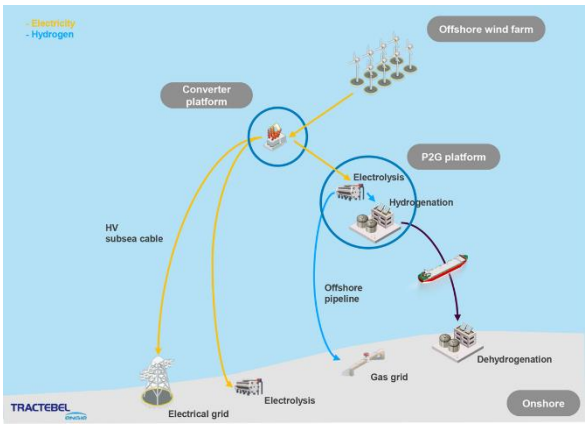

Fig. 3. Offshore hydrogen platform

In 2019 during the UN Conference on Climate Change held in Madrid, the Danish Minister for Climate and Energy, Dan Jørgensen, described the plans to build an artificial island for electrolysers in the North Sea. Which is planned to be operational by 2030, with an expected capacity of 10 at a cost of between 27,000 to 40,000 million euros. Tennet presented the feasibility study on behalf of the North Sea Wind Power Hub, to discuss this new concept. Its construction would take around eight years. Electrolyzers could be installed on sand islands, Caisson islands or those that use a gravity-based structure as the base.

4. Conclusion

The potential for renewable hydrogen generation through offshore wind power could reduce the energy deficit in a developing country like Mexico and ensure a sustainable energy supply. It is essential to consider offshore wind energy, as the trend in the future is increasing, and Mexico has a great capacity for using this energy. In general, an adequate strategy for technological development in offshore wind energy is required in Mexico. Regulations and a framework of rules are also required for the participation of the public and private sectors. On the other hand, the experience for generation displacement in small and large scale offshore wind farms is also an important factor.

Acknowledgements

The authors acknowledge the financial support from IPN multidisciplinary project SIP-2024 (2019-2020) and CONACYT: CEMIE-Ocean project 249795: Transversal Line I-LT1 and

Basic Science Project A1-S-15770. Malinalli Pérez Vigueras thanks the scholarship granted by CONACYT-Mexico.

References

[1] Ali, A.; Rahut, D.B.; Mottaleb, K.A.; Erenstein, O. Impacts of changing weather patterns on smallholder well-being. Int. J. Clim. Chang. Strateg. Manag. 2017, 9, 225–240.
[2] Uyar, T.S.; Be¸sikci, D. Integration of hydrogen energy systems into renewable energy systems for better design of 100% renewable energy communities. Int. J. Hydrogen Energy 2017, 42, 2453–2456.
[3] Gondal, I.A.; Masood, S.A.; Khan, R. Green hydrogen production potential for developing a hydrogen economy in Pakistan. Int. J. Hydrogen Energy. 2018, 43, 6011–6039.
[4] Ghandehariun Samane y Kumar Amit. Life cycle assessment of wind-based hydrogen production in Western Canada. International Journal of Hydrogen Energy. 2016, Volume 41, Issue 22, Pages 9696-9704, ISSN 0360-3199.
[5] Chi Jun & Yu Hongmei. Water electrolysis based on renewable energy for hydrogen production. Chinese Journal of Catalysis. 2018, Volume 39, Issue 3, Pages 390-394, ISSN 1872-2067. https://doi.org/10.1016/S1872-2067(17)62949-8.
[6] Mohsin M., Rasheed A.K., Saidur R. Economic viability and production capacity of wind generated renewable hydrogen. International Journal of Hydrogen Energy. 2018, Volume 43, Issue 5. Pages 2621-2630. ISSN 0360-3199
[7] International Renewable Energy Agency (IRENA). Renewable capacity statistics, Abu Dhabi, www.irena.org; 2019.
[8] Carta-Gonzalez J.A., Calero-Perez R., Colmenar-Santos A. & Castro-Gil M.A. Energía Eólica. En Centrales de Energías Renovables: Generación eléctrica con energías renovables. Madrid, España: Pearson Education, S.A.. 2009, pag 397-405.
[9] Roca, J. Los 10 mayores parques eólicos marinos del mundo: Walney Extension da un vuelco a la clasificación, https://elperiodicodelaenergia.com/los-10-mayores-parques-eolicos-marinos-del-mundo/ [accessed 13.03.19]
[10] Arantegui L., Roberto y Yutsa J.M. & Domínguez J. Offshore wind installation: Analysing the evidence behind improvements in installation time. Renewable and Sustainable Energy Reviews. 2018, Volume 92, Pag. 133-145.
[11] Huacuz, J. Energía Eólica. En Actualización del Programa de Investigación y Desarrollo Tecnológico en Sustentabilidad Energética. 2012, pag.113-119.
[12] Inventario Nacional de Energías Limpias (INEL), https://dgel.energia.gob.mx/INEL/mapa.html?lang=es#; 2019 [accessed 03.05.20]
[13] Atlas Nacional de Zonas con Alto Potencial de Energías Limpias (AZEL), https://dgel.energia.gob.mx/AZEL/mapa.html?lang=es, 2019 [accessed 03.03.19]
[14] Offshore Wind Technical Potential, https://energydata.info/dataset/offshore-wind-technical-potential, 2020 [accessed 01.07.20]

ID 023

Mixed Iron Oxides as Materials for Hydrogen Production: Thermochemical Cycles Studies

Lorenzo Antonio Cruz Santiago[1*], Ana Lidia Martínez Salazar[1], Benjamín Portales Martínez[2], Ana Adela Lemus Santana[2], Edilso Francisco Reguera Ruíz[2]

[1]Centro de Investigación en Petroquímica, Instituto Tecnológico de Ciudad Madero, Tamaulipas, México.
[2]Laboratorio Nacional de Conversión y Almacenamiento de Energía, Centro de Investigación en Ciencia Aplicada y Tecnología Avanzada - Unidad Legaría, IPN, CDMX, México.
*lacrus8@gmail.com

ABSTRACT

Mixed iron oxides are materials with great potential for two-step thermochemical cycles since these oxides contain divalent cations that confer the possibility of reducing the working temperatures of cycles. Two−step thermochemical processes are promising technologies for hydrogen production. In these processes, the first step is the endothermic reduction of a metal oxide at elevated temperatures by oxygen release, the second step corresponds to exothermic oxidation of reduced metal oxide at lower temperatures by taking oxygen from water and producing hydrogen via water−splitting reaction. In this work, $[Zn_xFe(III)_{1-x}]_{tet}[Mg_yFe(II)_{1-x-y}Fe(III)_{1+x}]_{oct}O_4^{2-}$ systems were synthesized through coprecipitation route. The $Zn(NO_3)_2$, $MgCl_2$, $Fe(NH_4)_2(SO_4)_2$ and $FeCl_3$ precursors at several ratios were mixed with constant stirring until homogenization was achieved. NaOH was used as a precipitating agent. The samples were characterized by thermogravimetric analysis and X−ray diffraction. Thermochemical studies were performed by thermogravimetry from room temperature to 1000 °C. Magnesium ferrite presented the highest loss mass (approximately 16%). X−ray patterns, reveal incremented zinc−magnesium ions insertion into magnetite structure as zinc−magnesium relative concentration increases, particularly in the plane (311). Powder patterns refinements of FZM2 samples were performed to evaluate the experimental lattice parameter and crystallite size. The characterization of these materials provides relevant information for its possible application in two−step thermochemical cycles in order to hydrogen production.

Keywords: mixed iron oxides; coprecipitation; two-step thermochemical cycles; powder pattern refinement

1. Introduction

Iron oxides are materials of great variety and commercial value, and within iron oxides classification is magnetite, which is an inverse spinel with structural formula $Fe(III)_{tet}[Fe(II)Fe(III)]_{oct}O_4^{2-}$. The general formula for spinel mineral is AB_2O_4 where A and B represent divalent and trivalent metallic cations, respectively. The spinel−type structure contains all divalent cations on tetrahedral sites and all trivalent cations on octahedral sites. In the inverse spinel structure, octahedral sites are occupied by divalent and trivalent cations [1]. Magnetite can be transformed into a mixed iron oxide MFe_2O_4, where M is divalent metal (i.e. Zn and Mg). Mixed iron oxides attract considerable interest as materials for potential applications in different fields.

An important application field where mixed iron oxides has been used as reference material is two-step thermochemical processes, which are promising technologies for the production of hydrogen. These processes involve the following stages [2]:

(1) Activation; in this step, the material is subjected to an endothermic reduction at elevated temperatures releasing oxygen.

$$MOn+heat \longrightarrow MOn\text{-}x+n2\ O2$$

(2) Hydrolysis; reduced material is reacted with water to reoxidize by taking oxygen from the water producing hydrogen by water−splitting.

$$MOn\text{-}x+xH2Og \longrightarrow MOn+xH2$$

where MO_{n-x} and MO_n denote reduction and oxidation states respectively.

Iron oxides systems have been evaluated in this type of process, where the activation temperature necessary for the reduction step exceeds 1500 °C causing material deactivation after several cycles. Mixed iron oxides show changes in activation temperature concerning conventional iron oxides and, therefore, allow better control reaction parameters. Some of the metals employed in mixed iron oxides are Mn, Co, Ni, and Zn, which in the last decade have been a topic of interest [3]. In order to evaluate mixed iron oxides in two-step thermochemical cycles, characterizations were performed on magnetite and zinc-magnesium ferrites. Samples' mass losses from room temperature to 1000 °C were analyzed, as well as the structural changes on the proposed materials.

2. Materials and Methods

2.1 Procedure

To prepare mixed iron oxides particles added 20 ml of $Fe(NH_4)_2(SO_4)_2 \cdot 6H_2O$ solution 0.2 M to 20 ml of $FeCl_3 \cdot 6H_2O$ solution 0.4 M and stir the solution continuously at 45 °C till complete dissolution is achieved. Then add 20 ml of sodium hydroxide solution 2 M drop by drop and allow the reaction to occur for around 120 minutes at 55 °C under constant stir. The resulting particles were then washed three times with deionized water. The precipitates were allowed to air dry and dried particles were ground in a mortar. For the preparation of zinc−magnesium ferrite particles, the above procedure is replicated by stoichiometrically replacing the Fe(II) precursor with $Zn(NO_3)_2 \cdot 6H_2O$ and $MgCl_2 \cdot 6H_2O$ according to following formula: $[Zn_xFe(III)_{1-x}]_{tet}[Mg_yFe(II)_{1-x-y}Fe(III)_{1+x}]_{oct}O_4^{2-}$. The x and y values for each sample are presented in the **Table 1**.

Table 1. x and y values for mixed iron oxides samples.

Sample	x = Zn	y = Mg	Zn [M]	Mg [M]	Fe(II) [M]	Fe(III) [M]
FZM0	0.00	0.00	0.00	0.00	0.20	0.40
FZM1	0.50	0.00	0.10	0.00	0.10	0.40
FZM2	0.00	0.50	0.00	0.10	0.10	0.40
FZM3	0.25	0.25	0.05	0.05	0.10	0.40

The general chemical equation for mixed iron oxides synthesis is given by:

$$M2{+}{+}2Fe3{+}{+}8OH{-}\longrightarrow MOH2\cdot 2Fe(OH)3$$

$$MOH2\cdot 2FeOH3\longrightarrow MFe2O4\cdot nH2O+(4-n)H2O$$

where M represents a divalent cation (Zn^{2+} or Mg^{2+}).

2.2 Analysis of samples

Crystalline and phase formation of the samples has been obtained using X-ray diffractograms by Bruker D8 Advance instrument through Cu−Kα1 (1.5406 Å) and Cu−Kα2 (1.5443 Å) radiations at room temperature in 2θ range 10−80°. The thermogravimetric analysis of particles were examined using Perkin Elmer TGA8000 module for TG (30−1000 °C). The heating ramps were at 10 °C/min in an inert atmosphere of N_2.

3. Results and Discussion

3.1 Thermal analysis

TG−DTG was used to determine the samples' mass losses from room temperature to 1000 °C (**Fig. 1**). In thermograms, a first section can be observed from room temperature to 200 °C, which is attributed to physisorbed water release, where the FZM2 sample showing the greatest loss. Chemisorbed water is released in the section that ranges from 200−400 °C. Subsequent mass losses from samples can be attributed to phase changes due to the release of oxygen.

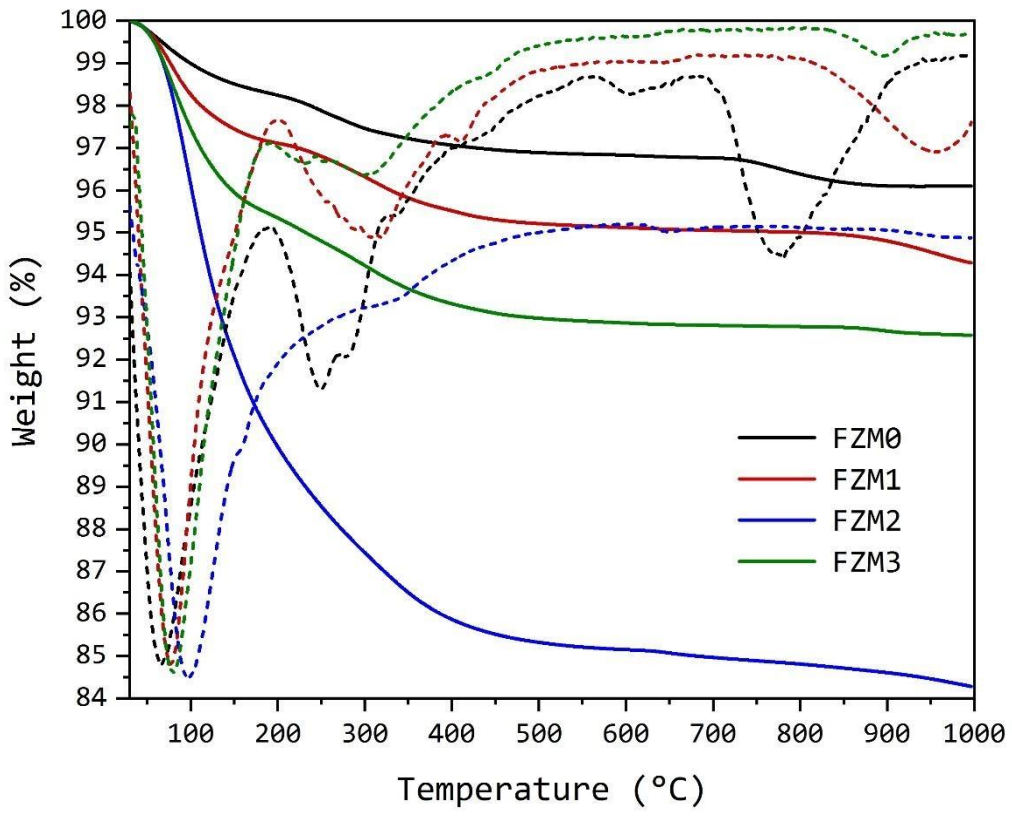

Fig. 1. TG–DTG curves of the samples.
Solid and dotted lines correspond to TG and DTG curves respectively.

3.1 X-ray diffraction

Before thermic treatment, magnetite and, zinc−magnesium ferrites were analyzed by X−ray diffraction and corresponded to a face−centered cubic spinel structure. The XRD patterns of samples are shown in **Fig. 2**. Diffractograms were characterized by several well-defined peaks, the most intense occurs at 2θ = 35.5° (311) [4–6].

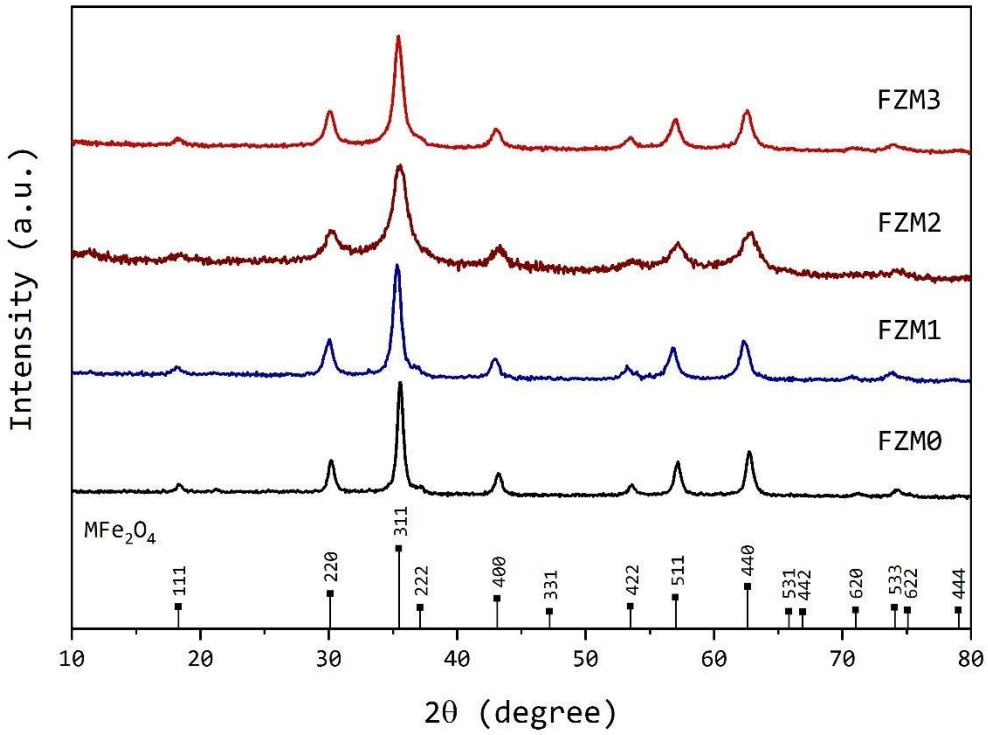

Fig. 2. XRD patterns (Cu−Kα1 radiation) of FZM0 to FZM3 samples before heat treatment. All samples match a spinel-like cubic structure (MFe_2O_4).

At the end of thermal treatment at 1000 °C, the samples were cooled in a nitrogen atmosphere and were subsequently analyzed by X−ray diffraction to verify any phase change. The XRD patterns of samples are shown in **Fig. 3**. In the diffractograms, well−defined peaks for rhombohedral structure of hematite (α−Fe_2O_3) are observed in all the samples [7,8], however, the mixed iron oxides that incorporate zinc and magnesium in their structure present a phase mixture with certain amounts of cubic spinel (MFe_2O_4).

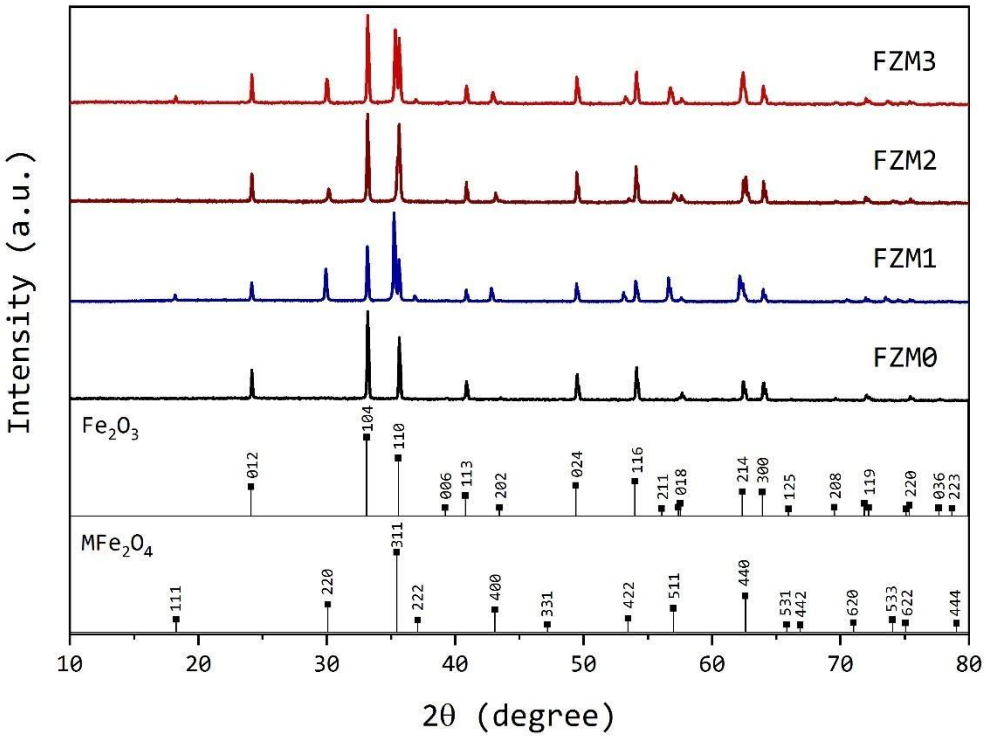

Fig. 3. XRD patterns (Cu−Kα1−Kα2 radiations) of FZM0 to FZM3 samples after heat treatment. A phase mixture is observed in mixed iron oxides (α−Fe_2O_3 and MFe_2O_4).

Considering that the FZM2 sample shows the greatest mass loss, a diffraction patterns refinement was carried out to analyze the structure and crystallite size of the oxides before and after the heat treatment. Refinement was performed using FullPROF program and results are illustrated in **Fig. 4**. A Thomson−Cox−Hastings pseudo−Voigt function was used to model peak profile, suitably reproducing the observed reflections. Refinement was continued until convergence with a good fit parameter (χ^2) around 1.0, and likewise, the residuals were used as fit quality numerical criteria on the diffraction pattern (**Table 2**) [9].

FZM2 sample increases on average 10 times crystallite size due to the increase in temperature. Phases mixture is due to that within the oxide structure there are Fe(II) ions that pass to Fe(III) causing the appearance of the α−Fe_2O_3 phase.

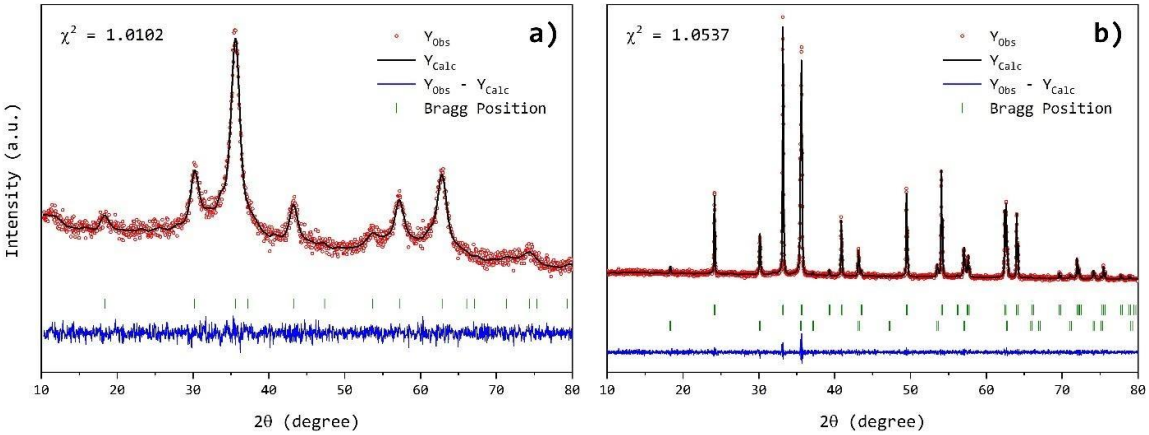

Fig. 4. Refined X-ray diffraction patterns of FZM2 sample: a) before and, b) after heat treatment.

After heat treatment, the majority phase is $\alpha-Fe_2O_3$ with 71.26% and mass loss can be explained through surface oxygen release in the plane (111) which are bound to Fe(III) in tetrahedral positions, these irons, in turn, contribute to hematite formation causing phase percentage to be favored.

Table 2. Refined structural parameters of FZM2 sample.

	Room temperature	1000 °C	
Cell parameters (Å)	F d -3 m a, b, c = 8.3586 α, β, γ = 90°	R -3 c a, b = 5.03577 c = 13.74749 α, β = 90° γ = 120°	F d -3 m a, b, c = 8.38342 α, β, γ = 90°
%Phase	100	71.26	28.74
V (Å)	583.983	301.915	589.200
R−factors	R_p = 39.0 R_{wp} = 26.8 R_{exp} = 26.67	R_p = 26.6 R_{wp} = 17.1 R_{exp} = 16.64	
χ^2	1.01	1.05	
Size (Å)	54.44	688.18	403.23
Strain (%)	29.1086	4.1543	4.1543

4. Conclusion

Mixed iron oxides presented here were transformed into a hematite phase due to Fe(II) presence, which was transformed into Fe(III) due to temperature increase. FZM2 sample is the one with highest mass loss of up to 16%, this behavior can be attributed to magnesium incorporation within the structure, this metal has octahedral sites preference which contributes to lattice stabilizing due to its unique valence state, in this way tetrahedral sites that contain Fe(III) are rearranged releasing small amounts of oxygen less than 2%.

X-ray diffraction pattern refinement of the FZM2 sample reveals that the hematite phase is predominant (71.26%) over the cubic spinel phase. To reduce the presence of the hematite phase, it is necessary not to incorporate Fe(II) during the synthesis process and to opt for use of divalent cations and Fe(III) in a spinel-type structure (zinc-magnesium ferrites). With results obtained, there are bases for materials redesign that allow a structural change towards a reduced phase of compound Fe_3O_4.

Acknowledgements

We thank Instituto Politécnico Nacional for providing the necessary resources to carry out the research.

We gratefully acknowledge the financial support of this work by Tecnológico Nacional de México.

References

[1] Usman M, Byrne JM, Chaudhary A, Orsetti S, Hanna K, Ruby C et al. Magnetite and Green Rust: Synthesis, Properties, and Environmental Applications of Mixed-Valent Iron Minerals. Chem Rev 2018;118(7):3251–304. https://doi.org/10.1021/acs.chemrev.7b00224.

[2] Fresno F, Fernández-Saavedra R, Belén Gómez-Mancebo M, Vidal A, Sánchez M, Isabel Rucandio M et al. Solar hydrogen production by two-step thermochemical cycles: Evaluation of the activity of commercial ferrites. International Journal of Hydrogen Energy 2009;34(7):2918–24. https://doi.org/10.1016/j.ijhydene.2009.02.020.

[3] Neises M, Roeb M, Schmücker M, Sattler C, Pitz-Paal R. Kinetic investigations of the hydrogen production step of a thermochemical cycle using mixed iron oxides coated on ceramic substrates. Int. J. Energy Res. 2009:n/a-n/a. https://doi.org/10.1002/er.1565.

[4] Saqib H, Rahman S, Susilo R, Chen B, Dai N. Structural, vibrational, electrical, and magnetic properties of mixed spinel ferrites Mg 1-x Zn x Fe 2 O 4 nanoparticles prepared by co-precipitation. AIP Advances 2019;9(5):55306. https://doi.org/10.1063/1.5093221.

[5] Liu Y, Wei SC, Wang YJ, Tian HL, Tong H, Xu BS. Characterization of (Mg, La) Substituted Ni-Zn Spinel Ferrite. Physics Procedia 2013;50:43–7. https://doi.org/10.1016/j.phpro.2013.11.009.

[6] Pan Y, Zhang Y, Wei X, Yuan C, Yin J, Cao D et al. MgFe2O4 nanoparticles as anode materials for lithium-ion batteries. Electrochimica Acta 2013;109:89–94. https://doi.org/10.1016/j.electacta.2013.07.026.
[7] Liu Y, Hsu J. The Use of Co-Precipitation to Produce Nano-Mn–Zn Ferrite ([MnxZn1−x]Fe2O4) from Waste Batteries. Applied Sciences 2018;8(6):1005. https://doi.org/10.3390/app8061005.
[8] Kostyukova D, Chung YH. Synthesis of Iron Oxide Nanoparticles Using Isobutanol. Journal of Nanomaterials 2016;2016:1–9. https://doi.org/10.1155/2016/4982675.
[9] Varshney D, Verma K. Substitutional effect on structural and dielectric properties of Ni1−xAxFe2O4 (A = Mg, Zn) mixed spinel ferrites. Materials Chemistry and Physics 2013;140(1):412–8. https://doi.org/10.1016/j.matchemphys.2013.03.062.

ID 059

Theoretical Aspects of Precursor Fibers to Activated Carbon Fibers to Store Hydrogen

Omar Rodríguez-Rivero[1], Fray de Landa Castillo-Alvarado[1], Teresa Ramírez-Rodríguez[2,*]

[1]Escuela Superior de Física y Matemáticas-Instituto Politécnico Nacional
[2]Escuela Superior de Ingeniería Textil-Instituto Politécnico Nacional
* Corresponding author: 43520891, teresa.ramirez7715@gmail.com

ABSTRACT

Among various precursors for producing carbon fibers, naturally occurring fibers such as lignocelluloses can adsorb hydrogen. In this study, we will focus on showing that cotton fibers that contain cellulose and lignin as main chemical compounds are a good precursor to obtain activated carbon fibers. Cotton cellulose is highly crystalline and oriented., For native crystalline cellulose (Cellulose I), this model assumes a monoclinic unit cell with space group P21 and two anti-parallel cellobiose chain segments occurring in opposite directions to along the fiber axis. Type II cellulose can be prepared by precipitating cellulose dissolved in an aqueous medium or also in mercerization. Preliminary work on moving type II cellulose, a two-cell unit cell; a = 8.14Å, b = 9.14Å, c = 10.3Å and γ = 62 °. Through molecular modeling and using the theory of the functional of the density based on local and semi-local approaches to the energy of electronic exchange-correlation (LDA and GGA) for which the Materials Studio software was used, taking as a point starting point that Generalized gradient approximations (GGA) seek to improve the precision of the local gyro density approximation (LSD) in electronic structure calculations and that, on the other hand, Perdew and Wang have developed a GGA based on the cut in space The actual long-range spurious components of the second-order gradient expansion for the exchange-correlation gap were chosen to perform these functional molecular modeling. The results of thermodynamic properties were obtained, which helped us to have an approximation of the behavior in the experimentation.

The mercerization process is an important treatment given to the cotton fiber, which allows the alkali to penetrate not only in the amorphous regions but also in the crystalline regions, achieving that the structure is accompanied by loss of resistance between the cellulose chains resulting in temporary weakening while the fiber remains swollen, the flattened shape of the fiber changes its characteristics to a rounded shape.

According to the visual analysis of each temperature, the alkali concentration, the temperature and their interaction had a significant effect on the secondary cell wall of the cotton, this due to the oxidation effect.

Keywords: activated carbon fibers; cotton fibers; mercerized

1. Introduction

Textile fiber is characterized by flexibility, finesse and a high length-to-thickness ratio. Fibers are long, thin units of matter. Its component atoms are joined into molecules, which are assembled into particular fine structures. [1]
The cotton fibers consist of a general proportion of the following compounds: cellulose 82-96%, hemicellulose 2-6-4%, lignin 1-5%, and pectin <1-7% [2]. Where cellulose is a natural linear polymer (polysaccharide) with a molecular repeating unit made up of a pair of D-anhydroglucose ring units linked by glycosidic oxygen bonds $\beta - 1 \rightarrow 4$ around which the molecular chain can bend and twist. Hemicelluloses, on the other hand, are linear or branched polymers and are essentially amorphous due to the many side groups attached to their heteropolysaccharide structures that contain sugar residues, including xylanes, mannans, arabinan and galactanes. Likewise, lignin is composed of oxyphenylpropane units that form a 3-D polymeric structure, free radicals polymerized from cinnamyl alcohols. The reaction of the lignin monomers with the lignin polymer can extend the molecular chain or form crosslinks. Lignin and hemicellulose act as cementing phases for cellulose. Pectins are found in plant tissue and, together with hemicelluloses and lignin, form the cell wall "matrix" for cellulose microfibril "fibers" in the form of a synthetic compound.

The first carbon fibers were produced around 1880 by Thomas Edison, who made cotton and bamboo filaments for use in lamps. But it wasn't until the early 1960s that the development of high-performance carbon fiber began. The prospect of new lightweight compounds ranging from sporting goods to aerospace applications sparked a “boom“in research on the processing, structure and mechanical properties of cellulose-based and polyacrylonitrile (PAN) carbon fibers. Considering cellulose-based carbon fibers only in fibers containing cellulose II. In the single chain configuration based on the level of covalent bonds, cellulose is a linear polysaccharide consisting of anhydroglucose units (AGUs) in the saddle conformation $^4C_1$ linked through glycosidic bonds $\beta(1 \rightarrow 4)$, so that in contrast to the amylose in the starch, which is a $\alpha(1 \rightarrow 4)$ linker, a linear chain conformation is easily generated. Moving from the simple chain to the bulk solid state, cellulose turns out to be a partially crystalline polymer. Biosynthesized cellulose crystallizes in the triclinic form I_α, or in the monoclinic space group $P2_1$, with the form I_β. The standard crystalline polymorph for mercerized (alkali-treated) cellulose is called cellulose II, indicating a monoclinic form of the space group $P2_1$, which is markedly different from native cellulose crystals.

In previous works we studied theoretically and through molecular modeling, using the Materials Studio software and based on the Functional Theory of Density, taking as a starting point the monomer that is part of the polymer with which the fiber is identified. of cotton, we locate by molecular modeling the hydroxyl groups, capable of modifying the surface of the cotton fiber and the effective way of activating them that directs us towards the conversion of conductive fibers. Obtaining a monoclinic cell belonging to the P21 space group that provides us with the type I cellulose crystal.

The focus of the work proposes the mercerizing of cotton fiber as a first phase to lead to obtaining activated carbon fiber, examining the molecular modeling that was carried out on the movement of type II cellulose, a two-cell unit cell; with network parameters; a = 8.14Å, b = 9.14Å, c = 10.3Å and γ = 62 °, giving us a better approximation of the functioning and behavior in experimentation. [3]

The mercerizing process was developed in 1844 by Jonh Mercer, a textile scientist born in Great Harwood, Lancashire, England, by treating cotton fibers with sodium hydroxide. In the Mercer version of the process it reduced the total size of the fabric, increasing its resistance and facilitating its subsequent dyeing. Said process became popular when H.A. Lowe developed its shape in 1890. By holding the cotton with a tension preventing it from shrinking, Lowe discovered that the fiber acquired a lustrous finish. Mercerization changes the chemical structure of the lignocellulosic fiber, transforming the initial structure (initial α α cellulose) into a polymorphic structure ($\beta\beta$ cellulose), consequently the cell wall of the fiber is inflated, this results in an increase in the total surface of the fiber. fiber and its reflectance, giving more shine and a softer touch. Although this process is, in general for cellulosic fibers, this application is focused exclusively on cotton, this in order to analyze the activated carbon precursor fiber (FCA).

2. Materials and Methods

PROCEDURE DESCRIPTION OF THE METHOD:
We start by making a cross-section of the cotton raw.

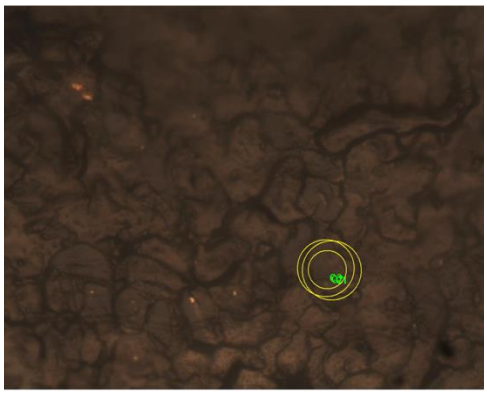

Figure 1. Natural Cotton cross section

1.1- CAUSTIC SODA SOLUTION PREPARATION OPERATION PROCESS 28º Be (15ºC).

Based on conversion table we take 28ºBe:

Table 1. allows the conversion of density from Baumé degrees to concentration expressed in solute percentage.

ºBe - % concentration (caustic soda at 15ºC to 1000ml)			
ºBe	% Concentration	gr NaOH	ml H2O
1	0,61	6,1	993,9
2	1,20	12	988
3	2,00	20	980
4	2,71	27,1	972,9
5	3,35	33,5	966,5
6	4,00	40	960
7	4,64	46,4	953,6
8	5,29	52,9	947,1
9	5,87	58,7	941,3
10	6,55	65,5	934,5
11	7,31	73,1	926,9
12	8,00	80	920
13	8,68	86,8	913,2
14	9,42	94,2	905,8
15	10,06	100,6	899,4
16	10,97	109,7	890,3
17	11,84	118,4	881,6
18	12,64	126,4	873,6
19	13,55	135,5	864,5
20	14,37	143,7	856,3
21	15,13	151,3	848,7
22	15,91	159,1	840,9
23	16,77	167,7	832,3
24	17,67	176,7	823,3
25	18,58	185,8	814,2
26	19,58	195,8	804,2
27	20,59	205,9	794,1
28	**21,62**	**216,2**	**783,8**

29	22,64	226,4	773,6
30	23,67	236,7	763,3
50	49,02	490,2	509,8

- Carefully add in three parts NaOH in flakes in H_2O at room temperature.

gr NaOH	ml H_2O
216,2 gr	1000 ml
108,1 gr	500 ml

Table 2. ratio gr of sodium hydroxide to ml of water

$$108{,}1gr \div 3\ parts = 36{,}03gr\ of\ NaOH\ for\ each\ 166{,}7ml\ of\ water(H_2O) \quad (1)$$

-Empty in container final solution and maintain temperature with ice around the container no more than 15ºC, constantly check this temperature with aerometer.

1.2- MERCERIZATION PROCESS WITH NaOH

-Cotton fibers were moistened to 50oC for 20 min in a stainless-steel container containing pre-prepared NaOH solution.

-The process is simple; we basically treat the fiber with a caustic soda solution under constant stress.

- Rinse with enough water for 5 min.
- Dry at room temperature
- It is not neutralized shows as we will be working in its alkaline or oxidation medium.
- Make mercerized sample cross-section

-Cotton fibers were moistened to 50oC for 20 min in a stainless-steel container containing pre-prepared NaOH solution.

-The process is simple; we basically treat the fiber with a caustic soda solution under constant stress.

- Rinse with enough water for 5 min.
- Dry at room temperature
- It is not neutralized shows as we will be working in its alkaline or oxidation medium.
- Make mercerized sample cross-section

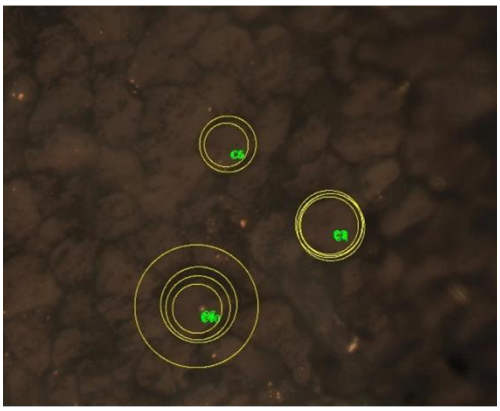

Figure 2. Cross section of mercerized Cotton.

1.3- OXIDATION PROCESS WITH H_2O

- We continue to moisturize sample with water (H_2O) by 5min
- We present the sample to different temperatures for a time of 2hrs, we start from temperature of 80ºC to a temperature of 100ºC with a decreasing temperature constant of 10 in 10
- The fibers were dehydrated in an oven at 80ºC for 2 hrs.
- Perform sample cross-section

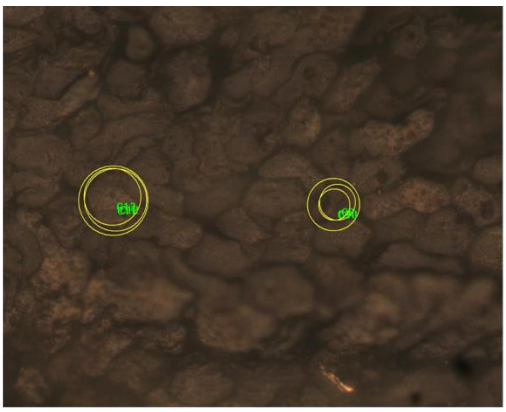

Figure 3. Cross section of cotton oxidized at 80ºC.

- The fibers were dehydrated in an oven at 90ºC for 2 hrs.
- Perform the cross-section

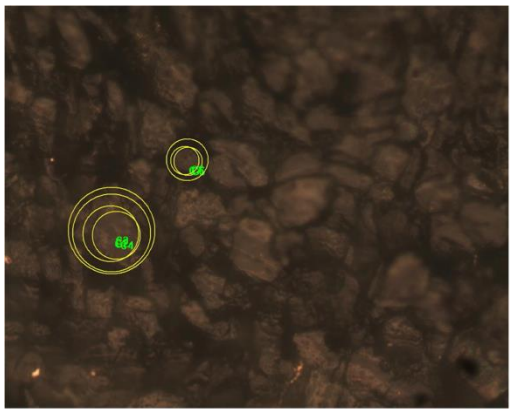

Figure 4. Cross section of cotton oxidized at 90ºC.

- The fibers were dehydrated in an oven at 100ºC for 2 hrs.
- Perform the cross-section

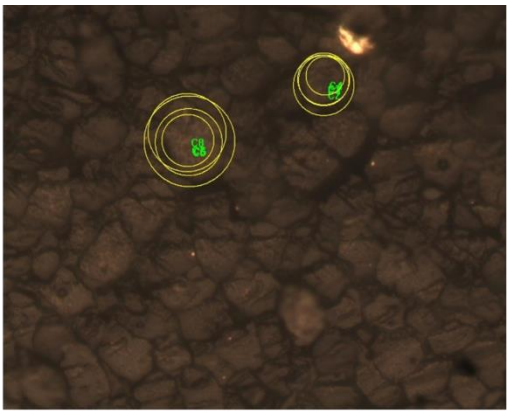

Figure 5. Cross section of cotton oxidized at 100ºC.

- We continue to perform the respective cross-sections at each different temperature of previously oxidized sample and obtain visual data on their behavior at different temperatures.

Measurements

Measurements were made in olympus Bx 41 electron microscopy, radio measurements were taken in each section, with a resolution of 4nm (0.004) and the total magnification of 10 x 40 = 400 magnification with a 40x objective.

3. Results and Discussion

Cellulose type II can be prepared by precipitating dissolved cellulose in an aqueous medium

or also in mercerization, that is, soaking the cellulose in aqueous NaOH (21.62% weight by volume). This process of transformation from type I cellulose to type II cellulose is considered irreversible.

$$\underline{Celulosa\ tipo\ I + NaOH \rightarrow Alcali - celulosa\ tipo\ II + H_2O}$$
$$\underline{Celulosa\ tipo\ I + NaOH \rightarrow Alcali - celulosa\ tipo\ II + H_2O}$$
$$Celulosa\ tipo\ I + NaOH \rightarrow Alcali - celulosa\ tipo\ II + H_2O \quad (2)$$

Mercerizing increases the number of possible reactive sites and allows better wetting, leads to fibrillation that causes the decomposition of the fiber beam, reduces the diameter of the fiber, thus increasing the aspect ratio leading to the development of a rough surface topography that results in better adhesion of the fiber interface and an increase in mechanical properties , increases the number of possible reactive sites.

In this process the cellulosic ligno fiber is usually treated with a concentrated solution of caustic soda of 21.62% with a certain time the alkali penetrates the fiber causing lateral swelling and longitudinal shrinking which allows the alkali to penetrate not only in the amorphous regions but also in the crystalline regions, the structure is accompanied by loss of resistance between cellulose chains resulting in a temporary weakening while the puffy fiber, the flattened shape of the fiber changes its characteristics to a rounded shape.

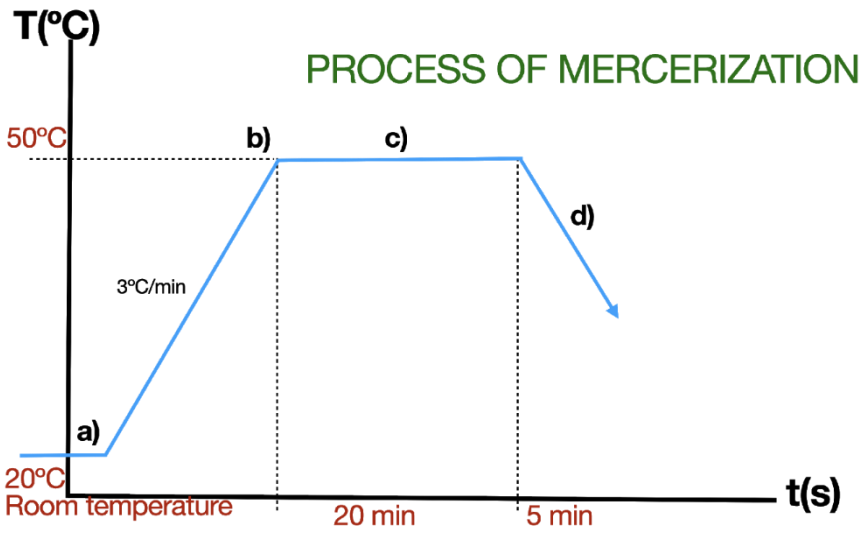

Graph 1 **(a)** Addition of sodium hydroxide solution to 21.62%;**b)**Temperature increase at 50°C; **c)**Keep temperature for 20 min; **d)** Rinse by overflowing with water for 5 min.

Lignocellulosic fibers, such as cotton fibers, under a hydrothermal treatment tend to reduce the amount of adsorbed moisture and increase their crystallinity. They have hydroxyl groups which are susceptible to modification, these groups may be involved in the hydrogen bond within cellulose molecules. Simple chemical treatments are applied to change surface tension and polarity by modifying the surface of the fiber. Chemical modification on the surface can activate these groups and effectively improve conversion to conductive fibers.
On the other hand, the study of the structure of the monomer that constitutes the cellulose of the cotton fiber before and after going through a doping phase with an oxidizing agent (in this case sodium hydroxide), optimizing the structure of the cellulose molecule type I and type II, the process of which is first: The evaluation of energy, the energy expression must be defined and evaluated for a given conformation. Energy expressions that include external restrictive terms, to skew optimization, can be defined in addition to the terms energy, second. The conformation is adjusted to reduce the value of the energy expression. A minimum can be found after an adjustment or may require thousands of interactions, depending on the nature of the algorithm's energy expression, and the size of the structure.

4. Conclusion

After the evaluation of the results by microscopy and measurement of secondary cell wall, it was concluded that the material obtained, after the process of cellulose mercerization with sodium hydroxide and oxidation with water at different temperatures, presented the characteristics that would be observed for an amorphous material, that is, that the methodology used allowed to obtain a cellulose with amorphous characteristics.

Cellulose morphology represents a well-organized architecture of fibrillar elements. The elemental fibril of native cellulose (type I cellulose) has been considered to be the smallest morphological unit with a diameter of approximately 3.5nm in the transverse direction. Hydroxyl groups in cellulose and chain shaping allow intermolecular and intramolecular hydrogen bonds to improve structure stiffness. Heat or reactions begin in the most accessible amorphous region and on the surface of the crystalline domain.

This study has been carried out with the aim of raising and finding the necessary conditions for the transformation of a lignocellulosic fiber, in this case cotton towards a conductive fiber by knowledge of its molecular geometry of cellulose type II.

Acknowledgements
Proyecto SIP-20201820 aprobado por el Instituto Politecnico Nacional
Escuela Superior De Ingenieria Textil
Escuela Superior De Fisica y Matematicas

References

[1] Eichhorn, S., Hearle, J. W. S., Jaffe, M., & Kikutani, T. (Eds.). (2009). Handbook of Textile Fibre Structure: Volume 1: Fundamentals and Manufactured Polymer Fibres. Elsevier.

[2] Eichhorn, S., Hearle, J. W., Jaffe, M., & Kikutani, T. (Eds.). (2009). Handbook of Textile Fibre Structure: Volume 2: Natural, Regenerated, Inorganic and Specialist Fibres. Elsevier.

[3] Memorias del Congreso Internacional de Investigación Academia Journals Celaya, (2017). ISSN 1946-5351, Volumen 11, No. 9: Modelamiento Molecular de la Microestructura del Polímero de la fibra de Algodón dopada con un Agente Oxidante.

ID 065

Corrosion Process Analysis on Anode of Nickel-plated Stainless Steel

J. A. Melo-Máximo[1*], E. M. Arce-Estrada[1], R. G. González-Huerta[2]

[1]Instituto Politécnico Nacional ESIQIE, Dep. de Ingeniería en Metalurgia y Materiales, UPALM, CP. 07738, CDMX.

[2]Instituto Politécnico Nacional ESIQIE, Laboratorio de Electroquímica, UPALM CP. 07738, CDMX.

* 5531321110 - jorgemelomaximo@hotmail.com

ABSTRACT

Alkaline electrolysis provides a sustainable solution to produce hydrogen replacing or enrichment conventional energy production ways, for example, internal combustion engines, atmospheric burners, etc. Unfortunately, secondary water electrolysis reactions lead to the formation of undesirable compounds, such as iron or nickel oxides, as well as ions in solution, among which hexavalent chromium (Cr (VI)) stands out for its high degree of toxicity. Alkaline electrolysis involves a series of electrochemical reactions that are carried out in an aggressive medium, with highly alkaline pH conditions (> 12) and oxidation potentials (E > 1.5 V) that accelerate the degradation of the material.

In this study, is boarded the main fundaments of the alkaline electrolysis, just as the electrochemical reactions generated into the alkaline media. A method is proposed to reduce the generation of Cr (VI) through the application of Ni films of 10 um thick obtained by electrodeposition techniques. It is taking as evidence that Ni is an

excellent material for its alkali resistance and electrocatalytic activity. Together with an austenitic steel-based system, the production of undesirable components in the system can be reduced or eliminated. in this step first, the characterization techniques used was cyclic voltammetry to detect Ni coating. As well as a microstructural test using Scanning Electron Microscopy (SEM) whit elemental analysis (EDS); before and after every electrochemical characterization to find the best structural characteristics of the coating. In the microstructural results, is observed that the coatings growth is in flakes form, and these form islands of around 10 um high and 2 um wide, they coalesce as the deposit grows. Furthermore, the results of the first electrochemical tests show the evolution of oxygen in the sample starting at 1.58V and there is the presence of Ni $(OH)_2$ at a potential of 1.4 V/RHE.

Keywords: Hydrogen; Electroplating; Stainless Steel; Nickel.

1. Introduction

Hydrogen is the cleanest source of energy since, in the presence of oxygen, they fuse to form water releasing energy, so the only waste generated is steam. For this reason, the use of hydrogen is free from the formation of greenhouse gases [1]. This gas is not free but is produced from different primary energy sources. Approximately only 4% of the gas generated in the world comes from water electrolysis; this percentage being represented by alkaline electrolysis and PEM technologies [2].

Alkaline electrolysis of water is a cheap method to produce hydrogen, which offers the advantage of simplicity. The challenges that prevent the widespread use of water electrolysis are to reduce its energy consumption, cost, and maintenance and to increase its reliability, durability, and safety. This technology has been used for many years to generate H_2 and O_2. However, it is necessary to design less expensive, more active, and robust cathode and anode electrodes. [3].

Alkaline electrolyzers operate at potential conditions close to 2 V per cell and can generate an efficiency close to 60 % [4]. However, electrolysis comprises two reactions: the hydrogen evolution reaction (HER) at the cathode and the oxygen evolution reaction (OER) at the anode. Given this, it has been obtained that in the electrode of the OER there is an over tension, being this identified as the major source of loss of efficiency by the process of self-corrosion generated in this one, obtaining this way major overpotentials and minor times of life [5].

Some studies have evaluated the dissolution of different metals in an alkaline medium, showing a lower corrosion process in noble metals [6]. However, their high costs prevent their use as substrates in large-scale alkaline electrolysis technologies. For this reason, the use of a technique of nickel electrodeposition on stainless steel is considered, which can mitigate the corrosive effects on the surface of the substrate [7][8]. Stainless steel

is considered one of the cheapest electrode materials used for alkaline electrolyzers. Stainless steel (304 and 316) consists of 18-22%w Cr, 8-11% Ni, and 2% Mo.

Stainless steel is chemically stable in an alkaline environment. But if the potential is >1.6 V is applied between the electrodes, corrosion processes occur at the anode, and when operated at these conditions, the presence of Fe3O4 and hexavalent chromium (Cr (IV)) can be generated at the anode, hence the importance of generating a coating [9].

In this work, we propose the modification of the AISI 304 stainless steel surface with nickel electrodeposition. It will be used as electrodes in chemical reactors, the nickel coatings are corrosion resistant in the service conditions of an alkaline electrolyzer, focusing on the anodes where the oxygen evolution reaction (OER) is performed.

2. Materials and Methods

2.1. Preparation of electrodes

Current density. The specific current density needed to obtain the best coating was evaluated by Hull Cell. This test was obtained using a trapezoidal acrylic vessel typical of this technique, as well as a 95 x 100 mm stainless steel plate as a cathode and a nickel plate as an anode. As the electrolyte, 267 ml of solution was taken from a Watt bath, immersing the steel plate at a temperature of about 50°C.

A stainless-steel bar AISI 304 of 0.635 cm diameter was used as the electrode substrate (anode). The sample was supported on a NYLACERO test tube, specially designed for electrochemical and microstructure tests. The electrodeposition was carried out by an electrochemical technique, in which a thin metallic layer of nickel was deposited on the surface of a substrate, based on Faraday's laws. The process of electrodeposition of stainless steel consists of three steps, each involving a specific solution that requires an electrochemical system, called

a) Cleaning: This procedure includes a metallographic preparation of the base metal surface, in addition to electrolytic anodic cleaning (AEC) of the electrodes to remove dust, grease, and particles left on the surface. In AEC, the anode is the working electrode and is placed in an alkaline electrolyte solution (3% w), and water electrolysis occurs at 3-7.5 A/dm2. The oxygen formed in the reaction cleans the surface by removing the dirt.
b) Surface pre-treatment (SP): A high degree of adhesion between the tank and the substrate is necessary for electroplating. In this case, the adhesion of nickel to the stainless steel becomes a very difficult task; a pre-treatment of the surface is necessary before nickel deposition. Good adhesion of nickel on a stainless-steel surface is achieved by electrochemical pretreatment with a solution consisting of $NiCl_2$ (240 g L-1) and HCl (130 ml/L-1). In SP, the cathode is the working electrode and is placed in an acidic electrolyte solution, and water electrolysis occurs at 2.5 V. The hydrogen formed in the reaction produces electrolytic pickling on the surface of the electrode.
c) Nickel deposit: The Watts method for nickel electrodeposition was used for this study. An electroplating bath was prepared by mixing 300 g/L-1 NiSO4*6H2O, 60 g/L-1 NiCl2*6H2O, and 45 g/L-1 H3BO3 at 55-60 °C, pH 4.5 to 4.3 A/dm2 and under constant stirring.

In the Watts bath solution, nickel sulfate helps to improve the conductivity and distribution of the metal on the surface of the base material. On the other hand, nickel

chloride improves the corrosion of the anodes, increases the conductivity, and improves the uniformity of the coating thickness distribution and helps refine the grain size. Boric acid is added to buffer the reaction, as deposits can crack and burn at low concentrations of boric acid [10].

Protection against corrosion depends mainly on the nickel layer. Also, the film thickness depends on the application. For example, the thickness can be 7 mm to protect the purity of the material, such as iron containers. Nickel coatings on automotive components, with hydraulic cylinders, cylinder liners, and shock absorbers, can be 125mm thick to provide corrosion and wear resistance. Equation (1) was used to calculate the thickness of the nickel layer, s in microns:

$$S=(m\cdot 1\times 10\text{^}5)/(d\cdot A)=(1.095\times 10\text{^}5\cdot I\cdot t\cdot \eta)/(8.0907\cdot A)=(0.123\times 10\text{^}5\cdot I\cdot t\cdot \eta)/A \quad (1)$$

Where m (g) is the amount of nickel deposited at the cathode (or dissolved at the anode), d (8.907 g/cm^{-3}) is the density of nickel, A (cm^2) is the electrode area, 1x10^5 is the conversion factor from cm to mm, I (A) is the electric current that flows through the plating tank, t (h) is the time that the current flows, and is the current efficiency ratio (95%). The proportionality constant 1.095 in g/Ah equals M/nF, where M is the atomic weight of nickel (58.69 gr/mol^{-1}), n is the number of electrons in the electrochemical reaction (2), and F is Faraday's constant, which is equal to 26.799 A-h (more commonly listed as 96,500 C).

2.2. Physical Characterization

For the electrochemical characterization were used a coated steel working electrode (WE) as an anode, a platinum mesh counter electrode (CE), and a reference electrode (RE) of Hg / HgO (E = 0.92 V vs. ENH).

Scanning electron microscopy (SEM) was used to determine the surface morphology of the nickel-plating using a JEOL JSM-6360 LV a 20kV microscope, equipped with EDS analysis ITESM-CEM.

3. Results and Discussion

3.1 Electrochemical Characterization

The electrochemical analysis was carried out by means of a cyclic voltammetry test. A NaOH electrolyte at %15w concentration was used. This concentration represents that of a real operating system. As a preliminary result, the performance of the coating in the alkaline environment can be observed. First, we looked for a potential window in which we could observe the evolution of oxygen from 1.58V. The presence of Ni (OH)3 was observed in a potential of 1.4V, figure 1 (A), coinciding with that shown in the Nickel Pourbaix diagram, figure 1 (B). Showing no presence of the base material, AISI304. After the potential of 1.58 V the evolution of oxygen is observed.

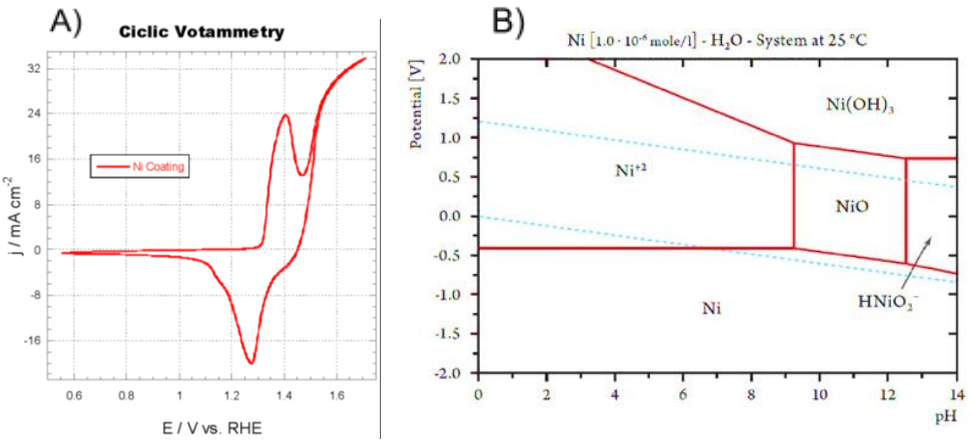

Fig. 1. A) Cyclic voltammetry of the Ni coating and B) Ni Pourbaix diagram.

Microstructural Analysis

The structural characteristics of the coating were observed. In zone 1, Fig 2, the size of the film thickness is approximately 10 µm, corresponding to the specific time established for obtaining these microns.

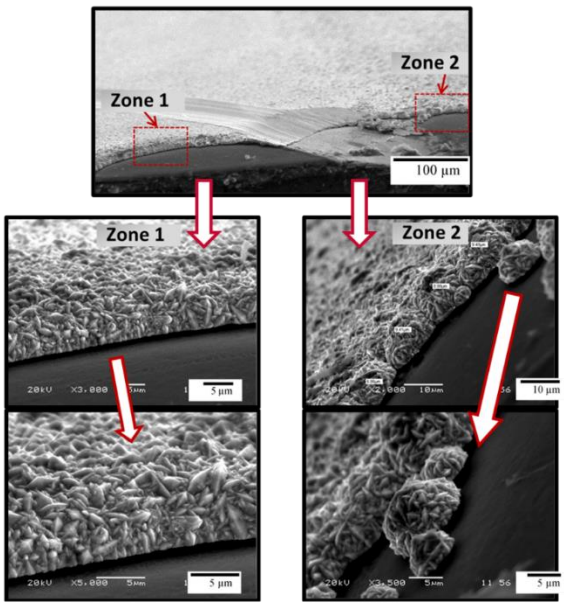

Fig. 2. SEM image corresponding to the coating morphology.

Also, in zone 2, it can be observed how the film growth is taking place. It can be deduced that this is taking place in the form of islands of a size of approximately 10 µm height by 2 µm width, these are formed by seeds from 2 to 3 µm long and 1 to 2 µm wide, the islands are coalescing as the deposit is growing and equal shape to obtain final thickness.

Besides, the ESD qualitative analysis provided details of the presence of the various elements that are present on the surface of the coated material. The data shows the presence of the deposited Ni from the surface, as well as a broad signal of Fe from the substrate material. It should be noted that no other stainless-steel materials such as Cr are present.

Once the electrochemical tests were performed, the microstructural characterization was repeated. The presence of Ni and Fe was observed in the EDS analysis and the existence of oxygen that was not observed in the first study. This is attributed to the presence of nickel oxide or nickel hydroxide generated at the surface along with the generation of oxygen. Likewise, it is to these that it can be attributed that the surface was modified, showing a film with grains with different morphology, Table 1.

Table 1. Comparison of EDS analysis with pre and post electrochemical test samples.

Signal	AISI 304	304-Ni untreated	304-Ni after electrochemical test

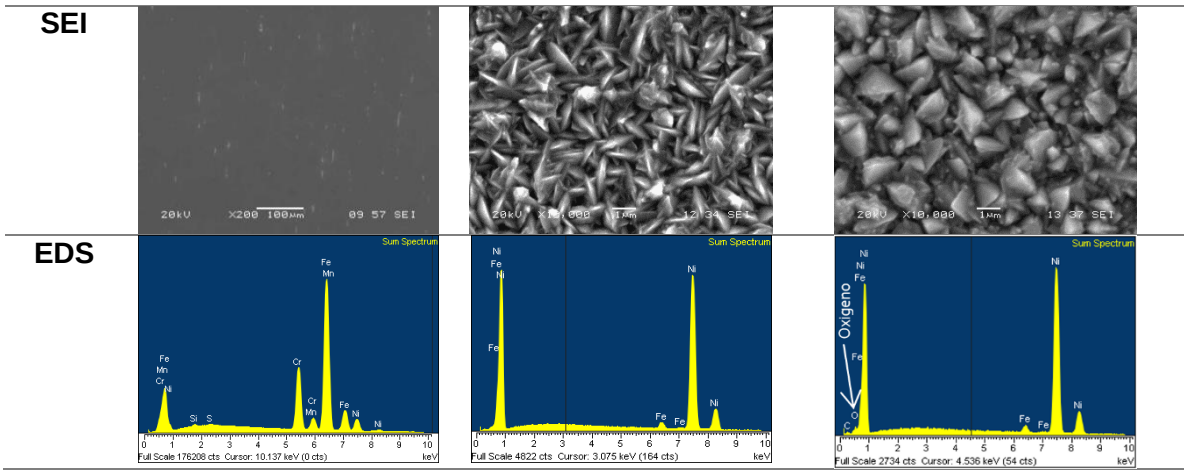

The elemental mapping of the coated samples was also analyzed before and after the electrochemical treatment. As can be seen from the mapping, the homogeneous distribution of nickel on the surface of the coated samples is evident. This is important to take into consideration, knowing that how the metal is distributed in the stainless-steel part is of great interest. Bad distribution of this could affect the whole experimental process.

Also, the study presented data on how iron was distributed on the surface after the electrochemical test. The presence of this metal in the mapping may be due to a signal from the substrate itself since in the EDS analysis no other metal was observed to contribute an extra signal, so we can conclude that the coating obtained is of good quality. The oxygen signal in the sample after treatment is also observed, this is mainly due to the oxygen signal that could be seen in the EDS analysis. The presence of oxygen on the surface is mainly due to the generation of nickel oxides generated in Cyclic Voltammetry. This element is widely distributed on the film and it can also be attributed to the modification in the morphology, Table 2.

Table 2. Elemental mapping of the surface of the Ni coated samples, before and after the electrochemical treatment.

Signal	AISI 304	304-Ni untreated	304- Ni after electrochemical test
SEI	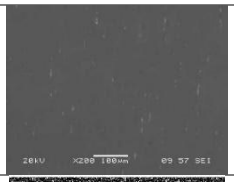	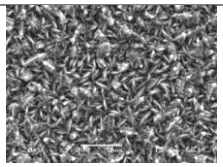	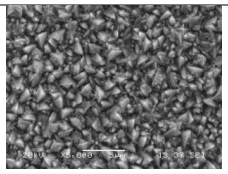
Ni	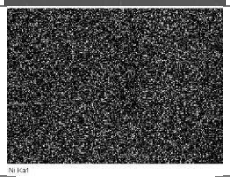	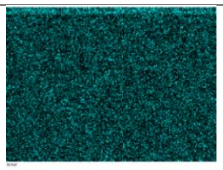	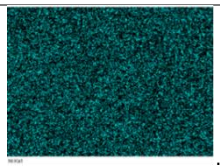
Fe	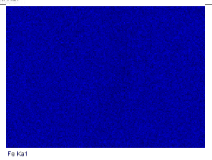	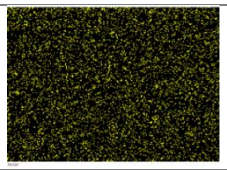	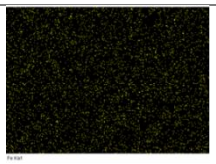
Cr	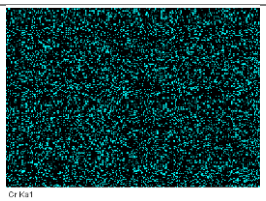	No Signal	No Signal
O	No Signal	No Signal	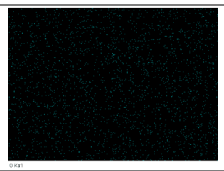

4. Conclusion

The presence of a nickel coating provided good results concerning oxygen evolution activity at the anode. It has been proven that having a coating present reduces the possibility of the formation of stainless-steel oxides. The main reason for the work was to eliminate the presence of Cr (VI) in the electrolyte and this has been achieved.
Thanks to these results, we will continue with the design of new electrodes with better electrodeposits, adding other metals that can increase the useful life and obtain less maintenance time in the alkaline electrolyzers.

Acknowledgements

The authors would like to thank IPN multidisciplinary project 2024, innovation project 20200935 and CONACYT CEMIE Oceano-249795, transversal line I-LT1 and project CB A1-S-15770.

References

[1]. Rashmi Chaubey, S. S. A review on development of industrial processes and emerging techniques for production of hydrogen from renewable and sustainable sources. *Renewable and Sustainable Energy Reviews*, 23, (2013), 443–462

[2]. Das, D. K. Recent developments in biological hydrogen production processes. *Chemical Industry & Chemical Engineering Quarterly*, 14, (2008), 57–67.

[3]. Soriano Moranchell FA at al., Electrodes modified with Ni electrodeposition decrease hexavalent chromium generation in alkaline electrolysis process, *International Journal of Hydrogen Energy*, 26, (2020), 13683-13692.

[4]. Ivy, J. Summary of Electrolytic Hydrogen Production. *Milestone Completion Report*, (2004).

[5]. Kjartansdóttir, C. K., & Møller, P. Development of Hydrogen Electrodes for Alkaline Water Electrolysis. DTU Mechanical Engineering, (2014)

[6]. Schalenbach, Maximilian, et al. "The electrochemical dissolution of noble metals in alkaline media." *Electrocatalysis* 9.2 (2018): 153-161.

[7]. Solmaz, Ramazan, and Gülfeza Kardaş. "Electrochemical deposition and characterization of NiFe coatings as electrocatalytic materials for alkaline water electrolysis." *Electrochimica Acta* 54.14 (2009): 3726-3734.

[8]. Solmaz, Ramazan, Ali Döner, and Gülfeza Kardaş. "The stability of hydrogen evolution activity and corrosion behavior of NiCu coatings with long-term electrolysis in alkaline solution." *International journal of hydrogen energy* 34.5 (2009): 2089-2094.

[9]. Shreir LL, Jarman RA, Burstein GT. In: Metal/environment reaction, corrosion. 3rd ed., vol 1. London, UK: Newnese Butterworths; 2000. Reprinted 2000.

[10].Jacobs, James A., and Stephen M. Testa. "Overview of chromium (VI) in the environment: background and history." *Chromium (VI) handbook* (2005): 1-21.

ID 066

Bioetanol steam reforming of Co-Ni/like-Hydrotalcites Catalysts to produce H_2

(The promoting effect of WOx and the long-term stability)

Jose L. Contreras [a*], Naomi N. González [a], Ricardo López M[a], Beatriz Zeifert[b], José Salmones[b], Tamara Vázquez[b], Gustavo A. Fuentes[c], Deyanira Angeles[a]

[a] Universidad Autónoma Metropolitana-Azcapotzalco, CBI-Energía, Ciudad de México, 02200, México.
[b] Instituto Politécnico Nacional, ESIQIE, UPALM, Zacatenco, Ciudad de México, 07738, México.
[c] Universidad Autónoma Metropolitana-Iztapalapa,CBI-IPH, Ciudad de México, 09340, México.

*Corresponding author: jlcl@correo.azc.uam.mx

ABSTRACT

For the production of H_2 by ethanol steam reforming (ESR), the calcined hydrotalcite-WOx-supported Ni-Co catalysts have been studied investigating the effect of the Ni / Co atomic ratio from 2.2 to 0.139 and the results were promising for the catalyst with ratio 2.2 in terms of selectivity to H_2. However, it was not known whether the addition of WOx to hydrotalcite could stabilize its structure thermally, preventing the reduction of the area of the support and of the Ni and Co crystallites and with it the deactivation by sintering. For this study, 6 catalysts were prepared varying the W concentration from 0.5wt% to 16wt%, maintaining the concentration of 10wt% Ni and 4.5wt% Co using the coprecipitation method. The ethanol conversion was total at 600 ° C and the selectivities were: 76% H_2, 21% CO_2, 1% CO, 2% CH_4, in N_2 stream using a H_2O / ethanol ratio 4 at atmospheric pressure.

Continuous evaluation showed that the catalyst with WOx was less deactivated than the catalyst without WOx. In our case we are still evaluating the catalysts in inert atmosphere or with a small amount of O_2 in the feed stream. Ni / Co catalysts showed carbon (coke) levels less than 4.9wt% for a 1440 min evaluation. By XRD the chemical species observed were: periclase MgO, alumina Al_2O_3, spinels of Co, Co_2O_3, bunsenite NiO, spinels of $MgAl_2O_4$. When we calcined the sample with 16 wt%W up to 800°C we observed a total transformation of the previous species by others with greater crystallinity. The graph of BET area versus W concentration (WOx) showed that effectively at low W contents (0.1 to 1wt%) the catalyst area was greater for the samples with W than the area for the sample without W at 450, 600 and 800 ° C.

Keywords: Ni-Co-Hydrotalcite-WOx ; catalysts, ESR of Ethanol, H_2 production

1. Introduction

Ethanol has several advantages as a fuel and can be stored more easily and without significant risk of handling and can be obtained in large quantities from biomass [1-2]. Then in order to produce H_2 by ESR, the catalysts must show high thermal stability, because the relative high operation temperatures at which reforming reactions take place, as well as high selectivity to H_2 production. Several studies have shown that supported noble metals such as: Ir, Pt, Pd, Ru or Rh [3, 4], or inexpensive metals such as Co [5-7], Ni [8], or bimetallic materials [9,10] are good options to catalyze the ESR reaction. Thereby, supports such as: MgO, ZnO, SiO_2, Al_2O_3, La_2O_3 or CeO_2, among others, are the most commonly used to support the active metals [11].

We have chosen the so-called hydrotalcite-like compounds as supports, also known as layered double hydroxides (LDHs) [12]. LDHs are a family of lamellar materials derived from brucite layers, which are currently of academic and industrial interest [12-14]. These compounds contain Mg^{2+} and Al^{3+} metal cations. In this study, bimetallic Ni-Co and hydrotalcite catalysts were prepared by the coprecipitation method and then evaluated in the ESR reaction.

2. Materials and Methods

The hydrotalcite was made by coprecipitation using two salt solutions as precursors. First, in a stirred reactor a salt solution of $Mg(NO_3)_2$ and $Al_2(NO_2)_3$ (J.T. Baker) with a molar ratio of 2:1 was made and a second solution of Na_2CO_3 (5%) and NaOH (pH = 10) (Carlo Erba) were prepared.

These two solutions were added simultaneously drop by drop to a third stirred reactor using water as solvent (60 drops/min) at 60°C maintaining an atomic ratio of Mg^{2+}/Al^{3+} of 1.55. In this step a solution of $(NH_4)_{12}W_{12}O_{41}\bullet 5H_2O$, (Aldrich) was added in order to get 0.5, 1, 4, 8 and 16%wtW of the final solid and also an aqueous solution containing $Ni(NO_3)_2$ and $Co(NO_3)_2$ (Aldrich) was added. The bimetallic Ni-Co catalysts were prepared with an atomic ratio of 2.22 (NiCo-1).

The hydrotalcite catalysts without metals were named: HT-450, HT-600 and HT-800. The bimetallic catalysts were named as follows: NC-0.5W, NC-1W, NC-4W, NC-8W and NC-16W . The final suspension in the reactor was maintained at 70°C and pH of 11 with stirring for 18 h. The solid precipitated was washed, dried at 110°C during 18 h and calcined at 450°C, 600°C and 800°C for 5 h.

This final suspension was maintained at 70°C in the reactor with stirring for 18 h. This precipitated solid was washed, dried and calcined at 450, 600 and 800°C for 5h. A sample of hydrotalcite without Ni or Co was prepared in a similar manner (sample HT). The solids obtained were characterized by X-ray diffraction (XRD) in a Phillips X´ Pert instrument. N_2 physisorption at 77 K was made in a Micromeritics 2000 instrument.

Each sample was pretreated at 200°C under vacuum (1 x 10^{-4} torr). The samples were analyzed by scanning electron microscope (SEM) using a microscope with high-resolution Jeol model JFM 6701 F, using secondary electrons. The qualitative chemical analysis and their corresponding spectra were obtained by coupling a probe SEM, and EDS (energy dispersive spectroscopy of X-rays).

The catalytic reaction was made in a U-shaped stainless steel fixed bed reactor.

The catalyst (1g) was charged and the feed of the reactants consisted of ethanol, water as steam and N_2. The gas mixture of H_2O and CH_3CH_2OH (molar ratio of 4/1) in N_2 stream was fed using two glass saturators.

The temperature of the catalyst was controlled to 450°C in flow of N_2 for 30 min to clean the catalyst surface and then the flow of reactants started at the same temperature. The catalyst was held at that temperature for 30 min in order to make three analyses. The analysis of the reactants and all the reaction products was carried out online by gas chromatography.

Inside an automated injection valve, the sample was divided into two portions which were then analyzed in order to obtain a complete quantification of the reaction products. H_2, CO, CO_2 and CH_4 were identified using a column of silica gel 12 grade 60/80 (18´x 1/8”) with a thermal conductivity detector (Gow-Mac apparatus). Also the ethanol, acetaldehyde were analized with a gas chromatograph Varian 3800 FID using a capillary column VF-1ms, 15 m, 0.25 mm, 0.25 µm.

3. Results and Discussion

3.1.- Texture and structure by XRD

The hydrotalcite samples (HT) promoted with WOx, showed the IV type hysteresis (Figure 1-3). The Ni-Co catalysts also corresponded with the hysteresis of type IV according to the IUPAC classification. The isotherms showed very low adsorption of N_2 at low relative pressures ($P/P° < 0.9$) revealing the absence of micropores, however a remarkable adsorption increase was observed at relative pressures greater than $P/P° > 0.9$ for all samples, which is due to the presence of interparticle porosity, with non-porous particles of nanometric sizes.

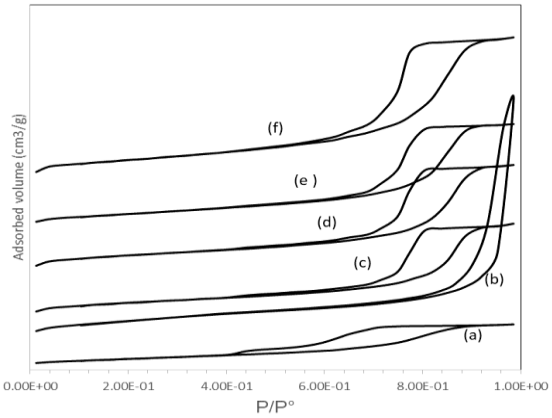

Figure 1. N_2 isotherms of samples with different concentrations of WOx: (a) 16W calcined at 450 ° C,(b) HT, (c) 8W, (d) 4W, (e) 0.5W and (f) 1W.

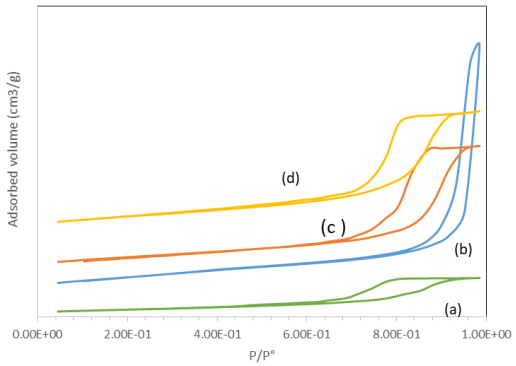

Figure 2. N_2 isotherms of samples with different concentrations of WOx calcined at 600 ° C. (a) 16W calcined at 600°C,(b) HT, (c) 4W, (d) 1W.

The presence of micropores was not observed, but the presence of meso and macropores was found in all the samples (Fig. 1-3). These catalysts were mesoporous and macroporous (see Table 1).

The surface area of the hydrotalcite, decreased when Ni and Co compounds were impregnated by coprecipitation and the pore diameter distributions showed mesopores and macropores (values did not change more than 15%). By XRD the presence of hydrotalcite (HTA), $MgNiO_2$, Periclase (MgO), κ-Al_2O_3 and Bunsenite (NiO) were observed (Figure 5-8).

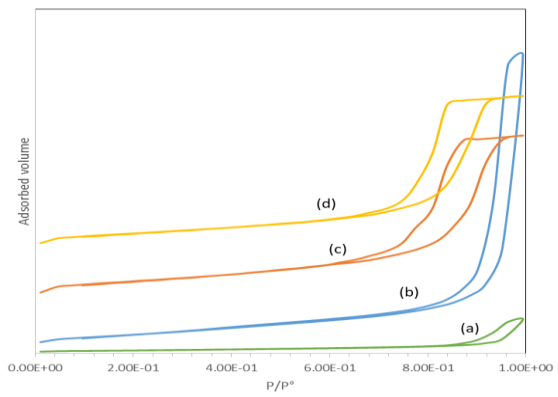

Figure 3. N2 isotherms of hydrotalcite samples with different concentrations of WOx calcined at 800 ° C. (a) 16W.(b) HT, (c) 8W, (d) 1W.

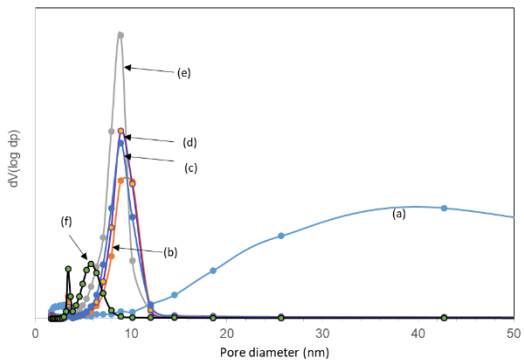

Figure 4. Pore diameter of the samples with different concentrations of WOx after calcining at 600 ° C.(a) HT, (b)

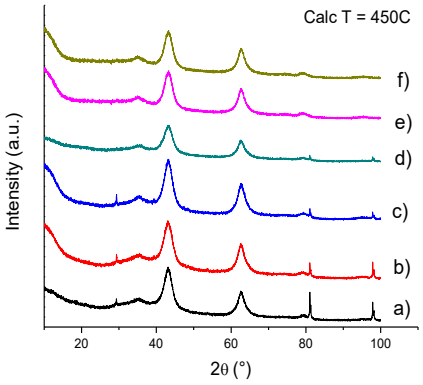

Figure 5. XRD of hydrotalcite samples with different concentrations of WOx after calcining at 450°C. a) 0% W, b) 0.5%W, c) 1%W, d) 4%W, e) 8%W, f) 16%W. (a)

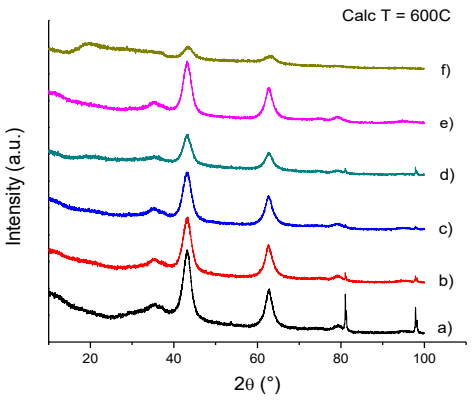

Figure 6. XRD of hydrotalcite samples with different concentrations of WOx after calcining at 600 ° C. a) 0% W, b) 0.5%W, c) 1%W, d) 4%W, e) 8%W, f) 16%W.

In the hydrotalcite sample, particles with diameters between 20-55 nm were observed by SEM having a lamellar shape (Figure 9) while in the catalysts already calcined (450°C) with Co and Ni, particles between 20 to 70 nm having a semi-cubic form were observed (Figure 10-12).

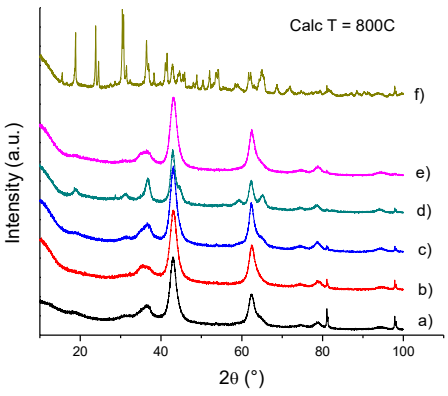

Figure 7. XRD of hydrotalcite samples with different concentrations of WOx after calcining at a) 0% W, b) 0.5%W, c) 1%W, d) 4%W, e) 8%W, f) 16%W. at 800 ° C.

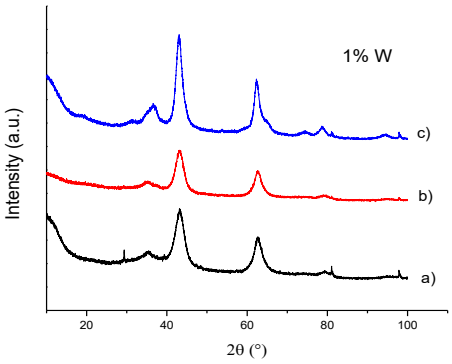

Figure 8. XRD of samples: (a) 1W-450, (b) 1W-600 and (c)1W-800 samples

It is observed in the XRD studies that the effect of the addition of WOx does not modify the reflections located at 2θ = 35, 42, 62, 79°, which correspond to the calcined HT without W. In other words, the W is exchanged with the structure It is generated already mentioned from spinel-type oxides of MgO, and Al_2O_3. On the other hand, when the calcination temperature is increased from 450, 600°C it is observed that all the reflections of the 16% W sample decreased while the samples with a lower content were maintained. This change could be related to a decrease in crystallinity, obtaining amorphous compounds linked to W.

In the case of samples calcined at 800°C, we can again observe changes in the sample at 4% W and 16% W. The sample with 4% W shows other reflections at 2θ = 31, 59° and 62.5 ° which indicates the possible formation of other compounds (not yet identified) that reappear in the sample of 16% W where a multitude of related peaks are observed. with the formation of Al and Mg tungstates.

Table 1. Surface area and texture of the hydrotalcite-WOx samples calcined at 450,600 and 800°C for 5 h.

Hydrotalcite	Surface Area (m^2/g)	Pore Volume (cm^3/g)	Pore Diameter (A)
HT-450	208,0	0,8417	161,9
0.05W -450	170,4	0,3429	80,48
1W -450	216,1	0,5107	94,51
4W -450	184,7	0,3872	83,85
8W -450	153,1	0,3713	96,99
16W -450	89,61	0,1554	69,37

Hydrotalcite	Surface Area (m^2/g)	Pore Volume (cm^3/g)	Pore Diameter (A)
HT-600	192,8	0,1004	208,4
0.05W -600	194,7	0,5279	108,5
1W -600	--,--	-,----	---,-

4W -600	212,1	0,5115	96,47
8W -600	--,--	-,----	--,--
16W -600	68,35	0,1558	91,15

Hydrotalcite	Surface Area (m^2/g)	Pore Volume (cm^3/g)	Pore Diameter (A)
HT-800	138,2	0,9409	272,3
0.05W-800	169,1	0,5326	126,0
1W-800	--,--	-,----	---,-
4W-800	158,7	0,5027	126,8
8W-800	--,--	-,----	---,-
16W-800	21,98	0,1075	195,6

3.2.- Catalytic Activity.

In relation to catalytic selectivity, it is observed in Figure 13 that in general the production of H_2 is maintained and the presence of CO_2, CO and CH_4 oscillates. A decrease in H_2 production is only observed in the sample containing the highest concentration of W (NC-16W).

The deactivation tests at 600 ° C observed in Figure 14 show that when the catalyst is synthesized at low concentrations of W, the activity is better maintained than when the concentration of W increases (NC-16W). This behavior is related to the formation of multiple Al or Mg tungstates that, although they have high thermal stability, are not as catalytically active.

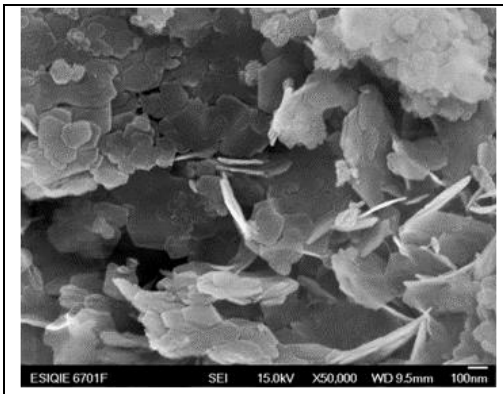

Figure 9. SEM of dry hydrotalcite

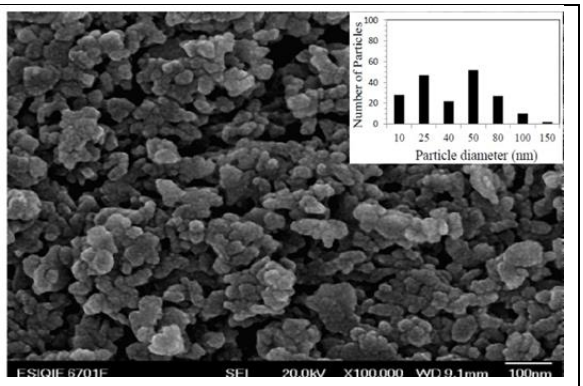

Figure 10. SEM of HT calcined at 450°C

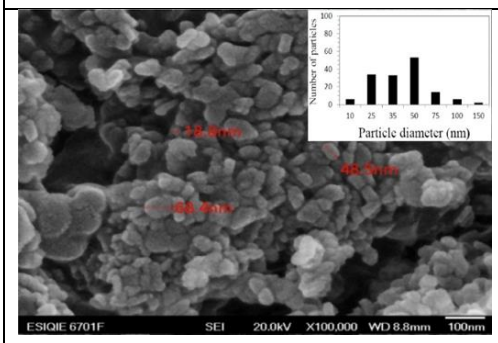

Figure 11. SEM of Co-18 calcined

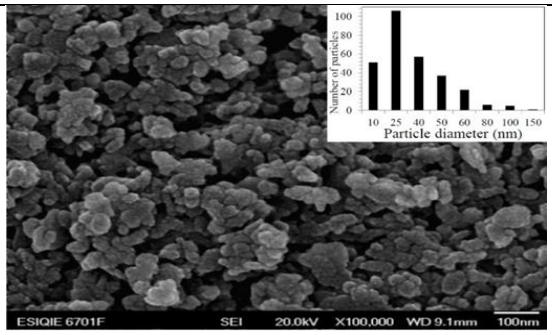

Figure 12.SEM of 0.05W-450 calcined catalyst

Table 2. Characterization of Ni-Co-hydrotalcite-WOx catalysts prepared by coprecipitation.

Catalyst	Ni wt%	Co wt%	W wt%	A_{BET} [m^2/g]	Dp [Å]	XRD[a] Compounds	SEM Particles	EDS Elements
HT	0	0	0	201	161	H,P,A	20-55nm	Mg,Al
NC-0.5W	10	4.5	0.5	169	80	H,M,P,N,	20-45	Mg,Al,Co,Ni
NC-1W	10	4.5	1	210	94	H,M,P,N,	----	Mg,Al,Co,Ni
NC-4W	10	4.5	4	180	83	H,M,P,N,	20-50	Mg,Al,Co,Ni
NC-8W	10	4.5	8	150	96	H,M,P,N,	---	Mg,Al,Co,Ni
NC-16W	10	4.5	16	87	69	H,M,P,N,	---	Mg,Al,Co,Ni

a H=hydrotalcite, M=MgNiO2,P=Periclase(MgO),A=κ-Al2O3,N=Bunsenite(NiO).

High H_2 selectivity and conversion were obtained at 450°C (Table 2) and no CO was observed in the bimetallic catalysts. These catalysts produced CH_4, CO_2 and H_2 and all the ethanol was converted. We did not find CH_3CHO and $CH_2{=}CH_2$.

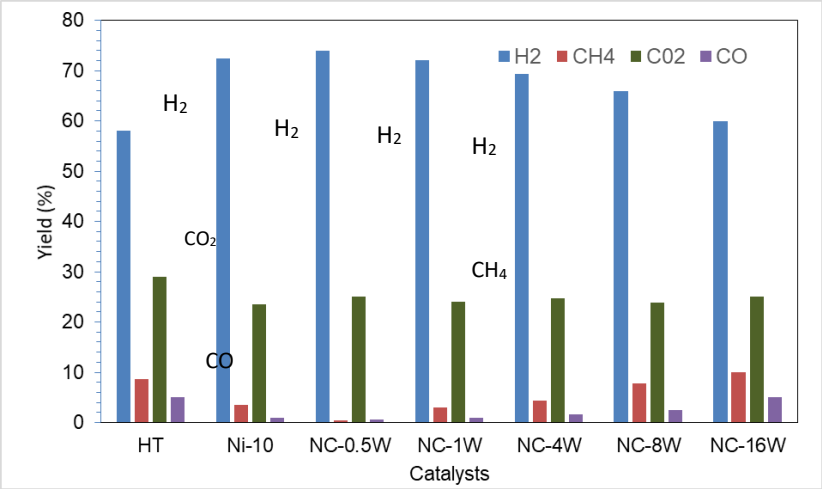

Figure 13. Selectivity and conversion for the ESR reaction of the NC-W catalysts.

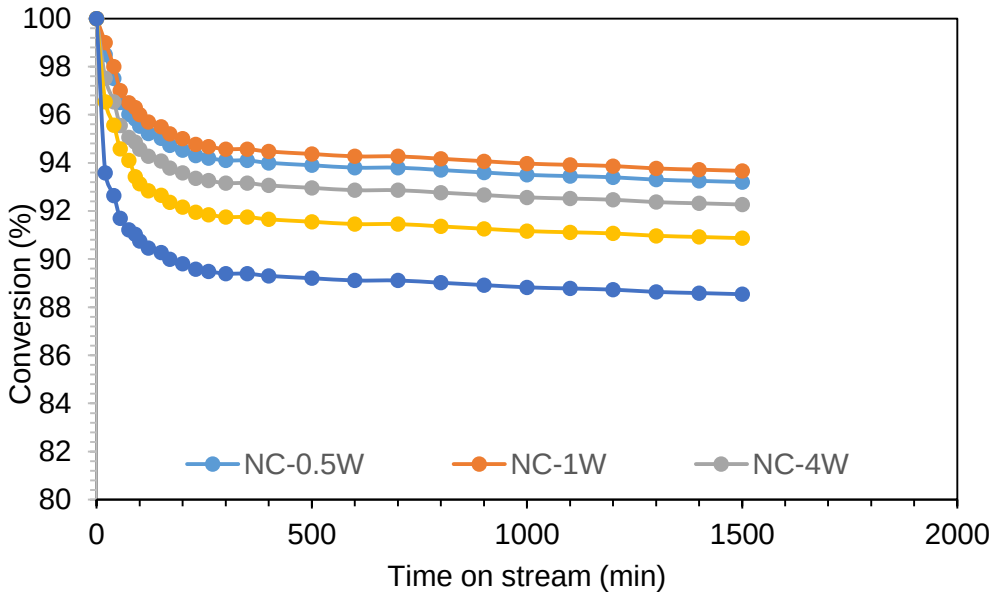

Fig. 14. Deactivation curves of the catalysts evaluated at 600°C.

4. Conclusion

Ni, Co catalysts supported on a hydrotalcite exchanged with W oxides (WOx) have been prepared and evaluated to provide greater thermal stability as well as modify the texture of the micropores and / or meso and macropores. Through three different calcination temperatures (450, 600 and 800 ° C, the texture and structure were studied as changes. These catalysts based on 10% Ni, 4.5% Co allowed to obtain high yields of H2 from the reaction of reformed with bioethanol (4/10 ratio, ethanol / water) at 600 ° C. The deactivation evaluations were carried out for 24 h.

Acknowledgements

To the UAM, the IMP and the IPN for their support in this investigation. Also to the company Síntesis y Aplicaciones Industriales SA

References

[1] R.D. Cortright, R.R. Davda, J.A. Dumesic, Nature 418, 964(2002).
[2] J. Llorca, N., Homs, J.Sales, J. L. G. Fierro and P. Ramírez de la Piscina, J. Catal. 222, 470-480(2004).
[3] J. L.Contreras, J. Salmones, L. A. García, A. Ponce, B. Zeifert and G.A. Fuentes, J. of New Materials for Electrochemical Systems 11, 109-117(2008).
[4] M. N.Barroso, M. F.Gómez, L.A.Arrúa, M. C.Abello, Appl. Catal. A: General 304, 116-123(2006).
[5] J. Llorca, N. Homs, J. Sales, and P. Ramírez de la Piscina, J. Catal. 209, 306-317(2002).
[6] K. Sing, D. Everett, R. Haul, L. Moscou, R. Pierotti, J. Rouquerol, and T. Siemieniewska, Pure Appl. Chem. 57, 603 (1985).
[7] L. D. Gelb, K. E. Gubbins, R. Radhakrishnan, and M. Sliwinska-Bartkowiak, Reports on Progress in Physics 62, 1573 (1999).
[8] S. Lowell, J. E. Shields, M. A. Thomas, and M. Thommes, Characterization of Porous Solid and Powders: Surface Area, Pore Size and Density, Kluwer Academic Publishers, (2004).
[9] M. del Arco, D. Carriazo, S. Gutiérrez, C. Martín and V. Rives, Inorg. Chem. 43, 375-384(2004).
[10] F. Basile, G. Fornasari, M. Gazzano, A. Vaccari, Appl. Clay. Sci. 16,185(2000).
[11]T.Shishido, M.Sukenobu, H.Morioka, R.Furukawa, H.lShirahase, K.Takehira, Catal. Lett.73, 21 (2001).
[12] C. Resini, T. Montenari, L. Barattini, G. Ramis, G. Busca, S. Presto, P. Riani, R. Marazza, M. Sisani, F. Marmottini, U. Costantino, Appl. Catal.A: General, 355, 83-93(2009).
[13] A. Bartecki and Dembicka, D. J. of Inorg. and Nuclear Chem.V.29,I.12, 2907-2916(1967).
[14] A. Iannibello, L. Villa, and S. Marengo, Gazzetta Chimica Italiana,109, 521(1979).

ID 075

Electrocatalytic materials for electrolysis in acid medium

A.M Fernandez*,[1] and J. Gutierrez-Castañeda[1].

[1]Instituto de Energias Renovables, Universidad Nacional Autonoma de Mexico,
Av. Xochicalco s/n, Col Ruben Jaramillo, 62580, Temixco, Mor. Mexico
* Corresponding author: afm@ier.unam.mx

ABSTRACT

The accelerated consumption of fossil fuels and their high emission of greenhouse gases have motivated the investigation of alternative fuels. Renewable energy has proven to be a promising option to replace fossil fuels since it is environmentally friendly and sustainable, and its sources such as solar, wind, maritime and geothermal energy are abundant on earth [1].

Hydrogen is often considered the best media for storing energy that comes from renewable and intermittent energy sources. With the increasing capacity of renewable energies that reach gigawatts, a storage system of equal magnitude is required. However, due to the low demand for electrolytic hydrogen in the last century, research on membrane water electrolysis (PEM) has been neglected [2].

The catalysts for the hydrogen evolution reaction are necessary for a hydrogen economy to be sustained since they are the best proposal to replace fossil fuels, in this work three Pt, Ru and Ir alloys were synthesized for use as catalysts in The production of hydrogen by electrolysis in an acid medium, the samples were characterized physicochemical and it was found that the best proportion of these metals is $Pt_{2.5}Ru_{0.5}Ir_{4.5}$ which presented characteristic kinetic parameters of Platinum without being pure Platinum, physical tests such as EDS and X-rays showed the appearance of the Ir-Pt phase and presence of very discrete ruthenium.

It is important to mention that water electrolysis has been recognized as the only current practical method for the production of hydrogen from renewable energy sources [3].

Keywords: water electrolysis, electrocatalitic materials, PEM-Electrolyzer component

---

1. Introduction

The last years for membrane-based electrolysis have been aimed at lowering the cost, this is achieved with better catalysts and configurations, in addition the main reason is to favor the reaction of hydrogen evolution (HER) that occurs in the cathode and the oxygen evolution reaction (OER) that occurs at the anode. Using the same electrocatalyst for both HER and OER has the advantage of simplifying the system and reducing cost. The electrocatalytic materials based on non-precious metals and efficient for both reactions, in strongly alkaline electrolytes, are metals such as Fe, Co and Ni and are more active for OER, these are the so-called metallic oxyhydroxides. [5].

Alkaline electrolysis has become a well-developed technology for the production of hydrogen up to the megawatt range and is the most widely used commercial technology. It is characterized by having two electrodes immersed in an alkaline electrolyte which is usually a potassium hydroxide solution between 20 to 30% vol. There are three problems associated with alkaline electrolyzers, a low partial charge range, limited current density, and low operating pressure.

1.1 Solid Oxide Electrolyzer (SOEC)

Since 1980 electrolyzer has been developed using solid oxides. Since then SOEC's have been of great interest as they convert electrical energy into chemical energy, producing hydrogen with high efficiency. SOEC technology is currently still under investigation and development. SOEC electrolyzer has enormous potential for future hydrogen production, as long as problems related to the durability of ceramic materials at high temperatures and long-term operation is resolved. [4].

1.2 Electrolisis de agua PEM.

In 1960 General Electric developed the first electrolyte water electrolyze based on an electrolyte concept solid polymer, the first proposal was a solid sulfonated polystyrene membrane as an electrolyte. This arrangement is known as proton exchange membrane water electrolysis or polymer electrolyte (both with the abbreviation PEM), and less often it is also called electrolysis Solid Polymer Electrolyte (SPE). Today it is known that the polymer electrolyte membrane (like Nafion®, Fumapem®) is responsible for providing high proton conductivity, low cross-over gases, compact system design and high-pressure operation. The small thickness of the membrane (20 to 300 micro m thick) is partly the reason why PEM is promising for storing energy intermittent. [4] Titanium-based bipolar plates (BPP) are commonly used in these electrolyzers as they can withstand the harsh operating conditions that occur within a running PEM electrolyzer [6].

Noble metal oxides such as iridium oxide (IrO2) and ruthenium oxide (RuO_2) have been performing well for OER, so the natural choice for the electrode material where OER occurs is metal oxide. Due to the high cost of noble metals, the application should be limited. In the early of 1973 electrolyzers based on Ir-based and Pt-Black catalysts with a high metal charge, and liquid acid electrolytes were built for both HER and OER. Likewise, it is known that to favor OER the use of Rh and Ir and Pt-Rh alloys is recommended, whose catalytic

activities decrease as follows: Pt <Pt-Rh <Rh <Ir. Currently, the loads for the anode catalyst layer range around 2mg / cm2

1.3 Electrocatalysts for the oxygen evolution reaction (OER).

The use of IrO_2 is generally recognized to promote OER in PEM electrolysis. RuO_2 is more active than IrO_2, but problems related to instability (corrosion) limit its use. Some publications about PEM electrolysis recommend the use of Ru and Ir catalysts, and their alloys, for OER. Using oxides such as Ta_2O_5, Nb_2O_5, Sb_2O_5 and their mixtures (eg SnO_2-IrO_2-Ta_2O_5), improve stability and durability. The use of the electrodes with Ti/IrO_2 showed good results in both needs and it was concluded that a rapid migration of O_2 towards the substrate appeared that was due to an electric field within the coating, this migration produces an insulator in TiO_2 which gives as a less effective electrode results after a while. [4]

1.4 Electro catalysts for the evolution reaction of hydrogen (HER).

In order to promote the HER, the use of black platinum has been proposed as a standard catalyst. However, despite the lower platinum loads compared to the side load of the anode, the cathode catalyst still represents a considerable part of the total cost of the system, especially if degradation or corrosion of the carbon support occurs [4]. Today, loads for the cathode side range from 0.5 to 1 mg/cm^2 and further reductions will always be desired, with the potential to reach values below 0.2 mg/cm^2. [6]. There are studies that attempt to reduce platinum loads [7], improve the use of catalysts (homogeneity, particle size) and potentially replace them (creating so-called platinum free catalysts).

The purpose of this work is work is to synthesize a $Pt_xRu_yIr_z$ alloy using minor proportions of Platinum in order to use it in the HER reaction. These proportions were studied extensively by Chen [8] who made 715 combinations with different proportions, Chen's conclusion is that the binary PtRu and tertiary $Pt_{4.5}Ru_4Ir_{0.5}$ are the best proposals to obtain bifunctional materials; in the case of a electrolyzer tertiary alloy seems to be a better option since it has more Pt.

2. Materials and Methods

Electrocatalytic materials were made using a thermal pyrolysis technique in a cylindrical furnace, brand Thermonlyne model 21100, into which a porcelain capsule (42.77 mm in diameter) was introduced, where salts of platinum $H_2PtCl_6{\cdot}6H_2O$, ruthenium $RuCl_3{\cdot}H_2O$ and iridium $IrBr_3{\cdot}H_2O$, adding drops of deionized water to mix them. The synthesis of the materials was carried out in a reducing atmosphere with a gas whose composition was 5% hydrogen and 95% nitrogen. The synthesis temperature was 550°C. Different types of heating/cooling ramps were used to achieve this temperature.

The electrochemical performance of the electrocatalytic material was carried out in a three-electrode cell containing a Pt mesh as a counter electrode (CE), and an Ag/AgCl/KCl electrode as a reference (REF) and as a working electrode (WE) a glassy carbon disc 7 mm in diameter, covered with electrocatalytic ink. The cell solution was 0.5 M H_2SO_4 purged with N_2 (Infra Co.; Ultra High Purity UHP, 99.999% MIN) and/or O_2 (Infra Co.; zero grade, UHP). Electrochemical techniques as Cyclic Voltammetry (CV), Linear Sweep Voltammetry (LSV)

and Rotating Disk Electrode (RDE) were carried out using Potentiostat/Galvanostat equipment (VSP-Biologic). The open circuit potential (OCP) of the electrodes was measured at the end of each experiment. Then, linear sweep voltammetry (LSV) measurements of the ORR were done in an electrolyte saturated with O2. The OCP for the ORR was measured for each catalyst and polarization curves were obtained in a range between E_{O2}^{OCP} and 0.658 V/NHE, at the scan rate of 5 mV/s. The rotation speed ranged from 100 to 1600 rpm.

3. Results and Discussion

3.1. X-ray energy dispersion spectrometry.

EDS analysis results are shown in Table 1. From this table it is observed that for sample N8, the presence of Ru and Pt, Similar occurs with sample N9 where Pt and Ru also appear. In the case, sample N10 shows the presence of Ir, according to this analysis.

Table 1.EDS analysis results for samples.

Sample	Element	Atomic Comp (At %)	Stoichiometry
N8	Pt	47.09	$Pt_{3.3}Ru_{2.19}Ir_0$
	Ru	53	
	Ir	0	
N9	Pt	15.82	$Pt_{2.45}Ru_{5.4}Ir_0$
	Ru	84-17	
	Ir	0	
N10	Pt	33.54	$Pt_{2.76}Ru_{0.7}Ir_{4.05}$
	Ru	13.09	
	Ir	4.05	

3.2. X-Ray Diffraction studies

Figure 1 shows the X-ray diffractogram for samples N8, N9 and N10, it is observed that more intense diffraction peaks correspond to planes (111), (200), (220) and (311). These peaks coincide with card 01-071-9289 that identifies the iridium and platinum phase, as seen in figure 1(a). The diffraction peaks corresponding to planes (100), (102) and (200) of card 01-071-9300 identify an iridium and ruthenium phase, for sample N9 (figure 1 (b)), in addition, the Planes (002), (110) and (200) correspond to card 00-046-1044 with an iridium phase only. On the other hand, the diffractogram of N10 figure 1(c) is compared like N8 with the card 01-071-9289 that indicates an iridium and platinum phase.

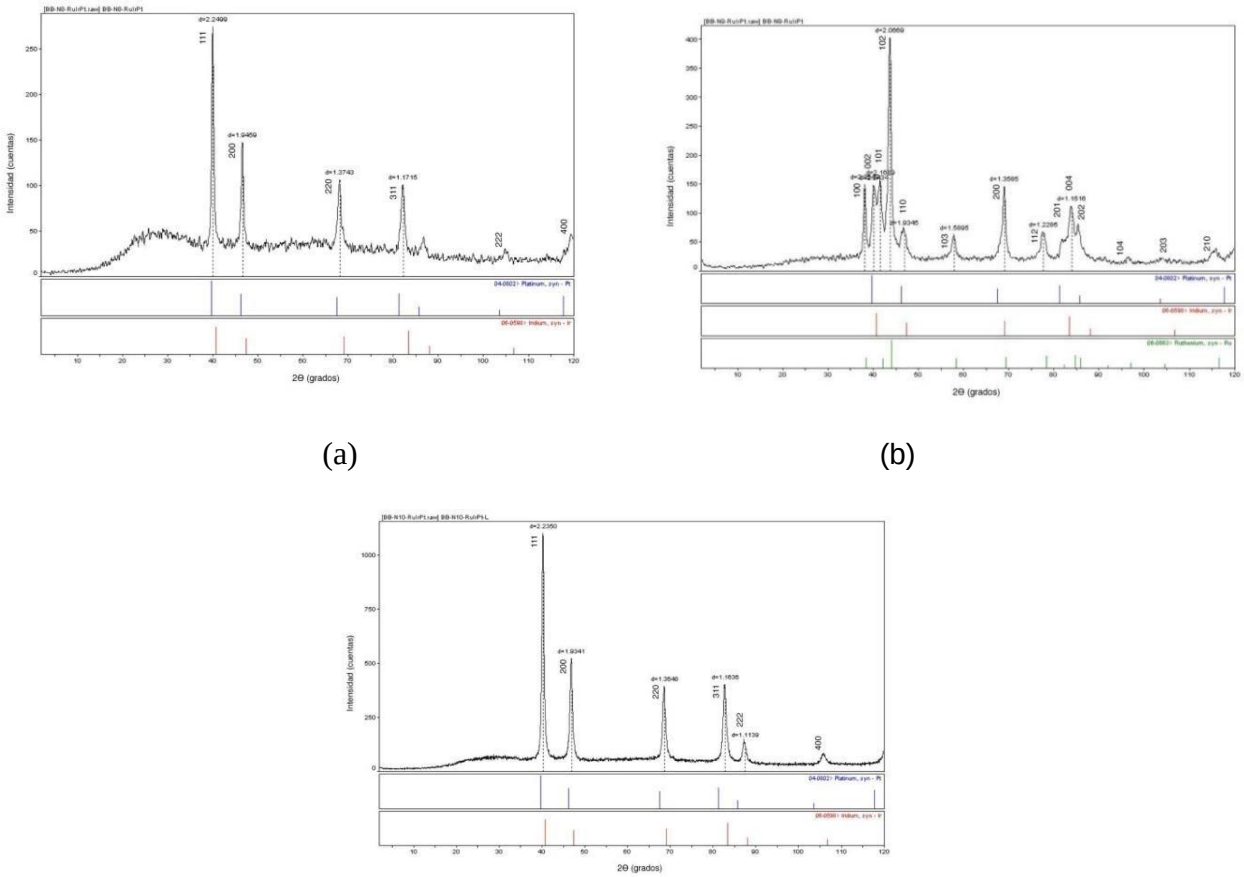

(a) (b)

(c)

Figure 1. XRD for samples N8 (a), N9 (b), and N10 (c).

3.3. Scanning Electron Microscopy (SEM).

Figure 2 shows the morphology of the elements (Pt, Ru, and Ir), made by thermal pyrolysis technique and to be used as a reference, and to be able to compare the morphology. From this same figure, the grain size was determined graphically. Table 2 shows the results.

Sample	Crystal size (nm)
Pt	25.16±7.4
Ru	85.93±30.6
Ir	93.27±29.4

From Figure 2 (a) a misty morphology for Pt can be observed, Ru has an amorphous hexagonal growth, see Figure 2 (b), while Ir has a larger cubic structure, as seen in figure 2 (c).

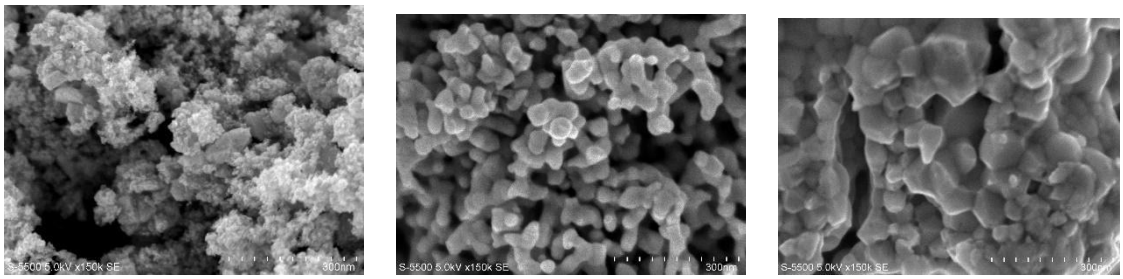

(a) (b) (c)

Figura 2, SEM images for (a) Pt, (b) Ru and (c) Ir made by thermal pyrolysis.

A cartoon of the morphology for each element, shown in Figure 2 could help to analyze the morphology of the synthesized samples, as shown in Figure 3.

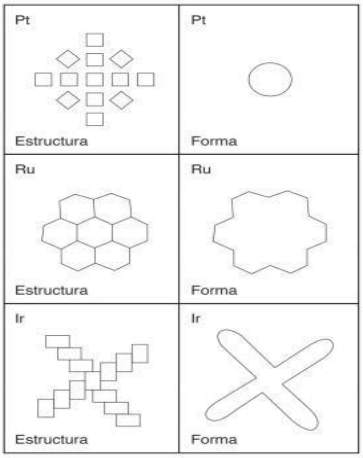

Figura 3. Outline of the morphology of each element (Pt, Ru, Ir) synthesized by thermal pyrolysis, according to figure 2

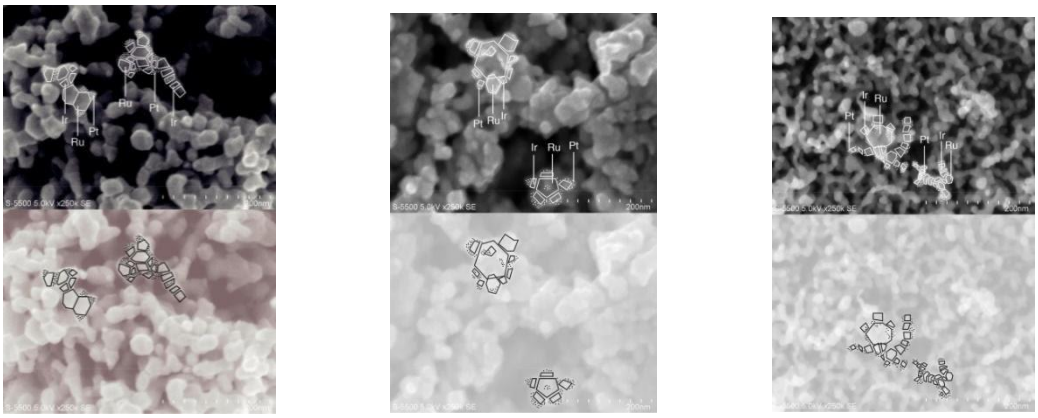

(a) (b) (c)

Figure 4. Overlapping sketches on the morphology of the samples. (a) N8, (b) N9 and (c) N10

Figure 4(a) shows the microphotograph obtained for sample N8 at 250kX and on which the sketches of figure 3 are superimposed. From this figure it is observed that in some regions the base is Ir crystals with terminations of Pt, long strips are due to Ru. In Figure 4 (b), the microphotograph for sample N9 is observed, where the growth of crystals on a Ru base is observed, this results in thicker branches due to the union of Ru and Ir, the Pt is Passes end of Ir at intersections between Ru and Ir.

Figure 4 (c) shows the growth of Ru and Ir crystals, forming chains with bifurcations, the Ir strips are divided by Ru junctions and platinum is found at the intersections and ends of Ir. According to the analysis of the images we can obey some general conclusions for the coupling of the structures. It was observed that platinum grows in the ends of the structures, it has a preferential growth in the ends of the iridium and in the faces of ruthenium, when accumulating in the lumps, similar to small spheres. However, iridium grew adequately. The iridium produces malformations or deformations in the base structures, in addition iridium is responsible for the connections between ruthenium structures, with the help of platinum fits and forms curves that unite the material as a whole. Finally, ruthenium tends to be the base of the structures, from it the crystals of the other materials grow and in some cases another ruthenium structure joins to form chains of hexagons where platinum fills the missing holes.

3.2. Electrochemical characterization.

3.2.1. Cyclic voltametry CV.

Figure 5 (a) shows the result for cyclic voltammetry for samples N8, N9 and N10. The voltamperogram for sample 8 shows a behavior very similar to Pt, as can be seen in Figure 5 (b), observing the two reduction and oxidation peaks. For sample N9, an envelope with a behavior similar to Ru is presented, with the peaks of the reduction process faded and travel to potentials near 0.1 V, and with a minimum of oxidation close to 0.4 V. For

sample N10, the characteristic peaks are observed. at Pt, but a mostly rectangular area is also observed, thereby indicating less wear.

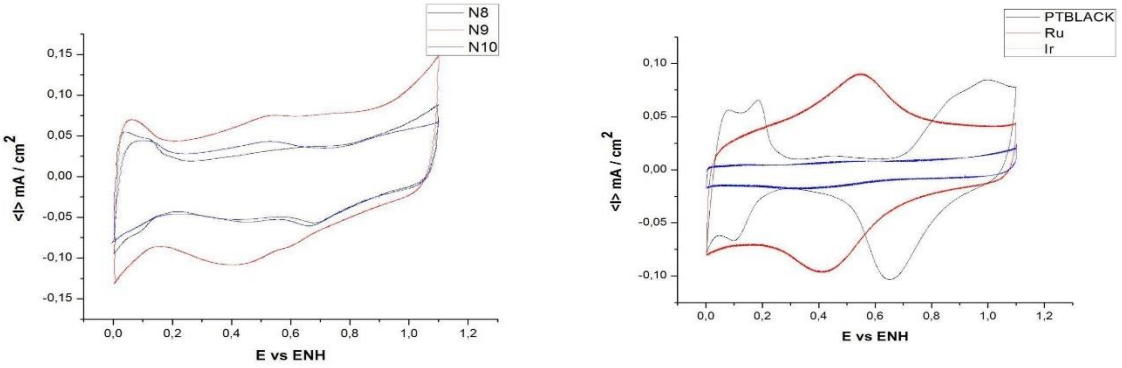

(a) (b)

Figure 5. Voltamperograms for samples (a) N8, N9 and N10, and (b) Pt, Ru and Ir synthesized under the same experimental conditions, as the samples. The measurement conditions are 0.5 M H_2SO_4 and a speed of 20 mV / s.

To determine the contribution of each of the metallic materials synthesized in the samples, the following graphic matrix was prepared, in Figure 6

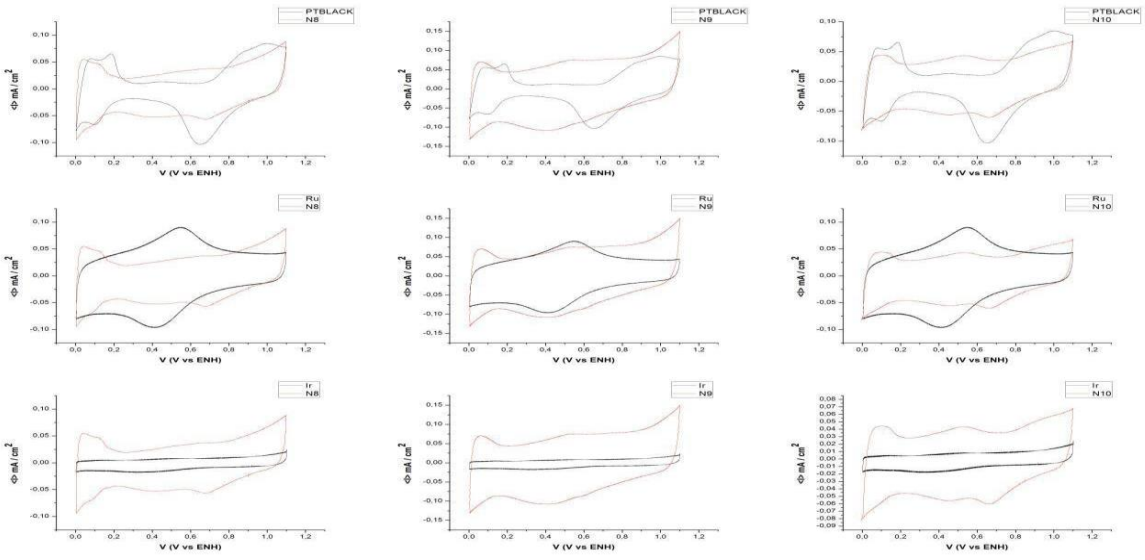

Figure 6. Matrix with the different permutations of synthesized materials and the references.

From figure 6, it can conclude that the contribution of Ir in the samples allows the samples to have greater stability, that is, it reduces the maximum and minimum oxidation and reduction, so it is basically inert. On the other hand, Platinum helps the production of hydrogen by being the best catalyst for said reaction, while Ru has the property of increasing the current produced, it is also appreciated that it is responsible for the displacement of the peaks of maximum and minimum.

3.2.2. Lineal Sweep Voltammetry (LSV).

LSV enables various kinetic parameters of the material to be determined, such as electron transfer, and Tafel slope analysis, and exchange current density. Graph 7 shows the LSV obtained for each sample.

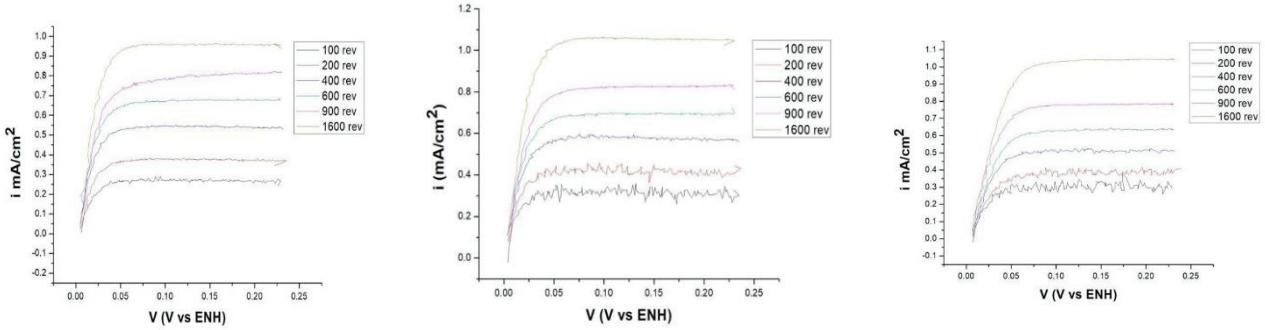

(a) (b) (c)

Figure 7. LSV of samples (a) N8, (b) N9, and (c) N10.

It is posible to observe in all the three graphs, the current obtained does not exceed the value of 1.1 mA/cm2 in any ef the cases. This result obeys the theoretician using in the Levich equation [9]

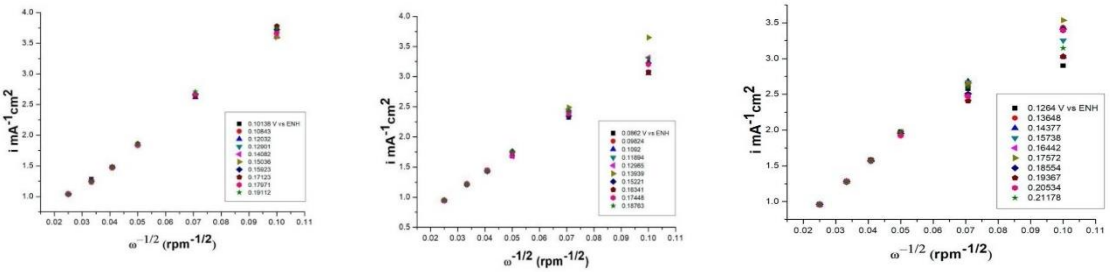

(a) (b) (c)

Figure 8. Koutecky-Levich graphs of samples (a) N8, (b) N9 and (N10), from 900 to 1600 revolutions.

The Koutecky-Levich graphs were constructed from the figure 7. In figure 8(a) it is shown that for sample N8, and between the revolutions of 900 and 1600 it is observed that the current for different voltages almost does not change, while for figure 8 (b), sample N9, the tendency to increase rotation is a stability in the current, of less magnitude than in N8 with regard to a minor electron transition. In figure 8(c), for sample N10, a scattering is presented with increasing rotation, this seems very large, so different electron transfer mechanisms may be occurred. In this case, different electron transfer mechanisms could be occurring, fast processes still predominate. Considering that, for this sample, and according to the EDS and XRD analyzes, which indicate a higher presence of Ir, these different processes may be due to the presence of this metal.

3.2.3. Kinetic parameters.

The kinetic parameters obtained for each of the materials are shown in Table 2

Table 2 Kinetic parameters obtained for the synthesized materials (N8, N9, N19) and Pt black

Sample	b mV/dec	**α**	**i_o**
N8	36.794	0.996	0.99
N9	49.121	0.995	0.99
N10	34.665	0.996	0.99
Pt black	36.835	0.996	0.99

The previous results compare those reported in the literature, where it is mentioned that for platinum-containing compounds, Tafel slope values of the order of 30 mV/dec are reported, in addition to the fact that the exchange current density is also very close to 1. [10-12]

Pt (110) Tafel slopes of the order of 28 mV/dec have been observed, while for Pt (100), this slope increases to 37 mV/dec, and Pt (111) have reported close values. at 112 mV/dec [10], in our case it is most likely a combination of the first two, that is call a Heyrovsky-Volmer process

It can be concluded that in the synthesized materials the reaction in Pt (100) occurs with a Heyrovsky-Volmer process, since the Tafel slopes range between 36 and 49 mV/dec.

Using precious metals OER/HER activity is scaled as follows according to Durst [13] Pt>Ir≥Rh>Pd. The anodic and cathodic transfer coefficients are similar for all these metals when supported on carbon, as it shown in this study.

4. Conclusion

Three electrocatalytic materials for the production of hydrogen in acid medium were synthesized by thermal pyrolysis with the following stoichiometry, $Pt_{2.5}Ru_{0.5}Ir_{0.5}$ (N8), $Pt_{2.5}Ru_{4.5}Ir_{0.5}$ (N9) and $Pt_{2.5}Ru_{0.5}Ir_{4.5}$ (N10). According to the cyclic and rotary disk voltammetry studies, Tafel slopes of 36.794 for N8, 49.121 for N9 and 34.665 for N10 were obtained, from the scanning microscopy studies it was concluded that the grain size is around 45.91 nm, 99.70 nm and 46.14 nm for N8, N9 and N10 respectively, and the Ir-Pt and Ir-Ru phases were found in some of the samples, the proportions were $Pt_{3.33}Ru_{2.19}Ir_{0}$ for N8, $Pt_{2.45}Ru_{5.4}Ir0$ for N9 and $Pt_{2.76}Ru_{0.7}Ir_{4.05}$ for N10.

According with the experimental results the best sample is the sample N10, due it shows stability, according to the cyclic voltammetry, in addition, it maintains observable redox pairs that indicate that no oxides are being formed in the surface that alter the catalytic activity, the EDS shows that it is the only sample with indications of all the materials that are sought are in the alloy, in addition to that SEM shows that its grouping has a shape that despite being lumpy maintains a high contact area and the slope of Tafel is very close to that of platinum without being pure platinum, that is, we have a material with catalytic behavior of platinum without a high load of it.

To improve the results obtained, it is recommended to allow materials to spend more time in a reducing atmosphere when synthesizing them, to maintain better temperature control, to carry out studies with more carefully calibrated electrodes, in addition, materials can be synthesized from the beginning with a support like Vulcan to see if this improves catalytic behavior.

Acknowledgements

One of the authors thanks the scholarship support to CONACYT. Also, we would like to thank Maria Luisa Ramon García for the XRD, Rogelio Morán Elvira for SEM measurements

References

[1] Francesco Valle, Electrocatalysts degradation in high temperature PEM fuel cells, PhD thesis, 04/2015.
[2] Ehab N, El Sawy and Viola Birss. Nano-porous iridium and iridium oxide thin films formed by high eficiency electrodeposition 2009, 19, 8244–8252.
[3] Mozota J, Conway. Surface and bulk processes at oxidized iridium electrodes- I. monolayer stage and transition to reversible oxide film behavior 1983;28;1-8.
[4] Feng Q, Xiao AZ, Gaoyang L, Bing W, Zhen Z, Hui L, and Haijiang W, A review of proton exchange membrane water electrolysis on degradation mechanisms and mitigation strategies. Journal of Power Sources, 2007; 366:33-55.
[5] Carmo M and Fritz DL, A comprehensive review on PEM water electrolysis. Int. J Hydrogen Energy 2013;38;1-8.

[6] Mart DC . Performance of a PEM electrolyzer using RuIrCoOx electrocatalysts for the oxygen evolution electrode, 2013:8:2-8.
]7] Morales-Salas L, Síntesis y caracterización de nano partículas electrocataliticas bifuncionales PtxRuyIrz para el electrodo de oxigeno de una celda regenerativa unificada. PhD thesis, UNAM, 2016.
[8] Chen G, De la Fuente DA, Sarangapani S, and Mallouk TE, Combinatorial discovery of bifunctional oxygen reduction-water oxidation electrocatalysts for regenerative fuel cells. Catalysis Today, 2001;67(4):341-355.
[9] Bard. Allen J and Faulkner. Larry R. Electrochemical Methods. Second Edition, 2001
[10] Ya-hui Fang and Zhi-pan Liu. Tafel Kinetics of Electrocatalytic Reactions: From Experiment to First-Principles. ACS Catalysis 2014;4;4364-4376.
[11] Uribe-Godinez J, Garcia-Montalvo V, Jimenez-Sandoval O., Study of the oxygen reduction and hydrogen oxidation reactions on RhIrRu-based catalysts. Int. J. Hydrogen Energy 2016,38, 3170-3173.
[12] Uribe-Godinez J, Castellanos RH, Borja-Arco E., Altamirano-Gutierrez A, Jimenez-Sandoval O, Novel osmium-based electrocatalysts for oxygen reduction and hydrogen oxidation in acid conditions 2008,177, 286-295.
[13] Durst Julien, Simon Christoph, Gasteiger Hubert A, Hydrogen Oxidation and Evolution Reaction Kinetics on Carbon Supported Pt , Ir , Rh , and Pd Electrocatalysts in Acidic Media. Journal of the Electrochemical Society, 2015, 162(1):F190-F203

ID 084

Effect of Piranha solution as oxidant in graphene oxide synthesis and in its behavior as photocatalyst for the hydrogen evolution

B. C. Hernández-Majalca, J. L. Dominguez-Arvizu, J. Jiménez-Miramontes, J. C. Pantoja-Espinoza, M.J. Melendez-Zaragoza, J.M. Salinas-Gutiérrez, A. López-Ortiz, V. Collins-Martínez*.

Departamento de Ingeniería y Química de Materiales, Centro de Investigación en Materiales Avanzados, S.C., Miguel de Cervantes 120, Chihuahua, Chih., 31136, México.

* Corresponding author: virginia.collins@cimav.edu.mx

ABSTRACT

Due to the two-dimensional nature of GO, a small superposition of the conduction and valence bands, can be presented in this material, which is responsible for its semimetal character, compared to a semiconductor whose bands must be separated. Depending on the GO oxidation level, the value of this separation, known as bandgap energy, can vary from 0 to 3.7 eV. The main aim of this study is to propose a fast and simple synthesis method for GO, which present self-tuning optoelectronic properties, advantageous features, for their application towards the photocatalytic hydrogen production. Graphene oxides (GO) were prepared through a modification of the Tour method from graphite powder by applying a microwave pretreatment. One GO sample was obtained by the oxidation using a mixture of H_2SO_4 and H_3PO_4 as main oxidants (T-GO). Another GO sample (P-GO) was oxidized employing a Piranha solution (H_2SO_4/H_2O_2). The study of morphology, crystalline structure, size, surface area and optical characterization of the material was carried out by SEM, XRD, TEM, BET and UV-Vis spectroscopy, respectively. Photocatalytic activity evaluation of the GOs towards hydrogen production through the water splitting reaction under visible light was followed by gas chromatography. Results indicate sample P-GO achieved a production of 8000 nmolH_2/g, while T-GO presented a negligible photocatalytic activity, under the same time and irradiation conditions. The difference of photocatalytic activity between these two GOs can be explained in terms of the oxidation degree of each material, so that the piranha solution was able to intercalate molecular oxygen allowing a controlled oxidation of graphite particles assisted by microwave heating.

Keywords: Piranha solution; Water splitting; Graphene oxide; Hydrogen production.

1. Introduction

Research of semiconductor materials with photocatalytic properties is today a major field of study, because the scientific community is constantly searching for new materials that can be used for renewable power generation and sustainable and environmentally friendly processes. Due to this, $BiVO_4$ [1], TiO_2 [1,2], WO_3 [3], CdS [2], C_3N_4 [4], and ZnO [5,6] have been explored in order to find alternatives to current photocatalysts that are prepared with precious metals such as Pt, to increase their efficiency in photocatalytic processes.

The inclusion of carbonaceous compounds in this research field has allowed the study of a wide a variety of materials with suitable optical properties for photocatalytic applications and have enhanced the growth of these in many research fields. Among these materials, the use of graphene in heterojunctions with other semiconductors [7], is one the most important applications.

Graphene is a family of materials where Graphene Oxide (GO) is included with two-dimensional and electronic properties, which are more than interesting such as zero forbidden band and very high conductivity [8] for its application in photocatalysis. However, obtaining a suitable graphene oxide for the generation of hydrogen is a difficult challenge, since the synthesized material must have adequate optical properties for this application. For example, one of them is that the photocatalyst must have the required over-potential for the splitting of the water molecule, which value is 1.23 eV [5]. For GO to acquire the proper properties for photocatalysis, it is necessary to modulate its band gap and to achieve this its oxidation level need to be modified. Therefore, the synthesis of GO plays a very important role, which is why in this study a comparison of two materials synthesized by two variations of the Tour method is studied in order to obtain the best option for its application towards the photocatalytic evolution of hydrogen.

2. Experimental

2.1. T-GO Synthesis

Graphite oxide was synthesized from pulverized graphite (grounded for 6.7 h in a Spex mill with a 10:1 ratio) according to a modification of the Tour method [9,10]. For the oxidation of graphite, 1 g of powdered graphite was subjected to a microwave pretreatment (Liu et al. 2014) for 15 s. Immediately after the microwave treatment, it was added to a concentrated solution with a 9:1 ratio of H_2SO_4 and H_3PO_4 (60 mL and 6.7 mL, respectively), this mixture was kept under stirring in a cold bath (4 °C) for 10 min. After that time 6 g of $KMnO_4$ were added for 3 h, the mixture was diluted with distilled H_2O (130 mL). Finally, a solution of H_2O_2 (12 mL 30%) and 10% HCl (13 mL) were added dropwise to the mixture under constant stirring until the vapors disappear (30 min). These mixtures were kept in an ice bath due to

the exothermic nature of reaction [11]. Finally, the GO was washed and filtered with tri-distilled water, and this aided by a vacuum pump until the acid and permanganate residues present in the mixture were removed. Once this step was completed, the GO was brought to dryness in a muffle at 65 °C.

2.2. P-GO Synthesis.

In this synthesis, like T-GO, it was synthesized following the modification of the Tour method. Briefly, 1g of pulverized graphite was subjected to a microwave pretreatment [12] for 15 s immediately after the microwave treatment. The next step is the difference in this synthesis, then it was added to a concentrated solution of H_2SO_4 and H_2O_2 (60 mL and 12 mL, respectively. Piranha solution) in a 5:1 ratio. This mixture was kept under constant stirring in a cold bath (4 °C) for 10 min. After that time, 6 g of $KMnO_4$ were added for 3 h, the mixture was then diluted with distilled H_2O (130 mL). Finally, even in a cold bath, a solution of H_2O_2 (12 mL 30%) and 10% HCl (13 mL) was added dropwise to the mixture under stirring until the vapors disappeared (30 min). The synthesis was concluded by following the same steps that were used during the synthesis of T-GO. This synthesis was used to synthesize P-GO2, to verify the repeatability of the method.

2.3. Characterization

In this study crystalline phases present in in each of the materials synthesized were determined by the x-ray diffraction technique using a Phillips Xpert-Pro diffractometer, which used a copper Cu-kα radiation (□□= 1.54056 Å) to obtain the diffraction patterns, with a 2□□sweep angle from 5° to 90°, with a step size of 0.05. Diffuse reflectance spectra were recorded using UV Visible Evolution 220 Thermo-spectrophotometer equipped with integration sphere, and the band gap energy was also estimated from the reflectance spectra using the Kubelka-Munk function. The BET surface area was determined with an Autosorb-1 brand Quantachrome using the N_2 physisorption method from 0.05 to 0.3 relative pressure (p/p^0). Sample morphology were examined by electronic field emission scanning (SEM) microscopy in a JEM-2200FS Transmission Electron Microscope Field Emission, where the sample was exposed to a beam of electrons generated from a tungsten filament, to minimize energy losses or deviations of the beam, the column employed an ultra-high vacuum of 10^{-8} Torr.

2.4. Photocatalytic Evaluation

The photocatalytic activity was evaluated based on the performance of the material for the production of hydrogen by the splitting of the water molecule, using as a 250W metal halide lamp as a source of energy, 2% methanol as a sacrifice agent. Photochemical reaction was monitored by gas chromatography using a Perking Elmer Clarus 580 gas chromatograph, taking samples at intervals of time of 1h with 8 repetitions.

3. Results and Discussion

3.1. X-ray diffraction

Fig. 1a) shows diffractograms of fresh graphite (GR), ground graphite (GM), graphene oxide by Tour (T-GO) and graphene oxide by piranha solution (P-GO). In the graphite diffraction pattern (GR), the majority signal can be clearly observed, at angle 2θ = 28 ° ≈ 3.18Å, which typically corresponds to graphite [13]. Also, in this Figure ground graphite (GM) diffraction pattern can be observed where its crystallinity decreases, due to the defects introduced by the milling process [14], it is expected that these defects potentiate the oxidation of graphite during the preparation of GO. In this same pattern, the growth of the peak can be observed at angle 2θ = 42°, corresponding to the crystalline plane (100) of graphene, this is presumably due to the exfoliation caused by the milling process [15, 16]. The asymmetry of the peak can be interpreted as a mixture of oriented graphite crystals and crystals with a larger interplanar space having lattice defects [8].

Furthermore, T-GO sample, which was synthesized from GM, exhibits a diffraction pattern where it is clearly observed that it presents a partial oxidation, since there is still non-oxidized graphitic material, in addition to present increased amorphicity.

Fig. 1b) shows a comparison of diffraction patterns between samples P-GO and P-GO2 in order to analyze and verify if the piranha solution is able to oxidize the graphite surface. In this Figure it can be seen that both materials shift from 2θ angle 28° to approximately 12° and 11° and this behavior is related to the introduction of oxidized functional groups [17]. This shift presumably denotes an increase in the interlaminar distance of the graphite sheets, thus considering that the P-GOX samples present typical structural characteristics of graphene oxide. It is worth mentioning that the reaction resulted in a fine dispersed powder in a suspension that is easier to clean than that obtained using the mixture of sulfuric and phosphoric acids (Tour method). Furthermore, this sample (T-GO) shows traces of oxidized graphite represented by the peak that appears at angle 2θ = 28 °.

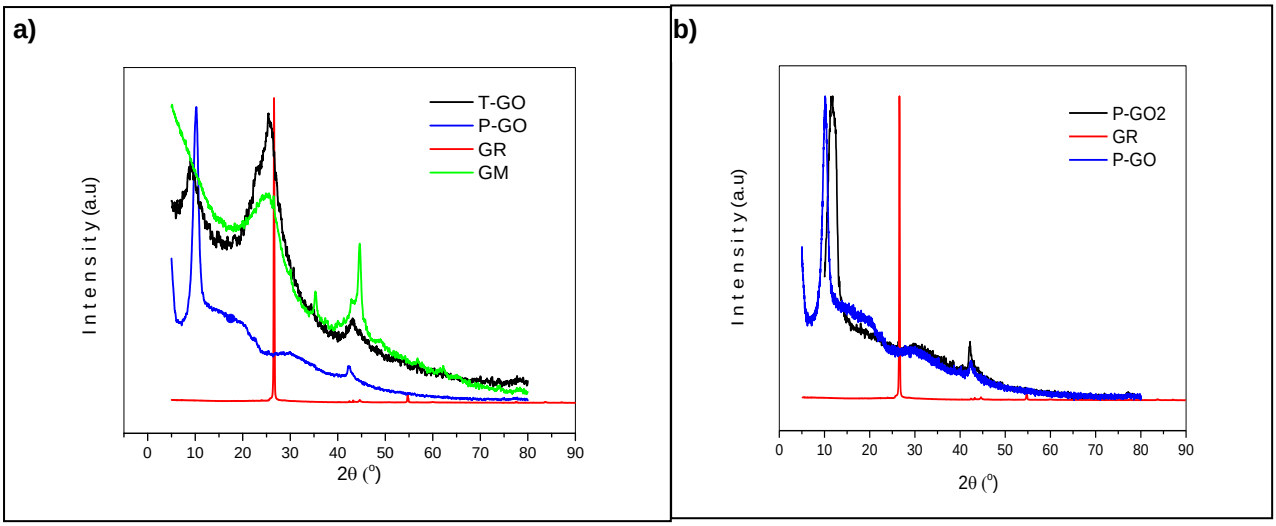

Fig. 1 a) XRD of samples: a) T-GO, P-GO, GR, GM. b) P-GO, GR, P-

3.2. Scanning electron microscopy (field emission)

SEM images of T-GO, P-GO and P-GO2 are shown in Fig. 2 a). In this Figure it can be seen that T-GO sheets are collapsed. However, it can be seen what could be an exfoliated thin layer, with dimensions in the order of microns. In the STEM mode micrograph Fig. 2 b) it can be seen that P-GO sample was exfoliated, since this image shows a spongy material, which can be explained by the research findings of Kurshid and Zhao [17,18]. They reported that the oxidation of graphitic surfaces with acid piranha solutions increase the presence of oxidized functional groups, as well as the generation of defects in the graphite sheet, which allows the increase of the hydroxyl groups at the edges, thus facilitating exfoliation [17,18]. However, the resolution of the micrograph does not allow to determine whether this is monolayer or multilayer, the image shows that this sheet has a certain flexibility, since folds of the sheet and certain curls on the edges can be noticed. While in Fig. C) it can be observed what presumably be an arrangement of a few GO sheets [19].

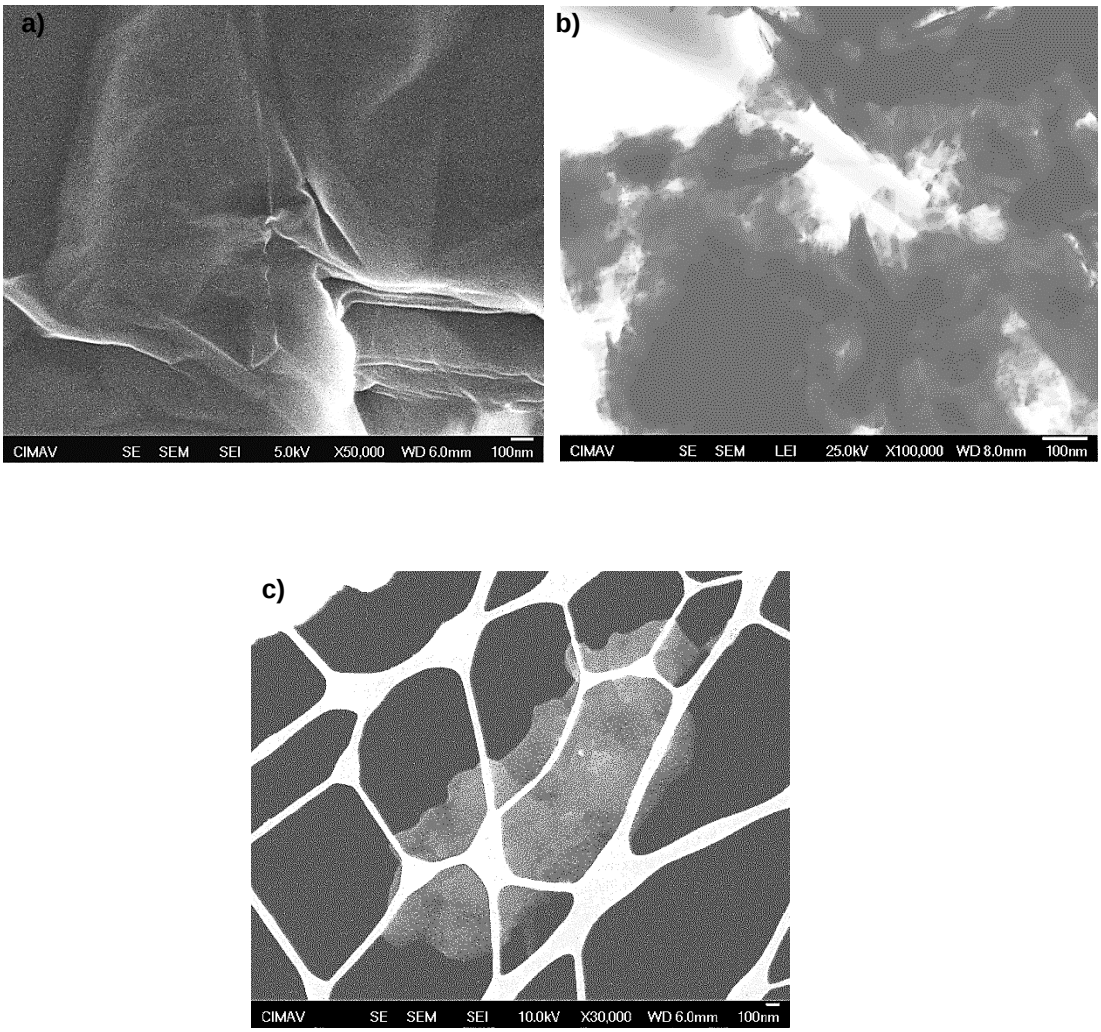

Fig. 2 SEM a) T-GO, b) P-GO, c) P-GO2.

3.3. Specific surface area (BET)

The specific surface area was evaluated by nitrogen physisorption isotherms, in Fig. 3 the GR sample shows a Type-III isotherm and does not exhibit porosity, reaching an area of 7m^2/g. The isotherm in Fig. 4 corresponds to graphite after 8h of ball milling, GM sample shows a Type-III isotherm and without porosity, with an area of 161 m^2/g, this increase in area is attributed to the decrease in particle size caused by high energy milling process [14].

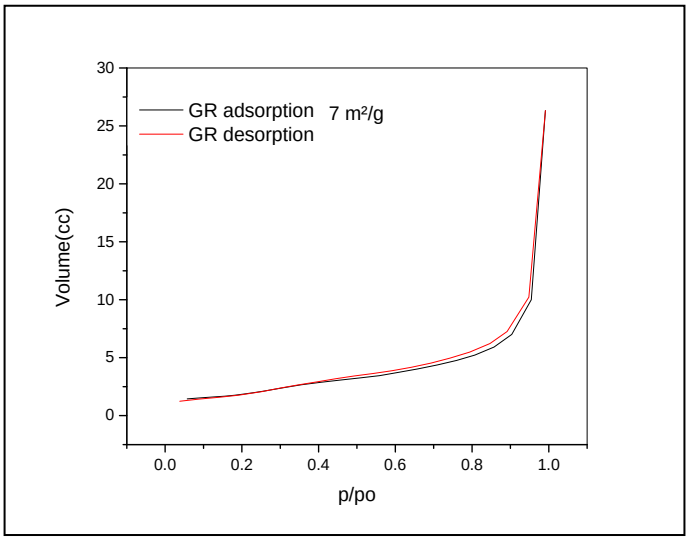

Fig. 3 GR Adsorption/desorption isot

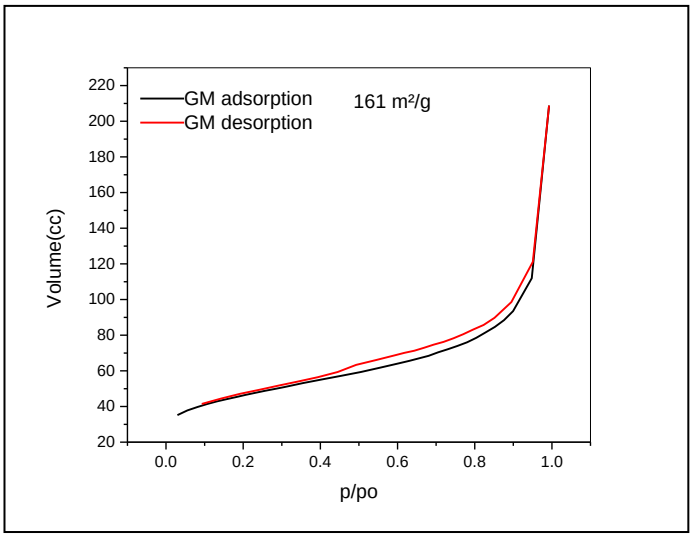

Fig. 4 GM Adsorption/desorption isotherm

In Fig. 5 the adsorption-desorption isotherm T-GO sample is presented, from the analysis of this curve it can be seen that this presents a Type-IV isotherm behavior, showing a slight hysteresis Type-H3 indicating a mesoporous material, while presenting a surface area of 144.2 m^2/g. This behavior can be interpreted as the inclusion of defects in the GO sheets due to the ball milling process. However, the decrease in area compared to that of its precursor can be attributed to the collapse of the sheets or the effect of agglomeration within the material [14].

.

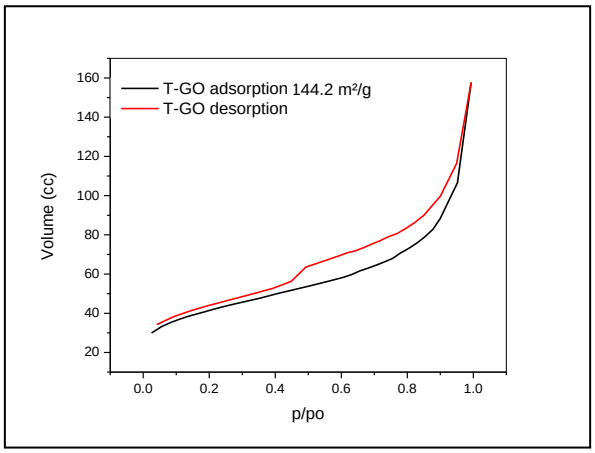

Fig. 5 T-GO Adsorption/desorption isotherm

Isotherm of the P-GO sample is presented in Fig. 6, which describes a Type-IV isotherm, showing a Type-H3 hysteresis, indicating a mesoporous material, reaching a specific surface area of 239 m^2/g. This same behavior is exhibited by sample P-GO2 (Fig. 7) with an area of 234 m^2/g.

The increase in surface area of the P-GO and P-GO2 materials is tied to the increase in the Inter-laminar distance, caused by the introduction of hydroxyl groups at the time of synthesis. This is correlated to a spongy texture of the material, which is shown in the micrographs and is in agreement with the increase in area that occurred due to exfoliation (spongy appearance) and/or porosity of the material [17,18].

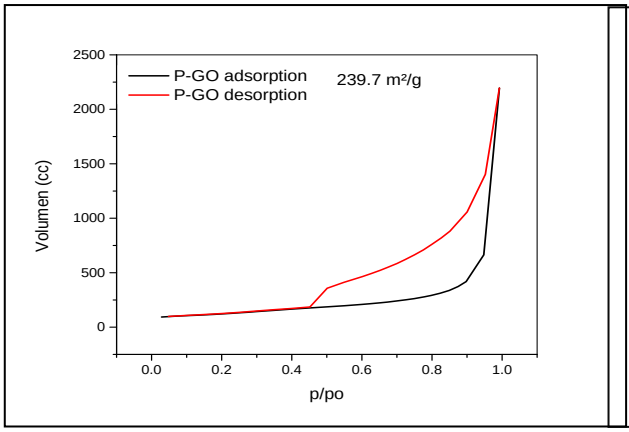

Fig. 6 P-GO adsorption/desorption Isotherm

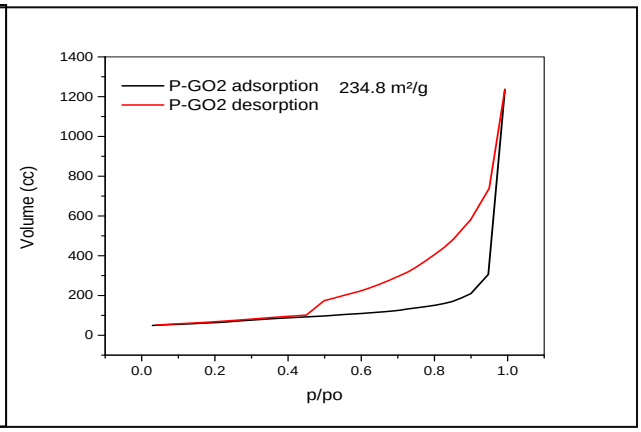

Fig. 7 P-GO2 adsorption/desorption Isotherm

3.4. Diffuse reflectance

The estimation of the forbidden band of P-GO, P-GO2 and T-GO materials was performed from the Kubelka-Munk function, where $[F(R_\infty)\cdot hv]^{(1/n)}$ is approximated to $(\square hv)^{(1/n)}$. Fig. 8 presents the Tauc plots both for the calculation of the forbidden band values for direct and indirect transitions, respectively. Estimated values that comprises 1.45, 1.27 and 1.15 eV for P-GO, P-GO2 and T-GO materials, respectively, while for the indirect transition values between 0.8 and 1.2 eV were found. The differences in the values of the forbidden band are related to the degree of oxidation of the material. The higher energy value of the forbidden band the greater amount of functional oxidation groups on the surface.

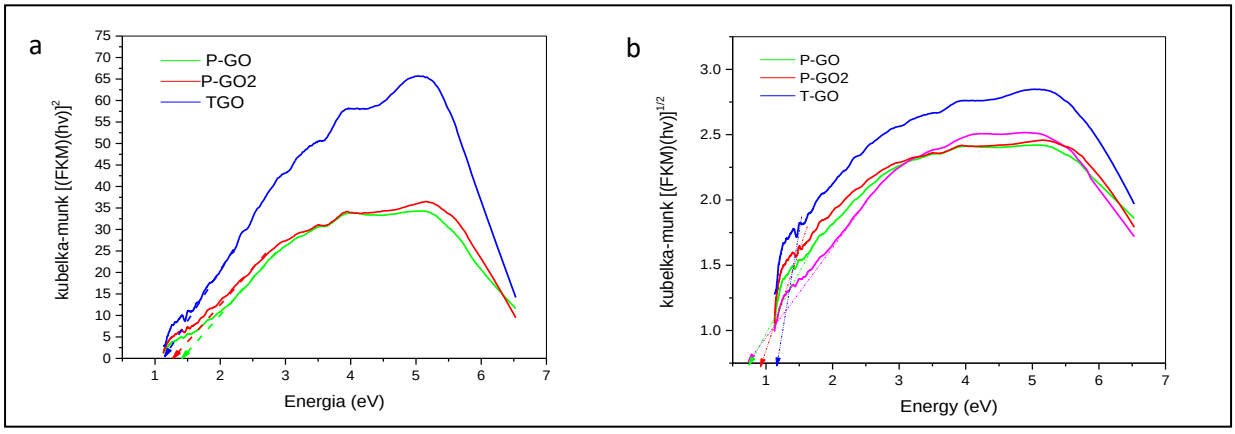

Fig. 8 GO Kubelka-Munk Approximation a) direct, b) indirect

3.5. Photocatalytic evaluation

Fig. 10 presents data for the photocatalytic hydrogen evolution of synthesized materials in water and a sacrificial agent (methanol) and under visible light irradiation. In this Figure it can be seen that the P-GO material presents a better photocatalytic performance compared to P-GO2 and T-GO samples.

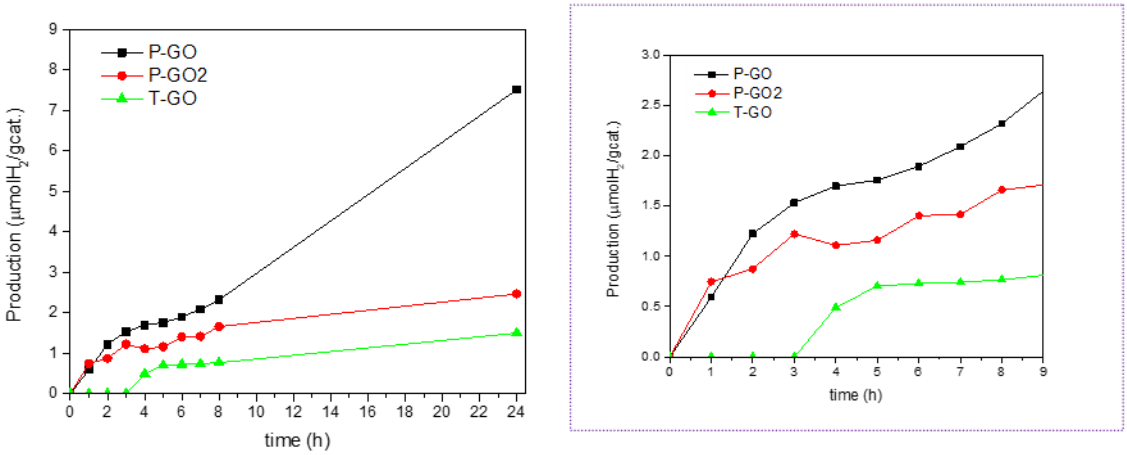

Fig. 10 Photocatalytic evaluation of P-GO2 and T-GO samples

The low photocatalytic performance of the P-GO2 and T-GO samples can be explained based on the energy values of the forbidden band obtained from these materials. For the P-GO2 sample, a band gap value of 1.27 eV was estimated, while the estimated value for the T-GO forbidden band was 1.15 eV. These energy values do not reach or are very limited to provide the required overpotential needed for the reaction of the splitting of the water molecule to take place (a minimum of 1.23 eV) [20].

The total production of 800 nmoles of H_2 in 24 h by the P-GO material can be attributed to a better distribution of the oxygenated groups. In comparison with the synthesis of the conventional Tour method, it can be considered that the oxidation generated by the acidic piranha solution to pulverized graphite and microwave pretreated, is more uniform and of greater stability.

4. Conclusion

The proposed synthesis method allowed the increase of the Interplanar distance of graphite to 7.64 Å. The oxygenated groups present in the materials and generated by the acidic piranha solution made it possible to obtain a value of the forbidden band by direct transition ranging from 1.27 to 1.45 eV. In this synthesis, a surface area of 239 m^2/g was obtained for GO and a production of 800 nmol of H_2, opening the possibility of an environmentally friendly synthesis of graphene oxide**.**

Acknowledgements

The authors acknowledge M.Sc. Ernesto Guerrero Lestarjette, M. Sc. Karla Campos Venegas, and Eng. Luis de la Torre Saenz for their contributions to the XRD, SEM, BET, results. Special thanks are given to Laboratorio Nacional de Nanotecnología in Centro de Investigación en Materiales Avanzados, S. C., for their support in the use of the facilities.

References

[1] Jia Q, Iwashina K, Kudo A. Facile fabrication of an efficient BiVO4 thin film electrode for water splitting under visible light irradiation. Proc Natl Acad Sci U S A 2012;109:11564–9. https://doi.org/10.1073/pnas.1204623109.
[2] Li Y, Hu Y, Peng S, Lu G, Li S. Synthesis of CdS Nanorods by an Ethylenediamine Assisted Hydrothermal Method for Photocatalytic Hydrogen Evolution. J Phys Chem C 2009;113:9352–8. https://doi.org/10.1021/jp901505j.
[3] Higashi M, Abe R, Takata T, Domen K. Photocatalytic Overall Water Splitting under Visible Light Using ATaO 2 N (A = Ca, Sr, Ba) and WO 3 in a IO 3 − /I − Shuttle Redox Mediated System. Chem Mater 2009;21:1543–9. https://doi.org/10.1021/cm803145n.
[4] Wang X, Maeda K, Thomas A, Takanabe K, Xin G, Carlsson JM, et al. A metal-free polymeric photocatalyst for hydrogen production from water under visible light. Nat Mater 2009;8:76–80. https://doi.org/10.1038/nmat2317.
[5] Fujishima A, Zhang X, Tryk DA. Heterogeneous photocatalysis: From water photolysis to applications in environmental cleanup. Int J Hydrogen Energy 2007;32:2664–72. https://doi.org/10.1016/j.ijhydene.2006.09.009.
[6] Amir M, Kurtan U, Baykal A. Rapid color degradation of organic dyes by Fe3O4@His@Ag recyclable magnetic nanocatalyst. J Ind Eng Chem 2015;27:347–53. https://doi.org/10.1016/j.jiec.2015.01.013.
[7] Jayavel R, Shanmugam M, Alsalme A, Alghamdi A. In-situ microwave synthesis of graphene–TiO2 nanocomposites with enhanced photocatalytic properties for the degradation of organic pollutants. J Photochem Photobiol B Biol 2016;163:216–23. https://doi.org/10.1016/j.jphotobiol.2016.08.029.
[8] Lee SH, Kang DS, Lee SM, Roh JS. X-ray diffraction analysis of the effect of ball milling time on crystallinity of milled polyacrylonitrile-based carbon fiber. Carbon Lett 2018;26:11–7. https://doi.org/10.5714/CL.2018.26.011.
[9] Zhang X, Wang H, Huang T, Wen L, Zhou L. Synthesis of graphene oxide through different oxidation degrees for solar cells. Mater Res Express 2018;5:035515. https://doi.org/10.1088/2053-1591/aab580.
[10] Dimiev AM, Tour JM. Mechanism of graphene oxide formation. ACS Nano 2014;8:3060–8. https://doi.org/10.1021/nn500606a.
[11] Dehghanzad B, Razavi Aghjeh MK, Rafeie O, Tavakoli A, Jameie Oskooie A. Synthesis and characterization of graphene and functionalized graphene via chemical and thermal treatment methods. RSC Adv 2016;6:3578–85.

https://doi.org/10.1039/C5RA19954A[12] Liu X, Zhan D, Chao D, Cao B, Yin J, Zhao J, et al. Microwave-assisted production of giant graphene sheets for high performance energy storage applications. J Mater Chem A 2014;2:12166–70. https://doi.org/10.1039/c4ta01979b.

[13]Chen X, Liu L, Niu Z, Zhang L. Structural diversity of bulky graphene materials. Small 2014;10:2200–14. https://doi.org/10.1002/smll.201400144.

[14]Chen Y, Gerald JF, Chadderton LT, Chaffron L. Nanoporous carbon produced by ball milling. Appl Phys Lett 1999;74:2782–4. https://doi.org/10.1063/1.124012.

[15]Zhu X, Zhang C, Wang Z, Sun P, Ren Y, Zhu J, et al. Facile synthesis and strongly microstructure-dependent electrochemical properties of graphene/manganese dioxide composites for supercapacitors. Nanoscale Res Lett 2014;9:1–8. https://doi.org/10.1186/1556-276X-9-490.

[16]Cai M, Thorpe D, Adamson DH, Schniepp HC. Methods of graphite exfoliation. J Mater Chem 2012;22:24992–5002. https://doi.org/10.1039/c2jm34517j.

[17]Khurshid AN, Mourad SH, Ismail AA, Abbas AM, Abdulrazzak FH. Influence of Acid and Base Piranha Oxidation Reagent on Adsorption Activity of Graphite 2017;2:30–4.

[18]Zhao H, Wang J, Zhang D, Dai Q, Han Q, Du P, et al. Chloro-benquinone Modified on Graphene Oxide as Metal-free Catalyst: Strong Promotion of Hydroxyl Radical and Generation of Ultra-Small Graphene Oxide. Sci Rep 2017;7. https://doi.org/10.1038/srep42643.

[19]Zhang T, Chang H, Wu Y, Xiao P, Yi N, Lu Y, et al. Macroscopic and direct light propulsion of bulk graphene material. Nat Photonics 2015;9:471–6. https://doi.org/10.1038/nphoton.2015.105.

[20]Yeh TF, Chan FF, Hsieh C Te, Teng H. Graphite oxide with different oxygenated levels for hydrogen and oxygen production from water under illumination: The band positions of graphite oxide. J Phys Chem C 2011;115:22587–97. https://doi.org/10.1021/jp204856c.

ID 085

Synthesis, Characterization and Photocatalytic Evaluation of g-C_3N_4/Ag/Zn_2TiO_4 Heterojunction for the Hydrogen Production under Visible Light

J. C. Pantoja-Espinoza, J. L. Domínguez-Arvizu, J. A. Jimenez-Miramontes, B. C. Hernández-Majalca, M. J. Meléndez-Zaragoza, J. M. Salinas-Gutiérrez, A. López-Ortiz, V. H. Collins-Martínez*

Departamento de Ingeniería y Química de Materiales, Centro de Investigación en Materiales Avanzados, S.C., Miguel de Cervantes 120, Chihuahua, Chih., 31136, México.
* Corresponding author: virginia.collins@cimav.edu.mx

ABSTRACT

In recent years, the exploration of clean energy has been growing due to the increase of industrial development. Current research for the production of hydrogen through photocatalysis aims to take advantage of the use of solar energy. Although this photocatalytic process has already been reported in the literature one remaining challenge is to find highly efficient photocatalysts to make it economically viable for larger scale hydrogen production. The objective of the present study is to synthesize, characterize and photocatalytically evaluate the g-C_3N_4/Ag/Zn_2TiO_4 heterojunction towards the hydrogen production under visible light. In order to prepare the hetero-linked photocatalyst, individual materials were first synthesized. g-C_3N_4 was obtained by urea pyrolysis at 325 °C during 1 hour followed by an additional 1 hour at 450 °C under air and nitrogen atmospheres, respectively. Zn_2TiO_4 powders were prepared by the modified Pechini method obtaining the crystal structure by calcination at 450 and 550 ° C for 2 and 1 hours, respectively. Ag/Zn_2TiO_4 and g-C_3N_4/Ag/Zn_2TiO_4 materials were prepared by photo-anchoring and impregnation, respectively. TGA was used to obtain urea pyrolysis and Zn_2TiO_4 calcination temperatures. Characterization of the materials was carried out using XRD, FT-IR, UV-Vis, BET and SEM, for the study of crystallinity, spectroscopic analysis, specific surface area and morphology, respectively. Photocatalytic evaluation of the materials was performed using triethanolamine as a sacrificial agent in aqueous solution employing a batch reactor irradiated with visible light. Results indicate that the greatest hydrogen production was achieved by g-C_3N_4/Ag/Zn_2TiO_4 heterojunction with 848 mmol $H_2/h{\cdot}g_{cat}$ after 8 h. This heterojunction was composed of 20% g-C_3N_4 and 80% of Ag/Zn_2TiO_4 and 1% Ag. This heterojunction can be considered as a high potential photocatalyst in the field of green hydrogen production.

Keywords: hydrogen production, photocatalysis, heterojunction, g-C_3N_4.

1. Introduction

For several decades, population growth has been tied to a continuous increase in pollutants caused by the use of fossil fuels. Therefore, the recent use of clean energies has spread the interest to contribute to the reduction of pollutants and to obtain economically viable fuels, with hydrogen as an energy vector being one of the possible solutions. Since Fujishima and Honda [1] who separated the water molecule by a photoelectrochemical process with TiO_2 activated under UV light, a large amount of research has been directed to the synthesis of materials for hydrogen production through the photocatalysis using visible light irradiation, with solar energy comprising almost 50% of the visible light electromagnetic spectrum. However, photocatalytic processes present the disadvantage of exhibiting low efficiency towards the production of hydrogen and this is manly caused by a high rate of recombination of electron-hole pairs in semiconductors, which are responsible for redox reactions.

In recent years, research has been oriented towards optimizing photocatalytic methods and/or processes for hydrogen production. One of the strategies consists in preparing heterojunctions as photocatalytic materials that, in addition to being active under visible light, also help to reduce the recombination rate of electron-hole pairs. There are three types of conventional heterojunctions: straddling gap (Type-I), those with a staggered gap (Type-II), and those with a broken gap (Type-III) [2]. It is worth to point out that Type-II heterojunction presents greater photocatalytic efficiency in the spatial separation of the electron-hole pairs by means of the alignment of the semiconductor bands, since in this arrangement both the conduction and valence band of semiconductor A, is greater than that of semiconductor B [3]. A variation of Type-II heterojunction is the arrangement in a Z scheme where the mechanism of the charge carriers is different as reported by Jiang et al. [4] in the synthesis of $AgCl/Ag/CaTiO_3$ for the production of hydrogen.

There are a number of existing research reported in the literature related to heterojunctions of different materials and evaluated photocatalytically for the production of hydrogen, some of them being between g-C_3N_4 and TiO_2, using Pt as a co-catalyst [5]. G-C_3N_4 has also shown good photocatalytic activity in heterojunctions with titanates such as $NiTiO_3$ [6] and using photostable Ag [7] to improve its catalytic efficiency. Some titanates such as Zn_2TiO_4 have shown good photocatalytic activity without heterojunctions as reported by Manchala et al. [8] obtaining a hydrogen production of 529 µmol H_2/h·gcat. Although g-C_3N_4 has been extensively studied, there is still no work that reports the heterojunction between g-C_3N_4 and Zn_2TiO_4 as a photocatalyst, since Pt is normally used as a co-catalyst when this last is photocatalytically evaluated for hydrogen production [5]. Alignment of conduction and valence bands potentials for g-C_3N_4 (-1.1, +1.6 eV) [7] and Zn_2TiO_4 (-0.9, +2.1 eV) [8] indicate that it is possible to construct a Type-II heterojunction with these materials. Therefore, the objective of the present work is to synthesize and characterize individual g-C_3N_4, Zn_2TiO_4 active materials under visible light and these in heterojunction with Ag, in different proportions to find an optimal composition of the heterojunction material with the highest photocatalytic activity towards the production of hydrogen.

2. Materials and Methods

2.1 Materials

For the synthesis of Zn_2TiO_4, zinc nitrate and titanium tetra n-butoxide were used as precursors; in addition, citric acid and ethylene glycol as polymerizing and chelating agents, respectively. Silver nitrate as a source of Ag^{+1} and its subsequent reduction to Ag^{o} (all reagents used were Sigma-Aldrich brand). Commercial urea was used as a precursor for the synthesis of g-C_3N_4.

2.2 Individual Zn_2TiO_4 and g-C_3N_4 synthesis

Zn_2TiO_4 was prepared by the modified Pechini method according to the method reported in the literature [9,10]. Zn_2TiO_4 preparation employed Zn:Ti precursors in a 1:2 molar ratio to obtain 1g of titanate material. As well as the sufficient quantity of citric acid with a molar ratio 1:2 and 1:4 with respect to Zn^{+1} and Ti^{+4}, respectively to ensure a sufficient quantity of carboxyl groups to facilitate the formation of the polymeric network. Also, considering the size of the Zn and Ti atoms, ethylene glycol was used in a 1:1 molar ratio with respect to citric acid. A gel was prepared by mixing citric acid and ethylene glycol in distilled water at 80 °C for 30 minutes, the gel was cooled to room temperature and zinc nitrate, previously dissolved in distilled water, was added, then the tetra-titanium n-butoxide was added dropwise while the temperature was increased again to 80 °C until a dry powder sample was obtained. The powders were calcined at 450 °C and 550 °C for 2 and 1 h, respectively to obtain the Zn_2TiO_4 crystal structure. The g-C_3N_4 was obtained from the pyrolysis of urea at two different temperatures at 325 °C and 450 °C for 1 h each one and under air and nitrogen atmospheres, respectively.

2.3 Ag/Zn_2TiO_4 and g-C_3N_4/Ag/Zn_2TiO_4 heterounion material synthesis

Ag/Zn_2TiO_4 was obtained by means of a photoassisted anchoring, according to the procedure described by Jiang et al. [4]. Certain quantities of Zn_2TiO_4 were added to a methanol-water solution and placed in an ultrasonic bath for 30 minutes, then specific quantities of 0.05 M $AgNO_3$ solution were added and stirred for 30 minutes in the dark, then the resulting mixture was placed in a Batch-type quartz tubular reactor and irradiated for 30 minutes with a 250 W metal halide lamp. The precipitate was separated in a centrifuge, rinsed with water and dried at 70 °C for 4 h. The same procedure was performed to obtain samples AZ0.5, AZ1.0, AZ1.5 and AZ2.0 indicating the Ag content from 0.5 to 2%. Heterounion g-C_3N_4/Ag/Zn_2TiO_4 materials were prepared by aqueous impregnation, keeping stirred for 1 hour different amounts of g-C_3N_4 and Ag/Zn_2TiO_4 at 1% Ag (AZ1.0), later the precipitate was separated in a centrifuge, washed with water and dried at 70 °C for 4 h. The samples were identified as 10CN-AZ1, 20CN-AZ1 and 30CN-AZ1 indicating the amount of 10, 20 and 30% of g-C3N4 and the remaining being Ag/Zn_2TiO_4.

2.4 Caracterización de los materiales individuales y heterounidos

La caracterización de los materiales individuales y las heterouniones consistieron en determinar su estructura cristalina, utilizando un difractometro de rayos X Panalytical XpertPRO equipado con radiación KCu□ (□ = 0.15405 nm). Los tipos de enlaces y las propiedades ópticas se estudiaron en los equipos FT-IR y UV-Vis modelos Frontier y Lambda 35, ambos de la marca Perkin-Elmer. The BET surface area was determined with an Autosorb-1 brand Quantachrome using the N_2 physisorption method from 0.05 to 0.3 relative pressure (p/p^0). La morfología de los materiales se analizó por electrones secundarios en un microscopio electrónico de barrido de Emisión de Campo JSM7401F.

2.5 Photocatalytic evaluation for hydrogen production

Photocatalytic evaluation for the hydrogen production of individual materials and heterojunctions was achieved by the splitting of the water molecule. The experimental tests were performed in a tubular quartz reactor in a batch arrangement. 50 mg of each of the prepared materials and 50 ml of a 10% aqueous solution of triethanolamine used as a sacrificial agent were placed in the reactor. Then the quartz reactor containing the material and the water-triethanolamine solution was irradiated using a metal-halide lamp that emits radiation in the visible spectrum. Hydrogen production was monitored for 8 hours in a Perkin-Elmer model Clarus 580 gas chromatograph equipped with a thermal conductivity detector (TCD), injecting a sample every hour to obtain the area under the curve of a calibration curve (mmol H_2 vs area under the curve) thus, hydrogen was quantified in □mol/h·g_{cat}.

3. Results and Discussion

3.1 XRD analysis

Fig. 1 shows X-ray diffractograms of individual materials g-C3N4, Zn_2TiO_4 and heterojunctions with Ag in their different proportions. In sample CN, two peaks with diffraction angles at 2□ = 27.3° and at 13.1° with lower intensity are observed, which agree to JCPDS 87-1526 diffraction pattern corresponding to the crystallographic structure of g-C3N4 and being consistent with that reported in the literature [11-13]. Otherwise, ZT sample diffraction peaks also are indexed with the 25-1164 JCPDS diffraction pattern corresponding to the crystallographic structure of Zn_2TiO_4. Whereas, diffractograms of the remaining samples show small diffraction peaks at 2□ = 38°, which corresponds to Ag^o with JCPDS 04-0783 card, verifying its presence within the heterojunction samples. Diffractograms of the heterojunctions containing g-C_3N_4 (10CN, 20CN and 30CN) with the AZT1 material exhibit small curves of lower intensity at 27.3°, indicating the presence of g-C3N4. No other peaks

were identified in the diffractograms, therefore the only presence of g-C_3N_4, Zn_2TiO_4, Ag/Zn_2TiO_4 and g-C_3N_4/Ag/Zn_2TiO_4 in the synthesized materials were be confirmed.

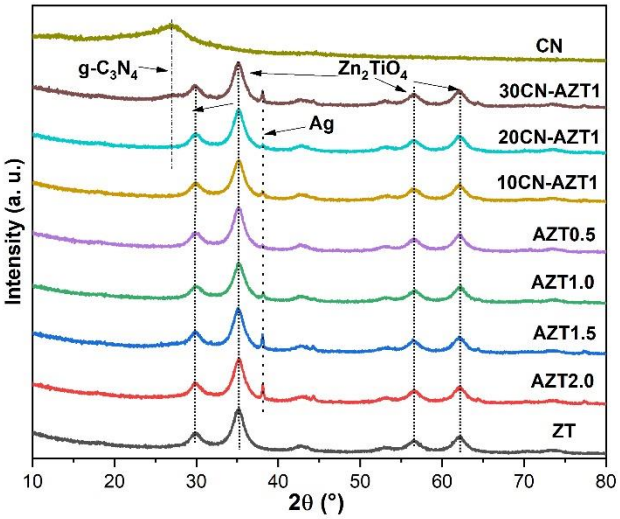

Fig. 1. XRD diffraction spectra of g-C_3N_4 and Zn_2TiO_4 samples as well as of heterojunctions of these materials with Ag.

3.2 FT-IR analysis

In Fig. 2 the FTIR spectra of the individual materials g-C_3N_4, Zn_2TiO_4 and of the heterojunctions with Ag in their different compositions are shown.

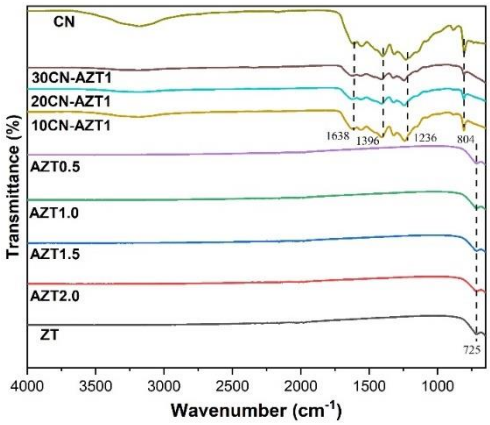

Fig. 2. FTIR spectra of the g-C_3N_4 and Zn_2TiO_4 samples, as well as the heterojunctions of these materials with Ag.

The absorption band at 725 cm^{-1} of the samples ZT, AZT0.5, 1.0, 1.5 and 2.0 is typical of metal oxides and is assigned to O-Metal bonds [8]. The absorption band in 804 cm^{-1} of CN sample is assigned to the tri-S-triazine rings that contain g-C3N4 [7]. Bands in the range of 1236 to 1638 cm^{-1} are assigned to the stretching modes of C-N heterocycles [6]. These absorption bands are also present in the FT-IR spectra of g-C_3N_4/Ag/Zn_2TiO_4 heterojunctions.

3.3 S-TEM analysis

Fig. 3 shows TEM images of C_3N_4/Ag/Zn_2TiO_4 heterojunction material obtained at 5000X (3a) and 35000X (3b) resolution. In these images particles with irregular morphology in aggregated (3a) and laminar structures or clusters of flat layers (3b) attributed to g-C_3N_4 [14] can be observed. The darker region in the images is possibly due to Zn_2TiO_4 and Ag/Zn_2TiO_4 particles of irregular shape and size.

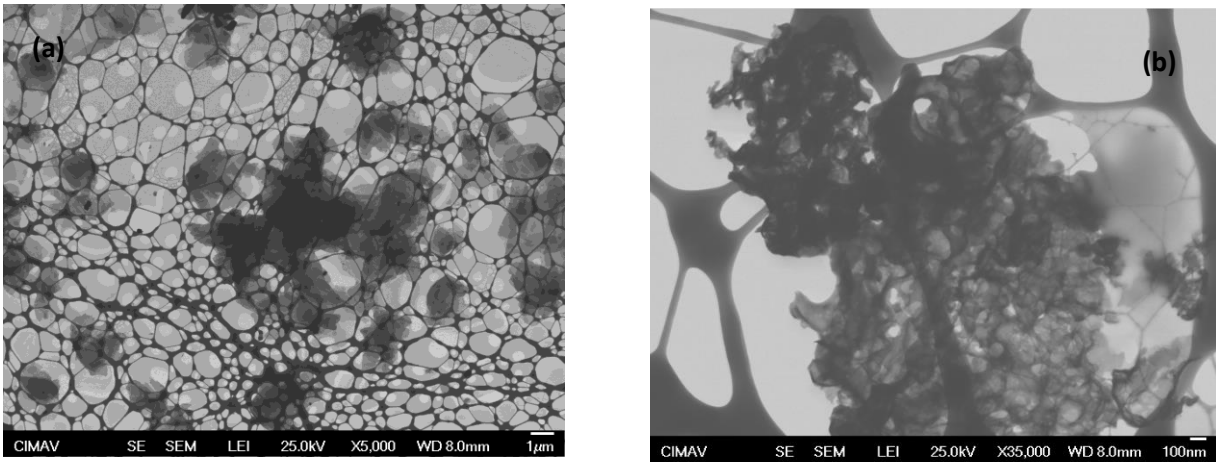

Fig. 3. Fig. 3. Micrographs of g-C_3N_4/Ag/Zn_2TiO_4 obtained at low (3a) and high resolutions (3b).

3.4 BET analysis

BET area of the synthesized materials was analyzed by nitrogen physisorption, thus obtaining the corresponding adsorption-desorption isotherms of each synthesized material. Fig. 4 shows the isotherms of Zn_2TiO_4 (Fig. 4a), g-C_3N_4 (Fig. 4b) and Ag/Zn_2TiO_4 (Fig. 4c) materials with their different Ag contents as well as that of the g-C_3N_4/Ag/Zn_2TiO_4 (Fig. 4d) heterojunction with the different g-C_3N_4 contents.

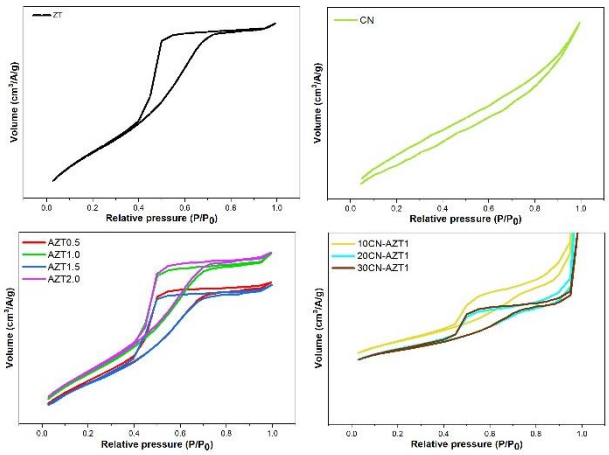

Fig. 4. Nitrogen adsorption-desorption isotherms of Zn_2TiO_4 (a), g-C_3N_4 (b), Ag/Zn_2TiO_4 (c) and g-C_3N_4/Ag/Zn_2TiO_4 (d) materials.

According to the IUPAC classification, the isotherms correspond to Type-IV characteristic of mesoporous materials with Type-H3 hysteresis, which is formed in materials whose pores are distributed between thin sheets [14].

Table 1 shows the BET surface area values of the synthesized samples in this work. The area of the individual materials Zn_2TiO_4 and g-C_3N_4 was 64.5 and 80.7 m^2/g, respectively. In all materials in heterojunction their surface areas decreased with respect to their individual components as reported in the literature when composites are prepared [5].

Whereas, within AZT materials their surface area decreased as the Ag loading on the surface of the Zn_2TiO_4 increased, however in the case of CN-AZT1 materials their surface area increased as the proportion of g-C_3N_4 also increased. This behavior can be attributed to the rearrangement of the materials when forming the heterojunction, which can cause a decrease in porosity and consequently a reduction in surface area.

Table 1. BET area of the single and heterojunction synthesized materials.

Sample	Area BET (m^2/g)	Sample	Area BET (m^2/g)	Sample	Area BET (m^2/g)
ZT	64.5	AZT1.0	58.6	20CN-AZT1.0	62.9
AZT2.0	42.1	AZT0.5	60.1	30CN-AZT1.0	65.8
AZT1.5	46.5	10CN-AZT1.0	61.3	CN	80.7

3.5 UV-Vis analysis

Optical properties of the synthesized materials were studied by obtaining their absorbance and reflectance spectra in the UV-Vis region. Fig. 5a shows the absorption spectra and Fig. 5b the Tauc plots for the estimation of the indirect band gaps by the Kubelka-Munk method. Individual and heterojunction materials exhibited absorption in the visible spectrum from 425 to 550 nm. The band gap values of g-C_3N_4 and Zn_2TiO_4 were 2.6 and 3.05 eV, respectively, being consistent with those reported in the literature [8,14]. band gaps of heterojunction materials were smaller than their individual components, confirming their absorption towards the visible spectrum.

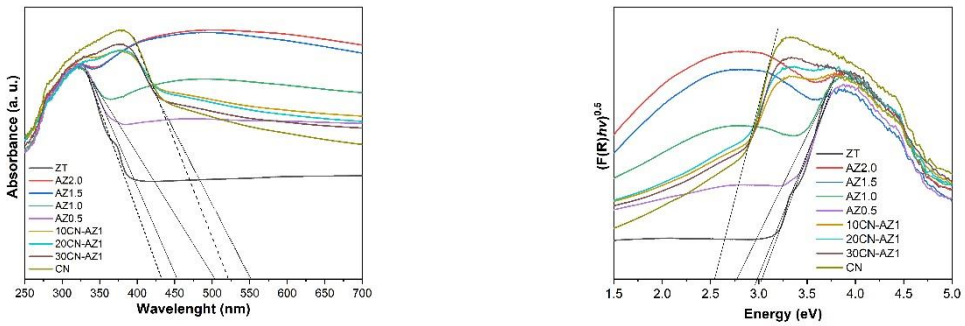

(**a**) (**b**)

Fig. 5. Absorption spectra (5a) and Tauc polts (5b) for estimating indirect band gaps of materials by the Kubelka-Munk method.

3.6 Photocatalytic evaluation for hydrogen production

Fig. 6 presents the hydrogen production rates indicated in µmol $H_2/h \cdot g_{cat}$ of g-C_3N_4 and Zn_2TiO_4 individual materials as well as for the heterojunction materials with Ag at different compositions, in aqueous solution using triethanolamine as sacrificial agent, under 8 hours of irradiation.

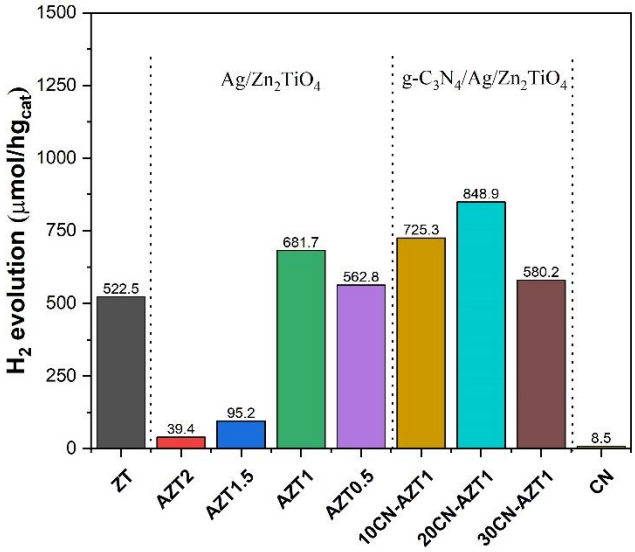

Fig. 6. Hydrogen production of the individual materials, as well as for materials in heterojunction under different compositions of g-C_3N_4, Ag and Zn_2TiO_4.

The low rate of pure g-C_3N_4 hydrogen production (8.5 µmol $H_2/h \cdot g_{cat}$) can be attributed to the fast recombination of electron-hole pairs in g-C_3N_4 and is comparable to that reported in the literature [5]. The hydrogen production of pure Zn_2TiO_4 (522.6 µmol $H_2/h \cdot g_{cat}$) is also consistent that reported ih the literature [8], while it increases with the incorporation of Ag, presumably attributed to the shifting of the forbidden band of the material towards an energy value found within the visible spectrum, reaching a maximum of 681.7 µmol $H_2/h \cdot g_{cat}$ with Zn_2TiO_4 and Ag at 1% (sample AZT1). However, a considerably lower hydrogen production is observed with an increase in Ag content of 1.5 and 2% in the materials. Optimal Ag/Zn_2TiO_4 (AZT1) heterojunctions and different compositions of g-C_3N_4 increased the hydrogen production to a maximum of 848.9 µmol $H_2/h \cdot g_{cat}$ at 20% of g-C3N4, which was higher than 10 and 30% of g-C_3N_4 content that managed to produce 725.3 and 580.2 µmol $H_2/h \cdot g_{cat}$, respectively. It is possible that the higher hydrogen production of the g-$C_3N_4/Ag/Zn_2TiO_4$ heterojunction, in addition to improving the absorption of light in the visible spectrum, also preserves a Z-scheme arrangement in which the charge carriers move from the CB of the g-C_3N_4 to the VB of Zn_2TiO_4 with Ag acting as quenching centers between these semiconductors [4], thus decreasing the recombination times of the electron-hole pair.

4. Conclusion

g-C_3N_4 and Zn_2TiO_4 materials were synthesized by urea pyrolysis and modified Pechini method, respectively. Ag heterojunction materials were obtained by photoanchoring-impregnation employing the individual materials. Characterization of the samples indicate that these materials presented porosity and specific surface areas of around 60 m^2/g, except for g-C_3N_4 sample, which reached an area of 80 m^2/g. The energy value of the forbidden band decreased as the silver content increased, from 3.05 eV presented by Zn_2TiO_4 to 2.75 eV when zinc titanate was doped with 1% Ag. In the same way, this value decreased even more with materials in heterojunction, presenting an energy value for their forbidden band of 2.55 eV. The g-C_3N_4/Ag/Zn_2TiO_4 (20CN-AZT-1) heterojunction composed of 20% of g-C_3N_4 and 80% of Ag/Zn_2TiO_4 at 1% of Ag exhibited higher photocatalytic activity towards the hydrogen production with 848 µmol $H_2/h \cdot g_{cat}$, followed by 10CN-AZT-1 with 725 µmol $H_2/h \cdot g_{cat}$.

Acknowledgements

First author is grateful for the support of the National Council of Science and Technology of Mexico (CONACYT) for the scholarship to complete a postdoctoral stay at Centro de Investigación en Materiales Avanzados, S. C. (CIMAV), Chihuahua unit. Authors greatly appreciate the help of Ph. D. Pedro Pizá Ruiz, M.Sc. Karla Campos Venegas, and Eng. Luis de la Torre Sáenz for their support in performing the XRD, SEM and BET analyzes. Also, thanks must be regarded to the National Nanotechnology Laboratory (NANOTECH) at CIMAV Chihuahua for their facilities to complete characterizations tests

References

[1] Fujishima, A., & Honda K. Electrochemical Photolysis of Water at a Semiconductor Electrode. Nature 1972;238:37–8. doi:10.1038/238037a0.
[2] Low J, Yu J, Jaroniec M, Wageh S, Al-Ghamdi AA. Heterojunction Photocatalysts. Adv Mater 2017;29. doi:10.1002/adma.201601694.
[3] Low J, Jiang C, Cheng B, Wageh S, Al-Ghamdi AA, Yu J. A Review of Direct Z-Scheme Photocatalysts. Small Methods 2017;1:1700080. doi:10.1002/smtd.201700080.
[4] Jiang Z, Pan J, Wang B, Li C. Two dimensional Z-scheme AgCl/Ag/CaTiO3 nano-heterojunctions for photocatalytic hydrogen production enhancement. Appl Surf Sci 2018;436:519–26. doi:10.1016/j.apsusc.2017.12.065.
[5] Alcudia-Ramos MA, Fuentez-Torres MO, Ortiz-Chi F, Espinosa-González CG, Hernández-Como N, García-Zaleta DS, et al. Fabrication of g-C3N4/TiO2 heterojunction composite for enhanced photocatalytic hydrogen production. Ceram Int 2020;46:38–45. doi:10.1016/j.ceramint.2019.08.228.
[6] Zeng Y, Wang Y, Chen J, Jiang Y, Kiani M, Li B, et al. Fabrication of high-activity hybrid NiTiO3/g-C3N4 heterostructured photocatalysts for water splitting to enhanced hydrogen production. Ceram Int 2016;42:12297–305. doi:10.1016/j.ceramint.2016.04.177.

[7] Kim SR, Jo WK. Application of a photostable silver-assisted Z-scheme NiTiO3 nanorod/g-C3N4 nanocomposite for efficient hydrogen generation. Int J Hydrogen Energy 2019;44:801–8. doi:10.1016/j.ijhydene.2018.11.014.
[8] Manchala S, Nagappagari LR, Muthukonda Venkatakrishnan S, Shanker V. Facile synthesis of noble-metal free polygonal Zn2TiO4 nanostructures for highly efficient photocatalytic hydrogen evolution under solar light irradiation. Int J Hydrogen Energy 2018;43:13145–57. doi:10.1016/j.ijhydene.2018.05.035.
[9] Domínguez-Arvizu JL, Jiménez-Miramontes JA, Salinas-Gutiérrez JM, Meléndez-Zaragoza MJ, López-Ortiz A, Collins-Martínez V. Optical properties determination of NiFe2O4 nanoparticles and their photocatalytic evaluation towards hydrogen production. Int J Hydrogen Energy 2017;42:30242–8. doi:10.1016/j.ijhydene.2017.09.180.
[10] Jiménez-Miramontes JA, Domínguez-Arvizu JL, Salinas-Gutiérrez JM, Meléndez-Zaragoza MJ, López-Ortiz A, Collins-Martínez V. Synthesis, characterization and photocatalytic evaluation of strontium ferrites towards H2 production by water splitting under visible light irradiation. Int J Hydrogen Energy 2017;42:30257–66. doi:10.1016/j.ijhydene.2017.09.162.
[11] Abdel Moneim SM, Gad-Allah TA, El-Shahat MF, Ashmawy AM, Ibrahim HS. Novel application of metal-free graphitic carbon nitride (g-C3N4) in photocatalytic reduction - Recovery of silver ions. J Environ Chem Eng 2016;4:4165–72. doi:10.1016/j.jece.2016.08.034.
[12] Meng J, Pei J, He Z, Wu S, Lin Q, Wei X, et al. Facile synthesis of g-C3N4 nanosheets loaded with WO3 nanoparticles with enhanced photocatalytic performance under visible light irradiation. RSC Adv 2017;7:24097–104. doi:10.1039/c7ra02297b.
[13] Dong Z, Wu Y, Thirugnanam N, Li G. Double Z-scheme ZnO/ZnS/ g-C3N4 ternary structure for efficient photocatalytic H2 production. Appl Surf Sci 2018;430:293–300. doi:10.1016/j.apsusc.2017.07.186.
[14] M.B. Shekardasht, M.H. Givianrad, P. Gharbani, Zohreh Mirjafary AM. Preparation of a novel Z-scheme g-C3N4/RGO/Bi2Fe4O9 nanophotocatalyst for degradation of Congo Red dye under visible light. Diam Relat Mater 2020. doi:https://doi.org/10.1016/j.diamond.2020.108008.

ID 086

Study of synthesis temperature effect on the photocatalytic properties of $MnCo_2O_4$ spinel towards the production of hydrogen by water splitting under visible light

J. A. Jiménez-Miramontes, J. L. Domínguez-Arvizu, B. C. Hernández-Majalca, J. C. Pantoja-Espinoza, J. M. Meléndez-Zaragoza, J. M. Salinas-Gutiérrez, A. López-Ortiz, V. Collins-Martínez*

Departamento de Ingeniería y Química de Materiales, Centro de Investigación en Materiales Avanzados, S.C., Miguel de Cervantes 120, Chihuahua, Chih., 31136, México
* Corresponding author: virginia.collins@cimav.edu.mx

ABSTRACT

Hydrogen generation through the photocatalytic separation of the water molecule has become a promising energy alternative with greater attention in recent years. One of the main reasons of this is due to the possibility of using sunlight as an energy source to carry out this process. However, this reaction is not thermodynamically feasible to proceed. Since, semiconductors with suitable optical properties to provide an overpotential of 1.23 eV to dissociate the water molecule are needed. For this reason, the search for materials that are photoactive under visible light, inexpensive, eco-friendly and having a band gap energy to overcome the water dissociation potential is essential. In this work, the calcination temperature effect on the photocatalytic performance of $MnCo_2O_4$ (MCO) was carried out, since the metallic cobaltite system theoretically presents adequate optical properties to be used in this type of process, while the information of these type of materials for this application is scarce. Cobaltites were synthesized by the Pechini method at temperatures of 350, 600, 900°C by four hours to obtain three MCO samples. Characterization of these materials consisted in X-Ray Diffraction (XRD), BET surface area by N_2 physisorption, Scanning Electron Microscopy (SEM) and UV-Vis spectroscopy. The diffractograms indicate the presence of $MnCo_2O_4$ in pure phase, with an increased crystallinity as temperature was raised. However, BET areas exhibited the opposite behavior, decreasing from 84 m^2/g to 1 m^2/g. Morphology of the obtained particles changed from irregular polygons to sintered polygons along with increasing temperature, with sizes ranging from ~50 nm to ~500 nm due to sintering. These MCOs presented a band gap of ~1.3 eV. The photocatalytic evaluation was performed by monitoring the hydrogen evolution by gas chromatography. MCO at 900°C presented the best photocatalytic performance achieving a production of 1152 nmol $H_2/g \cdot h$.

Keywords: water splitting; Spinel; Manganese cobaltite; hydrogen production.

1. Introduction

Pure hydrogen has been considered a promising alternative energy vector that has attracted the attention of researchers, since its combustion does not generate pollutants and is highly energetic. Water splitting is known as a clean technology used to generate hydrogen. This reaction is not thermodynamically feasible to proceed because the Gibbs free energy is +237 kJ/mol, in which the energy is provided by electrical or photonic energy. In order overcome this thermodynamic limitation, energy must be applied to a semiconductor (1.23 eV) [1] in the form of light to produce the separation of the water molecule to obtain hydrogen. Furthermore, the success of photochemical water splitting has emerged in recent years along with the development of solar energy technology [2].

At present, the photocatalytic process has been investigated multiple times, proposing new mechanisms, materials, etc. Many metal oxide semiconductors have been studied as photocatalysts, in order to find those that have the appropriate optical and electronic properties to provide the overpotential that is required for the reaction of the separation of the water molecule, TiO_2 has been the pioneer and preferred material, which its band gap (the difference between its conduction and valence band) has a value of 3.2 eV, however this material is not active under sunlight [3]. Other materials that have shown good results include photocatalysts based on $SrTiO_3$, Zn/In/S, Ta/O, Cd/S/Zn, K/Ti/O, and Ga/ZnO [4], each one with advantages and disadvantages compared to each other. To improve the performance of photocatalysts, doping with metals such as platinum, silver and gold [5–9] has proven to be a good strategy. This doping makes possible to reduce the recombination time of the electron-hole pair, thus enhancing the photocatalytic activity, but adding a higher cost to the process.

Wang et al [7] propose a new method to synthesize $Er^{3+}:Y_3Al_5O_{12}@Nb_2O_5/Pt/In_2O_3$ and use it as a photocatalyst, while Ding et al.[8] studied Zn-doped $CsPbBr_3$. Furthermore, Hunge et al. [10] prepared granular TiO_2 by the hydrothermal method, irradiated under visible light while employing Pt as a dopant. These recent investigations show the need to develop efficient photocatalysts aiming resistance to photocorrosion, low toxicity, high active area, band gap within the visible spectrum, inexpensive, easily accessible and environmentally friendly.

There are some bimetallic oxide materials with favorable properties that can be very employed for the production of hydrogen by means of photocatalysis and some of these semiconductors have been barely studied for this application. That is the case of spinel-type materials with main composition being AB_2O_4, where A and B are metal ions, forming a very extensive family containing one or more transition metals forming these materials. Due to these multiple compositions, electronic configurations, and valence states, spinels exhibit magnetic, optical, electrical, and catalytic properties that make them suitable for various applications.

One of the most common spinel-type systems are formed by iron (Fe) compounds, better known as metallic ferrites, with suitable optical properties to be used as photocatalysts aiming hydrogen production by the water splitting process [11–13]. Metal ferrites have the general formula MFe_2O_4, being the most common examples: $CuFe_2O_4$, $BaFe_2O_4$, $NiFe_2O_4$, $CoFe_2O_4$, $MgFe_2O_4$, $ZnFe_2O_4$ and $CaFe_2O_4$, where Ba, Ca and Sr ferrites have been investigated in catalytic reactions to degrade pollutants [14] and Zn, Co, Ba ferrites for photoelectrochemical separation of water [15]. They also have the advantage of having adequate band gap energies to work under visible light as well as the ability of band-gap tuning of other materials when used as supports and/or doping. [14,15].

As these ferrites present adequate properties and promising results, it is possible to expect that spinel-type cobaltites may have comparable or even better performance than ferrites materials mentioned above. Cobaltites have shown excellent performance in electrochemical and electrocatalytic processes, as well as catalysts. Some of these cobaltites present good catalytic properties and some convenient features such as: low preparation costs, being abundant, good electrical/ionic conductivity and rich redox behavior. Most known cobaltites are: $NiCo_2O_4$ [16–18], $MnCo_2O_4$[19,20], $MgCo_2O_4$[21,22] and $ZnCo_2O_4$[23,24] with band gap values between 2.0-2.2 eV [16,23,25,26]. Furthermore, $MnCo_2O_4$ cobaltite has been used mainly in electrochemical applications as anode and cathode electrodes, and as energy storage material. Also, this material presents several advantages such as chemical stability, rich redox reactions and being environmentally friendly [27–31]. Likewise, this cobaltite also presents adequate optical and catalytic properties to absorb visible light according to Zheng et al [29], although its band gap value varies from 1.21 to 2.1eV [25,32] according to studies reported by other researchers and specifically a research by Uke et al where they claim a value of 4.9 eV [33].

Therefore, in this work, $MnCo_2O_4$ (MCO), synthetized by the Pechini method, was characterized and evaluated as a photocatalyst for hydrogen generation by the water splitting reaction under visible light irradiation and specifically, the study of the calcination temperature effect on the photocatalytic performance of MCO was carried out.

2. Materials and Methods

Synthesis

$MnCo_2O_4$ spinel was synthetized by the Pechini Method. The synthesis consisted in the mixture of metallic precursors $Mn(NO_3)_2{\cdot}6H_2O$ and $Co(NO_3)_2{\cdot}6H_2O$ *Sigma-Aldrich*® in a stoichiometric ratio of 1:2. Citric acid and ethylene glycol (Sigma-Aldrich®) were used as chelating agents for the formation of the polymeric network. Ethylene glycol was first heated to 70°C, then citric acid was added and this kept under constant stirring until a translucent gel-like solution was reached. The product was allowed to cool to room temperature and then the metallic precursors were added while keeping this under constant stirring at a temperature of 80°C until a gel-like substance was obtained. This was finally left to dry to obtain a polymeric resin. Once dried, a thermogravimetric analysis of the organic resin was carried out to thermally decompose it and obtain the desired oxide.

Photocatalyst characterization

Material characterization was carried out by the thermogravimetry, X-ray diffraction and spectrophotometry techniques. Calcination temperature was determined to achieve the metallic cobaltite through the thermal decomposition of the resin by means of TGA in a Q500 from TA instruments, at temperatures between 25 to 980°C in air. The determination of the crystalline structure through X-ray diffraction analysis was carried out by means of a Panalytical XpertPRO X-ray diffractometer with copper radiation (αCu) at a step of 0.02 °/s in a range of 20-80°. An analysis by Field Emission scanning electron microscopy was carried out in a JEM-2200FS equipment to study of the morphology and particle size of the sample, with magnification settings at 50K-100K nm and 4-5 KV. Surface area was examined by nitrogen physisorption at its condensation temperature of 77.35°K, taking 11 adsorption points in a range of 0.05 to 0.3 relative pressure (P/Po) based on the Brunauer-Emmett-Teller method (BET) in a Quantachrome brand Autosorb-1 surface characterizer kit; to clean the surface, the sample was treated at 250°C for a minimum of 3 hours under vacuum. To determinate the value of the band gap energy, the absorption spectra by diffuse reflectance of the powders were obtained using a UV Visible Evolution 220 Thermo spectrophotometer with an integration sphere in a range from 100 to 1200 nm.

Cyclic voltammetry

Material electrochemical characterization was performed by Cyclic Voltammetry (VC) in a Pine Instruments bipotentiostat model AFCBP1 brand. The system consisted of a 3-electrode cell configuration: a vitreous carbon working electrode with a diameter of 0.5 cm (0.196 cm^2), a platinum foil as a counter-electrode with an area of 4.5 cm^2 (9 cm^2 on both sides) and an Ag/AgCl reference electrode with 3M KCl solution (0.210 V vs NHE). The electrolyte was potassium ferrocyanide trihydrate ($K_4Fe(CN)_6{\cdot}3H_2O$) 0.1 M, pH 7. The solution was bubbled with nitrogen for approximately 5 minutes to remove any possible content of dissolved oxygen before each measurement. The preparation of the working

electrode consisted in the dispersion of 30 mg of the material in 80 µL of isopropanol and 0.5 µL of Nafion®, the suspension was sonicated for a period of 10 minutes, then a drop of the sample was placed on the surface of the electrode and was allowed to evaporate obtaining a membrane of the material.

Photocatalytic H_2 evolution

The evaluation of the photocatalyst was carried out by measuring the hydrogen evolution using a Clarus 500 Perkin Elmer Gas Chromatograph with a TCD detector (Thermal Conductivity Detector) using a specific measurement method to measure hydrogen employing nitrogen as a carrier gas. The system consisted of a quartz tube reactor equipped with a with sampling valve at one end. Inside the reactor, a sample of MCO (200 mg) was added to 200 ml of distilled water with 4% methanol as a sacrificial agent. The reactor was kept at constant stirring for 8 hours, while a gas sample was taken every hour.

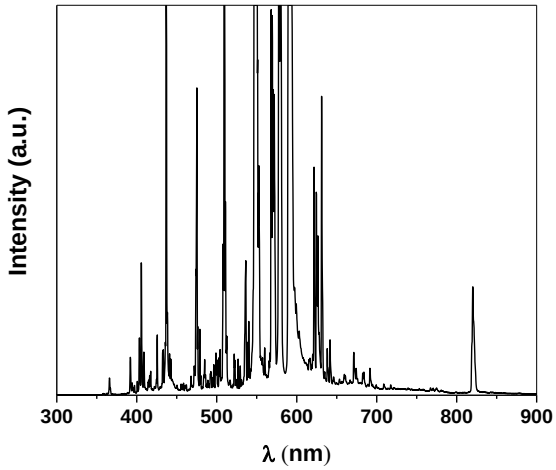

Fig. 1- Light emission spectrum of the lamp used in the photocatalytic evaluation.

The system was irradiated by a 250-watt metal-halide lamp emitting light in the visible range (Fig.1).

3. Results and Discussion

Thermogravimetric analysis

As a result of the modified Pechini's synthesis, the obtained precursor material is a mixture of manganese and cobalt metal ions bonded to organic compounds. Hence, a thermogravimetric analysis is performed in order to find the adequate temperature to obtain the expected MCO phase free of organic compounds. Fig.2 shows the thermogram of MCO where the temperature that reaches the greatest loss (46%) is approximately 370°C, also presenting a slight loss at 575°C.

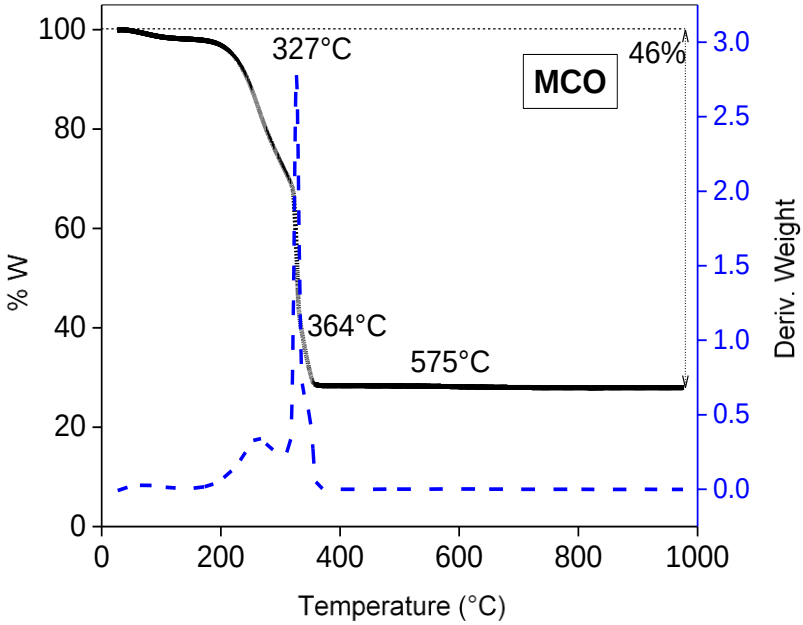

Fig. 2- Thermograms of the $MnCo_2O_4$ prior to calcination.

The literature presents a varied range of temperatures used to obtain the material, from 200 to 1000°C [19,34,35] in very different time intervals. For this reason, it was decided to calcine the material at different temperatures, being 350, 600, 900°C for 4 h in order to obtain 3 MCO samples and study the calcination temperature effect.

X-Ray Diffraction

XRD patterns of the samples calcined at different temperatures from 350, 600 and 900°C are shown in Fig 3 to investigate the influence of the calcination temperature on the crystalline structure. Results showed that with increasing calcination temperature, the intensity of peaks increases and the diffraction peaks become sharper and narrower. This indicates the enhancement of the crystallinity which originated from the increment of the crystalline volume ratio due to the size enlargement of the nuclei [36]. The diffractograms obtained from the material were indexed and compared with the crystallographic card ICDD 00-023-1237 of cobaltite in the ICDD database (*International Center for Diffraction Data*), verifying that the peaks were indicative of $MnCo_2O_4$ spinel.

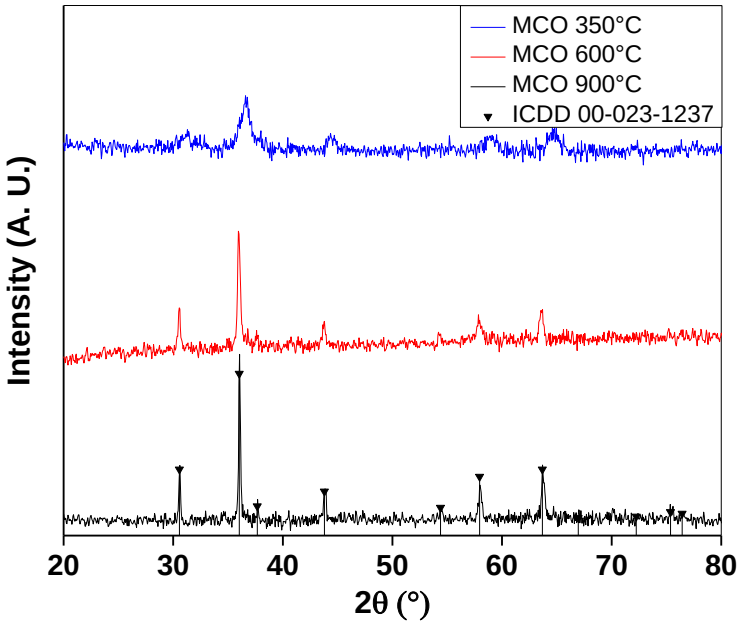

Fig. 3- Diffractograms of the synthetized spinel $MnCo_2O_4$ indexed with the ICDD pattern.

In order to obtain the cobaltite at a lower temperature, another calcination was carried out at 350°C, achieving the phase with wide peaks and not as sharp as the previous ones. In all cases, the peaks indexed to the crystallographic ICDD 00-023-1237, thus verifying that the spinel phase of the MCO was successfully reached.

SEM

Analysis of the particle size and morphology of each MCO was carried out by means of a field emission scanning electron microscope. Figs. 4 (a, b, c) show the SEM images obtained of the samples calcined at different temperatures. The first micrograph (Fig.4a) corresponds to the MCO 350 °C, in which particle sizes ranging between 30 and 50 nm are observed according to the count performed, although they are grouped in clusters, these particles have an irregular circular shape. The particle size obtained is small as expected from the calcination temperature used.

Fig. 4 b) presents a SEM image of MCO at 600°C. In this image an even greater degree of agglomeration of the particles can already be seen. The presence of a sintering effect due to temperature is reflected in sizes of approximately 300 nm, while maintaining an irregular shape. Furthermore, Fig.4c), the image of the sample calcined at 900°C is shown, here it can be observed that calcination temperature plays an important role, since particles are bigger (approx. 500 nm) and the presence of sintering a process is very noticeable in the

particles, while forming agglomerates greater than 1 micron. In these micrographs a wide range of particle sizes is clearly observed, from less than 100 nm to greater than 500 nm approximately. This shape is comparable to those obtained by Borges et al[36], also employing the Pechini method at 900°C.

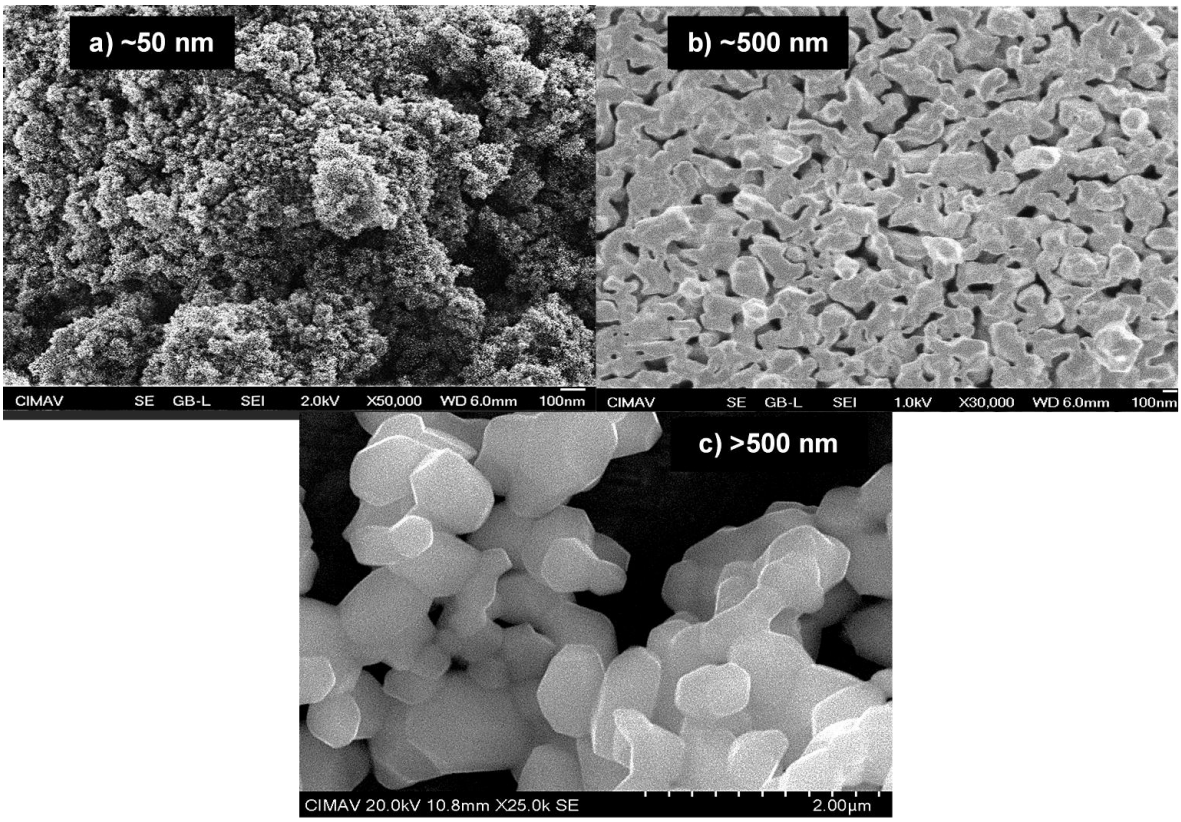

Fig. 4- Images of the $MnCo_2O_4$ calcinated at different temperatures: a) MCO350°C, b) MCO600°C and c) MCO900°C, respectively.

BET surface area

For the analysis of the surface area, the BET method [39] was used, obtaining the nitrogen adsorption isotherms presented in Fig. 5. They do not present hysteresis, so that no MCO has porosity. Table 1 shows the surface area obtained from each material, which values range between 1 and 84 m^2/g. These areas explain how by increasing the temperature, an increase in particle size is reflected in a reduction of the particles surface area that could affect their photocatalytic performance.

Table 1. BET Surface area

	A (m^2/g)
MCO 350°C	84
MCO 600°C	16
MCO 900 °C	1

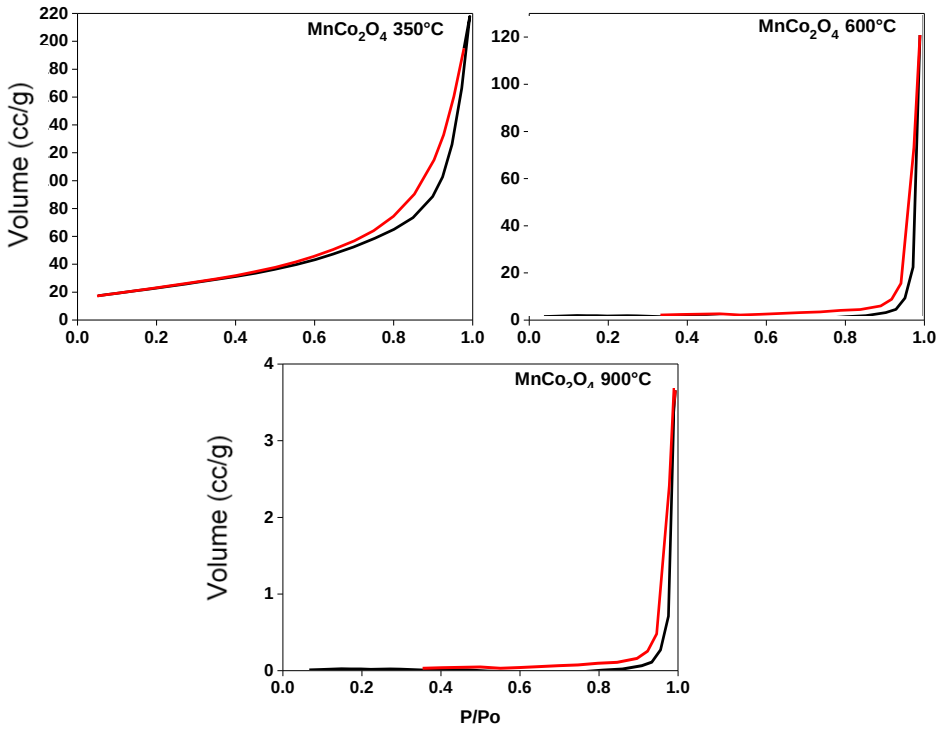

Fig. 5- BET isotherms for the $MnCo_2O_4$ calcined at different temperatures.

UV-Vis spectroscopy

UV-Vis spectroscopy analysis was performed on the MCO powders to determine the light spectrum absorption of the materials. In order to obtain the band gap, the kubelka Munk method was applied using the diffuse reflectance spectra of the material. This reflectance R is substituted in Eq. (1) of the Kubelka Munk function *ƒ(R)* [40]:

$$f(R) = \frac{(1-R)2}{2R} \qquad (1)$$

Table 2. Band gap

Sample	eV
MCO 350°C	1.29
MCO 600°C	1.30
MCO 900°C	1.35

This allows the construction of the Tauc Plot ($f(R)*hv)^n$ *vs hv*). For a direct band gap semiconductor, n = ½ and for indirect band gap materials, n=2. Depending of the material, it will show a linear Tauc Region just above the optical absorption edge. Extrapolation of this line to the photon energy axis yields to the semiconductor band gap value, a key indicator of its light absorption capacity under visible light illumination.

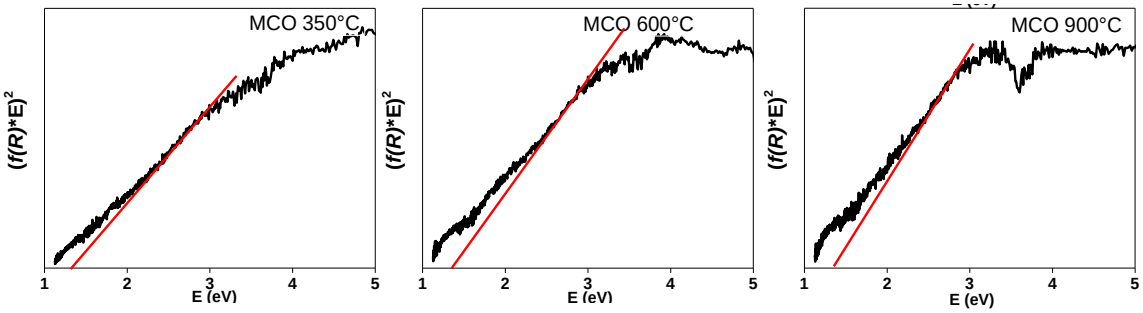

Fig. 6- Calculated band gap from Tauc Plots of the $MnCo_2O_4$ calcined at different temperatures.

Fig. 6 presents Tauc Plots for the MCO samples. The above-described procedure was performed for the three MCO, obtaining an approximate band gap value of about 1.30 eV (Table 2), with very similar values for the three samples. A very large difference between this value (1.30 eV) and those reported in the literature (1.21 and 4 eV) was found [25,32,33]. The value of 1.30 eV obtained in MCO samples are worrying, since in order to separate the

water molecule under visible light it is necessary to comply with the potential of 1.23 eV mentioned above. However, several studies indicate that the minimum energy required to drive a photocatalytic reaction is much higher, about 1.6 eV [1], due to energy losses that could be associated with the over-potentials required for the two chemical reactions and the charge carrier transport.

Photocatalytic H_2 evolution

Hydrogen evolution due to the separation of the water molecule via photocatalysis was carried out inside the reactor and measured every hour for a total of 8 hours. The performance of the MCO was evaluated for the samples calcined at 350°C, 600°C and 900°C obtaining the results presented in Fig. 7. Hydrogen production were reported in nmol of H_2/g_{cat} being evaluated by 8 hours total, while each sample was left to react 24 hours to observe the behavior at longer times.

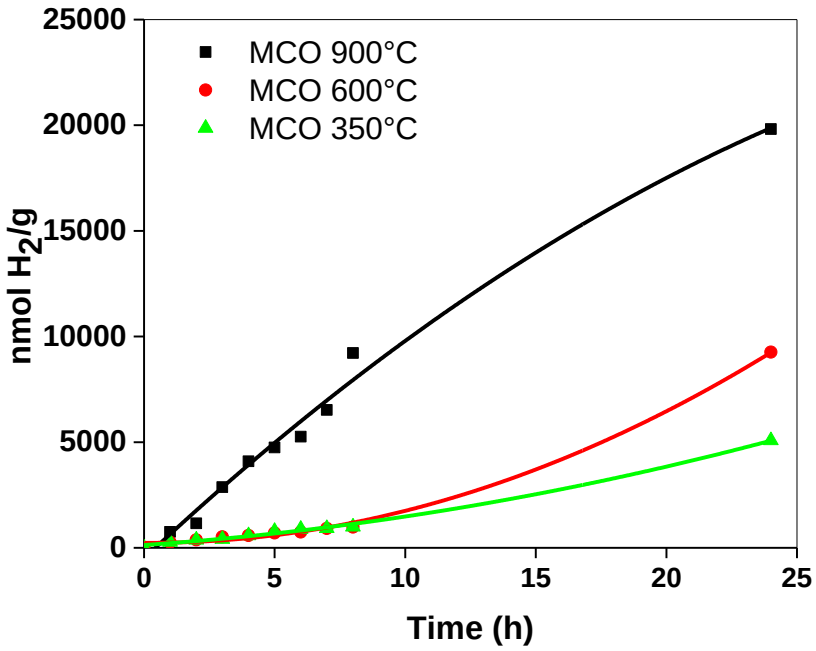

Fig. 7- Photocatalytic evaluation of the $MnCo_2O_4$ towards the H_2 production after 24 h under visible light irradiation.

Table 3 shows the comparison of the performance of the MCO at different calcination temperature against other photocatalysts considering their H_2 production by time and surface area. Materials synthetized in this work show a lower performance than previous ferrites synthetized by our group in other studies.

Table 3. Photocatalyst performance comparison of the MCO from this work, with respect to some common photocatalyst for H_2 production by water splitting.

	nmol H_2/g_{cat} at 8 h	**nmol H_2/g_{cat}·h**	**µmol H_2/m^2**	**Reference**
MCO 350°C	990	123	0.001	This work
MCO 600°C	1000	122	0.007	
MCO 900°C	9200	1152	1.152	
		µmol H_2/g_{cat}·h		
TiO_2		68	No info	[41]
ZnO		3	No info	[41]
$CoFe_2O_4$		21	21	[11]
$SrFe_2O_4$		730	324	[13]

The performance of the MCO-350°C was 990 nmol of H_2/g_{cat} at 8 hours of irradiation, in the MCO-600°C it was 1000 nmol of H_2/g_{cat} and finally, the MCO-900°C with a value of 9200 nmol of H_2/g_{cat}. The MCO-900°C sample obtained the best performance of all studied samples, which could be due to the calcination temperature used. The MCO with a lower calcination temperature obtained a very similar performance at 8 hours of irradiation, but when comparing their performance at 24 hours, it is observed that the MCO-600°C reaches a higher H_2 production. It is possible that this is due to the lack of treatment of MCO-350°C as mentioned above, since the temperature of 600°C promotes crystallinity in cobaltite [36] and as observed in MCO at 900°C, this high crystallinity improves performance. It is very important to note that although high temperature promotes crystallization and this improves performance, it also decreases the surface area of the MCO by the increase of particle size by sintering, which is undesirable for this application, therefore, results obtained in the production of H_2 are very low. Another very important reason for this low H_2 production could be due to the band gap that the material presents, not being enough energetic to promote the separation of the water molecule and for this reason is necessary to further characterize these materials in order to obtain their flat band values.

Cyclic voltammetry

Cyclic voltammetry measurements can reveal the band structure parameters; the corresponding anodic and cathodic peaks in the voltammograms can be attributed to the band edge positions and show a correlation between the optical band gap [42,43]. The electrochemical characterization of the material obtained at different temperatures by the Pechini method was carried out. Fig. 8 shows the voltammetry of the calcined MCO at different temperatures. In the first graph is show the Nafion, which works as a binder to adhere the material to the working electrode and being the conductor too.

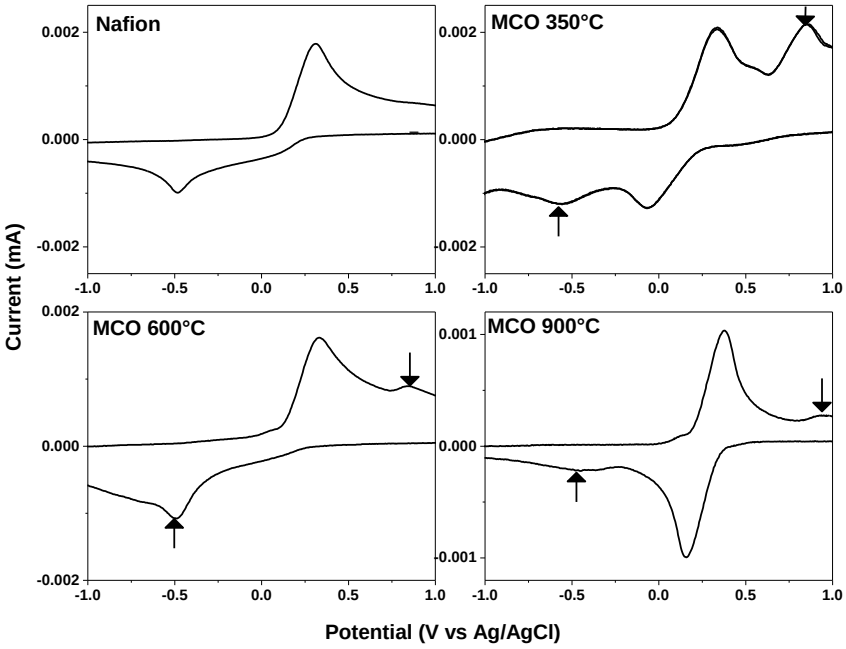

Fig. 8- Cyclic voltammetry of the $MnCo_2O_4$ calcined at different temperatures.

In the second graph in the same Fig. 8, the MCO calcined at 350°C is observed with the mark of the possible anodic and cathode energy bands, from left to right respectively. In this same figure the remaining graphs of the MCO samples are observed where values of the bands are found using the same procedure. It can be seen that the values of the conduction band remain very similar in the range of -0.5 V. This value indicates that the MCO have a reducing potential that is more negative than the redox potential of $H+/H_2$, 0 eV vs NHE. While the values of the valence band changed as the calcination temperature increases. This could be due to the crystallization of the material, as the temperature

increases, the crystalline lattice is modified, so the conduction band values differ from the previous MCO. Some authors claim that these slight changes may be due to a lower resistance to charge transfer, dopants or due to the same optical band gap of the material [44]. The measured values of the conduction and valence bands are presented in Table 4.

Table 4. Values obtained from the cyclic voltammetry.

	Conduction band	Reference	Valence band	Correction 0.205 V		Electrochemical Bg.	Optic Bg.
MCO 350°C	-0.53	0.69 V [29]	0.84	-0.325	1.045	1.37	1.29
MCO 600°C	-0.49		0.86	-0.285	1.065	1.35	1.30
MCO 900°C	-0.52		0.97	-0.315	1.175	1.69	1.35

In this table a comparison of these values with those reported in the literature can be observed. In the literature, the material obtained was synthesized by a solvothermal technique at a temperature of 500 °C for 4 hours. [29]. They reported a characterization by the Mott-Shottky method. This comparison is very similar when comparing the data obtained by UV-vis spectroscopy, where by calculating the band gap it is possible to obtain approximate values for the valence and conduction bands and This can done be using the following Eq. (4):

$$E_{BV} = E_g + E_{BC} \quad (2)$$

Where E_{BV} is the estimated value of the valence band, E_g the value of the band gap obtained by UV-Vis spectroscopy and E_{BC} the value of the conduction band estimated by cyclic voltammetry. In addition to this, it is important to take into account that a correction must be made to the values to be able to obtain the band gap of the material, since the value obtained is only against the Ag/AgCl electrode and it is necessary to convert this vs NHE, that is, the normal hydrogen electrode. These corrected values are included in Table 4. When comparing the gap calculated electrochemically with the optical one obtained previously, it can be observed that the difference is not very large. These values indicate that the reason that the MCO-900°C sample presents a better H_2 generation performance is presumably due to the value of its band gap, since as mentioned previously, a value greater than 1.23 eV is necessary, even >1.6 eV [1].

4. Conclusion

- $MnCo_2O_4$ was synthesized by the Pechini method, obtaining the spinel phase free of impurities.
- The MCO was calcined at different temperatures: 350°C, 600°C and 900°C, observing better crystallinity in the material as the temperature increased.
- Synthesized materials were nonporous and shown the presence of sintered agglomerates with the increase of temperature and consequently surface areas from 84 to 1 m^2/g.
- The MCO calcinated at different temperatures present a band gap of ~1.3 eV, which is close to the minimal energy for the photocatalytic H_2 generation under visible light.
- Performance of hydrogen generation at 8 hours for MCO-350°C, MCO-600°C and MCO-900°C were 990, 1000 and 9200 $nmolH_2/g_{cat}$, respectively.
- The low general performance of MCO samples are presumably due to their band gap of ~1.30 eV, even though they present a more negative value of the conduction band (-0.5eV) than the redox potential of $H+/H_2$ (0 eV vs NHE).

Acknowledgements

The authors acknowledge M.Sc. Ernesto Guerrero Lestarjette, M. Sc. Karla Campos Venegas, and Eng. Luis de la Torre Saenz for their contributions to the XRD, SEM, BET, results. Special thanks are given to Laboratorio Nacional de Nanotecnología in Centro de Investigación en Materiales Avanzados, S. C., for their support in the use of the facilities.

References

[1] Martin DJ. Investigation into High Efficiency Visible Light Photocatalysts for Water Reduction and Oxidation. Springer T. Switzerland: Springer International Publishing; 2015. https://doi.org/10.1007/978-3-319-18488-3.
[2] Zhao Q, Yan Z, Chen C, Chen J. Spinels: Controlled Preparation, Oxygen Reduction/Evolution Reaction Application, and beyond. Chem Rev 2017;117:10121–211. https://doi.org/10.1021/acs.chemrev.7b00051.
[3] Armatas GS. in Catalysis New and Future Developments in Catalysis. Elsevier B.V.; 2013. https://doi.org/10.1016/B978-0-444-53872-7.00022-4.
[4] Acar C, Dincer I, Zamfirescu C. A review on selected heterogeneous photocatalysts for hydrogen production. Int J Energy Res 2014;38:1903–1920. https://doi.org/10.1002/er.
[5] Rosseler O, Shankar M V, Du MK, Schmidlin L, Keller N, Keller V. Solar light photocatalytic hydrogen production from water over Pt and Au / TiO 2 (anatase / rutile) photocatalysts : Influence of noble metal and porogen promotion. J Catal 2010;269:179–90. https://doi.org/10.1016/j.jcat.2009.11.006.
[6] Selcuk MZ, Boroglu MS, Boz I. Hydrogen production by photocatalytic water-splitting using nitrogen and metal co-doped TiO2 powder photocatalyst. React Kinet Mech Catal 2012;106:313–24. https://doi.org/10.1007/s11144-012-0434-4.

[7] Wang D, Wang X, Liu J, Zhang M, Song Y, Zhang Z, et al. Preparation of high proportion of Z-scheme Er3+:Y3Al5O12@Nb2O5/Pt/In2O3 composite for enhanced visible-light driven photocatalytic hydrogen production. Mater Sci Eng B Solid-State Mater Adv Technol 2020;257:114549. https://doi.org/10.1016/j.mseb.2020.114549.
[8] Ding L, Shen C, Zhao Y, Chen Y, Yuan L, Yang H, et al. CsPbBr3 nanocrystals glass facilitated with Zn ions for photocatalytic hydrogen production via H2O splitting. Mol Catal 2020;483:1–7. https://doi.org/10.1016/j.mcat.2020.110764.
[9] Sadat N, Khameneh S, Mohammadpour R. Electrochimica Acta Band-gap narrowing and electrochemical properties in N-doped and reduced anodic TiO 2 nanotube arrays. Electrochim Acta 2018;270:245–55. https://doi.org/10.1016/j.electacta.2018.03.091.
[10]Hunge YM, Yadav AA, Mathe VL. Photocatalytic hydrogen production using TiO2 nanogranules prepared by hydrothermal route. Chem Phys Lett 2019;731:136582. https://doi.org/10.1016/j.cplett.2019.07.010.
[11]Ortega López Y, Medina Vázquez H, SalinasGutiérrez J, GuzmánVelderrain V, LópezOrtiz A, CollinsMartínez V. Synthesis method effect of CoFe2O4 on its photocatalytic properties for H2 production from water and visible light. J Nanomater 2015;76.
[12]Domínguez-Arvizu JL, Jiménez-Miramontes JA, Salinas-Gutiérrez JM, Meléndez-Zaragoza MJ, López-Ortiz A, Collins-Martínez V. Optical properties determination of NiFe2O4 nanoparticles and their photocatalytic evaluation towards hydrogen production. Int J Hydrogen Energy 2017;42:30242–8. https://doi.org/10.1016/j.ijhydene.2017.09.180.
[13]Jiménez-Miramontes JA, Domínguez-Arvizu JL, Salinas-Gutiérrez JM, Meléndez-Zaragoza MJ, López-Ortiz A, Collins-Martínez V. Synthesis, characterization and photocatalytic evaluation of strontium ferrites towards H<inf>2</inf>production by water splitting under visible light irradiation. Int J Hydrogen Energy 2017;42. https://doi.org/10.1016/j.ijhydene.2017.09.162.
[14]Li CJ, Wang JN, Li XY, Zhang LL. Functionalization of electrospun magnetically separable TiO 2-coated SrFe12O19 nanofibers: Strongly effective photocatalyst and magnetic separation. J Mater Sci 2011;46:2058–63. https://doi.org/10.1007/s10853-010-5038-7.
[15]Aziz AA, Yong KS, Ibrahim S, Pichiah S. Enhanced magnetic separation and photocatalytic activity of nitrogen doped titania photocatalyst supported on strontium ferrite. J Hazard Mater 2012;199–200:143–50. https://doi.org/10.1016/j.jhazmat.2011.10.069.
[16]Wu Z, Zhu Y, Ji X. NiCo2O4-based materials for electrochemical supercapacitors. J Mater Chem A 2014;2:14759–72. https://doi.org/10.1039/c4ta02390k.
[17]Fang L, Jiang Z, Xu H, Liu L, guan Y, Gu X, et al. Crystal-plane engineering of NiCo2O4electrocatalysts towards efficient overall water splitting. J Catal 2018;357:238–46. https://doi.org/10.1016/j.jcat.2017.11.017.
[18]Gao X, Zhang H, Li Q, Yu X, Hong Z, Zhang X, et al. Hierarchical NiCo2O4hollow microcuboids as bifunctional electrocatalysts for overall water-splitting. Angew Chemie - Int Ed 2016;55:6290–4. https://doi.org/10.1002/anie.201600525.
[19]Duan L, Gao F, Wang L, Jin S, Wu H. Hydrothermal synthesis and characterization of MnCo2O4 in the low-temperature hydrothermal process: Their magnetism and electrochemical properties. J Adv Ceram 2013;2:266–73. https://doi.org/10.1007/s40145-013-0070-0.

[20]Molin S, Jasinski P, Mikkelsen L, Zhang W, Chen M, Hendriksen P V. Low temperature processed MnCo2O4and MnCo1.8Fe0.2O4as effective protective coatings for solid oxide fuel cell interconnects at 750 ï¿½C. J Power Sources 2016;336:408–18. https://doi.org/10.1016/j.jpowsour.2016.11.011.
[21]Sharma Y, Sharma N, Subba Rao G V., Chowdari BVR. Studies on spinel cobaltites, FeCo2O4 and MgCo2O4 as anodes for Li-ion batteries. Solid State Ionics 2008;179:587–97. https://doi.org/10.1016/j.ssi.2008.04.007.
[22]Darbar D, Reddy M V., Sundarrajan S, Pattabiraman R, Ramakrishna S, Chowdari BVR. Anodic electrochemical performances of MgCo2O4synthesized by oxalate decomposition method and electrospinning technique for Li-ion battery application. Mater Res Bull 2016;73:369–76. https://doi.org/10.1016/j.materresbull.2015.09.025.
[23]Liu W-W, Jin MT, Shi WM, Deng JG, Lau W-M, Zhang YN. First-Principles Studies on the Structural Stability of Spinel ZnCo2O4 as an Electrode Material for Lithium-ion Batteries. Sci Rep 2016;6:36717. https://doi.org/10.1038/srep36717.
[24]Liu J, Xie Y, Nan Y, Gou G, Li X, Fang Y, et al. ZnCo2O4nanoparticles derived from dual-metal-organic-frameworks embedded in Multiwalled Carbon Nanotubes: a favorable electrocatalyst for the water splitting. Electrochim Acta 2017;257:233–42. https://doi.org/10.1016/j.electacta.2017.10.080.
[25]Shibli SMA, Arun PS, Raj A V. Exploration of octahedrally shaped MnCo2O4 catalyst particles for visible light driven photocatalytic water splitting reaction. RSC Adv 2015;5:19393–9. https://doi.org/10.1039/c4ra12646g.
[26]Zasada F, Gryboś J, Indyka P, Piskorz W, Kaczmarczyk J, Sojka Z. Surface structure and morphology of M[CoM′]O4 (M = Mg, Zn, Fe, Co and M′ = Ni, Al, Mn, Co) spinel nanocrystals-DFT+U and TEM screening investigations. J Phys Chem C 2014;118:19085–97. https://doi.org/10.1021/jp503737p.
[27]Darbar D, Anilkumar MR, Rajagopalan V, Bhattacharya I, Elim HI, Ramakrishnappa T, et al. Studies on spinel cobaltites, MCo 2 O 4 (M = Mn, Zn, Fe, Ni and Co) and their functional properties. Ceram Int 2018;44:4630–9. https://doi.org/10.1016/j.ceramint.2017.12.010.
[28]Mondal AK, Su D, Chen S, Ung A, Kim HS, Wang G. Mesoporous MnCo2O4with a flake-like structure as advanced electrode materials for lithium-ion batteries and supercapacitors. Chem - A Eur J 2015;21:1526–32. https://doi.org/10.1002/chem.201405698.
[29]Zheng J, Lei Z. Incorporation of CoO nanoparticles in 3D marigold flower-like hierarchical architecture MnCo2O4 for highly boosting solar light photo-oxidation and reduction ability. Appl Catal B Environ 2018;237:1–8. https://doi.org/10.1016/j.apcatb.2018.05.060.
[30]Jadhav HS, Roy A, Chung WJ, Seo JG. Free standing growth of MnCo2O4 nanoflakes as an electrocatalyst for methanol electro-oxidation. New J Chem 2017;41:15058–63. https://doi.org/10.1039/c7nj03180g.
[31]Fan LQ, Huang JL, Wang YL, Geng CL, Sun SJ, Huang YF, et al. High-capacity MnCo2O4 supported by reduced graphene oxide as an anode for lithium-ion capacitors. J Energy Storage 2020;30:101427. https://doi.org/10.1016/j.est.2020.101427.
[32]Habibi MH, Bagheri P. Enhanced photo-catalytic degradation of naphthol blue black on nano-structure MnCo2O4: charge separation of the photo-generated electron–hole pair. J Mater Sci Mater Electron 2017;28:289–94. https://doi.org/10.1007/s10854-016-5523-0.

[33]Uke SJ, Akhare VP, Meshram SP, Bambole DR, Thakre DS, Chaudhari GN, et al. FABRICATION OF SPHERICAL NANOCRYSTALLINE MnCo 2 O 4 VIA SOL- GEL CITRATE ROUTE FOR SUPERCAPACITOR 2018:254–61.
[34]Yoon MY, Lee EJ, Song RH, Hwang HJ. Preparation and properties of a MnCo2O4 for ceramic interconnect of solid oxide fuel cell via glycine nitrate process. Met Mater Int 2011;17:1039–43. https://doi.org/10.1007/s12540-011-6025-5.
[35]Lesani P, Babaei A, Ataie A, Mostafavi E. Nanostructured MnCo2O4synthesized via co-precipitation method for SOFC interconnect application. Int J Hydrogen Energy 2016;41:20640–9. https://doi.org/10.1016/j.ijhydene.2016.07.216.
[36]Borges FMM, Melo DMA, Câmara MSA, Martinelli AE, Soares JM, de Araújo JH, et al. Magnetic behavior of nanocrystalline MnCo2O4 spinels. J Magn Magn Mater 2006;302:273–7. https://doi.org/10.1016/j.jmmm.2005.09.017.
[37]Krittayavathananon A, Pettong T, Kidkhunthod P, Sawangphruk M. Insight into the charge storage mechanism and capacity retention fading of MnCo2O4 used as supercapacitor electrodes. Electrochim Acta 2017;258:1008–15. https://doi.org/10.1016/j.electacta.2017.11.152.
[38]Jiménez-Miramontes JA, Domínguez-Arvizu JL, Salinas-Gutiérrez JM, Meléndez-Zaragoza MJ, López-Ortiz A, Collins-Martínez V. Synthesis, characterization and photocatalytic evaluation of strontium ferrites towards H 2 production by water splitting under visible light irradiation. Int J Hydrogen Energy 2017;42:30257–66. https://doi.org/10.1016/j.ijhydene.2017.09.162.
[39]Brunauer S, Emmett PH, Teller E. Adsorption of Gases in Multimolecular Layers. J Am Chem Soc 1938;60:309–19. https://doi.org/10.1021/ja01269a023.
[40]Pike Technologies. Diffuse Reflectance – Theory and Applications. Appl Note 2011:2. https://doi.org/10.1016/j.soilbio.2011.02.019.
[41]Xie MY, Su KY, Peng XY, Wu RJ, Chavali M, Chang WC. Hydrogen production by photocatalytic water-splitting on Pt-doped TiO2-ZnO under visible light. J Taiwan Inst Chem Eng 2017;70:161–7. https://doi.org/10.1016/j.jtice.2016.10.034.
[42]Inamdar SN, Ingole PP, Haram SK. Determination of band structure parameters and the quasi-particle gap of CdSe quantum dots by cyclic voltammetry. ChemPhysChem 2008;9:2574–9. https://doi.org/10.1002/cphc.200800482.
[43]Kucur E, Riegler J, Urban GA, Nann T. Determination of quantum confinement in CdSe nanocrystals by cyclic voltammetry. J Chem Phys 2003;119:2333–7. https://doi.org/10.1063/1.1582834.
[44]Venkata C, Reddy IN, Sreedhar A, Shim J. Applied Surface Science Investigation of dopant and Ag plasmonic effect on α-Fe 2 O 3 photoelectrode for photoelectrochemical water splitting activity. Appl Surf Sci 2019;488:629–38. https://doi.org/10.1016/j.apsusc.2019.05.316.

ID 087

$CoFe_2O_4/Cu_2O$ heterojunction study as photocatalyst for visible light hydrogen production

J. L. Domínguez-Arvizu, J. A. Jiménez-Miramontes, B. C. Hernández-Majalca, J. C. Pantoja-Espinoza, J. M. Meléndez-Zaragoza, J. M. Salinas-Gutiérrez, A. López-Ortiz, V. Collins-Martínez*

Departamento de Ingeniería y Química de Materiales, Centro de Investigación en Materiales Avanzados, S.C., Miguel de Cervantes 120, Chihuahua, Chih., 31136, Mexico

* Corresponding author: virginia.collins@cimav.edu.mx

ABSTRACT

In recent years, research related to visible light-driven photocatalysts has attracted a lot of attention towards hydrogen production using solar energy. However, single phase photocatalysts studies have suggested that their optoelectronic properties can be improved by means of heterojunction generation with other semiconductors, turning this into a higher visible light absorption and quantum yield bringing a superior hydrogen production. In this research we study the $CoFe_2O_4/Cu_2O$ heterojunction by comparing their photocatalytic activity with the individual materials synthesized by Pechini´s method and Benedict reaction respectively. Hydrogen content was measured by gas chromatography observing a significant ten times higher activity in heterojunction than the individual oxides. Synthesized materials were characterized through XRD, SEM, TGA, UV-Vis and BET surface area techniques whilst their electrochemical properties by means of cyclic voltammetry and electrochemical impedance spectroscopy were employed to elaborate the Mott-Schottky plots and calculate band gap edge positions of individual materials.

Keywords: Hydrogen production, photocatalysis, heterojunctions, visible light photocatalyst

1. Introduction

Nowadays, hydrogen is considered the future fuel since it can be obtained from renewable sources. However, 95 % is produced from fossil fuels while only 5% of hydrogen is obtained from renewables [1].

In 1972 Honda and Fujishima, discovered the photocatalysis phenomenon using TiO_2 and platinum as electrodes and irradiating the system with solar energy as a renewable source, afterwards, photocatalysis has demonstrated to have a wide variety of applications like photocatalytic water splitting, whereas process efficiency depends mainly on semiconductor opto-electronic properties such as radiation absorption capacity, charge carrier density and recombination time [2-4].

Up to date, the most used and studied photocatalyst is TiO_2 which is active under UV light. This represents a disadvantage since UV light is only 4 % from solar irradiation. Is in this sense that the search for visible light-driven photocatalysts represents one of the main challenges for photocatalytic water splitting research [3]. Furthermore, semiconductor materials in individual phase as a rule, show low efficiencies for hydrogen production. Therefore, the strategy to add dopants or other materials in heterojunction to photocatalysts has been proposed aiming to modify their opto-electronic properties as well as charge-carrier separation efficiencies (electron-hole pair) in order to increase their recombination times [5, 6].

There are in general three types of heterojunctions: Type I (Figure 1a), where conduction band (CB) and valence band (VB) of the narrowest bandgap semiconductor are bound with the largest band gap material. In this case both electrons and holes flow to the narrowest band gap photocatalyst. Type II (Figure 1b), where BC and BV are interposed between both semiconductors, causing an opposite flow between holes and electrons achieving the objective of more efficient charge carrier separation. Type III (Figure 1c), where BC is under the other semiconductor VB, resulting in a faster recombination charge-carrier recombination kinetics and henceforth, making this heterojunction inefficient for photocatalytic water splitting [7, 8].

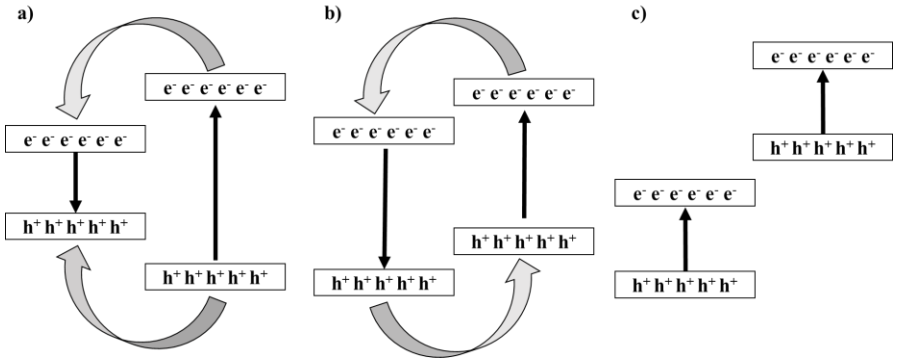

Figure 1: Types of heterojunctions of coupled semiconductors, arrows indicate the charge-carrier flow throughout heterojunctions [8].

Regarding to individual materials as photocalaysts, there are some studies where spinel ferrites (MFe_2O_4) are used (i.e. M = Mg, Sr, Co, Ni or Zn) [9-12]. It has been demonstrated that spinel ferrites have an adequate band gap to be active under visible light and due to its crystal structure, which favors charge transfer processes: They need less energy due to its high packing degree of O^{2-}, M^{2+} and Fe^{3+} ions on its octahedral and tetrahedral sites in crystal lattice besides their low cost and nontoxic nature [13, 14]. Studies with oxides as individual photocatalysts, α-Fe_2O_3 has been used as photoanode for water splitting [15], WO_3 with FTO and Cu_2O as solar light photocatalyst [16, 17]. Furthermore, there is research related to both materials used in heterojunctions in photocatalytic water splitting, like $NiFe_2O_4/Fe_2O_3$ for photoelectrochemical water splitting [18], $ZnFe_2O_4$/α-Fe_2O_3 doped with aluminum [19] or $ZnFe_2O_4$/ZnO [20], thus showing that these type of heterojunctions have a great potential to be used in photocatalytic water splitting for hydrogen production.

In this work we propose the use of $CoFe_2O_4/Cu_2O$ heterojunction for the photocatalytic hydrogen production by water splitting due to their individual properties aimed to enhance the hydrogen generation under visible light irradiation and because of the lack of studies based on these materials. Furthermore, very few characterization studies have been reported on these materials such as band edge positions and cyclic voltammetry in order to evaluate their photocatalytic properties.

2. Materials and Methods

$CoFe_2O_4$ synthesis

The synthesis was carried out by Pechini´s method first preparing a 1:1 solution of ethylene glycol (EG) and citric acid (CA) and maintaining this under constant vigorous stirring and heating until a 90 °C temperature was reached. Later, $Co(NO_3)_2.6H_2O$ and $Fe(NO_3)_3.9H_2O$ reagents (Sigma Aldrich) in adequate stoichiometric ratios were mixed in a

way that the molar ratios respect to CA were 2:1 and 3:1 respectively. This solution was maintained under stirring at 80 °C until the whole water content was evaporated obtaining an olive-green color gel which was pulverized in an agate mortar. The powder was subjected to TGA analysis in order to determine its calcination temperature (600 °C for 4 hour) to finally obtain the $CoFe_2O_4$ nanoparticles.

Cu_2O synthesis

To synthesize the Cu_2O particles, the Benedict reaction was employed by preparing a $Cu(NO_3)_2.2.5H_2O$, Na_2CO_4 and sodium citrate dihydrate solution (Benedict reagent) at 0.67, 0.94 and 0.07 M concentrations respectively. Then an excess of D-Glucose was added and the resultant mixture was heated up to 80 °C for a half hour under permanent stirring. Subsequently, the reaction could be verified by the observation of the reduction of cupric nitrate Cu^{2+} ions resulting in the appearance of a brick-red color precipitate, corresponding to Cu_2O particles. The obtained product was recovered by means of micro glass fiber filters and washed with distilled water and ethanol at 80 °C.

$CoFe_2O_4/Cu_2O$ heterojunction

Heterojunction was generated from a 50 % mass mixture of individual materials and using and impregnation method as follows: An ethanol material mixture suspension was kept under stirring by 6 hours and then the ethanol content was evaporated at 60 °C, then the generated mixture was pulverized in an agate mortar and calcinated at 200 °C by 2 hours.

Characterization

Calcination temperature obtained from $CoFe_2O_4$ and thermal stability of Cu_2O synthesis were determined by TGA analysis in a Q 500 TA instruments equipment. Crystal phase identification of both materials was performed by X Ray Diffraction (XRD) with a PANalytical X'pert PRO diffractometer with X'Celerator detector. Materials morphology by field emission scanning electron microscopy in a JEM-2200-FS microscope. Band gap was estimated by UV-Vis spectroscopy in a Lambda 35 from Perkin Elmer spectrometer and finally, BET surface area was obtained from an Autosorb-1C gas equipment Sorption System from Quantachrome.

Electrochemical Characterization

Valence (VB) and conduction (CB) band gap positions and energy values were estimated by cyclic voltammetry (CV) in a 3-electrode electrochemical cell using a bipotenciostat model AFCBP1 from Pine instruments. System configuration consisted of a vitreous carbon as working electrode of 0.5 cm diameter (0.196 cm^2), a platinum sheet with 4.5 cm^2 area by each face as counter electrode and Ag/AgCl with 3M KCl solution as reference electrode (0.21 V vs NHE). $K_4Fe(CN)_6.3H_2O$ electrolyte was used at 0.1 M concentration with pH~7 which was bubbled with N_2 by 10 minutes each measurement in order to eliminate the possible content of diluted oxygen in solution. The working electrode was prepared as follows: 30 mg of each material was dispersed in 80 µL of isopropanol and 0.5 µL of Nafion® was added, then the suspension was sonicated by 10 minutes and a drop was deposited in the vitreous carbon working electrode heating at 60 °C for 5 minutes in order to evaporate the isopropanol content and finally obtaining a membrane of the semiconductor sealed by Nafion®. The possible chemical species adsorbed in the material were eliminated making 40 cycles at 200 mV/s sweep rate and then a rate of 20 mV/s sweeping was carried out to obtain the voltammetry of each material.

Mott-Schottky plots

Same configuration as in CV was used as well as the same working electrode preparation and electrolyte. Working electrode capacitance was computed through electrochemical impedance spectroscopy (EIS) with an electrochemical interface system SI 1287 coupled to a frequency response analyzer (FRA) model SI 1260 both from Solartron. Impedance was determined at a frequency of 50 kHz for each material using an amplitude of 20 mV and sweeping from 1 to -1 V in direct current.

Photocatalytic hydrogen production measurement

For individual materials and heterojunction, 20 cm x 4.5 cm of diameter quartz tube reactors were used holding their hermeticity by means of two neoprene gaskets in both sides of the quartz tube pressed by two brides held by four screwed metal rods and a septum in the top bride to take the sample. 200 mg of each material were dispersed in 200 ml of water 2% (v/v) of methanol as sacrificial reagent. Reaction monitoring was carried out by gas chromatography in a Clarus 500 chromatograph by Perkin Elmer equipped with Porapak Q and Carboxen columns taking simples of 0.2 mL with a strynge each hour by a period of 8 hours for each material, the reactors were maintained under stirring and irradiated by a 200 Watts metallic halide lamp from Phillips. The whole experimental set up is shown in Figure 2.

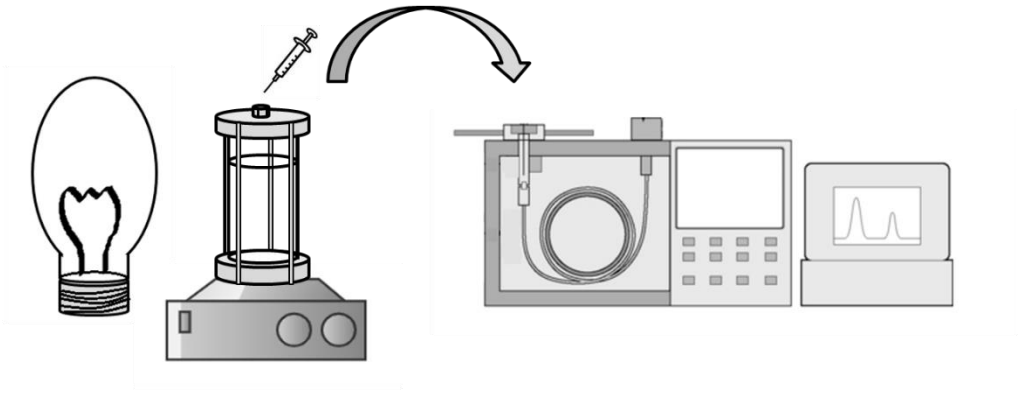

Figure 2. Experimental set up for photocatalytic water splitting measurement of individual materials and heterojunction.

3. Results and Discussion

Characterization

In Figure 3 the TGA plots of each individual photocatalyst are shown. Figure 3a shows the thermogram of the gel for $CoFe_2O_4$ nanoparticles synthesis. It can be seen a first pronounced steep of weight percent around 200 °C, which indicates the loss of bound water, while organic content in gel starts to burn out around 300 °C reaching thermal stability at about 400 °C. Therefore, calcination temperature was fixed at 600 °C in order to insure the whole removal of water and organic content in the material and be able to achieve its crystallinity. On the other hand, Figure 3b shows TGA analysis of thermal stability of Cu_2O particles with the purpose of establishing a temperature to generate the heterojunction by impregnation method when the material mixture is calcinated. It can be appreciated a pronounced weight percentage increase around 300 °C and thermal stability is reached at 500 °C with around 10 g weight increment based on 100 grams of material. Calculating the stoichiometric quantities for the whole oxidation of this mass 11 grams of oxygen to reach the complete oxidation is needed.

Crystallinity analysis of each material was established by XRD. In Figure 4 the corresponding diffractograms for both materials can be appreciated. In both cases the matching diffraction peaks show that there is no evidence of other crystalline phase in each semiconductor, since only the corresponding individual crystalline phases were found and these being diffraction peaks in 4a those that correspond to the cubic spinel ferrite with spatial group Fd-3m and in 4b those that agrees with spatial group Pn-3m (both cubic). Each diffractogram is compared to the ICDD database.

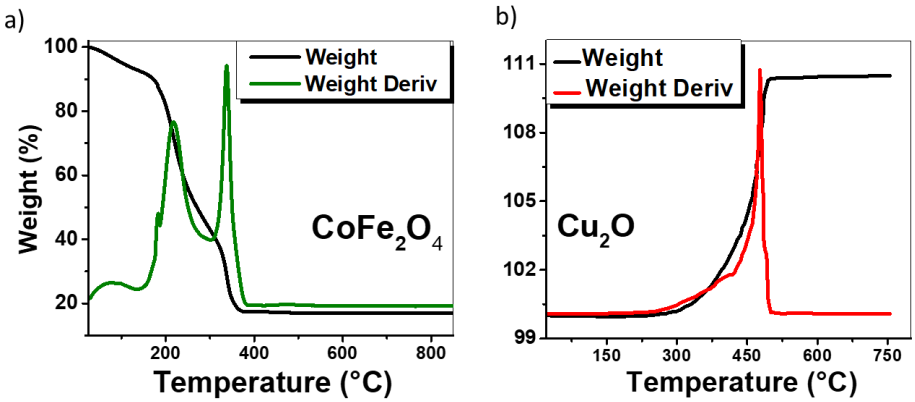

Figure 3. TGA analysis from both individual materials with their corresponding weight derivative of each material.

Crystallite size for each phase was estimated with Scherrer equation taking the most intense peak of each diffractogram:

$$L = \frac{K\lambda}{B(2\theta)cos\theta}$$

Where *B(2θ)* is FWHM of the most intense peak, *L* is the crystallite size in nm, λ the X-ray wavelength of α-Cu electrode equal to 0.154 nm, *θ* the diffraction Bragg's angle in diffractogram and *K* the correction factor equal to 0.9. Results obtained for crystallite size were 56 nm for $CoFe_2O_4$ and 1400 nm for Cu_2O, a value which exceeds the limit of size determination with Scherrer's equation which is 100-200 nm [21]. However this value is used to make the comparison between the grade of crystallinity between both phases in a qualitative way rather than calculate an exact value of *L*.

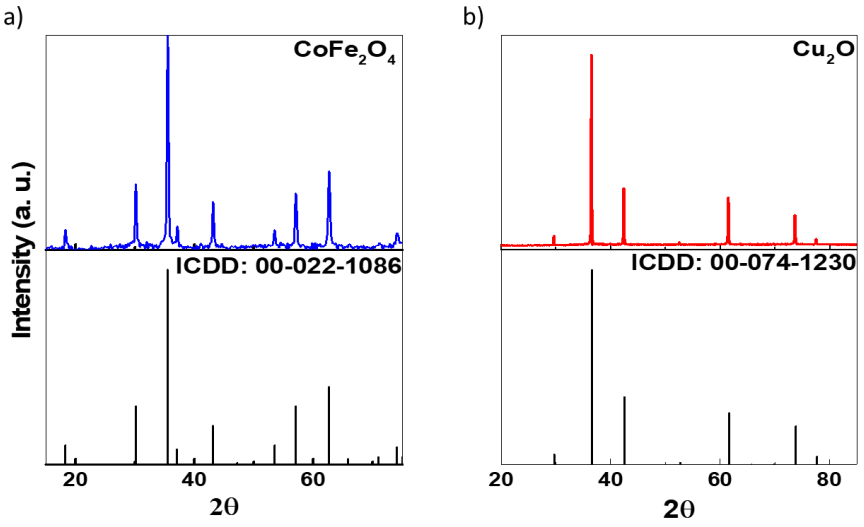

Figure 4. Diffractograms compared to his ICDD crystallographic sheet for each individual material.

BET surface analysis results of sorption isotherms are shown in Figure 5. Both plots show that material surface area is attributed only to the materials morphology and not to an appreciable porosity in each semiconductor due to an absence of a significative hysteresis in each adsorption-desorption isotherm.

However, comparing surface areas between photocatalysts, it can be observed a difference of almost one order magnitude between $CoFe_2O_4$ (11.85 m^2/g) and Cu_2O (1.23 m^2/g). This agrees with the highest crystal size discussed previously of Cu_2O particles which indicates a possible greater particle size in the photocatalyst compared to $CoFe_2O_4$ material and it can be confirmed in the SEM micrographs shown in Figure 6 where an averaged estimated particle size for Cu_2O phase is ~ 2 micrometers while particle size for $CoFe_2O_4$ is around 150 nm which is approximately 13 times smaller.

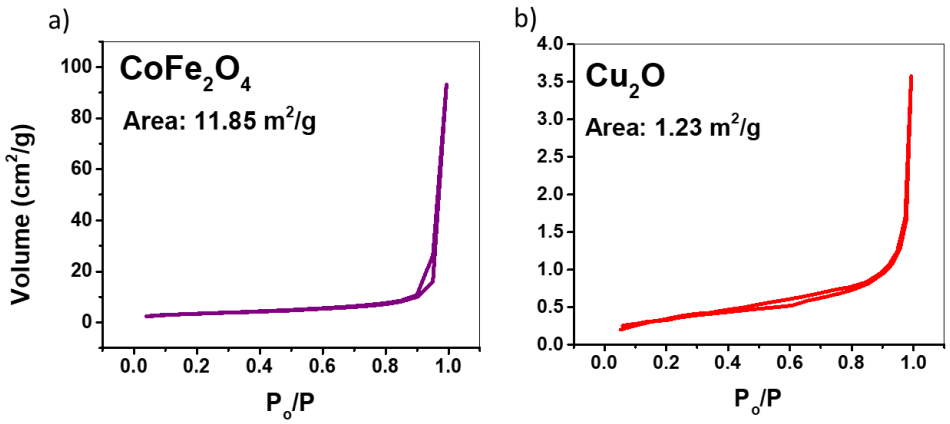

Figure 5. BET surface analysis from both phases: a) $CoFe_2O_4$ nanoparticles and b) Cu_2O particles estimated surface area.

Moreover, it can be observed that morphology between both materials is very different being nanoparticle type in $CoFe_2O_4$ that it is worth noting that can be observed a certain grade of sintering probably due to the high temperature and time employed in calcination (600 °C for 4 h) while in Cu_2O a morphology between polyhedral and micrometric cube particles can be observed.

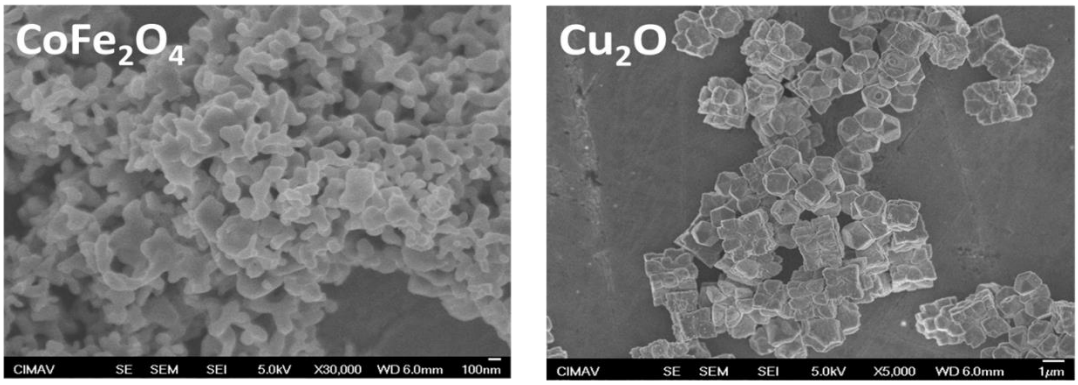

Figure 6. SEM micrographs of $CoFe_2O_4$ and Cu_2O synthesized particles.

Figure 7 shows the Kublelka-Munk plots calculated from UV-Vis spectra for the direct band gap of both individual materials. A value of 1.32 eV for $CoFe_2O_4$ can be observed, which is very similar to the one obtained by López et al. [13] and synthesized by the coprecipitation method and obtaining a band gap value of 1.38 eV. On the other hand, calculated band gap for Cu_2O is 1.95 eV, De Jongh et al. [22] obtained a value 2.0 eV synthesized by thin-film electrodeposition on transparent substrates.

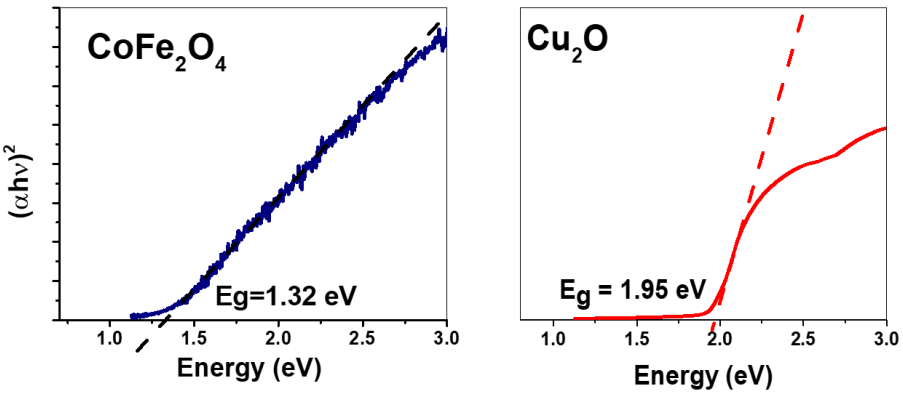

Figure 7. Estimated direct band gap value from both individual semiconductors.

Electrochemical characterization

In Figure 8 the Mott-Schottky (MS) plots obtained for individual materials are shown to obtain each CB positions through flat band estimations. There is a vast literature information about conduction band estimation in semiconductors using MS plots where potential is plotted against the inverse of squared capacitance, which is computed by the following equation:

$$\frac{1}{C^2} = 2\pi\nu Z'$$

Where *C* is capacitance, *v* the frequency employed in FRA instrument (50 kHz in this case) and *Z'* the complex part of the measured impedance. This is made under the assumption to calculate the CB through the intercept of potential by MS equation for n-type semiconductor (which is the case for both materials due to their positive slope in each material plot) using the following simple algebraic steps:

$$\frac{1}{C^2} = \frac{2}{\epsilon_o \epsilon e N_d}\left(E - E_{fb} - \frac{kT}{e}\right)$$

And if $1/C^2$ is zero and since $E \gg kT/e$ then:

$$E = E_{fb}$$

Moreover, in order to confirm the obtained CB values, a cyclic voltammetry was performed. According to Inamdar et al. [23] band edge positions can be estimated through cyclic voltammetry measurement attributing the cathodic peak to the CB and the anodic to VB in the working electrode.

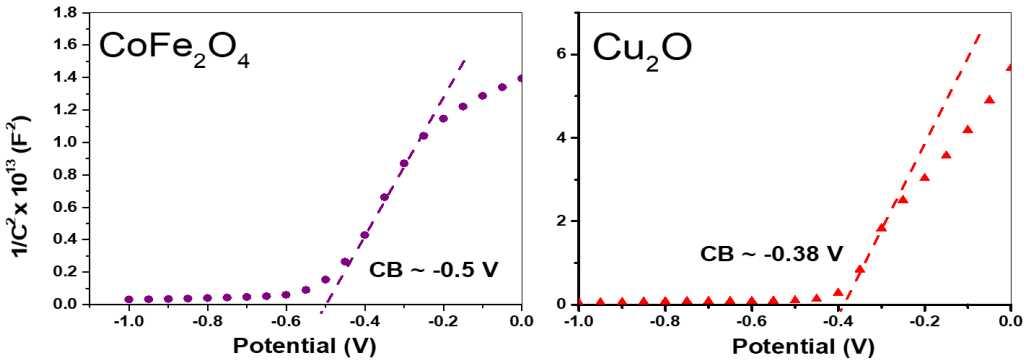

Figure 8. Mott-Schottky plots obtained for both individual materials, as can be seen each material has a n-type semiconductor nature.

Once the cathodic peak is determined from the obtained value from MS plots, the anodic peak can be deducted from the peak which value is nearest to the sum of estimated CB and the material band gap. Figure 9 shows the cyclic voltammetry plots for $CoFe_2O_4$ (a and b for CB and VB, respectively) and the cyclic voltammetry for Cu_2O particles (CB and VB estimation in c). The other peaks are attributed to adsorption of electrolyte and water.

Finally, Table 1 summarizes the electrochemical parameters estimated by both methods converted to NHE as reference electrode and makes a comparison between them with the band gap value calculated by UV-Vis spectroscopy. It is worthy to note that the difference between CB and CV obtained from cyclic voltammetry is very similar to the obtained band gap value in each material and due to CB and VB positions. It is possible to conclude that the type of heterojunction corresponds to Type II as in Figure 1 being Cu_2O with the superior band edge positions.

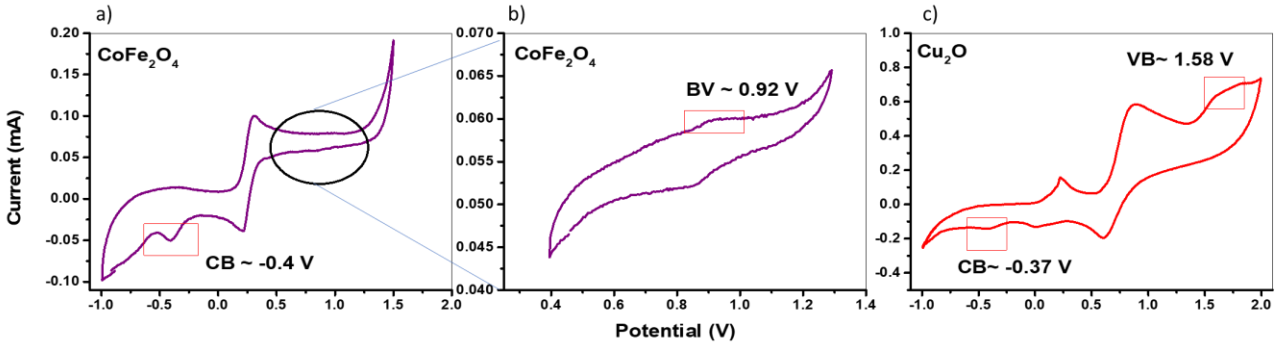

Figure 9. Cyclic voltammetry obtained from each individual semiconductor, in Figure b is shown a "zoom" of $CoFe_2O_4$ nanoparticles measuring at this potential window.

Table 1. Summary of electrochemical estimated properties of each individual material.

Material	CB CV	VB CV	CB MS	CBG	MBG	MSL
$CoFe_2O_4$	-0.19	1.13	-0.29	1.32	1.32	-0.25[24]
Cu_2O	-0.16	1.79	-0.17	1.96	1.95	-0.14[25]

Acronyms: CV-cyclic voltammetry, CBG-Calculated band gap, MBG-Measured band gap, MSL-Mott-Schottky value obtained from literature.

Photocatalytic evaluation

Figure 10, shows hydrogen production in µmol of H_2 per gram of photocatalyst for the 3 materials: $CoFe_2O_4$, Cu_2O and heterojunction (Figures a, b and c respectively).

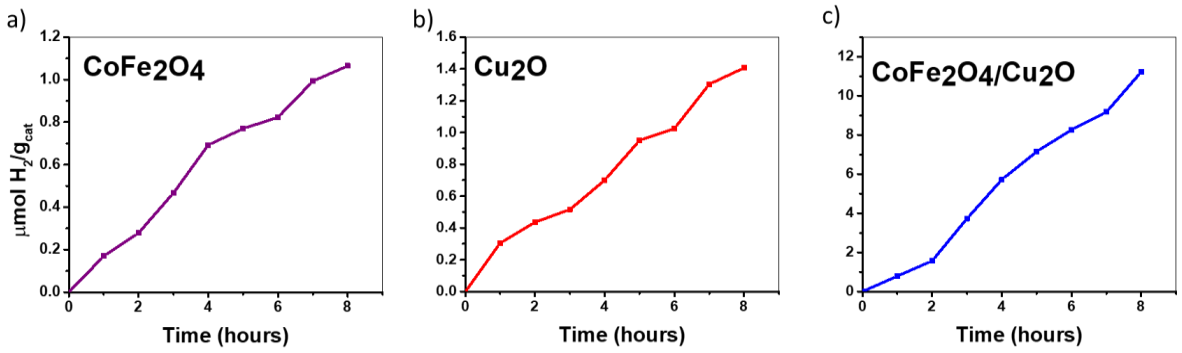

Figure 10. Photocatalytic Hydrogen production of each individual material (a and b) and for the heterojunction (c) in µmol of H_2 per gram of photocatalyst.

It can be appreciated that both ferrite and cuprous oxide have similar production at 8 hours of evaluation with 1.1 and 1.4 µmol respectively, while heterojunction exhibits a value about 10 times greater (~12 µmol) confirming the synergic interaction between both materials despite the pronounced differences of particles and areas.

4. Conclusions

$CoFe_2O_4$ and Cu_2O phases were synthesized with no evidence of other phases as could be seen in DRX results. Moreover, cyclic voltammetry and Mott-Schottky methods resulted to be complementary in order to compare and confirm results of the gap positions and to place a potential to discard the other peaks in cyclic voltammetry with CB estimation with Mott-Schottky plots. Finally, due to photocatalytic activity results observed and the band gap positions of both materials, it can be concluded that the type II heterojunction between $CoFe_2O_4$ and Cu_2O was successfully generated despite the size and area particle differences and this can be observed in the synergic effect between materials which causes an enhancement in a photocatalytic activity producing around ten times greater hydrogen with the heterojunction than those of individual phases.

Acknowledgements

Authors of this work acknowledge to MSc Karla Campos, Eng. Luis De la Torre, Dr. Daniel Lardizabal, Dr. Pedro Piza, Dr. Martha Ochoa and Dr. Francisco Espinoza for the equipment facilities and the characterization of materials as well as to SMH and XVII International Congress of the Mexican Hydrogen Society for the opportunity to participate.

References

[1] Ni, M., Leung, M. K., Leung, D. Y., & Sumathy, K. (2007). A review and recent developments in photocatalytic water-splitting using TiO2 for hydrogen production. Renewable and Sustainable Energy Reviews, 11(3), 401-425.

[2] Li, Q., Guo, B., Yu, J., Ran, J., Zhang, B., Yan, H., & Gong, J. R. (2011). Highly efficient visiblelight-driven photocatalytic hydrogen production of CdS-cluster-decorated graphene nanosheets. Journal of the American Chemical Society, 133(28), 10878-10884.

[3] Tang, J., Durrant, J. R., & Klug, D. R. (2008). Mechanism of photocatalytic water splitting in TiO2. Reaction of water with photoholes, importance of charge carrier dynamics, and evidence for four-hole chemistry. Journal of the American Chemical Society, 130(42), 13885-13891

[4] He, W., Kim, H. K., Wamer, W. G., Melka, D., Callahan, J. H., & Yin, J. J. (2013). Photogenerated charge carriers and reactive oxygen species in ZnO/Au hybrid nanostructures with enhanced photocatalytic and antibacterial activity. Journal of the American Chemical Society, 136(2), 750-757.

[5] Hong, Y., Jiang, Y., Li, C., Fan, W., Yan, X., Yan, M., & Shi, W. (2016). In-situ synthesis of direct solid-state Z-scheme V2O5/g-C3N4 heterojunctions with enhanced visible light

efficiency in photocatalytic degradation of pollutants. Applied Catalysis B: Environmental, 180, 663-673.
[6] QingáLu, G. (2009). Enhanced photocatalytic hydrogen evolution by prolonging the lifetime of carriers in ZnO/CdS heterostructures. Chemical communications, (23), 3452-3454.
[7] Kittel, C. (2005). Introduction to solid state physics (8va ed., pp. 507-508). New York: Editorial John Wiley & sons.
[8] Saha, S., Gyanprakash, M., Khan, R., Sivakumar, S., & Pala, R. G. (2017). Engineering Semiconductor Interfaces Via Non-Native Nanostructures to Facilitate Electron-Hole Separation. ECS Transactions, 77(6), 85-94.
[9] Rekhila, G., Bessekhouad, Y., & Trari, M. (2013). Visible light hydrogen production on the novel ferrite NiFe2O4. International journal of hydrogen energy, 38(15), 6335-6343.
[10] Lv, H., Ma, L., Zeng, P., Ke, D., & Peng, T. (2010). Synthesis of floriated ZnFe2O4 with porous nanorod structures and its photocatalytic hydrogen production under visible light. Journal of Materials Chemistry, 20(18), 3665-3672.
[11] Boudjemaa, A., Popescu, I., Juzsakova, T., Kebir, M., Helaili, N., Bachari, K., & Marcu, I. C. (2016). M-substituted (M= Co, Ni and Cu) zinc ferrite photo-catalysts for hydrogen production by water photo-reduction. International Journal of Hydrogen Energy, 41(26), 11108-11118.
[12] Jiménez-Miramontes, J. A., Domínguez-Arvizu, J. L., Salinas-Gutiérrez, J. M., Meléndez-Zaragoza, M. J., López-Ortiz, A., & Collins-Martínez, V. (2017). Synthesis, characterization and photocatalytic evaluation of strontium ferrites towards H2 production by water splitting under visible light irradiation. International Journal of Hydrogen Energy, 42(51), 30257-30266
[13] López, Y. O., Vázquez, H. M., Gutiérrez, J. S., Velderrain, V. G., Ortiz, A. L., & Martínez, V. C. (2015). Synthesis method effect of CoFe2O4 on its photocatalytic properties for H2 production from water and visible light. Journal of Nanomaterials, 16(1), 76.
[14] Casbeer, E., Sharma, V. K., & Li, X. Z. (2012). Synthesis and photocatalytic activity of ferrites under visible light: a review. Separation and Purification Technology, 87, 1-14.
[15] Sivula, K., Le Formal, F., & Grätzel, M. (2011). Solar water splitting: progress using hematite (α-Fe2O3) photoelectrodes. ChemSusChem, 4(4), 432-449.
[16] Jelinska, A., Bienkowski, K., Jadwiszczak, M., Pisarek, M., Strawski, M., Kurzydlowski, D., ... & Augustynski, J. (2018). Enhanced photocatalytic water splitting on very thin WO3 films activated by high-temperature annealing. ACS Catalysis, 8(11), 10573-10580.
[17] Kondo, J. (1998). Cu 2 O as a photocatalyst for overall water splitting under visible light irradiation. Chemical Communications, (3), 357-358.
[18] Zhang, Y., He, J., Yang, Q., Zhu, H., Wang, Q., Xue, Q., & Yu, L. (2019). Solution quenched in-situ growth of hierarchical flower-like NiFe2O4/Fe2O3 heterojunction for wide-range light absorption. Journal of Power Sources, 440, 227120.
[19] Xu, Y. F., Rao, H. S., Wang, X. D., Chen, H. Y., Kuang, D. B., & Su, C. Y. (2016). In situ formation of zinc ferrite modified Al-doped ZnO nanowire arrays for solar water splitting. Journal of Materials Chemistry A, 4(14), 5124-5129.
[20] Yang, M., Zhang, Y., Cheng, R., Sun, J., Peng, Y., & Yu, J. (2020). Highly Efficient Solar Hydrogen Evolution by Photoelectro-Chemical Water Splitting over ZnFe2O4-ZnO Heterojunction. energy, 6, 7.

[21] Vallat-Sauvain, E., Kroll, U., Meier, J., Shah, A., & Pohl, J. (2000). Evolution of the microstructure in microcrystalline silicon prepared by very high frequency glow-discharge using hydrogen dilution. Journal of Applied Physics, 87(6), 3137-3142.
[22] De Jongh, P. E., Vanmaekelbergh, D., & Kelly, J. J. (1999). Cu2O: electrodeposition and characterization. Chemistry of materials, 11(12), 3512-3517.
[23] Inamdar, S. N., Ingole, P. P., & Haram, S. K. (2008). Determination of Band Structure Parameters and the Quasi-Particle Gap of CdSe Quantum Dots by Cyclic Voltammetry. ChemPhysChem, 9(17), 2574-2579.
[24] Archer, M. D., Morris, G. C., & Yim, G. K. (1981). Electrochemical approaches to solar energy conversion: A brief overview and preliminary results obtained with n-type cobalt ferrite. Journal of Electroanalytical Chemistry and Interfacial Electrochemistry, 118, 89-100.
[25] Hsu, Y. K., Yu, C. H., Chen, Y. C., & Lin, Y. G. (2013). Synthesis of novel Cu2O micro/nanostructural photocathode for solar water splitting. Electrochimica Acta, 105, 62-68.

Fuel Cells components and stacks

ID 001

Improved preparation of membrane-electrode assembly for PEM electrolysis through automatic catalytic ink application system

A. Martínez-Septimo[1,2], M. A. Valenzuela-Zapata[2], R. G. González-Huerta[3]*

[1]Instituto Politécnico Nacional-ESIQIE, Lab. Catálisis y Materiales, Zacatenco, C.P. 07738, CDMX, México
[2]Instituto Politecnico Nacional ESIQIE, Laboratorio de Electroquímica, UPALM, C.P. 07738, CDMX, México
* rosgonzalez_h@yahoo.com.mx

ABSTRACT

Currently, hydrogen has been proposed as a viable energy vector. One of the most efficient and cleanest method for the hydrogen production is proton exchange membrane water electrolysis (PEMWE) [1]. Therefore, the efficiency and stability in PEMWE has to be improved based on the design of gas diffusion layer, bipolar plates and membrane-electrodes assembly (MEA). For this propose, a MEA was made through an innovate method based in an automatic catalytic ink application system additionally, a new PEMWE was designed and made in-home. The new PEMWE designed, was integrated with the improved MEA, which was feed with deionized water (≥18 MΩcm) @25°C and tested using a DC power source. The experiments were recorded in the current range from 0.1 to 0.6 A cm^{-2} at 300 s. At the same current density (0.2 A cm^{-2}) the potential of the new PEMWE design with the improved MEA was lower (3 V) than the potential measured in a older made in-home design (5 V) with a MEA made through a manual spraying catalytic ink application. These better results are attributed to an improvement in water distribution into gas diffuser (porous titanium) and a better dispersion and adhesion of the catalytic layer on the membrane.

Keywords: PEM water electrolysis; Supported catalyst; TiO_2; Ir-Ru based anode; iridium oxide; ruthenium oxide.

1. Introduction

Since the industrial revolution, humanity has been using fossil fuels such oil and its derivatives, as well as natural gas and coal, these energy sources produce a high rate of pollution (CO_2, NO_X, SO_X, etc), which significantly contributes to climate change and are not renewable. Hence, there is an immediate need to accelerate in large-scale implementation of clean and renewable energy systems. However, these kind of energy systems are intermittent in nature and do not provide constant power [1]. Therefore, the need arises to develop energy vectors capable of being produced with excess energy to store and supply energy when there are energy deficits [2]. Several studies have shown that a viable energy vector is hydrogen, since it has several advantages over fossil fuels: higher energy density (33 kWh kg^{-1}) and its combustion by-products are water vapor and a small amount of nitrogen oxides, which do not significantly impact the environment as a result of their low concentrations [3]–[5]. Electrochemical water electrolysis for hydrogen generation are viable for industrial and domestic applications using renewable energy sources as principal power supply [6]–[8], an example of a coupled clean energy system with hydrogen as energy vector is the HyBalance project in Denmark where renewable electricity will be produced from wind turbines to help balance the power grid, hydrogen will be produced from excess energy through electrolysis of water, which will be stored for use in clean transport and industrial applications, allowing cheap storage of renewable electricity.[9].

Nowdays, there are three types of water electrolysis systems: alkaline, proton exchange membrane (PEM) and solid oxide. Each one have specific advantages and weaknesses, solid oxide electrolyzers (SOE) has been proposed like the most energy-efficient electrolyzers since the theoretical potential to dissociate the water molecule in SOE is lower than PEM and alkaline, nevertheless, its high temperature operation (>600°C), and a power still on a laboratory-scale , make SOE technology unfeasible for large-scale application [10], [11]. Alkaline water electrolysis the widely used technology in industry due to its maturity and the existence of large-scale systems [12] however, this electrolysis technology use a liquid electrolyte, which reduces ionic conductivity, increasing the total system resistance compared to PEMWE in addition, PEMWE can produce the same hydrogen flow in a more compact stack than alkaline and SOE, since it can work with a higher current density (4 A cm^{-2}@65°C), its proton exchange membrane (i.e. solid electrolyte) has a response time of <1 s and, PEMWE can produces high purity hydrogen (~99.99% w) reducing the costs of post-production purification systems [13], [14]. This makes PEMWE technology the best alternative to operate in a dynamic energy regime such as that of renewable energies [15].

The proton exchange membrane used in industrial-scale PEMWE is made of sulphonated polymers teflon-based with terminal sulphonyl groups, thus, PEM water electrolysis takes place in acidic media and the materials used on the anodic and cathodic electrodes must be stable at low pH (<1) and high corrosion potentials, E<-0.1 V/RHE in the cathode and E>1.5 V/RHE in the anode, where the oxygen evolution reaction (OER) and hydrogen evolution reaction (REH) take place, respectively. Commercial catalysts for the OER are made of mixtures of IrO_2-RuO_2-based since several studies have shown that these oxides are the most active and stable OER catalysts in acidic media, in the other hand, Pt supported (ca. 20 wt.%) on high-surface area carbon (e.g. carbon Vulcan®) is used for the

(REH) [16]–[18]. Consequently, operation parameters like efficiency and stability PEMWE has to be improved using cheaper materials and/or innovating manufacturing methodology and new designs of gas diffusion layer, bipolar plates and membrane-electrodes assembly (MEA). such as the methodology developed in this paper [19][20] In this work, we developed a methodology for automatic impregnation of catalytic ink on the membrane and a new test electrolyzer design made in-home which improves the energy efficiency of the electrolyzer.

2. Materials and Methods

Proton exchange membrane water electrolyzes (PEMWEs) are constituted by several components; the central structure is the membrane electrode assembly (MEA), where the molecular oxygen and molecular hydrogen are electrochemically formed from water and an electrical power. In this work, porous titanium and a titanium plates were used like gas diffusion layers and current collector (Figure 1) respectively, in order to improve the electrical conductivity, mass transport and mitigate the passivation/corrosion, compared to the gas diffusion layers and current collectors of the old test electrolyzer which were made of a stainless-steel mesh and plate, respectively. The components used for the new PEMWE design and construction are the next:

- Acrylic cases: 'A1' and 'A2'
- Titanium current collector plates: 'C1' and 'C2'
- Seals of EPDM rubber: 'D1' and 'D2'
- Porous titanium mesh gas diffusers: 'E1' and 'E2'
- A Nafion® membrane like solid proton transport electrolyte

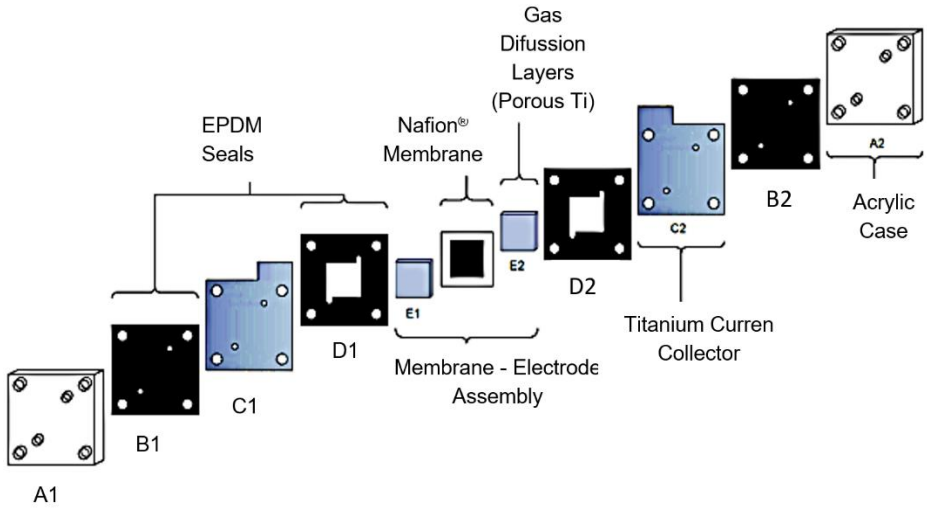

Fig. 1. Internal components of the new test electrolyzer design.

1. *MEA preparation:*

Before the MEAs assemble, the membrane is protonate in a H_2SO_4 1M solution for 1 h, washed several times with deionized H_2O (18 MΩ cm) and then is embedded in a vacuum table as shows the Figure 2. The anodic catalytic ink is prepared as follows: for an active area of 4 cm^2 and a loading of 3 $mg_{(IrO2+RuO2)}$ cm^2, 12 mg of a mechanical mixture of 75%RuO_2-25%IrO_2, 960 µL of anhydrous ethyl alcohol, 24 µL of deionized water and 72 µL of Nafion perfluorinated solution (Sigma-Aldrich, 5 wt.% in lower aliphatic alcohols and water) are placed into an ultrasonic ice bath for 30 minutes for the purpose of form a homogeneous RuO_2-IrO_2 dispersion. When the membrane is dry, the anode is painted on it using a spraying system.

The proton exchange membrane used which acted as a solid electrolyte was made of Nafion® 115 having 127 µm thickness, for the cathodic part of the MEA, a commercial carbon fabric electrode with a Pt coating supported in Vulcan Carbon at 40% w Pt was used to catalyze the hydrogen evolution reaction. In the other hand, the anodic coating of the MEA was applied using a ValveMate 8040 automatic liquid spray system consisting of three main parts; the spray nozzle, the pressure regulation system, and the software-driven axes, Figure 2.Once the anode has been painted, the MEA is integrated by a sintering process. The vacuum pressure of the table, height of the valve nozzle tip to the membrane surface, the valve opening time, the delay time between an impregnation were optimized. The atomizing pressure of the fluid was kept constant at 1kgf cm^{-2}. Different MEAs were prepared with the mechanical 75%RuO_2-25%IrO_2 mixture for the anode and tested in the old and new test electrolyzer design by a power supply to determine the performance curves.

Fig. 2. Left, automatic catalytic ink application system with vacuum table.

2. *Assemble and characterization of the Eest Electrolyzer:*

The pieces showed in the Figure 1 were assembled as follows: the acrylic case 'A1' was place over the EPDM seal 'B1', the distributor plate 'C1', the EPDM seal 'D1' and the diffuser 'E1', the membrane is placed with the anode ink on the diffuser 'E1'. Subsequently, the EPDM seal 'D2' and the diffuser 'E2' are placed on the commercial catalyst and finally the distributor plate 'C2', the EPDM seal 'B1' and the 'A2' case. The test electrolyzer is compressed by screw studs, insulated by Teflon, plastic plugs, washer bolts and nuts. It is connected to water supply tanks and to an electrical power source by alligator clips.

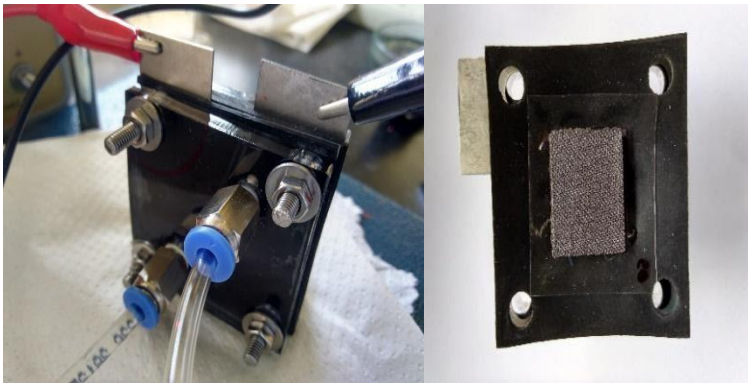

Fig. 3. Left, Assembled Electrolyzer, right, Nafion membrane, EPDM Seals, Porous Titanium Mesh and Titanium Current Colector before the ink application and electrolyzer assembly

For the performance curves, the electrolyzer was connected to a power source, the current increased from 0 to 0.1 Amperes (A) with variations of 0.02 A, once the value of 0.1 A reached, the current intensity varied in 0.1 A until 2 A is reached, obtaining the different voltage values, each current increase was hold constant for 1 minute in order to reach an stable voltage in the electrolysis system. The performance curves were recorded for the old and new electrolyzer design.

According to the Figure 6, the performance in the new test electrolyzer is higher than the old design test electrolyzer, since for all the MEAs, the cell voltage is lower. Current values higher than 0.3 A were no recorded at the old design electrolyzer due to its voltage was too high for a PEMWE at room temperature (>4V) so, those results are not representative. The MEA which obtained the best performance was the 75% IrO_2-25% RuO_2 since at 1.5 A it demanded a lower cell voltage (2.7 V. For the old test prototype, this presented a low performance, since at a current of 0.2 A, it demanded a cell voltage higher than 3V with all the IrO_2-RuO_2 MEA's.

This is attributed to the fact that the stainless steel mesh current collector of the old desing generates considerable resistance due to the passivation/corrotion, which decreases significatively the performance of the electrolyzer, additionally, this current collector does not have a good contact with the MEA; due the inclusion of a water pool in the case design which increased the hydrostatic pressure and a ionic resistance due to the high amount of deionized water over the active electrode surface, this prevents the correct desorption of the gases generated in both electrodes and a good electronic conduction, respectively

3. Results and Discussion

After catalytic ink impregnation, the membranes were superimposed on the light, several voids were visible where deposition had not adhered and had detached after drying, Figure 5. To prevent the ink from coming off, several tests were carried out in which the following parameters were optimized: the height of the valve to the membrane was set at 5.7 cm, and an opening time for each atomization was adjusted to 13 ms since it was found that this is the minimum time necessary for the fluid to be able to pass from the storage container to the valve, pass through it and be atomized. The delay time (time that the valve continues to operate by expelling air in the absence of fluid) was fixed at 3 s since this was the time needed to expel enough air to completely dry the newly atomized ink. Once this was done, uniformly coated membranes were obtained in which no voids were observed when exposed to light, Figure 4.

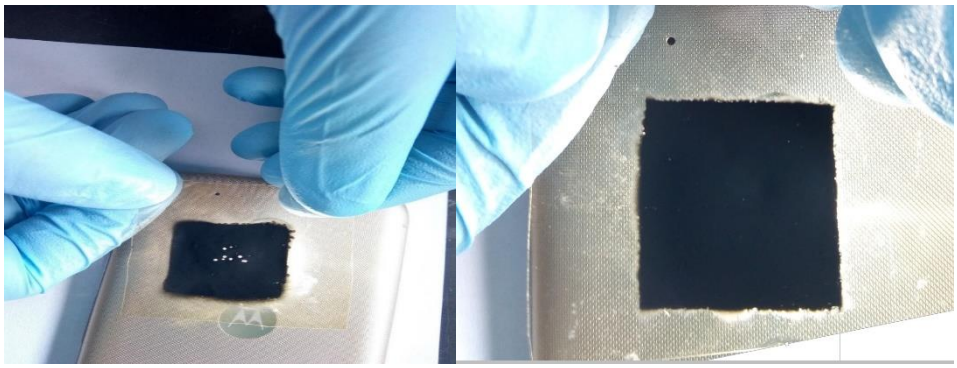

Fig. 4. Left, swollen membrane with areas without catalytic ink, right, flat membrane with uniform catalytic ink coating.

According to the Figure 5, the performance in the new test electrolyzer is higher than the old design test electrolyzer, since for all the MEAs, the cell voltage is lower. Current values higher than 0.3 A were no recorded at the old design electrolyzer due to its voltage was too high for a PEMWE at room temperature (>4V) so, those results are not representative. The MEA which obtained the best performance was the 75% IrO_2-25% RuO_2 since at 1.5 A it demanded a lower cell voltage (2.7 V. For the old test prototype, this presented a low performance, since at a current of 0.2 A, it demanded a cell voltage higher than 3V with all the IrO_2-RuO_2 MEA's. This is attributed to the fact that the stainless steel mesh current collector of the old desing generates considerable resistance due to the passivation/corrotion, which decreases significatively the performance of the electrolyzer, additionally, this current collector does not have a good contact with the MEA; due the inclusion of a water pool in the case design which increased the hydrostatic pressure and a ionic resistance due to the high amount of deionized water over the active electrode surface, this prevents the correct desorption of the gases generated in both electrodes and a good electronic conduction, respectively.

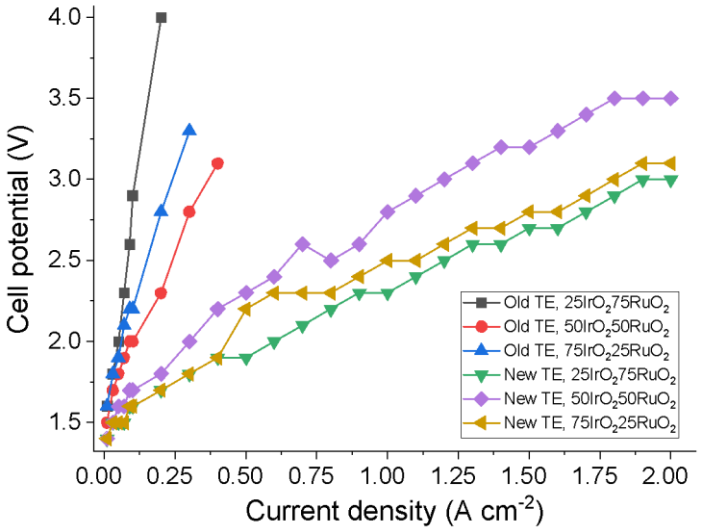

Fig. 5. Performance curves of the old and new test electrolyzer design.

4. Conclusion

A new made in-home design and catalytic ink application system for a PEMWE cell prototype was developed which significantly improved the performance of the system compared with the older one by requiring a lower power to generate the same hydrogen amount at room temperature. The performance curves of the new test electrolyzer show a better performance for all the MEAs, at an applied current, the demanded voltage was lower due to the better contact and catalyst dispersion over the MEA. More theoretical studies and improvements in the test PEMWE designs have to be done in order to understand the contribution of each process variable and design factors. The next step, is to assembly and test a PEMWE system able to work continuously at 65°C and 4 A.

Acknowledgements
The authors would like to thank IPN multidisciplinary project 2024 and CONACYT CEMIE Oceano-249795, transversal line I-LT1 and project CB A1-S-15770.

References

The reference format should be as the examples provided, if a specific reference is not include in the examples, please visit the Guide for authors in International Journal of Hydrogen Energy, Elsevier.

[1] G. Notton et al., “Intermittent and stochastic character of renewable energy sources: Consequences, cost of intermittence and benefit of forecasting,” Renew. Sustain. Energy Rev., vol. 87, no. February, pp. 96–105, 2018.

[2] N. Kittner, F. Lill, and D. M. Kammen, “Energy storage deployment and innovation for the clean energy transition,” Nat. Energy, vol. 2, no. 9, pp. 1–6, 2017.

[3] S. Shiva Kumar and V. Himabindu, “Hydrogen production by PEM water electrolysis – A review,” Mater. Sci. Energy Technol., vol. 2, no. 3, pp. 442–454, 2019.

[4] J. O. Abe, A. P. I. Popoola, E. Ajenifuja, and O. M. Popoola, “Hydrogen energy, economy and storage: Review and recommendation,” Int. J. Hydrogen Energy, vol. 44, no. 29, pp. 15072–15086, 2019.
[5] J. D. Fonseca, M. Camargo, J. M. Commenge, L. Falk, and I. D. Gil, “Trends in design of distributed energy systems using hydrogen as energy vector: A systematic literature review,” Int. J. Hydrogen Energy, vol. 4, pp. 9486–9504, 2019.
[6] A. Mohammadi and M. Mehrpooya, “A comprehensive review on coupling different types of electrolyzer to renewable energy sources,” Energy, vol. 158, pp. 632–655, 2018.
[7] A. Buttler and H. Spliethoff, “Current status of water electrolysis for energy storage, grid balancing and sector coupling via power-to-gas and power-to-liquids: A review,” Renew. Sustain. Energy Rev., vol. 82, no. February 2017, pp. 2440–2454, 2018.
[8] J. Chi and H. Yu, “Water electrolysis based on renewable energy for hydrogen production,” Cuihua Xuebao/Chinese J. Catal., vol. 39, no. 3, pp. 390–394, 2018.
[9] H.-V. AirLiquide, Hydrogenics, Ludwig-Bolkow-Systemtechnik, Centrica, “HyBalance,” 2020. [Online]. Available: http://hybalance.eu/. [Accessed: 31-May-2020].
[10] Y. Zheng et al., “A review of high temperature co-electrolysis of H2O and CO2 to produce sustainable fuels using solid oxide electrolysis cells (SOECs): Advanced materials and technology,” Chem. Soc. Rev., vol. 46, no. 5, pp. 1427–1463, 2017.
[11] J. Kim et al., “Hybrid-solid oxide electrolysis cell: A new strategy for efficient hydrogen production,” Nano Energy, vol. 44, no. July 2017, pp. 121–126, 2018.
[12] M. David, C. Ocampo-Martínez, and R. Sánchez-Peña, “Advances in alkaline water electrolyzers: A review,” J. Energy Storage, vol. 23, no. August 2018, pp. 392–403, 2019.
[13] F. M. Sapountzi, J. M. Gracia, C. J. (Kee. J. Weststrate, H. O. A. Fredriksson, and J. W. (Hans. Niemantsverdriet, “Electrocatalysts for the generation of hydrogen, oxygen and synthesis gas,” Prog. Energy Combust. Sci., vol. 58, pp. 1–35, 2017.
[14] M. Carmo et al., “PEM water electrolysis: Innovative approaches towards catalyst separation, recovery and recycling,” Int. J. Hydrogen Energy, vol. 44, no. 7, pp. 3450–3455, 2019.
[15] S. Giddey, S. P. S. Badwal, and H. K. Ju, Polymer electrolyte membrane technologies integrated with renewable energy for hydrogen production. Elsevier Inc., 2018.
[16] R. G. González-Huerta, G. Ramos-Sánchez, and P. B. Balbuena, “Oxygen evolution in Co-doped RuO2 and IrO2: Experimental and theoretical insights to diminish electrolysis overpotential,” J. Power Sources, vol. 268, pp. 69–76, 2014.
[17] S. Siracusano, N. Van Dijk, R. Backhouse, L. Merlo, V. Baglio, and A. S. Aricò, “Degradation issues of PEM electrolysis MEAs,” Renew. Energy, vol. 123, pp. 52–57, 2018.
[18] E. Mayousse, F. Maillard, F. Fouda-Onana, O. Sicardy, and N. Guillet, “Synthesis and characterization of electrocatalysts for the oxygen evolution in PEM water electrolysis,” Int. J. Hydrogen Energy, vol. 36, no. 17, pp. 10474–10481, 2011.
[19] P. Lettenmeier et al., “Durable Membrane Electrode Assemblies for Proton Exchange Membrane Electrolyzer Systems Operating at High Current Densities,” Electrochim. Acta, vol. 210, pp. 502–511, 2016.
[20] A. S. Gago, P. Lettenmeier, S. Stiber, A. S. Ansar, L. Wang, and K. A. Friedrich, “Cost-effective PEM electrolysis: The quest to achieve superior efficiencies with reduced investment,” ECS Trans., vol. 85, no. 13, pp. 3–13, 2018.

ID 011

Analysis of ordered and disordered conductive phases in a PEMFC synthetic catalyst layer

C.Pacheco[1], B. Escobar[1, *], A. Rodriguez[2], R. Barbosa[2, *]

[1] Centro de Investigación Científica de Yucatán, A.C. Carretera Sierra Papacal Chuburna Puerto Km 5, C.P. 97302, Sierra Papacal, Yucatán, México.
[2]Universidad de Quintana Roo, Boulevard Bahía s/n, C.P 77019, Chetumal, Q. Roo, México.
* Tel: +52 9999300205; e-mail: beatriz.escobar@cicy.mx
* Tel: +52 9831566032; e-mail: romelix1@gmail.com

ABSTRACT

The current research analyzes the behavior of effective transport coefficient (ETC) through the disorder process of real and simulated micrographs of a polymeric electrolyte fuel cell (PEFC) electrode. The suggested methodology examines an ordered bar system that evolves into a heterogeneous stochastic system, which uses simulated images generated by computational algorithms and experimental images from the scanning electron microscope (SEM). The behavior of the electrode microstructure was studied through images with different surface fractions of the conductive phase. Microstructural variation is imposed by statistical moments of reconstruction by simulated annealing (SA). The ETC was determined numerically by the finite volume method (FVM) and generalized by a conduction efficiency (ek). The case studies showed that the microstructure ordered in bars has a load transport equal to the surface fraction of the study phase, and through the disorder process, the value of ek (%) decreases until it reaches a stable value of ek (%). For example, for the 70% surface fraction, the initial ek is 70.55 ± 0.05%, after 100 iterations of the disorder process the new ek is 21.28 ± 0.26%, and after 1000 iterations, the value of ek gets steady at 20.56% with a standard deviation of 0.20%. The trend of the ek results was similar in systems with different surface fractions. Then, our research proposes an innovative methodology, as a design tool, to improve the load transport in fuel cell electrodes.

Keywords: Effective transport coefficient; PEFC; Aligned composites; Catalyst layer

1. Introducción

Los compositos permiten la asociación de materiales con características diferentes, pero complementarios, que combinados sinérgicamente generan un ensamblaje con propiedades originales. Estos materiales encuentran nicho en aplicaciones donde los materiales tradicionales no pueden satisfacer los criterios de diseño. Algunos ejemplos de sus aplicaciones son: para ahorrar peso mientras se mantienen las propiedades mecánicas de alto rendimiento [1], alta resistencia a la corrosión [2], mejor transporte eléctrico [3]. Diferentes sectores como el aeroespacial, industria energética, se sienten atraídos por los materiales compuestos [4].

Cuando los materiales compuestos alinean sus fases pueden mejorar algunas de las propiedades físicas [5]. Por ejemplo, en electrodos electroquímicos existen muchas expectativas de tener materiales compuestos unidireccionales que proporcionen una reducción a la resistencia interna y faciliten la difusión de los iones. Un electrodo alineado permite que este exhiba mejores rendimientos electroquímicos [5,6]. En la actualidad han sido estudiadas varias estrategias para fabricar compositos electrolíticos que proporcionen alta conductividad iónica. Los análisis de tortuosidad sugieren que las partículas cerámicas verticalmente interconectadas son la configuración óptima para crear vías de alta conductividad iónica en baterías de ion litio [7]. Liu W. et al. demostró que alinear verticalmente fibras incrementa la conductividad iónica de 1.78×10^{-7} S cm^{-1} a 6.05×10^{-5} S cm^{-1} a 30 °C [8]. Wang et al. Presentan un estudio sobre baterías recargables con compositos cerámicos/polímeros alineados verticalmente donde la fase cerámica alienada en el electrolito compuesto permite la conducción rápida de iones de litio, alcanzando una conducción de 1.67×10^{-4} S cm^{-1} a temperatura ambiente, 6.9 veces mayor que cuando el compuesto cerámico se encuentra disperso en el electrolito [7,9].

En las PEFC, el transporte de masa en la capa catalítica sigue siendo una de las principales características que determina el rendimiento de la celda, porque el transporte efectivo de electrones, iones y gases reactantes son prerrequisitos para que ocurran las reacciones electroquímicas completas [10–12]. Los fenómenos de transporte son asociados con la morfología heterogénea de los compositos que forman la capa catalítica, ionomero y poros. Para mejorar la estructura de la capa catalítica a nano escalas se propone el uso Platino (Pt) soportado en nanotubos de carbón alineados verticalmente (Pt/ VACNT), adoptando el uso de VACNT como soporte de carbón la capa catalítica puede formar caminos efectivos para el transporte del electrones y poros de estructura continua para transporte de masa [13,14]. Yasuda et al. Desarrollo una capa catalítica de nanotubos de carbón dopado con nitrógeno de hierro utilizando VACNT, demostró que la capa catalítica soportada en VACNT exhibió mayor reacción a la reducción de oxígeno en comparación a la capa catalítica convencional soportada en carbón, lo que resulto en una mejor eficiencia en el transporte de masa [15]. Tian et al. Reportó que los VACNT pueden proporcionar mejoras significativas en la fabricación de los ensambles membrana electrodo (MEA) de baja carga de Pt cuando se usan como soporte de carbono porque hay vías adecuadas para el transporte de electrones, protones y reactivos en la capa catalítica de VACNT lo que permite un mejor uso del catalizador [16]. Las capas catalíticas establecidas sobre VACNT

exhiben rendimientos similares a las capas catalíticas convencionales incluso cuando se utilizan cargas muy bajas de Pt son depositadas en la superficie de las VACNT. Murata et al. Demostró que los VACNT utilizados como soporte de carbón permitieron la operación de una PEFC a altas densidades de corriente con una baja carga de Pt, principalmente debido a la continuidad mejorada de los poros y al contacto eléctrico [17]. Los compositos pueden ser estudiados como un material heterogéneo aleatorio (RHA). Los coeficientes de proporcionalidad, o coeficiente efectivo de transporte (ETC), para el transporte de masa, carga y energía son afectados por las propiedades de las fases que los conforman, la fracción superficial de las fases y por la microestructura, como lo describe la ecuación 1 [18]:

$$Ke = fK1, K2, \ldots, KM; 1, 2, \ldots, M; , \quad (1)$$

donde el subíndice de las variables indica la fase en cuestión, K es la constante de proporcionalidad de la fase, la fracción volumétrica de la fase y la información microestructural del medio [19].

Existen diferentes relaciones matemáticas para determinar los ETC´s. Garnett [20] desarrolló una relación para determinar propiedades ópticas de dispersiones de esferas uniformes diluidas. Una de las metodologías más usadas es la de Bruggeman [21], la cual se puede aplicar a sistemas con dispersiones aleatorias de partículas esféricas con diferentes rangos de tamaño. Sin embargo, la reconstrucción estocástica permite definir la microestructura en una malla de nodos para estudiar los ETC con mayor detalle [18].

2. Materiales y metodología

Se aplicó el método de reconstrucción estocástica para generar microestructuras sintéticas, se partió de un sustrato generado mediante algoritmos computacionales y esta misma imagen se desordeno (cambio de píxel aleatorio) bajo cierto número de iteraciones hasta alcanzar una imagen completamente isotrópica y heterogénea. Las estructuras son caracterizadas estadísticamente mediante funciones de correlación de dos puntos y camino lineal. La reconstrucción se hace a partir de un sustrato ordenado el cual se va desordenando mediante SA, en determinados puntos del desorden se realiza el cálculo del ETC. Para determinar las conductividades efectivas eléctricas de diferentes estructuras, se resuelve la ecuación de continuidad de transporte de carga en una malla bidimensional de volúmenes de control finitos [22,23]. La reconstrucción estocástica, la caracterización estadística y la determinación de la conductividad eléctrica y protónica de varías muestras de una CL sintética de dimensiones de 300 x 300 pixeles con un total de 90,000 elementos se realizaron en tiempos significativamente menores.

La metodología inicia con la generación de dos sistemas digitales, cada sistema cuenta con fases identificables de color blanco y de color negro. Los sistemas son definidos por

condiciones iniciales: el tamaño (*n x n*) y la fracción superficial (Φ) de las fases. El sistema origen es condicionado a presentar barras alineadas verticalmente (de sur a norte). Las microestructuras generadas son caracterizadas mediante la función de correlación de dos puntos (FS2). SA es utilizado para obtener un ensamble () que caracteriza un momento estadístico de la agitación SA. Cada momento de SA se presenta como un sistema de estudio, en donde está compuesto por 5 realizaciones aleatorias (W=5). Los resultados presentan la respuesta de la función de correlación y la eficiencia de conducción (ek), aplicado para ambas fases.

Se aplica FVM a la malla de volúmenes de control reconstruidos, en donde cada nodo identifica la conductividad de la fase. FVM, se puede implementar en diferentes escalas de materiales sintetizados y modelado de fenómenos de transporte en 2D o 3D de un medio heterogéneo [24]. La normalización y generalización de los resultados se realiza mediante el cálculo de las resistividades para estimar una eficiencia de conducción ek [17].

ek= effM , (2)

donde, eff es la conductividad efectiva y M la conductividad nominal.

La función de correlación de dos puntos FS2 (xa,xb) es la probabilidad de que el punto inicial xa y el punto final xb de una recta de longitud r caen dentro de la misma fase j. Considerando estadísticamente un medio isotrópico y homogéneo, FS2 puede ser definida en función de la distancia r:

FS2(r)=⟨TJ(x)TJ(x+r)⟩, (3)

donde ⟨⟩ se refiere al promedio estadístico que resulta al evaluar todo el dominio de cómputo, de cada una de las realizaciones . T es la función índice, del dominio de cómputo, la cual es T=1 cuando el nodo pertenece a la fase conductora (fase de estudio) y T=0 cuando el nodo es la fase no conductora.

3. Resultados y discusión

Estos resultados teóricos fueron orientados a determinar la tasa de eficiencia de conducción eléctrica en una CL sintética con diferentes condiciones estructurales: 1) fracción superficial de la fase conductora en el electrodo (color negro) en un rango del 40 a 80%.

Cada una de las muestras fue estudiada a diferentes puntos del desorden para conocer las eficiencias de conducción en estos puntos. En la tabla 1 se presentan las diferentes fracciones superficiales de las muestras estudiadas.

Tabla 1 Fracciones superficiales de las estructuras simuladas.

Muestra	Fase conductora
B04	**40%**
B05	**50%**
B06	**60%**
B07	**70%**
B08	**80%**
BSKPH	**22%**
B9KX	**19%**
BSINTE	**50%**

Las muestras *B04* a la *B08* son las denominadas sintéticas y partieron de un orden en sus fases (barras verticales), la muestra BSKPH es una micrografía de un electrodo manufacturado con biocarbón, de igual manera se parte de un sustrato ordenado y se lleva a la microestructura objetivo. *BSINTE* es una muestra sintética con una microestructura final formada por polígonos.

La metodología planteada propone el estudio de las siguientes CL´s: 7 muestras sintéticas con diferentes porcentajes de fase conductora y 1 micrografía SEM con fase conductora de 78%. Contemplando que cada muestra es analizada en 25 diferentes puntos del proceso de reconstrucción tenemos un total de 120 estructuras analizadas. El equipo de cómputo utilizado fue una laptop de 16 GB de memoria RAM y 2.60 GHz de velocidad del procesador, el tiempo para la obtención de los resultados es de ~150 horas.

3.1 Microestructuras reconstruidas

A continuación, en la Tabla 2 se presentan las microestructurales de las CL´s reconstruidas. Se estudió la eficiencia de conductividad eléctrica en la fase sólida (blanca). Se puede observar que en todos los casos se parte de un sustrato ordenado, el cual con el paso de las iteraciones se va desordenado hasta llegar a la función objetivo, la columna REA muestra las imágenes reconstruidas y que estadísticamente son similares al objetivo.

Es importante recalcar que las condiciones de reconstrucción para todos los casos fueron las siguientes, se fijó una temperatura inicial de $1x10^{-4}$ 1x10-4 y un error mínimo de $1x10^{-6}$ 1x10-6, con estos parámetros se obtuvieron los mejores resultados al realizar las reconstrucciones.

Tabla 2 Resumen de microestructuras estudiadas.

Muestra	Sustrato inicial (ordenado)	Función objetivo	REA
B04	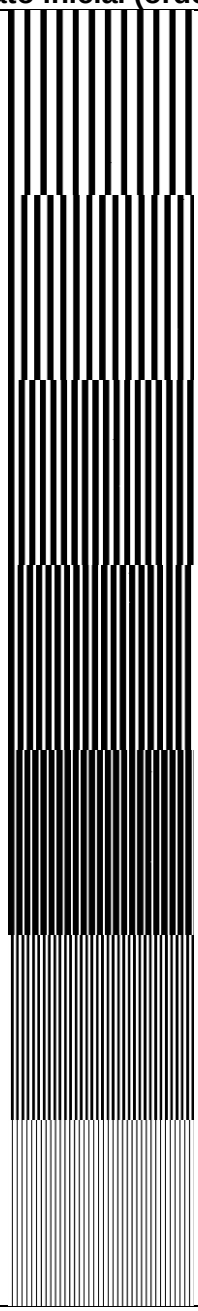	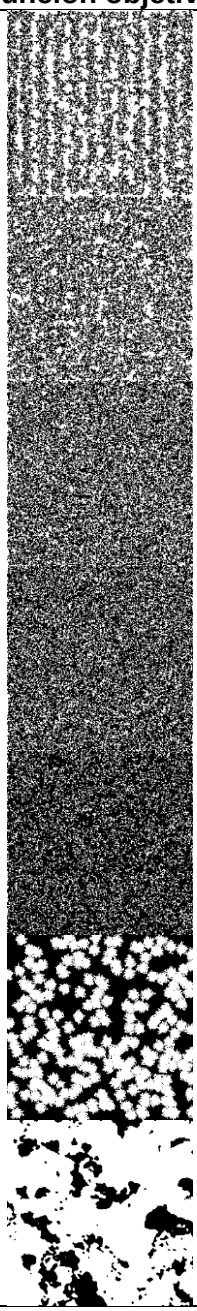	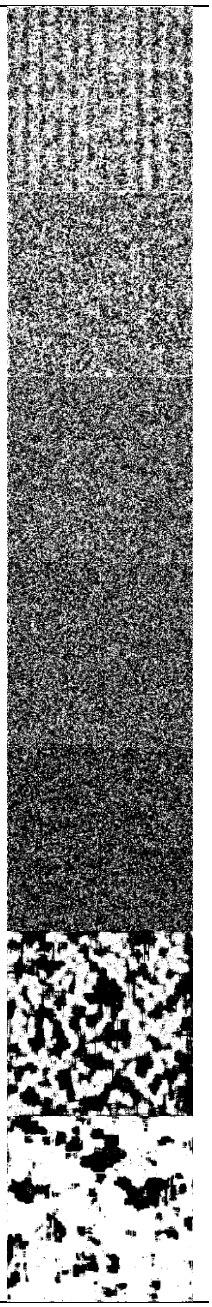
B05			
B06			
B07			
B08			
BSINTE			
BSKPH			

La fig. 2 muestra la función de correlación de dos puntos (FS2) obtenida para algunas estructuras reconstruidas de cada una de las muestras estudiadas. Los resultados son graficados versus la distancia adimensional *r/N,* donde *r* es la distancia entre los dos puntos y *N* dimensión del dominio de cómputo. Como se observa en la figura, cuando se tiene r=

0 FS2 representa el valor de la fracción volumétrica de la fase caracterizada, en este caso la fase sólida (negro). Todas las funciones de dos puntos decaen exponencialmente hasta el cuadrado de la fracción volumétrica, a partir del cual su valor es independiente de *r*.

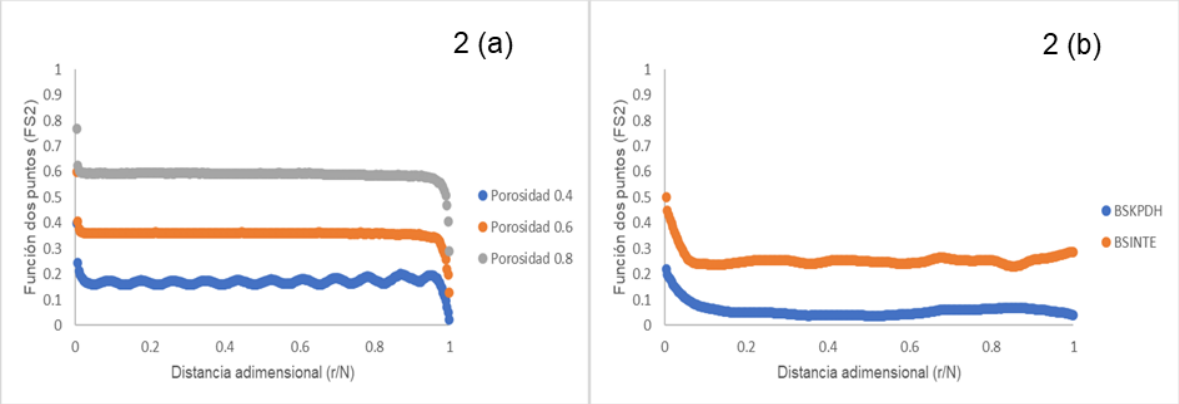

Fig. 2 de Correlación de dos puntos (FS2) versus distancia adimensional (r/N) para algunas estructuras representativas. 2(a) muestra las FS2 para la fase carbón para las muestras B04, B06 y B08, donde cada curva corresponde a diferentes porosidades y 2(b) muestra las FS2 para la fase carbón en las muestras BSKPDH y BSINTE, cada curva corresponde a las porosidades, según el caso.

En la fig.3 se presenta la comparativa de la función de correlación FS2 de la función objetivo versus la reconstruida. Se observa que las curvas son idénticas, teniendo una desviación estándar de 8.21x10^{-5} 8.21x10-5, siendo un valor muy reducido lo cual indica que las reconstrucciones, estadísticamente, son bastante cercanas a las funciones objetivo. Lo que permite realizar los estudios de ETC sin que se pierda información microestructural. En todos los casos de estudio se presenta una desviación estándar pequeña, por lo cual se ejemplifica en la muestra BSINTE.

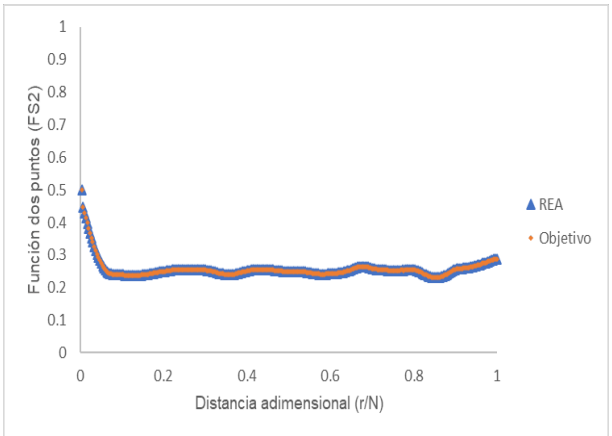

Fig. 3 Comparativa FS2 de la función objetivo versus REA de la muestra BSINTE, donde se aprecia una desviación estandar de 8.21x10^{-5} *8.21x10-5*.

3.2 Estimación del coeficiente efectivo de transporte en la fase sólida

Después de finalizada la reconstrucción, el programa genera una malla microestructural de la CL's, con la cual se procede a realizar el cálculo de la respuesta al transporte de carga. Debido a que las estructuras son homogéneas, el lado del dominio de la estructura que será asignado como entrada de flujo de corriente es indistinto, sin embargo, la salida debe ser del lado opuesto. En el lado seleccionado como entrada, se designa un potencial de 1.1 V especificado exclusivamente en las caras de la fase de estudio, mientras que en las caras de la fase porosa la condición de frontera es un flujo nulo de corriente. Asimismo, la salida se especifica con 1 V solo para las caras de la fase de estudio, por lo que el gradiente de potencial es de 0.1 V. Estos valores han sido propuestos únicamente con el propósito de determinar la eficiencia de conducción y no representan la distribución del voltaje real [23].

Se calcularon los ETC en diferentes puntos del desorden para diferentes muestras con diferentes porcentajes de fracción superficial de la fase conductora, iniciando con el sustrato de barras ordenadas, donde la fracción de carbón (pixeles negros) y poros (fracción blanca) se encuentran ordenados. Se puede apreciar que, al realizar el cálculo de los ETC en el primer punto de desorden, es decir, cuando las barras se encuentran desordenadas, el valor del ETC es igual a la fracción superficial del elemento estudiado (respuesta analítica de conducción de carga en un circuito de conductores ordenados en serie en sentido del fenómeno de transporte), debido a que al momento de calcular los ETC el flujo de corriente tiene un sentido norte-sur, al estar ordenadas las fases no existen perdidas. En la tabla 3 se presentan los valores del ETC de las muestras cuando son ordenadas.

Tabla 3 ETC muestras ordenadas.

Muestra	% fracción conductora	ETC (%)
B03	30	30
B04	40	40
B05	50	48.11
B06	60	59.91
B07	70	70.05
B08	80	80.11
BSINTE	50	49.76

La Fig. 4 muestra el efecto del cambio en la eficiencia de transporte de carga electrónica respecto al momento estadístico de desorden ocasionado por la reconstrucción por recocido simulado. Las dimensiones del dominio computacional para las reconstrucciones fueron 300 x 300 para las muestras sintéticas y 350 x 350 para la muestra SEM. El proceso REA fue corrido durante 4 millones de iteraciones, donde la temperatura ficticia fue disminuyendo de 1 x 10-6 hasta el valor de aceptación. En los incisos B, D, F, H, J, L y N, están representados gráficamente el porcentaje de eficiencia de transporte de la fase negra para diferentes fracciones superficiales. Se observa un comportamiento similar en todas las muestras, al iniciar el proceso de desorden de la microestructura el porcentaje del ETC

disminuye hasta un valor finito. Al irse incrementando el valor de la fracción superficial de la fase conductora (incisos A, C, E, G, I, K y M) el ETC va incrementando. Esto es debido a que al incrementar el volumen de la fase conductora más partículas se encuentran activas y conectadas entre sí, lo cual no ocurre cuando la fracción superficial es menor, contrariamente los poros (fase blanca) se encuentran conectados de mejor manera [24]. Finalmente, la conducción eléctrica en la fase conductora depende del porcentaje de su fracción superficial, al ser esta mayor da como resultados una mejor conducción ya que las partículas se encuentran conectadas entre sí.

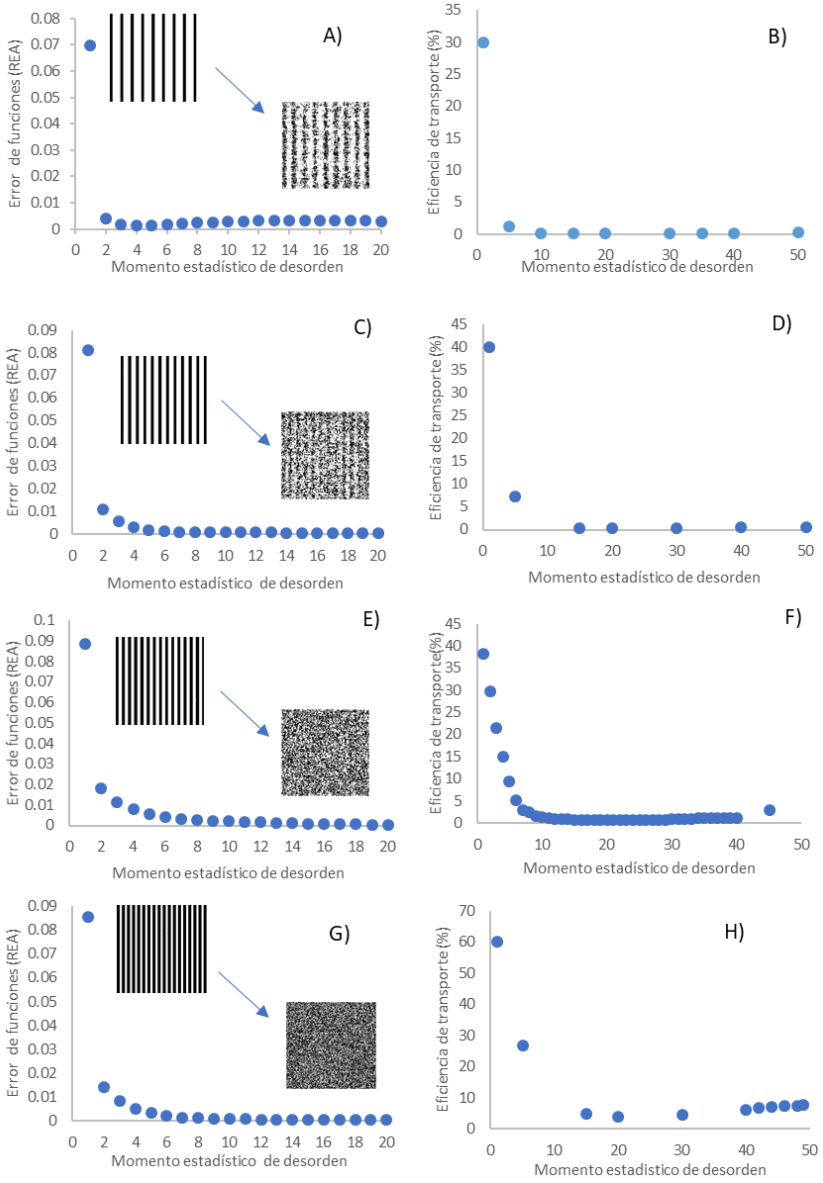

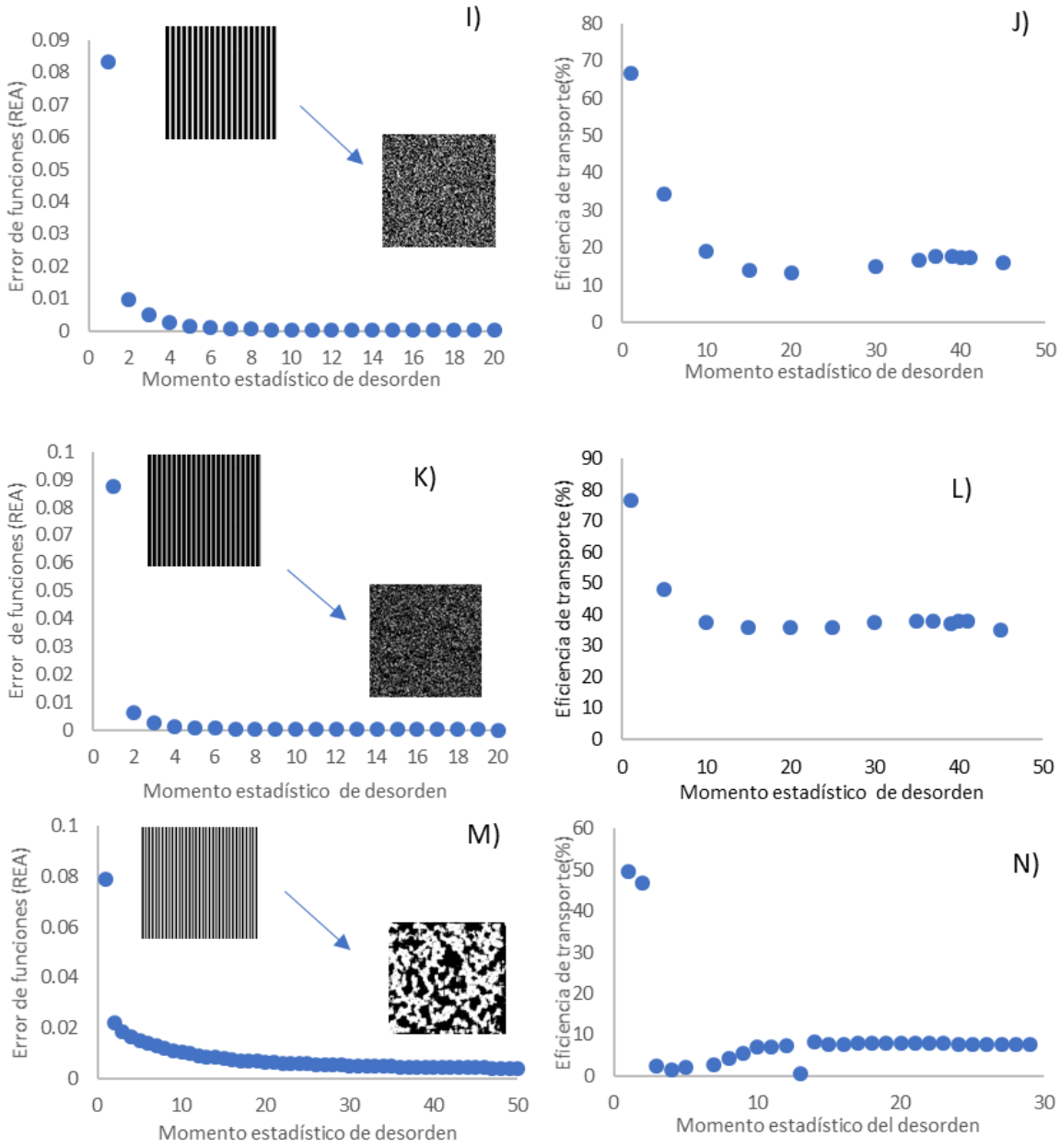

Fig. 4 Resultados numéricos del efecto del orden sobre la eficiencia al transporte de carga para microestructuras sintéticas. Inciso A y B, corresponden a fracción superficial de 30% fase conductora (color negro). Inciso C y D, corresponden a fracción superficial de 40% de la fase conductora (color negro). Inciso E y F, corresponden a fracción superficial de 50% fase conductora (color negro). Inciso G y H, corresponden a fracción superficial de 60% de la fase conductora (color negro). Inciso I y J, corresponden a fracción superficial de 70% fase conductora (color negro). Inciso K y L, corresponden a fracción superficial de 80% de la fase conductora (color negro). Inciso M y N, corresponden a fracción superficial de 50% de la fase conductora (color negro).

4. Conclusión

Se propone una metodología que puede ser aplicada como herramienta de diseño para mejorar el transporte de carga en electrodos de celdas de combustible. El método de SA permite simular la evolución del momento estadistico de desorden del composito alineado hasta un sistema disperso. El momento estadístico de desorden tiene un efecto sobre el ETC, en el momento 0 del desorden el ETC presenta el mismo valor que la fracción superficial de su fase y al incrementar el desorden el ETC disminuye hasta llegar a estabilizarse. Esta herramienta permitirá el diseño de mejores microestructuras debido a que se puede conocer en qué momento estadístico presenta mayor porcentaje de eficiencia de conducción.

Agradecimientos
Los autores quieren agradecer a CONACYT por el financiamiento otorgado bajo el proyecto Problemas Nacionales 2266.

Referencias

[1] Lin M-C, Lou C-W, Lin J-Y, Lin TA, Lin J-H. Mechanical property evaluations of flexible laminated composites reinforced by high-performance Kevlar filaments: Tensile strength, peel load, and static puncture resistance. Compos Part B Eng 2019;166:139–47. https://doi.org/10.1016/J.COMPOSITESB.2018.11.138.

[2] Huang ZH, Zhou YJ, Nguyen TT. Study of nickel matrix composite coatings deposited from electroless plating bath loaded with TiB2, ZrB2 and TiC particles for improved wear and corrosion resistance. Surf Coatings Technol 2019;364:323–9. https://doi.org/10.1016/J.SURFCOAT.2019.01.060.

[3] Han B, Chen H, Hu T, Ye H, Xu L. High electrical conductivity in polydimethylsiloxane composite with tailored graphene foam architecture. J Mol Struct 2020;1203:127416. https://doi.org/10.1016/J.MOLSTRUC.2019.127416.

[4] Blassiau S, Thionnet A, Bunsell AR. Micromechanisms of load transfer in a unidirectional carbon fibre-reinforced epoxy composite due to fibre failures: Part 3. Multiscale reconstruction of composite behaviour. Compos Struct 2008;83:312–23. https://doi.org/10.1016/j.compstruct.2007.05.004.

[5] Wu X, Tang L, Zheng S, Huang Y, Yang J, Liu Z, et al. Hierarchical unidirectional graphene aerogel/polyaniline composite for high performance supercapacitors. J Power Sources 2018. https://doi.org/10.1016/j.jpowsour.2018.07.031.

[6] Mao N, Chen W, Meng J, Li Y, Zhang K, Qin X, et al. Enhanced electrochemical properties of hierarchically sheath-core aligned carbon nanofibers coated carbon fiber yarn electrode-based supercapacitor via polyaniline nanowire array modification. J Power Sources 2018. https://doi.org/10.1016/j.jpowsour.2018.07.022.

[7] Wang X, Zhai H, Qie B, Cheng Q, Li A, Borovilas J, et al. Rechargeable solid-state lithium metal batteries with vertically aligned ceramic nanoparticle/polymer composite electrolyte. Nano Energy 2019;60:205–12. https://doi.org/10.1016/J.NANOEN.2019.03.051.

[8] Liu W, Lee SW, Lin D, Shi F, Wang S, Sendek AD, et al. Enhancing ionic conductivity in composite polymer electrolytes with well-aligned ceramic nanowires. Nat Energy 2017;2:17035.
[9] Pacheco C, Barbosa R, Rodriguez A, Oskam G, Ruiz-Gómez M, Escobar B. Numerical Simulation to Determine the Effect of Topological Entropy on the Effective Transport Coefficient of Unidirectional Composites. Crystals 2020;10:423.
[10] Shin S, Liu J, Akbar A, Um S. Nanoscale transport characteristics and catalyst utilization of vertically aligned carbon nanotube catalyst layers for fuel cell applications: Comprehensive stochastic modeling of composite morphological structures. J Catal 2019;377:465–79.
[11] Mench MM. Fuel cell engines. John Wiley & Sons; 2008.
[12] O'hayre R, Cha S-W, Colella W, Prinz FB. Fuel cell fundamentals. John Wiley & Sons; 2016.
[13] Chhowalla M, Teo KBK, Ducati C, Rupesinghe NL, Amaratunga GAJ, Ferrari AC, et al. Growth process conditions of vertically aligned carbon nanotubes using plasma enhanced chemical vapor deposition. J Appl Phys 2001;90:5308–17.
[14] Jakubinek MB, White MA, Li G, Jayasinghe C, Cho W, Schulz MJ, et al. Thermal and electrical conductivity of tall, vertically aligned carbon nanotube arrays. Carbon N Y 2010;48:3947–52.
[15] Yasuda S, Furuya A, Uchibori Y, Kim J, Murakoshi K. Iron–nitrogen-doped vertically aligned carbon nanotube electrocatalyst for the oxygen reduction reaction. Adv Funct Mater 2016;26:738–44.
[16] Tian ZQ, Lim SH, Poh CK, Tang Z, Xia Z, Luo Z, et al. A highly order-structured membrane electrode assembly with vertically aligned carbon nanotubes for ultra-low Pt loading PEM fuel cells. Adv Energy Mater 2011;1:1205–14.
[17] Murata S, Imanishi M, Hasegawa S, Namba R. Vertically aligned carbon nanotube electrodes for high current density operating proton exchange membrane fuel cells. J Power Sources 2014;253:104–13.
[18] Barbosa R, Andaverde J, Escobar B, Cano U. Stochastic reconstruction and a scaling method to determine effective transport coefficients of a proton exchange membrane fuel cell catalyst layer. J Power Sources 2011;196:1248–57. https://doi.org/10.1016/j.jpowsour.2010.08.033.
[19] Torquato S. Theory of random heterogeneous materials. Handb. Mater. Model., Springer; 2005, p. 1333–57.
[20] Garnett JCM. Colours in metal glasses, in metallic films and in metallic solutions.—II. Proc R Soc Lond A 1905;76:370–3.
[21] Bruggeman DAG. Berechnung verschiedener physikalischer Konstanten von heterogenen Substanzen. II. Dielektrizitätskonstanten und Leitfähigkeiten von Vielkristallen der nichtregulären Systeme. Ann Phys 1936;417:645–72.
[22] Barbosa R, Escobar B, Cano U, Pedicini R, Ornelas R, Passalacqua E. Stochastic reconstruction at two scales and experimental validation to determine the effective electrical resistivity of a PEMFC catalyst layer. ECS Trans 2011;41:2061–71.
[23] Barbosa R. Estudio teórico-experimental de la capa catalítica y su influencia en los fenómenos de transporte en un PEMFC. Universidad Nacional Autónoma de México, 2012.
[24] Lange KJ, Sui P-C, Djilali N. Determination of effective transport properties in a PEMFC catalyst layer using different reconstruction algorithms. J Power Sources 2012;208:354–65. https://doi.org/10.1016/J.JPOWSOUR.2011.11.001.

Influence of Sulfonation Time On Thermal Properties And Solubility Of Poly (Styrene-Co-Butyl Acrylate) Membranes

L. Francisco-Vieira, L. Da Silva, D. Morales-Acosta*, R. Benavides*

Centro de Investigación de Química Aplicada, Blvd Enrique Reyna No. 140, Col. San José de los Cerritos, 25290. Saltillo, Coahuila, México
*Tel: +52844-4389830 E-mail: roberto.benavides@ciqa.edu.mx; diana.morales@ciqa.edu.mx

ABSTRACT

Sulfonation is a powerful strategy for the modification of hydrocarbon polymers used for the preparation of membranes for fuel cell technologies and involves the substitution of hydrogen atoms (H) by sulfonic acid (-SO_3H) groups in the polymer chain, enabling its ion exchange capacity (IEC). The sulfonation degree (DS) can be controlled through time and temperature during the reaction with different sulfonation agents. In this context, the sulfonation of poly (styrene – co – butyl acrylate) (StBuA) was carried out with sulfuric acid at a molar ratio of 150% relative to the theoretical molar amount of benzene rings and a temperature of 40 ºC. Reaction times of 2, 3, 4 and 5h were tested and even longer periods of 7, 9 and 12h were also evaluated. The sulfonated copolymers were dissolved in polar aprotic solvents and membranes prepared by casting and differences followed by characterization techniques as FTIR and TGA. It was observed, through FTIR, that as the reaction time increases, a widening of the absorption bands characteristic of the SO_3H groups occurs. Thermal gravimetric analysis (TGA) confirmed the successful sulfonation through the weight loss due to sulfonic groups, as well as a good thermal stability over 380 °C for the longest reaction time of 12h. sStBuA membranes exhibited color changes through the sulfonation time, starting with yellowness and ending with brownish for 12h.

Keywords: membranes; styrene-co-butyl acrylate; sulfonated copolymers; fuel cells.

1. Introduction

Proton exchange membrane fuel cells (PEMFCs) has been considered as one of the most promising clean energy technologies used to solve the problems on resources, energy and environment, due to its high efficiency and low environmental impact [1,2].

Aromatic polymers are an attractive kind of materials widely applied, basically due to their peculiar properties imparted by planar and rigid aromatic rings. The presence of such ring in each monomer unit encourages high thermal stability and excellent mechanical properties; even though their use is limited due to its high hydrophobicity and suggests modifications in order to improve properties of better wettability and modifying solubility in common organic solvents [3].

Sulfonation is a powerful and versatile route to modify aromatic polymers, where the sulfonating agent reacts in the aromatic ring, and a proton (H) of benzene is replaced by a group of sulfonic acid (SO_3H). The later converts aromatic polymers into ionomers, able to conduct protons and allowing its use as proton exchange membranes (PEM). Polymers can be sulfonated in the initial stage of synthesis, as monomers, or once is a polymer (post-sulfonation) [4,5]. The main problems of the sulfonation are side reactions combined with polymer degradation, high toxicity of sulfonating agent, heterogeneity of the reaction media, low control over the sulfonation level. As a consequence of the above, there is a tendency of the polymer to crosslink via sulfone formation and to degradation of the polymers by oxidation or chain scission [3]. These effects have been attributed to the sulfonating agent, time and temperature of the sulfonation reaction.

Ngadiwiyana and coworkers [6] studied the modification of polystyrene (Styrofoam) by a sulfonation reaction during times of 1 to 5h. They obtained sulfonated PS that presented a IEC value 1.55 $meq \cdot g^{-1}$ with 4h; however, with 5h sPS suffered a decrease in IEC and sulfonation degree; they attributed the fact that such sPS was more soluble in water, which in turn resulted in a higher possibility for side reactions.

Parreño y coworkers [7] studied the direct sulfonation reaction in fibers of polybenzoxazine (PBz) using H_2SO_4 as sulfonating agent and reaction times of 3, 6, 12h and even 72h. The authors acquired IEC that varied of 1.78 at 3h and 2.27 $meq \cdot g^{-1}$ at 24h. The fibers presented color changes when 72h was used as sulfonation time, from light brown to reddish-brown and eventually up to black. Gel formation was also observed during washing with deionized water.

Our research group has been working on sulfonated cheap hydrocarbon copolymers based on styrene (St) combined with different monomers, such as divinylbenzene, acrylic acid [8,9], acrylonitrile and butyl acrylate [10]. The St monomer is known to form intrinsically rigid and brittle structures; then, in some cases the combination is necessary to improve such characteristics for its application as membranes.

The copolymer of poly(styrene-co-butyl acrylate) (StBuA) was synthesized and sulfonated with different acid concentrations with a fixed reaction time of 2h. Membranes obtained had IEC values varied from 0.83 to 1.18 $meq \cdot g^{-1}$, depending on the sulfonation degree. They also exhibited a proton conductivity of 9.77 $x10^{-5}$ $S \cdot cm^{-1}$ for the StBuA membrane with less acid concentration, which is two orders of magnitude lower than the commercial Nafion membrane [10].

In this context, in this present work the copolymer StBuA was sulfonated with H_2SO_4 as sulfonating agent, an acid concentration of 150%mol relatives to the molar amount of

benzene rings, theoretically present in the composition (90:10), but with variation of the reaction time, a set ranging from 2 to 5h and a longer set for 7, 9 and 12h. The effect of the reaction time in the properties of solubility and thermal of the membranes is reported.

2. Materials and Methods

2.1. *Materials*

Sulfuric acid (H_2SO_4, 95-98%), potassium hydroxide (KOH, ≥85%), tetrahydrofuran (THF) were purchased from Sigma-Aldrich. Dichloromethane (DCM), xylene and hydrochloric acid (HCl, 37%) were obtained from J. T. Baker. All solvents were used as received without further purification.

2.2. *Sulfonation of poly(styrene-co-butyl acrylate)*

Poly (styrene-co-butyl acrylate) was synthesized with a molar ratio of 90:10, with the highest concentration for the styrene monomer, as it was previously reported [10].
The sulfonation reaction was carried out dissolving 20 g of the copolymer StBuA in 700 mL of DCM and heated to 40 °C, under N_2 atmosphere into a jacketed glass reactor equipped with a condenser and mechanical stirring. After the complete solubility of the copolymer, concentrated sulfuric acid (H_2SO_4, 98%) was added as the sulfonating agent. The reaction was stopped by pouring the sulfonated solution into a beaker with distilled water immersed in an ice bath. The solid sulfonated copolymer was washed several times until neutral pH. To ensure removal of residual acid, the materials were washed with an alkaline solution of KOH maintaining it under stirring for 6 hours, then HCl was added, keeping the stirring overnight. The material was washed again with distilled water and dried at 50 °C in a vacuum oven for 48 hours to remove residual water. The sulfonating agent was added at concentrations of 150 mol% (relative to the molar amount of benzene rings, theoretically present in the composition). The sulfonation reaction time was varied for 2, 3, 4, 5, 7, 9 and 12h. The synthetic route scheme is presented in Figure 1.

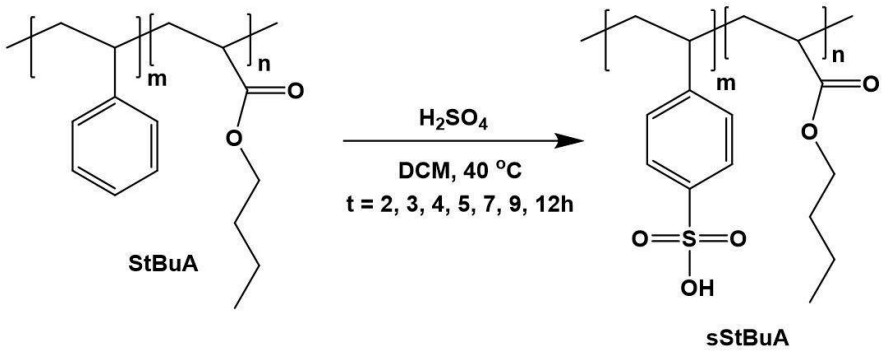

Fig. 1. Scheme for sulfonation of poly(styrene-co-butyl acrylate).

2.3. *Solubility of the sulfonated copolymers*

Solubility tests are a needed step previous to membrane preparation. The following solvents were evaluated: chloroform, tetrahydrofuran, xylene, dimethylsulfoxide, dimethylformamide, and the mixtures of tetrahydrofuran/dimethylsulfoxide, tetrahydrofuran/dimethylformamide and tetrahydrofuran/xylene.

2.4. Preparation of the membranes

Membranes of sStBuA were prepared by the casting method. The preparation consisted of a concentration that was prepared of 0.3 $g \cdot mL^{-1}$ copolymer/solvent. The solubilized copolymers were poured into glass molds and dried at room temperature. The casted membranes were put in a vacuum oven at 50 ^{o}C for 24 h, to remove residual solvent.

2.5. *Characterization of membranes*

FTIR spectroscopy of the copolymers, before and after sulfonation, were carried out in a Bruker Vertex 70v spectrophotometer, through diamond ATR, with 64 scans and a nominal resolution of 4 cm^{-1} in the region of 4000 - 500 cm^{-1}. The thermal stability of the StBuA and sStBuA copolymers was evaluated by TGA analysis in a Linseis apparatus, model STA (Simultaneous Thermal Analysis) PT 1600. Thermal runs were performed between 30 ^{o}C and 800 ^{o}C with a heating rate of 10 $^{o}C \cdot min^{-1}$ under N_2 atmosphere.

3. Results and Discussion

FTIR analysis was used to confirm the chemical modification of the copolymers, regarding the efficiency of the electrophilic $-SO_3H$ introduction in the structure of polymer through the sulfonation reaction. Figure 2 shows the spectra differences of the sulfonated copolymers (sStBuA) along the reaction time (from 2 up to 12h). Additionally, the spectrum of the un-sulfonated copolymer StBuA 9010 was included.

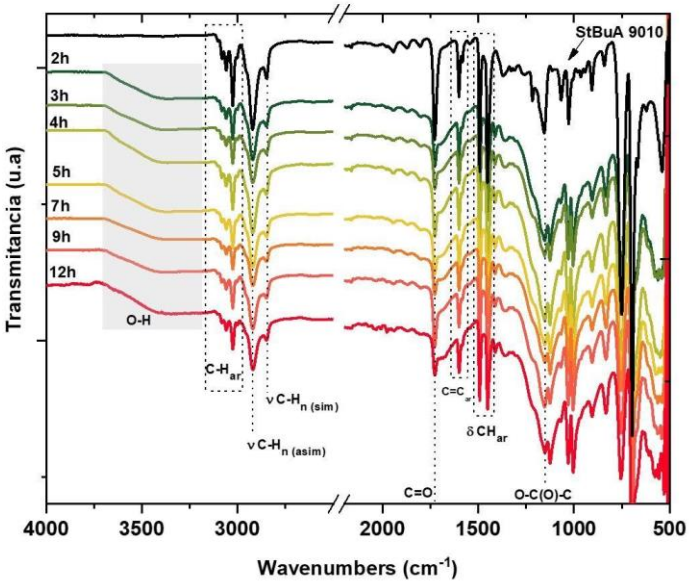

Fig. 2. FTIR spectra of copolymers sStBuA with different sulfonation reaction time.

The main absorption bands characteristic of a hydrocarbonated aromatic polymer chain are observed between 3100-3000 cm^{-1}, attributes of the stretching vibration of the C-H_{ar}, while the bands at 2962-2850 cm^{-1} are assigned to the CH_2 and CH_3 groups in the aliphatic side of the polymer chain (asymmetric and symmetrical deformation, respectively). The typical signal of the ester group present in the BuA monomer is observed as the intense absorption band at 1722 cm^{-1} corresponding to the C=O group. Then at 1152 cm^{-1} the absorption band corresponds to the stretching vibration of O-C (O) -C [11].

For the sulfonated copolymers, it is appreciated that the -SO_3H electrophilic substitution happened by observing the appearance of new vibrations related to the sulfonic acid functions, including the broad band of the region between 3600 – 3200 cm^{-1} attributed to stretching vibration of the O-H bonds from the sulfonic groups.

Detailed bands assigned to the sulfonic group presence are better observed in Figure 3, where amplified spectra can be seen. The intense and broadened bands between 1240 – 1004 cm^{-1}, are assigned to vibrations of the S=O; particularly, the absorption bands at 1220 cm^{-1} is characteristic of the asymmetric stretching of the S=O bond in the sulfonic acid group. It is also noticeable the appearance of a new absorption band at 1125 cm^{-1} as the symmetric vibration from this same group [12].

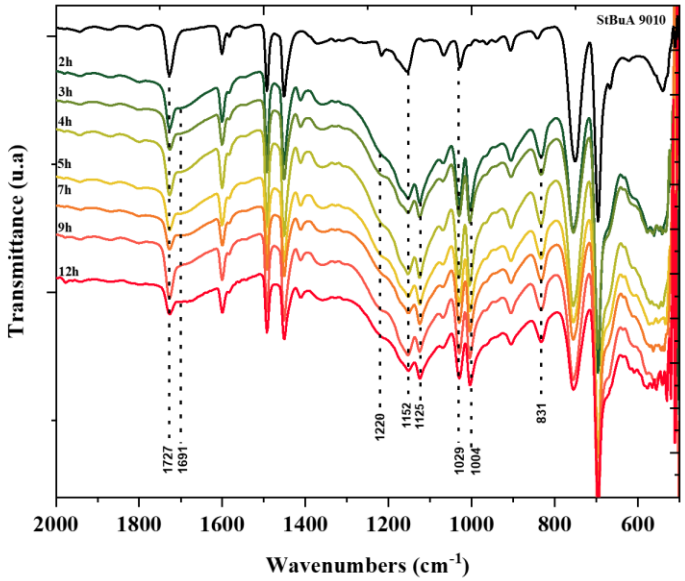

Fig. 3. FTIR spectra of copolymers sStBuA with different sulfonation reaction times in the spectra region between 2000 – 550 cm^{-1}.

The absorption bands at 1125 and 1004 cm^{-1}, for all sulfonated copolymers, have been associated with the in-plane band of the aromatic ring substituted with sulfonic groups at *para*-position [13]. Regarding the previous, it can also be observed the band in the region in 831 cm^{-1}, indicating the presence of *para*-substituted phenyl rings (1,4 – disubstituted – Fig.1) in the structure of sulfonated aromatic polymers [3].

It is known that some kind of compounds with C=O bond shows a strong stretching absorption band in the region of 1870-1540 cm^{-1}, such as ketones, aldehydes, carboxylic acids, esters, acid halides, anhydrides and lactams. The position of the C=O stretching band is determined by the following factors: sample physical state, electronic and mass effects of the neighboring substituent, conjugation, hydrogen bonding (inter and intramolecular), and ring strain [14].

In accordance with Melo and coworkers [8], the copolymers after sulfonation reaction are able to form cyclic structures in the polymer chains after photo-oxidation and loss of carbonyl groups. However, when H_2SO_4 was employed as sulfonating agent, the carbonyl signal does not suffer any shift toward lower wavenumbers, only a reduction in intensity. They associated this behavior with the formation of chemical crosslinks through sulfone groups between aromatic rings.

Considering this effect, the absorption bands of the carbonyl groups suffered some changes in intensity and width after the sulfonation reaction. It is also possible to see the appearance of a shoulder next to the main band (1727 cm^{-1}), specifically at 1691 cm^{-1}, which could be associated to the resonance effect between the carbonyl group and the S of the sulfonic group, caused by the sulfone-type crosslinking from the high acid concentration.

Solubility differences arising from the introduction of sulfonic acid groups can be the result of changes in the polarity of the polymers and intermolecular forces related to hydrogen bonds [15]. Solubilities of sStBuA copolymers were tested, and the results are listed in Table 1.

Table 1. Solubility of the copolymers sStBuA.

StBuA	Solvents								
150%S	$CHCl_3$	THF	Xylene	DMSO	DMF	THF/DMSO	THF/DMF	THF/Xylene	H_2O
2h	++	++	+	-	-	*	*	+	-
3h	++	++	+	-	-	*	*	+	-
4h	++	++	+	-	-	*	*	+	-
5h	+	+	+	-	-	*	*	+	-
7h	+	+	-	-	-	*	*	+	-
9h	-	+	-	-	-	*	*	+	-
12h	-	+	-	-	-	*	*	+	-

++ Soluble with stirring
+ Soluble with stirring and heating
* Gelatinous material
- Insoluble

Copolymers sulfonated during 2 – 4h are easily soluble in solvents like chloroform, THF, and xylene, not the case for the rest. It is known that sulfonation reaction time defines some of the characteristics of the polymers, since such process will increase hydrophilicity and its proton conductivity by the presence of sulfonate groups in the polymer chain. However, the main sulfonation problems commonly occur due to side reactions during the procedure, sometimes resulting in degradation or sulfone type crosslinking in the polymer chains [3]. Under such modification, the polymers become efficient water absorbents, but could also inhibit their solubility.

It is noticeable that after 5h of reaction, the materials sulfonated show less solubility in all solvents. This can be attributed to the possible crosslinking formation, consequently, the solubility of these materials decreases as the reaction time increases. In the case of copolymers qualified as gelatinous material (*), with solvent mixtures (THF/DMSO and THF/DMF) the solution presented only a change in the viscosity, since once the solvent enters in contact with the copolymer, the precipitated gel is formed, so total solubility was not possible.

In general, it is also observed that all the materials have low or no solubility in water. In this context, a mixture of THF and xylene were used as solvents for the preparation of the membranes by the casting method.

A picture of the membranes obtained through the casting method is presented in Fig 4. It is observed that the membranes exhibited a change in the color as an increase in the time sulfonation reaction, which changed of yellow-transparent to brown-light.

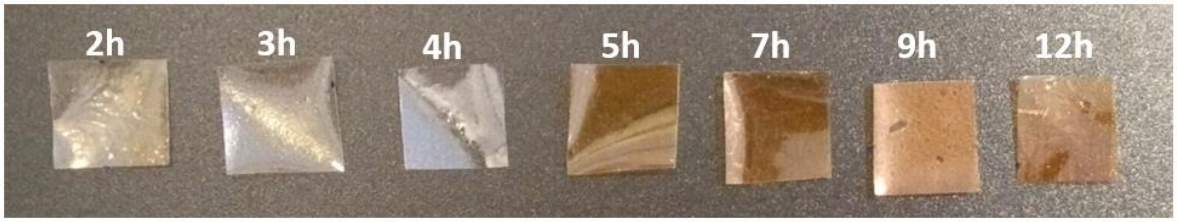

Fig. 4. Membranes of the sulfonated copolymer StBuA in different time sulfonation reactions.

An increase in coloration is observed along reaction time. Membranes were analyzed with the help of the numeric computer scale of red, green and blue (RGB color), which once combined those numbers indicated changes of color starting with grays for 2 – 4h membranes.

Merle and coworkers mentioned that when copolymers are crosslinked, membranes exhibited a change of color, from transparent for un-crosslinking membranes to a brownish color for a crosslinking material [16].

It is clearly observed that membranes changed coloration from gray to brown color along sulfonation time and RGB system indicated a high level of yellow color for the 12h sulfonated membrane, as much as 76% of yellowness. The later could be a consequence of crosslinking promoted by the long reaction time, an effect also suggested from FTIR analysis.

The thermal decomposition properties of non-sulfonated (StBuA) and sulfonated at the extreme 12h of sulfonation time (sStBuA) copolymers are presented in Fig. 5. Firstly, it is possible to confirm that the non-sulfonated copolymer has high thermal stability for our application purpose, since it stable over 380 ^{o}C, after it undergoes main chain degradation. On the other hand, sulfonated copolymer shows a reduced stability with a trend of weight loss in three steps.

The first step (130 – 280 °C) is assigned to the decomposition or loss of pendant sulfonic acid groups (-SO_3H); this step is particular for sulfonated materials. The second loss weight (300 - 400 ^{o}C) is attributed to the decomposition of the main chain or polymer backbone. Finally, the third loss above 400 ^{o}C is related to the total decomposition of the material residues, which could be crosslinked material [17].

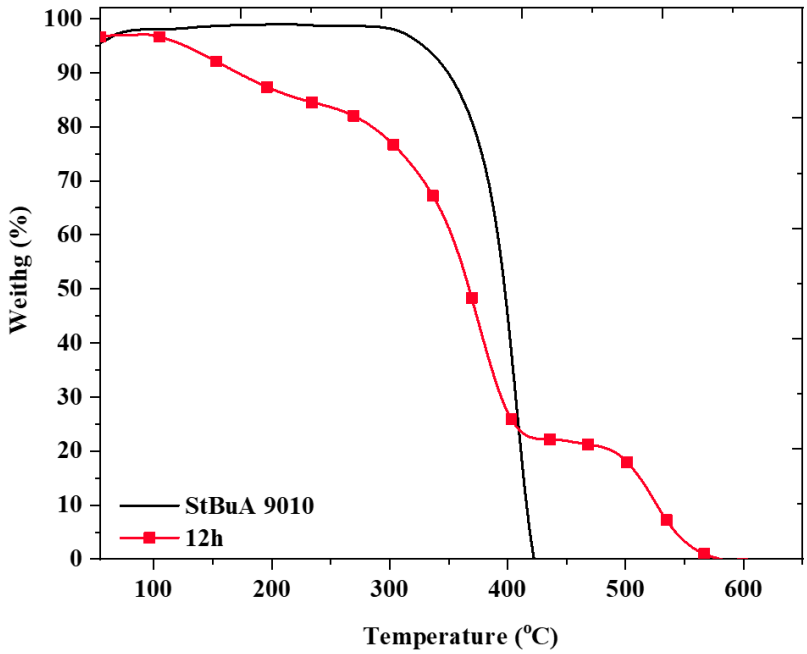

Fig. 5. TGA thermograms of copolymers StBuA and sStBuA with 12h of sulfonation reaction.

The non-sulfonated and most sulfonated materials were first considered for this test to have an initial view of materials behavior under thermal treatment; however, all intermediate sulfonation time conditions will be further evaluated as well. These results envisage that even the most sulfonated copolymer has stability over 150 °C, which useful as material to face fuel cell operation temperature.

4. Conclusion

The copolymers of sStBuA with different reaction times were successfully sulfonated, as confirmed by FTIR analysis, they also showed good solubility in common solvents, capable of membrane preparation. Thermal properties were also obtained and indicated thermal stability over 150 °C by TGA.

Acknowledgments

Authors acknowledge to CONACyT through project grants FC3004 and CB259010, and Ph.D. scholarship for LFV.

References

[1] Kim DJ, Lee BN, Nam SY. Characterization of highly sulfonated PEEK based membrane for the fuel cell application. Int J Hydrogen Energy 2017;42:23768–75. doi:10.1016/j.ijhydene.2017.04.082.

[2] Jin X, Li L, Xu R, Liu Q, Ding L, Pan Y, et al. Effects of Thermal Cross-Linking on the Structure and Property of Asymmetric Membrane Prepared from the Polyacrylonitrile. Polymers (Basel) 2018;10:539. doi:10.3390/polym10050539.

[3] Wolska J, Walkowiak-Kulikowska J. On the sulfonation of fluorinated aromatic polymers: Synthesis, characterization and effect of fluorinated side groups on sulfonation degree. Eur Polym J 2020;129:109635. doi:https://doi.org/10.1016/j.eurpolymj.2020.109635.
[4] Al Lafi AG. The sulfonation of poly(ether ether ketone) as investigated by two-dimensional FTIR correlation spectroscopy. J Appl Polym Sci 2015;132. doi:doi:10.1002/app.41242.
[5] Yee RSL, Zhang K, Ladewig BP. The Effects of Sulfonated Poly(ether ether ketone) Ion Exchange Preparation Conditions on Membrane Properties. Membranes (Basel) 2013;3:182–95. doi:10.3390/membranes3030182.
[6] Ngadiwiyana, Ismiyarto, Gunawan, Purbowatiningrum RS, Prasetya NBA, Kusworo TD, et al. Sulfonated polystyrene and its characterization as a material of electrolyte polymer. J Phys Conf Ser 2018;1025:12133. doi:10.1088/1742-6596/1025/1/012133.
[7] Parreño RP, Liu Y-L, Beltran AB, Carandang MB. Effect of a direct sulfonation reaction on the functional properties of thermally-crosslinked electrospun polybenzoxazine (PBz) nanofibers. RSC Adv 2020;10:14198–207. doi:10.1039/D0RA01285H.
[8] Melo L, Benavides R, Martínez G, Da Silva L, Paula MMS. Degradation reactions during sulphonation of poly(styrene-co-acrylic acid) used as membranes. Polym Degrad Stab 2014;109:343–52. doi:10.1016/J.POLYMDEGRADSTAB.2014.06.002.
[9] Da Silva L, Pedrosa RP, Coelho F, Vieira LF, Benavides R, Dal-Bó AG, et al. Synthesis and Characterization of Sulfonated Poly-(styrene-co-acrylic acid) for Applications as Pronton Exchange Membranes. Macromol Symp 2014;343:51–8. doi:doi:10.1002/masy.201300188.
[10] Francisco-Vieira L, Benavides R, Cuara-Diaz E, Morales-Acosta D. Styrene-co-butyl acrylate copolymers with potential application as membranes in PEM fuel cell. Int J Hydrogen Energy 2019. doi:10.1016/J.IJHYDENE.2019.01.181.
[11] Fuente L, Ferna M. Characterization and Thermal Properties of Poly (n-butyl acrylate-g-styrene) Graft Copolymers. J Appl Polym Sci 2000;80:783–9. doi:10.1002/1097-4628(20010502)80:5<783::AID-APP1155>3.0.CO;2-5.
[12] Xi J, Li Z, Yu L, Yin B, Wang L, Liu L, et al. Effect of degree of sulfonation and casting solvent on sulfonated poly(ether ether ketone) membrane for vanadium redox flow battery. J Power Sources 2015;285:195–204. doi:10.1016/j.jpowsour.2015.03.104.
[13] Becker CM, Biagini AB, Forte MMC, Amico SC, Vargas JVC, Azambuja DS. Sulfonation and characterization of styrene-indene copolymers for the development of proton conducting polymer membranes. Polímeros 2012;22:395–400. doi:10.1590/S0104-14282012005000069.
[14] Robert M. Silverstein, Francis X. Webster DJK. Spectrometric identification of organic compounds. 7th ed. New York: Jonh Wiley & Sons, Inc; 2005. doi:10.1016/0022-2860(76)87024-X.
[15] Gao Y, Robertson GP, Guiver MD, Jian X, Mikhailenko SD, Wang K, et al. Sulfonation of poly(phthalazinones) with fuming sulfuric acid mixtures for proton exchange membrane materials. J Memb Sci 2003;227:39–50. doi:10.1016/j.memsci.2003.08.020.
[16] Merle G, Ioana FC, Demco DE, Saakes M, Hosseiny SS. Friedel-Crafts Crosslinked Highly Sulfonated Polyether Ether Ketone (SPEEK) Membranes for a Vanadium/Air Redox Flow Battery. Membranes (Basel) 2013;4:1–19. doi:10.3390/membranes4010001.
[17] Wang Q, Lu Y, Li N. Preparation, characterization and performance of sulfonated poly(styrene-ethylene/butylene-styrene) block copolymer membranes for water desalination by pervaporation. Desalination 2016;390:33–46. doi:https://doi.org/10.1016/j.desal.2016.04.005.

ID 024

Study of the integration of a System PEMFC (580W) – Charger – Li-Ion Battery Module for an Electric Vehicle

J.L. Díaz-Bernabé[1], A. Rodríguez-Castellanos[1], S. Citalán-Cigarroa[1], O. Solorza-Feria[1*]

[1] Departamento de Química, Centro de Investigación y de Estudios Avanzados del IPN, Av. Instituto Politécnico Nacional No. 2508, Sn. Pedro Zacatenco, Ciudad de México, México.
* Corresponding author: osolorza@cinvestav.mx

ABSTRACT

In this communication the behavior of an integrated system consisting of 580W Proton Exchange Membrane Fuel Cell (PEMFC) stack - battery charger - Li-Ion battery module, for its use in an hybrid electric vehicle will be presented. A Buck-Boost converter was designed to regulate the current and voltage of the battery module in Charging-Mode. The ideal behavior of the whole system is estimated by modeling the main components and the responses of PEMFC stack, charger, and battery module are followed by means of simulation results, performed in SPICE. Results show that the PEMFC device is sensitive to changes of the load requirements (battery charging-current), so an oversize of its power level is necessary in a practical implementation. The followed methodology will be presented and discussed in this presentation which can be easily adapted to higher power levels in electric vehicular applications.

Keywords: PEMFC systems, Li-Ion Battery, DC-DC Simulation;

1. Introduction

The polymer electrolyte membrane fuel cell (PEMFC) has long been accepted as a promising zero-emissions, versatile, and modular power source for a wide range of applications [1]. It is suitable for electric vehicle (EV) applications because it has low operation temperature, small design, and no many deterioration difficulties. In spite of their advantages, EV's have a limited driving autonomy and an extensive battery module recharging phase. A PEMFC stack, separately from main energy supply, permits to recharge the battery modules and to improve the autonomy of an EV.

Fig. 1 shows a simplified of PEMFC system for an EV which integrates a PEMFC stack, a DC-DC converter as battery charger, and battery modules M1 and M2 (energy storage system) in serial configuration. It is assumed that since their restricted energy capacity and performance limitations, PEMFC stack charges module M1 while module M2 feeds the electronic speed controller (ESC). Conversely, module M1 feeds the ESC as PEMFC stack charges module M2. In order to evaluate the behavior and design constraints of the PEMFC system every component ought to be modeled and simulated. The combination of these component yields a simulation model of the entire system.

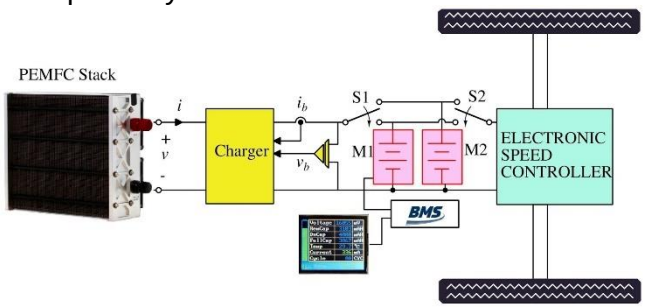

Fig. 1. PEMFC system for an electric vehicle.

Functional and behavioral methods are suitable to carry out simulations of a whole PEMFC resource in powertrain environments [2-8]. These modeling approaches do not consider in-depth single cells but describe comprehensive properties of a PEMFC stack. A number of mathematical, electrochemical, and electrical modeling formulations for Li-Ion batteries and cells have been reviewed in references [9-16]. Containing a lattice of N_P x N_S single cells, the battery modules enlarge the autonomy of an electric vehicle. A string of N_S cells increases the output voltage and an array of N_P parallel cells increases the current rate. By expanding the electrical model of a single cell proposed by Chen and Rincón-Mora [9], the behavior of a Li-Ion battery module is investigated. This method makes the previous analysis of Li-Ion cells applicable to Li-Ion modules for EV applications.

Simulation Program Integrated Circuit Emphasis (SPICE) is a general-purpose analog electronics circuit simulator which provides a technique to examine the performance of complex circuits and batteries [11] by means of analog behavioral models [17- 19]. A behavioral model for PEMFC stack was built based on a non-linear relation whose simulated response match well to the experimental current-voltage curve. Then, an equivalent circuit was implemented to produce a PEMFC device inside SPICE simulation environment. In the same way, the behavioral models for the DC-DC converter and the Li-Ion battery module were developed in order to shape a simulation model of the complete PEMFC system. This article is organized in the following way: Section 2 shows the modeling of the main components of the PEMFC system, section 3 presents the simulation results, and final section gives the conclusions of the developed work.

2. System Modeling

2.1 *PEMFC stack behavioral Model*

In [3] the behavior of the PEMFC stack is estimated with the non-linear equations (1) and (2), for every operation point (*i*,*v*) inside of the curve. The stack voltage *v* (V) as a function of the output current *i* (A) is approximated by:

$$v = v_{OC} - iR_S - B\log(1000i) - i_m.m.\exp(n.i_m) \quad (1)$$

$$i_m = \begin{cases} 0 & for \;\; i < i_d \\ i - i_d & for \;\; i > i_d \end{cases} \quad (2)$$

where v_{oc} is the open-circuit voltage, R_S is the parasitic resistance in the route of current, B (mv/dec) is the sum of the Tafel slope of all individual cells in the stack, i_d is the value of output current at the point where the voltage goes away from linearity, and m and n parameters are adjusted to agree with the curve in the region of mass transfer. Fig. 2 shows an equivalent circuit proposed for the PEMFC stack where the linear current-controlled voltage source H1 correspond to the output current *i*, and the behavioral sources B1 and B2 stand for logarithmic and exponential terms respectively of Eq. (1).

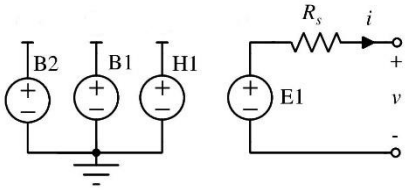

Fig. 2. Equivalent circuit for a PEMFC stack.

2.2 Buck-Boost converter

Figure 3 shows the arrangement of the ideal no-inverting Buck-Boost converter which contains an inductor L_1, a capacitance C_1, and the switches S1 and S2 modulated with a Pulse Width Modulate (PWM) signal. This circuit allows to increase or to decrease the output voltage v_b with respect to the voltage *v* of the PEMFC stack, depending on the value of a control signal *u*.

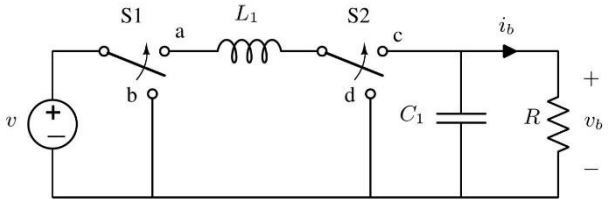

Fig. 3. Non-inverting Buck-Boost converter.

Figure 4 shows the averaged circuit model of a Buck-Boost converter for continuous current mode (CCM) [20]. This circuit gives the low-frequency response of the converter necessary to abbreviate time-consuming simulations of battery modules.

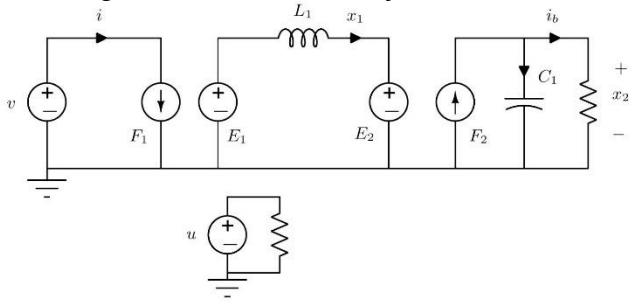

Fig. 4. Averaged circuit model for Buck-Boost converter [20].

The control variable $u = [1, 0]$ is related to the positive width (on-time) of the PWM signal, and L_1 and C_1 are constant parameters. Non-linear dependent current and voltage sources F_1, F_2, E_1, and E_2 are defined in the set of equations (3):

$$F_1 = ux_1, \quad F_2 = u'x_1$$
$$E_1 = uv, \quad E_2 = u'x_2 \quad (3)$$

where $u'=1-u$ is the negative width (off-time) of the PWM signal, and the state variables x_1 and x_2 are the current at L_1 and the voltage at C_1, respectively.

2.3

Figure 5 presents an equivalent circuit for the Li-Ion cell where at the right side a capacitor C_{SOC} is the nominal charge storage capacity of the cell. The current source F_{ib} increases or diminishes the state-of-charge of battery (SOC) so a value equals 1.0V at node SOC indicates that the cell is fully charged. At the left side, the voltage-controlled voltage source E_{SOC} is the open-circuit voltage as a function of SOC, the R_1, R_2, and R_3 engross the equivalent series resistance and the networks R_1C_1 and R_2C_2 stand for transient response.

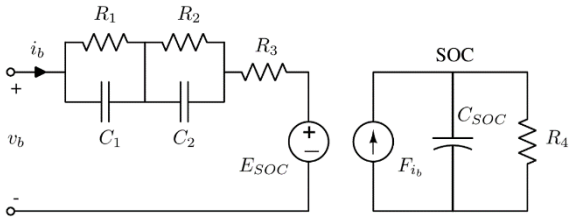

Fig. 5. Equivalent circuit of Li-ion cell [9].

The SOC is continuously estimated in simulation by means of the voltage at node SOC:

$$SOC(\tau) = \frac{SOC_0}{C_{SOC}} \int_0^{\tau} F_{i_b}(\tau)\, d\tau \qquad (4)$$

where $SOC_0 = [0, 1]$ is the initial condition of *SOC*, Fi_b is proportional to the output-current. The capacitor C_{SOC} is the cell charge storage capacity and its value is determined by:

$$C_{SOC} = 3600\, C_{Cell}\, f_1\, f_2 \qquad (5)$$

where *3600* is the conversion from seconds to hours, C_{cell} is the nominal capacity of cell in units of *Ahr*, f_1 (<1.0) is an aging factor because charging-discharging cycles reduce the nominal capacity of battery, and f_2 (<1.0) is the temperature effect that reduces nominal capacity too.

As has been shown in ref [9], the set of equations in (6) carries out the update of the parameters in simulation, where it has assumed a widespread Li-Ion cell with a nominal voltage of 3.685V.

$$\begin{aligned}
E_{SOC} &= 0.3201 SOC^3 - 0.1178 SOC^2 + 0.2156 SOC - 1.031 \exp(-35.SOC) + 3.685 \\
R_1(SOC) &= 0.04984 + 6.603 \exp(-155.2\, SOC) \\
R_2(SOC) &= 0.04669 + 0.3208 \exp(-29.14\, SOC) \\
R_3(SOC) &= 0.07446 + 0.1562 \exp(-24.37\, SOC) \\
C_1(SOC) &= 703.6 - 752.9 \exp(-13.51 SOC) \\
C_2(SOC) &= 4475 - 6056 \exp(-27.12\, SOC)
\end{aligned} \qquad (6)$$

Li-Ion battery module was developed by means of a circuit for an array of N_P parallel cells. This building block is connected N_S times in series in a way to shape the entire battery module, see Fig. 6. The array of N_P cells required to modify the equations for R_1, R_2, and R_3 by a factor of $1/N_P$ and the equations for the C_{SOC}, C_1, and C_2 by a factor of N_P.

3. Simulation Results

Figure 6 presents the simulation model of the PEMFC system with a single battery module developed in NGSPICE [19]. The PEMFC stack, Buck-Boost charger, and battery module make calls to sub-circuits from X1 to X12 respectively. The Control sub-circuit X13

needs the current i_b and voltage v_b to update the duty cycle u of buck-boost converter so the charging profile of a Li-Ion battery module is accomplished.

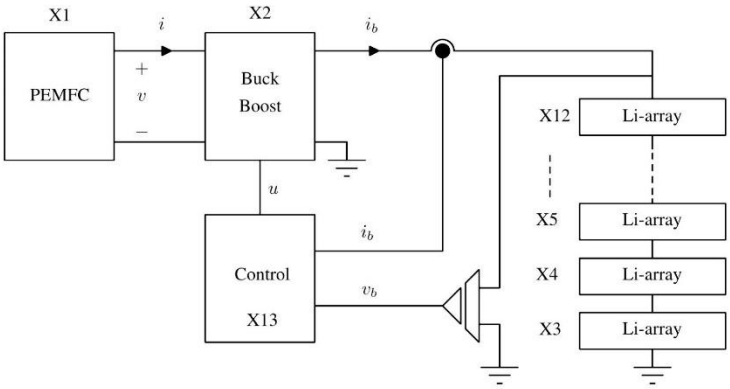

Fig. 6. SPICE simulation model for the PEMFC system.

Table 1 shows the main specifications of the experimental PEMFC stack, Table 2 exhibits the requirements of a buck-boost circuit designed to operate in CCM, and Table 3 indicates the main parameters of the battery module.

Table 1. Specifications of a 580W PEMFC stack.

Type	Nominal Power (W)	Number of cells	Material and Concentration (weight/C)	MEA area a (cm^2)	Reactants	Reactants pressure (atmospheres)
PEM	580	48	Pt, 20%	123	H_2/Air	0.3/0.0

Table 2. Requirements of a Buck-Boost converter in CCM.

F_s (kHz)	L_1(uH)	C_1(uF)	S_1, S2
60	220	100	IRF254

Table 3. Specifications of a Li-Ion of battery module.

Cell Part Number	Capacity (Ahr)	Voltage (V)	Series Number	Parallel Number	Module Power (W)
INR18650M26 [21]	2.6	3.685	10	5	480

Figure 7 shows the experimental and simulated performances of a 580W PEMFC stack by means of its current-voltage curve. Since parameters *B*, *m* and *n* of Eq. (1) and (2)

are properly chosen, the simulated trace is similar to that experimental. The safe operating range (SOR) of the PEMFC source should drop where both curves touch themselves, between10A and 35A, in the curve. Figure 8 displays the voltage response of the PEMFC stack to an upward stair current stimulus similar to that could appear when a battery module or an electric vehicle increases its power requirement. Because the variations are inside the SOR span, the voltage decreases linearly with the increasable output current.

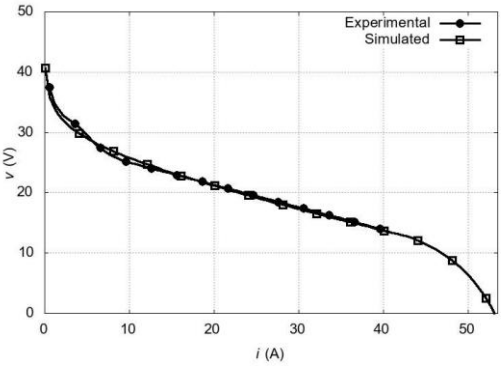

Fig. 7. Current-voltage curve of a 580W PEMFC

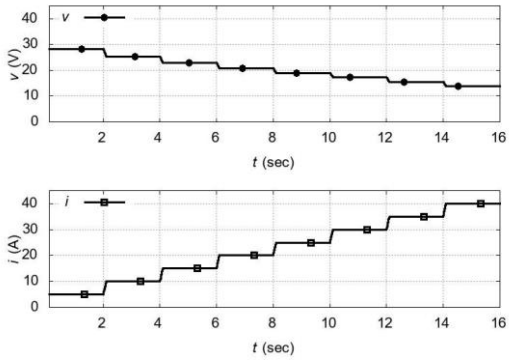

Fig. 8. Response of the PEMFC stack to an upward stair stimulus

In figure 9 is shown the voltage of the battery module in discharge-mode with three different constant discharge current rates: 3C, 2C and 1C. The Fig. 10 displays the expected diminution of battery SOC with the three constant discharge current rates respectively.

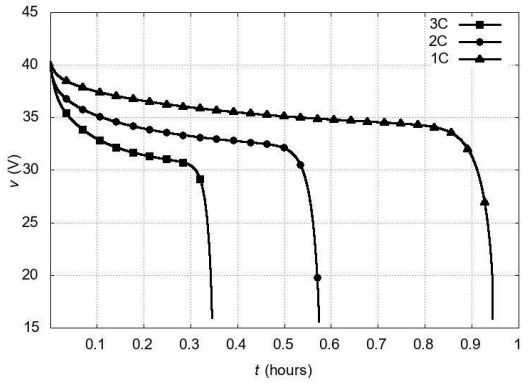

Fig. 9. Battery module voltage with three different discharge current rates.

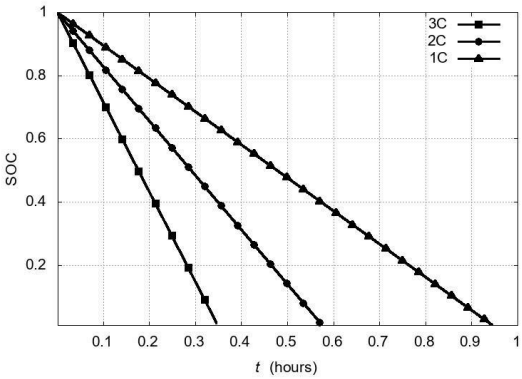

Fig. 10. Variation of SOC with three different discharge current rates.

Figure 11 exposes the behavior of the voltage v_b and current i_b of Li-ion battery module in charging- mode. In the first part of the recharging profile, the battery voltage slowly rises up as the control algorithm makes the battery current to remain stable at 0.45 times the nominal current (13A). Then, the control algorithm regulates the voltage at 42V as charging current exponentially decreases. The Fig. 12 shows the behavior of voltage *v* and current *i* of the PEMFC stack in charging-mode. In the first part of the recharging profile, the voltage falls from its open-circuit value and remains stable as an increasing output current is drawn from PEMFC stack. At the end of charging profile, the voltage grows toward its open-circuit value and the current exponentially goes down. This behavior demonstrates the sensitively response of the PEMFC voltage to changes on the battery current in charging-mode.

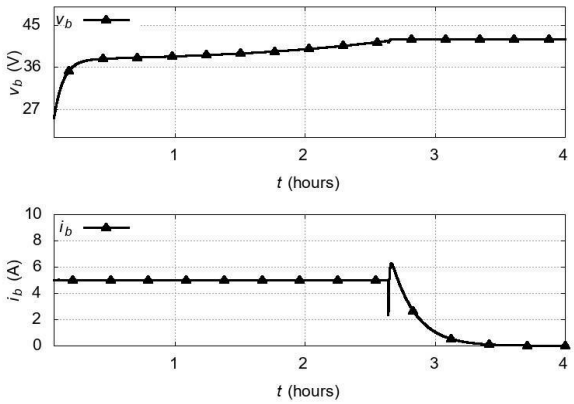

Fig. 11. Behavior of voltage and current of battery module in charging-mode.

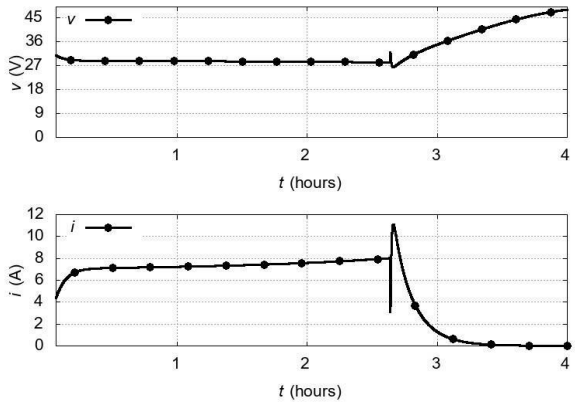

Fig. 12. Behavior of the voltage and current of PEMFC stack in charging-mode.

4. Conclusion

This paper shows the modeling and simulation of a PEMFC system for a hybrid electric vehicle. The PEMFC stack global properties was approximated by a simple non-linear equation and Li-Ion battery module was analyzed by expanding the parameters of a single cell. PEMFC *I-V* curve and transient response were independently studied with the proposed modeling. Li-Ion battery module discharge and estimated SOC examples demonstrates the functionality of a Li-Ion battery device in SPICE environment. Finally, the simulation findings of the entire PEMFC system were completed by showing the behavior of currents and voltages of PEMFC stack and battery module in charging-mode. The method and simulations outlined in this paper can be adapted to other oversized PEMFC systems for EV by modifying some other important parameters.

Acknowledgements

This work was supported with funding granted by projects CONACYT-246920 and SEP-CINVESTAV-015.

References

[1] Rodríguez-Castellanos, A., et al. Development and applications of portable systems based on conventional PEM fuel cells, in Portable Hydrogen Energy Systems. Academic Press, 2018. 91-106.

[2] Bagotsky, V.S., 2009. In Fuel Cells: Problems and Solutions. ECS-John Wiley & Sons, New Jersey.

[3] D. Chu, R. Jiang and C. Walker, Analysis Of PEM Fuel Cell Stacks using an Empirical Current-Voltage Equation. Journal of Applied Electrochemistry 30: 365–370 (2000). https://doi-org.access.biblioteca.cinvestav.mx/10.1023/A:1003905109007.

[4] Squadrito, G., Maggio, G., Passalacqua, E. et al. An Empirical Equation For Polymer Electrolyte Fuel Cell (PEFC) Behaviour. Journal of Applied Electrochemistry 29, 1449–1455 (1999). https://doi-org.access.biblioteca.cinvestav.mx/10.1023/A:1003890219394.

[5] Ticianelli, E. A., Derouin, C. R., Redondo, A., & Srinivasan, S. (1988). Methods to Advance Technology of Proton Exchange Membrane Fuel Cells. Journal of The Electrochemical Society, 135(9), 2209-2214.

[6] Yu, D., & Yuvarajan, S. (2004, February). A Novel Circuit Model for PEM Fuel Cells. Nineteenth Annual IEEE Applied Power Electronics Conference and Exposition, 2004. APEC'04. (Vol. 1, pp. 362-366). IEEE.

[7] Jia, J., Li, Q., Wang, Y., Cham, Y. T., & Han, M. (2009). Modeling and Dynamic Characteristic Simulation of a Proton Exchange Membrane Fuel Cell. IEEE Transactions on Energy Conversion, 24(1), 283-291.

[8] Musio, Fabio, et al. PEMFC system simulation in MATLAB-Simulink® environment, International Journal of Hydrogen Energy 36.13 (2011): 8045-8052.

[9] Chen, M., & Rincon-Mora, G. A. (2006). Accurate Electrical Battery Model Capable of Predicting Runtime and I-V Performance. IEEE transactions on Energy Conversion, 21(2), 504-511.

[10] Seaman, A., Dao, T. S., & McPhee, J. (2014). A Survey of Mathematics-Based Equivalent-Circuit and Electrochemical Battery Models for Hybrid and Electric Vehicle Simulation. Journal of Power Sources, 256, 410-423.

[11] Hageman, S. C. (1993). Using PSpice to Simulate the Discharge Behavior of Common Batteries. EDN Mag, 260-286.

[12] Piller, S., Perrin, M., & Jossen, A. (2001). Methods For State-of-Charge Determination and their Applications. Journal of Power Sources, 96(1), 113-120.

[13] Kroeze, R. C., & Krein, P. T. (2008, June). Electrical Battery Model for Use in Dynamic Electric Vehicle Simulations. In 2008 IEEE Power Electronics Specialists Conference (pp. 1336-1342). IEEE.

[14] Gao, L., Liu, S., & Dougal, R. A. (2002). Dynamic Lithium-Ion Battery Model for System Simulation. IEEE transactions on components and packaging technologies, 25(3), 495-505.

[15] He, H., Xiong, R., Guo, H., & Li, S. (2012). Comparison Study on The Battery Models Used for the Energy Management of Batteries In Electric Vehicles. Energy Conversion and Management, 64, 113-121.

[16] Jongerden, M. R., & Haverkort, B. R. H. M. (2008). Battery Modeling. Enschede, January, 38.

[17] Dennis Dennis Fitzpatrick, Analog Behavioral Models, in Analog Design and Simulation Using OrCAD Capture and PSpice, Second Edition, ISBN: 9780081025062, 452 pages.

[18] Duran P.A. (1998) Modeling and Simulation Background, in A Practical Guide to Analog Behavioral Modeling for IC System Design. Springer, Boston, MA. https://doi.org/10.1007/978-1-4419-8630-6_2.

[19] Holger Vogt, Marcel Hendrix, and Paolo Nenzi, Mixed-Mode and Behavioral Modeling with XSPICE, in NGSPICE User's Manual Version 32, May 2nd, 2020. Available in: http://ngspice.sourceforge.net/docs/ngspice-manual.pdf

[20] R.W. Erickson and D. Maksimovic , Circuit Averaging and Averaged Switch Modeling, in Fundamentals of Power Electronics, Second edition, ISBN: 0-7923-7270-0, pp. 226-247.

[21] Kim, Dong Myung, Rechargeable Lithium Ion Battery Model INR18650 M26, LG Product Specification, Document No. LRB-PS-CY2600-M26, Date: 2015-04-08, Rev. 0

ID 026

Influence of resorcinol-formaldehyde molar ratio in the properties of Mesoporous Carbon Supports for PEMFC Catalysts

E.T. Zanoni, R. Benavides, L. Da Silva, D. Morales-Acosta*

Centro de Investigación de Química Aplicada, Blvd Enrique Reyna No. 140, Col. San José de los Cerritos, 25290. Saltillo, Coahuila, México
* Corresponding author: diana.morales@ciqa.edu.mx

ABSTRACT

Carbon materials from mesoporous phenolic resins are considered an advanced class of high-stable mesoporous materials with potential application as fuel cell support electrodes. The performance of these carbons depends greatly of the structure and purity of polymeric precursors, and could be easily controlled to get the final properties required. Resorcinol-formaldehyde (RF) resins, with 1:2 and 1:3 molar ratios, were synthesized using Pluronic ® F127 as structure director. Synthesized RF resins were subsequently carbonized at 700 °C to obtain mesoporous carbon (MC). RF resins and their corresponding MC were characterized by FT-IR, TGA, RAMAN, TEM, BET and SAXS techniques. The obtained results indicate that resin with R/F=1:3 shows a greater thermal stability near to 300 °C and a higher percentage of residues, which in turn suggests an enhanced crosslinking mechanism. For the MC obtained from this resin (R/F= 1:3) a disordered structure and a low specific surface area value (S_{BET} = 35.9 m^2/g) was observed. In contrast, a highly ordered mesostructure was obtained for the MC from the resin R/F=1:2, with larger pore size (7 nm) and the highest specific surface area (S_{BET} = 107 m^2/ g); a partial crystalline mesostructure was confirmed by SAXS. In the RAMAN spectrum for the carbonized samples, two peaks were observed, corresponding to amorphous carbon (peak D at 1333 cm^{-1}) and crystalline graphite (peak G at 1598 cm^{-1}), with an intensity ratio (I_D / I_G) of 0.86 for both MC, indicating a high order of crystalline graphite regardless of the R/F molar ratio. The results suggest that a low content of formaldehyde in the resin promotes the formation of a mesophase during the polycondensation reaction, generating a carbon material with better textural properties for their application as electrodes in fuel cells.

Keywords: *Resin, Resorcinol-Formaldehyde, Mesopores, Carbon*

1. Introduction

A fuel cell (FC) is an electrochemical device, which converts the chemical energy of a fuel directly into electrical energy [1]. These are considered as an alternative for the generation of clean and efficient energy, with application in both portable devices and automobiles. In a FC, the electrodes are responsible for the energy conversion, through electrochemical reactions. In electrodes, nanostructured carbon materials with different morphologies and unique characteristics have been extensively studied as a support material for nanoparticulate catalysts (eg Pt and Pd) [2,3]. Among the various carbon structures, mesoporous carbon (MC) has attracted attention for its characteristics as high surface area, chemical, physical and thermal stability, in addition to its abundant mesopore structure that promote rapid mass transfer and diffusion of ions [4].

In recent decades, various methods have been developed to obtain MC, among which the two best-known routes are: hard-templating and soft-templating. The soft-templating method is simpler, requires fewer steps and is more economical. This method consists of using block copolymers, the best known and used being poly (ethylene oxide) -b-poly (propylene oxide) -b-poly (ethylene oxide) of the Pluronic® family [5]. In a polymerization reaction for the formation of resins, Pluronic®, acts in situ as a directional agent of structure between resorcinol or phenol, with formaldehyde. Resorcinol is chemically similar to phenol; however, the additional hydroxyl gives it greater reactivity, obtaining 3 reactive sites located in the hydrogens adjacent to the hydroxyl (ortho and para positions of the ring), obtaining a polymeric structure as indicated in the Figure 1.

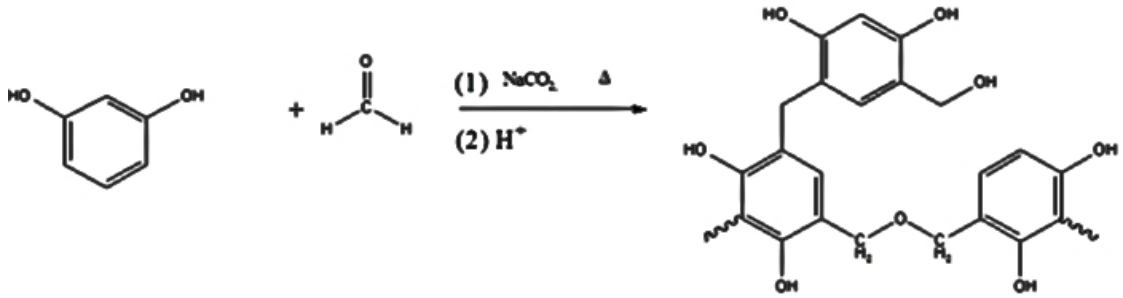

Fig. 1. Scheme of polymerization between resorcinol and formaldehyde.

From the RF resin, followed by heat treatment (carbonization) at high temperatures, the MC is obtained [6–9]. Various materials with a mesoporous structure, obtained from this resin, have been evaluated as a catalytic support [10]. Obtaining MC with a relatively long pore structure is important in the application as a catalytic support in fuel cells that use gaseous or liquid fuels, since fuel diffusion is essential for its performance. Although this method has been successful for the preparation of MC with different mesopore geometry, the influence of the R / F ratio on the textural properties still remains a challenge in obtaining MC.

In this work, the influence of the molar ratio of resorcinol-formaldehyde (RF) on the synthesis of organic resins for subsequent preparation of mesoporous carbon (MC) is evaluated in terms of chemical, structural, thermal and textural properties.

2. Materials and Methods

2.1 Reagents

Resorcinol, 37% formaldehyde (wt), anhydrous sodium carbonate, Pluronic F127® and sodium hydroxide were purchased from Sigma-Aldrich. HCl 37% (wt) was obtained from Fermont.

2.2 Synthesis of RF resins

The synthesis of the resins resorcinol-formaldehyde (RF) was performed using the method described by Pekala [11] and adapted in the working group [10]. Two different molar ratios of R: F: 1: 2 and 1: 3 were considered, using Pluronic ® F127 as structure director. The obtained resins were labeled as RF1 and RF2, respectively.

For the synthesis of RF1 resins, 8.8 g (0.08 mol) of resorcinol were reacted with 11.9 ml (0.16 mol) of formaldehyde, together with 0.044 g (0.41 mmol) of anhydrous sodium carbonate. The mixture was stirred for 1 h and then a solution containing 12.8 g of Pluronic® F127 in 50 ml of ethanol and 32 ml of distilled water was added, the system remaining for more 1 hour under stirring. Subsequently, a 16 ml volume of a 2 M HCl solution was slowly added into the system to catalyze the polycondensation and generate polymer gel. All stages of synthesis occurred at room temperature. The gel was cured in an oven for 24 hours at 60 °C. For the RF2 resin, the same procedure was followed, reacting 8.8 g (0.08 mol) of resorcinol with 17.8 ml (0.24 mol) of formaldehyde.

2.4 Carbonization

The RF1 and RF2 resins were heat-treated in a tubular furnace in an inert N_2 atmosphere for 3 hours at 700 °C with a heating ramp of 2 °C/min to obtain MC. The carbonized samples were named respectively RF1-700 and RF2-700.

2.5 Characterization

The thermogravimetry (TGA) characterization of the RF resins was performed on a TA Instruments Q500, up to 700 °C with a heating ramp of 10 °C/min. The carbonized samples were evaluated by Raman spectroscopy in a confocal µsurf Horiba XploRA microscope equipped with a 532 nm laser. The specific surface area and mean pore size of carbonized RF resin were evaluated on a Quantachrome AutosorbIQ. Before measurements, the samples were degassed at 250 °C for 10 hours under vacuum conditions. The surface area was determined using the Brunauer-Emmett-Teller (BET) method with N_2 adsorption-desorption isotherm and the mean pore size using the Barrett-Joyner-Halenda (BJH) method derived from the desorption isotherm. Small-angle X-ray scattering (SAXS) measurements were performed at a Bruker NanoStar equipped with a

turbo rotating anode (50 kV and 50 mA), Göbel mirrors selecting Cu Kα radiation (1.5418 Å) and a Vantec 2D detector. The SAXS patterns were corrected for empty cell scattering and sample transmission. Transmission electron microscopy (TEM) was performed on a FEI model TITAN 80-300kv equipment to analyze the morphology of the samples. FT-IR spectra of resin before and after the carbonization process were obtained in a Bruker Vertex 70V infrared spectrometer by transmission technique using KBr tablets.

3. Results and Discussion

Figure 2 shows the thermal characterization results obtained by TGA for RF1 and RF2 resins. In the thermogram, it is possible to observe the resins degradation occurs in various stages, registering two important weight losses with the greatest above 300 ° C. The first weight loss (<130 °C) is due to the decomposition of remaining water. The second loss in weight (130-270 °C) can be related to condensation reactions of remaining groups and release of water in the resins. RF2 presents a superior thermal stability on the entire temperature range, and greater quantity of carbonaceous residues compared with RF1, which can be related to the high content of formaldehyde, compared to RF1. This is confirmed by the

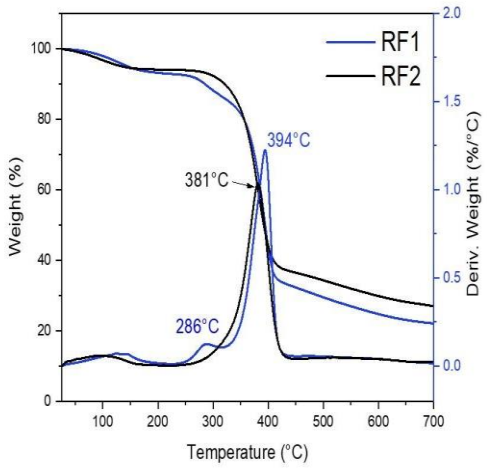

Fig. 2. Thermograms (TGA / DTGA) for the RF1 and RF2 resin samples.

The RF1 and RF2 resins were heat treated at 700 °C to obtain mesoporous carbon, being named RF1-700 and RF2-700, respectively. RF1-700 and RF2-700 were characterized by FT-IR, Raman, SAXS TEM, and BET nitrogen adsorption/desorption technique. The FT-IR spectra for the RF1-700 and RF2-700 carbonized resins are shown in Figure 3A. Both resins present the same main bands after carbonization process: at 3442 cm^{-1} is related groups -OH, related from adsorbed water or from hydroxyl groups incorporated in the surface of the pores of the graphitic material. At 1577 cm^{-1} is assigned to the vibration of C=C of the material and at ~ 1100 cm^{-1}, characteristic of a type bond (C-O-C), which can be from the ether bond generated in the synthesis of the resin, as reported in the literature [12,13].

Figure 3B shows the Raman spectra obtained for the resins (RF1-700 and RF2-700). Both resins exhibit the D-band related to disorder-induced, and G band corresponding to crystalline graphitic structures. The first at ~ 1333 cm^{-1} (D-band) is assigned to C-C bonds with sp^3-type hybridization, characterized by single and tetragonal bonds in the carbonaceous material. This band is associated with the defects created in the structure and the disorder introduced in the carbon network. The second at 1598 cm^{-1} (G-band) is related to sp^2-type bonds present in the graphite phase. The presence of G-band confirms that the materials structure is mainly composed of graphitic carbon, although with some an amorphous component. The intensity ratio of the D and G bands (I_D / I_G) is associated with evolution with the degree of graphitization and disorder in sp^2-hybridized carbon. The calculated I_D / I_G values for samples RF1-700 and RF2-700 were 0.87 and 0.86, respectively, indicating that the degree of graphitization and defects are very similar.

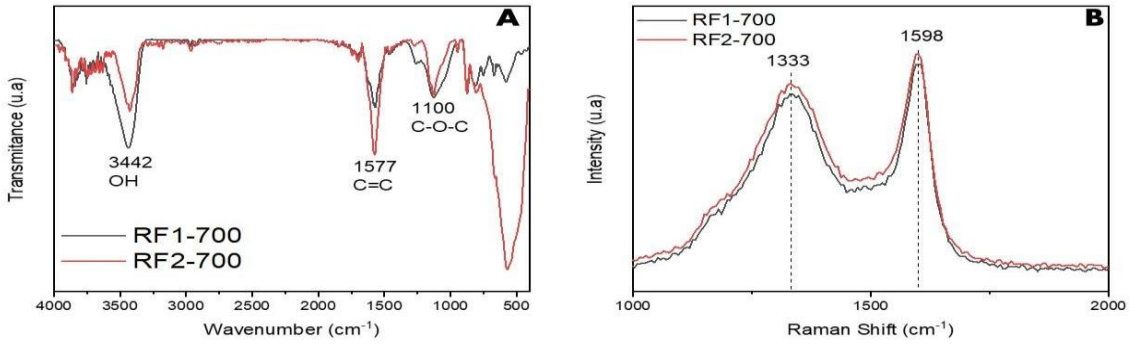

Fig. 3. FT-IR spectra (A) and RAMAN (B) spectra for carbonized resins.

The textural properties were analyzed using N_2 adsorption-desorption isotherms. As seen in Figure 4A, the isotherm for RF1-700 shows a type IV isotherm with a type H4 hysteresis loop, which is a behavior associated with capillary condensation in mesopores and confirming the formation of mesopores. In contrast, RF2-700 shows a type I isotherm, characteristic of microporous materials. The latter is confirmed by pore size distribution that varies from 5 to 15 nm with a surface area of 107 m^2 / g for sample RF1-700. This value is considerably greater compared to RF2-700 (20 m^2 / g). The observed differences are attributed to the higher formaldehyde molar ratio in RF2-700, that generates a more closed crosslinked polymeric structure and, consequently, smaller size and total pore volume (V_t) are observed for RF2-700 with a V_t value of 0.103 cm^3 / g versus 0.675 cm^3 / g for RF1-700.

In addition, SAXS pattern for RF1-700 shows a well-resolved scattering peak around q= 0.46 nm^{-1}, which has been assigned to C (100), suggesting some ordered mesoporous with 2D structure. In contrast, no peak was observed for RF2-700.

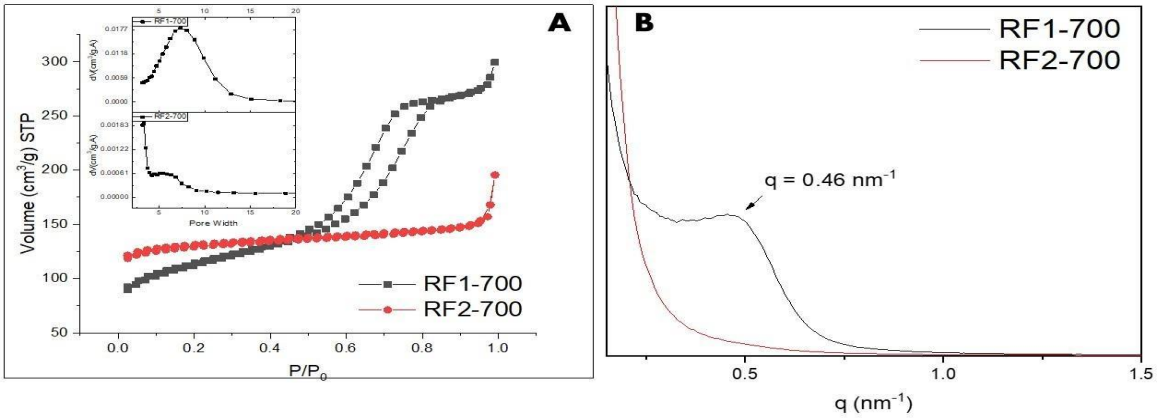

Fig. 4. Adsorption-desorption isotherms (A) and small angle X-ray scattering (SAXS) (B) for carbonized resins.

Figure 5 shows TEM images of the carbonized resin samples. For sample RF2-700 (C-D), it was possible to observe the presence of micro and mesopores with a disordered structure known as worm-like [9], which is according to N_2 adsorption-desorption isotherm and SAXS observations.

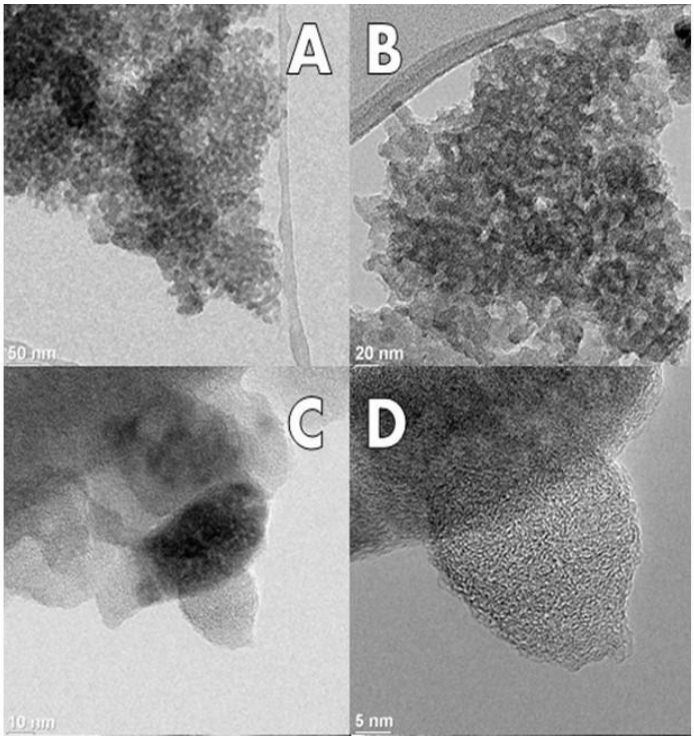

Fig. 5. Transmission microscopy images for RF1 and RF2 carbonized resins at 700 ° C: RF1-700 (A-B) and RF2-700 (C-D).

4. Conclusion

Formaldehyde and resorcinol resins were successfully synthesized in proportions of 1: 2 and 1: 3 (R:F), with higher thermal stability for the resin with high F content (RF2). For RF1-700 a mesoporous structure was obtained, with a pore size distribution from 5 to 15 nm and a surface area of 107 m^2 / g. The obtained results suggest the formaldehyde molar ratio has a direct effect on textural properties due to a high degree of crosslinking. The higher R / F molar ratio provided lower texture properties, presenting lower volume and pore size, making it difficult to obtain an ordered mesoporous structure. This may be related to the crosslinking of the resin caused by excess formaldehyde. In summary, the resin with a 1:2 ratio of resorcinol-formaldehyde obtained the best results with promising results to obtain mesoporous carbon for electrochemical applications in fuel cells.

Acknowledgements

Authors acknowledge to CONACyT through grants FC3004 and CB259010, and PhD scholarship for ETZ.

References

[1] Goor M, Menkin S, Peled E. High power direct methanol fuel cell for mobility and portable applications. Int J Hydrogen Energy 2019;44:3138–43. https://doi.org/10.1016/j.ijhydene.2018.12.019.
[2] Samad S, Loh KS, Wong WY, Lee TK, Sunarso J, Chong ST, et al. Carbon and non-carbon support materials for platinum-based catalysts in fuel cells. Int J Hydrogen Energy 2018;43:7823–54. https://doi.org/10.1016/j.ijhydene.2018.02.154.
[3] Antolini E. Carbon supports for low-temperature fuel cell catalysts. Appl Catal B Environ 2009;88:1–24. https://doi.org/10.1016/j.apcatb.2008.09.030.
[4] Hwang SW, Hyun SH. Capacitance control of carbon aerogel electrodes. J Non Cryst Solids 2004;347:238–45. https://doi.org/10.1016/j.jnoncrysol.2004.07.075.
[5] Chuenchom L, Kraehnert R, Smarsly BM. Recent progress in soft-templating of porous carbon materials. Soft Matter 2012;8:10801–12. https://doi.org/10.1039/c2sm07448f.
[6] Zanto EJ, Al-Muhtaseb SA, Ritter JA. Sol-gel-derived carbon aerogels and xerogels: Design of experiments approach to materials synthesis. Ind Eng Chem Res 2002;41:3151–62. https://doi.org/10.1021/ie020048g.
[7] Lin C, Ritter JA. Carbonization and activation of sol-gel derived carbon xerogels. Carbon N Y 2000;38:849–61. https://doi.org/10.1016/S0008-6223(99)00189-X.
[8] Sanchez-Sanchez A, Izquierdo MT, Medjahdi G, Ghanbaja J, Celzard A, Fierro V. Ordered mesoporous carbons obtained by soft-templating of tannin in mild conditions. Microporous Mesoporous Mater 2018;270:127–39. https://doi.org/10.1016/j.micromeso.2018.05.017.
[9] Xu J, Wang A, Zhang T. A two-step synthesis of ordered mesoporous resorcinol–formaldehyde polymer and carbon. Carbon N Y 2012;50:1807–16. https://doi.org/10.1016/j.carbon.2011.12.028.

[10]Morales-Acosta D, Rodríguez-Varela FJ, Benavides R. Template-free synthesis of ordered mesoporous carbon: Application as support of highly active Pt nanoparticles for the oxidation of organic fuels. Int J Hydrogen Energy 2016;41:3387–98. https://doi.org/10.1016/j.ijhydene.2015.10.114.
[11]Pekala RW. Organic aerogels from the polycondensation of resorcinol with formaldehyde. J Mater Sci 1989;24:3221–7. https://doi.org/10.1007/BF01139044.
[12]Merline DJ, Vukusic S, Abdala AA. Melamine formaldehyde: Curing studies and reaction mechanism. Polym J 2013;45:413–9. https://doi.org/10.1038/pj.2012.162.
[13]Elkhatat AM, Al-Muhtaseb SA. Advances in tailoring resorcinol-formaldehyde organic and carbon gels. Adv Mater 2011;23:2887–903. https://doi.org/10.1002/adma.201100283.

ID 027

Synthesis of Random Polystyrene-co-Acrylonitrile-co-Butyl Acrylate Terpolymers as potential solid electrolytes for fuel cells

L.G. Delgado Interial, R. Benavides*, L. Da silva*, D. Morales-Acosta, L. Francisco-Vieira

Centro de Investigación en Química Aplicada, Blvd. Enrique Reyna H. 140, Saltillo Coah. 25294
* E-mail: roberto.benavides@ciqa.edu.mx, luciano.dasilva@ciqa.edu.mx

ABSTRACT

Nafion® electrolytes in fuel cells have been the most commercialized polymeric membranes; even though it has some drawbacks such as high cost and limited operating temperature (<100°C). Styrenic sulfonated membranes are an alternative to Nafion®, since polystyrene is a low-cost material with processing feasibility and high mechanical properties. However, it has also some drawbacks, like a low flexibility and a poor chemical resistance. Copolymerization techniques have been implemented to enhance mechanical and chemical properties of polystyrene. Terpolymers containing styrene (St) as a molecular base, butyl acrylate (BuA) as flexible component and acrylonitrile (ACN) to enhance chemical stability, were prepared by free radical polymerization. Several molar composition ratios of the St:ACN:BuA were prepared: 70:10:20, 70:15:15, 70:20:10, 80:05:15, 80:10:10 and 80:15:05. FTIR vibrational bands indicate the formation of terpolymers and ^{1}H and ^{13}C NMR chemical shifts from the corresponding functional groups associated with the comonomers confirmed the proposed structure, even though some differences in comonomer composition. The terpolymers exhibited the ability of forming a flexible film and showed variations in solubility with respect to pure polystyrene. According to GPC, terpolymers showed MW values up to 150,000 g/mol. DSC thermal analysis indicated Tg values from 64 to 80ºC, depending on the content of comonomers, while TGA showed decomposition temperatures over 350°C. Complex modulus values obtained from TMA flexure experiments decrease along the content of BuA (~3600 to 1500 MPa); on the contrary, when ACN content is increased, modulus goes from ~3600 to 4500 MPa.

Keywords: Polystyrene membranes; terpolymers; solid electrolytes; fuel cells

1. Introduction

Due to its chemical structure and its excellent properties, Nafion® has been the most employed membrane for its use as an electrolyte in PEM fuel cells. [1]. The Nafion® membrane has a structure of a copolymer, which consists of a perfluorinated basic structure (fluoro 3,6-dioxo 4,6-octane) and sulfonic acid ends [2]. Nafion® membranes have excellent mechanical, chemical and proton conductivity properties, attributed to its complex structure [3]. The perfluorinated structure contributes to the hydrolytic and oxidative stability (hydrophobic domain), and the sulfonic acid in the structure (ionic part) promotes the ionic exchange (hydrophilic domain). Despite the attractive properties of perfluorosulfonic membranes, they have a high cost, its efficiency dramatically decreases at elevated temperatures (80-100°C) and low humidity (<40%) [4] and exhibits high methanol permeability in DMFCs (Direct Methanol Fuel Cells) that hinders their application. Due to such drawbacks, other not perfluorinated polymers have been considered, for example, Polyetheretherketone (PEEK), Polybenzimidazole (PBI), Polystyrene (PS), etc [5]. In particular, Polystyrene has been of great interest, due to its low cost and processing feasibility. Also, when polystyrene is sulfonated (PSS), it exhibits ion exchange capacity. Nevertheless, polystyrene (PS) has some drawbacks, as its stiffness and poor chemical resistance. Due to this, styrene copolymerization techniques, have been implemented to improve its mechanical and chemical properties [6]·[7].
This work is the search of a polymer basis involving novel random terpolymers of polystyrene-co-acrylonitrile-co-butyl acrylate in different compositions, synthesized by free radical polymerization to enhance chemical and mechanical properties in polystyrene. Such materials could be further sulfonated to provide ion exchange properties, to use them as PEM membranes.

2. Materials and Methods

2.1 Materials

Monomers of Styrene (St, 99%, Aldrich), Acrylonitrile (ACN, 99%, Aldrich) and Butyl Acrylate (BuA, 99%, Aldrich) were purified to remove inhibitors. Benzoyl Peroxide (BPO, Aldrich) to use as initiator and tetrahydrofuran (THF, 98%, J. T Baker), ketone (98%, J. T Baker), methanol (≥99%, Aldrich), chloroform, dichloromethane (98%, J. T Baker) and deutered chloroform ($CDCl_3$, ≥99%) used as solvents.

2.2 Methods

2.2.1 Copolimerization

The terpolymers were prepared by bulk free radical copolymerization. The St:ACN:BuA molar compositions employed were: 70:10:20, 70:15:15, 70:20:10, 80:05:15, 80:10:10 and 80:15:05. Reactions were carried out at 100°C for 4 h in a glass reactor, under inert atmosphere (N2) and reflux (Figure 1). The obtained terpolymers were solubilized in dichloromethane and precipitated in methanol to remove residual monomer three times. After, the terpolymers were dried at 40°C for 48 h, the scheme of reaction is presented in Figure 1.

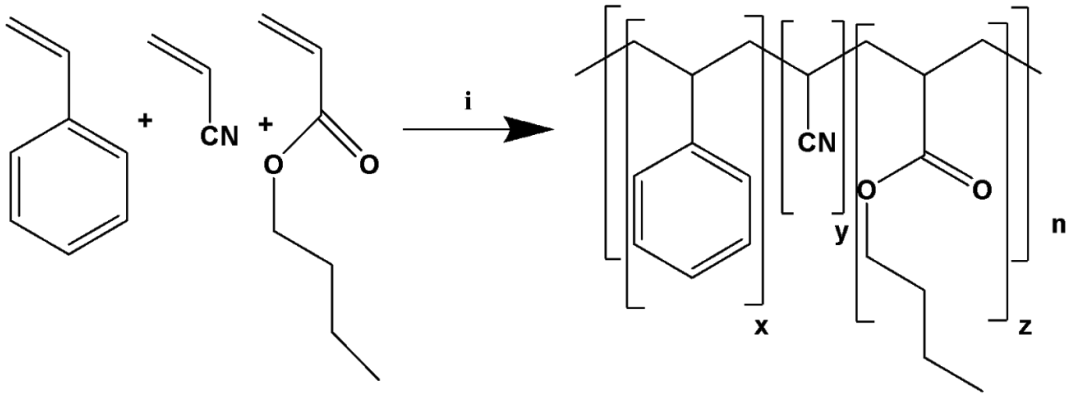

Figure 1. Reaction scheme of free radical polymerization of styrene, acrylonitrile and butyl acrylate. (i) : 4h, N2, BPO, 100°C, stirring and reflux. 70% of yield.

2.2.2 Membranes

For all synthesized compositions, films of terpolymers were prepared by casting. The general procedure was: 2mg of terpolymers were solubilized in 2ml of chloroform and were poured into a mold. The solvent was evaporated and the film was carefully removed.

2.3 Characterization

Chemical structure of random terpolymers was analyzed by Fourier Transform Infrared Spectrometer (FTIR-Bruker Vertex 70) in transmission-mode at 64 scans and also corroborated by Nuclear Magnetic Resonance Spectroscopy (NMR-Bruker Avance 3 400Mhz) of ^{1}H and ^{13}C using $CDCl_3$ as a solvent and TMS as the standard reference. Molecular weight and its distribution were analyzed by GPC (Waters Alliance 2695), using polystyrene as the standard (DLS and UV detectors). Solubility tests were carried out in different solvents (H_2O, methanol, ketone, chloroform, dichloromethane and tetrahydrofuran). Thermal stability properties were analyzed by TGA using a Linseis STA instrument with a heating speed of 10°C·min^{-1} and N_2 atmosphere. Vitreous transitions were analyzed by DSC (TA Instruments Q2000) at 10°C·min^{-1} from -54 to 260°C. Mechanical properties were analyzed by thermomechanical analysis using a TA Instruments Q400 in flexure mode (three points), isothermal (35°C) and applying a force ramp of 0.001 to 0.010 N at 0.001 N.min^{-1}.

3. Results and Discussion

The molecular structure of the random terpolymers prepared was corroborated with FTIR, were all characteristic vibrational bands of the comonomers are observed in the spectra (Figure 2). The vibrational band belonging to styrene comonomer (δC-H) is shown at 3160-3060 cm^{-1} and the ones related to the stretching of (C=C) are at 1600cm^{-1}, 1492cm^{-1}and 1450cm^{-1} [8]. The typical vibrational band related to the comonomer acrylonitrile (C≡N) is observed at 2236 cm^{-1}, and the one for Butyl acrylate (C=O) is observed at 1728 cm^{-1}[9].

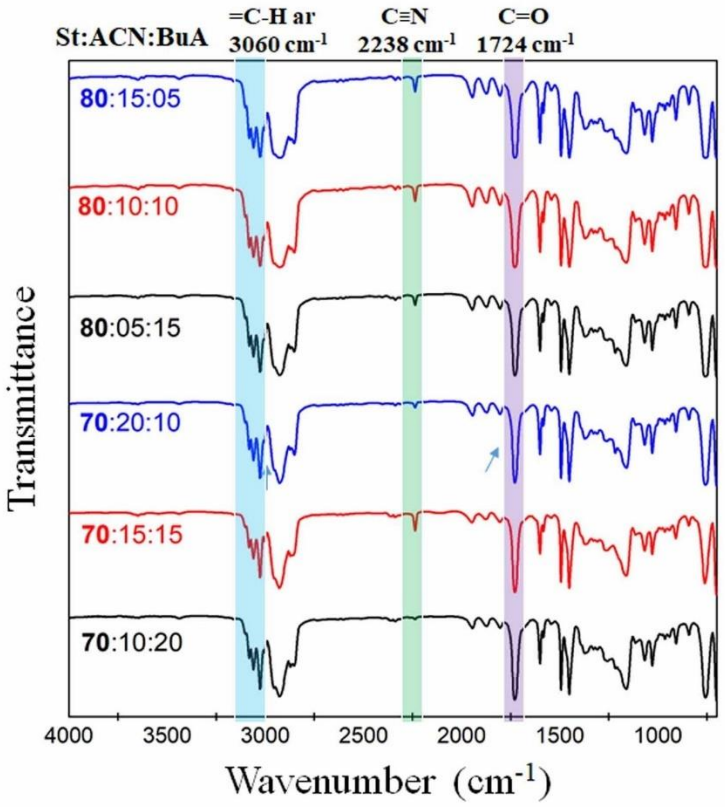

Figure 2. Random terpolymers FTIR spectra for all compositions.

The NMR spectra also confirmed the random terpolymer formation, by showing the correspondent shifting signals of their comonomers. The compositions were also analyzed by ^{1}H and ^{13}C ig (Inverse gated decoupling sequence) [10] as seen in Figure 3b and 3c respectively.

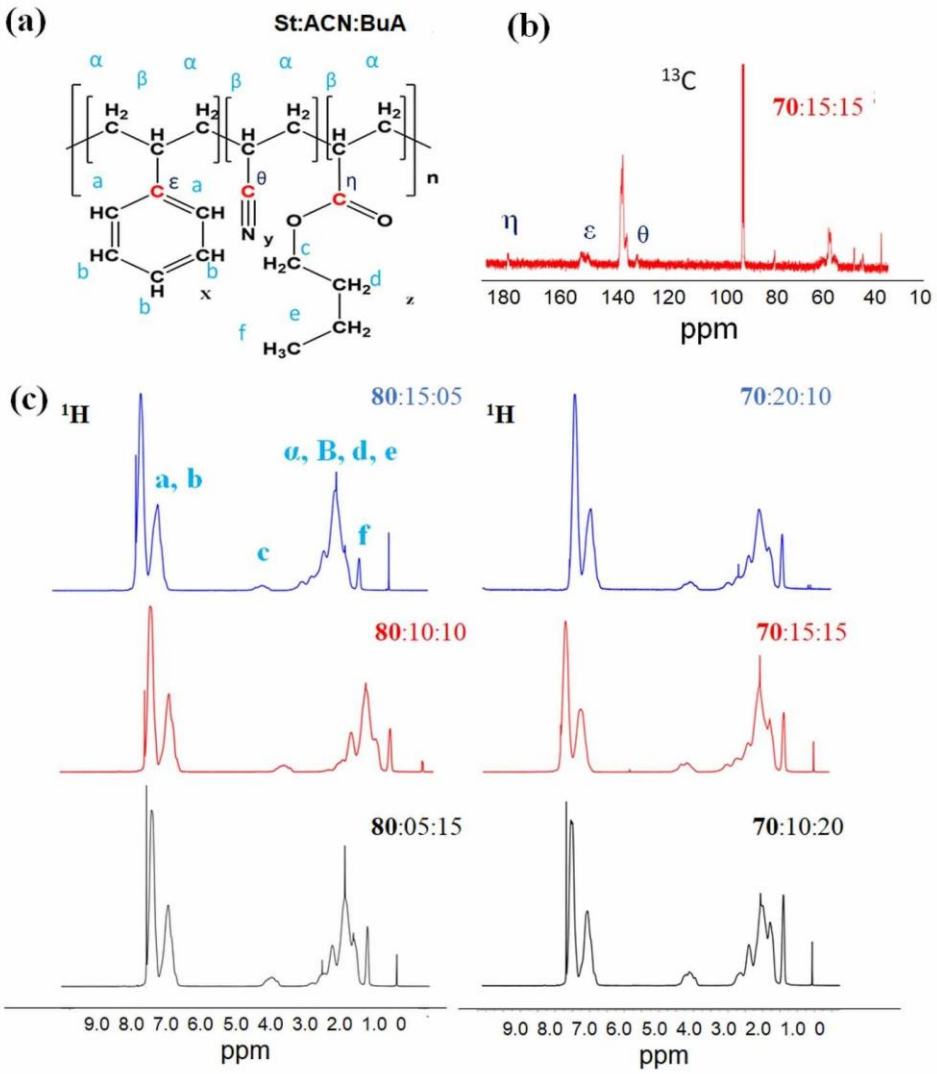

Figure 3. (a) Chemical structure, (b) ^{13}C-NMR spectra for 70:15:15 and (c) ^{1}H-NMR spectra of terpolymers.

The methylene (-CH2) and methine (-CH) protons of the random terpolymers overlap in the region 1.25–3.20 ppm (indicated as α and β in Figure 3b). The aromatic protons of polystyrene, shift as a multiplet around 6.4–7.5 ppm [11]. The protons for butyl acrylate (BuA), (-OCH_2-) are observed on 3.4 to 4 ppm and the terminal methyl from the pending chain (-CH_3) appears at 0.90 ppm (Figure 3c).

A representative carbon spectrum for all compositions is shown in Figure 3b and the important carbons from the functional groups of comonomers were analyzed in the region 100-180 ppm. The different carbon from aromatic system from polystyrene were observed as multiplets around 138–146.5 ppm. The carbon from carbonyl group (-C=O) from butyl acrylate shows multiplets around 173–178.5 ppm, while the quaternary carbon from acrylonitrile (-C≡N) has signals around 124 ppm.

Reactivity of comonomers during copolymerization reactions are important, being the reason of exothermicity and providing different composition than raw comonomers ratio predicts. The reactivity of comonomers at 80-100°C found in texts are [12],[13]: 0.39 (St), 0.20 (BuA) and (0.06) for ACN. Compositions calculated from ^{1}H and ^{13}C signals are shown in Table 1. It is observed that copolymerization reactions were affected for these reactivity values during the propagation step. It is possible to observe that styrene was the rich monomeric unit in the terpolymers, whereas, butyl acrylate held its composition closer to the desired composition and acrylonitrile composition was lower than the desired composition.

Table 1. Composition by ^{1}H-NMR and ^{13}C-NMR

Original Comonomer composition (%mol) St:ACN:BuA	**Calculated Composition**	
	^{1}H-NMR	**^{13}C-NMR**
70:10:20	80:02:18	-
70:15:15	70:15:15	70:13:17
70:20:10	85:09:06	76:15:09
80:05:15	85:09:06	-
80:10:10	81:00:00	-
80:15:05	76:19:05	80:13:07

Resistance to solvents was enhanced with the incorporation of comonomers, comparing with pure polystyrene, since they needed more time, mechanical stirring and temperature to reach solubility than pure polystyrene. In general, terpolymers dissolve simply by stirring in tetrahydrofuran and chloroform and needed stirring and heating for ketone and dichloromethane. Random terpolymers did not show solubility in water and methanol.

It is well known that atactic polystyrene exhibit high molecular weight, up to 100,000 with a distribution (D) around ~2 when is polymerized by free radicals[14]. On the other hand, polyacrylonitrile and polibutyl acrylate exhibit molecular weights of 86,000 and 100,000 respectively [15] [16]. The molecular weight and distribution of the random terpolymers prepared are shown in Figure 4, exhibiting Mw values over 100,000 and a relatively narrow and unimodal molecular weight distribution. The later conditions usually mean a high possibility to prepare membranes with them.

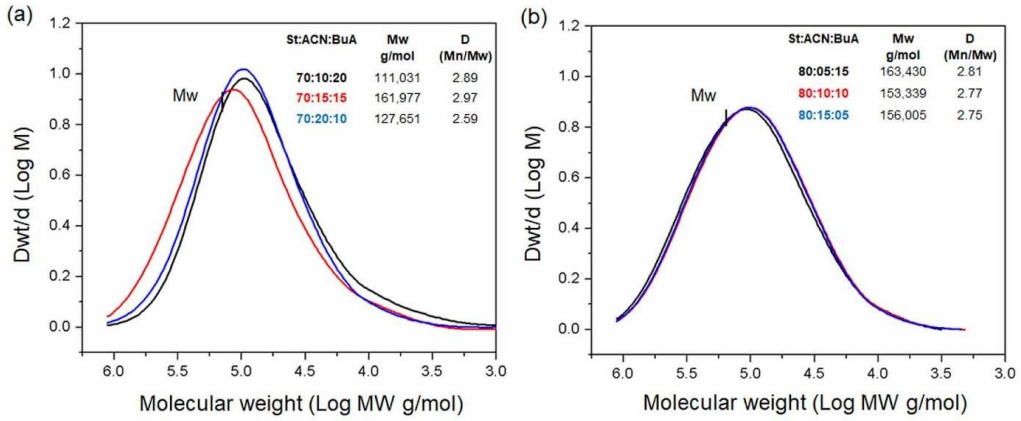

Figure 4. Molecular weight distribution of random terpolymers. a) 70% and b) 80% styrene.

Thermal studies are important to evaluate physical chemical properties, Figure 5 shows TGA traces and mechanical behavior along comonomer composition of terpolymers. Thermal stability is desired for polymers used in fuel cells since such devices work at low and high temperatures. Polystyrene by itself shows stability up to ~370°C [17] while copolymerized with acrylonitrile or butyl acrylate have stability around 350°C [9] [6]. TGA thermograms of random terpolymers show stability over 350ºC, as can be seen in Figure 5a. The weight loss happens in one step and is attributed to the decomposition of the main chain. This temperature allows its application as a polymer basis for further sulfonation.

Thermal transitions were analyzed by DSC and terpolymers didn't show any sign of crystallinity. The vitreous transition was affected by the content of comonomer: at high content of acrylonitrile, Tg increases closer to 100°C (Tg of Ps) and increasing BuA content, Tg value decreases down to 60°C. This is attributed to the Tg of the homopolymers (Tg of styrene is 100°C, PAN 105°C [9] and PBU 54°C).

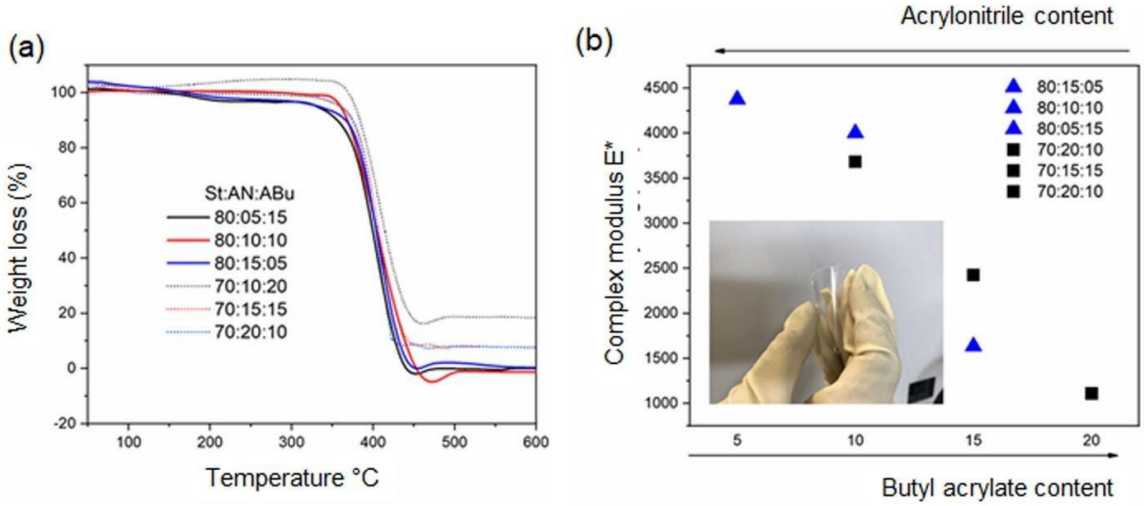

Figure 5. (a) Random terpolymers thermograms (TGA) and (b) Complex modulus (E*) of terpolymers obtained from TMA.

Complex modulus (E*), calculated from TMA experiments and representative of mechanical properties, follow the same trend as Tg values. Terpolymers decreased modulus when increasing Butyl acrylate (BuA) comonomer, attributed to its aliphatic chain mobility. On the other hand, the content of acrylonitrile increases modulus, due to the steric effect in the polymeric chains. Polystyrene by itself is related to a high complex modulus. The complex modulus values of random terpolymers are observed in Figure 5b.

4. Conclusion

The synthesis of random terpolymers St:AN:BuA in different compositions by bulk-free radicals polymerization was corroborated by FTIR and NMR. Reactivity of comonomers affected the composition of the pretended random terpolymers. Terpolymers presented molecular weight Mw values over 100,000 g/mol and unimodal distribution. They also showed resistance to different organic solvents and no solubility in methanol and water. Thermal analysis by TGA showed high thermal stability (up to 300°C), Vitreous transition by DSC, was affected by comonomers content: BuA promotes flexibility and acrylonitrile increases stiffness properties to the terpolymer. These results are promising for its use as a polymer basis for further sulfonation for its use as electrolytes in fuel cells.

Acknowledgements

This work has been supported by the Mexican Council of Science and Technology (CONACyT) through project FC-3004. The MSc grant given to LGDI from CONACyT is also appreciated.

References

[1] Rikukawa M, Sanui K. Proton-conducting polymer electrolyte membranes based on hydrocarbon polymers. Prog Polym Sci 2000;25:1463–502. doi:10.1016/S0079-6700(00)00032-0.

[2] Peighambardoust SJ, Rowshanzamir S, Amjadi M. Review of the proton exchange membranes for fuel cell applications. vol. 35. 2010. doi:10.1016/j.ijhydene.2010.05.017.

[3] Mulijani S, Dahlan K, Wulanawati A. Sulfonated Polystyrene Copolymer: Synthesis, Characterization and Its Application of Membrane for Direct Methanol Fuel Cell (DMFC). Int J Mater Mech Manuf 2013;2:36–40. doi:10.7763/ijmmm.2014.v2.95.

[4] Zhicheng Z, Elena C, Mark F, Chunmei W, Serguei NL, Sridhar K, et al. Synthesis and Characterization of Poly(vinylidene fluoride)-<italic>g</italic>-Sulfonated Polystyrene Graft Copolymers for Proton Exchange Membrane. Fuel Cell Chem Oper 2010;1040:31–48. doi:doi:10.1021/bk-2010-1040.ch003.

[5] Walkowiak-Kulikowska J, Wolska J, Koroniak H. Polymers application in proton exchange membranes for fuel cells (PEMFCs). Phys Sci Rev 2017;2:1–34. doi:10.1515/psr-2017-0018.
[6] Francisco-Vieira L, Benavides R, Cuara-Diaz E, Morales-Acosta D. Styrene-co-butyl acrylate copolymers with potential application as membranes in PEM fuel cell. Int J Hydrogen Energy 2019;44:12492–9. doi:10.1016/j.ijhydene.2019.01.181.
[7] Melo L, Benavides R, Martínez G, Morales-Acosta D, Paula MMS, Da Silva L. Mechanical properties and morphology of polystyrene-co-acrylic acid synthesized as membranes for fuel cells. Int J Hydrogen Energy 2017;42:21880–5. doi:10.1016/j.ijhydene.2017.02.210.
[8] Fang J, Xuan Y, Li Q. Preparation of polystyrene spheres in different particle sizes and assembly of the PS colloidal crystals. Sci China Technol Sci 2010;53:3088–93. doi:10.1007/s11431-010-4110-5.
[9] Silva ALA, Takase I, Pereira RP, Rocco AM. Poly(styrene-co-acrylonitrile) based proton conductive membranes. Eur Polym J 2008;44:1462–74. doi:10.1016/j.eurpolymj.2008.02.025.
[10] Giraudeau P, Baguet E. Improvement of the inverse-gated-decoupling sequence for a faster quantitative analysis of various samples by 13C NMR spectroscopy. J Magn Reson 2006;180:110–7. doi:10.1016/j.jmr.2006.01.015.
[11] Brar AS, Hekmatyar SK. Microstructure determination of the acrylonitrile-styrenemethyl methacrylate terpolymers by NMR spectroscopy. J Appl Polym Sci 1999;74:3026–32. doi:10.1002/(SICI)1097-4628(19991220)74:13<3026::AID-APP3>3.0.CO;2-C.
[12] Ziaee F, Nekoomanesh M. Monomer reactivity ratios of styrene-butyl acrylate copolymers at low and high conversions. Polymer (Guildf) 1998;39:203–7. doi:10.1016/S0032-3861(97)00249-8.
[13] Priddy DB. Thermal discoloration chemistry of styrene-co-acrylonitrile. Adv Polym Sci 1995;121:122–54. doi:10.1007/bfb0018580.
[14] Sisido M. Encyclopedia of Polymeric Nanomaterials. 2021. doi:10.1007/978-3-642-36199-9.
[15] Enzel P, Bein T. Poly(acrylonitrile) Chains in Zeolite Channels: Polymerization and Pyrolysis. Chem Mater 1992;4:819–24. doi:10.1021/cm00022a014.
[16] Beevers RB. Dependence of the glass transition temperature of polyacrylonitrile on molecular weight. J Polym Sci Part A Gen Pap 1964;2:5257–65. doi:10.1002/pol.1964.100021221.
[17] Liang XM, Jiang HC, Fang JL, Hua M, Pan XH, Jiang JC. Thermal analysis of the styrene bulk polymerization and characterization of polystyrene initiated by two methods. Chem Eng Commun 2019;206:432–43. doi:10.1080/00986445.2018.1494586.

Solid Oxide Fuel Cell: Metallic Interconnectors Analysis

José Juan Alvarado Flores[1, *], María Liliana Ávalos Rodríguez[2], José Guadalupe Rutiaga Quiñones[1], Jaime Espino Valencia[3] and Jorge Víctor Alcaraz Vera[4]

[1]Facultad de Ingeniería en Tecnología de la Madera, Universidad Michoacana de San Nicolás de Hidalgo. Santiago Tapia 403, CP 58000, Morelia, Michoacán, México.
[2]Centro de Investigación en Geografía Ambiental, Universidad Nacional Autónoma de México. Antigua Carretera a Pátzcuaro No. 8701, C.P. 58190, Morelia, Michoacán, México.
[3]Facultad de Ingeniería Química, Universidad Michoacana de San Nicolás de Hidalgo. Francisco J. Mújica S/N, Col. Felicitas del Rio, C.P. 58000, Morelia, Michoacán, México.
[4]Instituto de Investigaciones Económicas y Empresariales, Universidad Michoacana de San Nicolás de Hidalgo. Francisco J. Mújica S/N, Col. Felicitas del Rio, C.P. 58000, Morelia, Michoacán, México.
* Corresponding author: doctor.ambientalista@gmail.com

ABSTRACT

Today, alternative sources of energy have been considered as an option to reduce the cost of oil, because they are environmentally friendly and do not generate pollution as high as that derived from fossil fuels. In large-scale electricity generation systems, solid oxide fuel cells (SOFCs) offer several advances over other fuel cell technologies, because they can have a very high conversion efficiency (35-55%) and also have the ability to be used with a wide variety of fuels. Interest in SOFC stems from their higher efficiencies and lower levels of emitted pollutants, compared to traditional power production methods. Interconnects are a critical part in SOFC stacks, which connect cells in series electrically, and also separate air or oxygen at the cathode side from fuel at the anode side. Therefore, the requirements of interconnects are the most demanding, i.e., to maintain high electrical conductivity, good stability in both reducing and oxidizing atmospheres, and close thermal expansion coefficient (TEC) match and good compatibility with other SOFC ceramic components. This paper reviewed the interconnect materials, and coatings for metallic interconnect materials in a SOFC cell.

Keywords: solid oxide fuel cells (SOFC); interconnect; spinel; coating

1. Introduction

Fuel cells are energy conversion devices that produce electricity directly from a gaseous fuel by electrochemical combination of the fuel with an oxidant. Solid Oxide Fuel Cell (SOFC) technology has become an increasingly attractive method of power generation due to its low emissions, fuel flexibility and high efficiency compared to traditional energy conversion systems. The main applications of SOFCs are: stationary power generation, serving as an auxiliary power unit (APU) and military applications. The high operating temperature in this type of cell, compared to other types of fuel cells (PEM, AFC, PAFC), makes them ideal for application in combined SOFC/gas turbine (GT) cycles, and thus obtains an efficiency between 70-80% [1].

The fundamental mechanism of operation in an SOFC is the oxidation of hydrogen and other fuels at the anode, and the reduction of oxygen at the cathode, to create a potential difference between the two electrodes. Depending on the fuel used, the reaction products can be water and CO_2. The chemical energy is released both in electrical energy and in the form of heat due to polarizations and ohmic losses [2]. An SOFC cell consists of an electrolyte, an anode and a cathode. The electrolyte is a non-porous ceramic solid, usually made of Y_2O_3-stabilised ZrO_2 (YSZ). The SOFC cell operates at a temperature between 600 and 1000°C, where the ceramic electrolyte is an oxygen ion conductor, O^{2-}, but not an electron conductor. The high operating temperature has some advantages such as minimizing polarization losses and tolerance of the catalyst to poisoning by impurities in the fuel [3,4]. Generally, the anode is made of yttria-stabilized nickel-zirconia cermet (Ni-YSZ) and the cathode is a perovskite-type electronic conductor of Sr doped with $LaMnO_3$ cermet (LSM), in addition to other materials with perovskite structure.

2. The interconnector in an SOFC cell

Interconnectors provide the electrical connection between the anode of one cell and the cathode of the adjacent cell and also act as a physical barrier to prevent any contact between reducing and oxidizing atmospheres. In general terms, the interconnector must meet the following requirements [5,6]:

- Excellent electrical conductivity. It is considered an acceptable value below 0.1 $\Omega.cm^2$ in relation to the specific area resistance (ASR);
- Adequate stability in terms of dimensions, microstructure, chemistry and phases of the material at an operating temperature of around 800°C, in both oxidizing and reducing atmospheres for 40,000 hours (long-term service);
- Excellent impermeability to oxygen and hydrogen to prevent the direct combination of fuel and oxidant during operation;
- Compatibility of the thermal expansion coefficient (TEC) with the electrodes and electrolyte with a value of around 10.5 X 10^{-6} K^{-1}, so that the thermal stresses developed at the beginning and end of operation are reduced to a minimum;
- There should be no reaction or interdiffusion between the interconnector and its adjacent components;
- Excellent resistance to carbon oxidation, sulphurisation and cementation;

- Optimum creep resistance at high temperatures;
- Be low cost, as well as easy to fabricate and forming.

3. Lanthanum chromite as an interconnector

The traditional material used for the interconnection of an SOFC is lanthanum chromite ($LaCrO_3$) for high temperature applications (~1000°C). First of all, this material exhibits remarkably high electrical conductivity, under operating conditions, compared to other ceramics commonly used in SOFC cells. It should be noted that the conductivity can be significantly increased by means of Mg, Sr or Ca doping. Secondly, the melting point of the $LaCrO_3$ cermet is 2783 ± 20 K and it can remain stable in both cathodic and anodic environments. Finally, the coefficient of thermal expansion (TEC) of $LaCrO_3$ is $9.5X10^{-6}$ K^{-1}, which is quite close to the TEC of the YSZ material ($10.5X10^{-6}$ K^{-1}) [7].

4. Metal alloys as interconnectors

Almost all known alloys for SOFC cell interconnectors, which contain Cr and Al (Si is a third possibility, but much less used), are candidates that provide resistance to oxidation, due to the formation of oxide layers types: Cr_2O_3 (chromium) and Al_2O_3 (alumina), respectively. For chromium formation, there must be sufficient chromium in the alloy to form a continuous layer of this oxide to efficiently provide high oxidation resistance under SOFC operating conditions. Considering the insulating nature of the alumina in these alloys, the aluminum content should be controlled, in order to avoid the formation of a continuous layer of alumina [8].

4.1. Chrome-based alloys

At high temperatures, between 900 and 1000°C, chromium-based reinforced oxide dispersion (ODS) alloys are especially used to replace the $LaCrO_3$ cermet. The Ducrolloy alloy (Cr-5Fe-1Y_2O_3), designed by the *Plansee company*, was developed to improve the compatibility of the coefficient of thermal expansion with the other components of the SOFC7 cell. Some other ODS base alloys include: Cr-5Fe-1.3La_2O_3, Cr-5Fe-0.5CeO_2, Cr-5Fe-0.3Ti-0.5Y_2O_3 and others. The reason for choosing chrome-based alloys (chromium formation) is that chromium has high conductivity compared to other oxides [9].

4.2. Fe-Cr base alloys

To obtain a continuous layer of chromium oxide, the alloy substrate must have sufficient Cr. In the literature, the strict Cr13 content has been summarized, which varies between approximately 20-25% to ensure the formation of a continuous protective Cr_2O_3 layer. It should be noted that a low Cr content (5-10%) used as an interconnector significantly reduces the oxidation resistance. Low (<5%) Cr steels are practically composed of Fe oxide accompanied by Cr_2O_3 precipitates and/or $FeCr_2O_4$ spinels. With increasing Cr content, the layers become richer in spinels and chromias, which decreases the growth rate [10]. The nominal composition of Fe-Cr base alloys is shown in table 1.

Table 1. Nominal composition of Fe base alloys

Alloy	Concentration (W, %)										
	Fe	Cr	Mn	Mo	W	Si	Al	Ti	Y	Zr	La
Fe-10Cr	Balance	10	<0.02		<0.1						
1.4724	Balance	13					1.0				
SUS 430	Balance	16-17	0.2-1.0			0.4-1.0	≤0.2				
Fe-17Cr-0.2Y	Balance	17							90.2		
1.4016	Balance	17									
Ferrotherm (1.4742)	Balance	17-18	0.3-0.7		0.8-0.9	0.9-1.0					
Fe-18Cr-9W	Balance	18			9						
Fe-20Cr-7W	Balance	20			7	0.3	0.6			0.3	
Fe-20Cr	Balance	20	<0.02		<0.1					0.2	0.04
AL 453	Balance	22	0.3			0.3	0.6	0.02			0.1
1.4763 (446)	Balance	24-26	0.7-1.5	≤0.05		0.4-1		<0.05			
FeCrMn(LaTi)	Balance	16-25	?					?			?
Fe-Cr-Mn	Balance	16-25	?								
Fe-25Cr-DIN 50049	Balance	25	0.3		0.7		0.01				
Fe-25Cr-0.1Y-2.5Ti	Balance	25						2.5	0.1		
Fe-25Cr-0.2Y-1.6Mn	Balance	25	1.6						0.2		
Fe-25Cr-0.4La	Balance										0.4
Fe-25Cr-0.3Zr	Balance	25								0.3	
Fe26CrTiY	Balance	26	0.1	<0.02		<0.05	<0.05	0.3	0.4		
Fe26CrTiNbY	Balance	26	Composition not provided, but presumably equal to $Fe_{26}CrTiY$ with Nb								
Fe26CrMoTiY	Balance	26	0.1	2	<0.05	<0.05	0.3	0.3			
E-Brite	Balance	26-27	≤0.1	1	0.03-0.2	≤0.05	≤0.05	≤0.01			
Al29-4C	Balance	27	0.3	4	0.3		?				
Fe-30Cr	Balance	30	<0.02		<0.1						

During operation of an SOFC cell, the interconnector can reduce the anode side and oxidize the cathode side. Therefore, simulated tests under real operating conditions with exposure to the $H_2O + H_2$ gas mixture at the anode and with a dual air/H_2 atmosphere at the cathode have been reported in several reports. With the mixture of $H_2O + H_2$ gas, the morphology of the chromium is slightly modified and the adhesion of the protective layer is improved. In the dual atmosphere, the layer formed contains iron-rich spinels or Fe_2O_3 nodules, which were not present on both sides of the alloy when it was exposed to air. This suggests that the mobility of iron is increased by hydrogen on the anode side [11].

4.3. Ni-Cr base alloys

Compared to Fe-Cr base alloys, Ni-Cr alloys have always shown higher oxidation resistance as well as satisfactory electrical conductivity. To obtain a continuous chromium layer, 15% Cr is required to establish a reasonable resistance to high temperature corrosion, which is lower compared to the Fe-Cr alloy where 18-19% Cr is required. Nominal compositions of Ni base alloys are shown in table 2.

Table 2. Nominal composition of Ni base alloys for application in SOFC cell interconnectors.

Alloy	Concentration (%, W)									
	Ni	Cr	Fe	Co	Mn	Mo	Nb	Ti	Si	Al
Inconel 600	Balance	14-16	6-9		0.4-1			0.2-0.4	0.2-0.5	0.2
ASL 528	Balance	16	7.1		0.3			0.3	0.2	
Haynes R-41 (Rene 14)	Balance	19	5	11	0.1	10		3.1	0.5	1.5
Inconel 718	Balance	22	18	1	0.4	1.9				
Haynes 230	Balance	22-26	3	5	0.5-0.7	1-2			0.3	
Hastelloy X	Balance	24	19	1.5	1.0	5.3				
Inconel 625	Balance	25	5.4	1.0	0.6	5.7				
Nicrofer 6025HT	Balance	25	9.5		0.1	0.5			0.5	0.15
Hastelloy G-30	Balance	30	1.5	5	1.5	5.5	1.5	1.8	1	

In the presence of hydrogen, most Ni-Cr based alloys show excellent resistance to oxidation, through the growth of a thin film of Cr_2O_3 and (Mn, Cr, Ni)$_3O_4$ spinels, and can therefore be used at the anode of a cell as a metal coating. In an oxidizing medium, Cr-containing alloys, e.g. Haynes 230 and Hastelloy S, form a thin film, mainly composed of Cr_2O_3 and (Mn, Cr, Ni)$_3O_4$ spinels when exposed to high temperatures, while low Cr-containing alloys such as *Haynes 242* develop a thick double layer of NiO on top of a chromium rich substrate, which is of great interest due to its oxidation resistance for interconnector applications[12]. Recently, researchers from the National Energy Technology Laboratory (NETL, Pittsburgh, USA), have developed a new series of Ni-Cr based alloys containing W, Mo, Al, Ti, etc., with potential application in interconnectors for SOFCs. After testing at high temperature, as well as at room temperature for more than one thousand hours, it was found that alloy J5 presents good properties, comparable to the commercial *Haynes 230* alloy. The nominal composition of alloy J5 is Cr-12.5%, Ti-1.0%, Al-0.1%, Mo-22.5%, Mn-0.5%, Y-0.1%, Ni-equilibrium [13].

4.4. Problems when using metallic materials as interconnectors

The application of ferritic stainless steel still presents some challenges, even at reduced temperatures, among which are: (1) unacceptably high corrosion rate; (2) presence of fracture and deformation of the formed oxide film, when subjected to thermal cycling; (3) high volatilization of chromium species (Cr) in the form of CrO_3 or $Cr(OH)_2O_2$.

5. Interconnector coating

With the main objective of mitigating excessive chromium growth and chromium poisoning, several coatings have recently been developed for the metal interconnectors of SOFCs. In selecting the coating material, the following characteristics should be considered: (1) the diffusion coefficients of Cr and O in the coating should be as small as possible, to avoid transporting chromium and oxygen in their entirety; (2) it should be chemically stable and compatible with respect to the substrate, electrodes, sealing materials and contact pastes; (3) in the applied temperature range, it must be thermodynamically stable in both reducing and oxidizing atmospheres; (4) it must have low ohmic resistance to

maximize electrical efficiency; (5) the coefficients of thermal expansion must be compatible with the substrate so that the coating is resistant to fracture during the thermal cycle [7]. Of the interconnector coatings that have been highlighted, those of the nitride (Ny) type (MxNy with M = Cr, Al, Sm, Co, Ti), have been widely used in tools due to their greater resistance to wear. On the other hand, this type of coating can be an alternative in SOFC applications, due to its low resistance and stability at high temperature [14]. Another coating that can also be mentioned is the perovskite type in its ABO_3 form. The $LaCrO_3$ material is a traditional interconnector, which has been applied by the sputtering technique [15]. LSM cermet, on the other hand, has been widely used as a cathodic material in an SOFC. This material has also been investigated as a possible interconnector coating due to its high electrical conductivity, thermal compatibility and stability in oxidizing environments. The presence of the LSM coating can be crucial in maintaining a low level of contact resistance at high temperatures over extended periods of time. This coating has been investigated on the *SUS 430* substrate [16]. Spinels are another option as a lining for an SOFC interconnector. Compared to perovskites, some spinels have shown better performance in preventing internal oxygen diffusion as well as Cr diffusion to the outside. However, Cr diffusion is still a problem for Cr containing spinels. The compound $MnCr_2O_4$ has been reported as a product of the reaction between chromium oxide and Mn diffusion of the *Crofer 22* type substrate, but the evaporation of Cr is imperceptible. It has been reported that long periods are necessary to test the efficiency of coatings, for example $CoCr_2O_4$ material, does not reduce the performance of the cell in 1000 h of use [17]. Among the various compositions of $Mn_{1+\delta}Co_{2-\delta}O_4$ spinel, the structures $Mn_{0.5}Co_{2.5}O_4$ (δ = -0.5) and $MnCo_2O_4$ (δ = 0), have a cubic spinel phase, with Mn located at the octahedral interstitial sites and Co located at both the octahedral and tetrahedral sites of the FCC cubic network. While the spinels $Mn_{2.5}Co_{0.5}O_4$ (δ = 1.5) and Mn_2CoO_4 (δ = 1.0), show tetragonal structure. When δ = 0.5, the $Mn_{1.5}Co_{1.5}O_4$ spinel turned out to be a dual phase material, containing both the cubic and tetragonal phase [18]. Regarding the conductivity of spinels, there are currently several spinels ($Mn_{1+\delta}Co_{2-\delta}O_4$), which are good electrical conductors. For example, tests performed on the $Mn_{1.5}Co_{1.5}O_4$ spinel indicate an electrical conductivity of ~ 60 $S.cm^{-1}$ at 800°C in air, which is 2-4 orders of magnitude higher compared to Cr_2O_3 and $MnCr_2O_4$ structures [19]. One of the most important parameters is the thermal expansion coefficient (TEC), in this sense we can mention the spinel $Mn_{1.5}Co_{1.5}O_4$, which exhibited acceptable linearity with respect to temperature (11.5 x 10^{-6} K^{-1}, 20 - 800°C). Furthermore, this spinel has shown to be compatible with the TEC of ferritic stainless steel such as Crofer 22 APU and AISI 430, as well as with perovskite phase cathodic structures such as $La_{0.8}Sr_{0.2}MnO_3$ and $La_{0.8}Sr_{0.2}FeO_{3.54}$ [19]. The TEC of the $MnCo_2O_4$ spinel, on the other hand, is very close to the $Mn_{1.5}Co_{1.5}O_4$ material below 1000°C.

6. Conclusion

In recent years, great progress has been made in the development of interconnectors for SOFCs and their coatings. Therefore, several coatings have demonstrated potential for use

in interconnectors due to their high oxidation resistance and chromium retention capacity. According to the proposed strategies, coatings with spinel structure can be considered the most promising candidates for use in SOFC interconnectors, such is the case of the dual phase spinel $Mn_{1.5}Co_{1.5}O_4$ containing both the cubic and tetragonal phase, has shown an electrical conductivity of ~ 60 $S.cm^{-1}$ at 800°C in air, being 2-4 orders of magnitude higher compared to Cr_2O_3 and $MnCr_2O_4$ structures. Furthermore, this spinel has shown to be compatible with the TEC of several types of steels such as Crofer 22 APU and AISI 430, as well as with perovskite phase cathodic structures such as $La_{0.8}Sr_{0.2}MnO_3$ and $La_{0.8}Sr_{0.2}FeO_{3.54}$.

References

[1] M.C. Williams, J.P. Strakey and W.A. Surdoval: J. Power Sources, 2005, 143, 191.
[2] O. Yamamoto: Electrochim. Acta, 2000, 45, 2423.
[3] S. Kaka，c, A. Pramuanjaroenkij and X. Zhou: Int. J. Hydrogen Energ., 2007, 32, 761.
[4] F. Alcaide, P. Cabot and E. Brillas: J. Power Sources, 2006, 153, 47.
[5] W.Z. Zhu and S.C. Deevi: Mater. Sci. Eng. A, 2003, 348(1-2), 227.
[6] S. Fontana, R. Amendola, S. Chevalier, P. Piccardo, G. Caboche, M. Viviani, R. Molins and M. Sennour: J. Power Sources, 2007, 171, 652.
[7] W. Vielstich, A. Hubert, M. Gasteiger and A. Lamm: Handbook of Fuel Cells-Fundamentals, Technology and Applications; Fuel Cell Technology and Applications, chapter 74, Wiley, New York, 2003.
[8] Z. Yang, K. Weil, D. Paxton and J. Stevenson: J. Electrochem. Soc., 2003, 150, A1188.
[9] J. Fergus: Solid State Ionics, 2004, 171, 1.
[10] S. Geng, J. Zhu, M. Brady, H. Anderson, X. Zhou and Z. Yang: J. Power Sources, 2007, 172, 775.
[11] J. Fergus: Mater. Sci. Eng. A, 2005, 397, 271.
[12] Z. Yang, G. Xia and J. Stevenson: J. Power Sources, 2006, 160, 1104.
[13] P. Jablonski and D. Alman: Int J. Hydrogen Energ., 2007, 32, 3705.
[14] S. Dey and S. Deevi: Mater. Sci. Eng. A, 2003, 324, 58.
[15] N. Orlovskaya, A. Coratolo, C. Johnson and R. Gemmen: J. Am. Ceram. Soc., 2004, 87, 1981.
[16] J. Kim, R. Song and S. Hyun: Solid State Ionics, 2004, 174, 185
[17] C. Johnson, J. Wu, X. Liu and R.. Gemmen: ASME Fuel Cell Conference, New York, 2007
[18] Z. Yang, G. Xia, X. Li and J. Stevenson: Int. J. Hydrogen Energ., 2007, 32, 3648.
[19] J. Stevenson, Y. Chou, O. Marina, S. Simner, K. Weil, Z. Yang and P. Singh: SECA Core Technology Program: Materials Development at PNNL, SECA Core Technology Program Review Meeting, Lakewood, CO, October 25, 2005.

ID 029

Study of Water Management In Solid Styrene Electrolytes

L. Da Silva*, M.M. Salas, L. F. Vieira, L.G. D. Interial, D. Morales-Acosta, A. de León Santillán, R. Benavides

Centro de Investigación en Química Aplicada, Blvd. Enrique Reyna H. 140, Saltillo, Coah. 25294, Mexico.
* Corresponding author E-mail: luciano.dasilva@ciqa.edu.mx

ABSTRACT

The variety of polymeric materials with distinct chemical structures that precisely control the molecular architecture underlies the numerous industrial uses of polymers over the past few decades. Polymer electrolytes or gel-type polymer electrolytes, for example, are interesting alternatives to substitute liquid electrolytes in different systems such as fuel cells (FC) and dye-sensitized solar cells (DSSC). For application in FC, the Nafion electrolyte is the most widely studied. However, this material is highly dependent on hydration and operating temperature. To a certain extent, concepts and models of proton conductivity in bulk water carry over to proton conductivity in Nafion and other polymer electrolyte membranes. To understand how water acts on these systems, in this work we conducted a study to identify the kind of interaction between the adsorbed water and the electrolyte structure of membrane. Differents copolymers were synthesized from styrene as the main comonomer and characterized chemically and thermally. Membranes were prepared by casting, hydrated and the Water Uptake (WU) and Water Content (WC) were determined. Differential Scaning Calorimetry (DSC) was used to determine the kinds of present water. We observed that several compositions absorb a lot of water and do not showed conductivity because it is basically free water and does not interact with the copolymer. For other side, when the copolymer structure allows strong interaction with water, the kind of water present also changes and this is reflected in the ionic properties of the membrane.

Keywords: *Polystyrene membranes; water management; solid electrolyte; Fuel cells*

1. Introduction

Water is considered the most important compound on earth, being found in different physical states, both solid and liquid and vapor [1]. Compared to other common liquids, water is characterized by high boiling, melting and critical temperatures, high specific heat,

and high surface tension, among other properties [2]. The variety of polymeric biomaterials with distinct chemical structures that precisely control the molecular architecture underlies the numerous industrial uses of polymers over the past few decades. For example, sulfonated aromatic copolymers, due to their high thermal stability, strength, cost competitiveness, and high resistance to membrane decomposition in an acidic water medium, have been considered a promising alternative to Nafion [3–6]. However, particularly when the membranes from these materials have a high degree of sulfonation, to increase proton conductivity, they tend to suffer from poor performance in reducing methanol crossover and water uptake. Meanwhile, considering the fact that protons in fuel cell membranes move forward via water channels, the management of water molecules in water-swollen membranes is said to be crucial in determining transport properties such as proton conductivity, methanol permeability, and selectivity. Therefore, the control and understanding of the state of water in polymers structure is must be essential for breaking through the technical limits of the water-swollen proton conductors.

For this purpose, various terms have been used to characterize the water adsorbed in materials, mainly in membranes where water plays an important role in different processes in which they are used. Bound water, imbibed water, water of constitution, adsorbed water and saturation point are some of the terms that have been used to describe the water in membranes. The origin of each term can be traced to either theoretical considerations or to the experimental method of measurement. Bound water has been the most popular term used to describe the associated water. Bulk water or free water is that portion of water not associated (or not bound) within the membrane.

There are different techniques that can be used to determine the kind of water present in the membrane, but two techniques are especially important to quantified and identify different kinds of water present in the membrane, these are thermal analysis techniques: 1) Thermogravimetric analysis - A wet membrane sample is heated under controlled conditions to obtain the mass loss curve. The loss of mass at temperatures below 200 ^{o}C is usually associated with the water content in the membrane. The loss of mass rates is highly dependent upon the diffusion rates and the geometry of the sample; 2) Differential Scanning Calorimeter analysis - When a wet membrane sample is cooled well below 0 °C, the free water freezes but the bound water remains in the non-frozen state. When the frozen sample is heated in a calorimeter, the heat required to melt the frozen water can be measured. Non-frozen water, which is defined as the bound water, is the difference between the total water and the frozen water. The freezing of free water and non-freezing of bound water are thermodynamic phenomena, so the measurement is absolute, but as the bound water is calculated by difference, the measurement is indirect. The bound water is measured only at the freezing point [7-9].

Knowing these properties, we used the calorimetric techniques to determine the type of water present in the membrane. In this work, we describe the methodology used to quantify and qualify the different types of water present in the polymeric electrolyte membrane. The results demonstrate a strong relationship between the presence of ionizable hydrogen atoms and the kind of water present in the membrane.

2. Materials and Methods

2.1. General Information

The solvents and chemicals were purchased from Sigma-Aldrich and J. T Baker and used as received. The mass spectrometer was operated in negative ion mode. FT-IR (ATR) spectra were recorded on a Bruker Vertex 70. Molecular weight and its distribution were analyzed by GPC (Waters Alliance 2695), using polystyrene as the narrow standard (DLS and UV detectors). ^{1}HNMR (Hydrogen Nuclear Magnetic Resonance) and ^{13}CNMR (Carbon Nuclear Magnetic Resonance) spectra were recorded in a Bruker Avance 3 - 400Mhz spectrometer. Thermal stability properties were analyzed by TGA using a Linseis (STA instrument) and DSC (TA instruments Q2000).

2.2. Synthesis

2.2.1 Preparation of membranes

The membranes used were the same as those prepared in a previous experiment [10-14] i.e., membranes of styrene copolymers (involving different concentrations of a second comonomer) prepared by casting in DMF. For comparison, the styrene-acrylonitrile copolymer (StAN, 50:50) was prepared and used in this work as a standard. This system has an acrylonitrile group, quite hygroscopic, but it does not have ionizable hydrogen, which does not allow ionic conductivity.

2.3 Thermal analysis

2.3.1 Determination of the states of water

Before starting the water characterization tests, the different compositions were used to prepare membranes by casting. After, the membrane were dried in a vacuum oven at 50 ^{o}C for 24 hours, and than, immersed in deionized water during 24 hours for full hydration.

- Using DSC (Q2000, TA Instruments): The fully hydrated sample was placed in an alumina sample pan for scanning, the sample was cooled to − 80 °C at 20 °C/min and then kept at − 80 °C for 5 min before heating to 40 °C at 2.0 °C/min under a nitrogen atmosphere.

- Using TGA (STA PT1000, Linseis): The measurements were made in an alumina pan. For scanning, the sample was heated to 50 °C and kept isothermal for 5 min before heating to 250 °C at 10.0 °C/min under a nitrogen atmosphere.

2.4 Membrane Morphology

The samples' surface morphological characteristics was carried out by Atomic Force Microscopy (AFM) on a Dimension™3100 from Digital Instruments with Pt-coated Si tip with 15 nm nominal radius model: OSCM-PT Bruker, the images were obtained in the tapping mode at a scanning rate of 1.0 Hz during 256 lines.

3. Results and Discussion

The copolymers were synthesized and characterized as described in the literature. The Table 1 shows the composition (%St) weight average molecular weight (Mw) and dispersity (Mw/Mn) of the membranes StCo-1, StCo-2, StCo-3, StCo-4 and StAN.

Table 1. Percentage of styrene ($\%_{St}$) and molecular weight (Mw) of copolymers.

Sample	$\%_{St}$ (moles)	Mw (Daltons)	Mw/Mn
StCo-1	60.0	45,345	4.543
StCo-2	70.0	45,193	3.818
StCo-3	80.0	33,634	2.628

StCo-4	90.0	56,784	3,742
StAN	50.0	58,670	3.573

Thermal analyzes were performed by Thermogravimetric Analysis (TGA) and Differential Scanning Calorimetry (DSC). The TGA analysis was achieved at a heating rate of 10 °C/min under nitrogen atmosphere (Fig. 1 and Fig. 2) and the results are listed in **Table 1**. It is observed that all copolymers have three stages of mass loss. The first stage occurs at temperatures below 200 ^{o}C, the second stage occurs at temperatures between 200 and 280 ^{o}C and the third stage occurs at temperatures between 290 and 450 ^{o}C. In order to have a better view of the dehydration process, an expanded section of TGA traces are shown in Figure 2a for the 4 copolymers and in Figure 2b when the standard StAN is included.

The first stage of mass loss is associated with the polymer dehydration process (Fig. 2a). This way, knowing the mass used in the analysis and the percentage of loss that occurs up to a temperature of 180 ^{o}C, it is possible to determine the total amount of water present in the polymer. The amount of water determined by TGA was called Total Water ($\mathbf{W_T}$). As can be seen in Fig. 2b, we also add the standard StAN copolymer absorbs much more water than the other copolymers.

Water Content (**WC**) and Water Uptake (**WU**) are two denominations for total water absorbed in a sample determined by using an analytical balance. Then, **WU** and **WC** can be calculated as follows:

(1)

$$WU\ (\%) = [(W_{wet} - W_{dry})/W_{dry}] \times 100$$

(2)

$$WC\ (\%) = [(W_{wet} - W_{dry})/W_{wet}] \times 100$$

Where, W_{wet} and W_{dry} correspond to the weight of wet membrane and weight of dry membrane, respectively.

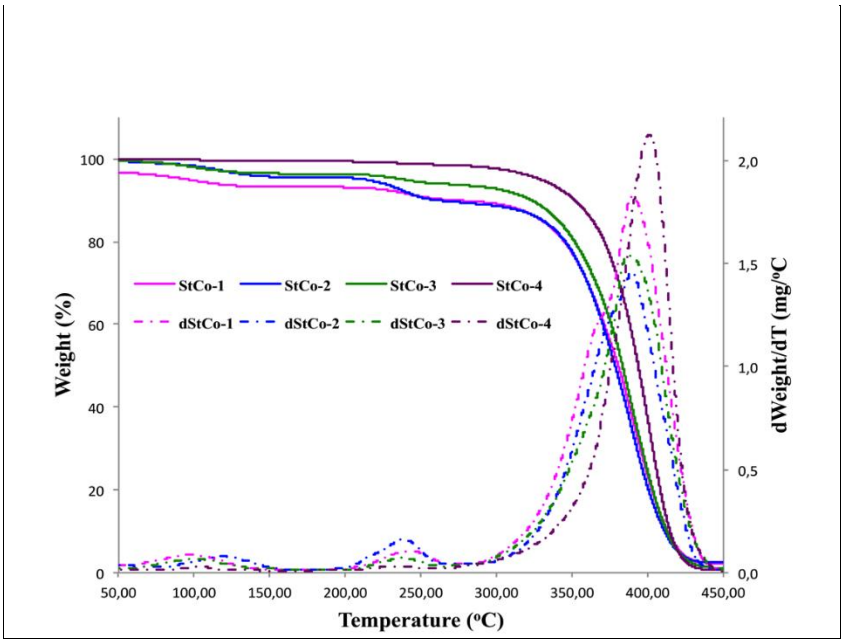

Fig. 1. TGA and DTG curves of copolymers StCo-1, StCo-2, StCo-3 and StCo-4.

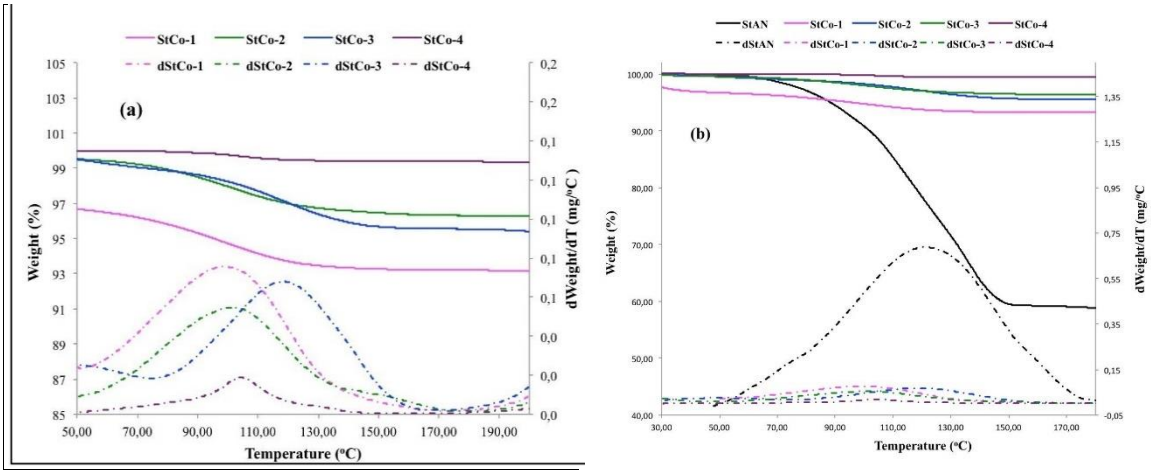

Fig. 2. Expanded region of TGA and DTG curves of copolymers. (a) StCo-1, StCo-2, StCo-3 and StCo-4 expanded in the region between 50 and 200C; (b) StCo-1, StCo-2, StCo-3, StCo-4 and StAN;

Table 1. Results of TG/DTG analysis of the copolymers **StCo-1**, **StCo-2**, **StCo-3** and **StCo-4**.

Copolymer	Loss mass 1		Loss mass 2		Loss mass 3	
	$T_{initial}$ (°C)	T_F (°C)	$T_{initial}$ (°C)	T_F (°C)	$T_{initial}$ (°C)	T_F (°C)
StCo-1	54.3	168.0	204.2	279.4	278.4	389.8
StCo-2	53.4	172.2	192.4	270.6	280.8	387.3
StCo-3	75.4	161.2	175.4	278.4	287.3	389.4
StCo-4	68.1	139.0	200.1	270.8	270.7	400.8

The **W_T**, **WU** and **WC** values obtained for the prepared membranes from different copolymers are shown in **Table 2**. The **W_T** values were determined based on the TGA spectra (Fig. 2a), observed at temperatures below 180 degrees. For this test, TGA equipment has been programmed to stabilize the sample at 40 °C for 10 min and heated at a rate of 10 °C/min, in a nitrogen atmosphere, up to a temperature of 200 °C. To determine **WC** and **WU**, the dry membrane was weighed before being hydrated (W_{dry}) and after hydrating (W_{wet}).

Table 2. Water uptake (WU), water content (WC) and total water (**W_T**) for copolymers **StCo-1**, **StCo-2**, **StCo-3, StCo-4** and **StAN.**

Copolymer	WU (%)	WC (%)	W_T (%)
StCo-1	25.90	20.50	8.35
StCo-2	48.10	32.50	8.30
StCo-3	26.60	20.90	7.60
StCo-4	7.50	6.20	2.88
StAN	2.80	6.99	49.51

It is observed that the amount of **WU** and **WC** are different values, also different from **W_T** values. **W_T** was obtained by TGA analysis while **WU** and **WC** were obtained by the difference in mass between the vacuum dried membrane and the hydrated membrane. Considering that to obtain the weight of wet membrane (Wwet), the determination depends a lot on how the experiment is carried out since the excess water present on the membrane surface must be discarded, it is possible that part of such excess water is still present in the Wwet value. Parameters such as porosity and sample dimensions should also influence Wwet determination. For the purpose of interpretation of results, the amount of total water present will be used the value of **W_T**.

The amount and interaction mechanism of water with the polymer structure could be an important factor to understand the behavior of these materials. Considering the membrane hydration process, the water could be classified in three states according to mobility that could be described as **linked water**, one ordered water structure in the vicinity

of different surfaces, having low molecular mobility; **free water** - water with higher mobility; **intermediated water** - water that behaves similarly to linked water. Linked water is tightly bound to the surface and theses interactions are very strong, while water–water interactions are very weak. Intermediate water interacts moderately with the surface (stronger than free but weaker than linked water) involving both water-surface and water–water interactions. Free water hardly interacts with the surface and there is mainly water–water interaction. According to the difference of intermolecular hydrogen bonding, including water/polymer bonding, weakened water/water bonding, and normal water/water bonding, the structure of the hydrated polymer network could be represented as depicted in Fig. 3.

When a sample of the hydrated copolymer is cooled well below 0°C, the free water and intermediate water freezes but the linked water remains in the non-frozen state. When the frozen sample is heated in a calorimeter, the heat required to melt the frozen water can be measured. Non-frozen water, which is defined as the linked water, is the difference between the total water (water content) and the frozen water. The frozen water (W_{fs}) could be determined using equation 4.

$$(4)\ W_{fs}\ (\%) = \frac{\Delta H_{\text{polymer hydrated}}}{\Delta H^{\circ}_{m\ water}} \times 100$$

Where: $\Delta H^{0}_{m,\ water} = 333.5(J/g)$ and $\Delta H_{\text{polymer hydrated}}$ is the sum of all the melting enthalpy in the heating trace of DSC of hydrated copolymer.
The linked water (W_{liked}) could be determined by difference between water content (W_T) and frozen water (W_{fs}) using the equation 5.

$$(5)\ W_{liked}\ (\%) = W_T - W_{fs}$$

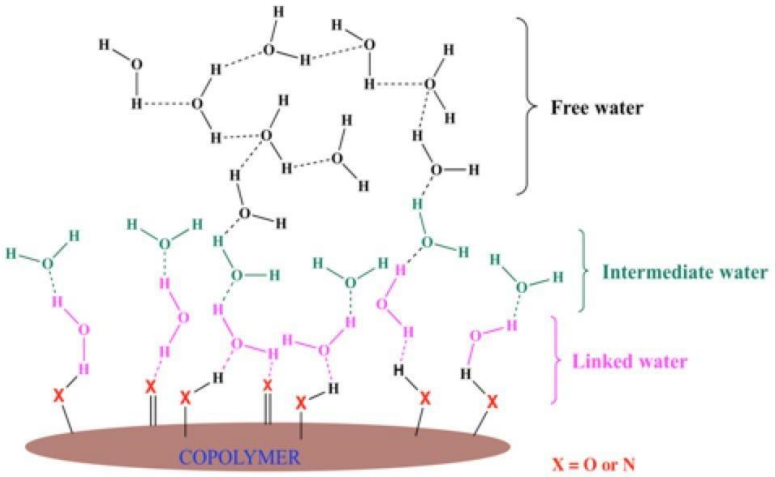

Fig. 3. Schematic representation of the water in the copolymer network.

Fig. 4 shows the thermograms obtained by DSC for heating from -20 C to 30 C for all copolymers evaluated and their respective melting enthalpy values are summarized in Table 3.

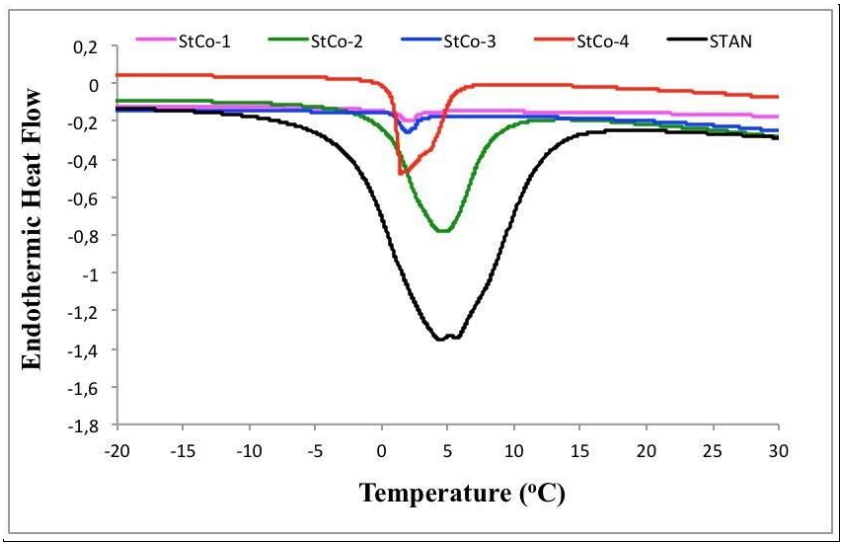

Fig. 4. DSC thermograms for the StCo-1, StCo-2, StCo-3, StCo-4 and StAN composites.

Table 3. Melting enthalpy and W_{linked} values for the StCo-1, StCo-2, StCo-3, StCo-4 and StAN composites.

Copolymer	W_T (%)	$\Delta H_{polymer\ hydrate}$ (J/g)	W_{fs} (%)	W_{liked} (%)
StCo-1	8.35	3.40	1.02	7.33
StCo-2	8.30	22.93	6.87	1.43
StCo-3	7.60	10.42	3.12	4.48
StCo-4	2.88	0.87	0.26	2.62
StAN	49.51	161.8	48.52	0.99

It is observed that the StAN copolymer is the material that absorbs the largest amount of water (> W_T) and also the one that has the lowest amount of linked water (< W_{linked}). All the water absorbed in StAN is in the form of free or intermediate water.

AFM was used for the determination of phase morphology, heterogeneity, or homogeneity of the membranes. In addition, the surface roughness of the membranes was also determined. The selected AFM images of membranes are presented in Fig. 5. In the comparison, it is possible to differentiate the morphology between the two types of materials, StAN and StCo-1.

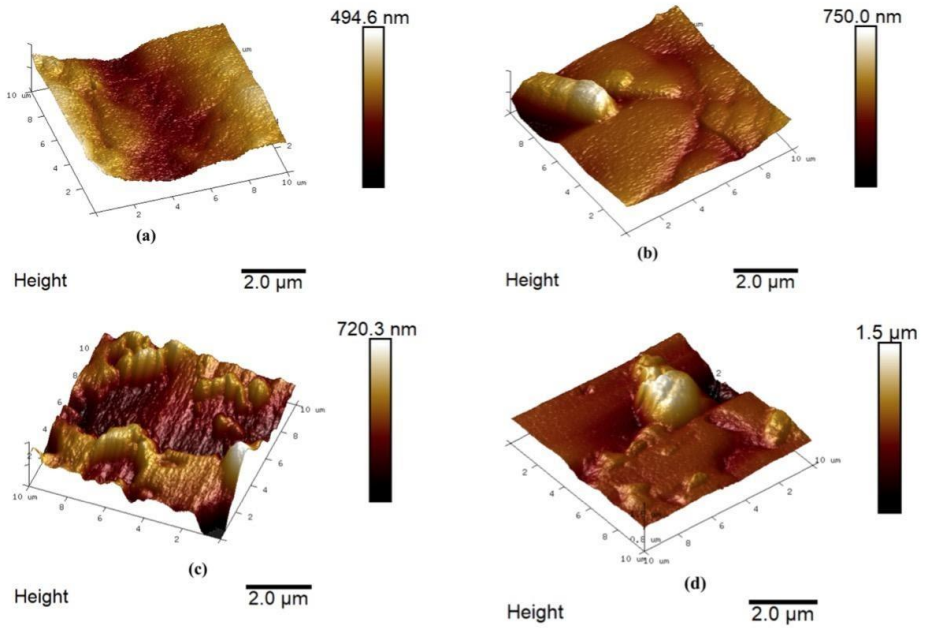

Fig. 5. AFM pictures of (a) StAN dry, (b) StAN hydrated, (c) StCo-1 dry and (d) StCo-1 hydrated.

4. Conclusion

Styrene copolymers were synthesized and characterized. Membranes of these copolymers were prepared by casting. Theses membranes were hydrated and the amount of water was determined by thermal analysis. The results demonstrate that there is a difference in how water is in the membrane and how much water is directly linked to the material surface. Complementary results are necessary, but it is possible that there is a direct relationship between the type of water present in the material and ionic conductivity properties, which is highly dependent on the presence of water in the membrane.

Acknowledgements

This work was supported by CIQA - Call for internal projects - 2019.

References

[1] Robinson, G. W.; Singh, S.; Zhu, S-B.; Evans, M.W. Water in Biology, Chemistry, and Physics: Experimental Overviews and Computational Methodologies; World Scientific: Singapore, 1996.

[2] Ratner, B. D., Role of water in biomaterials. In Biomaterials Science: An Introduction to Materials in Medicine; Ratner, B.D., Ed.; Academic Press: Cambridge, MA, USA, 2012; pp. 55-59.

[3] Steel, B. C. H., Heinzel, A., Materials for fuel-cell technologies, Nature, 2001, 414, 345-352.

[4] M.A. Hickner, H. Ghassemi, Y.S. Kim, B.R. Einsla, J.E. McGrath, Alternative polymer systems for proton exchange membranes (PEMs), Chem. Rev., 2004, 104, 4587-4612.

[5] Hill, M. L., Hill, Y. S., Kim, B. R., Einsla, J. E., McGrath, Zirconium hydrogen phosphate/ disulfonated poly(arylene ether sulfone) copolymer composite membranes for proton exchange membrane fuel cells, J. Membr. Sci., 2006, 283, 102-108.

[6] Neburchilov, V., Martin, J., Wang, H., Zhang, J., A review of polymer electrolyte membranes for direct methanol fuel cells, J. Power Sources, 2007, 169, 221-238.

[7] Hechter, O.M., Wittstruck, T., McNiven, N., Lester, G., Modification of the structure of water in agar gels. Proc. Natl. Acad. Sci. USA 1960, 46, 783-787.

[8] Sterling, C., Masuzawa, M., Gel/water relationships in hydrophilic polymers: Nuclear magnetic resonance. Makromol. Chem. Phys. 1968, 116, 140-145.

[9] McBrierty, V. J., Martin, S. J., Karasz, F. E., Understanding hydrated polymers: The perspective of NMR. J. Mol. Liq. 1999, 80, 179-205.

[10] Benavides, R. C., Urbano, R., Morales-Acosta, D., Martinez-Pardo, M. E., Carrasco, H., Paula, M. M. S., Da Silva, L., INT J HYDROGEN ENER, 2018, 44, 24, 12525-12528.

[11] Melo, L., Benavides, R., Martínez, G., Morales-Acosta, D., Paula, M. M. S., Silva, L. Int J Hydrogen Ener., 2017, 42, 21880-21885.

[12] Da Silva Paula, M. M., De Souza, H. J., Búrigo, C., Langbehn, J. T., Baesso, A. S., Da Silva, L., Da Silva, P. R. P., Benavides, R., Alonso-Núñez, G., Collins, V., COLLOID SURFACE A, 2017, 520, 78-84.

[13] Melo, L., Benavides, R., Martínez, G., Morales-Acosta, D., Paula, M.M.S., Da Silva, L., Int J Hydrogen Ener, 2017, 1, 1-10.

[14] Cantu, R. B., Rodrigues, J. C. O., Melo, L., Morales-Acosta, D., Paula, M.M.S., Da Silva, L., J. Appl. Electrochem. 2015, 45, 1211-1215

[15] Benavides, R., Oenning, L. W., Paula, M. M. S. ; Da Silva, L., Int J Hydrogen Ener, 2015, 40, 17413-17420.

ID 034

Preparation of Sulfonated PEEK and Graphene Oxide Materials for Proton Exchange Membranes

A. Saldívar-Martínez, D. Morales-Acosta*, P.C. Flores-Escareño, R. Benavides*, L. Da Silva.

Centro de Investigación de Química Aplicada, Blvd Enrique Reyna No. 140, Col. San José de los Cerritos, 25290. Saltillo, Coahuila, México
* E-mail: roberto.benavides@ciqa.edu.mx; diana.morales@ciqa.edu.mx

ABSTRACT

Sulfonated polyether ether ketone (sPEEK) and their composites are considered one of the most promising alternative polymeric materials for the development of proton exchange membranes (PEM) due to good mechanical properties, resistance to high temperatures and excellent chemical resistance. The degree of sulfonation (DS) of PEEK can be controlled by reaction time and temperature, as well as the sulfonating agent. This study reports the preparation of sPEEK with varying DS and sulfonated reduced graphene oxide (srGO) for their potential application as composite proton exchange membranes for fuel cells. The sulfonation of PEEK was carried out using concentrated sulfuric acid (H_2SO_4) at 70 ºC and several reaction times (3-5h). GO synthesized by Tour's method was further reduced and chemically modified using the same sulfonating agent at 70 ºC. The sulfonation of PEEK and rGO was characterized by 1H NMR, FT-IR, and TGA-DSC techniques. FT-IR and 1H NMR confirmed the successful sulfonation of sPEEK and it was observed through TGA and 1H NMR that long reaction time increases the DS from 50 to 76% while maintaining good thermal stability over 300 °C for all reaction times. On the other hand, the sulfonation of rGO and its effects were characterized by FT-IR and TGA to evaluate its potential of becoming a prospect for application in PEMFC.

Keywords: PEEK; sulfonated PEEK; sulfonated reduced graphene oxide; PEM fuel cells

1. Introduction

The polyether ether ketone (PEEK) family of materials is a new generation of polymers with a semi-crystalline structure that has a unique combination of high mechanical properties, high-temperature and chemical resistance. Especially for polymer electrolyte membrane fuel cells (PEMFC), sulfonated PEEK (sPEEK) derivatives offer a lower-cost alternative to commercial Nafion membranes. The PEEK aromatic structure helps maintain thermal and mechanical stability, allowing chemical modification through electrophilic substitution (sulfonation). Sulfonation provides the ion exchange capacity and increases solubility to common solvents, facilitating processing for the obtainment of membranes [1] with improved hydrophilicity and water uptake capacity. Sulfonation ($-SO_3H$) of PEEK in H_2SO_4 occurs preferably in the hydroquinone segment of the polymer chain and is activated by the electrophilic substitution of the ether bond [2].

According to previous reports in the literature, the degree of sulfonation (DS) can be controlled by time, reaction temperature, and sulfonating agent; however, sulfonation conditions have not been optimized yet. Preliminary studies by our research group have suggested that PEEK may be sulfonated in short reaction periods, since substitution in other aromatic rings may occur as well when using higher temperatures (70-90 ºC).

On the other hand, the use of modified inorganic fillers such as graphene oxide (GO) in the sPEEK matrix, could increase the mechanical and thermal properties. Additionally, when GO is chemically modified by sulfonation ion conduction properties are also promoted.

This study reports the chemical modification of PEEK with concentrated sulfuric acid to obtain sPEEK with varying DS using different reaction times. The synthesis and sulfonation of GO are reported as well, with the perspective of developing composite membranes for PEMFC applications.

2. Materials and Methods

2.1 PEEK sulfonation

PEEK was obtained from Victrex® as a powder. 1 g of resin powder was dissolved in 10 ml of sulfuric acid (H_2SO_4 95-98%) and stirred at 70 ºC for the desired time, ranging from 2 to 5 hours. The polymer solution was then poured into ice water and washed several times with deionized water. The polymer precipitate was dried under vacuum at 40 ºC for 24 hours. The sulfonated polymers were labeled as sPEEK 70X, considering the reaction temperature (70 ºC) and X indicated the reaction time (3-5 hours), for example, sPEEK 705.

2.2 GO synthesis, reduction, and sulfonation

GO was synthesized from graphite (Sigma-Aldrich) using the Tour's method [3]. In a round flask, 2 g of graphite were mixed with 10 mL of H_3PO_4 and 46 mL of H_2SO_4. The mixture

was cooled to below 10 °C. Once the temperature was reached, 6 g of $KMnO_4$ were slowly added. The mixture was heated to 60 °C, then after 30 min 90 mL of deionized water was added. The reaction was maintained at 60 ºC and with magnetic stirring for 5 hours. Finally, 30 mL of a 3% H_2O_2 solution was added. The suspension obtained was washed and centrifuged with distilled water until neutral pH was reached, and dried at 60 ° C to obtain a film.

To partially remove the functional groups on the surface, GO was chemically reduced. Initially, 700 mg of GO were dispersed in 300 mL of deionized water with the aid of ultrasonic stirring. A solution of 4.2 mL of $NaBH_4$ (12%) in 56 mL of deionized water was prepared and added to the GO dispersion. The mixture was stirred for 1 hour. The suspension was washed with distilled water until neutral pH was reached. The suspension was decanted and dried at 60 °C until a film was obtained, which was labeled rGO.

Sulfonated reduced graphene oxide was prepared using H_2SO_4. 150 gr of rGO was ground and added into a two-necked ball flask containing 75 mL of H_2SO_4. The mixture was heated to 70 ºC with a heating mantle. The reaction was kept at a constant temperature for 8 hours, with magnetic stirring and under reflux. At the end of the reaction, the solution was diluted in 1.5 L of distilled water. Excess water was decanted, and the resulting suspension washed with distilled water until pH 5-6 was reached. The filtered material was dried at 60 °C for 24 hours. A thin film was obtained and labeled srGO.

3. Physicochemical characterization of sPEEK, GO, rGO, and srGO

The modification of the polymer structure derived from the sulfonation was evaluated by 1H NMR and FT-IR. The 1H NMR spectra of samples of the copolymers were obtained using a Bruker Advance 3 spectrometer at a resonance frequency of 400 MHz, using deuterated DMSO as the solvent. FT-IR spectra were obtained on a Bruker Vertex-70 spectrometer. The IR spectra were recorded between 4000 and 400 cm^{-1} at a resolution of 8 cm^{-1} using a diamond Attenuated Total Reflection (ATR) accessory. The formation of GO from graphite was confirmed by FT-IR spectroscopy. This technique also provided information about the oxygen-containing functional groups, their reduction, and those introduced by sulfonation. The IR spectra were recorded between 4000 and 600 cm^{-1} at a resolution of 8 cm^{-1} using a Ge ATR accessory.

DSC and TGA thermal analyses were performed to obtain the thermal transitions in sPEEK, as well as the decomposition pattern of the polymers before and after sulfonation. The TGA measurements were carried out on a TA Instruments Q800 thermobalance with thermal scans of 25 to 800 °C under a N_2 atmosphere and a 5-minute isotherm under an O_2 atmosphere; with a heating rate of 10 °C/min. For DSC analyses, a TA Instruments model Q2000 calorimeter was used, with thermal scans from 25 to 380 ºC at a rate of 10 ºC/min under a N_2 atmosphere. TGA analysis was also carried out to observe the differences in mass loss between graphite, GO, rGO, and srGO; as well as the thermal stability of the samples. The thermal scans went from 25 to 600 °C under a N_2 atmosphere and from 600 to 800 ºC under an O_2 atmosphere; with a heating rate of 10 °C/min.

4. Degree of sulfonation

The DS is defined as the percentage of repetitive PEEK units that have been sulfonated and can be determined from the data obtained from 1H NMR and TGA analyses [1].
From the TGA measurements, the weight loss of the curve between 200-300 °C is considered, which corresponds to the loss of the sulfonic groups [4], using the following equation:

$$DS = \frac{M(PEEK)\,m\Delta m}{M(SO_3H)} \quad (1)$$

where m= molar mass of sPEEK, Δm= weight loss of the sulfonic group in the TGA curve between 200-300 °C, and M(PEEK) and M(SO_3H) are the molar masses of PEEK and the sulfonic acid group (SO_3H), respectively.

The degree of sulfonation can also be determined quantitatively by 1H NMR. In the 1H NMR spectra, the presence of a sulfonic acid group in the hydroquinone ring of sPEEK causes a down-field shift of the 2' hydrogen compared to other protons present in the repeating unit [1,5].
The nomenclature of the aromatic protons for the sPEEK repeat unit is shown in Fig. 1.

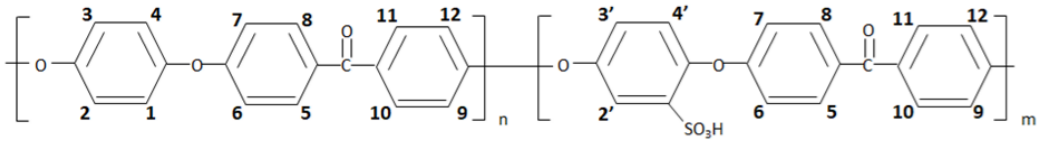

Fig. 1. Nomenclature of the aromatic protons for PEEK and sPEEK repeat units.

The intensity of the $H_{2'}$ signal is directly correlated to the $-SO_3H$ group content. The ratio between the peak area of the $H_{2'}$ signal and the integrated peak area of the signal corresponding to the $H_{5,8,10,11}$ hydrogens is an estimate for the content of sulfonic acid groups. A simplified equation to determine the DS is expressed as:

(2)

where $A_{H5,8,10,11}$ is the integrated peak area of the signal corresponding to the 5,8,10, and 11 hydrogens.

3. Results and Discussion

The modification of the chemical structure of PEEK was analyzed using FT-IR. Fig. 2 shows the spectra for the sPEEK materials at different reaction times.

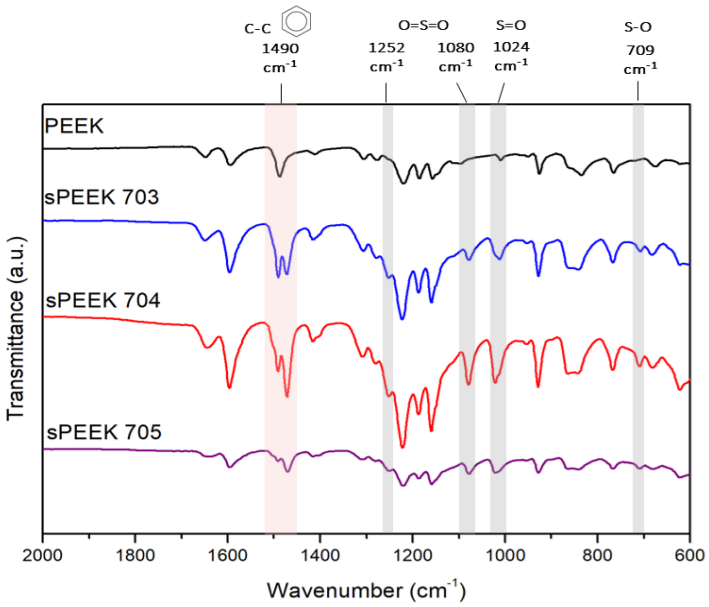

Fig. 2. FT-IR spectra of PEEK and sPEEK.

The presence of the $-SO_3H$ groups are observed with the absorption peaks at 1252, 1080, 1024, and 709 cm^{-1}; corresponding to the following bonds: asymmetrical and symmetrical stretching vibrations of the O=S=O group, and stretching vibrations of the S=O and S-O bonds, respectively. The aromatic C-C peak at 1490 cm^{-1} suffers splitting after sulfonation, the intensity of the new signal, at ~1472 cm^{-1}, increases with sulfonation time [6].

The sPEEK samples were also evaluated by 1H NMR to confirm the sulfonation of the polymer and to obtain the DS. The limitation of this analysis is that PEEK and sPEEK with low sulfonation levels present limited solubility in common organic solvents. For this reason, it was only possible to analyze the sulfonated materials. 1H NMR spectrum of sPEEK 703 dissolved in deuterated DMSO is shown in Fig. 3. The presence of the $-SO_3H$ group causes a significant shift of the $H_{2'}$ proton to ~ 7.5 ppm, compared to the $H_{3'}$ and $H_{4'}$ protons in the hydroquinone ring. The spectra for sPEEK 704 and 705 (not shown here) display similar behaviors.

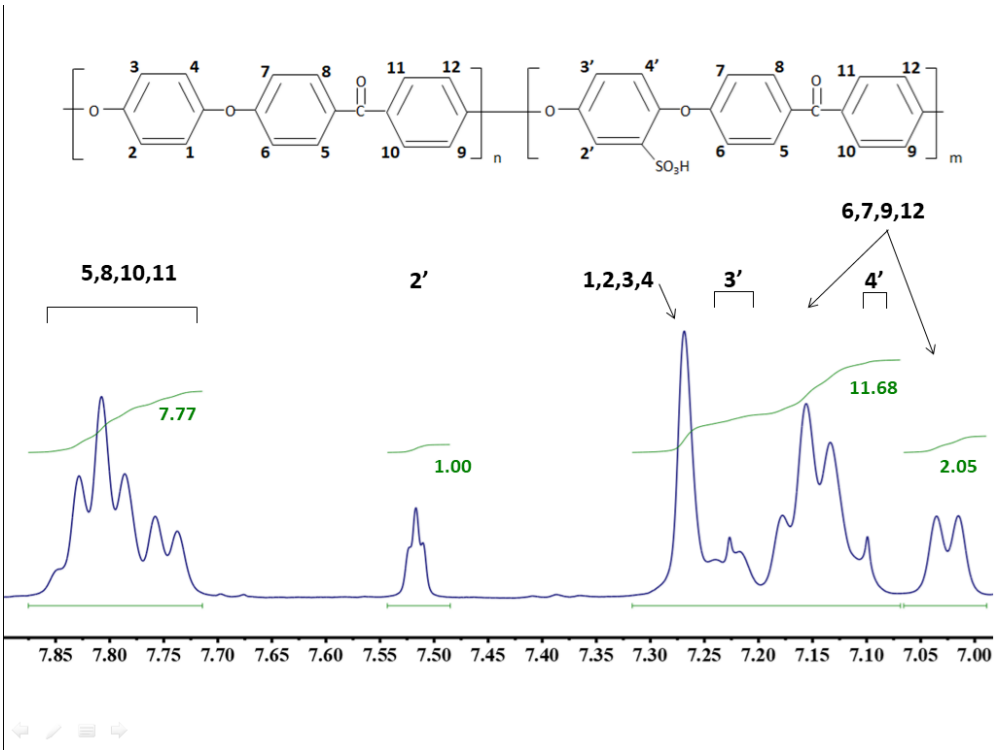

Fig. 3. 1H NMR spectrum of sPEEK 703.

The thermogravimetric curves for sPEEK with different sulfonation times (Fig. 4a) show three important regions of weight loss, unlike unsulfonated PEEK. The first loss occurs below 100 ºC and is related to the evaporation of water that is absorbed in the sample's surface, the second loss near 300 ºC is attributed to the loss of the $–SO_3H$ groups, and finally, the loss around 450 ºC corresponds to the degradation of the main polymer chain [7]. As expected, sulfonation affects the thermal stability of the polymer due to the decomposition of the acid group, displacing the onset of decomposition to a temperature range of 340 to 350 °C. This confirms that sulfonated PEEK at 70 °C maintains stability over a wide temperature range, which is above the common operating temperature for PEMFC (80-120 °C).

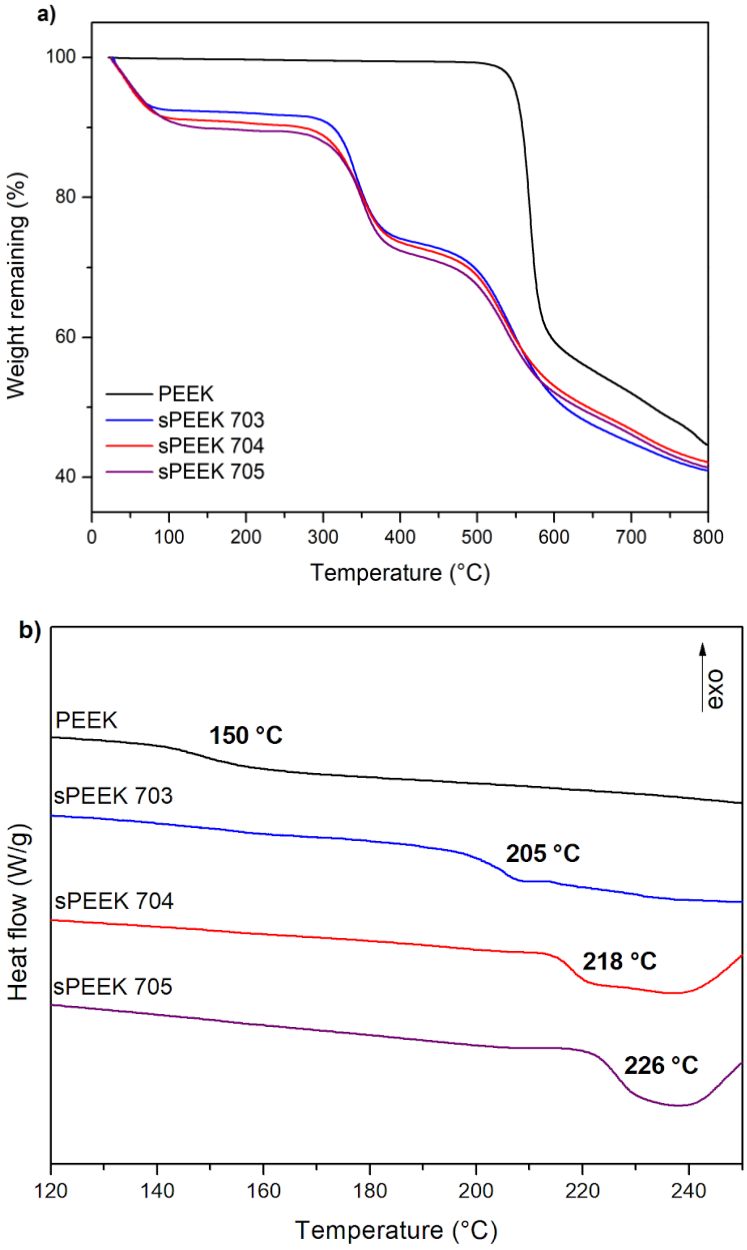

Fig. 4. TGA (a) and DSC (b) curves of sPEEK

The DSC thermograms (Fig. 4b), show that T_g tends to increase at higher DS. For sample sPEEK 705 the introduction of the -SO_3H group into the polymer chain displaced the T_g to ~ 76°C over the unsulfonated PEEK (150 °C). This increase in T_g results from the intermolecular interaction by hydrogen bonds that surge between the sulfonic groups. The decrease in free volume due to the introduction of the –SO_3H group may also contribute to reducing the mobility of the polymer chain [1].

From the values of the weight loss attributed to the removal of the sulfonic acid group (near to 300 °C), an estimate of the DS can be calculated. Table 1 presents the DS values obtained from the TGA and NMR data.

Table 1. DS obtained from TGA and 1H NMR analyses

Sample	DS obtained from TGA (%)	DS obtained from 1H NMR (%)
sPEEK 703	78	52
sPEEK 704	79	68
sPEEK 705	78	76

The DS values obtained from TGA, for the three different reaction times, remains almost constant (DS ~ 78%). It is observed that the temperature promotes a high level of sulfonation from low reaction times. However, DS from NMR data, using the integration of the $H_{5,8,10,11}$ peaks in relation to the integration of the H_2 peak of the spectra, indicate a clear tendency of higher DS values with increasing reaction time. Sulfonation proceeded rapidly, with DS starting at a value of 52% up until 76% for the longest reaction time.

The difference in the DS values obtained through TGA and 1H NMR can be attributed to the precision of each technique, besides, we are assuming the weight loss near 300 ºC in the TGA curves corresponds to just the sulfonic acid groups present in the sample, when some other subproduct may be getting released during the thermal process.

GO is capable of holding several oxygen-containing groups, such as carbonyl (C=O), hydroxyl (-OH), carboxyl (-COOH), as well as oxygen epoxide groups. The successful synthesis of GO from graphite was analyzed using FT-IR and thermal decomposition through TGA (Fig. 5).

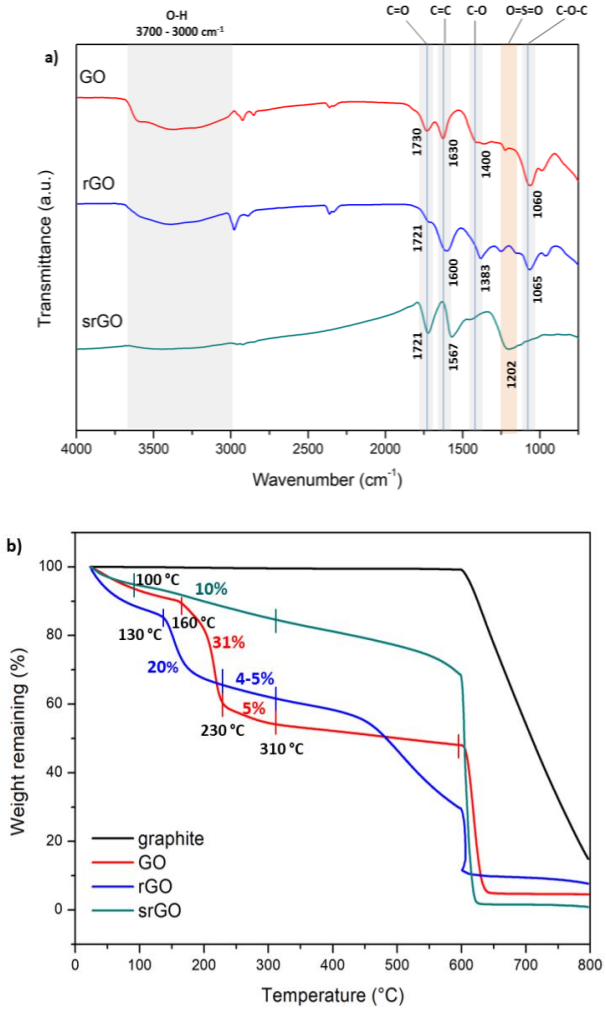

Fig. 5. FT-IR spectra (a) and TGA thermograms (b) of GO, rGO and srGO.

FT-IR GO spectrum shows a characteristic broad band for intermolecular hydrogen bonds at the 3000-3700 cm^{-1} region due to –OH on the GO surface [8]. The spectrum also shows peaks at 1730, 1630, 1400, and 1060 cm^{-1} which correspond to the stretching of the C=O bonds from the carbonyl groups, the vibration of the C=C bond associated to aromatic rings within the GO carbon skeleton structure (CC sp2 bonds that remain unoxidized), the stretching of the C-O bond from the carboxyl group, and the stretching of the C-O-C bonds from the epoxide groups, respectively.

The spectrum for rGO shows some differences in contrast to the GO spectrum. The peak at 1600 cm^{-1} is due to the stretching of the C=C bond, and the small shoulder at 1721 cm^{-1} is due to the remaining C=O groups in rGO. The peaks at 1383 and 1065 cm^{-1} are associated with the stretching of the C-O and C-O-C bonds, respectively, from the carboxyl and epoxide groups remaining even after the reduction reaction [3].

The modification by sulfonation of the rGO can be confirmed with the appearance of a new peak at 1202 cm^{-1} in the srGO spectrum, which corresponds to the symmetrical and asymmetrical stretching of the O=S=O groups present in the sulfonic acid groups. The peak associated with the C=C bond suffers a shift to 1567 cm^{-1} allowing the visibility of the peak at 1721 cm^{-1}, associated with the C=O bond.

The thermal stability of graphite, GO, rGO, and srGO examined by TGA analysis is observed in Fig. 5b. Evidently, graphite exhibits one clear step of weight loss at 600 °C once the introduction of the oxygen atmosphere starts. GO and rGO decompose in three main steps. For GO, the first loss (up to 160°C) is associated with the release of water molecules from the surface or trapped between GO sheets. The second weight loss from 160 to 230 °C, which comprises 31% of the total weight, is due to the loss of less stable oxygenated functional groups, such as hydroxyl and epoxide groups. The lower weight loss of 5% is related to more stable oxygen-containing groups, whose pyrolysis yield CO y CO_2. The rGO curve shows similar characteristics but with lower amounts of weight loss compared to GO, particularly in the second weight loss, from 130 to 230°C, which shows a 20% weight loss of the more labile oxygen-containing functional groups. This confirms the reduction of GO, decreasing the content of oxygenated functional groups in the GO structure [9,10].

Focusing on the same region, the curve for srGO shows a loss of just 10% until 310°C, due to the release of the $–SO_3H$ group and some more stable oxygen-containing groups present in the srGO structure.

5. Conclusion

PEEK was successfully modified via sulfonation to introduce $–SO_3H$ groups. The sulfonated material shows a high DS (52-76% by 1H NMR) with good thermal properties which are fit to be potentially used as membranes in PEMFC. Additionally, GO was synthesized and further reduced and sulfonated, to become an adequate prospect in the future development of sPEEK composite membranes.

Acknowledgments

This work has been supported by the Mexican National Council of Science and Technology (CONACyT) through grants CB259010 and FC3004. ASM is thankful to CONACyT for the scholarship. The authors are also grateful to the National Laboratory of Graphene Materials (LNMG).

References

[1] Zaidi SMJ. Polymer Sulfonation – A versatile Route to prepare proton -conducting membrane material for advanced technologies. Arab J Sci Eng 2003;28:183–94.

[2] Xing P, Robertson GP, Guiver MD, Mikhailenko SD, Wang K, Kaliaguine S. Synthesis and characterization of sulfonated poly (ether ether ketone) for proton exchange membranes. J Memb Sci 2004;229:95–106.

[3] Morales-Acosta D, Flores-Oyervides JD, Rodríguez-González JA, Sánchez-Padilla NM, Benavides R, Fernández-Tavizón S, et al. Comparative methods for reduction and sulfonation of graphene oxide for fuel cell electrode applications. Int J Hydrogen Energy 2019;44:12356–64.

[4] Flores-Escareño PC, Morales-Acosta D, Benavides R. Chemical modification of polyether ether ketone and the obtainment of proton exchange membranes. Doctoral thesis. In process. 2019.

[5] Huang RYM, Shao P, Burns CM, Feng X. Sulfonation of Poly (Ether Ether Ketone)(PEEK): Kinetic Study and Characterization. J Appl Polym Sci 2001;82:2651–60.

[6] Araby R, Attia NK, Khafagi M, Mostafa T. Characterization and sulfonation degree of sulfonated polyether ether ketone using Fourier transform infrared spectroscopy Characterization and Sulfonation Degree of Sulfonated Poly. World Appl Sci J 2014;32:2239–44.

[7] Knauth P, Hou H, Bloch E, Sgreccia E, Vona ML Di. Thermogravimetric analysis of SPEEK membranes : Thermal stability, degree of sulfonation and cross-linking reaction. J Anal Appl Pyrolysis 2011;92:361–5.

[8] Dai W, Shen Y, Li Z, Yu L, Xi J, Qiu X. SPEEK/Graphene oxide nanocomposite membranes with superior cyclability for highly efficient vanadium redox flow battery. J Mater Chem A 2014;2:12423–32.

[9] Chen J, Yao B, Li C, Shi G. An improved Hummers method for eco-friendly synthesis of graphene oxide. Carbon N Y 2013;64:225–9.

[10] Loryuenyong V, Totepvimarn K, Eimburanapravat P, Boonchompoo W, Buasri A. Preparation and Characterization of Reduced Graphene Oxide Sheets via Water-Based Exfoliation and Reduction Methods. Adv Mater Sci Eng 2013;2013:1–5.

ID 036

CFD PEMFC simulation with different levels of enriched air

Eduardo A. Rosado Vázquez[1], Humberto J. Mandujano Ramírez[1], Sandra J. Figueroa Ramírez[1], Juan M. Sierra Grajeda[1,*]

[1]Universidad Autónoma del Carmen, Facultad de Ingeniería, zip code 24180. Cd del Carmen Campeche, México

* Corresponding author: 7771843585; jsierra@pampano.unacar.mx

ABSTRACT

The present work, is about the simulation and analysis using computational fluid dynamic (CFD) on a proton exchange membrane fuel cell (PEMFC) considering steady state and non-isothermal conditions, different scenarios were evaluated varying oxygen concentration for enriched air at the cathode entrance. The model consists of a 3D mono-cell with a channel in each plate that meanders in a squared shape eight times in order to cover its area. The model includes a membrane, catalytic layers, diffusion layers, monopolar plates. The mesh is a hexahedral type with 569,088 elements. The operation conditions were 1 atm and 300 K considering one phase. Properties as pressure, temperature, current density, species concentration are obtained at different components of the membrane-electrodes ensemble. Analyzing the processed results, one can observe, when the oxygen arrives to the catalytic layer is enough and approximately homogeneous, the grater the oxygen concentration at the cathode entrance the more is the generated current density at the catalytic layer. The protonic conductivity and the ionic current density have a similar behavior. Moreover, the obtained properties distribution at the diffusion layer, catalytic layer and the membrane, the heterogeneity at these components is very similar for different oxygen concentration at the cathode entrance but with ranges of values that depends on this parameter. This way, the ranges' upper limit on current density, relative humidity, oxygen concentration, protonic conductivity, and temperature, increase with increasing oxygen concentration at the cathode entrance. Besides, it is observed that at very high rates the polarization curves separation is less compared with an optimal rates range. Also, at very low rates, this sensibility to oxygen concentration is low because the oxygen is not enough at the catalytic layer. It was observed an optimal range of rates where sensibility to oxygen concentration at the cathode entrance is noticeable and important due to enriched air adds to the system´s electric power in an appreciable way.

Keywords: PEMFC; enriched air; CFD;

1. Introduction

Proton exchange membranes fuel cells (PEMFC) are considered as green friendly way to have a portable source of energy for mobile applications, because of its characteristics for consume oxygen and hydrogen to produce, electric power, heat and water. Additionally, hydrogen gas, can be produced from hydrocarbons but also from green energy sources like Eolic, Photovoltaic, Solar, etc. Despites there are some environmental impact issues, due to the manufacturing parts of the PEMFC, these can be importantly reduced by recycling. Daniel et al. made an environmental impact comparison review for gasoline internal combustion engine (ICE), diesel ICE, Methanol PEMFC, no green hydrogen PEMFC, and PEMFC with hydrogen from wind. They reveal the hydrogen green PEMFC potential to substantially reduce greenhouse gas emissions, environmental noise and vehicle vibrations due to much less moving parts, routine maintenance and higher mileage too. One of the principal conclusions was that recycling, will help to reduce in a great way the PEMFC manufacturing environmental impact on acidizing, global warming and energy resources [1].

The PEMFC consist of an electrochemical system that converts the chemical energy contained in hydrogen and oxygen into electricity. Jiao & Ni made a review of challenges and opportunities about research of this device behavior under several operation conditions and modeling considerations [2].

The flow fields design is important to provide a uniform spatial distribution of the reacting gas front advance to the membrane in order to get a homogeneous distribution of current density at the cell. P.Y.A. Chuang et al. made experimental comparison of three flow field designs, straight parallel, multiple channel serpentine and single channel serpentine. They concluded that the single serpentine channel behaves better over a variety of operating conditions [3].

There are experimental works about PEM Fuel Cell operation with air enriched with higher oxygen concentrations. F. Javier Pinar et al. evaluated a high temperature (HT) PEMFC performance and degradation under operation with oxygen enriched cathode air and hydrogen from synthetic reformate. They observed experimentally that the system provides solutions to achieve higher efficiencies only when cathode oxygen concentration does not exceed 30 % V/V and they reported after some electrochemical test, this was due to oxygen concentration that improves the kinetics and prevent corrosion occurring for higher concentrations [4]. Jay Benziger et al. made experimental work considering two configurations: a one-dimensional stirred tank reactor (STR) PEMFC and two-dimensional parallel flow channel PEMFC. In the first experiment instead of flowing gas channels, there is stagnant gas at constant concentration. For both experiments he evaluated several scenarios to generate polarization curves considering an specific oxygen concentration at the cathode gas inlet for each polarization curve generation. They concluded that reducing oxygen concentration at the cathode channel to air, reduces significantly the current or the cell voltage at the PEMFC and also they mention about oxygen lateral transport from cathode channel to the cathode catalyst layer that reduces highly the local current density [5]. Hamelin et al., obtained the experimental polarization curves and the power efficiency curves for different levels of oxygen gas enrichment. They evaluated three methods to

produce oxygen: pressure swing adsorption, membrane separation and oxygen recuperation as an electrolysis byproduct. In the energy efficiency analysis, they considered that feeding with oxygen instead of air, would leads to handling concerns and additional cost and complexity. In this way, considering all this system in the energy efficiency evaluation, they concluded that none of the studied systems for enriched oxygen would increase the available power comparing with using oxygen from air only. Also, they reported that without considering the oxygen providing system, the best increment in power was at oxygen concentration at the cathode injected gas between 21% y 40 % [6].

2. Materials and Methods

This work is based on a computational fluid dynamic (CFD) model about a proton exchange membrane fuel cell (PEMFC) considering steady state and non-isothermal conditions [7]. The implemented mesh was hexahedral with 569,088 elements. For solution equations were used a commercial software with a segregated method for discretization equations and applied simple algorithm for pressure velocity coupling. The model consists in a 3D cell with 52 mm large along *x* axis, 18 mm width in *y* axis and 3.72 mm high *z* axis. This cell contains one proton exchange membrane, two catalyst layers, two gas diffusion layers and two monopolar plates. The cathode and anode electrodes have, each one, a channel distributed in a square serpentine way. The channel width is 1 mm and the height is 1 mm too. Both channels cover the whole cell's active area. Each of these channels is engraved at the interior face of each monopolar plate and the external face is the external electric contact. In this way, the electric circuit is closed when both electric external contacts are connected to an electric load. Next to the internal face of each monopolar plate is the gas diffusion layer and beside the later we have the catalyst layer embedded in the membrane located at the center of the cell. In this way the membrane has catalyst layers at both sides one for anode and the other for cathode reactions with hydrogen and oxygen respectively as reactants [8], [9]. The hydrogen gas is injected to the cell by the entrance of the anode channel and the oxygen gas at the entrance of the cathode channel. While they flow along each channel, one part diffuses to the catalyst layer, through the diffusion layer. At the anode catalyst layer the hydrogen gas react producing two protons and two electrons, these electrons migrate from the anode catalyst layer to the anode external contact in direction to the electric load and the protons migrate from the anode catalyst layer to the cathode catalyst layer through the membrane. At the cathode catalyst layer electrons arrive from the external cathode electric contact, connected to the load, and encounters with the oxygen and protons generating heat and water and providing electric current. In figure 1 it can be seen the structure of the PEMFC.

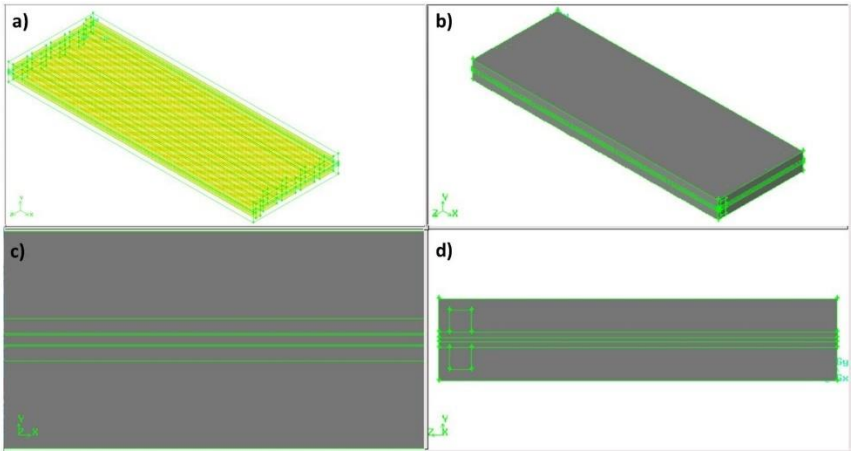

Fig. 1. PEMFC model structure from different views. (a) Structure isometric view with channels grid elements. (b) Solid and isometric view with the external boundaries. (c) Side view with all PEMFC layers. (d) Front view with layers and output boundaries, one for anode and other for cathode.

The electric boundary conditions consider zero potential for the external anode and constant cell potential for external cathode. So, there is electric current flux through external anode and external cathode, but not across any other external boundary. In the case of inlets boundary conditions, we consider for the cathode channel inlet, in the upper electrode, constant oxygen enriched air flow rate and for the anode channel inlet, in the lower electrode, constant hydrogen flow rate. For both channels outlets, anode and cathode, the boundary condition is constant atmospheric pressure.

In the first stage of the work we made an electric power sensibility to the oxygen concentration in the gas at the cathode entrance (enriched air) and to the flow rate of enriched air at the cathode entrance. This permitted to choose a flow rate were electric power is sensible to the level of enriched air.

In the second stage the simulated scenarios considered different levels of enriched air to generate polarization curves for each different oxygen concentration. So, we also simulated scenarios with different cell voltage to sweep the whole polarization curve for each oxygen concentration. These simulations permitted to visualize the polarization curves' zones sensibility to the level of enriched air.

In the third part of the work it was analyzed some spatial distribution properties in many parts of the cell, principally at the cathode catalyst layer as will be shown in some figures in the next section. All these analyses give information about how oxygen spatial distribution properties, that depends on enriched air level, influence the PEMFC electrical behavior.

3. Results and Discussion

Results from sensibility of PEMC´s electric power to enriched air level and flow rate is shown in the next figure for cell potential of 0.6 volts. The electric power density behaves like a no symmetric bell while varying the flow rate at cathode inlet. The low rate side ramped linearly, and the high flowrate side is strongly damped as can be observed at 100 % O_2 and 20.9 % O_2 curves.
Also, as we increase the enriched air level, the bell´s maximum increases nonlinearly and occurs at lower flow rate. The pure oxygen maximum represents approximately 20 % increase respect the just air maximum scenario as can be calculated from the figure.

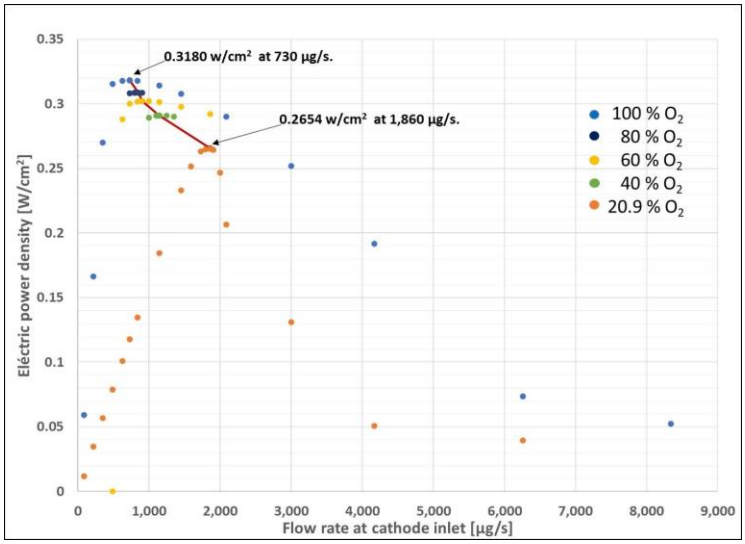

Fig. 2. Electric power density sensibility to both, flow rate and enriched air level at cathode entrance for 0.6 V.

In the other hand, looking for electric power density sensibility to enriched air level, it can be seen that it´s very sensible at the pure oxygen maximum power´s flow rate and much less sensible at just air maximum power´s flow rate. Because we want to look for enriched air level influence on PEMFC behavior and because low flow rate is more practical, we chose 730 µg/s as the flow rate considered at the cathode entrance in order to do the next analysis where we additionally change the cell voltage to investigate the polarization curves sensibility to the enriched air level variation at the cathode inlet. In the study of the next results, we considered nine enriched air levels since just air to pure oxygen at the gas entrance to the cathode channel. For each enriched air level were simulated multiple scenarios each of them with different cell voltage as can be seen in the next figure. It can be observed a sensibility of the zone of loses due to mass transport where the limit current is located to higher values and for lower voltages when the enriched air level increases. Also, the zone of energy loses due to Ohmic resistance increases its current interval including higher currents and lower voltages as the enriched air level is increased. Also, for most of the range from Ohmic losses zone all enriched air level polarization curves approximately follow the same envelop traced by the pure oxygen cases, getting away from it, in the higher current density part of this zone.

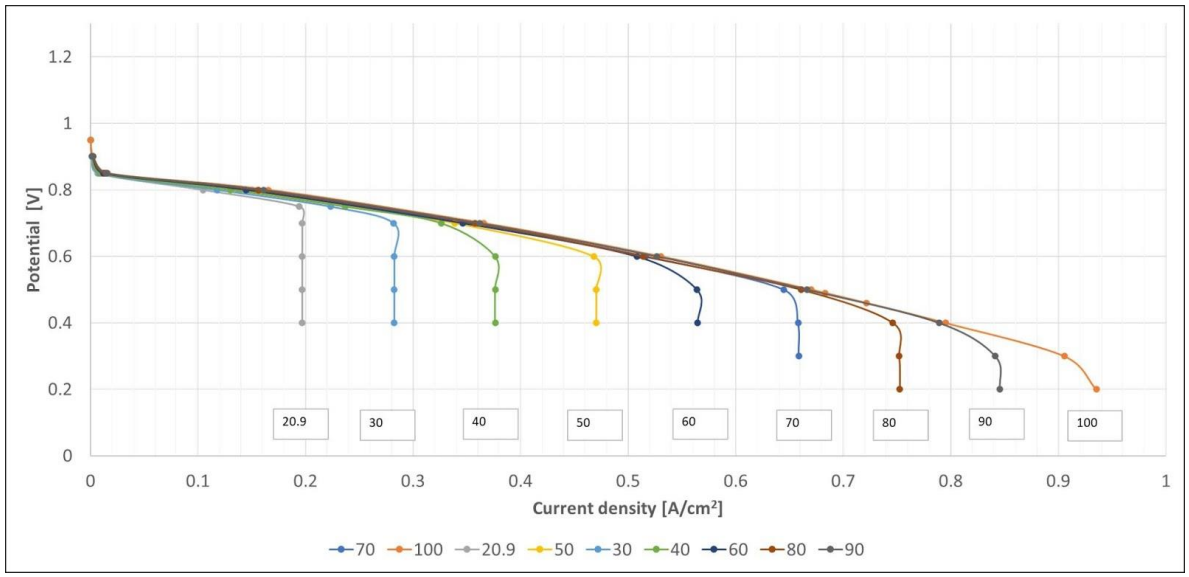

Fig. 3. Polarization curves sensibility to enriched air level at cathode inlet.

For all these scenarios it was calculated the electric power density, in the next figure can be seen the power density behavior with the current density variations. Each power density curve corresponds to a polarization curve. Consider that as current density increases the voltage decreases, and at current limit the voltage can decrease. As current density increase for low currents, the power density increase linearly until getting a maximum to suddenly drop for low enriched air levels and as the enriched air level is increased the maximum is reached in a more soft way and the drop after the maximum is softer in a way that for pure oxygen in the neighboring maximum zone can be approximated as constant 0.334 W/cm^2. In the same figure it can be seen the segmented line for scenarios with different enriched air levels but with the same cell voltage of 0.6 volts. Along this segmented line, it can be appreciated that the power density increases, due to enriched air level at cathode increases. This is substantial for enriched air levels lower than 60 % oxygen and for greater enriched air levels de increase in the power density is marginal. This observation stablishes that for 0.6 volts, 60 % air enriched level technically is an optimal oxygen concentration for the gas at the entrance of the cathode channel.

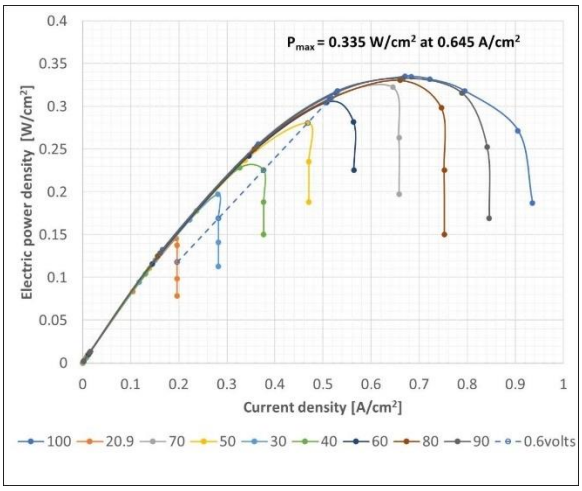

Fig. 4. Power density polarization curves.

To reinforce this asseveration let see some properties distributions at the catalyst layer cathode for 0.6 volts scenarios in figure 5.

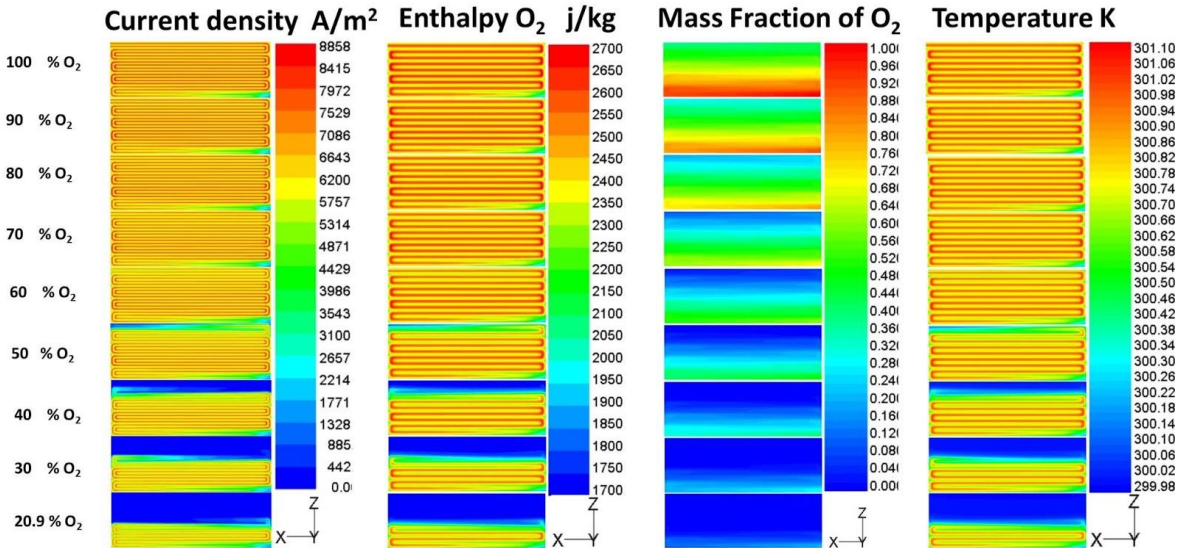

Fig. 5. Properties distributions for 0.6 V at catalyst layer cathode. The enriched air level or oxygen mass percentage at the cathode channel inlet can be read to the left.

In the last figure it can be appreciated that for enriched air levels lower than 60 % as the enriched air lever is increased the utilized cell active area increase adding substantially more current density to the cell current and incrementing the cell electric power. It can be seen also a strong correlation between the current density and the oxygen enthalpy distribution. This oxygen enthalpy distribution could be generated by the temperature distribution detonated by the mass fraction of oxygen distribution, results of the enriched air level at the cathode channel inlet.

4. Conclusions

The increment of enriched air level or told in another way the increment of oxygen concentration at the inlet of the cathode channel, increases the PEMFC's electric power.

The increment of enriched air level above certain value, the optimal value, produce a marginal increment in electric power.

The increment of enriched air level below certain value, the optimal value, produce a substantial increment in electric power.

The optimal level of enriched air injected in the cathode inlet, for 0.6 V of cell's potential from the simulated scenarios in this work, is identified as 60 % of oxygen mass fraction.

This work shows a methodology to calculate a technically optimal value of enriched air level at the cathode channel inlet for a PEMFC.

Acknowledgements

The authors gratefully acknowledge to UNACAR and CONACyT for the financial support from the project No. 254667 "Consolidación del Laboratorio de Energía Renovable del Sureste (LENERSE)".

References

[1] Daniel Garraín, Yolanda Lechón, Cristina de la Rúa. Polymer electrolyte membrane fuel cells (PEMFC) in automotive applications: environmental relevance of the manufacturing stage. Smart Grid and Renewable Energy 2011;2:68-74.
[2] Jiao, K., Ni, M. Challenges and opportunities in modelling of proton exchange membrane fuel cells (PEMFC). Int. J Energy Res. 2017; 1-5.
[3] Mojica, F., Rahman, M. A., Mora, J. M., Ocon, J. D., & Chuang, P. Y. Experimental Study of Three Channel Designs with Model Comparison in a PEM Fuel Cell. Fuel Cells 2020; No. 0: 1-11.
[4] F. Javier Pinar, Nadine Pilinski, Maren Rastedt, Peter Wagner. Performance of a high-temperature PEM fuel cell operated with oxygen enriched cathode air and hydrogen from synthetic reformate. International Journal of Hydrogen Energy 2015; 40: 5432-5438.
[5] Jay Benziger, Erin Kimball, Raquel Mejia-Ariza, and Ioannis Kevrekidis. Oxygen Mass Transport Limitations at the Cathode of Polymer Electrolyte Membrane Fuel Cells. AIChE J 2011; 57:2505-2517.
[6] Fournier, M., Hamelin, J., Agbossou, K., and Bose, T. K. Fuel cell operation with oxygen enrichment. Fuel Cells 2002; 2 No.2: 117-122.
[7] ANSYS FLUENT 12.0 Fuel Cells Module Manual 2009; 1-12.
[8] BARBIR, F. PEM Fuel Cells Theory and Practice. Storrs, CT: Elsevier; 2005.
[9] Colleen S. Spiegel. Designing & Building Fuel Cells. 1st ed. New York: Mc Graw Hill; 2007.

ID 037

Effect of Polymer Sulfonation on the thermal and Ion Exchange Capacity Properties of SPEEK Membranes for PEMFC

P.C. Flores Escareño, R. Benavides*, L. Da Silva, D. Morales Acosta*

Centro de Investigación en Química Aplicada, Blvd. Enrique Reyna No. 140, Col. San José de los Cerritos, 25290. Saltillo, Coahuila, México.
*Tel: +52844-4389830 E-mail: roberto.benavides@ciqa.edu.mx; diana.morales@ciqa.edu.mx

ABSTRACT

Poly(ether-ether-ketone) is an alternative polymeric material for the development of proton exchange membrane for fuel cell application. In this work, the chemical modification of poly(ether-ether-ketone) by electrophilic sulfonation was carried out using sulfuric acid at several temperatures 70 y 80°C and several reaction times (1-5 h). SPEEK membranes were obtained by casting. The physicochemical, thermal, mechanical, and ionic conductive properties of sulfonated PEEK and membranes were evaluated. The sulfonation of PEEK was confirmed for all conditions established. The sulfonated PEEK long times (SPEEK 804 y SPEEK 805), the low solubility and/or high hydrophilicity affect their processing confirmed by FTIR and ^{1}HNMR, while the sulfonation degree (DS) was calculated by ^{1}H NMR, and the results were similar than those reported in the literature (48 to 68 %). Thermal stability as well as the glass transition varied with respect to the DS. SAXS results show the increasing amorphous nature of the membranes with increase DS value. Depending on the degree of sulfonation, the water uptake (WU) and ion exchange capacity (IEC) of the membranes varied from 4%-112% and 0.78-2.28 meq g^{-1}, respectively, which in some cases were higher than those obtained for commercial NAFION® membrane (WU=13% and IEC= 0.91 meq g^{-1}). Results regarding proton conductivity from the latter will be presented as well.

Keywords: PEEK, Sulfonation, membranes, Fuel Cells.

1. Introduction

The increasing demand for energy has been generated from domestic devices to various means of transport, it also increases the need to develop further research to find alternative and clean sources of power generation to meet global demand. Fuel cells (FC) are electrochemical devices that have a particular attention for their high power density on stationary or mobile applications, and also because they generate low impact on the environment[1]. It should be emphasized that the proper performance of the FC depends to a largely extent on the polymer exchange membranes (PEM), which is responsible for proton transportation from the anode to the cathode. Traditionally in proton exchange fuel cells (PEMFC), the most used membrane is the commercially known as NAFION®. Sulfonated poly(ether ether ketone) (SPEEK) has been widely employed during the last decade to fabricate membranes operating in the range from 90-120ºC. The degree of sulfonation (DS) is defined as the number of sulfonic acid groups per repeating unit and can be controlled by reaction conditions.
In this work, the sulfonation of PEEK was carried out at different temperatures (70-80°C) and reaction times (1-5h), to obtain SPEEK with a high level of sulfonation and film forming capacity. The sulfonated polymers were characterized by FTIR and TGA. The effect of sulfonation degree in polymer solubility and film formation capacity were evaluated, as well as the ion exchange capacity and water uptake properties.

2. Materials and Methods

Poly (ether-ether-ketone) was acquired from Good Fellow in the form of pellets, Sulfuric Acid (H_2SO_4 98-99%) and dimethylacetamide (DMAc 98%) were purchased from Aldrich.

2.2 Sulfonation reaction

The sulfonation of PEEK was carried out using concentrated sulfuric acid as sulfonating agent. PEEK powder was dissolved in concentrated sulfuric acid with a PEEK/H_2SO_4 ratio of 1:10 w/v. Subsequently the solution was heated at a specific temperature (70 or 80ºC) during different times (1, 2, 3, 4 and 5h) under a nitrogen atmosphere and reflux conditions. The reaction was stopped by pouring the sulfonated polymer solution into a beaker with distilled water immersed in an ice bath. The solid sulfonated polymer was washed several times with distilled water until neutral pH was reached and subsequently dried in a vacuum oven at 60°C for 48 h, to remove residual water. The samples were labelled as SPEEK-X-Y (X=70, 80 ºC and Y= 1, 2, 3, 4, 5 h) [2].

2.3 Membrane preparation

The sulfonated PEEK membranes were prepared by the casting method using DMAc as solvent. 0.2g of SPEEK were dissolved in 20mL of solvent, then poured into a flat glass container to let solvent evaporates. The casted membranes were dried at 50ºC in a vacuum oven for 24 h, to remove residual solvent.

2.4 Characterization of polymers and membranes

FTIR measurements were performed in an instrument Bruker Vertex-70 infrared spectrometer, with a nominal resolution of 4 cm^{-1} in the 4000-500 cm^{-1} region. Thermal stability was determined by TGA analysis, using an equipment TA Instruments model Q500 under nitrogen atmosphere and a heating rate of 10 °C/min^{-1}, from 30 to 600ºC. Water uptake (WU) measurements of the SPEEK membranes were conducted by immersing the membrane samples into distilled water at room temperature for 24h for full equilibrium. Then, the membrane surface was wiped off with a tissue paper and weighed immediately in order to obtain the wet weight (W_{wet}). Membranes were dried at 80°C in a vacuum oven for 2h and later weighed to determine the dry weight (W_{dry}). The percentage of water uptake is calculated by differences between dry/wet weights (in gr.), according to the equation [3]:

$$WU\% = \frac{Wwet - Wdry}{Wdry} \cdot 100 \qquad (1)$$

The ion exchange capacity (IEC) and degree sulfonation of the sulfonated PEEK membranes were evaluated by an acid-base titration method using a potentiometric titrator from Metrohm. The dried membrane was immersed into a 1M HCl solution for 24h; then rinsed and immersed into deionized water. Finally, the membrane was rinsed into 1M NaCl solution for 24h and the resultant solution was titrated with a 0.005M of NaOH solution. The IEC and sulfonation degree (DS) of SPEEK were calculated using the following equations:

$$IEC = \frac{V_{NaOH} \cdot N_{NaOH}}{Wdry} \cdot 100 \qquad (2)$$

$$DS\% = \frac{IEC.Mw(polìmero)}{1-(IEC.MwSO3H)} \cdot 100 \qquad (3)$$

where V_{NaOH} (mL) and N_{NaOH} (mL) is the volume consumed and concentration of NaOH (mmol·mL^{-1} ~meq·mL^{-1}), W_{dry} is the dry weight of the polymer membrane, Mw PEEK (g·mol^{-1}) is the molecular weight of the polymer (PEEK or SPEEK) and Mw SO_3H (g.mol^{-1}) is the molecular weight of the sulfonic group.
DS was also calculated from the TGA thermograms, using the following equation:

(4)

$$DS\,(\%) = \frac{MwPEEK}{\{(\frac{m}{\Delta m-1})\}.MSO3H} \cdot 100$$

where m is the molecular mass of the SPEEK, Δm is the first loss in weight in the thermograms of the sulfonated polymers, corresponding to the weight loss by the decomposition of the sulfonic group.

The ^{1}H RMN spectra for the sulfonated samples were obtained on a Bruker Advance instrument operating at frequencies of 500 MHz and 125 MHz, respectively. The conditions of the analysis were: test temperature at 25 °C, central peak of $DMSO_d$ assigned to 7.26 ppm(^{1}H).
DSC analyses were performed on a TA Instruments model Q200 calorimeter. Considering the glass transition temperatures of SPEEK, the thermal range used for sulfonated polymers was 20-380 °C with a heating ramp of 20°C.min^{-1}. All were made in nitrogen atmosphere.
Two-dimensional wide-angle X-ray scattering was acquired using a diffractometer equipped with a CCD detector and CuK, α (1.54184 Å) radiation operated at 35 mA. Measurements were performed at room temperature with exposure times of 200 seconds.

3. Results and Discussion

The sulfonation of PEEK to various reaction conditions allowed to observe very different products, all precipitated from the same established temperature and time conditions. However, it is worth mentioning that for temperature of 80°C and reaction times of 3 to 5 hours, difficulties during for washing during neutralization were observed. Apparently, not only hydrophilicity was affected for the high number of sulfonic groups introduced, but also changes in polarity which in turn affects solubility.

SPEEK materials 703, 704, 705, 801, 802, 803, 804 and 805 were capable to form membranes and convenient to follow characterization. Figure 1 shows images of the membranes obtained. The precipitates SPEEK 701 had partial solubility while the SPEEK 702 sample was mostly soluble.

Fig. 1. Membranes obtained with DMAc solvent.

It can be seen that in SPEEK 70 and 80 samples, coloration changes as the sulfonation time increases, from white to transparent; it can be attributed to the level of sulfonation, modifying the crystallinity of the material.
Regarding FTIR spectra from materials, Figure 2 shows the differences between 1 and 5 h of sulfonation (a) and the differences between 70 and 80ºC (b), with the extreme condition (30ºC and 30h) for comparison.

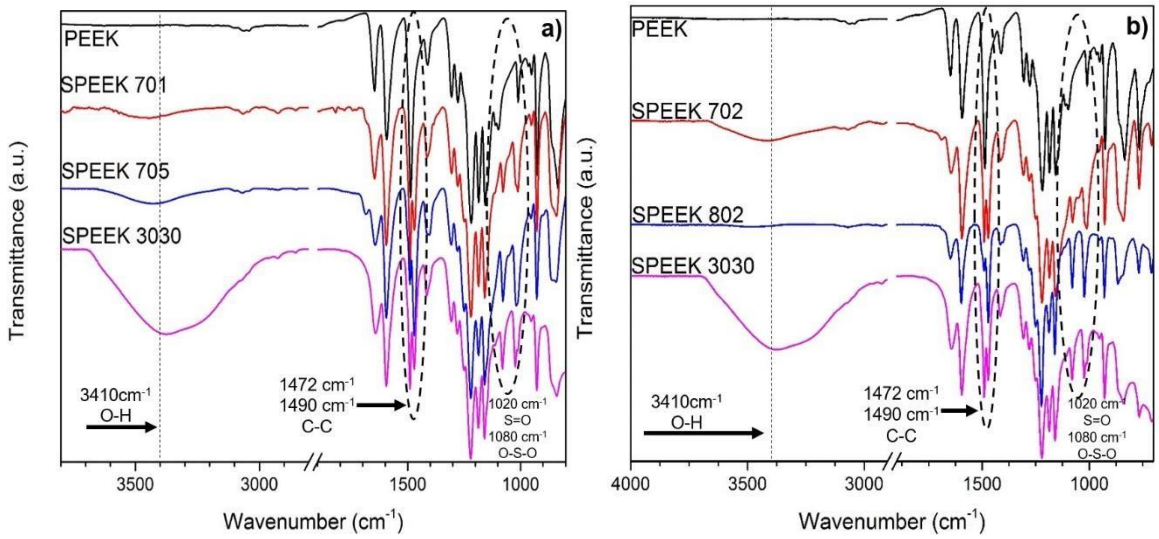

Fig 2. FT-IR spectra for PEEK sulfonated at different times (a) 1, 5 and 30 h different temperatures 70, 80 and 30 °C (b).

The untreated PEEK contains the characteristic absorption bands at 1649-1651 cm^{-1} [6,7] corresponding to the C-C link of the main chain replacement and the band to 1223 cm^{-1} which is the presence of the C-O-C link of the main chain. Once PEEK is sulfonated, the presence of some characteristic groups appears. The increase in O-H vibration of the sulfonic acid groups at 3410 cm^{-1} is clearly observed [9, 10] increasing with sulfonation time (Fig. 2a), although changing from 70 to 80ºC (Fig. 2b) makes no difference in OH intensity; it is more clear for the SPEEK 3030.

On the other hand, the regions that undergo changes by sulfonation is the band of the aromatic C-C vibration at 1490 cm^{-1}, which is divided generating a band at 1472 cm^{-1}, and increases with the reaction time. The bands at 1080 and 1020 cm^{-1} are attributed to symmetrical and asymmetrical vibrations between the oxygen-sulfur S=O. The later suffers a change in intensity with respect to temperature conditions.

It is notorious that the extreme condition of 30h at 30ºC of sulfonation reaction, produces a highly sulfonated material with a very intense band of the OH vibration coming from the presence of the sulfonic group inserted into the polymer. Moving reaction temperature (from 70 to 80ºC), at least for 2 h of reaction, does not have the same effect.

^{1}H NMR is used for characterization, but in our case is also with the purpose of obtaining the degree of sulfonation of polymers. It is done by calculating the molar composition through the relative integration of the peak corresponding to the H 10' [28]. Figure 3 shows the ^{1}H NMR spectra of SPEEK samples, (a) for the series 70 with reaction times of 2-5 hours, and (b) for variation from 70 to 80ºC at a fixed 2h of reaction time.

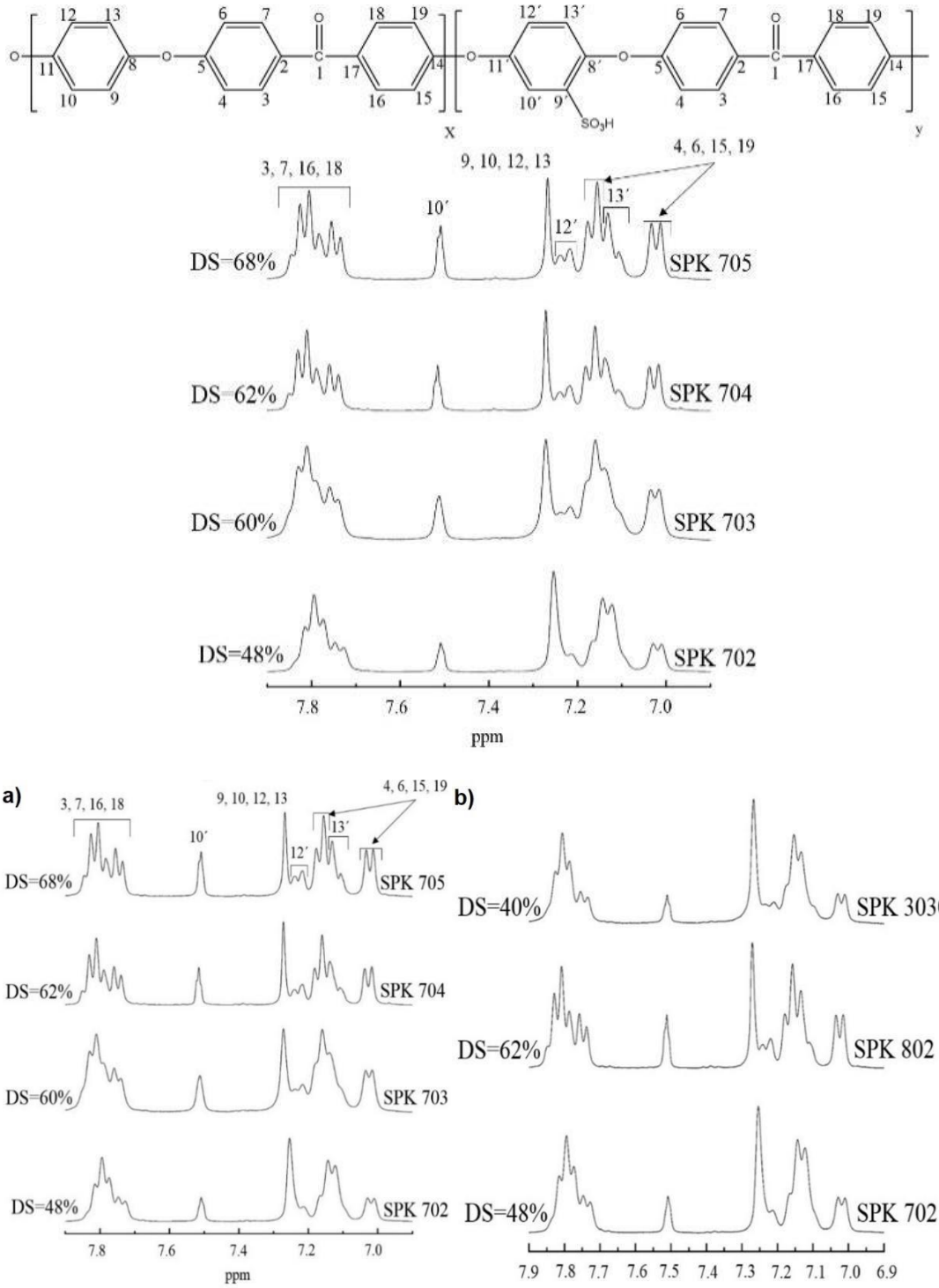

Fig. 3 ^{1}H NMR analysis and DS calculated for SPEEK with variation in reaction time (a) SPEEK 70 °C, 2-5 h (b) SPEEK 30°C 30h, SPEEK 80°C 2h, SPEEK 70°C 2h.

The former resulted with sulfonation values from 48% to 68%, while the change in temperature resulted in moving from 40 to 62% of DS. It is worthy to note that SPEEK 3030, with the high intensity in the OH band from FTIR results, only gets 40% of DS. With respect other alternatives for obtain the DS value, using TGA method the results were from 19-95% and by IEC method were from 24-80%. The comparison between the three method was varied due to the precision in each one and the factors that are considered.

TGA analysis was carried out in order to observe the decomposition temperature of the PEEK and the sulfonated samples, as well as to envisage the stability considering the usual working temperatures in a fuel cell. The calorimetric measurements (DSC) were carried out for evaluation of vitreous transition (Tg) changes after sulfonation reactions. Thermograms TGA and DSC for PEEK and sulfonated PEEK at 70ºC are shown in the figure 4.

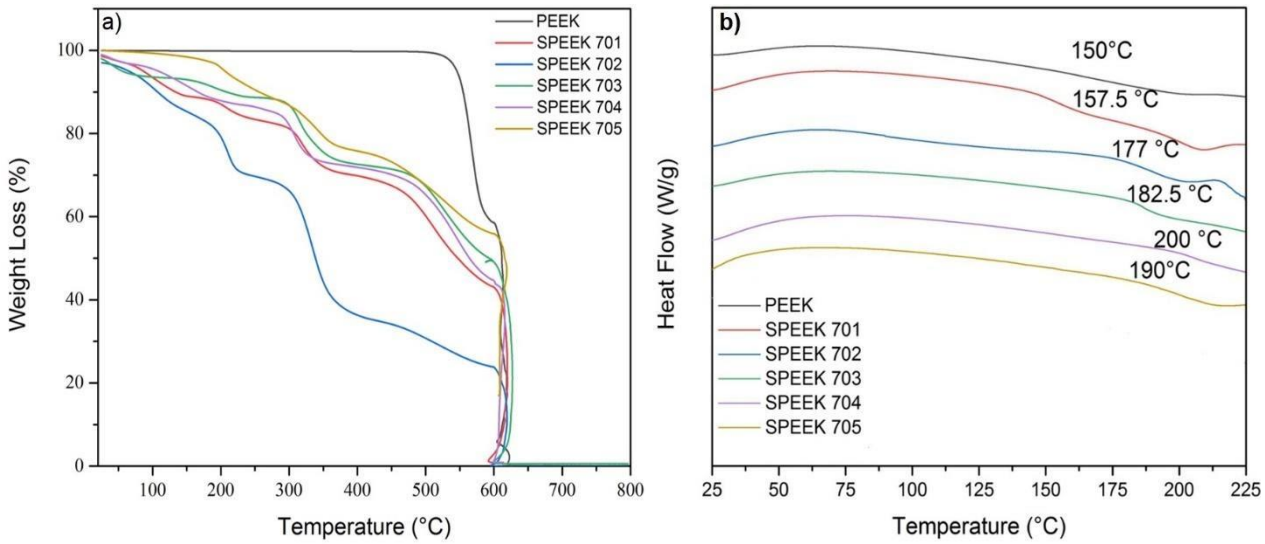

Fig. 4 Thermograms of PEEK samples sulfonated at 70ºC, (a) TGA, (b) DSC

The TGA thermogram for PEEK shows excellent stability above 500°C, while sulfonated polymers, show a progressive deterioration in their thermal stability. Peixiang [7] observed a degradation in the thermal stability of their sulfonated polymers depending on the degree of sulfonation compared to the PEEK. All SPEEK exhibit a singular trend for its degradation along the level of sulfonation [4,12]; however, three main steps in degradation are almost common to all of them: the first two steps are associated with the loss of the sulfonic groups in the range of 200-350°C and the second is related to the breakdown of the main polymer chain, in the range of 400-580°C. It should be noted that this last stage for sulfonated materials are at lower temperature than for PEEK; a catalytic degradation caused by the sulfonic group (-SO_3H) could be the reason. The DSC results of sulfonated samples showed the effect of sulfonation on the vitreous transition temperature and is clear that sulfonation enhance Tg values along sulfonation time for all materials. The later has been found by other authors, as has been reported previously [4,11]. The increase in the values of Tg is commonly observed in ionomeric polymers, and in our case is due to strong interactions among sulfonic groups [7]. Structural modification of polymeric materials directly affects their physical properties affecting physicochemical and thermal properties of sulfonated

polymers. The crystalline structure of PEEK has been investigated previously [11]. The wide-angle X-ray diffraction of PEEK and SPEEK (not shown here) show the intensity of four crystalline peaks: 2°: 19°, 21°, 23° and 29°; similarly same peaks has been reported in the literature [5, 6, 8] and correspond to diffraction planes (110)-(110)*, (111), (200) and (211) respectively [20,27]. Once PEEK is sulfonated, the intensity of the crystalline peaks is reduced, which is due to the introduction of sulfonic group into the polymeric structure. For samples SPEEK 701, 702, 703 and even SPEEK 705, there is only a slightly presence of the peak located at 18.72º, while for the SPEEK 704, a wide peak indicates a highly amorphous material. Water retention (WU) into a membrane is important to be able to generate conduction channels that optimize the transfer of protons; however, an excess absorption of water can also cause undesirable dimensional changes in the membrane. The values of WU for our SPEEK materials were higher than at NAFION ® commercial membrane (WU=13%), with values ranging from 4 to 112%. The high WU values usually result in an increase in IEC values, although in our results it is only a general trend, since for some materials, particularly for 80ºC sulfonated materials, the values remain constant. The later indicates that not always exists proportional relationship between the WU with the IEC, as reported in NAFION® membranes [13]. It is worth mentioning that values obtained for IEC in our materials are higher (from 0.78 to 2.28 meq.g^{-1}) than that reported in literature for the NAFION membrane (0.91 meq.g^{-1}), which is of great advantage.

4. Conclusions

All sulfonated SPEEK samples, independently of temperature or time of reaction, showed greater hydrophilicity. Materials SPEEK 701, SPEEK 702 were unable to form membranes. TGA demonstrates thermal stability above 200°C even for higher temperatures and longer times, as well as DSC demonstrated the change in the vitreous transition temperature of the material with the degree of sulfonation. FTIR and ^{1}H NMR characterization confirm the presence of the characteristic bands of a sulfonated material and sulfonation degrees ranging in 48 to 68 % for SPEEK 70°C 1-5 h and of 62% for SPEEK 802.
A total amorphous structure was observed for SPEEK 704, according to XRD and WU values of 4 to 112%, higher than the NAFION ® commercial membrane (WU=13%). High IEC values from 0.78 to 2.28 meq.g^{-1} were also found, which is also higher than value reported for NAFION ® (0.91 meq.g^{-1}).

Acknowledgements

This work has been supported by the Mexican Council of Science and Technology (CONACyT) through grants 259010. PCFE thanks CONACyT for the support through the PhD scholarship.

References

[1] Stambouli AB. Fuel cells: The expectations for an environmental-friendly and sustainable source of energy. Renew Sustain Energy Rev 2011:4507–20.
[2] Yee R, Zhang K, Ladewig B. The Effects of Sulfonated Poly(ether ether ketone) Ion Exchange Preparation Conditions on Membrane Properties. Membranes (Basel) 2013;3:182–95
[3] Khanh Ngan T. Do DK, Department. Synthesis and Characterization of Homogeneously Sulfonated Poly(ether ether ketone) Membranes: Effect of Casting Solvent Khanh. J Appl Polym Sci 2008;110:1763–70.
[4] Huang RYM, Shao P, Burns CM, Feng X. Sulfonation of poly(ether ether ketone)(PEEK): Kinetic study and characterization. J Appl Polym Sci 2001;82:2651–60.
[5] Yee R, Zhang K, Ladewig B. The Effects of Sulfonated Poly(ether ether ketone) Ion Exchange Preparation Conditions on Membrane Properties. Membranes (Basel) 2013;3:182–95.
[6] Xing P, Robertson G, Guiver M, D Mikhailenko S, Wang K, Kaliaguine S. Synthesis and characterization of sulfonated poly(ether ether ketone) for proton exchange membranes. vol. 229. 2004.
[7] Conceição TF, Bertolino JR, Barra GMO, Pires ATN. Poly (ether ether ketone) derivatives: Synthetic route and characterization of nitrated and sulfonated polymers. Mater Sci. Eng C 2009; 29:575–82.
[8] K. Nakanishi. Infrared Absorption Spectroscopy. Science (80-) 1963; 140:648.
[9] Krimm S. The infrared spectra of complex molecules, Vol. 1 (3rd ed.), L. J. Bellamy, Halsted Press, a division of John Wiley & Sons, Inc., New York, 1975, 433 pp. J Polym Sci Polym Lett Ed 1976; 14:121.
[10] Jin X, T. Bishop M, S. Ellis T, E. Karasz F. A sulphonated poly (aryl ether ketone). vol. 17. 1985.
[11] Iulianelli A, Clarizia G, Gugliuzza A, Ebrasu D, Bevilacqua A, Trotta F, et al. Sulfonation of PEEKWC polymer via chloro-sulfonic acid for potential PEM fuel cell applications. Int J Hydrogen Energy 2010; 35:12688–95.
[12] Shan J, Vaivars G, Luo H, Mohamed R, Linkov V. Sulfonated polyether ether ketone (PEEKWC)/phosphotungstic acid composite: Preparation and characterization of the fuel cell membranes. Pure Appl Chem 2006; 78:1781–91.
[13] Berezina NP, Kononenko NA, Dyomina OA, Gnusin NP. Characterization of ion-exchange membrane materials: Properties vs structure. Adv Colloid Interface Sci 2008; 139:3–28.

ID 067

SOFC solid electrolytes based on the CeO_2-Ln_2O_3 system; effect of sintering aids on their electrical properties

D.E. Puente-Martínez[1], K.A. González-García[1], J.A. Díaz-Guillén[1*], S. Martínez-Montemayor[2], J.C. Díaz-Guillén[3], G. Ochoa-Hernández[4], M.E. Bazaldúa-Medellín[5], K.P. Padmasree[5], A. F. Fuentes[5].

[1]Tecnológico Nacional de México- IT de Saltillo, 25280-Saltillo, Coahuila México.
[2]Centro de Investigación en Química Aplicada, 25294-Saltillo, Coahuila México
[3]COMIMSA-CONACYT, 25290- Saltillo, Coahuila México
[4]Universidad Virtual del Estado de Michoacán, 58147-Morelia, Michoacán México
[5]Cinvestav Unidad Saltillo, 25900-Ramos Arizpe, Coahuila México.

l*Corresponding author e-mail: jadiaz@itsaltillo.edu.mx (José Alonso Díaz-Guillén)

ABSTRACT

Ceramic materials based on cerium oxide CeO_2 (ceria) are known by their interesting ionic conduction properties at intermediate temperatures, which make them interesting candidates to be used as solid electrolytes in Solid Oxide Fuel Cells (SOFC). These electrical properties can be improved with the incorporation of different elements (in solid solution) in the cubic structure of ceria, due mainly to the increase of the number of oxygen vacancies in the unit cell or the modification of the lattice parameter. This project evaluates the viability of mechanical milling (mechanochemistry) to generate a composition of the system CeO_2-Er_2O_3 ($Er_{0.1}Ce_{0.9}O_{1.95}$). This powder processing method allows obtaining metastable phases at room temperature, which include a large number of structural defects, which will have an interesting effect on their electrical properties. XRD analysis revealed that this system can be synthesized after 20 hours of milling, by using a planetary mill and ZrO_2 containers and balls. Post-milling thermal treatments at 1500°C promotes the cubic structure of this fluorite-type composition. Their electrical properties were analyzed (in sintered pellets) by impedance spectroscopy for pure $Er_{0.1}Ce_{0.9}O_{1.95}$ and the same system mixed with 2 wt. % of CaO, ZnO, MgO and TiO_2 as sintering aids. Results reveal that these materials show high ionic conductivities at temperatures of 650°C. These properties are improved with the incorporation of sintering aids and are comparable with such reported by different reports on ceria-based materials. These results corroborate the viability of these materials to be used as solid electrolytes in SOFC.

Keywords: *SOFC; Doped ceria; Solid electrolytes; Mechanochemistry*

1. Introduction

Low-Temperature Solid Oxide Fuel Cells (LT-SOFC) represent an interesting prospect technology to generate electrical energy from an electrochemical reaction between hydrogen and oxygen at temperatures below 650°C, generating only water steam as a by-product. [1] The interest in this technology has been increased in the last decades looking to overcome the environmental world problems produced by the constant use of fossil fuels.
In this context, the evolution of SOFC (which currently operate at 750 - 1000°C) to LT-SOFC requires to solve some problems related with the stability and properties of the current components, which include an 8YSZ (8% mol yttria-stabilized zirconia) solid electrolyte, a $(LaSr)MnO_3$ cathode and a Ni-8YSZ cermet anode. Decreasing the operating temperatures can contribute to the increasing of the lifetime of the fuel cell, but it implies a necessary increase of the efficiency of its components, e. g. high ionic conductivity (~10^{-2} Scm^{-1}) in the solid electrolyte at lower temperatures (<650°C). Developing new materials with higher ionic conductivities at lower temperatures, just like the proposed in this research (doped CeO_2), can be a way to solve this problem in SOFC. The incorporation of new materials with high efficiency at low temperatures to the fuel cells could also help to overcome some other issues that have decreased their applicability, such as the high-performance degradation rates, the presence of isolating phases produced by reactions at the cathode/electrolyte interface and the slow startup and shot dawn cycles, to mention some. [2-6]
Different materials have been proposed to replace the 8YSZ as a solid electrolyte, all of them showing high ionic conductivity, which represents the most important property for the solid electrolyte in a SOFC. Among these materials, pure or doped lanthanide zirconates, titanates, or hafnates (with general formula $Ln_2B_2O_7$, where Ln = lanthanides and Y; B = Zr, Ti or Hf) with cubic pyrochlore or fluorite has been proposed. These materials show high thermal stability over 1500°C and conductivities comparable with different ionic conductors. [7-10]

Better results have been obtained with ceria (CeO_2), which present a cubic fluorite-type structure from room temperature to its melting point, and whose ionic conductivity (σ) can be improved when it is doped by different elements, including lanthanides. For example, L. Li et al reported a value of σ = 3.71 x 10^{-4} Scm^{-1} at 650°C for pure CeO_2 [11], while different authors report higher values σ for Gd (1.6 x 10^{-2} Scm^{-1} (700°C) [12]), Sm (2.03 x 10^{-2} Scm^{-1} (700°C) [13]) and Dy (7.74x10^{-2} Scm^{-1} (800°C) [14]) doped CeO_2. Additionally, we have reported values of conductivity of 1 x $10^{-1.91}$ Scm^{-1} at 650°C for the system $Dy_{0.1}Ce_{0.9}O_{1.95}$ [15]. The reason of the increase of conductivity is the increase of the number of oxygen vacancies generated by the substitution of tetravalent ions (Ce^{4+}) by trivalent ones (Ln^{3+}). Consequently, these vacancies allow the diffusion process of oxygen ions at high temperatures and their contribution to the charge transport.
Even though the electrical properties of Dy-doped ceria are promising for use in LT-SOFC, we have found some issues in the sintering process. The problem consists of the presence of bubbles and macrocracks on the surface on samples sintered at 1500°C (related to the generation of gaseous oxygen during the reduction reaction of CeO_2 to Ce_2O_3 (Ce^{4+} to Ce^{3+})). This behavior has been also reported by Zhou et al. for undoped ceria at temperatures over 1200°C [16], and according to the reaction:

$$CeO_2 \rightarrow Ce_2O_3 + ½\ O_2 \qquad (1)$$

A decrease in sintering temperature avoids these defects, but generates morphologies not dense in pellets, with remnant porosity. These reported results generated the necessity of improving the densification of sintered pellets of doped ceria by the use of sintering aids (such as CaO, MgO, TiO_2, and ZnO).
In this context, this study involves the synthesis by mechanical milling, characterization, and analysis of electrical properties of a representative system of doped ceria with composition $Er_{0.1}Ce_{0.9}O_{1.95}$. Additionally, the effect of the incorporation of the mentioned sintering aids on the densification and electrical properties of this composition is also analyzed.

2. Materials and Methods

A composition of Er-doped Ceria of formula $Er_{0.1}Ce_{0.9}O_{1.95}$ was obtained by mechanical milling, by using a RESTCH PM100 planetary mill, by using YSZ containers and balls. CeO_2 and Dy_2O_3 were using as starting reagents and were milled together in stoichiometric relation at different times (1, 6, 10, and 20 hours), to promote a mechanically induced reaction. The evolution of mixtures with milling time was followed by X-Ray Powder Diffraction (XRD) in a Rigaku Model IV diffractometer, with a wavelength Kα of Cu = 1.54 Å, a current of 30 mA and a voltage of 40 kV. Synthesized samples (20 hours of milling) were then fired at different temperatures (from 800 to 1200°C for 6 h) and analyzed by XRD to evaluate their structural evolution with temperature. Milled powders of pure $Er_{0.1}Ce_{0.9}O_{1.95}$ and mixed with CaO, MgO, TiO_2 or ZnO (2 w %) were uniaxially pressed and sintered at 1200 and 1500°C. Morphology of these pellets was studied by Field-Emission Scanning Electron Microscopy (TESCAN-MIRA 3 microscope). Previously to these studies, pellets were coated with a gold-palladium nanometric layer. Analysis of electrical properties was developed by impedance spectroscopy in sintered pellets (1200°C), with dimensions of ~1 mm of thickness and ~9 mm of diameter. Before the analysis pellets were coated with silver paint on both opposite faces (which will act as blocking electrodes), and dried at 600°C for 6 h, to harden the Ag coatings. Analysis of electrical properties was performed in air, as a function of temperature (200-650 °C) and frequency (100 Hz-1 MHz) in a Solartron 1260 Frequency Response Analyzer (FRA). The conductivity (σ_{dc}) was determined from these studies for each composition.

3. Results and Discussion

The X-ray diffraction pattern corresponding to the CeO_2-Er_2O_3 mixture at 1, 6, 10, and 20 hours of milling are showed in Figure 1(a). After one hour of milling, the pattern of the starting mixture reveals the presence of similar reflections of cubic fluorite-type CeO_2, according to the reference pattern for this oxide (ICDD, PDF 00-075-0390) showed in Figure 1(a). A reflection of lower intensity, corresponding to the Er_2O_3 (ICDD, PDF 00-077-777) is also evident in this pattern at 29.2° (2θ). The low intensity of reflections and increasing of their width is evident for all times of milling, due to the impacts of the balls with the powders, generating new surfaces, and creating lattice defects, surface radicals, and broken bonds. As milling time increases, the main peak of Er_2O_3 decreases in intensity.

The reason of this behavior is the incorporation of Er into the CeO_2 structure, giving place to a substitutional solid solution. For longer times of milling, XRD patterns are similar to the corresponding to the cubic structure of CeO_2 without relevant changes.
The XRD patterns obtained for the same composition milled for 20 h and thermally treated at 800-1200°C for 6 h are shown in Figure 1(b). Increasing of crystallinity for this composition is evident with the increase in the intensity of reflections at higher temperatures. All patterns revealed a set of peaks corresponding to fluorite-type materials and the absence of reflections of secondary phases is evident. Nevertheless, there is a reflection at ~25.78° corresponding to the main reflection of CeO_2 for the Cu K beta wavelength. All patterns of Figure 1 show this reflection, which is present because the device used to monochromatize the radiation does not completely attenuate the K Beta radiation.
After 20 hours of milling, powders were uniaxially pressed and sintered at 1500°C for 6 hours. SEM morphologies of the same composition $Er_{0.1}Ce_{0.9}O_{1.95}$ is showed in Figure 2(a-d). Well-defined and clean borders between grains are appreciated at higher magnifications, but the presence of small bubbles and macrocracks on the surface on this composition is evident at lower magnifications. This behavior could be related to the mentioned generation of gaseous oxygen during the reduction reaction of CeO_2 to Ce_2O_3. These results are similar to such obtained by the same group of work for Dy-doped Ceria. [15] The same composition was then sintered at 1200°C, looking to obtain morphology free of these defects. Figure 3 shows such morphology at 50,000 magnifications. Remnant porosity in this sample is still present and the diameter of grain is in all cases around 500 nm. Surface bubbles and cracks were absent for this sintering temperature. Figure 4 shows a comparison of morphologies (at 100,000 magnifications) of the composition $Er_{0.1}Ce_{0.9}O_{1.95}$ milled for 20 hours and mixed with different oxides to promote densification (TiO_2, MgO, CaO and ZnO), and sintered at 1200°C for 6 hours. This figure reveals the positive effect of such oxides since densification is almost complete for all four samples. The absence of porosity is evident and grains seem well defined. The surface of the samples is not flat since these were not previously polished.
After corroborating the positive results of sintering aids on the densification of this studied composition, the effect of the same on the electrical properties was studied.

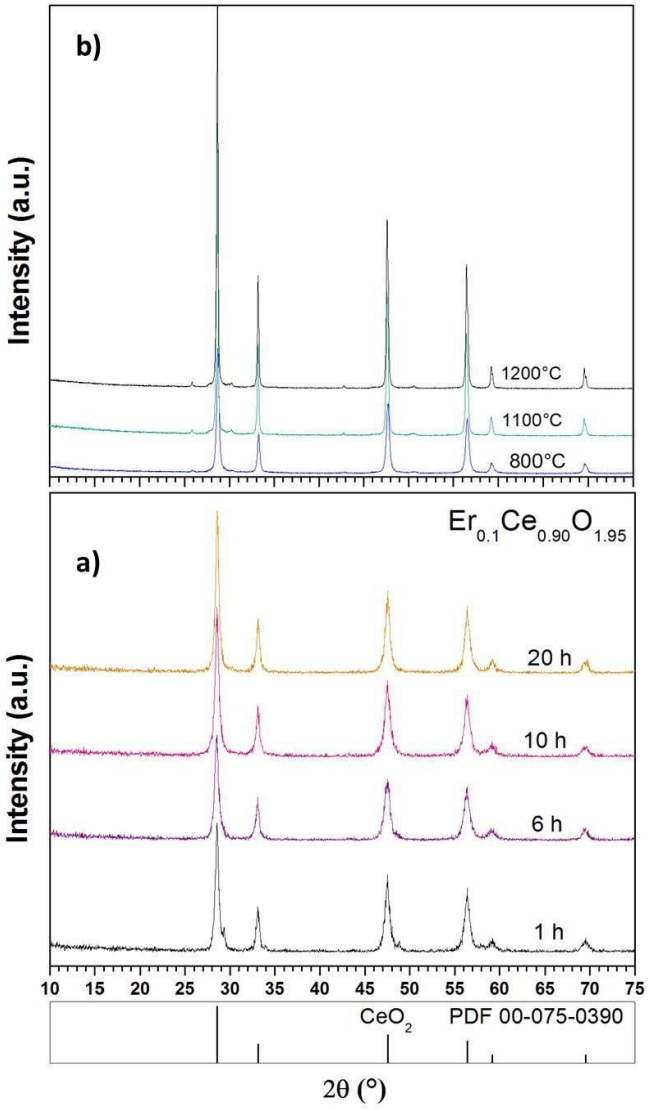

Fig. 1. Diffraction patterns corresponding to the starting mixture (CeO_2 - Er_2O_3) of the system $Er_{0.1}Ce_{0.9}O_{1.95}$ milled at different times (a) and after thermal treatments at 800-1200°C (b).

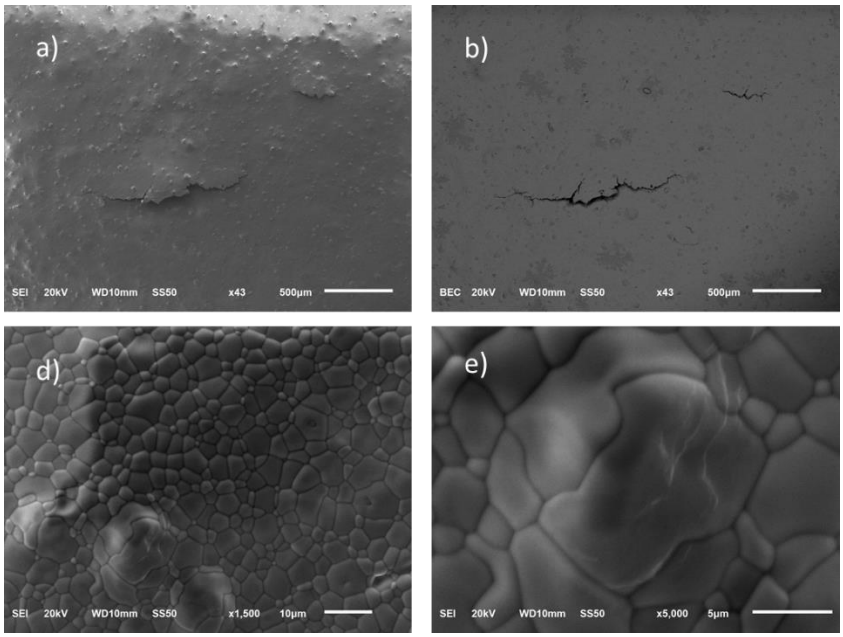

Fig. 2. Morphology at different magnifications of the composition $Er_{0.1}Ce_{0.9}O_{1.95}$ sintered at 1500 °C for 6 h (SEM) (a-d).

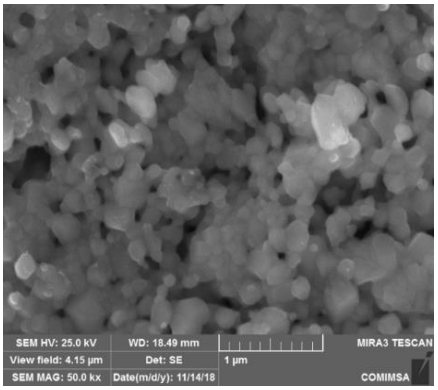

Fig. 3. Morphology of the composition $Er_{0.1}Ce_{0.9}O_{1.95}$ sintered at 1200 °C for 6 h (FE-SEM).

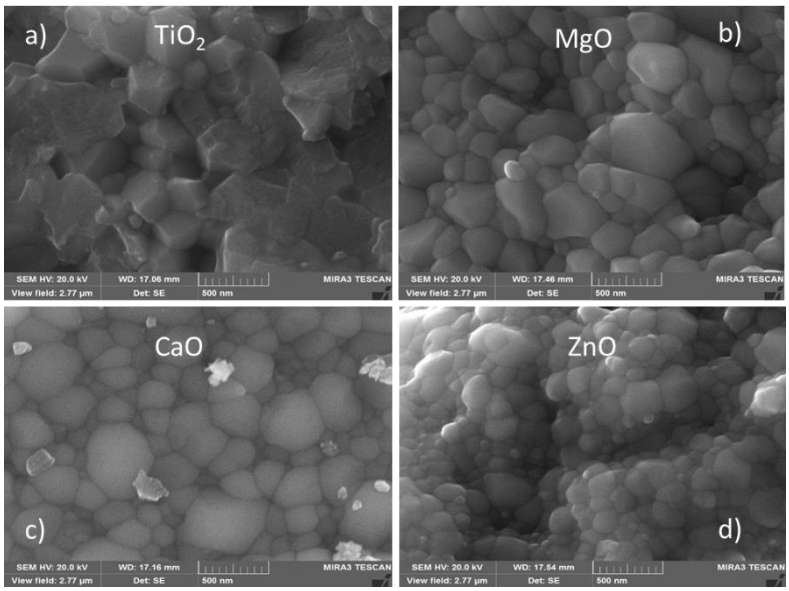

Fig. 4. Morphology (FE-SEM) of the composition $Er_{0.1}Ce_{0.9}O_{1.95}$ milled for 20 hours and mixed with 2 w% of TiO_2 (a), MgO (b), CaO (C), and ZnO (d). All samples were sintered at 1200 °C for 6 h.

The dependence of the conductivity with temperature (from 200 to 650°C) and frequency (100 Hz to 1 MHz) in logarithmic scale is showed in Fig. 4 (a) and b for the composition $Er_{0.1}Ce_{0.9}O_{1.95}$, pure and mixed with CaO, respectively. In this type of representation, an increase in ionic conductivity with temperature is evident and corroborates the ionic nature of these materials. Additionally, there is a potential dependence of the ionic conductivity with the frequency at low temperatures and high frequencies, which is known as Universal Dynamic Response (UDR) and is showed by most ionic conductors, and is described by the equation [17]:

$$\sigma^*(\omega) = \sigma_{dc}[(1 + (j\omega/\omega_p)^n] \quad where \quad 0 \le n \le 1 \qquad (2)$$

where σ_{dc} is the dc conductivity (or bulk conductivity) and ω_p is the crossover frequency related to the characteristic time of the conduction process t_p (t_p = 1/ ω_p). For lower frequencies than ω_p or longer times than t_p, the ions are at a long-range conduction process. On the other hand, for higher frequencies than ω_p or shorter times than t_p, the ions are jumping to neighboring positions, in a process described by the UDR. The exponent *n* describes the degree of interaction of the charge carriers (O^{2-} Ions) in the conduction process. If *n* = 0 there will be no interaction between the carriers and a Debye type behavior with constant frequency conductivity will occur, even though this last behavior is not common in ionic conductors. The value of the dc conductivity in these representations at each temperature is manifested as a plateau, where σ is independent of the frequency. From figure 5 (a) and (b), it is clear that the incorporation of CaO as sintering aids has a positive effect on the electrical conductivity since an increase in dc conductivity is evident in the sample $Er_{0.1}Ce_{0.9}O_{1.95}$ – CaO with respect the pure $Er_{0.1}Ce_{0.9}O_{1.95}$. The behavior of conductivity vs frequency and temperature was similar for all five analyzed samples, just like the characteristic of ionic conductors.

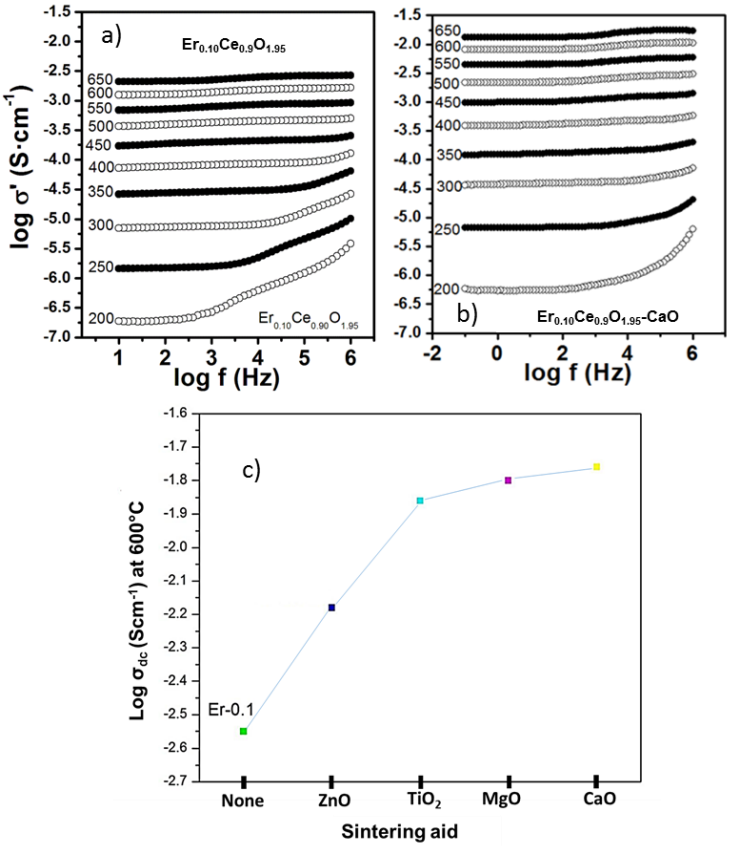

Fig. 5. Representation of the dc conductivity σ_{dc} vs. frequency in a double logarithmic scale at different temperatures (in °C) for the composition $Er_{0.1}Ce_{0.9}O_{1.95}$ pure (a) and mixed with CaO as sintering aid (b), both sintered at 1200°C. Effect of the sintering aids incorporation on the ionic conductivity σ_{dc} of the composition $Er_{0.1}Ce_{0.9}O_{1.95}$ at 600°C (c).

Figure 5(c) shows the effect of incorporation of sintering aids on the dc conductivity σ_{dc} measured at 650 °C by impedance spectroscopy. Conductivity values for all five cases are comparable with those obtained for similar ionic conductors [12-15]. The value of σ_{dc} for $Er_{0.1}Ce_{0.9}O_{1.95}$ is 1 x $10^{-2.55}$ Scm^{-1}, and increases almost one order of magnitude with the incorporation of CaO (σ_{dc} for $Er_{0.1}Ce_{0.9}O_{1.95}$-CaO is 1 x $10^{-1.76}$ Scm^{-1}) as a sintering aid. This last value represents one of the highest conductivity at 600°C reported for lanthanide-doped ceria.

The increasing of dc conductivity in pure $Er_{0.1}Ce_{0.9}O_{1.95}$ concerning the CeO_2 is due to the presence of oxygen vacancies because these empty spaces represent a path for oxygen ions, which are responsible for conduction in these materials, to move through these vacant sites and give functionality to the solid electrolyte in a SOFC.

These vacancies are generated when Ce^{4+} is replaced by a different element (such as Er^{3+}) and a substitutional solid solution is formed. This process is described by the following general equation:

$$0.05\ Er_2O_3 + 0.9\ CeO_2 \rightarrow Er_{0.1}Ce_{0.9}O_{2-\delta} \qquad (3)$$

where δ = 0.05 and represents the amount of oxygen that should be removed from the system to maintain the charge electroneutrality, giving place to the formula $Er_{0.1}Ce_{0.9}O_{1.95}$.

These removed oxygen atoms represent vacancies, responsible for the good electrical properties of these materials.
Otherwise, the incorporation of low quantities of sintering aids enhances the densification process at high temperatures. This decrease of porosity contributes to the improving of almost one order of magnitude in conductivity, corroborating the viability of the studied composition for its use in LT-SOFC.

4. Conclusions

The system $Er_{0.1}Ce_{0.9}O_{1.95}$ was synthesized by mechanochemistry (20 h of milling) in a planetary mill, starting from oxides of the involved elements. This obtained phase showed a disordered fluorite-like structure. The crystallinity of this Er-doped ceria increases notoriously with temperature, and the fluorite structure prevails at temperatures as high as 1200°C. Analysis of electrical properties by Impedance spectroscopy corroborated the high ionic conductivity ($1 \times 10^{-2.55}$ Scm^{-1} at 600°C) showed by this system, and also confirmed an improving of conductivity when $Er_{0.1}Ce_{0.9}O_{1.95}$ is mixed with low quantities of TiO_2, MgO, CaO and ZnO as sintering aids, reaching a maximum in conductivity for CaO ($1 \times 10^{-1.76}$ Scm^{-1} at 600°C). The presence of sintering aids promotes the densification during sintering at 1200°C, giving place to materials with a dense morphology and well-defined grains. The high ionic conductivity at 600°C in these materials corroborates their viability to be used as solid electrolytes in Low-Temperature SOFC.

Acknowledgements

This work was financially supported by Mexican TecNM (grant 7779.20-P). D. E. Puente-Martínez and K.A. González-García thank Mexican CONACYT for the scholarship (grants 557621 and 860984 respectively) granted for their Ph. D. studies.

References

[1] Gao Z, Mogni LV, Miller EC, Railsback JG,Barnett SA. A perspective on low-temperature solid oxide fuel cells. Energy Environ. Sci., 2016;9;1602-44. https://doi.org/10.1039/C5EE03858H.
[2] Wachsman ED, Lee KT. Lowering the Temperature of Solid Oxide Fuel Cells. Science 2011; 334:935-939. DOI: 10.1126/science.1204090
[3] Mahato N, Banerjee A, Gupta A, Omar S, Balani K. Progress in material selection for solid oxide fuel cell technology: A review. Prog Mater Sci 2015; 72:141-337
[4] Minh NQ, Solid oxide fuel cell technology-features and applications, Solid State Ionics 2004; 174:271-277.
[5] Labrincha JA, Frade JR, Marques FMB. La2Zr2O7 formed at ceramic electrode / YSZ contacts. J Mater Sci 1993; 28:3809-3815.
[6] Mitterdorfer A, Gauckler LJ. La2Zr2O7 formation between yttria-stabilized zirconia and La0.85Sr0.15MnO3 at 1773 K. MRS Proceedings 1996; 453: 525-530.

[7] Liu ZG, Ouyang JH, Sun KN, Xia XL. Preparation, characterization and electrical conductivity studies of NdYb1-xGdxZr2O7 (0 ≤ x ≤ 1.0) ceramics. Electrochim Acta 2010; 55: 8466-8470.
[8] López-Cota FA, Cepeda-Sánchez NM, Díaz-Guillén JA, Dura OJ, López de la Torre MA, Maczka M, Ptak M, Fuentes AF. Electrical and thermophysical properties of mechanochemically obtained lanthanide hafnates. J Am Ceram Soc. 2017;100:1994–2004.
[9] Cepeda-Sánchez NM, Díaz-Guillén JA, Maczka M, Amador U, Fuentes AF. Mechanochemical synthesis, crystal structure and ion conduction in the Gd2Hf2−xTixO7 system. J Mater Sci 2017;52: 11933-11946.
[10] Valdés-Ibarra MR, Díaz-Guillén JA, Padmasree KP, Montemayor SM, Rodríguez-Varela FJ, Fuentes AF. Oxygen ion conducting pyrochlore oxides prepared by an ultrasound-assisted wet chemistry route: Ca-doped Gd2Ti2O7 nanocrystals. Int J of Hydrogen Energy 2019; 44 (24): 12515-12524. doi.org/10.1016/j.ijhydene.2018.09.216.
[11] Li L, Zhu B, Zhang J, Yan C, Wu Y. Electrical properties of nanocube CeO2 in advanced solid oxide fuel cells. Int J Hydrogen Energy 2018;43(28):12909-16. https://doi.org/10.1016/j.ijhydene.2018.05.120.
[12] Anjaneya KC, Singh MP. Synthesis and properties of gadolinium doped ceria electrolyte for IT-SOFCs by EDTA citrate complexing method. J Alloy Comp 2017;695(25):871-6.
[13] Aygün B, Özdemir H, Öksüzömer MAF. Structural, morphological and conductivity properties of samaria doped ceria (SmxCe1-xO2-x/2) electrolytes synthesized by electrospinning method. Materials Chemistry and Physics 2019;232:82-87. https://doi.org/10.1016/j.matchemphys.2019.04.067.
[14] Yahiro H, Eguchi Y, Eguchi K, Arai H. Oxygen ion conductivity of the ceria- samarium oxide system with fluorite structure. J Appl Electrochem 1998;18:527-31. https://doi.org/10.1007/BF01022246.
[15] Puente-Martínez DE, Díaz-Guillén JA, Montemayor SM, Díaz-Guillén JC, Burciaga-Díaz O, Bazaldúa-Medellín ME, Díaz-Guillén MR, Fuentes AF, High ionic conductivity in CeO2 SOFC solid electrolytes; effect of Dy doping on their electrical properties, International Journal of Hydrogen Energy 2020;45(27),14062-70, https://doi.org/10.1016/j.ijhydene.2019.11.032.
[16] Zhou YC, Rahaman MN. Hydrothermal synthesis and sintering of ultrafine CeO2 powders. J Mater Res 1993;8(7):1680-6.
[17] Jonscher AK. Dielectric relaxation in solids. Chelsea Dielectric London. 1983.

ID 079

Experimental characterization of the clamping and pressure distribution in a PEM electrolyzer: gasket materials and bolt torques.

R. Moreno Soriano[1], N. Rojas [2], E. Nieto[2], R. González-Huerta[1*], J. Sandoval-Pineda[1*]

[1]Instituto Politécnico Nacional – ESIME – Azc, SEPI, Av. De las Granjas, No 682, Azcapotzalco, CP 02250, México
[2]Centro Nacional del Hidrógeno, Prolongación Fernando el Santo s/n, CP 13500 Puertollano, Spain.
* Corresponding author: beto.mec@outlook.es

ABSTRACT

To keep all elements of an electrolysis cell optimally connected is one of the most important criteria in its design. The main parameters affected by the clamping force are: compression pressure distribution, water/gas handling, contact resistance and mass transfer limitations in the cell. The homogeneous distribution of the compression pressure over the cell active area ensures a greater number of contact points between components. More contact points, means a better electric current distribution, decreasing the contact resistance and increasing cell performance. The optimal distribution and value of the clamping points is crucial for increasing the cell performance.

In this work, the compression pressure distribution inside a PEM electrolysis cell with an active area of 25 cm^2 was experimentally evaluated, using different materials (Teflon®, Viton®, Ethylene and Nitrile) with different thicknesses. The evaluation of the sealing material was performed taking as performance indicators: total compressed area (%) and compression pressure on the area active, for different torques applied. The experimental values obtained were compared with theoretical ones. Pressure distribution was obtained by using pressure-sensitive films, analyzing the distribution of pressure points from 3D graphics, and quantifying the intensities of the images obtained. The results obtained showed that the distribution of the pressure points depends on the stiffness and thickness of the gasket materials. For a tightening torque of 3.70 Nm, a pressure of 2.23 Mpa is obtained with 85 % of the compressed active area using Nitrile-Ethylene gaskets. Finally, the electrochemical characterization of the cell was performed through I/V curves, the cell performance for a current density of 2.0 A/cm^2, is 2.40 V with an overall efficiency of 58.78 % and electrical consumption of 6.07 kWh/Nm^3.

Keywords: Proton exchange membrane electrolysis; Gasket materials; Bolt torque; Clamping pressure.

1. Introduction

Water electrolysis could become one of the key technologies for converting electricity from fluctuating renewable energy sources to chemical energy (hydrogen), overcoming the limitations of the intermittency typically occurring in these systems and serving as a coupling element between different sectors of the industry, forming the backbone of future energy system [1].In this context, proton exchange membrane (PEM) water electrolysis is highlighted from other water electrolysis technologies. Since the initial development of PEM electrolyzers, significant improvements in cell performance, efficiency and durability of the components of these systems have been reported. Currently great efforts are being made in R&D by industry and researchers to reduced investment costs, increase system efficiency and increase the useful life of components, improving, optimizing and reducing their costs [2].

In a PEM electrolyzer, all components usually are assembled between clamping plates by applying torque to the bolts. As a result, the applied torque plays an important role in the performance and service life of the cell components. The torque applied to the bolts has direct relationship to the compression pressure applied to the cell. However, this pressure should not be too high as it can damage the cell components by decreasing the life of the cell [3]. However, a cell with insufficient and uneven compression pressure has a high interfacial electrical resistance between components. Cell performance can increase by increasing the torque on the bolts up to an optimal value. Beyond this value the performance begins to decrease due to mass transfer limitations and water management in the cell [4]. Main parameters affected by the torque for cell clamping are: pressure distribution, water / gas management, contact resistance and mass transfer limitations caused by deformations in cell components. A uniform magnitude and distribution of compression pressure ensure more contact points, which is a requirement for proper mounting and higher performance on PEM electrolyzers [5].

Within the literature, few studies have been conducted to investigate the influence of bolt torque and gasket materials for PEM electrolyzers. Selament, et al [5] investigates the effects of bolt torque on contact resistance and performance in a PEM electrolysis cell, for different gasket materials. Obtaining a maximum performance of 1,93 V at 1 A / cm^2 for EPDM gaskets with a bolt torque of 15 N.m. Borgardt et al [3] evaluated the effect of clamping pressure on the performance of a PEM electrolyzer for different cell configurations. Determining an optimal range of 2.0 - 3.0 Mpa for compression pressure according to the designs evaluated. Higher pressures lead to large ohmic and mass transport losses, decreasing cell performance. Shakhshir et al [6] study the effects of compression pressure on PEM electrolysis cell performance, hydrogen, and water crossover through the membrane and hydrogen and oxygen production rate.

In this work, the optimization of the clamping pressure of a PEM electrolysis cell was addressed, through the experimental evaluation of the compression pressure to which the internal elements of the cell are subjected. Different torques and sealing materials like Teflon®, Viton®, Ethylene and Nitrile have been evaluated. The objectives intended are primarily to maintain the sealing of the cell (avoid leakage of water, hydrogen and oxygen) and to achieve optimal contact between the components so that the cell performance is

maximized through the reduction of the ohmic loss while avoiding the obstruction of multiphase flow (liquid-gas) and structural damage to the components.

2. Materials and Methods

2.1 Cell components

Tests were carried out on a single cell with an active area of 25 cm^2. Terminal plates were made in stainless steel (AISI 321) of 15 mm thickness with a high stiffness. Due to corrosive environment inside the cell, bipolar plates were made of titanium, with 2 mm of thickness and 85 mm x 70 mm of total area. These plates, house the flow channels with a U-type (inverse) flow configuration. Sintered titanium porous electrodes with 0.90 mm of thickness and 25 cm^2 of area were used. The Pt (cathodic) and IrOx (anodic) catalysts were deposited on the surface of the Ti electrodes on the cathode and anode side respectively. A Nafion® 115 membrane (125 µm) with a rectangular area of 85 x 70 mm was used like electrolyte. The cell was fastened using eight hexagonal bolts (M10), nuts and washers. A torque wrench was used to tighten the screws to the desired torque.

Equation 1 describe the compression force applied F_C, where N, is the bolts number symmetrically distributed around the cell; T is torque applied on each bolt (N/m); f is the friction coefficient (0.20 for steel bolts) and D, the bolt diameter (m) [6].

$$F_C = \frac{N_P * T}{f * D_P} \quad (1)$$

Applied pressure P_c is a function of the clamping force F_c and the compressed area A_c, as is defined in equation 2.

$$P_c = \frac{F_C}{A_C} P_c = \frac{F_C}{A_C} \quad (2)$$

In this work, A_C is defined like the total dimension of the bipolar plates (85 x 70 mm). Fig. 1 shown the CAD 3D model of the cells components used and the dimensions and design of the gaskets.

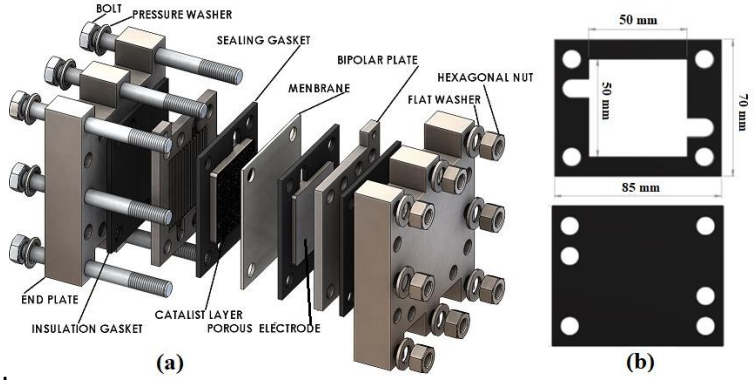

Fig. 1. Electrolysis PEM cell: (a) components 3D diagram (b): dimensions and design of the gaskets evaluated.

2.2 Gasket material selection

In order to analyze the contribution of the material tested like gasket on the magnitude, distribution of the compression pressure and the sealing capacity of the cell, four materials were evaluated. Materials were select by commercial availability and cost criteria, Teflon®, Viton®, Ethylene and Nitrile were selected. Different thicknesses and combinations of them were tested. Table 1 shows the thicknesses used according to the gasket material.

2.3 Clamping pressure measurement and analysis

Pressure film (Fujifilm Prescale - LLW) were used to provide a topographical image of pressure variation across the contact area. A dedicated software FPD-8010E, was used to convert Prescale density values into pressure values. The applied torque values were defined in sensitivity range of the films (0.50 - 2.50 Mpa). Pressure distributions over the total membrane area were obtained for each material type and torque value. During tests, membrane was replaced by the pressure films. Since the films are placed between the sealing gasket and the thickness of the films is minimal, compared to the total thickness of the cell, it is not considered any influence of change in thickness on the results obtained. Table 1 shows the experimental conditions for the tests performed.

Table 1. Experimental conditions for the materials tested

	Gasket material				
	Viton®	Teflon®	Ethylene	Nitrile	
Thickness (mm)	1.000	1.000	0.900	1.400	
	Compression applied				
Torque (N.m)	**N_p (#)**	**D_p (m)**	**F_c (N)**	**A_c (m^2)**	**P_c(Mpa)**
1	8	0.010	4000	0.006	0.067
1.500	8	0.010	6000	0.006	1.010
2.000	8	0.010	8000	0.006	1.340
3.000	8	0.010	12000	0.006	2.020
3.700	8	0.010	14000	0.006	2.490

Fig. 2, shows the flow diagrams follow, as well as the order of screw tightening (a) and the results obtained in the main stages of the test (b-f).

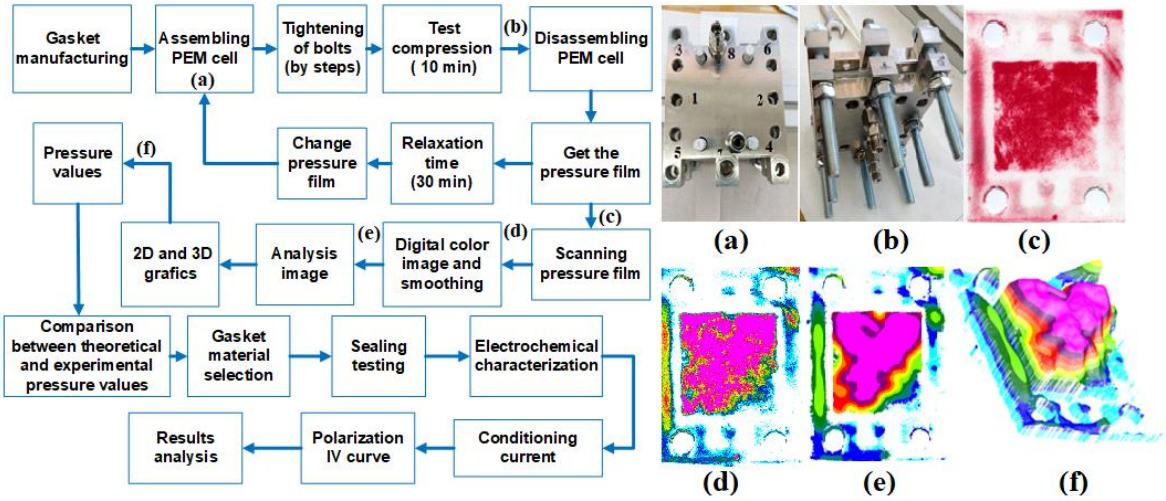

Fig. 2. Flow diagram for the compression process: (a) order of screw tightening and (b-f) the results obtained in the main stages of the test.

A tightening order (1-8) of the bolts in the cell assembly was established and repeated in all test. The bolts were not compressed directly, were tightened gradually (in steps) following the prescribed order. The prints obtained on the films, gone through a scanning process for digitization, and then a smoothing process was performed with the software to delimit the measurement errors generated by the high resolution of the images obtained. 3D graphics were used to obtain the distribution profile of the compression pressure. Only the impressions generated on the membrane area were taken into account.

2.4 Electrochemical characterization

Cell electrochemical characterization was carried out through the implementation of polarization I/V curves. Tests were performed in a test bench for the characterization of PEM electrolyzers (BE- PEME) installed at the CNH2. The polarization curves were done under two different step sizes according to the applied current density and for two types of conditioning currents, as described in Table 2. The conditioning protocols for the cell were established according to reference [2].

Table 2. Experimental conditions for electrochemical characterization.

Pre-conditioning					
Water Flow (L/min)	**Temperature (°C)**	**Current (A)**	**Total time (s)**	**Time delay (s)**	**Time acquisition (s)**
0.30	75	15	1800	150	1
0.30	75	37.50	1800	150	1

Polarization I/V curve			
Step: 1 Current interval: 0 - 0.10 A/cm^2		**Step: 2** Current interval: 0.20 – 2.00 A/cm^2	
Steps number	5	Steps number	5
Increase	0.02 A/cm^2	Increase	0.20 A/cm^2
Time	300 (s)	Time	300 (s)
Time delay	150 (s)	Time delay	150 (s)
Time acquisition	1 (s)	Time acquisition	1 (s)

3. Results and Discussion

Distribution and measurement of the compression pressure developed in the membrane was evaluated from the intensity of the color generated in the impressions films obtained (red). The higher the pressure exerted on the films the more intense the color of the printed in the films. The Fig. 3 (a), shows the comparison of the prints obtained in the tested films, as well as the images obtained with the mapping software, for a maximum torque of 3.70 N.m and the development of average pressures in the membrane area according to the torque and material evaluated is shown in Fig 3 (b). Clamping pressure changed depending on the thickness and stiffness of the material used in the gaskets, as well as the torque applied.

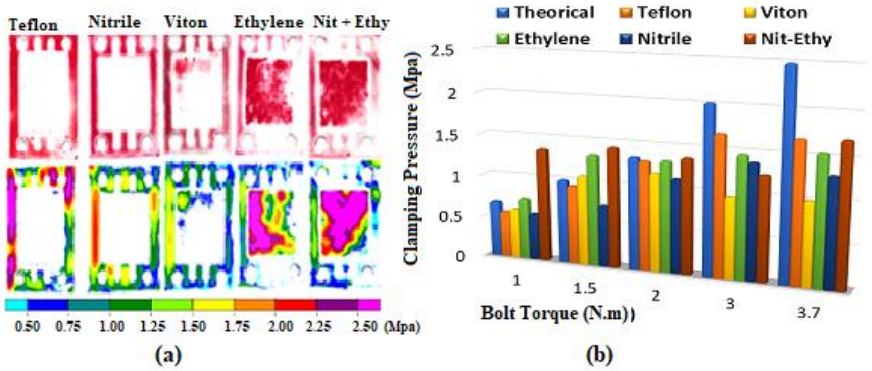

Fig. 3. Result of pressure distribution on membrane area for materials evaluated (a): impression films obtained for each compression torque applied (b): clamping average pressure for bolts torques and materials.

Two behaviors were observed depending on the thicknesses and materials used. For cases (Nitrile, Teflon® or Viton®), where the thickness of the gasket was greater than of the electrode or the stiffness of the material was high, there was a minimum deformation in the gasket. It could be caused because the gasket could absorb a minimum amount of energy transmitted by the bolt torque, transmitting directly the compression pressure on the sealing area (high coloration zone). For cases, (ethylene and nitrile-ethylene) where the thickness of the gasket is equal to that of the electrodes, the thickness and minimum stiffness of the material cause greater deformation in the gasket. This causes a better cell sealing (low coloration zone) due to deformation and energy absorbed by gasket.

3.1 Gasket material selection

Fig. 4, shown the comparison of the distribution and magnitude in clamping pressure on the membrane area through 3D graphs for a maximum torque of 3.70 N.m in ethylene (a) and nitrile–ethylene (b) gaskets. In both cases, no total contact between the electrodes and the cell membrane was achieved, so no total contact was observed (the gasket does not adhere) between the gasket materials and the membrane area (sealing failure), this behavior was most evident in ethylene gasket. But it was observed that a higher percentage (about 80 %) of surface area was compressed for nitrile-ethylene combinations that for ethylene (about 40%). This behavior could be attributed to the order of the bolt torque. This produced a preload on the side by which the torque was started to be applied on the bolts, causing an inefficient distribution in the compression of the cell. Uniform application of the load could substantially improve the distribution of pressure in the total area of the membrane.

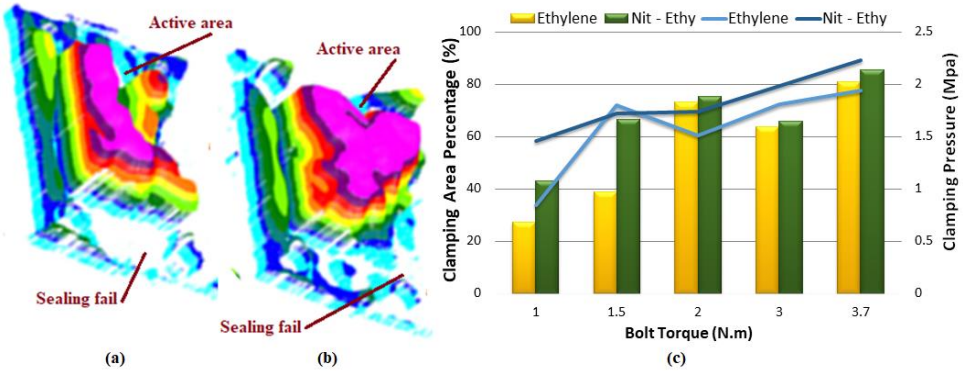

Fig. 4. 3D graphs for the distribution and magnitude of clamping pressure for ethylene (a) and nitrile-ethylene (b). Clamping pressure and clamping area percentage for torque applied (c).

The clamping pressure and clamping area percentage depended on the gasket material and the applied torque (Fig. 4 (c)). For a torque of 3.70 N.m., an average clamping pressure of 1.94 Mpa was obtained with 81.40% clamping active area of the membrane for ethylene gasket. For the combination of nitrile–ethylene gaskets, an average pressure of 2.23 Mpa was obtained with 85.48 % of clamping active area of the membrane. Nitrile was selected as the ideal material for the manufacture of insulation gaskets and ethylene as the ideal material for the manufacture of sealing gasket in the cell. The results obtained, showed an almost homogeneous distribution of the clamping pressure in the cell using these materials. In addition, for these materials, was observed that when the torque in the bolts increases, an increase in clamping pressure was obtained, decreasing the sealing failures detected (Fig.4 (b)).

3.2 Electrochemical performance.

The combination of nitrile-ethylene gasket was mounted in a PEM water electrolysis cell and it was electrochemical tested trough I/V curves determination. Small liquid leaks were detected mainly in the cell input and output connections. In order to increase the sealing capacity of the gasket was applied a clamping pressure of 4.03 Mpa, eliminating the presence of liquid leaks in the cell (the torque was applied by steps of 1.5, 3 and 6 N.M).

Cell performance was evaluated based on a pre-conditioning current of 15 A (E.A.E-2) and 37.50 A (E.A.E-4). Fig. 5 presents the comparison of the performance obtained in the cell, for each pre-conditioning current evaluated.

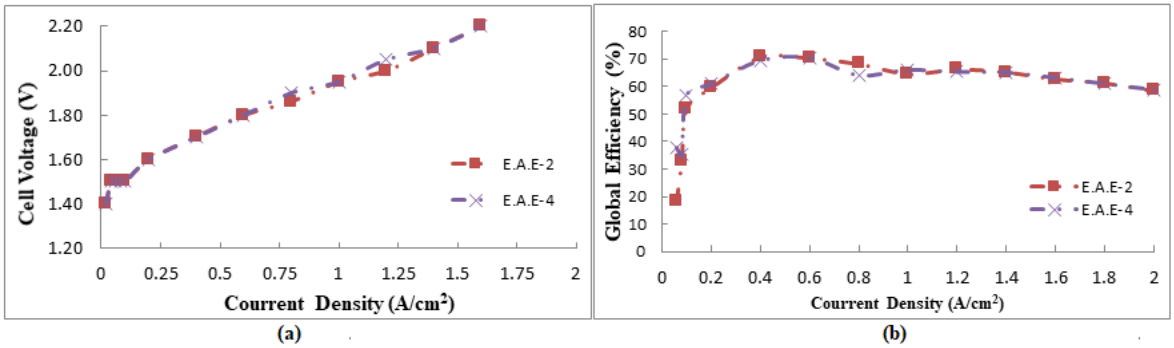

Fig. 5. Polarization I/V curves (a) and global efficiency (b) of the PEM electrolysis cell, for each current applied.

Linearity of the polarization curves was attributed to the dependence between the applied current and the voltage developed in the cell: Losses due to the ohmic resistances determine the performance of the PEM electrolysis cell. At minimum current densities, maximum cell performance was observed. Maximum cell efficiency was achieved at a current density of 0.60 A/cm^2, as current density increases, overall efficiency decreases. Table 3 summarizes the operating conditions in the cell for each conditioning current, evaluating the optimal and maximum operating points.

Table 3.Operating conditions in the PEM electrolysis cell.

Test	Temperature (°C)	Cell voltage (V)	Flow H_2 (L/hr)	$\eta_{Faraday}$ (%)	$\eta_{Voltage}$ (%)	η_{Global} (%)	Electric consumption (kWh/ Nm^3)
Current density: 0.60 A/cm^2							
E.A.E-2	73.40	1.80	5.10	81.95	82.22	67.78	5.30
E.A.E-4	72.83	1.80	5.33	85.67	82.22	70.44	5.07
Current density: 2.00 A/cm^2							
E.A.E-2	73.40	2.39	19.57	94.34	61.96	58.45	6.10
E.A.E-4	72.83	2.40	19.78	95.32	61.67	58.78	6.07

4. Conclusions

Experimental results allowed identifying the main points of contact between the cell components in the sealing areas and the active area of the membrane. The digitization of these points made it possible to quantify clamping pressure values in the areas of interest. The best results were obtained for the combination of nitrile-ethylene gaskets, with an average clamping pressure of 2.23 Mpa and 85.48 % compression in the active area of the membrane. Insulation gasket made of nitrile with a thickness of 1.40 mm and sealing gasket made of ethylene with a thickness of 0.90 mm were selected to improve the distribution of the clamping pressure on the active area of the membrane, applying a bolt torque of 6 N.m. for an order established in the bolts.

For a conditioning current of 37.50 A, a maximize cell performance was achieved. Cell performance was evaluated through a hysteresis polarization curve, the results obtained showed great similarity at most points of the curve with a maximum deviation of 0.018 % in the voltage values obtained. Cell performance for 2.0 A/cm^2 was 2.40 V with a η_{globa}l of 58.78 % and electrical consumption of 6.07 kWh/Nm$_3$. From the electrical consumption and production conditions of H_2, optimal operating conditions in the cell was observed selected for a performance of 0.60 A/cm^2 to 1.80 V with a η_{global} of 67.12 % and electrical consumption of 5.31 kWh/Nm$_3$. Performance obtained for the PEM cell tested was comparable with the reported yields for PEM electrolysis in the literature, demonstrating the viability of the selected materials as gaskets and applied bolt torques.

Acknowledgements

The authors of this work, thank the Consejo Nacional de Ciencia y Tecnología (CONACYT) for the international scholarship granted for the realization of international research stay in the “CENTRO NACIONAL DE EXPERIMENTACION DE TECNOLOGIAS DEL HIDRÓGENO Y PILAS DE COMBUSTIBLE (CNH2)” in Puerto llano Spain, in order to carry out this research work.

References

[1] Babic,U, Tarik M, Schmidt TJ, Gubler L. Understanding the effects of material properties and operating conditions on component aging in polymer electrolyte water electrolyzers. J Power Sources.2000;451;227778.

[2] Bender G, Carmo M, Smolinka T, Gago A, Danilovic N, Mueller M. Initial approaches in benchmarking and round robin testing for proton exchange membrane water electrolyzers. Int. J. Hydrog. Energy 2019;44: 9174-9187.

[3] Borgardt E, Giesenberg L, Reska M, Müller M, Wippermann K, Langemann M, Stolten D.Impact of clamping pressure and stress relaxation on the performance of different polymer electrolyte membrane water electrolysis cell designs. Int. J. Hydrog. Energy 2019;44: 23556-23567.

[4] Gatto, I., Urbani, F., Giacoppo, G., Barbera, O., & Passalacqua, E. (2011). Influence of the bolt torque on PEFC performance with different gasket materials. Int. J. Hydrog. Energy 2011;36: 13043-13050.

[5] Selamet OF, Ergoktas M S. Effects of bolt torque and contact resistance on the performance of the polymer electrolyte membrane electrolyzers. *J* Power Sources, 2015;281:103-113.

[6] Al Shakhshir S, Cui X, Frensch S,Kær SK. In-situ experimental characterization of the clamping pressure effects on low temperature polymer electrolyte membrane electrolysis. Int. J. Hydrog. Energy 2015; 42:21597-21606.
[7] Carmo M, Fritz DL, Mergel J,Stolten D. A comprehensive review on PEM water electrolysis. Int. J. . Hydrog. Energy, 2013:38, :4901-4934.
[8] Buttler A,Spliethoff H. Current status of water electrolysis for energy storage, grid balancing and sector coupling via power-to-gas and power-to-liquids: A review. Renew. Sust. Energ. Rev., 2018;82:2440-2454.
[9] Van der Merwe J, Uren K, Van Schoor G, Bessarabov D. Characterisation tools development for PEM electrolysers. *Int. J. Hydrog. Energy,2014; 39*:14212-14221.
[10] Bertuccioli L, Chan A, Hart D, Lehner F, Madden B, Standen E. Development of water electrolysis in the European Union. Fuel cells and hydrogen joint undertaking, 2014;83.
[11] Frensch S H, Olesen A C, Araya S S, Kær S K. Model-supported characterization of a PEM water electrolysis cell for the effect of compression. Electrochim. Acta,2018; 263:228-236.
[12] Verdin B, Fouda-Onana F, Germe S, Serre G, Jacques P A, Millet P. Operando current mapping on PEM water electrolysis cells. Influence of mechanical stress. Int. J. Hydrog. Energy,*2017;42*:25848-25859.

Nanostructured materials

ID 004

Au@Pd/C core shell structures for enhance the oxygen reduction reaction at PEM-FC

E. Y. Cervantes-Aspeitia[1,2], M. L. Hernández-Pichardo[1,*], P. Del Angel[3,*],

[1] Instituto Politécnico Nacional-ESIQIE, Laboratorio de Nanomateriales Sustentables, México City, 07738, México.
[2] Instituto Politécnico Nacional-ESIQIE, Laboratorio de Electroquímica, México City, 07738, México.
[3] Instituto Mexicano del Petróleo, Caracterización de Materiales Naturales y Sintéticos, México City, 07730, México.

* Corresponding author e-mail: pangel@imp.mx, mhernandezp@ipn.mx

ABSTRACT

Many electrochemical properties of metallic and bimetallic nanoparticles (NPs) are highly dependent on their morphology and size. In this work, a seed-growth method was used to synthesize dendritic core-shell Au@Pd nanoparticles supported on carbon (Au@Pd/C). The composition, morphology, and particle size of these catalysts were analyzed by HRTEM, HAADF-STEM, EDS mapping, XRD, and XPS. The Pd growth mechanism over the Au surface generated by this synthesis method drives to the formation of a dendritic-type porous Pd shell covering the Au core. This result was attributed to a poor capping ability of cetyltrimethylammonium chloride (CTAC), along with a sluggish reduction of Pd by ascorbic acid. The dendrite formation on the Au surface was attributed to the nucleation and epitaxial growth of Pd atoms on some facets of the Au NP, in the presence of adsorbed CTAC. Meanwhile, anisotropic growth occurred at all the other uncapped planes of the gold core. The electrocatalytic activity of the as-prepared catalysts was assessed through the oxygen reduction reaction (ORR), and it was compared to the activity of a commercial Pd/C catalyst. The Au@Pd/C catalyst exhibited a superior electrocatalytic activity due to the formation of a non-homogeneous Pd shell, as well as to the synergistic effects at the Au-Pd interfaces. The dendritic structure allowed for an increased number of exposed active sites, and the interplay between both metals favored the suppression of the adsorption of hydroxyl and super hydroxyl groups on the active sites, enhancing the oxygen reduction reaction kinetics of the Pd shell in acidic media.

Keywords: Au@Pd Nanoparticles; Carbon, Oxygen Reduction Reaction, Electrocatalysis.

1. Introduction

One of the most promising technologies to cover the world energy demand is proton exchange membrane fuel cells (PEMFCs) due to their high efficiency, low working temperatures, and low emissions [1]. This technology owns the most promising devices to achieve the commercialization stage. A key challenge in the development of more efficient PEMFCs is the sluggish reaction rate at the cathode, where the oxygen reduction reaction (ORR) is six orders of magnitude slower than the anodic reaction [2]. Therefore, the development of innovative metallic materials to catalyze the cathodic reaction is a crucial factor for the commercialization of fuel cell systems [3]. Platinum is the most effective electrocatalyst for ORR, but this metal is rare and expensive. The recent advances in electrocatalysts for ORR are mainly focused on the low- and non-platinum materials, including platinum alloys, core-shell structures, and palladium-based catalysts with novel structures and compositions [4].

Pd based materials are among the best candidates for ORR in acid media. It has also been found that multi-metallic Pd-based nanoparticles present several advantages for the ORR, in comparison to the corresponding monometallic components [5]. The incorporation of a second metal, as well as the nanoparticles (NP) shape, also plays an important role in improving the Pd catalytic effects of Pd for this reaction [6]. Thus, binary metallic core-shell nanoparticles have attracted attention due to their improved electrocatalytic properties, which can be tuned by controlling the size, shape, and interfacial structure [7,8]. The incorporation of a second metal (Pt, Ni, Co, Fe, Cu, Au) to form alloys [9] or core-shell structures [10] to enhance the Pd activity has also been studied.

In the case of the bimetallic Au-Pd-containing systems, it has been reported that gold may increase the chemical stability [11] and modify palladium electrochemical properties. These systems increase the electrocatalytic activity through synergistic Au-Pd effects [12], the architecture influence of Au@Pd core-shell nanoparticles, or by means of the particle size reduction [13,14]. Recently, dendritic Au@Pd NP have also attracted considerable attention due to their higher surface area and surface defects that result in increased electrocatalytic activity [15]. However, the electrochemical performance of supported dendritic Au@Pd NP has been scarcely reported. Then, the main objective of this work is to synthesize dendritic Au@Pd NP supported on carbon and investigate the influence of the dendritic structure on the oxygen reduction reaction.

2. Materials and Methods

2.1 Reagents and Chemicals

Cetyltrimethylammonium bromide (CTAB), cetyltrimethylammonium chloride (CTAC), sodium borohydride ($NaBH_4$), tetrachloroauric (III) acid ($HAuCl_4 \cdot H_2O$), trisodium citrate (Na3Cit), palladium chloride ($PdCl_2$), ascorbic acid (AA), and Nafion® (5%) were purchased from Sigma-Aldrich and HCl from Fermont. A 0.01 M solution of dihydrogen tetrachloropalladate (II) (H_2PdCl_4) was prepared by mixing 44.5 mg of $PdCl_2$ in 25 mL of HCl (20 mM) aqueous solution under stirring at room temperature until complete dissolution. The Pd/C catalyst (10 % Pd mass loading containing 5−6.5 nm Pd NP) and Vulcan carbon XC-72R was obtained from Fuel Cell. Ultrapure deionized water was used for all the preparation

of all the solutions. The bimetallic sample was prepared with nominal contents of 5 wt. % Au and 5 wt. % Pd.

2.2 Synthesis of the dendritic Au@Pd/C catalysts by the seed-growth method

A three-step synthesis method was followed for the preparation of Au@Pd. The first step consists of the preparation of a seed solution similar to that reported by Jana and coworkers [16] to obtain Au nanoparticles of 5 ± 0.8 nm of diameter. In a conical flask, 300 µL of $HAuCl_4$ (10 mM) and 2 mL of trisodium citrate (2.5 mM) were mixed. Next, 0.6 mL of ice-cold, freshly prepared $NaBH_4$ (0.1 M) solution was added to the solution while stirring. The solution was kept under slow stirring for 3 h to assure the total decomposition of $NaBH_4$. The second step was the preparation of the growth solution (octahedral Au nanoparticles). 200 µL of $HAuCl_4$ (10 mM), 5 mL of CTAB (0.1 M), and 2 mL ascorbic acid (0.1 M) were diluted in 35 mL of Milli-Q water. Then, 0.3 mL of seed solution were added, mixed for 3 min, and left undisturbed overnight. In the third step, a dendritic core-shell Au@Pd nanoparticles solution was prepared. 4 mL of the growth solution were mixed with 32 mL of Milli-Q water, and 5 mL of CTAC (0.1 M) were mixed with 400 µL of H_2PdCl_4 (0.01 M). These solutions were mixed and stirred for 3 min; after this, 0.1 mL of ascorbic acid (0.1 M) was added. The solution was mixed for 10 min and left undisturbed overnight. Finally, the supported Au@Pd/C NP were prepared by mixing Vulcan carbon, ethanol, and the Au@Pd NP solution, and by drying at 90 °C for 8 h to obtain a Pd load of 5 wt. % Au and 5 wt. % Pd.

2.3 Electrochemical measurements

The electrocatalytic ink for both samples, Au@Pd/C and commercial Pd/C, were prepared as follows: 5 mg of catalyst powder were mixed with 750 µL of isopropanol, 250 µL of Milli-Q water and 70 µL of Nafion® solution, and sonicated for 45 min. Then, 9 µL of this suspension were dropped on a glassy carbon electrode (0.196 cm^2) previously polished at mirror-finish. The Pd loadings on the glassy carbon was 21.5 µg cm^{-2} and 10.7 µg cm^{-2} in commercial Pd/C and Au@Pd/C, respectively, which is consistent with the literature recommendation [17]. Finally, the glassy carbon electrode was dried by rotating at 500 rpm at room temperature. All the electrochemical experiments were carried using a potentiostat Autolab PGSTAT302N. For all the electrochemical measurements, a standard three-electrode glass cell was used. A Pt mesh and a reversible hydrogen electrode (RHE) were used as counter and reference electrodes, respectively. A glassy carbon rotating disk electrode (RDE) was used as a working electrode, and the electrolyte was 0.1 M $HClO_4$. The electrochemical measurements were carried out at 25 °C. Cyclic voltammetry (CV) and linear sweep voltammetry (LSV) techniques were carried out in saturated Ar and O_2, respectively. The CV profiles were recorded from 0.05 to 1.2 V vs. RHE, at 50 mV s^{-1}. LSV polarization curves were obtained from open circuit potential (OCP) to 0.25 V vs. RHE, at 5 mV s^{-1}, with a rotation speeds of 100, 200, 400, 900 and 1600 rpm. The electrocatalytic activity was evaluated in the oxygen reduction reaction (ORR) in 0.1 M $HClO_4$. The CO-stripping technique was used to calculate the electrochemical active surface area (ECSA). Firstly, the solution was saturated with CO for 5 min, and finally, the residual CO in the solution was removed by bubbling Ar for 20 min, all the time under a set potential of 0.1 V vs. RHE.

2.4 Structural characterization

XRD patterns were collected on a Bruker AXS D8 diffractometer with Cu Kα radiation (λ =1.5418 Å). High resolution transmission electron microscopy (HRTEM) images were acquired on a FEI TITAN 80-300 operated at 300 kV with a Cs corrector. Scanning transmission electron microscopy (STEM) analyses were obtained on a JEOL JEM-ARM

200CF operated at 200 kV and equipped with a Cs probe corrector. In this instrument was obtained high angle annular dark field (HAADF-STEM) images, chemical compositions, mapping, and line scanning profiles by energy dispersive spectroscopy (EDS-STEM). Samples for HRTEM and STEM analyses were prepared by depositing a single drop of diluted NP dispersion in isopropanol on lacey formvar/carbon-coated copper grids. X-ray photoelectron spectroscopy (XPS) was carried out using a K-alpha from Thermo Fischer Scientific spectrometer with a monochromatic Al ka X-ray source (1486.6 eV).

3. Results and Discussion

3.1 High-resolution transmission electron microscopy (HRTEM) and scanning transmission electron microscopy (STEM)

HRTEM images were obtained at the atomic level for the monometallic Au seeds, the octahedral Au NP, and the bimetallic dendritic Au@Pd NP to explore the growth mechanism and Pd aggregation state over the Au nanoparticles. Fig. 1(a-b) present TEM images of the Au seeds, showing the formation of spherical Au NP with an average size of 5 ± 0.8 nm. In this case, trisodium citrate was used as a reducing and stabilizing agent of the size of the nanoparticles; the citrate ions changed the negative surface charge causing the nanoparticles to repel from each other, thus preventing the growth of the Au seeds. Besides, sodium borohydride owns a high capacity for reduction, producing a large number of Au seeds. Due to its high nucleation ability, it does not allow the growth of the NP, generating a high concentration of Au NP [18]. Fig. 1(c) shows the HRTEM image of an octahedral Au nanoparticle coming from the growth solution with an average size of 25 ± 1.6 nm. Since ascorbic acid is not a strong reducing agent, it allows the heterogeneous deposition of gold on the surface of the seeds, and, along with the use of CTAB as a surfactant, it enables the anisotropic growth of truncated NP in aqueous solution and prevents their aggregation [19]. The intermediate magnification BF-TEM image (Fig. 1(d)) shows the formation of dendritic Au@Pd NP with an average size of 35 ± 2.5 nm. The inner part of the nanoparticles appears darker compared with their edges, due to the difference in their atomic number of Au and Pd (79 and 46, respectively).Some studies have reported that the rapid growth of metals in a CTAC solution contributed to the fast formation of metallic shells on gold nanostructures, generating a non-uniform growth of the shell over the core [20]. To determine the formation of the dendritic Au@Pd core-shell NP at the atomic level, a deeper analysis by using HAADF-STEM, EDS elemental mapping, and EDS line scanning profiles was performed. Fig. 1(e) shows an Au@Pd core-shell nanoparticle obtained at intermediate magnification by HAADF-STEM; this nanoparticle exhibits a contrast difference between the Au core (atomic number 79) and the Pd shell (atomic number 46). Considering that the HAADF-STEM technique can distinguish chemical elements with an atomic number difference ≥ 7; this is the case of Au, which is heavier than Pd. In the same Au@Pd nanoparticle, high-resolution HAADF-STEM images from two different regions were obtained, over Pd (Fig. 1(f)) and Au (Fig. 1(g)), indicated by red and green squares, respectively. Over the red square, the measured interplanar distance was 0.224 nm, corresponding to the (111) plane of the metallic palladium with fcc structure. The measurement in the green square was 0.236 nm, which corresponds to the (111) plane of the metallic gold, with the same fcc structure

as that of Pd. The atomic planes measurements confirmed that palladium was covering the gold surface NP. Since they have the same crystallographic structure (fcc), they present a high lattice match, and it is possible to observe that the continuation of the atomic planes from the core (Au) to the shell (Pd), along the (111) plane. This result is the confirmation of the epitaxial growth of the Pd on some Au facets.

Another critical issue is how Pd covers the Au surface; from Fig. 1(d-e), the irregular growth of a Pd shell with the formation of some Pd dendrites on the Au surface is observed. Some studies have stated that irregular growth exhibits an excellent electrocatalytic activity toward the ORR [6]. The corresponding EDS line scanning profile is shown in Fig. 1(h). It corroborates that the Au@Pd core-shell NP consist of an Au-rich center (green line) and a Pd-rich edge (red line). The HAADF-STEM image and the EDS elemental mapping of the same particle are shown in Fig. 1(i-l). The EDS elemental mapping (Fig. 1(k)) shows that the Pd is covering completely to the gold because its signal is continuous over all the nanoparticle. The Au core maintains a 25 nm size, and the Pd shell thickness is about 12-15 nm. In the seed-mediated growth method, both thermodynamic and kinetic factors should be taken into consideration for understanding the formation mechanism of Pd nanocrystals [21]. If kinetic factors prevail, the shape of Pd nanocrystals will be determined by the growth rate of different crystal faces. In this sense, the chemical species used (reducing, stabilizing, or capping agents) for the preparation of core-shell nanoparticles may also play a key role in the overgrowth process since they may modify the growth kinetics [13,22]. In this work, it was observed that the growth mechanism of Pd over the Au surface using this synthesis method led to the formation of a dendritic-type porous Pd shell, covering the Au core. This fact was attributed to the poor CTAC capping ability because this surfactant exhibits weaker electrostatic interactions than CTAB. It has been reported that the binding strength of the halides to the Au particle surface increases in the order $Cl^- < Br^- < I^-$. Moreover, by theoretical studies, it has been found that Cl^- ions preferentially remain in the solution, in contrast to Br- ions, which are strongly adsorbed on the gold surface [23].

After that, by using CTAC for the Pd growth, some crystal Au planes remain uncapped and exposed to Pd nucleation. Then, the slow reduction by AA favored the Pd growth on those facets. The formation of some dendrites on the Au NP has been ascribed to the nucleation and epitaxial growth of Pd atoms over some facets of the Au NP in the presence of adsorbed CTAC, whereas anisotropic growth was occurred on the uncapped planes of the gold core, forming a heterogeneous shell.

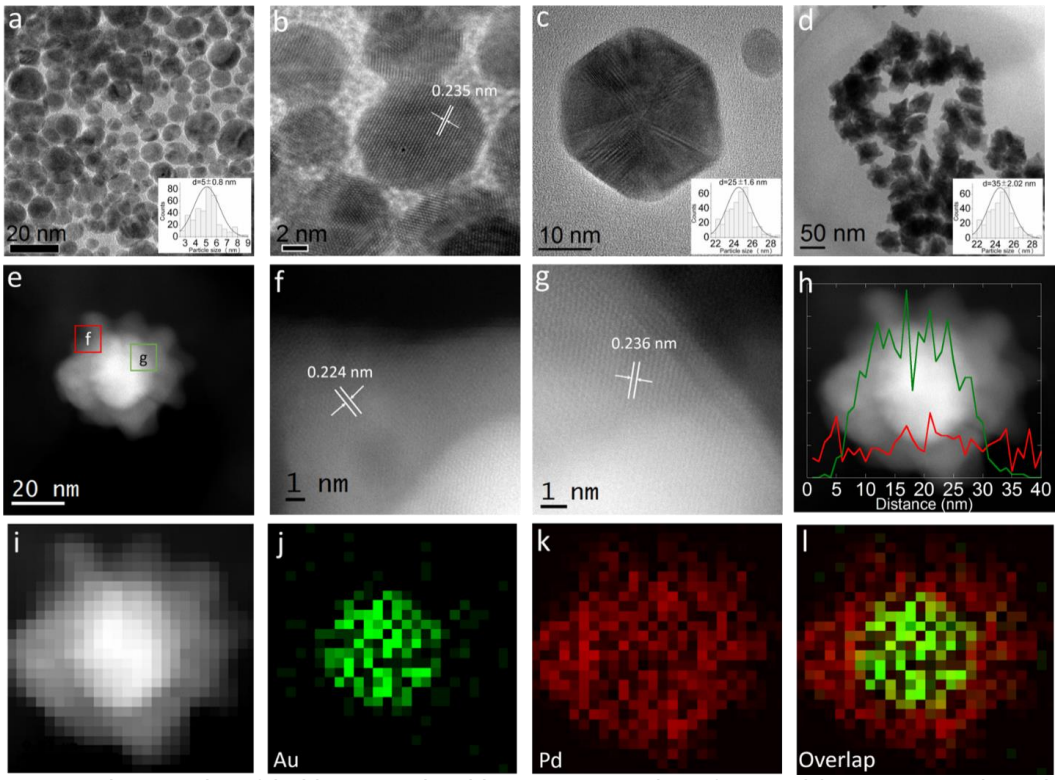

Fig. 1. TEM micrographs of (a-b) Au seeds with an average size of 5 nm, (c) Au truncated octahedral NP with an average size of 25 nm, (d) Dendritic-like Au@Pd core-shell NP, with an average size of 35 nm, (e) HAADF image of the Au@Pd core-shell nanoparticle, showing the Au core and the Pd shell in two regions (f and g), (f) high-resolution HAADF image of the Pd shell, (g) high-resolution HAADF image of the Au core, (h) EDS line scanning profiles of an Au@Pd nanoparticle (Au is in green and Pd in red) and (i-l) HAADF image and its corresponding EDS elemental mapping.

3.2 X-ray diffraction (XRD) and X-ray photoelectron spectroscopy (XPS)

XRD patterns for Au@Pd/C and the commercial Pd/C samples are shown in Fig. 2(a). The reflection peaks at 40.1°, 46.5° and 68° in 2-theta correspond to the (111), (200) and (220) atomic planes of the metallic Pd (01-089-4897 JCPDS card), respectively. The (111) peak of the Pd is observed in both samples. The other two reflections ((200) and (220)) are not observed clearly due to the polycrystalline nature (high background) of Vulcan carbon support (00-050-0926 JCPDS card). The Au peaks (00-001-1172 JCPDS card) are at 38.2°, 44.5°, and 64.89° in 2-theta; however, in the Au@Pd/C sample only the (111) reflection is observed, due to the Vulcan carbon background. The peak positions of the core-shell nanoparticles correspond to pure Au and Pd metals with fcc structure, according to the JCPDS cards, confirming that the Pd-shell is thick enough to produce reflections assigned to Pd0. The PdO in the commercial sample is observed like a slight hump at 33.5° in 2-theta corresponding to the (022) plane of the PdO (43-1024 JCPDS card).

Fig. 2(b) shows the general XPS spectra, verifying the presence of Au, Pd, and C in the as-prepared sample. It is observed that the intensity of the Au signal is quite low compared to that of Pd. Considering the results obtained by HRTEM, they indicate that the metal on the surface is mainly palladium since the XPS analysis is a surface-sensitive technique. This

result confirms those obtained by electron microscopy, which showed that the Pd shell thickness is about 12-15 nm and corroborates the formation of core-shell Au@Pd NP. The Au 4f and Pd 3d high resolution spectra for Au@Pd/C are shown in Fig. 2(c-d). For Au@Pd/C, the binding energy of Au 4f was found at 87.4 eV and 83.5 eV corresponding to 4f5/2 and 4f7/2, respectively, assigned to Au at zero-valent state [24]. The XPS spectra of commercial Pd/C and Au@Pd/C for Pd 3d were deconvoluted into two pairs of doublets. The most intense doublet at 335.2 and 340.5 eV for both catalysts corresponded to the metallic Pd. The weakest doublet (336.7 and 341.8 eV) could be assigned to Pd at oxidized state, showing that Pd is not completely reduced to metallic palladium [14]. According to the peak intensity, the surface atomic ratio of Pd to Au is about 9:1, indicating that there are Pd atoms on the surface mainly, and not all the Au particle is covered by gold. Then, compared to the Pd 3d5/2 and 3d3/2 binding energies of the commercial Pd/C catalyst, no apparent shift was observed in the Au@Pd/C catalyst, probably due to the wide Pd shell thickness of the Au@Pd/C.

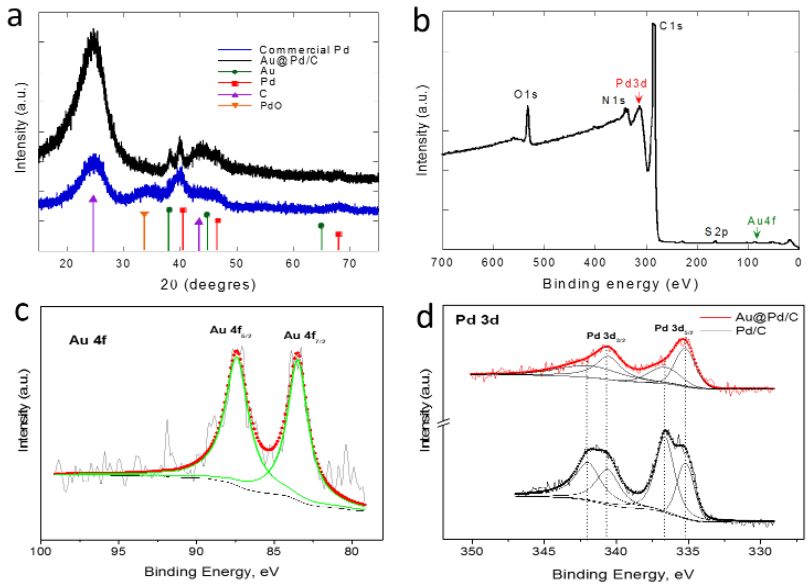

Fig. 2. (a) XRD patterns of Au@Pd/C and commercial Pd/C samples, (b) XPS general spectra for Au@Pd/C. High-resolution XPS spectra in the (c) Au 4f and (d) Pd 3d regions.

3.2 Electrochemical characterization

Electrochemical studies of the Au@Pd/C and commercial Pd/C catalysts were performed in $HClO_4$. The current density was normalized to 1 mg of palladium loading and the geometrical area of the glassy carbon electrode. The cyclic voltammograms (CV) of Au@Pd/C and commercial Pd/C materials were evaluated in Ar saturated atmosphere and scan rate of 50 mV s^{-1}. Fig. 3(a) shows the electrochemical behavior in a potential window from 0.05 to 1.2 V/RHE, starting at an open circuit potential of 0.870 V /RHE toward a positive-going scan. Regions of hydrogen adsorption/desorption can be observed at the potential interval ranging from 0.05 to 0.38 V/RHE, where a higher current density for Au@Pd/C than for the commercial Pd/C was obtained. The Au@Pd/C electrode did not present the characteristic

voltammogram peaks associated with the adsorption/desorption of hydrogen of the polycrystalline noble metals. This could be due to a bigger particle size [7] and irregular and porous Pd shell, which may favor hydrogen adsorption on different planes. The Pd-O formation on-set potential was 0.74 and 0.85 V/RHE for commercial Pd/C and Au@Pd/C, respectively; this shift of 0.09 V/RHE was attributed to the interaction between the Au core and Pd shell because it suppressed the adsorption of hydroxyl and super hydroxyl groups on active sites [25,26]. The reduction peak potential has a positive shift of 30 mV between the two materials, being of 0.75 and 0.72 V /RHE for Au@Pd/C and commercial Pd/C, respectively, which indicates that the oxides formed on Au@Pd/C are more easily to be reduced than the oxides formed on Pd/C; this result suggests that Au@Pd/C will be a better catalyst than Pd/C in ORR. The typical ORR linear sweep voltammetry plot for Au@Pd/C and commercial Pd/C are shown in Fig. 3(b), where the OCP values had a difference of 0.03 V /RHE, being higher for Au@Pd/C and consistent with a positive shift of the reduction peak potential observed in the CV. The half-wave potentials ($E_{1/2}$) were in the order 0.79 V/RHE (Au@Pd/C) > 0.76 V /RHE (commercial Pd/C), it presents a shift of 30 mV, to more positive values, demonstrating an increase in the electrocatalytic activity toward the ORR. The enhanced electrochemical activity of Au@Pd/C compared to the commercial Pd/C is related to the porous dendritic structure, which exhibits a larger specific area and the higher number of active sites, probably generated by a significant amount of defects on the surface [27,28]. The way Pd nanoparticles grow on the gold surface prevents agglomeration because they are independent of each other, making them more efficient. Besides, using Eq. (1) [29], the ECSA was calculated from the CO stripping reaction at the electrode interface, in acid medium ($HClO_4$ 0.1 M).

$$ECSA_{CO}\ (m^2 g^{-1}) = \left[\frac{Q_{CO}(C)}{420\ (\mu C\ cm^{-2}) L_{Pd}(mg\ cm^{-2}) A_g(cm^2)}\right] 10^5 \quad (1)$$

Where Q_{CO} is the charge for the CO induced adsorption, 420 (μC cm^{-2}) is the charge required to oxidize the monolayer of CO [30], L_{Pd} is the Pd catalyst loading on the working electrode, and A_g is the geometric surface area of the glassy carbon electrode (0.196 cm^2). Fig. 3(c-d) show the CO stripping voltammograms for commercial Pd/C and Au@Pd/C materials, where the peaks associated with the CO oxidation to CO_2 were found at 0.91 V /RHE and 1.04 V /RHE for commercial Pd/C and Au@Pd/C, respectively. The calculated ECSA and the obtained CO stripping reaction parameters (Eonset-CO, ICO, and ECO) are reported in Table 1. According to the obtained results, ECSA for the Au@Pd/C catalyst is 1.17 times higher than one for the commercial Pd/C catalyst.

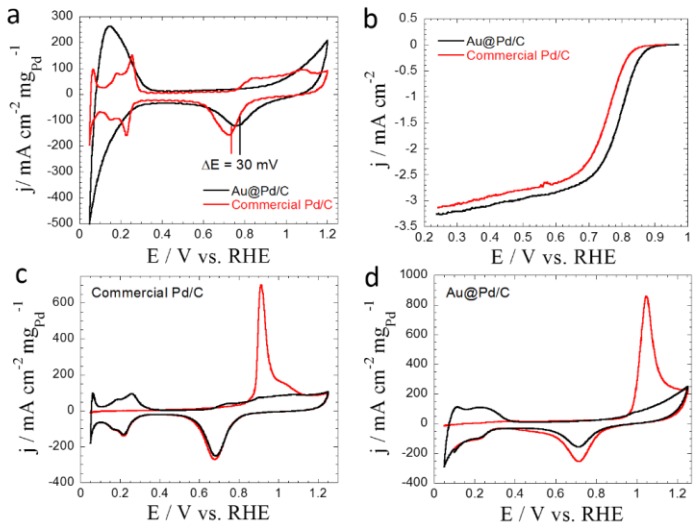

Fig. 3. Electrochemical measurements in $HClO_4$ solution. (a) CVs for Au@Pd/C and commercial Pd/C in Ar saturated atmosphere at a scan rate of 50 mV s^{-1}, (b) ORR polarization curves for Au@Pd/C and commercial Pd/C in O2 saturated solution, at a scan rate of 5 mV s^{-1} and a rotation rate of 1,600 rpm, (c) and (d) CO stripping voltammograms at a scan rate of 20 mV s^{-1} for commercial Pd/C and Au@Pd/C, respectively.

Table 1. The electrochemical surface area and the obtained CO stripping reaction parameters for commercial Pd/C and Au@Pd/C catalysts.

Catalyst	ECSA [m^2 g^{-1}]	$E_{onset-CO}$ [E /V vs. RHE]	I_{CO} [mA cm^{-2} mg^{-1}]	E_{CO} [E /V vs. RHE]
Commercial Pd/C	73.4	0.68	699.8	0.91
Au@Pd/C	86.3	0.91	859.6	1.04

Fig. 4(a) shows the polarization curves at different rotation rates of the Au@Pd/C catalyst, in oxygen saturated 0.1 M $HClO_4$ solution at 25 °C. The main characteristics in the polarization curve are the defined charge transfer control and the mixed and mass transfer region. The inset figure represents the Koutecky–Levich plot for the Au@Pd/C catalyst, where the inverse current density (j^{-1}) is a function of the inverse of the square root of the rotation rate ($\omega^{-1/2}$). The linearity of these lines indicates that the number of electrons transferred in the reaction does not change significantly within the studied potential range. Fig. 4(b) shows the Tafel plot, where the slopes were determined a range at more positive potentials and the measured current densities were mainly due to an electronic transfer control for the ORR. In this region, kinetic parameters such as Tafel slope value (b) and transfer coefficient (⟨), which are reported in Table 2, were calculated respecting that this range covers a minimum of one decade of current. The potential values, E, which were obtained for j=0.01 mA cm^{-2}, are also included in Table 2. In summary, the Tafel slope values around of 60 mV dec^{-1} determined on noble metal samples (Au@Pd/C and Pd/C) at low overpotentials, are in good agreement with those reported in the literature [31] and explained in terms of an electrode surface saturated with adsorbed oxygen, where the rate-determining

step of the overall molecular oxygen reduction is controlled by the first charge- transfer step, i.e., $(O_2)_{ads} + e^- \rightarrow (O_2^-)_{ads}$. The transfer coefficient values are consistent with the obtained Tafel slopes. However, the higher potential reached (0.94 V) at 0.01 mA cm-2 for the Au@Pd/C catalyst, with respect to the potential reached by the commercial Pt/C (only 0.90 V), should be noted. These results indicate that the Au@Pd/C catalyst exhibited enhanced catalytic activity toward oxygen reduction reaction compared to the commercial Pd/C catalyst in a perchloric acid solution. The improved catalytic activity should be attributed to two principal reasons: (a) the way that the Pd growth on the Au surface allows the formation of a porous core-shell structure and exposes more active sites to adsorb oxygen. It can provide an increase in the electrochemical surface area and, in turn, the number of active sites, which is favorable for the enhancement of catalytic activity [28]; and (b) the interaction between Au and Pd can modify the electronic structure of Pd, resulting in the ability to suppress the adsorption of hydroxyl and super hydroxyl groups on active sites [25], thus providing a synergistic effect to increase the catalytic activity of Pd.

Table 2. Kinetic parameters for the commercial Pd/C and Au@Pd/C catalysts.

Catalyst	*b* [mV dec^{-1}]	α	E at 0.01 mA cm^{-2} [V]
Commercial Pd/C	64.35	0.910	0.90
Au@Pd/C	61.45	0.988	0.94

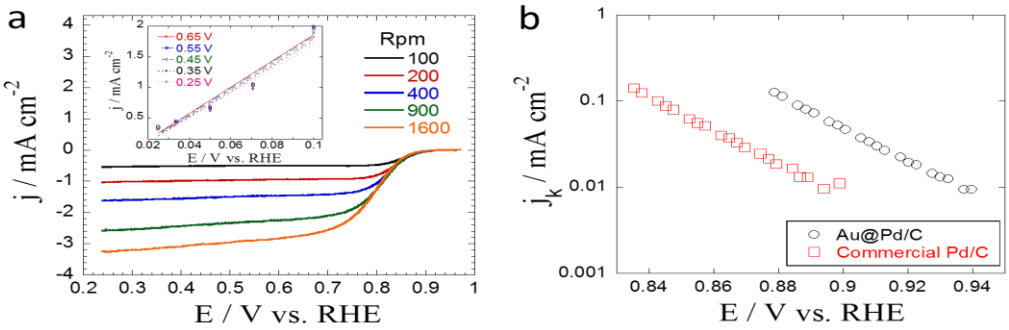

Fig. 4. (a) ORR polarization curves for the Au@Pd/C catalyst at different rotation rates, in oxygen saturated and 0.1 M $HClO_4$ electrolyte. The inset shows the Koutecky-Levich plot at various electrode potentials and (b) Tafel slopes for the Au@Pd/C and commercial Pd/C catalysts.

4. Conclusion

In the present work, a dendritic core-shell Au@Pd/C catalyst was successfully prepared by a seeded-growth method. HAADF-STEM results showed the formation of dendritic core-shell nanoparticles obtained by the epitaxial overgrowth of Pd over some uncovered Au facets. The electrocatalytic activity of these NP was compared with that of a commercial Pd/C catalyst. The slow Pd reduction in the presence of CTAC over the Au surface resulted in the formation of a porous shell, which increased the electrochemical surface area. The Au@Pd/C catalyst exhibited a higher oxygen reduction reaction activity than the commercial Pd/C in acid media, due to the porous Pd surface, with more exposed active sites, and the

synergetic effects between the Au core and the Pd shell. The dendritic structure produced a suppression of the adsorption of hydroxyl and super hydroxyl groups on the active sites, thus enhancing the catalytic activity. The Au@Pd/C catalyst is a promising candidate to be used as a cathode electrocatalyst in proton exchange membrane fuel cells.

Acknowledgements

This work was supported by the Instituto Politécnico Nacional [20200541 and SIP-2024], E.Y.C.A. thanks the financial support from CONACyT [Ph.D. scholarship number 787438].

References

[1] Wang Y, Chen KS, Mishler J, Cho SC, Adroher XC. A review of polymer electrolyte membrane fuel cells: Technology, applications, and needs on fundamental research. Appl Energy 2011;88:981–1007. https://doi.org/10.1016/j.apenergy.2010.09.030.

[2] Zhang L, Chae SR, Hendren Z, Park JS, Wiesner MR. Recent advances in proton exchange membranes for fuel cell applications. Chem Eng J 2012;204–205:87–97. https://doi.org/10.1016/j.cej.2012.07.103.

[3] Vignarooban K, Lin J, Arvay A, Kolli S, Kruusenberg I, Tammeveski K, et al. Nano-electrocatalyst materials for low temperature fuel cells: A review. Chinese J Catal 2015;36:458–72. https://doi.org/10.1016/S1872-2067(14)60175-3.

[4] Wang Y, Li J, Wei Z. Recent Progress of Carbon-Based Materials in Oxygen Reduction Reaction Catalysis. ChemElectroChem 2018;5:1764–74. https://doi.org/10.1002/celc.201701335.

[5] Kuai L, Yu X, Wang S, Sang Y, Geng B. Au-Pd alloy and core-shell nanostructures: One-pot coreduction preparation, formation mechanism, and electrochemical properties. Langmuir 2012;28:7168–73. https://doi.org/10.1021/la300813z.

[6] Fu G, Liu Z, Chen Y, Lin J, Tang Y, Lu T. Synthesis and electrocatalytic activity of Au@Pd core-shell nanothorns for the oxygen reduction reaction. Nano Res 2014;7:1205–14. https://doi.org/10.1007/s12274-014-0483-2.

[7] Salvador-Pascual JJ, Citalán-Cigarroa S, Solorza-Feria O. Kinetics of oxygen reduction reaction on nanosized Pd electrocatalyst in acid media. J Power Sources 2007;172:229–34. https://doi.org/10.1016/j.jpowsour.2007.05.093.

[8] Londono-Calderon A, Bahena D, Yacaman MJ. Controlled Synthesis of Au@AgAu Yolk–Shell Cuboctahedra with Well-Defined Facets. Langmuir 2016;32:7572–81. https://doi.org/10.1021/acs.langmuir.6b01888.

[9] Shao MH, Huang T, Liu P, Zhang J, Sasaki K, Vukmirovic MB, et al. Palladium monolayer and palladium alloy electrocatalysts for oxygen reduction. Langmuir 2006;22:10409–15. https://doi.org/10.1021/la0610553.

[10] Guo S, Zhang S, Su D, Sun S. Seed-mediated synthesis of core/shell FePtM/FePt (M = Pd, Au) nanowires and their electrocatalysis for oxygen reduction reaction. J Am Chem Soc 2013;135:13879–84. https://doi.org/10.1021/ja406091p.

[11] Juárez MF, Soldano G, Guesmi H, Tielens F, Santos E. Catalytic properties of Au electrodes modified by an underlayer of Pd. Surf Sci 2015;631:235–47. https://doi.org/10.1016/j.susc.2014.06.015.

[12] Londono-Calderon A, Campos-Roldan CA, González-Huerta RG, Hernandez-Pichardo ML, del Angel P, Yacaman MJ. Influence of the architecture of Au–Ag–Pt nanoparticles on the electrocatalytic activity for hydrogen evolution reaction. Int J Hydrogen Energy 2017;42:30208–15. https://doi.org/10.1016/j.ijhydene.2017.08.042.
[13] Lee YW, Kim M, Kim ZH, Han SW. One-Step Synthesis of Au@Pd Core−Shell Nanooctahedron. J Am Chem Soc 2009;131:17036–7. https://doi.org/10.1021/ja905603p.
[14] Chen D, Li C, Liu H, Ye F, Yang J. Core-shell Au@Pd nanoparticles with enhanced catalytic activity for oxygen reduction reaction via core-shell Au@Ag/Pd constructions. Sci Rep 2015;5:1–9. https://doi.org/10.1038/srep11949.
[15] Zhou Y, Wang D, Li Y. Pd and Au@Pd nanodendrites: a one-pot synthesis and their superior catalytic properties. Chem Commun 2014;50:6141. https://doi.org/10.1039/c4cc02081b.
[16] Jana NR, Gearheart L, Murphy CJ. Seeding growth for size control of 5-40 nm diameter gold nanoparticles. Langmuir 2001;17:6782–6. https://doi.org/10.1021/la0104323.
[17] Garsany Y, Baturina OA, Swider-Lyons KE, Kocha SS. Experimental Methods for Quantifying the Activity of Platinum Electrocatalysts for the Oxygen Reduction Reaction. Anal Chem 2010;82:6321–8. https://doi.org/10.1021/ac100306c.
[18] Oliveira JP, Prado AR, Keijok WJ, Ribeiro MRN, Pontes MJ, Nogueira B V., et al. A helpful method for controlled synthesis of monodisperse gold nanoparticles through response surface modeling. Arab J Chem 2020;13:216–26. https://doi.org/10.1016/j.arabjc.2017.04.003.
[19] Smith DK, Korgel BA. The importance of the CTAB surfactant on the colloidal seed-mediated synthesis of gold nanorods. Langmuir 2008;24:644–9. https://doi.org/10.1021/la703625a.
[20] Okuno Y, Nishioka K, Nakashima N, Niidome Y. Rapid formation of silver shells on gold nanorods in a micellar solution of hexadecyltrimethylammonium chloride. Chem Lett 2009;38:60–1. https://doi.org/10.1246/cl.2009.60.
[21] Zhang H, Jin M, Xiong Y, Lim B, Xia Y. Shape-Controlled Synthesis of Pd Nanocrystals and Their Catalytic Applications. Acc Chem Res 2013;46:1783–94. https://doi.org/10.1021/ar300209w.
[22] Lim B, Kobayashi H, Yu T, Wang J, Kim MJ, Li Z-Y, et al. Synthesis of Pd−Au Bimetallic Nanocrystals via Controlled Overgrowth. J Am Chem Soc 2010;132:2506–7. https://doi.org/10.1021/ja909787h.
[23] Meena SK, Celiksoy S, Schäfer P, Henkel A, Sönnichsen C, Sulpizi M. The role of halide ions in the anisotropic growth of gold nanoparticles: a microscopic, atomistic perspective. Phys Chem Chem Phys 2016;18:13246–54. https://doi.org/10.1039/C6CP01076H.
[24] Sun J, Han Y, Fu H, Qu X, Xu Z, Zheng S. Au@Pd/TiO2 with atomically dispersed Pd as highly active catalyst for solvent-free aerobic oxidation of benzyl alcohol. Chem Eng J 2017;313:1–9. https://doi.org/10.1016/j.cej.2016.12.024.
[25] Ramos-Sánchez G, Yee-Madeira H, Solorza-Feria O. PdNi electrocatalyst for oxygen reduction in acid media. Int J Hydrogen Energy 2008;33:3596–600. https://doi.org/https://doi.org/10.1016/j.ijhydene.2008.03.004.
[26] Martínez-Casillas DC, Vázquez-Huerta G, Pérez-Robles JF, Solorza-Feria O. Electrocatalytic reduction of dioxygen on PdCu for polymer electrolyte membrane fuel cells. J Power Sources 2011;196:4468–74. https://doi.org/https://doi.org/10.1016/j.jpowsour.2011.01.050.
[27] Shi Q, Liang H, Feng D, Wang J, Stucky GD. Porous carbon and carbon/metal oxide microfibers with well-controlled pore structure and interface. J Am Chem Soc 2008;130:5034–5. https://doi.org/10.1021/ja800376t.

[28] Wang L, Yamauchi Y. Autoprogrammed synthesis of triple-layered Au@Pd@Pt core-shell nanoparticles consisting of a Au@Pd bimetallic core and nanoporous Pt shell. J Am Chem Soc 2010;132:13636–8. https://doi.org/10.1021/ja105640p.
[29] Vidaković T, Christov M, Sundmacher K. The use of CO stripping for in situ fuel cell catalyst characterization. Electrochim Acta 2007;52:5606–13. https://doi.org/10.1016/j.electacta.2006.12.057.
[30] Zadick A, Dubau L, Demirci UB, Chatenet M. Effects of Pd Nanoparticle Size and Solution Reducer Strength on Pd/C Electrocatalyst Stability in Alkaline Electrolyte. J Electrochem Soc 2016;163:F781–7. https://doi.org/10.1149/2.0141608jes.
[31] Ruiz Camacho B, Torres Rodríguez M, Solorza-Feria O. Synthesis and Charactarization of Pt and Pt-Au Oxygen Reduction Electrocatalysts. J New Mater Electrochem Syst 2009;12:43–7.

ID 016

Pt and Pt-Sn nanoparticles supported on zeolite-carbon for oxygen reduction reaction in acid medium

P.J. Pérez-Díaz[1,*], B. Ruiz-Camacho[1], A. Medina-Ramírez[1]

[1]Department of Chemical Engineering, University of Guanajuato, DCNE, Col. Noria Alta s/n, C.P. 36050, Guanajuato, Gto., Mexico
* Corresponding author: +52 1 2282515360 pperezdiaz01@gmail.com

ABSTRACT

Fuel cells are devices capable of generating electric power in a direct and clean way, capable of substituting the conventional batteries even the engines. It has been demonstrated that the proton exchange membrane fuel cells (PEMFCs) are the most promising devices, one of them are the direct methanol fuel cells (DMFC) that use methanol as fuel. The methanol is a good option as fuel due to it is found naturally in the liquid form, this makes the methanol easy to manage and store. The oxygen reduction reaction (ORR) is the cathodic reaction and it is the limiting reaction of the process due to its low kinetics of electron transfer compared to anodic reaction. In other hand, zeolites as the second catalyst can give stability and can improve the ORR. The zeolites are compounds of crystalline aluminosilicate of Si, Al y O with a tetrahedral structure; this property will allow enhancing the Pt dispersion and nucleation. Moreover, a bimetallic catalyst of Pt-Sn was proposed with the aim to increase the methanol tolerance. In this work three different electrocatalyst for ORR were evaluated in acid medium in presence and absence of methanol. For the preparation of the electrocatalysts, a X zeolite-carbon with a wt. % ratio 3:1 was synthesized by sol-gel method as substrate of Pt and Pt:Sn with a wt. % ratio 1:1. Additionally, Pt/C was tested at same conditions, with the objective of analyze the effect of the support in the ORR. It was demonstrated that the presence of Sn in the catalysts increases the methanol tolerance, and it allows to diminish the Pt load reducing the final cost of the electrocatalyst. XRD results showed the crystalline structure of the materials synthesized, and TEM images demonstrated the nanoparticles size and the metals dispersion onto the support material.

Keywords: oxygen reduction reaction; fuel cell; X zeolite; methanol tolerance

1. Introduction

In recent years the energy production is an issue of discussion, since the energy is as important as it is the economy base of a country, yet its production has a lot of negative effects in the environment because it is mostly produced by fossil oils. A clean way to produce electric energy is through the fuel cells. Fuel cells are galvanic cells, which are devices capable of generate electric power in a direct way, capable of substitute the conventional batteries even the engines. In these devices the free energy of a chemical reaction is converted into electrical energy [1], it has been demonstrated that they are a clean, silence and efficiency source energy, among which proton exchange membrane fuel cells (PEMFCs) are the most promising mechanisms [2]. The direct methanol fuel cells (DMFC) are a type of PEMFCs, using the methanol as fuel which is fed directly to the cell. The reactions that take place in a DMFC are the methanol oxidation reaction (MOR) in the anode, and the oxygen reduction reaction (ORR) in the cathode. The ORR is the most important reaction in a fuel cell due to is the reaction that limit the full process and the commercialization because of its low kinetics of electron transfer [3]. The ORR is a multi-electron reaction which can occur by two paths: I) the direct reduction path of four electrons from O_2 to H_2O; and II) the indirect reduction path of two electrons from O_2 to H_2O_2 [4]. The activity of those reactions depends of the electrocatalyst used, typically Pt supported on carbon, Pt/C(Vulcan X-72) is one of the most used catalysts in PEMFC and DMFC [5].

It has been demonstrated that catalyst based on Pt are the best for fuel cells for performance and durability [6]; but this has negative implications in the final cost of the fuel cell due to the high price of the precious metal. A good way to reduce the cost, is diminish the Pt load or using Pt alloys with metal cheaper. According to literature, the carbon as Pt support trends to degrade under the operation conditions affecting the performance of Pt and therefore dismissing the electrodes useful life [7-8]. For this reason, it is necessary a material that gives support and stability to electrocatalysts, in that order, the zeolite Faujasite NaX (zeolite X) type is proposed as second support material that will offer those characteristics.

Zeolites are compounds of crystalline aluminosilicate of Si, Al and O with a tetrahedral structure, which ones have four oxygen atoms around a cation [10]; this property will allow enhancing the Pt dispersion and nucleation [11]. Due to Pt as electrocatalyst is very expensive, several Pt-X materials have been research in order to reduce cost, and also to reduce the overpotential that the Pt implies. Among the Pt alloys that have been studied are Fe [12], Ni [13], Co [14], Cr [15], Sn [15-17], and Ru [18]. The aim of this work was the study of the electrocatalytic activity of Pt and Pt:Sn supported on zeolite-carbon composite for the oxygen reduction reaction in acid medium in presence and absence of methanol to investigated the tolerance to methanol. The results were compared with Pt/C material synthesized at same conditions.

2. Materials and Methods

2.1. Materials

Fly ash was used as the precursor for zeolite X synthesis, the details and the properties are reported in Medina et al. [19]. Aluminum hydroxide (J. T. Baker) was used for the support zeolite-carbon synthesis. Hexacloraplatinic acid ($H_2PtCl_6 \cdot 6H_2O$), isopropyl alcohol, methanol, sulfuric acid, and 5 wt.% solution of Nafion were purchased from Sigma Aldrich analytical grade. Distilled water was used as solvent.

2. Synthesis of zeolite X-C supports.

The support of zeolite X-Carbon was prepared with ratio of wt. % 3:1. First, the zeolite X was added to distilled water and it was stirred for 10 min. Then, the corresponding amount of carbon was added, the suspension was kept under stirring for 10 minutes more. After that, the mixture was put into an ultrasonic bath and the aluminum hydroxide was added. This mixture was stirred for 24 h. Following this time, it was filtered under vacuum and the recovered solid was dried in an oven at 80° C for 24 h. Subsequent, the powder obtained was submitted to heat treatment in a furnace at 300° C for 3 h in air atmosphere.

3. Preparation of the electrocatalyst Pt/zeolite X-C, Pt/C and Pt:Sn/zeolite X-C

The preparation of Pt nanoparticles by reduction method was previously reported Ruiz-Camacho et al [20]. Briefly, 85 mg of the previously prepared zeolite-carbon support plus were added to 50 mL of 0.5 mM solution of hexachloroplatinic acid. 60 mL of isopropyl alcohol was added as reducing agent to the previous suspension and put it in an ultrasonic bath (42 kHz) for 2 h. Finally, the solvent was removed by evaporation. The electrocatalysts obtained, following this technique, were (1) Pt/C, (2) Pt:Sn/X zeolite-C and (3) Pt/X zeolite-C

2.4 Physical characterization

The X ray diffraction patterns of the samples were characterized using a PANalytical Model X-ray diffractometer with a Cu K α radiation source (λ = 1.5406 Å) in the range of 10-80° 2θ. The study of the morphology and structural properties of the samples was performed by TEM using a TEM JEOL 1010 field emission microscope, operated at 80 kV, each one.

4. Electrochemical characterization

A potentiostat/galvanostat GAMRY Instrument reference 1000 T was used to determinate the electrocatalytic activity of the materials synthesized through lineal voltammetry (LV) using a rotatory disk electrode at different rotation rates (100, 200, 400, 900 y 1600 rpm). Electrocatalytic tests were performed using the three-electrode system,

which consists of a counter electrode of graphite, a reference electrode of standard saturated Calomel electrode (SCE = 0.246 V) and a working electrode (5 mm diameter) of glassy carbon disk. The catalytic ink was prepared with 6 mg of the catalyst powder, which was dispersed by ultrasonic bath for 2 hours in 500 µL of an isopropanol solution and 50 µL of a 5 wt.% Nafion solution. 11 µL of the ink was deposited on the surface of the working electrode. Potentials measurements in this work were referred to the normal hydrogen electrode (NHE).

3. Results and Discussion

Fig. 1 shows the physical characterization of XRD for a) Pt/zeolite X-C and bimetallic catalyst, and b) Pt/C catalyst. Both images show the crystalline face-centered cubic structure (fcc) of platinum at 2θ values of 39.85°, 46.35°, 67.66° corresponding to the planes (111), (200) and (220), indicated with a diamond (JCPDS 01-087-0642). In Fig. 1 a), bimetallic catalyst presents a smaller diffraction peaks of Pt than the Pt peaks of monometallic sample, Pt/X zeolite catalyst. This is the effect of having the half of Pt metal in the bimetallic catalyst. The peaks corresponding to Sn are not shown in this pattern due to the level of Sn in the electrocatalyst is not detectable by the XRD test. In other hand, Pt/X zeolite-C shows the crystalline structure of X zeolite, indicated with a circle. With diamond, the peaks of Pt are indicated in Fig. 1 b). Those peaks are well defined because Pt is the only metallic element present in this material.

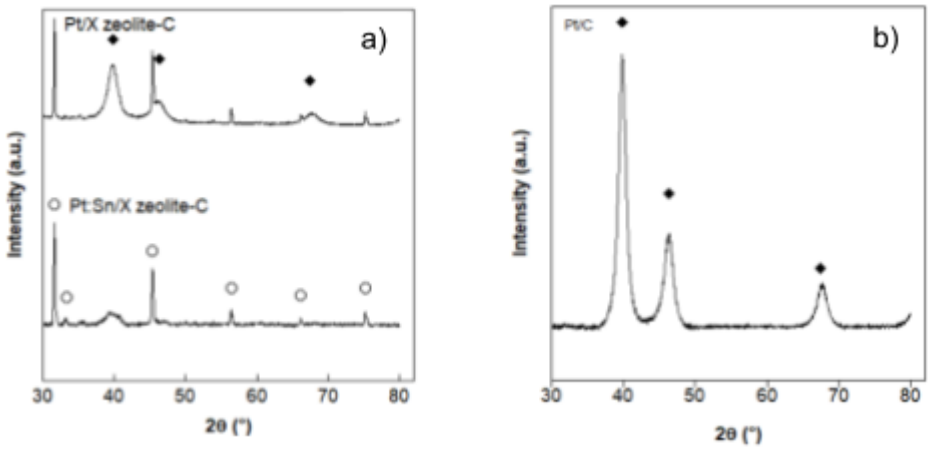

Fig. 1. XRD patterns of (a) Pt/X zeolite-C and Pt:Sn\X zeolite-C. (b) Pt supported on Carbon Vulcan. ♦ Pt, ○ X-zeolite.

Fig. 2, shows the TEM images of the (a) Pt/zeolite X-C, (b) Pt-Sn/zeolite X-C and (c) Pt/Carbon Vulcan. The particle size and dispersion vary according to the type of substrate. For example, a smaller Pt particle size and greater dispersion were obtained on the bimetallic composite, compared to zeolite X-C composite and Pt/C. Furthermore, a core-shell morphology between Pt and Sn is observed in Fig. 2b.

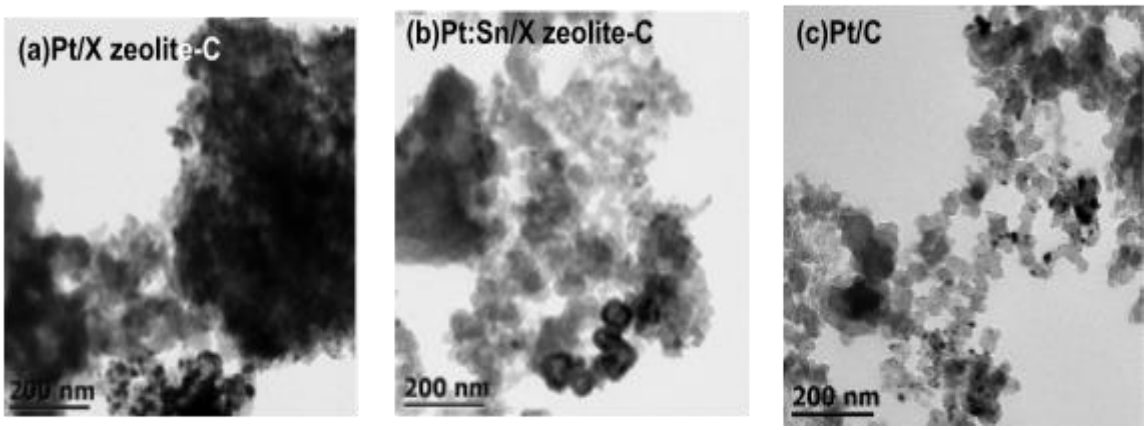

Fig. 2. TEM images of Pt catalysts supported on (a) C-zeolite X, (b) Pt:Sn/zeolite X-C and (c) carbon Vulcan.

The electrochemical results are shown in Figure 3. Figure 3, a) corresponds to lineal voltammetry in acid medium, 0.5 M sulfuric acid, saturated with oxygen at 900 rpm. At 0.9 V, the Pt/C presents 0.031 mA cm^{-2}, while Pt/X zeolite-C presents 0.013 mA cm^{-2}, and Pt:Sn/X zeolite-C 0.004 mA cm^{-2} meaning that the Pt/C presents a better electrochemical answer in the ORR, since this reaction may occur faster. Figure 3, b) shows the results of the lineal voltammetry in 0.5 M acid medium plus methanol, where it is observed that the Pt/C catalyst is the one presenting the less tolerance at methanol, since it has an overpotential of 230 over 225 and 200 mV of Pt/X zeolite-C and Pt:Sn/X zeolite-C, respectively. Figure 3, c) shows those results more clearly. Moreover, it can be said from those results that the bimetallic catalyst not only decreases the Pt load, decreasing the final cost, but it increases the methanol tolerance. For what concern to the zeolite, it increases the methanol tolerance, although the overpotential obtained with this catalyst is very close to the Pt/C catalyst. Figures 3 d, e and f show the Koutecky-Levich plots of the three electrocatalyst. It can be seen that those lines do not have an intersection in zero meaning that the ORR is not only controlled by diffusion processes but also the kinetic process is associated to this mass transfer [21]. The experimental average slope found is 11.19, 14.83, 15.15 mA^{-1} $rpm^{1/2}$ for Pt/C, Pt/X zeolite-C and Pt:Sn/X zeolite-C respectively, while the theorical slope for four and two electrons transfer are 9.90 and 19.81 mA^{-1} $rpm^{1/2}$ respectively.

Fig. 3. Linear sweep voltammetry of Pt/X zeolite-C, Pt:Sn/X zeolite-C, and Pt/C in a) 0.5 M sulfuric acid, b) 0.5 M sulfuric acid plus methanol, c) zoom of b) at 900 rpm, and scan rate 5 mV s^{-1} RT. Koutecky-Levich plots of d) Pt/C, e) Pt/X zeolite-C, and f) Pt:Sn/X zeolite-C.

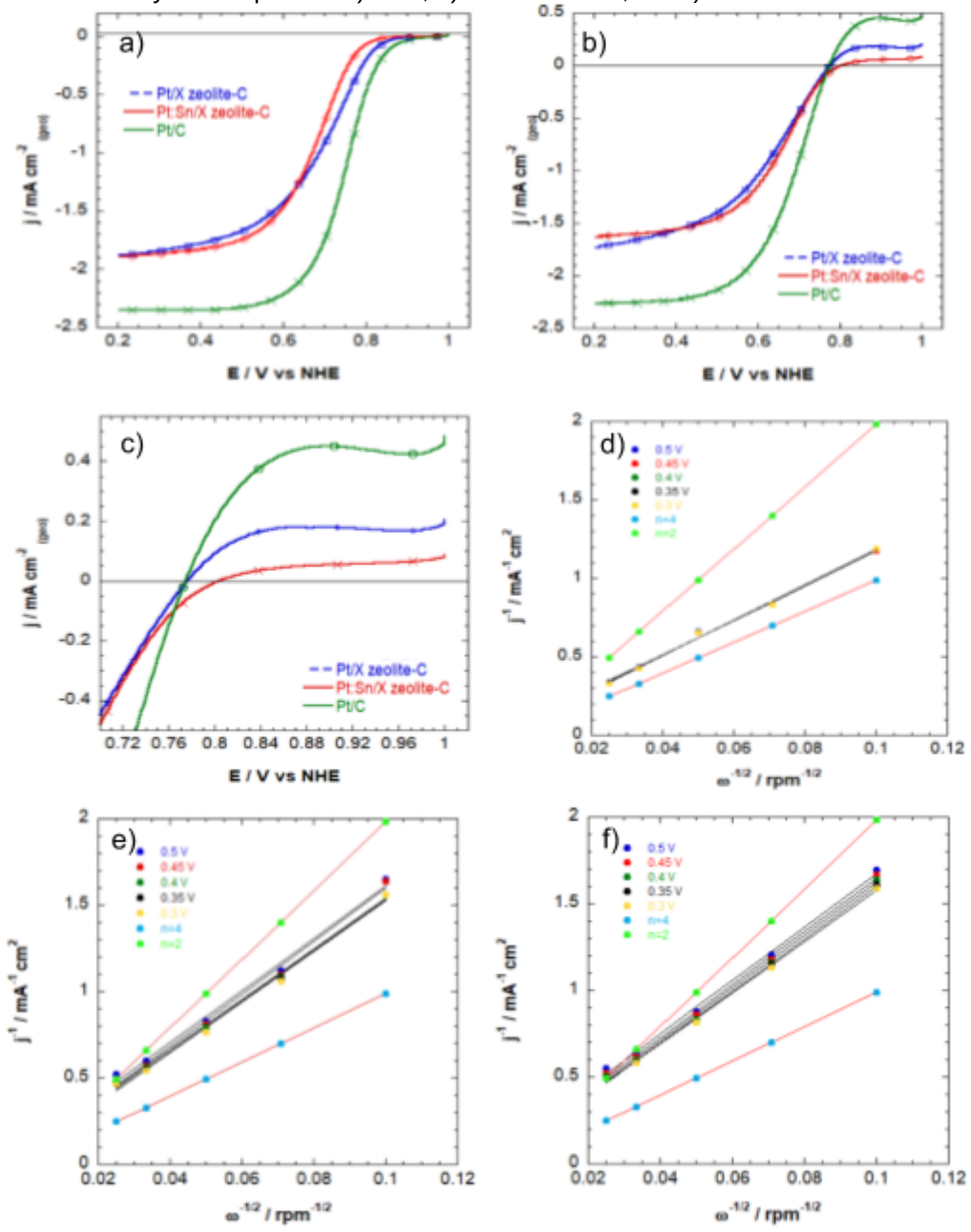

With the Koutecky-Levich plots the limits current densities were calculated for each rotation speed of the electrode by $j_l=\omega^{1/2}/B$, where ω is the rotation speed, and B is the experimental slopes calculated. The results are shown in table 1. It is observed that j_L increases when the

rotation speed increases too, and that the Pt/C electrocatalyst is the one presenting the highest current density in all the speed range.

Table 1. Diffusion limit current densities at different rotation speed.

	j_L / mA cm^{-2}				
Catalyst	**100 rpm**	**200 rpm**	**400 rpm**	**900 rpm**	**1600 rpm**
Pt/C	0.893	1.263	1.786	2.679	3.572
Pt/X zeolite-C	0.674	0.953	1.348	2.002	2.696
Pt:Sn/X zeolite-C	0.66	0.933	1.320	1.979	2.639

The information of table 1 was used to made a correction of j_k, kinetic current, using the equation of Koutecky-Levich:

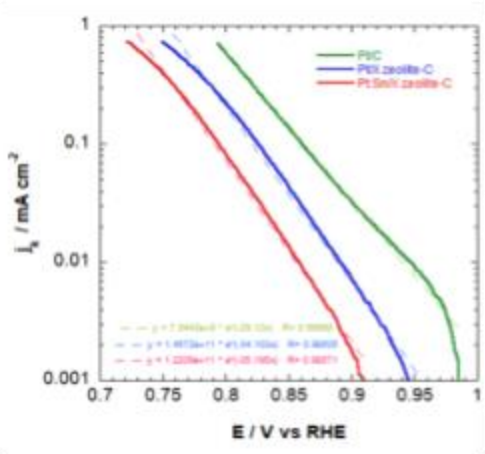

Fig. 4. Tafel plots of Pt/C, Pt/X zeolite-C and Pt:Sn/X zeolite-C.

$$j_k = \frac{j j_l}{j_l - j}$$

then, the Tafel plots were obteined. It is observed that the Pt/C material presents the higest current density of all three at 0.9 V, wich is 0.0329 mA versus 0.0068 and 0.0021 of Pt/X zeolite-X and Pt:Sn/X zeolite-C, respectevily.

4. Conclusions

In summary, mono and bi-metallic nanoparticles of Pt and Pt:Sn were tested on ORR in a DMFC. Pt/C was synthesized and tested at the same conditions for comparison purposes. It was proved that the tolerance of methanol was improved by the bimetallic material because the overpotential dismisses in comparison with the Pt/C material. This occurs because of the interaction between the tin and platinum, which modifies the electronic density of platinum. Moreover, the presence of tin in the bimetallic material, besides the

decrease in overpotential, dismisses the Pt load decreasing the total cost of the entire cell, obtaining results so close to that without tin. In other hand, it sems that the addition of X-zeolite only apport stability to the electrocatalyst but it does not improve the ORR having an inclination to the path of two electrons and not the four electrons path as does the Pt/C electrocatalyst, which one also presents the highest current density of all three.

Acknowledgements

The authors are grateful for University of Guanajuato through the DAIP office (076/2020) for providing financial support for the present research. We also thank Lourdes Palma Tirado (Neurobiology Institute-UNAM) for TEM characterization. Finally, we thank SMH and XIX International Congress of the Mexican Hydrogen Society for providing a space where to present this work.

References

[1] Daas BM & Ghosh S. Fuel cell applications of chemically synthesized zeolite modified electrode (ZME) as catalyst for alcohol electro-oxidation - A review. J Electroanal Chem 2016;783:308–315.
[2] Arvia, A.J., & Giordano, M. C. (1983). Introducción a la electrocatalisis-Monografía.
[3] Zhang, J. PEM Fuel Cell. Electrocatalyst and Catalyst Layers: Fundamentals and applications. London: Springer, 2008.
[4] C. Song y J. Zhang, «Electrocatalytic Oxygen Reduction Reaction,» de PEM fuel cell electrocatalyst and catalyst layers: Fundamentals and applications, London: Springer, 2008, pp. 88-134.
[5] Kinoshita K. Electrochemical Oxygen Technology. New York: Wiley-Interscience Pubilications; 1992.
[6] Moghaddam RB, Shahgaldi S & Li X. A facile synthesis of high activity cube-like Pt/carbon composites for fuel cell application. Front Energy 2017;11:245–253.
[7] Vogel W, Timperman L, Alonso-Vante N. Probing metal substrate interaction of Pt nanoparticles: structural XRD analysis and oxygen reduction reaction. Appl Catal A 2010;377:167-173.
[8] Dhanushkodi SR, Tam M, Kundu S, Fowler MW, Pritzker MD. Carbon corrosion fingerprint development and deconvolution of performance loss according to degradation mechanism in PEM fuel cells. J Power Sources 2013;240:114-121.
[10] Coombs DS, Recommended nomenclature for zeolite minerals: report of the sub-committee on zeolites of the International Mineralogical Association. Can Mineral 1997;35:1571–1606.
[11] Mojovic Z, Bankovic P, Jovic-Jovicic N, Milutinovic-Nikolic A, Rabi-Stankovic AA, Jovanovic D. Electrocatalytic behavior of nickel impregnated zeolite electrode. Int J Hydrogen Energy 2011;36:13343-13351.
[12] Chen W, Kim J, Sun S, Chen S. Electrocatalytic reduction of oxygen by FePt alloy nanoparticles. J Phys Chem 2008; 112:3891-3898

[13] Yang H, Vogel W, Lamy C, Alonso-Vante N. Structure and electrocatalytic activity of carbon-supported Pt-Ni alloy nanoparticles toward the oxygen reduction reaction. J Phys Chem B 2004;108:11024-11034
[14] Chen S, Shen W., Yabuuchi N, Ferreira PJ, Allard L, Shao-Horn Y. Origin of oxygen reduction reaction activity on "Pt_3Co" nanoparticles: atomically resolved chemical compositions and structures. J Phys Chem 2009;113:1109-1125
[17] Antolini E, Salgado JRC, Santos, LGRA, García, G, Ticianelli EA, Pastor E, Gonzalez ER. Carbon supported Pt-Cr alloys as oxygen-reduction catalyst for direct methanol fuel cells. J Appl Electrochem 2006;36:355-362
[15] Beyhan S, Sahin NE, Pronier S, Léger JM, Kadirgan F. Comparison of oxygen reduction reaction on Pt/C, Pt-Sn/C, Pt-Ni/C, and Pt-Sn-Ni/C catalysts prepared by Bönnemann method: A rotating ring disk electrode study. Electrochim Acta, 2015;151:565-573
[16] Jeyabharathi C, Venkateshkumar P, Mathiyarasu J, Phani KLN. Platinum-tin bimetallic nanoparticles for methanol tolerant oxygen-reduction activity. Electrochim Acta 2008;54:448-454
[17] Knani S, chirchi L, Napporn WT, Baranton S, Léger JM, Ghorbel A. Promising ternary Pt–Co–Sn catalyst for the oxygen reduction reaction. J Electroanal Chem 2015;738:145-153
[18] Takasu Y, Fujiwara T, Murakami Y, Sasaki K, Oguri M, Asaki T, Sugimoto W. Effect of structure of carbon-supported PtRu electrocatalysts on the electrochemical oxidation of methanol. J Electrochem Soc 2000;147
[19] Medina A, Gamero P, Almanza JM, Vargas A, Montoya A, Vargas G, Izquierdo M. Fly ash from a mexican mineral coal I: mineralogical and chemical characterization. J Hazard Mater 2010;181:91-104.
[20] Ruiz-Camacho B, Martínez Álvarez O, Rodríguez-Santoyo HH, López Pérez PA, Fuentes-Ramírez R. Mono and bi-metallic electrocatalysts of Pt and Ag for oxygen reduction reaction synthesized by sonication. Electrochemm Comm 2015;61:5-9.
[21] Z. Qi. Electrochemical methods for catalyst activity evaluation. In: Jiujun Zhang editor. PEM fuel cell electrocatalyst and catalyst layers: Fundamentals and applications, London: Springer; 2008, pp. 547-604.

ID 020

Cost effective synthesis of NiCu electrocatalyst as anode for direct ethanol fuel cell in alkaline media

Gladys Gallardo-Espinoza[1], José G. Becerra-Salais[1], Enrique Rocha-Rangel[1], José A. Rodriguez-Garcia[1], P. C. Melendez-Gonzalez[2], W. J. Pech-Rodríguez [1*].

[1]Universidad Politécnica de Victoria, Parque Científico y Tecnológico de Tamaulipas, Ciudad Victoria, Tamaulipas 87138, México
[2]Cinvestav Unidad Saltillo, Av. Industria Metalúrgica 1062, Parque Industrial Ramos Arizpe, 25900 Ramos Arizpe, Coahuila, México
* Corresponding author: wpechr@upv.edu.mx

ABSTRACT

Herein, we report a facile and cheap process to synthetize NiCu nanoparticles to be used as electrocatalyst for the Ethanol Oxidation Reaction (EOR). For that, an intermittent microwave assisted polyol process was used to synthetize NiCu in two steps. The, obtained material was characterized by FTIR measurements to determine the existing bonding between O, Ni and Cu. Also, to determine the capacity to oxidize ethanol in alkaline media a set of electrochemical experiments were performed. From the FTIR results it is demonstrated the presence of Cu-O bindings and also Ni-Cu binding. The results from CVs suggest that Cu great improve the performance of Ni to achieve the ethanol oxidation. The enhancing in current density for EOR in NiCu electrocatalysts can be explained by the well-known bifunctional theory that state that a second metal can provides OH groups at low potential that facilitate the rapid oxidation of ethanol onto the active metal, in this case Ni. Therefore, with this investigation we demonstrate a cost effective process to obtain active electrocatlysts for EOR and also this open the doors to further investigation of non-noble metals as electrocatalysts for this relevant electrochemical reaction.

Keywords: Synthesis, nanoparticles, electrocatalysts, oxidation.

---

1. Introduction

The alkaline anion exchange membrane fuel cell (AAEMFC) has gained great interest because they can operate with high efficiency due to the rapid kinetic reaction at the anode and cathode compartment [1]. In addition, they represent a potentially revolutionary technology because they do not use a combustion process to generate electrical energy [2].

Currently, noble metals have been used as electrocatalysts for anodic and cathodic reactions. However, to make the fuel cell a viable technology, it is necessary to reduce the load of these precious metals or to use low-cost nanomaterials. Since these devices use Pt electrocatalyst and this is expensive and scarce element, it contributes to raising the production cost of the fuel cells [3].
Therefore, this has propitiated the study of non-noble metals such as Ni, Sn, Mo, Cu and others as cocatalysts for the Ethanol oxidation reaction (EOR). In this sense, Ni nanostructures have been synthesized and used as an electrocatalyst for EOR. One of the studies made with NiCu alloys can be seen in the article published by Danaee and coworkers, where nickel and carbon electrodes were fabricated and studied for Methanol oxidation reaction (MOR). The electrocatalysts were prepared by galvanostatic deposition by examining the redox process. This group conducted experiments in 0.3 M of methanol + 1 M NaOH to estimate the ability of GC/NiCu to oxidize methanol. They found that GC/NiCu present good electrochemical activity for MOR.

Onthe other hand, the research group of Jafarian studied a modified Ni electrode with copper nanoparticles for MOR. They carried out an investigation to determine the effect of methanol oxidation at different molar concentrations and they found a linear relationship between methanol concentration and current densities. For example, at 0.5 mol L^{-1} a current close to 1 mA was obtained while a 2 mol L^{-1} 4 mA was observed. [4]

It is well-know that the method of synthesis plays a key role into the final properties of the materials. Here, we used the microwave assisted polyol process to synthesize NiCu nanoparticles and the obtained material was used as electrocatalysts for EOR. The results shown that NiCu present better electrochemical activity for ethanol oxidation in contrast with the synthesized Ni electrocatalyst.

2. Materials and Methods

Ni and NiCu nanoparticles were synthesized by the polyol process were Ethylene glycol (EG) was used as solvent and reducing agent. For Ni material the desired amount of $NiCl_2$ was dispersed 14 mL of EG by ultrasonic bath. Then, 1.5 mol L^{-1} of NaOH was aggregated under magnetic stirring the resulted solution was transferred at round bottom flask and heated under two sequence of microwave hating of 2 min. The resulted slurry was cool down at room temperature and filtered and washed with deionized water. Meanwhile, NiCu nanoestructures were developed by two step synthesis. First, Ni nanoparticles was obtained by the aforementioned procedure and then a mixture of $CuSO_4$ + NaOH was added to the obtained Ni slurry as summited to microwave heating.

The electrocatalytic activity of the NiCu nanoparticles for EOR was investigated in a three-electrode cell using a Gill AC potenciostat/galvanostat with a Ag/AgCl as reference electrode and graphite bar as counter electrode. The glassy carbon working electrode was modified by transferring an aliquot of catalytic ink composed of 5 mg of NiCu or Ni catalysts + 0.5 mL of 2-propanol and 15 µL of Nafion®.

3. Results and Discussion

The surface chemical groups of the obtained material were studied by FTIR measurements. Figure 1 shows the FTIR spectra of the synthesized NiCu. The perturbation at 620 cm^{-1} is attributed to interactions between Cu-O species. This suggest that Cu nanoparticles were successfully reduced onto the surface of Ni. Furthermore, the band located at 676 cm^{-1} is due to the stretching vibration of Ni-O. The OH group interaction with the sample was observed at 1630 cm^{-1} and 3450 cm^{-1}. [3]

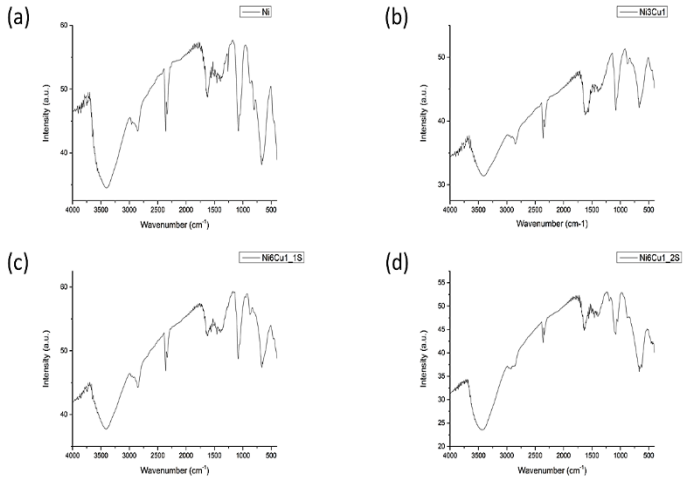

Figure 1. FTIR spectra of the synthesized NiCu electrocatalyst

Figure 2 shows the cyclic voltammogram for the synthesized Ni electrocatalysts. The experiment was conducted in 0.5 mol L^{-1} NaOH with a windows potential from 0.1 to 0.7 V vs Ag/Ag Cl at scan rate of 20 mV s^{-1}. As can be observed in the forward direction an anodic peak was observed close to 0.47 V vs Ag/AgCl that was ascribed to Ni species. The reduction of the Ni peak occurs at the backward direction at 0.42 V [5].

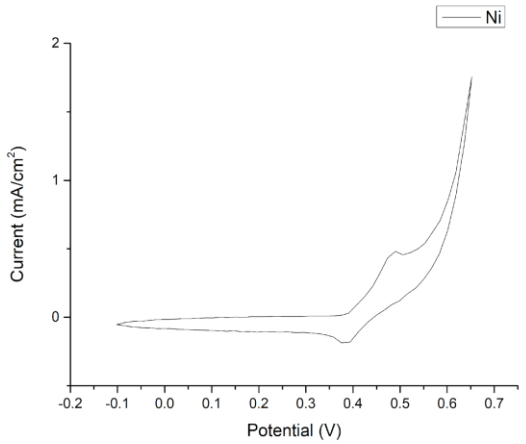

Figure 2. Nickel Voltammogram in 0.5 mol L⁻¹NaOH at 20 mV s⁻¹.

The CV for ethanol oxidation reaction (EOR) at different concentrations on Ni electrocatalysts is depicted in Figure 3. The anodic and cathodic peak of Ni disappears and only one peak is observed that is attributed to the EOR. At 0.5 mol L^{-1} of ethanol the Ni electrocatalysts deliver 2.7 mA cm^{-2} of current density and this value has a linear relationship with the ethanol concentration.

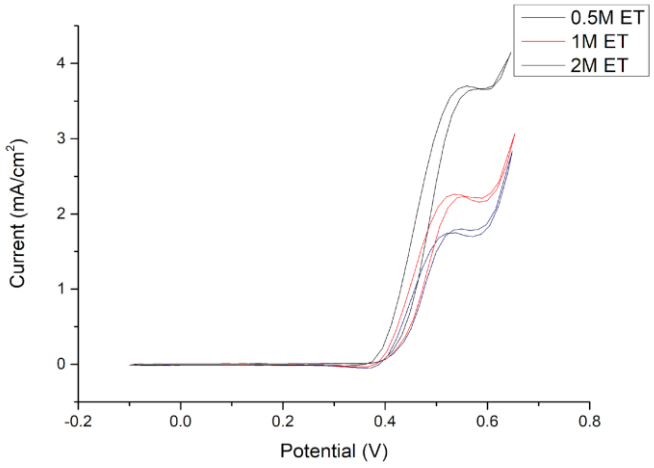

Figure 3. Nickel behavior with different ethanol concentrations in 0.5 mol L⁻¹ NaOH at 20 mV s⁻¹.

Figure 4 shows the CV for EOR at NiCu electrocatalysts. As in the case of Ni, current densities have a linear trend with ethanol concentration. Moreover, NiCu has better current densities compared with only Ni. For example, NiCu present 25 mA cm^{-2} at 1 mol L^{-1} EtOH while Ni electrocatalysts has only 3 mA cm^{-2}.

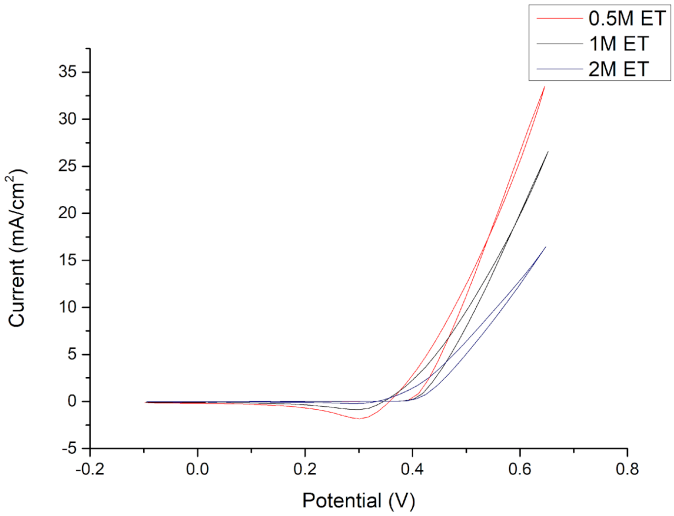

Figure 4. Behavior of the NiCu in the ratio Ni: Cu = 6:1, with different ethanol concentrations in 0.5 mol L^{-1} NaOH at 20 mV s^{-1}.

4. Conclusion

Herein, it is demonstrated the successful synthesis of NiCu electrocatalysts for fuel cell applications. From CV it was observed that NiCu has better electrocatalytic activity for ethanol oxidation than Ni. The enhanced performance for EOR in NiCu can be due to beneficial effect of Cu that change the binding energies for ethanol adsorption.

Acknowledgements
I thank CONACYT for the scholarship granted to G. Gallardo-Espinoza. In addition, I am grateful to the SMH and XVII International Congress of the Mexican Hydrogen Society for the acceptance in this congress.

References

[1] I. Danaee, M. Jafarian, F. Forouzandeh, F. Gobal, and M. G. Mahjani, “Electrocatalytic oxidation of methanol on Ni and NiCu alloy modified glassy carbon electrode,” Int. J. Hydrogen Energy, vol. 33, no. 16, pp. 4367–4376, 2008, doi: https://doi.org/10.1016/j.ijhydene.2008.05.075.
[2] U. C. Castillo, “generación de electricidad limpia y eficiente vía electroquímica,” 1999.
[3] D. Chen, F. Giroud, and S. D. Minteer, “Nickel Cysteine Complexes as Anodic Electrocatalysts for Fuel Cells,” vol. 161, no. 9, pp. 933–939, 2014, doi: 10.1149/2.0811409jes.
[4] M. Jafarian, R. B. Moghaddam, M. G. Mahjani, and F. Gobal, “Electro-catalytic oxidation of methanol on a Ni – Cu alloy in alkaline medium,” pp. 913–918, 2006, doi: 10.1007/s10800-006-9155-6.
[5] Y. Fu, L. Zhang, and G. Chen, “Preparation of a carbon nanotube-copper nanoparticle hybrid by chemical reduction for use in the electrochemical sensing of carbohydrates,” Carbon N. Y., vol. 50, no. 7, pp. 2563–2570, 2012, doi: 10.1016/j.carbon.2012.02.014.

ID 054

High-performance Pd nanocatalyst supported on Vulcan XC-72 functionalized with Cu organometallic compounds for the Ethanol Oxidation Reaction in alkaline media

P.C. Meléndez González[1], M.E. Sánchez-Castro[1,2], I.L. Alonso-Lemus[3], B. Escobar-Morales[4], W.J. Pech-Rodríguez[5], Teko W. Napporn[6], F.J. Rodríguez-Varela[1,2*].

[1]Programa de Nanociencias y Nanotecnología, Cinvestav Unidad Saltillo, Av. Industria Metalúrgica 1062, Parque Industrial Ramos Arizpe. Ramos Arizpe, Coahuila, C.P 25900, México.
[2]Programa de Sustentabilidad de los Recursos Naturales y Energía, Cinvestav Unidad Saltillo.
[3]CONACYT, Sustentabilidad de los Recursos Naturales y Energía, Cinvestav Unidad Saltillo.
[4]CONACYT. CICY. Calle 43 No. 130 Col. Chuburná de Hidalgo, Mérida, Yucatán, C.P. 97200, México.
[5]Universidad Politécnica de Victoria, Av. Nuevas Tecnologías 5902, Parque Científico y Tecnológico de Tamaulipas, Cd Victoria, Tamps., C.P.87138, México
[6]Université de Poitiers, IC2MP UMR 7285 CNRS, «Equipe SAMCat», 4, rue Michel Brunet, B27, TSA 51106, 86073 Poitiers Cedex 09, France.

ABSTRACT

The most widely used support of metal nanoparticles in fuel cells applications is the commercially available Vulcan XC-72. Herein, we report its functionalization XC-72 with home-obtained mesityl copper (Cu-mes) and Cu coordinate (Cu(dmpz)L2) organometallic compounds. Pd nanoparticles are dispersed on the novel supports by the polyol method, obtaining Pd/$C_{Cu\text{-}mes}$ and Pd/$C_{Cu(dmpz)L2}$. The aim of the surface modification of the support is to promote the formation of functional groups and alloyed phases between Cu from the compounds and the Pd nanoparticles being dispersed on it. The catalytic activity of the nanocatalysts for the Ethanol Oxidation Reaction (EOR) in 0.5 mol L^{-1} KOH was evaluated. Characterization of the functionalized Vulcan by FTIR analysis shows the successful incorporation of the organometallic compounds. The XRD patterns demonstrate a shift towards higher 2θ angles at Pd/$C_{Cu\text{-}mes}$ and Pd/$C_{Cu(dmpz)L2}$, compared to conventional Pd/C, indicating the formation of alloyed Pd-Cu phases. Analysis by EDS shows that the organometallic compounds are chemically stable, maintaining a high Cu concentration after the synthesis of the nanocatalysts. In electrochemical characterization, the polarization curves of the EOR at the nanocatalysts show that Pd/$C_{Cu\text{-}mes}$ promotes the reaction at a more negative onset potential, i.e., E_{onset} = 0.38 V/RHE, compared to 0.41 V/RHE of Pd/C and Pd/$C_{Cu(dmpz)L2}$. The current density j delivered by Pd/$_{CCu\text{-}mes}$ is considerable higher (119.11 mA cm^{-2}), followed by Pd/$C_{Cu(dmpz)L2}$ and Pd/C (73.63 and 54.57 mA cm^{-2}, respectively). In AEM-DEFC tests, the cell equipped with a Pd/$C_{Cu\text{-}mes}$ anode nanocatalyst demonstrated the highest open circuit voltage (OCV, 0.60 V) followed by 0.50 and 0.38 V at the cells having Pd/C and Pd/$C_{Cu(dmpz)L2}$ anodes, respectively. The maximum cell power density of 0.14 W cm^{-2} at 0.5 A cm^{-2} has been generated by Pd/$C_{Cu\text{-}mes}$. Due to its high catalytic activity, Pd/$C_{Cu\text{-}mes}$ can find application in AEM-DEFCs.

Keywords: Pd nanocatalysts, organometallic, EOR, Vulcan XC-72.

1. Introduction

Anion Exchange Membrane- Direct Ethanol Fuel Cells (AEM-DEFCs) are considered efficient clean energy technologies with low environmental impact, offering several advantages compared to conventional energy devices and the acid DEFC, such as i) the possibility of using renewable ethanol that can be easily handled in its liquid form; ii) a higher conversion efficiency; iii) faster kinetics in anode and cathode electrochemical reactions, and iv) longer useful life [1-2]. However, one of the scientific-technological challenges is to increase its performance, particularly at the anode reaction, where the oxidation molecule generates several reaction intermediaries. Therefore, the design of highly active nanocatalysts is necessary.

Vulcan XC-72 is one of the most used carbonaceous materials as metal nanoparticle supports, since it has suitable surface chemistry for anchoring nanoparticles, along with a high electrical conductivity [3]. Having a hydrophobic surface, it has been submitted to diverse oxidative fictionalizing treatments that modify the textural properties of the carbon, decreasing its electrical conductivity [4-5]. In this context, it is important to point out that the organometallic compounds are less aggressive functionalizing agents than oxidative treatments, but strong enough to chemically modify the carbonaceous surface creating functional groups that promote the anchorage and adequate dispersion of nanoparticles. Furthermore, the surface modification creates active metal sites from the compound that promote alloying phases with the base metal that is deposited on the surface of the carbon [6].

In the present work, the electrochemical characterization of the 20 wt. % Pd/$C_{Cu\text{-}mes}$ and Pd/$C_{Cu(dmPz)L2}$ nanocatalysts during the EOR in alkaline media is presented and compared to that of a conventional Pd/C nanocatalysts. The characterization includes the full AEM-DAFC test.

2. Materials and Methods

2.1 Reagents

The chemical reagents used were analytical grade. Vulcan XC-72 was purchased from Cabot Inc. Copper chloride (I) (99.9 %), 1,4-dioxane (99.8 %), ether (99 %), 3,5 dimethylpyrazole (99 %), copper (II) acetate monohydrate (99 %), terephtalic acid (97.5 %) and THF (99.9 %), $PdCl_6(NH_4)_2$ (99 %), ethylene glycol (99.8 %), NaOH (97 %) and H_2SO_4 (95-99 %) were used. For the electrochemical tests we used: KOH (90 %), Nafion ® 117 (5 wt. %), 2-propanol (95 %), and ethanol (99.8 %) were acquired from Sigma-Aldrich. Metallic sodium (Na^0) was obtained from Jamlek. High purity Argon (Ar) (> 99 %) was purchased from INFRA.

2.2 Synthesis of organometallic compounds

Cu-mes was synthesized under Ar atmosphere using the Schlenk technique. Solvents (dioxane, THF, and ether) were distilled before use. Magnesium mesitylbromide was slowly mixed with a suspension of CuCl (I) in THF under vigorous magnetic stirring for 12 h at room temperature. Dioxane was added to the mixture, maintaining stirring for 2 h, then allowing precipitation for 1 h. The obtained product was filtered via cannula and dried under vacuum

conditions. Ether was added to produce a solution that was precipitated and filtered to obtain Cu-mes crystals [7].

Cu(dmpz)L2 was synthesized as follows: a solution of copper (II) acetate in methanol was added to a methanol solution containing dimethylpyrazole (dmpz) and terephtalic acid (L2) under continuous stirring. The resulting solution was dispersed for 45 min by ultrasound at room temperature, left to precipitate for 1 h, and the resulting blue crystals filtered, washed with methanol, and dried under vacuum [8].

2.3 Functionalization of Vulcan

A mixture of Vulcan and the corresponding organometallic compound (1:10 molar ratio) was dispersed in THF under Ar atmosphere and refluxing conditions for 48 h at 130°C. The obtained product was transferred to a Schlenk tube, subsequently washed with THF, water, and ethanol then dried under vacuum conditions [9].

2.4 Synthesis of nanocatalysts

The nanocatalysts were synthesized using the polyol method [10]. For example, $C_{Cu\text{-}mes}$ and the Pd precursor were dispersed in 46 and 4 mL of ethylene glycol (EG), by sonication for 30 min. Subsequently, The Pd and $C_{Cu\text{-}mes}$ solutions were mixed under magnetic stirring for 15 min, then the pH of the solution was adjusted to 12 by adding a 1 mol L^{-1} NaOH solution. The resulting mixture was heated and stirred under refluxing conditions at 160° C for 3 h. At the end of this time, the mixture was left to cool down, followed by the modification of the pH to 2, using 1 mol L^{-1}, H_2SO_4, filtered and dried. The same producer was followed for the Pd/C nanocatalysts, using non-functionalized Vulcan.

2.5 Physicochemical Characterization

$C_{Cu\text{-}mes}$ and $C_{Cu(dmpz)L2}$ were characterized by FTIR in WQF-S10A FTIR Rayleigh instrument. The nanocatalysts were characterized by EDS microanalysis in a Philips XL SERIES Scanning Electron Microscope (SEM). XRD patterns were obtained in Brunker D2 Phase 2nd Gen equipment. The crystallite size (d) was estimated from data of the Pd (220) reflection planes with the Scherrer equation [11].

2.6 Electrochemical Characterization

Evaluation of the nanocatalysts was carried out in a three-electrodes electrochemical half-cell using a Pine Wave Driver 20 bipotentiostat. The counter was a Pt wire, while the reference electrodes was of the Ag/AgCl type. Potentials have been referenced against the Reversible Hydrogen Electrode (RHE). Catalytic inks were prepared by separately mixing by ultrasound 10 mg of nanocatalyst, 5 µL of Nafion® and 1 mL of 2-propanol. An aliquot of 10 µL was deposited on a 5 mm diam glassy carbon disc to from the working electrode. CVs were acquired in Ar-saturated 0.5 mol L^{-1} KOH in a potential range between 0.05 and 1.2 V /RHE at a scan rate of 20 mV s^{-1}. The catalytic activity of the EOR of the nanocatalysts was evaluated adding a 0.5 mol L^{-1} solution of EtOH to the electrolyte. The polarization curves were obtained under the same conditions as in the CVs. Polarization curves in an AEM-

DEFC test were obtained in a homemade electrochemical cell with the same nanocatalysts at the anodes and cathodes. The fuel was EtOH 0.5 mol L^{-1} + KOH. The AEM was a Fumatech ® FAA. Cathode was fed with a flow of O_2 + KOH.

3. Results and Discussion

The FTIR spectra of the supports are shown in Fig. 1. Nonfunctionalized Vulcan (C) shows a band at around 3440 cm^{-1} due to the OH stretching vibration from hydroxyl groups. It also displays the band around 2900 cm^{-1} attributed to C-H vibrations of alkane and alkyl groups. The band at 2368 cm^{-1} corresponds to O-H stretching and COOH group vibrations. In the 1700-1200 cm^{-1} range, signals emerge due to HCOO- carbonyl and carboxyl groups stretching vibrations [12-16]. Additionally, $C_{Cu\text{-}mes}$ shows a band in the 660-520 cm^{-1} range attributed to Cu-O stretching vibration [17-18]. Also, $C_{Cu(dmpz)L2}$ shows characteristic peaks that correspond to carboxylate and NH bands of the (dmpz) ligand, which suggest the coordination of the compound [19].

Table 1 shows the chemical composition of carbon functionalized with organometallic compounds. $C_{Cu\text{-}mes}$ has 80.51, 12.89 and 6.59 (wt. %) C, Cu and O content, respectively. Its Cu concentration is lower than the theoretically calculated (20 wt. %) due to the presence of O, which appears probably due to the formation of copper oxides phases and oxygen in the carbon. Meanwhile, the C, Cu and O content at $C_{Cu(dmpz)L2}$ are 71.31, 22.36, and 6.32 (wt. %), respectively.

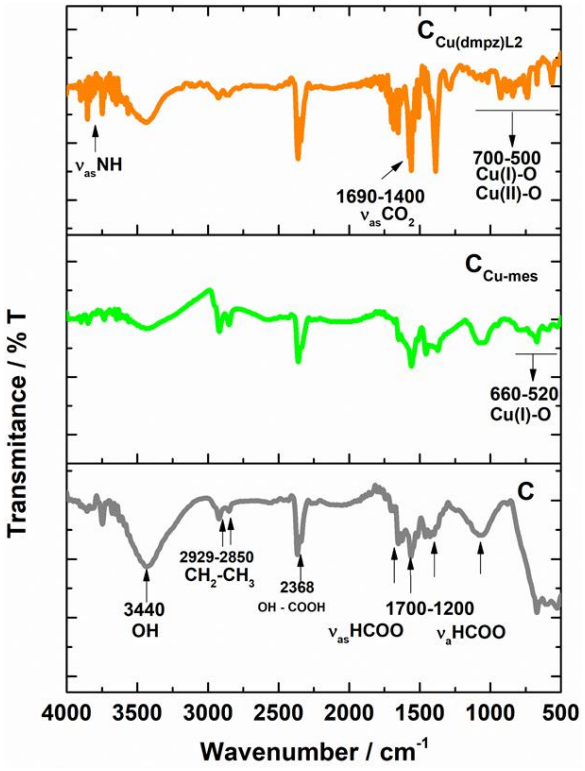

Fig. 1. FTIR spectra of C, $C_{Cu\text{-}mes}$ and $C_{Cu(dmpz)L2}$.

Table 1. Chemical composition of $C_{Cu\text{-}mes}$ and $C_{Cu(dmpz)L2}$.

Support	Chemical Composition (wt. %)		
	C	Cu	O
$C_{cu\text{-}mes}$	80.51±0.86	12.89±1.38	6.59±0.60
$C_{Cu(dmpz)L2}$	71.31±0.18	22.36±0.37	6.32±0.29

Fig. 2 shows the XRD patterns of the nanocatalysts. In the diffractogram of Pd/C, the (002) plane due to the carbon structure can be observed, followed by the (111), (200), (220), and (311) reflections corresponding to the fcc structure of Pd. In the case of $Pd/C_{Cu\text{-}mes}$, the peaks due to the Pd planes shift towards higher degrees (2 theta), which suggests a modification in the Pd lattice due to the formation of Pd-Cu alloyed phases [20]. Such displacement in the Pd planes is more evident in $Pd/C_{Cu(dmpz)L2}$. Furthermore, this nanocatalysts shows several peaks in the 15-25 (2 theta) interval attributed to the organometallic compound. Table 2 shows the d values of the nanocatalysts. $Pd/C_{Cu\text{-}mes}$ has the smallest d, compared to Pd/C and $Pd/C_{Cu(dmpz)L2}$.

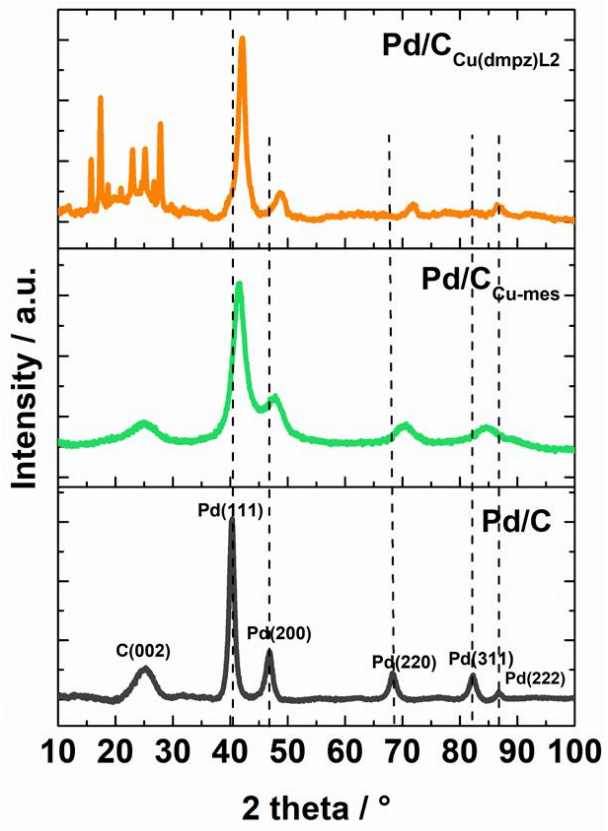

Fig. 2. XRD patterns of Pd/C, $Pd/C_{Cu\text{-}mes}$ and $Pd/C_{Cu(dmpz)L2}$.

Table 2. Crystallite size of the nanocatalysts.

Nanocatalyst	Crystallite size (nm)
Pd/C	6.9
$Pd/C_{Cu\text{-}mes}$	2.9
$Pd/C_{Cu(dmpz)L2}$	6.3

In Fig. 3 a) the CVs of the nanocatalysts supported on functionalized Vulcan show a higher j over the potential scanned, particularly a remarkable increase in the peak due to the reduction of Pd oxides, compared to Pd/C. The j peak at ca. 0.9 V/RHE observed at $Pd/C_{Cu\text{-}mes}$ and $Pd/C_{Cu(dmpz)L2}$ is due to the presence of copper oxides, because of the organometallic functionalization of Vulcan. Fig. 3 b) shows the polarization curves of the nanocatalysts. $Pd/C_{Cu\text{-}mes}$ promotes the reaction at a more negative E_{onset} compared to Pd/C and $Pd/C_{Cu(dmpz)L2}$ (Table 3). Moreover, the peak j is considerable higher at $Pd/C_{Cu\text{-}mes}$ (119.11 mA cm^{-2}), followed by $Pd/C_{Cu(dmpz)L2}$ (73.63 mA cm^{-2}) and Pd/C (54.57 mA cm^{-2}). Thus, the nanocatalysts supported in functionalized Vulcan show enhanced behavior for the EOR, attributed to a combination of the bifunctional mechanism and the electronic interaction between Pd and Cu that induce a modification in the adsorption energy of species such as ethanol and/or intermediates.

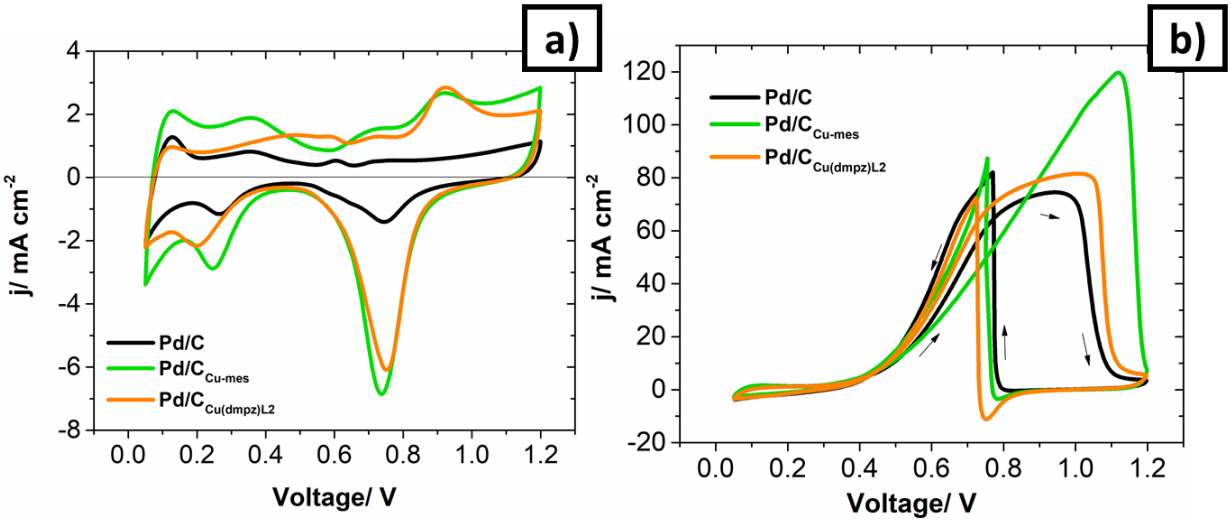

Fig. 3. a) CVs of Pd/C, $Pd/C_{Cu\text{-}mes}$ and $Pd/C_{Cu(dmpz)L2}$. Electrolyte: 0.5 mol L^{-1} KOH. Scan rate: 20 mV s^{-1}. b) Polarization curves of the EOR at the nanocatalysts. Same scan rate. Electrolyte: 0.5 mol L^{-1} KOH + 0.5 mol L^{-1} EtOH.

Table 3. Electrochemical parameters of the EOR at the nanocatalysts in half-cell and AEM-DEFC.

Nanocatalyst	E_{onset}	j	OCV	P_{cell}
	(V)	(mA cm^{-2})	(V)	(W cm^{-2})
Pd/C	0.41	54.57	0.50	0.09
$Pd/C_{Cu\text{-}mes}$	0.38	119.11	0.60	0.15
$Pd/C_{Cu(dmpz)L2}$	0.41	73.63	0.38	0.04

The polarization curves of the EOR in an AEM-DAFC are show in Fig. 4 a). Pd/$C_{Cu\text{-}mes}$ as the anode nanocatalyst generates the highest open circuit voltage (OCV) (Table 3), with a value of 0.60 V, followed by Pd/C (OCV= 0.50V) and Pd/$C_{Cu(dmpz)L2}$ (OCV = 0.38). The maximum power density (P_{cell}) value is 0.15 W cm^{-2} when Pd/$C_{Cu\text{-}mes}$ is the anode (Fig. 4b). The enhanced performance of the Pd/$C_{Cu\text{-}mes}$ nanocatalysts is attributed to a synergistic effect due to incorporation of Cu into the Pd structure after Vulcan functionalization, catalyzing the EOR and promoting the oxidative removal of adsorbed intermediates, thus increasing the power density generated by the AEM-DEFC.

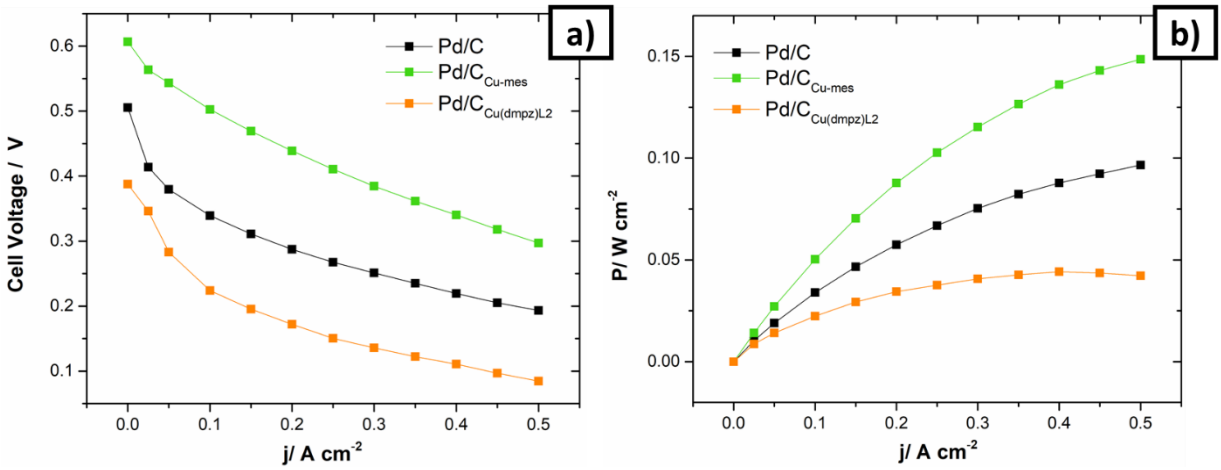

Fig. 4. a) Polarization curves and b) power density curves of an AEM-DEFC equipped with the nanocatalysts as anodes and cathodes. Fuel: 0.5 mol L^{-1} EtOH + KOH. AEM: Fumatech® FAA. Feed at the cathode: O_2 + KOH.

4. Conclusions

The functionalization of Vulcan with Cu organometallic compounds was successfully achieved, promoting the formation of functional groups and Cu species sites. The presence of Cu promoted the formation of alloyed Pd-Cu phases, increasing the catalytic activity of Pd/$C_{Cu\text{-}mes}$ and Pd/$C_{Cu(dmpz)L2}$ for the EOR in half-cell tests in alkaline media. In a complete AEM-DEFC, Pd/$C_{Cu\text{-}mes}$ showed the best performance compared to Pd/C and Pd/$C_{Cu(dmpz)L2}$. The results presented in this work show that Pd/$C_{Cu\text{-}mes}$ can be used as high-performance anode in an AEM-DEFC.

Acknowledgements

We acknowledge the support from CONACYT México through project 241526 and doctorate scholarship to PCMG.

References

[1] Cermenek B., Ranninger J., Hacker V. Alkaline Direct Ethanol Fuel Cells. In: Besile A., Lulianelli A., Dalena F., Veziroglu N., editors. Ethanol, Amsterdam: Elsevier B.V; 2019, p.383-405.
[2] Wang L., Lavacchi A., Bevilcqua M., Bellini M., Fornasiero P., Filippi J., Innocenti M., Marchionni A., Miller H. A., Vizza Francesco. Energy efficiency of alkaline direct ethanol fuel cells employing nanoestructured palladium electrocatalysts. Chem CatChem 2015;7 2214-2221.
[3] Zhu Y., Kang Y., Zou Z., Zhou Q., Zheng J., Xia B., Yang H., A facile preparation of carbon-supported Pd nanoparticles for electrocatalytic oxidation of formic acid. Electrochem. Commun. 2008;10 802-805.
[4] Yang S., Zhang X., Mi H., Ye X. Pd nanoparticles supported on functionalized multi-walled carbon nanotubes (MWCNTs) and electrooxidation for formic acid. J. Power Sources 2008; 175 26-32.
[5] Salgado J.R.C., Duarte R.G., Ilharco L.M., Botelho do Rego A.M., Ferraira A.M., Ferreira M.G.S. Effect of functionalized carbon as Pt electrocatalysts support on the methanol oxidation reaction. Aplp. Catal. B; -Environ. 2011;102 496-504.
[6] Siller-Ceniceros A.A., Sánchez-Castro M.E., Morales-Acosta D., Torres-Lubian J.R. Martínez Guerra E., Rodríguez-Varela F.J. Innovative functionalization of Vulcan XC-72 with Ru organometallic complex: Significant enhancement in catalytic activity of Pt/C electrocatalysts for the methanol oxidation reaction (MOR). App. Catal. B-Environ. 2017;209 445-467.
[7] Stollenz M., Meyer F. Mesitylcopper-A powerful tool in synthetic chemistry. Appl. Organomet. Chem. 2012;31 7708-7727.
[8] Jin S-W., Ye X-H., Jin L., Zheng L., Li J-W., Jin B-P, Wang D-Q. Syntheses and structural characterization of nine coordination compounds assembled from copper acetate, 3,5-dimethylpyrazole and carboxylates. Polyhedron 2014;81 382-395.
[9] Siller-Ceniceros A.A., Sánchez-Castro M.E., Morales-Acosta D., Torres-Lubian J.R. Martínez Guerra E., Rodríguez-Varela F.J. Functionalizing reduced Graphene oxide with Re-organometallic compounds as an effective strategy to produce high-performance Pt nanocatalysts for the methanol oxidation reaction. Chem. Electro. Chem. 2019;6 4902-4916.
[10] González-Quijano D., Pech-Rodríguez W.J., González-Quijano J. A., Escalante-García J. I., Morais C., Napporn T. W., Rodríguez-Varela F. J. Performance and In-Situ FTIR evaluation of Pt−Sn/C electrocatalysts with several Pt: Sn atomic ratios for the ethanol oxidation reaction in acidic media. Chem. Electro. Chem. 2018;5 3540-3547.
[11] Pech-Rodríguez W. J., Calles-Arriaga C., González-Quijano D., Vargas-Gutiérrez G., Morais C., Napporn T. W., Rodríguez-Varela F. J. Electrocatalysis of the ethylene glycol oxidation reaction and in situ Fourier-transform infrared study on PtMo/C electrocatalysts in alkaline and acid media. J. Power Sources 2018;375 335-344.
[12] Abidat I., Morais C., Pronier S., Guignard N., Comparot J.D., Canaff C., Napporn T.W., Habrioux A., Mamede A.S. Lamoinier J.F. Kokoh K.B. Effect of gradual reduction of graphene oxide on the CO tolerance of supported platinum nanoparticles. Carbon 2016;111 849-858.
[13] Kok Poh C., Hua Lim S., Pan H., Lin J., Yang Lee J. Citric acid functionalized carbon materials for fuel cell applications. J. Power Sources 2008;176 70-75.

[14] Yin S., Lou L., Xu C., Zhao Y., Qiang Y., Mu S. Functionalizing carbon nanotubes for effective electrocatalysts supports by and intermittent microwave heating method. J. Power Sources 2012;198 1-6.
[15] Yin S., Kang Shen P., Song S., Ping Jiang S. Functionalization of carbon nanotubes by an effective intermittent microwave heating-assisted HF/H_2O_2 treatment for electrocatalysts support of fuel cells. Electrochim. Acta. 2009;54 6954-6958.
[16] Lakshmi N., Rajalakshmi N., Dhathathreyan K., Fuctionalization of various carbons for proton exchange membrane fuel cell electrodes: analysis and characterization. J. Phys. D: Appl. Phys. 2006;39 2785-2790.
[17] Ethiraj A.S., Kang D.J. Synthesis and characterization of CuO nanowires by a simple wet chemical method. Nanoscale Res. Lett. 2012; 7:70 1-5.
[18] Cerník M., Thekkae Padil V.V. Green synthesis of copper oxide nanoparticles using gum karaya as a biotemplate and their antibacterial application. In. J. Nanomedicine. 2013;8 889-899.
[19] Ying-Ji S., Peng C., Shi-ping Y., Zong-Hul J., Dai-Zheng L., Pan-Wen S. Novel Zinc (II) and cobalt (II) chain complexes with 3,5-dimethylpyrazole and thiocyanate. J. Coord. Chem., 2020;55:3 363-372.
[20] Shao M., Shoemaker K., Peles A., Kaneko K., Protsailo L. Pt monolayer on porous Pd-Cu alloys as oxygen reduction electrocatalysts. J. AM. Chem. Soc. 2010;132 9253-9255.

ID 083

Kinetics of the Oxygen Reduction Reaction for Pt nanoparticles supported on novel reduced graphene oxide-polyindole

N.M. Sánchez-Padilla[1,2], J. Manríquez[2], L. Da Silva[1], R. Benavides[1]*, D. Morales-Acosta[1]*

[1]Centro de Investigación en Química Aplicada, Blvd Enrique Reyna No. 140, Col. San José de los Cerritos, Saltillo, 25294; Coahuila, México.

[2]Centro de Investigación y Desarrollo Tecnológico en Electroquímica S.C., Parque Tecnológico Querétaro s/n, Sanfandila, 76703, Pedro Escobedo, Querétaro, México.

* diana.morales@ciqa.edu.mx

ABSTRACT

Electrochemical study of the electron-transfer pathways associated with the O_2 reduction reaction (ORR) is typically carried out by linear-sweep voltammetry using a rotating disk electrode (LSV-RDE). In this investigation, ORR was studied using the Koutecký-Levich and the Andrieux-Savéant approaches on Pt nanoparticles (prepared by means of the polyol process) supported on reduced graphene oxide (rGO)-polyindole (PIN) hybrids (rGO_x-PIN_y, where x and y subfixes denote the fractions of rGO and PIN, respectively). Three types of Pt-modified rGO_x-PIN_y materials (Pt/rGO_x-PIN_y) were electrochemically tested by means of LSV-RDE deposited on glassy carbon electrode: Pt/rGO_{90}-PIN_{10}, Pt/rGO_{50}-PIN_{50}, Pt/rGO_{10}-PIN_{90}. For comparison purposes, analysis of the electrochemical responses was carried out by employing the theoretical models described by Andrieux-Savéant (AS) and Koutecky-Levich (KL) looking for understanding the effect of the PIN on the ORR kinetics. To achieve this, O_2-transfer ($k°_{O2}$, from the electrolyte to the electrocatalytic sites) and electron-transfer ($k°_{et}$, from the O_2 molecules to the electrode surface) constants were estimated by means of the AS and KL approaches, respectively. Both types of kinetic constants were compilation as follows: system **Pt/rGO** ($k°_{O2,AS}$ = 3.8×10^{-2} cm s^{-1}, $k°_{et,AS}$= 1.1×10^{-6} cm s^{-1}; $k°_{et,KL}$= 1.13×10^{-6} cm s^{-1}), system **Pt/rGO$_{90}$-PIN$_{10}$** ($k°_{O2,AS}$ = 2.2×10^{-2} cm s^{-1}, $k°_{et,AS}$= 0.69×10^{-6} cm s^{-1}; $k°_{et,KL}$= 1.9×10^{-6} cm s^{-1}, system **Pt/rGO$_{50}$-PIN$_{50}$** ($k°_{O2,AS}$ = 4.0×10^{-2} cm s^{-1}, $k°_{et,AS}$= 1.4×10^{-5} cm s^{-1}; $k°_{et,KL}$= 1.5×10^{-5} cm s^{-1}), and system **Pt/rGO$_{10}$-PIN$_{90}$** ($k°_{O2,AS}$ = 1.6×10^{-2} cm s^{-1}, $k°_{et,AS}$= 0.97×10^{-5} cm s^{-1}; $k°_{et,KL}$= 1.18×10^{-5} cm s^{-1} $k°_{O2}$ was the same magnitude order, at all the electrocatalytic systems, thus indicating that O_2 was firstly adsorbed at the junction **Pt|rGO.** Thereafter, the values of $k°_{et}$ were increased at the same time the content of PIN according to the next order **Pt|rGO < Pt/rGO$_{90}$-PIN$_{10}$ < Pt/rGO$_{50}$-PIN$_{50}$ ≈ Pt/rGO$_{10}$-PIN$_{90}$**, thus indicating that the activation energy of the ORR (GORR0) was strongly decreased in the presence of the junction **PIN$_y$|Pt|rGO$_x$**. Consequently, K-L and AS provide a reliable and facile approach for evaluating the performance fuel cell electrocatalysts systems.

Keywords: Pt/rGO_x-PIN_yhybrids, *ORR,* electrocatalysis, activation energy

1. Introduction

Oxygen reduction reaction (ORR) is one of the most important electrochemical reactions that proceeds in electrochemical devices as fuel cells (FC) and metal air batteries. In FC, reaction at the cathode is the catalysis of oxygen reduction reaction (ORR), which is the rate-determining factor affecting overall system performance. Therefore, to increase the rate of ORR for enhanced system performances, the development of efficient electrocatalysts is essential. In this manner, one approach is to prove novel supports who increment the catalytic activity of the catalysts used to promote the ORR. The kinetic ORR is a quite complex and involve many intermediate and two sequential steps: (a) the chemical adsorption of the O_2 molecules on the electrocatalytic sites to form an activated adduct and, (b) the electron-transfer process between the electrode and the chemically-activated adduct to promote the electrocatalysis of the ORR. Both are dependent on the nature of the catalyst and electrolyte in which in alkaline electrolytes.

Carbon Vulcan is the widely used support of Pt nanoparticles, in recent years graphene and its derivatives have been proposed as an alternative to Vulcan due to better properties as high electrochemical stability and faster charge transfer process [1]. Nonetheless, graphene materials tend to re-stack due to strong interactions (π- π). The surface modification of these materials is an effective way to minimize this strong interaction[2–4]. One of the surface modifications approaches is using a conductive polymer as polyindole[5] to improve the properties of graphene, Pt nanoparticles and Pt-graphene interaction during ORR.

In this context, the theoretical approach reported by Andrieux and Savéant can be alternatively employed for obtaining physicochemical parameters associated with two sequential steps: (a) the chemical adsorption of the O_2 molecules on the electrocatalytic sites to form an activated adduct and, (b) the electron-transfer process between the electrode and the chemically-activated adduct to promote the electrocatalysis of the ORR.

In this study, reduced graphene oxide- polyindole (rGO_x-PIN_y) was evaluated as support for Pt nanoparticles, consideration three different rGO_x-PIN_y compositions: Pt/rGO_{90}-PIN10, Pt/rGO50-PIN50, Pt/rGO10-PIN90). The Pt/rGO_{90}-PIN_{10}, Pt/rGO_{50}-PIN_{50}, Pt/rGO_{10}-PIN_{90} catalysts were electrochemically evaluated by LSV-RDE the electrochemical responses for ORR was analyzed by the Koutecky-Levich and the Andrieux-Savéant approaches and determinate the effect of the incorporation of a polymer in the support in the ORR, and thus to test which composition could be the best to improve the Pt catalytic activity.

2. Materials and methods

Graphene oxide (GO) was synthetized by Tour's method [6]. Hybrid materials with polyindole (PIN) were prepared by oxidative polymerization of indole in presence of GO in three different compositions (GO_x-PIN_y, where subfixes x and y stand denote GO and PIN content, being the proportions 10-90, 50-50 and 90-10 in weight). The three materials were used as support to deposit Pt nanoparticles by polyol method, thus obtaining the materials Pt/rGO_x-PIN_y (the GO phase was reduced to rGO after polyol method). As comparative a Pt/rGO were prepared in similar way.

The Pt/rGO_{90}-PIN_{10}, Pt/rGO_{50}-PIN_{50}, Pt/rGO_{10}-PIN_{90} catalysts were characterized by linear-sweep voltammetry using a rotating disk electrode (LSV-RDE). The electrode was prepared as a catalytic ink as follows: the catalyst powder was dispersed in isopropanol and Nafion (5 μL) by ultrasound to form an ink with catalyst loading of 10 mg mL^{-1}. Then, an aliquot of 20 μL of the catalytic ink was deposited onto a glassy carbon disk (0.196 cm^2 as geometrical area), previously polished until mirror-finished surface. After drying, the working electrodes were obtained.

The catalytic activity was measured in a SP-300 (Biologic) bipotenciostat connected to an RDE (Pine Inst.) in an electrochemical cell. A Pt wire was used as counter electrode, while Ag/AgCl served as reference. All experiments were carried out in alkaline media (0.1 KOH) N_2-saturated. After 40 cycles at 50 mV s^{-1} cyclic voltammetry (CV) activation and CV profile at 20 mV s^{-1}, the ORR activity was measured at different rotation rates (400 until 2000 rpm) in a O_2-saturated electrolyte. CV was carried out to test the activity at 5 mV s^{-1}.

For the kinetic detailed study of the materials the Koutecky-Levich (equation 1) and Andrieux-Seavéant (equation 2) approaches were carried out.

$$ik=1i()-1iL-1 \quad (1)$$
$$jk=1j()-1jL-1jads-1 \quad (2)$$

3. Results

The LSVs of the materials Pt/rGO_{10}-PIN_{90}, Pt/rGO_{50}-PIN_{50}, Pt/rGO_{90}-PIN_{10} and Pt/rGO are shown in **Figure 1**. It is observed that all the materials possess catalytic activity to reduce oxygen, with three observable regions: i) the kinetic region between 1.2 to 0.95 V, from this section the kinetic and thermodynamic parameters of the ORR are established as the onset potential (E_0); ii) the mixed control region between 0.75 and 0.8 V, governed by mixed transport and kinetic processes; and lastly iii) the region controlled by the mass transport between 0.7 and 0.05 V, this zone is controlled by processes involved in the transport of mass such as the diffusion of oxygen and gives us information about the limited current density released by the catalyst (j_L) .As it is observable, the E_0 of the catalysts Pt/rGO_{10}-PIN_{90}, Pt/rGO_{90}-PIN_{10} and Pt/rGO are similar to each other (1 V). However, Pt/rGO_{50}-PIN_{50}, has a higher E_0 than the others. The increase in catalytic performance of Pt/rGOx-PINy catalysts can be attributed to the addition of PIN that modifies the π-π interactions of rGO and improves the exposure of Pt nanoparticles [7]. Besides, Pt/rGO_{50}-PIN_{50} has the greater j_L (8 mA cm^{-2}).

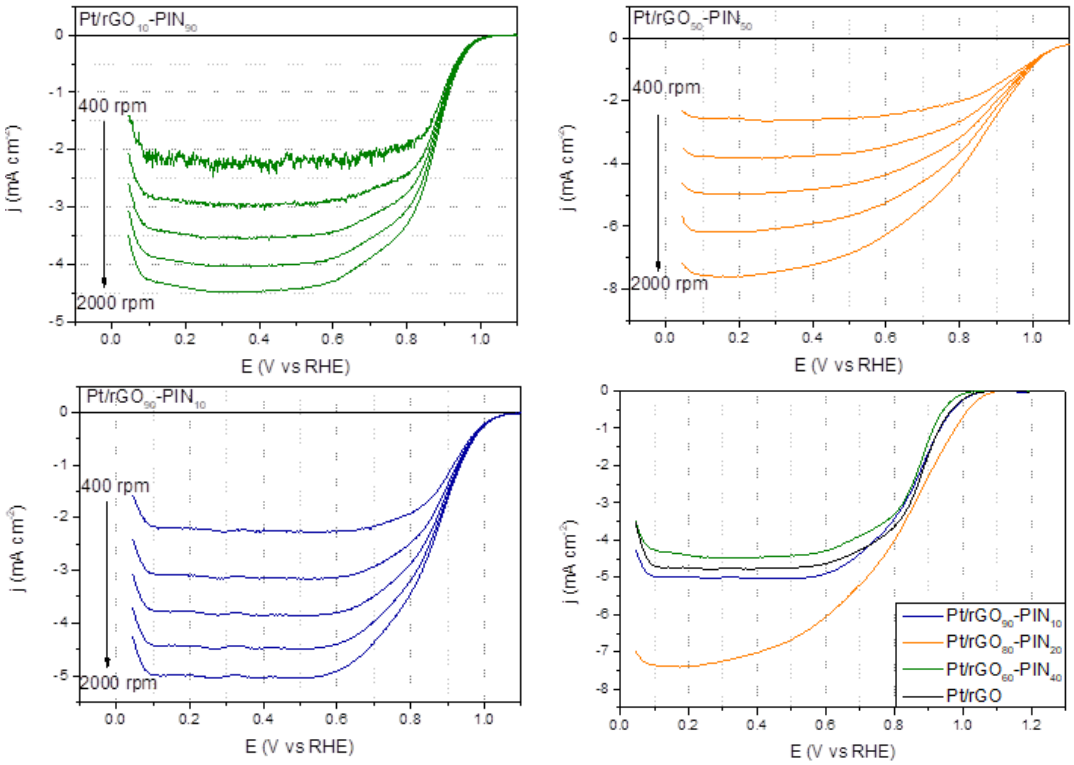

Fig. 1. LSV of for Pt/rGO_{10}-PIN_{90}, Pt/rGO_{50}-PIN_{50}, Pt/rGO_{90}-PIN_{10} and a comparison to 2000 rpm of the three catalysts with Pt/rGO.

a. Koutecký-Levich approach

Figure 2 shows the j_k vs η curves obtained by the Koutecký-Levich (K-L) approach (equation 2) using the data obtained by the LSV curves. As can be observed, in increasing overpotentials (η) the kinetical current density also increases. In lower η it is observable that linear behaviors that belongs to the Tafel regimen. In the later zone the K-L analysis were carried out.

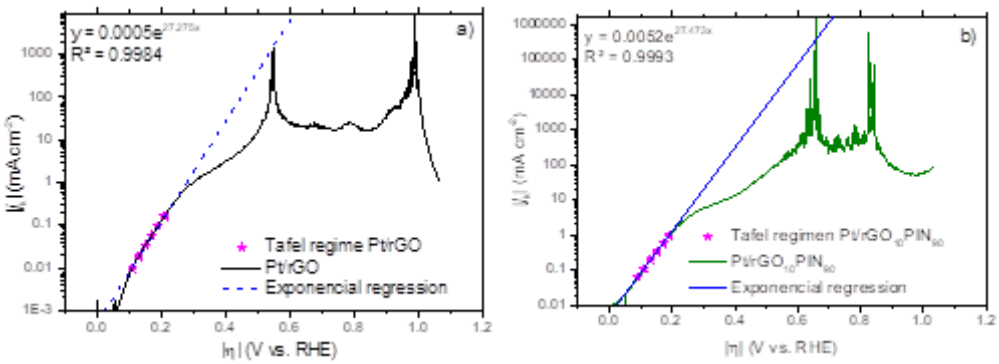

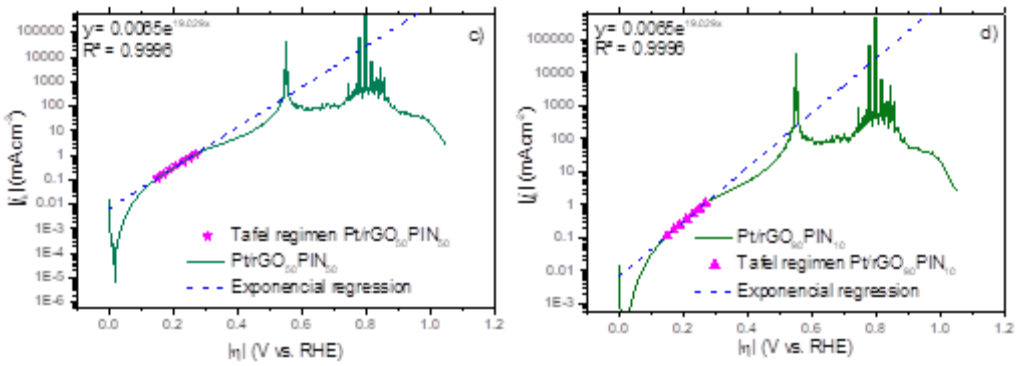

Fig. 2. Koutecky-Levich approach for a) Pt/rGO, b) Pt/rGO$_{10}$-PIN$_{90}$, Pt/rGO$_{50}$-PIN$_{50}$, and Pt/rGO$_{90}$-PIN$_{10}$.

b. Andrieux-Savéant

Figure 3 shows the j_k vs η curves obtained in the Andrieux-Savéant (A-S) approach.in similar manner to the K-L analysis the data obtained by the LSV curves is used but the subtraction of the adsorption current density (j_{ads}) must be taken account.. as K-L approach, in lower η it is observable linear behaviors that belongs to the Tafel regimen. In this zone the A-S analysis were carried out.

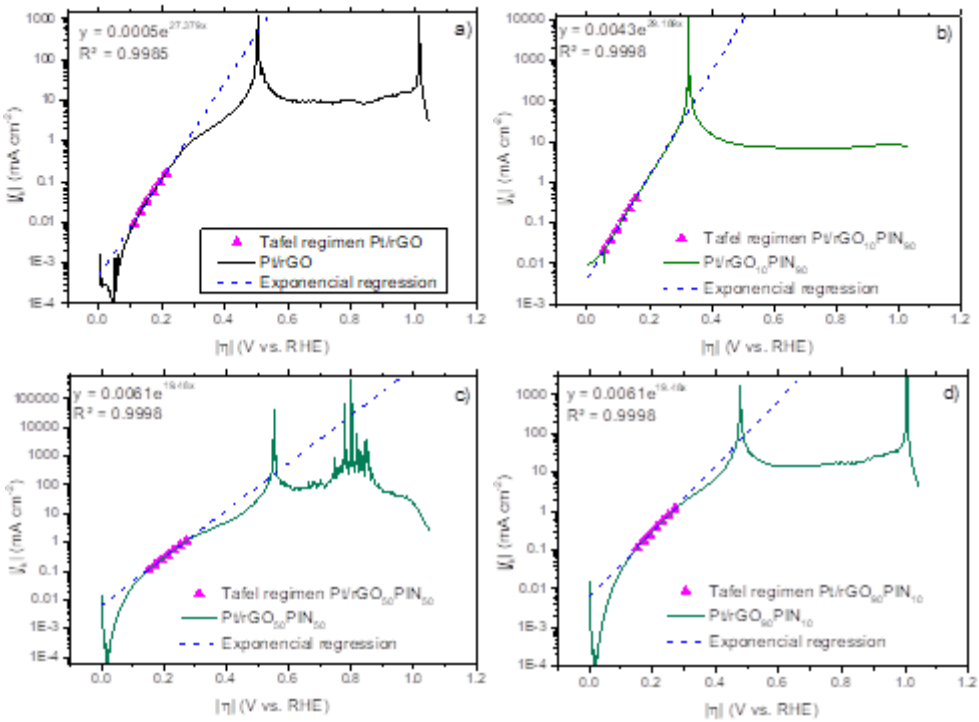

Fig. 3. Andrieux-Savéant approach for a) Pt/rGO, b) Pt/rGO$_{10}$-PIN$_{90}$, Pt/rGO$_{50}$-PIN$_{50}$, and Pt/rGO$_{90}$-PIN$_{10}$.

Table 1 summarize Koutecký-Levich and Andrieux-Savéant kinetic parameters approaches.

Table 1. Parameters calculated through KL and AS approaches

Parameters	Pt/rGO$_{10}$-PIN$_{90}$	Pt/rGO$_{50}$-PIN$_{50}$	Pt/rGO$_{90}$-PIN$_{10}$	Pt/rGO
j0 (Koutecky-Levich)	5.2 x10-6 A cm-2	6.5x10-6 A cm-2	8 x10-7 A cm-2	5x10-7 A cm-2
k0 (Koutecky-Levich)	1.18 x10-5cm s-1	1.5x10-5cm s-1	1.9 x10-6cm s-1	1.13x10-6cm s-1
a (Koutecky-Levich)	0.3564	0.2468	0.2684	0.3538
b (Tafel slope-KL)	36.39 mV	52.55 mV	48.32 mV	36.66 mV
j0 (Andriex-Savéant)	4.3 x10-6 A cm-2	6.1x10-6 A cm-2	3 x10-7 A cm-2	5x10-7 A cm-2
k0 (Andriex-Savéant)	0.97 x10-5cm s-1	1.4x10-5cm s-1	0.69x10-6cm s-1	1.1x10-6cm s-1
a (Andriex-Savéant)	0.3787	0.2527	0.3642	0.3552
b (Tafel slope-AS)	34.26 mV	34.25 mV	35.61 mV	36.52 mV
ket0	1.6 x10-2 cm s-1	4.0x10-2 cm s-1	2.2 x10-2 cm s-1	3.8x10-2 cm s-1

The Andrieux-Savéant approach involve an extra parameter (ket0) useful to compare the interaction between the analyte and the catalytic interface as well as the adduct products electro-adsorbed on the catalysts surface, while the Koutecký-Levich approach does not.ket0 is the electron transfer constant from the O_2 molecules to the electrode surface, which is influenced by chemical interaction between rGO and PIN with Pt. With the values observed it seem that polymer increase the ket0 and then enhance the adsorption between O_2 and the electroactive phase Pt|rGO by incrementing the interfacial interaction O_2-Pt|rGO. In this manner, the catalytic activity is controlled by the enthalpy and the use of the PIN decrease the ΔG, i.e., the polymer lowers the activation energy for the electronic transfer process by lowering the energy barrier.

4. Conclusions

The exchange current densities and the Tafel slopes obtained between the two approaches are closer. However, a detailed comparison between the other parameters allowed observing that the magnitude order of the $k°_{O2}$ was the same at all the electrocatalytic systems, thus indicating that O_2 was firstly adsorbed at the junction **Pt|rGO.** Thereafter, the values of $k°_{et}$ were increased at the same time the content of PIN according to the next order **Pt|rGO < Pt/rGO$_{90}$-PIN$_{10}$ < Pt/rGO$_{50}$-PIN$_{50}$ ≈ Pt/rGO$_{10}$-PIN$_{90}$,** thus indicating that the activation energy of the ORR (GORR0) was strongly decreased in the presence of the junction **PIN$_y$|Pt|rGO$_x$**.

Acknowledgment

The authors are grateful to the National Council of Science and Technology (Conacyt) through the CB259010 and FC3004 projects. NMSP is thankful to Conacyt for the PhD scholarship. Authors also are grateful to Graphene Materials National Laboratory (LNMG) and to the Research Center for Technological Development in Electrochemistry (CIDETEQ) for the facilities provided for the use of some of its installations.

References

[1] A.L. Dicks, The role of carbon in fuel cells, J Power Sources. 156 (2006) 128–141.

[2] Z. Cui, P.J. Kulesza, C.M. Li, W. Xing, S.P. Jiang, Pd nanoparticles supported on HPMo-PDDA-MWCNT and their activity for formic acid oxidation reaction of fuel cells, Int. J. Hydrogen Energy. 36 (2011) 8508–8517. https://doi.org/10.1016/j.ijhydene.2011.04.072.

[3] Y. Hong, L. Zhang, W. Jiang, S. Hwa, ScienceDirect Pd nanoparticles supported on PDDA-functionalized carbon black with enhanced ORR activity in alkaline medium, Int. J. Hydrogen Energy. 39 (2014) 8449–8456. https://doi.org/10.1016/j.ijhydene.2014.03.165.

[4] D. Nguyen-Thanh, A.I. Frenkel, J. Wang, S. O'Brien, D.L. Akins, Cobalt-polypyrrole-carbon black (Co-PPY-CB) electrocatalysts for the oxygen reduction reaction (ORR) in fuel cells: Composition and kinetic activity, Appl. Catal. B Environ. 105 (2011) 50–60. https://doi.org/10.1016/j.apcatb.2011.03.034.

[5] S.H. Hosseini, M. Ashjari, Synthesis and characterization of polyindole with liquid crystalline azobenzene as side chains, Int. J. Phys. Sci. 8 (2013) 1611–1622. https://doi.org/10.5897/IJPS12.107.

[6] D.C. Marcano, D. V. Kosynkin, J.M. Berlin, A. Sinitskii, Z. Sun, A. Slesarev, L.B. Alemany, W. Lu, J.M. Tour, Improved synthesis of graphene oxide, ACS Nano. 4 (2010) 4806–4814. https://doi.org/10.1021/nn1006368.

[7] S. Lin, C. Shen, D. Lu, C. Wang, H.J. Gao, Synthesis of Pt nanoparticles anchored on graphene-encapsulated Fe3O4magnetic nanospheres and their use as catalysts for methanol oxidation, Carbon N. Y. 53 (2013) 112–119. https://doi.org/10.1016/j.carbon.2012.10.037.

ID 092

Novel and cheaper process for the development of carbon nanoestructures by using Orange peel waste for the generation of carbons applied to supercapacitors

Gladis G. Suárez-Velázquez[a,b*], José A. Ramírez de León[a], Juan F. Castañón-Rodríguez J.F.[a]
Wilian J. Pech-Rodríguez[b]

[a] Unidad académica de Trabajo Social y Ciencias para las humanidades. Universidad Autónoma de Tamaulipas, Centro universitario, 87120 Cd. Victoria, Tamaulipas, México.

[b] Ingeniería Mecatrónica, Universidad Politécnica de Victoria, Av. Nuevas tecnologías 5902, parque científico y Tecnológico de Tamaulipas, 87138 Cd. Victoria, Tamaulipas, México.

* gsuarezv@upv.edu.mx

ABSTRACT

Today, human kind is facing energy and environmental issues due to the increasing demand for electrical energy. In this regard, extensive investigation has been carried out to develop efficient technologies to generate and storage electrical energy. One alternative to face these problems is by using raw or waste biomass such as orange skin, coconut shell and others.

In this work is presented a novel and effective thermal process for the development of conductive carbon nanostructures by using orange peel waste for energy storage applications. The Orange peel waste sample was first cleaned and treated under an ultrasonic bath then, was summited at thermal treatment by using high-temperature alumina crucibles while the atmospheric air was limited by covering the sample with fine-grain silica sand. The obtained carbonaceous material was physical and chemically characterized by XRD, FTIR, and SEM-EDS measurements. Cyclic voltammetry measurement was conducted in order to study the electric-double layer capacitance. The XRD analysis shows that the obtained sample was composed of a graphitized carbon phase also CaO and CaCO3 phases were observed with high crystalline quality. On the other hand, from FTIR spectrogram was observed in the presence of C-O, C=O and Ca-O species on the surface of the obtained carbon nanostructure.

The CV's curves were analyzed and the electrical double layer capacitance was estimated for the sample the results were compared with the non-modified glassy carbon electrode. The electrochemical results reveal that the as-synthesized carbonaceous material under a controlled air atmosphere has prominent capacitance and thus can be used for energy storage applications. Therefore, herein is demonstrated that by the proposed novel thermal process is possible to obtain graphitized carbon nanostructure with good electrochemical properties at low cost.

Keywords: orange peel; supercapacitors; cyclic voltammetry

INTRODUCTION

Currently supercapacitors are devices that are positioning themselves as favorites among energy storage systems. This, due to their high power density and high energy characteristics, which have proven to be superior to batteries and double layer capacitors. However, one of the main drawbacks for the commercialization of SCs has been the high cost of manufacturing them. The above has led to the search for inexpensive materials and methods that, in turn, satisfy technical criteria, such as fast load-unload operation, high power density, high specific capacity, wide operating temperature and energy conservation.

Activated carbon (AC) based plants and fruits peel are studied (Wei et al., 2019) as cheaper electrode material for supercapacitors. On this regard, bamboo (Yang et al., 2014), pine cone (Bello et al., 2016), nutshells (Natalia et al., 2013) and, orange peel shows good electrical properties (Ranaweera et al., 2017)(Maharjan et al., 2017).

The annual world production of oranges is more than 62.3 million tons (Lugo-Lugo et al., 2012). México produces approximately 4,444 tons representing a critical amount of waste material, mostly based in the orange peel (OP). Frequently orange peel is used to feed animals or is disposed of in municipal garbage dumps.

Orange peel have been used by diverse authors for the preparation of activated carbon applied to supercapacitors. Arie et al. (Arie et al., 2014)) synthesized materials for lithium-ion capacitors and prepared cathodes for the same purpose. While, other authors have focused their attention on the effect of the conditions of carbonization (Xiang et al., 2017), Ma et al., 1993) and the impact of activation on the coals obtained (Wang et al., 2019)

The carbonization process has been carried out mostly under inert atmospheres by using argon and nitrogen gas (Xiang et al., 2017) (Wang et al., 2019). These conditions allowed them to reach temperatures above 400 ° C, without converting the raw material in ash. However, the process involves sophisticated equipment as oven tube furnace and expensive materials such as the consumed gas. For this reason, in this work, we propose to produce CA without the need to use an inert atmosphere to obtaining coal from the orange peel. Using a muffle and fine-grain sand was possible to reach coal with good characteristics conductive and capacities. The structural and electrochemical properties of biocarbons were characterized by SEM, DRX, FTIR and cyclic voltammetry.

MATERIALS AND METHODS

The orange peel was obtained from fresh fruits. The OP was washed with soap and water and cut into pieces of approximately 1 cm2. They were subsequently washed following the procedure described in (Shamsuddin et al., 2016). Once clean, they were left to dry in the sun for 3 hours. To remove the rest of the water, they were placed in a muffle at 120 ° C for 2 hours. The dehydrated

samples were packed in hermetic bags for later use. The dehydrated OP was placed in a crucible and then covered with fine-grain sand and carbonized at 1000 °C within a muffle for 60 minutes.

The carbons obtained were characterized using X-ray diffraction analysis in a Philips-X'Pert diffraction meter at 40 kV using Cu K〈 radiation. The detection of functional groups was analyzed by Fourier transform spectroscopy (FTIR, IFS66 V / S & HYPERION 3000, Bruker Optiks). The morphology of the samples was carried out on a Philips XL30-SEM-EDS equipment at 25 kV. Electron microscopy was performed on the FEM-SEM-S-4800 equipment, Hitachi. Electrochemical tests were performed using a Gill-AC-ACM instruments Ltd brand potentiostat, at a rate of 20 mVs^{-1}.

RESULTS

Figure **1** shows the SEM micrograph for the thermal treated orange peel. The sample is composed of large and small rough flakes with high porosity. Figure 2 shows the EDS analysis of the obtained sample. As expected, the sample is mainly composed by carbon. Calcium element (Ca) was present in considerable amount, followed by potassium (K) and phosphorous (P). Other elements such as Mg, S and O were observed in small quantities.

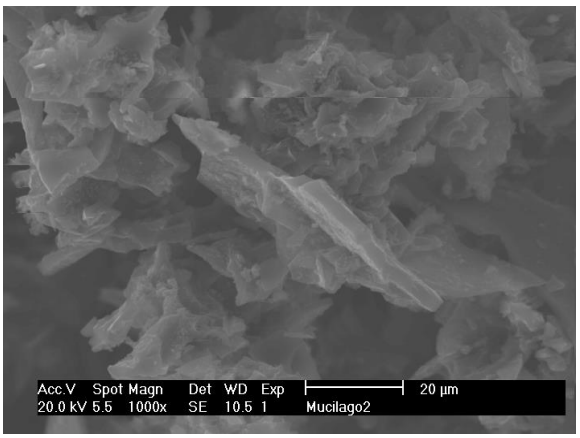

Figure 1. SEM of orange peel at 1000 °C

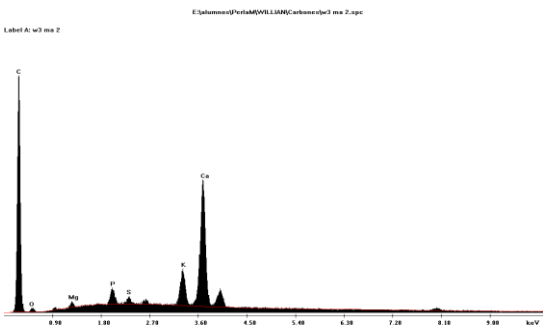

Figure 2. EDS of orange peel at 1000 °C

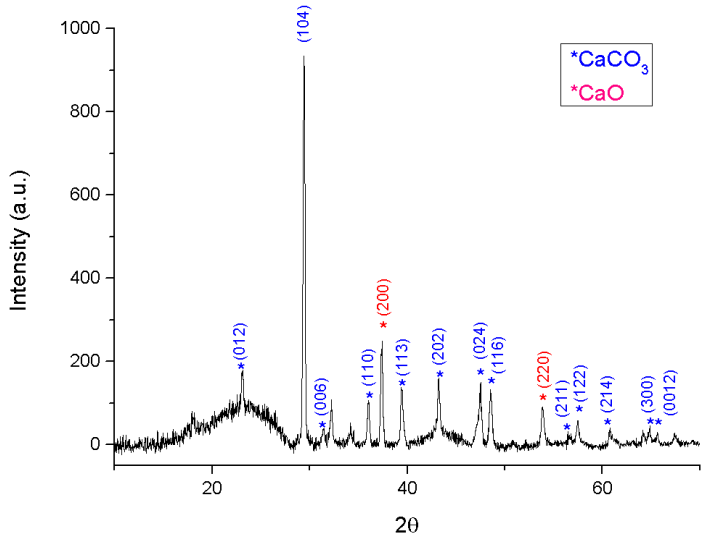

Figure 3. XR Difractogram of orange peel at 1000

The XRD difractogram is shown in Figure 3. It can be observed the diffraction peaks of graphite structure located between 15-30° 2θ and 40-50° 2θ ascribed to 002 and 101 plane. These peaks are broad in nature suggesting that the obtained carbon is in nanostructure range or amorphous form. The carbon peak is overlapped with the CaCO3 structure (JCPDS data file 00-005-0586) that is present with high crystalline quality. Also, there is observed the characteristic peaks of CaO at 33, 37.5 and 54° 2θ according to the (JCPDS data file 004-0777) card. These results are in good agreement with the SEM-EDS measurements where C and Ca were the major elements in the sample. The superficial chemical group of the bio-carbon was studied by FTIR measurements in KBr pellets. The band located at 1080 cm^{-1} was ascribed to the stretching vibrations of C-O (Gaudenzi et al., 2004). The signal for carbonate species was observed at 1795 cm^{-1} that is due to the C=O interaction and at 1439 cm^{-1} for C-O group(Miguel Galván-Ruiz, Juan Hernández, Leticia Baños, 2009) .Also, a perturbation was observed at 799 cm^{-1} and this peak was attributed to Ca-O.

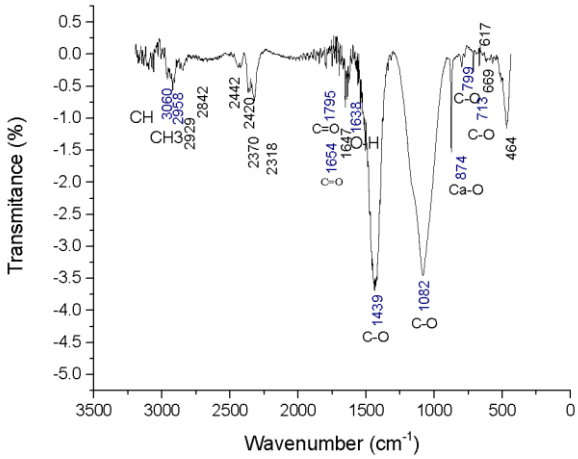

Figure 4. FTIR analysis of orange peel at 1000 °C

The electrochemical properties of the developed bio-carbon were studied by cyclic voltammetry in H_2SO_4 0.5 mol L^{-1} at scan rate of 20 mVs^{-1}. Figure 5 shows the CV´s for the no-modified glassy carbon (GC) and the obtained carbon nanostructure. The CV for glassy carbon shows low current densities along the studied potentials. Meanwhile, the thermal treated carbon displays significant current densities in the same potential range. On the other hand, the bio-carbon delivers high current densities between 0.1 V to -0.2 V that is attributed to the hydrogen adsorption region on the surface of the carbon. These results are very important, because carbonaceous nanostructures have been used as support in the area of fuel cell electrocatalyst.

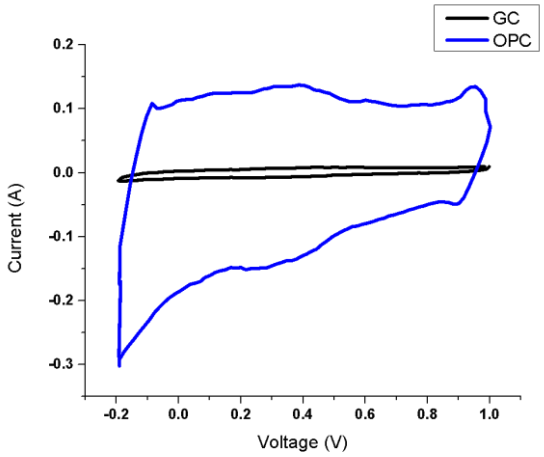

Figure. 5 Cyclic voltametry of OP-1000°C

Tan and coworkers studied graphite oxide for supercapacitor applications and they proposed a method for calculating the capacitive behavior of the material through the cyclic voltammetry (Tan et al., 2013). The capacitive behavior of the sample was calculated from the CV considering the

pseudo capacitance and the bio-carbon has a 0.058F/cm^{-2} while the capacitance of glassy carbon was of 0.00268 Fcm^{-2}.

CONCLUSIONS

In this work, the synthesis of carbons based orange peel (OPC) was obtained by a novel method without using a gas-induced inert atmosphere. The morphology and composition characteristics of obtained OPC were analyzed by SEM-EDS, DRX, FTIR. SEM studies revealed large and small rough flakes with high porosity. DRX and EDS analysis indicated that OPC contains mostly carbon and calcium. VC shows that OPC has a capacitance of 0.058 Fcm^{-2}, which is superior to the glassy carbon 0.00268 Fcm^{-2}. Results obtained suggest that the methodology developed is promising for obtaining materials for supercapacitors applications.

REFERENCES

Arie, A. A., Kristianto, H., Suharto, I., Halim, M., & Lee, J. K. (2014). *Preparation of Orange Peel Based Activated Carbons as cathodes in Lithium Ion Capacitors*. *896*, 95–99. https://doi.org/10.4028/www.scientific.net/AMR.896.95

Bello, A., Manyala, N., Barzegar, F., Khaleed, A. A., Momodu, D. Y., & Dangbegnon, J. K. (2016). Renewable pine cone biomass derived carbon materials for supercapacitor application. *RSC Advances*, *6*(3), 1800–1809. https://doi.org/10.1039/c5ra21708c

Gaudenzi, S., Pozzi, D., Toro, P., Silvestri, I., Morrone, S., & Congiu Castellano, A. (2004). Cell apoptosis specific marker found by Fourier Transform Infrared Spectroscopy. *Spectroscopy*, *18*(3), 415–422. https://doi.org/10.1155/2004/483591

Lugo-Lugo, V., Barrera-Díaz, C., Ureña-Núñez, F., Bilyeu, B., & Linares-Hernández, I. (2012). Biosorption of Cr(III) and Fe(III) in single and binary systems onto pretreated orange peel. *Journal of Environmental Management*, *112*, 120–127. https://doi.org/10.1016/j.jenvman.2012.07.009

Maharjan, M., Ulaganathan, M., Aravindan, V., Sreejith, S., Yan, Q., Madhavi, S., Wang J-Y. , & Aravindan, V. (2017). *Fabrication of High Energy Li–Ion Capacitors from Orange Peel Derived Porous Carbon*. 5051–5058. https://doi.org/10.1002/slct.201700574

Galván-Ruiz, M.,Hernández, J., Baños, L., Noriega-Montes, J., & Rodríguez-García, M. E. (2009). *Characterization of Calcium Carbonate, Calcium Oxide, and Calcium Hydroxide as Starting Point to the Improvement of Lime for Their Use in Construction*. *November*, 1–19.

Natalia, M., Sudhakar, Y. N., & Selvakumar, M. (2013). Activated carbon derived from natural sources and electrochemical capacitance of double layer capacitor. *Indian Journal of Chemical Technology*, *20*(6), 392–399.

Ranaweera, C. K., Kahol, P. K., Ghimire, M., Mishra, S. R., & Gupta, R. K. (2017). *Orange-Peel-Derived Carbon: Designing Sustainable and High-Performance Supercapacitor Electrodes*. https://doi.org/10.3390/c3030025

Tan, Y., Xu, C., Chen, G., Liu, Z., Ma, M., Xie, Q., Zheng, N., & Yao, S. (2013). Synthesis of ultrathin nitrogen-doped graphitic carbon nanocages as advanced electrode materials for supercapacitor. *ACS Applied Materials and Interfaces*, *5*(6), 2241–2248. https://doi.org/10.1021/am400001g

Wang, W., Xu, S., Wang, K., Liang, J., & Zhang, W. (2019). De-intercalation of the intercalated potassium in the preparation of activated carbons by KOH activation. *Fuel Processing Technology*, *189*(December 2018), 74–79. https://doi.org/10.1016/j.fuproc.2019.03.001

Wei, Q., Chen, Z., Cheng, Y., Wang, X., Yang, X., & Wang, Z. (2019). Preparation and electrochemical performance of orange peel based-activated carbons activated by different activators. *Colloids and Surfaces A: Physicochemical and Engineering Aspects*, *574*, 221–227. https://doi.org/10.1016/j.colsurfa.2019.04.065

Xiang, J., Lv, W., Mu, C., Zhao, J., & Wang, B. (2017). Activated hard carbon from orange peel for lithium/sodium ion battery anode with long cycle life. *Journal of Alloys and Compounds*, *701*, 870–874. https://doi.org/10.1016/j.jallcom.2017.01.206

Yang, C. S., Jang, Y. S., & Jeong, H. K. (2014). Bamboo-based activated carbon for supercapacitor applications. *Current Applied Physics*, *14*(12), 1616–1620. https://doi.org/10.1016/j.cap.2014.09.021

Bioelectrochemical cells

ID 010

Use microbial fuel cells for degradation of Used Lubricating Oils (ULO) and production of energy

Esther Ibarra Altamirano[1]; Miguel Mauricio Aguilera Flores[1]; Verónica Ávila Vázquez[1]*

[1]Instituto Politécnico Nacional – Unidad Profesional Interdisciplinaria de Ingeniería Campus Zacatecas. Blvd. del Bote 202 Cerro del Gato Ejido La Escondida, Col. Ciudad Administrativa 98160 Zacatecas, Zac. Phone. 01-492-92-42-419, 01-492-92-55-998
* Corresponding author: vav_taba@hotmail.com

ABSTRACT

Microbial fuel cells (MFC) have gained great interest as an alternative energy conversion system for generating bioenergy. MFC technology is a promising sustainable energy alternative to combat problems related to non-renewable energy consumption, climate change and environmental pollution. Used Lubricating Oils (ULO) are defined as hazardous waste and their generation is increasing every year. In this work, a discontinuous cycle of 55 days was performed in a MFC, using ULO as substrate and potting soil as inoculum. Physicochemical and electrochemical tests were carried out to validate the degradation of ULO. Results show a MFC stabilization between day 9 and day 11, obtaining an open-circuit voltage up to 553 mV, DP_{max} of 0.24 mWm^{-2} and i_{max} of 2.35 mAm^{-2} from an initial potential of 223 mV. Turbidity reduction efficiency of 88% was found, and total and volatile solids reduction efficiencies of 40% and 10%, respectively, were found. These results demonstrate that MFC allows energy generation from the degradation of ULO, so it is presented as an alternative to the treatment of water contaminated with this type of hydrocarbons and as an alternative energy option.

Keywords: Environmental pollution, MFC, ULO.

1. Introduction

Nowadays, climate change and energy shortages are two leading problems, as fossil fuels accounting for approximately 80% of total global energy demand [1]. In Mexico, the main source of electrical energy generation is natural gas. The burning of natural gas emits various greenhouse gases, mainly CO_2, which are responsible for global warming and climate change. As for renewable electricity generation in Mexico, the main one is wind, which generates 13,074 GWh, and in fifth place is waste, with a generation of 484 GWh [2]. One of the characteristics of renewable energy is that it takes advantage of energy products generated or produced in each area. Microbial fuel cells (MFC) are a type of bioelectrochemical system that provide an ecological alternative to produce energy at low cost [1].

A MFC is a device that obtains electrical energy through microorganisms, and under proper conditions. The microorganisms convert the chemical energy of their metabolic activity during the degradation of a substrate, into electrical energy [3]. MFC can be designed with a single or double chamber, and ULO could be used as substrate.

In Mexico, during the 2004-2019 period, used oils represented 20% of total hazardous waste generated with 547,374.53 tons. The 54.6% of them corresponds to ULO [4]; less than 4% being recycled [5]. When the ULO is inadequately managed, this pollutes the atmosphere by its burning, and the soil and water by shedding, causing contamination of water tables, rivers, lakes and seas [6].

Since there is a large generation of ULO, these could easily be used as substrate in a MFC for their degradation, and energy generation. MFC technology is a promising sustainable energy alternative to combat problems related to non-renewable energy consumption, climate change and environmental pollution [7].

This technology is versatile as it offers direct energy but also degradation of contaminants. Therefore, any pilot study, field test or prototype installation, adds valuable knowledge to contribute to the technological readiness for real-world implementation and a wider market, and MFC are the only electrochemical system that provides waste treatment [8]. Therefore, this project will provide input for future studies.

2. Materials and Methods

2.1 Construction of MFC

The experiment consisted of a MFC which is composed of a clay pot with a capacity of 70 mL, acting as a container and as a proton-exchange membrane. A Platinum cloth cathode was integrated to the outside of the structure (5 cm x 12.6 cm) held with a stainless steel wire at the top and bottom (the wire helps to support and collect the current). Inside the cell, the graphite-felt anode (5 cm x 9 cm) was placed with a small stainless steel mesh insert as a current collector. The methodology was followed according to Enciso Hernández (2018) [9].

2.2 Inoculum and Substrate

The substrate was prepared with a homogeneous mixture of 70 mL of common water, 0.1 µL of Tween 20, and 0.75 mL of ULO (1%), according to the suggested procedure by Zhao et. al, 2019 [10]. 1.5 g of potting soil was used as inoculum. A light source was placed on the MFC to provide heat and maintain a temperature of 35 °C [11].

2.3 Preliminary test: ULO degradation cycle

The ULO degradation cycle was monitored. The open-circuit voltage was measured daily for 55 days, until a voltage dropped was identified, which meant that the degradation cycle has ended.

2.4 Linear voltammetry: Polarization curve.

The Versa STAT equipment was used. The working electrode was placed on the cathode current collector and the reference and counter electrode were connected to the anode current collector. A potential sweep was performed from 0.28 V to 0.05 V at a speed of 0.0001 mV/s.

2.5 Electrochemical Impedance Spectroscopy

The Electrochemical Impedance Spectroscopy technique was used to identify the solution resistance (R_s) and the charge transfer Resistance (R_{ct}) of the MFC, applying a scan from 0.1 to 10,000 Hz, with a 60 s conditioning time at open-circuit voltage.

2.6 Chronoamperometry: Stability curve

Versa Stat 3 equipment was used to perform the chronoamperometry. The position of the electrodes was inverted, the working electrode was placed in the anode current collector, while the reference and counter electrode were placed in the cathode current collector. 89 mV was the voltage used during the analysis with a duration of 600 s.

2.7 Physicochemical Analysis

The turbidity was determined based on the Mexican standard procedure NMX-AA-038-SCFI-2001. Total Solids (TS) and Volatile Solids (VS) were determined based on the Mexican standard procedure NMX-AA-034-SCFI-2015.

3. Results and Discussion

3.1 Identification of the ULO degradation cycle in the MFC

Figure 1a, shows open-circuit voltage of the MFC. While Figure 1b shows the bacterial population growth curve (latency or adaptation (Lag), exponential, stationary, and death phases).

The Lag interval can be short or long, depending on the nature of the inoculum and the medium [12]. Comparing the results between Figure 1a and Figure 1b, it can be seen that the Lag phase is not visualized, because occurs in a short time. The exponential phase was carried out approximately from day 1 to day 11, when the maximum potential was reached. After, the stationary phase occurred from day 12 to day 35, the bacterial population growth did not increase due to the exhaustion of some essential nutrient (of ULO for this case), so its concentration decreased, achieving the partial elimination of the contaminant. Finally, the cell death phase occurred from day 36 to day 55.

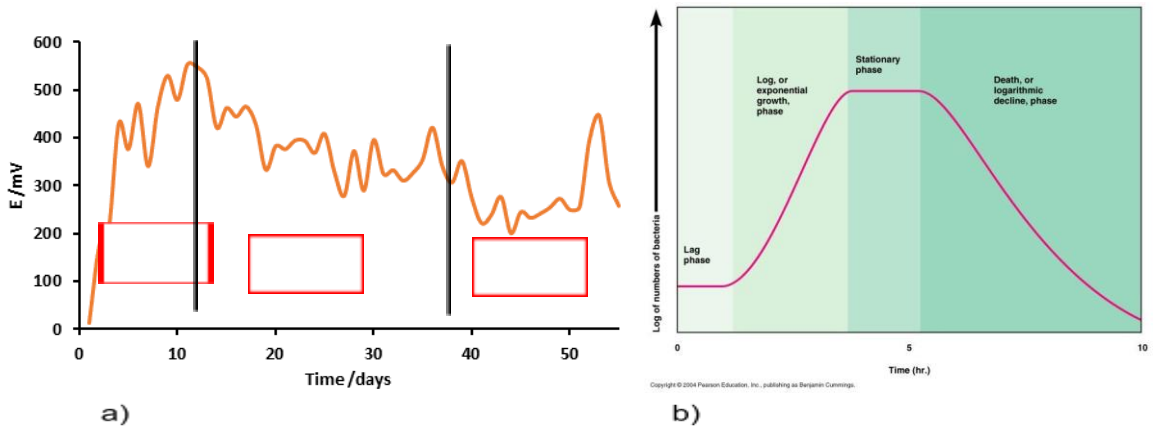

Fig. 1. a) MFC open-circuit voltage; b) Bacterial growth curve. Source: [13]

3.2 Linear voltammetry: Voltage and power generated

The polarization and potential curve in the MFC is shown in Figure 2. It can be seen a generation of voltage (E_i) of 223 mV, current density (i) of 2.35 mAm^{-2}, and a Power Density (PD) of 0.24 mWm^{-2}. The potential curve shows the three loss regions associated to activation, ohmic and mass transport, being reflected in the MFC yield.

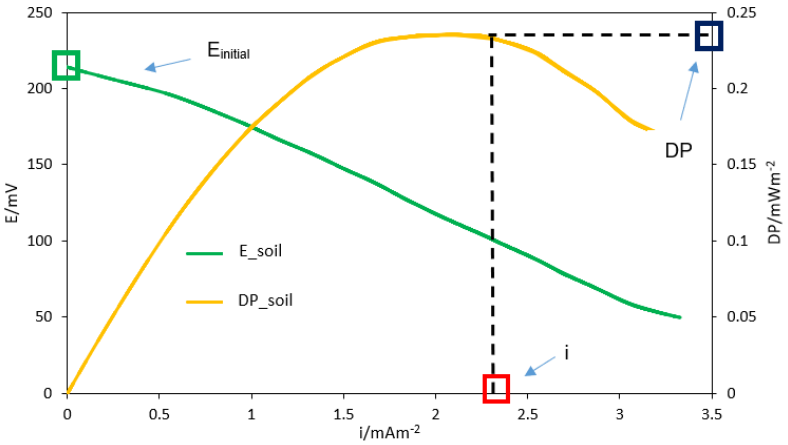

Fig. 2. Polarization and potential curve in the MFC.

3.3 Electrochemical Impedance Spectroscopy (EIS)

The overall internal resistance of a MFC has many factors including solution resistance (R_s) and charge transfer resistance (R_{ct}) [14]. Figure 3 shows the Nyquist diagram in the MFC. It can be seen approximate values of 1.7 and 8.7 Ωcm^{-2} for R_s and R_{ct}, respectively. These resistances can be considered minimum, favoring the energy generation.

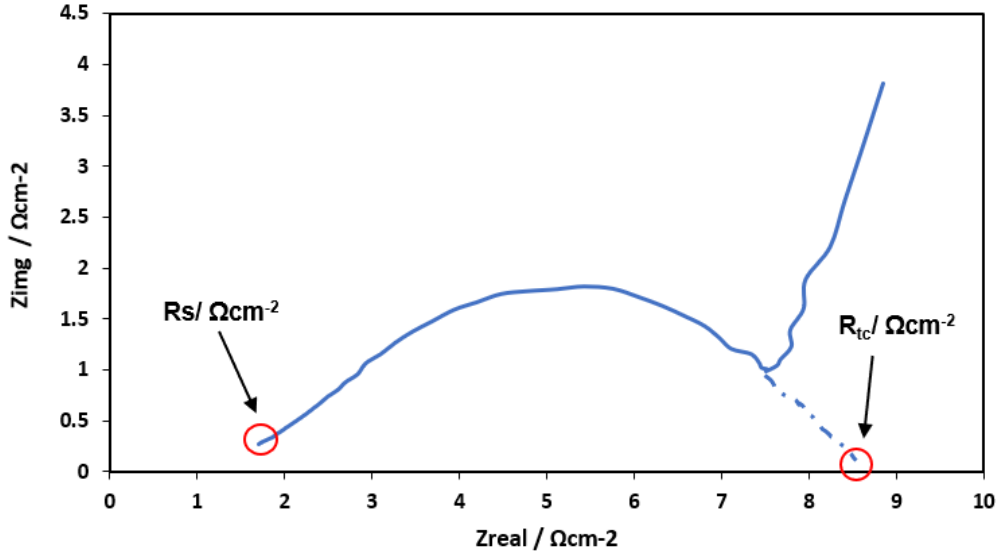

Fig. 3. Nyquist diagram in the MFC.

3.4 Chronoamperometry: stability curve

Figure 4 shows the stability curve in the MFC with a fixed voltage of 89 mV, giving an initial current of 500 µA. The stabilization was achieved to 50 µA, demonstrating that the MFC is stable to the working conditions.

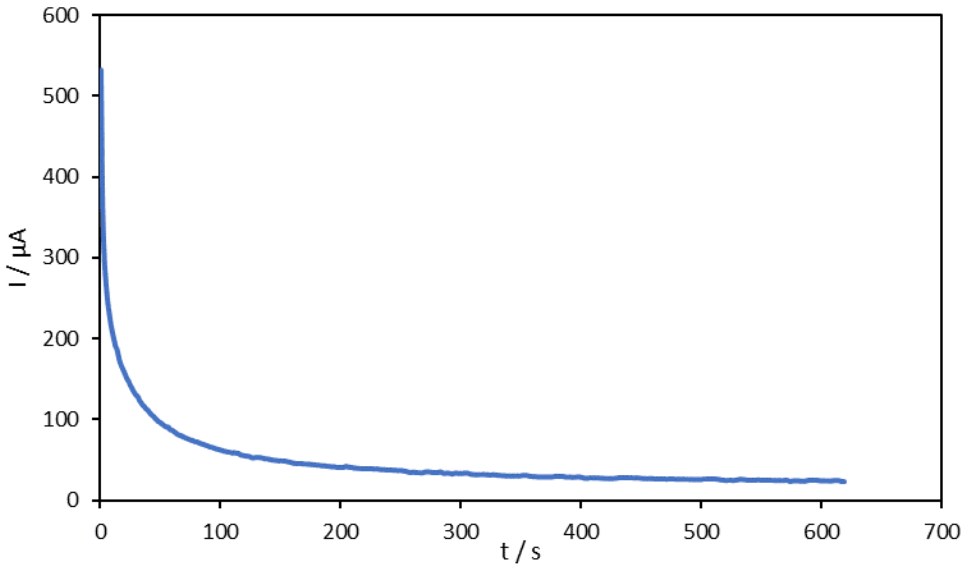

Fig. 4. Stability curve in the MFC.

Table 1 shows the percentages of removal of the physic parameters analyzed before (day 1) and after (day 55), during the operation of the MFC. The percentages of removal obtained suggest the degradation of the ULO, however, this must be verified by more rigorous analytical techniques.

Table 1. Percentages of removal obtained.

Physic parameter	Removal (%)
Turbidity	88
Total Solids	40
Volatile Solids	10

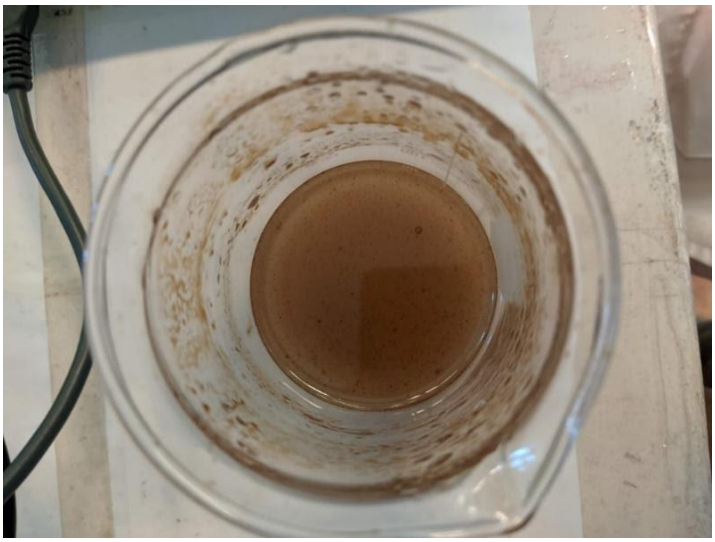

4. Conclusion

The maximum open-circuit potential recorded was 553 mV for day 11, having a 55-day ULO degradation cycle. The polarization curve for the MFC showed a DP_{max} of 0.24 mWm^{-2}, i_{max} of 2.35 mAm^{-2}, and in the Nyquist diagram, the R_{ct} and R_s were 8.7 and 1.7 Ωcm^{-2}, respectively. The MFC showed a stable curve for relatively long periods. In addition, turbidity reduction efficiency, and total and volatile solids reduction efficiencies found, suggesting the ULO degradation, however, this must be verified by more rigorous techniques.

Acknowledgements

The authors would like to thank to the technical staff of the 'Laboratorio de Energías Renovables' at the 'Universidad Autónoma de Zacatecas' and the ''Laboratorio de Ingeniería Ambiental' at the 'Unidad Profesional Interdisciplinaria de Ingeniería Campus Zacatecas' of the 'Instituto Politécnico Nacional' for the technical and analytical support.

References

[1] Shabani, M., Younesi, H., Pontié, M., Rahimpour, A., Rahimnejad, M., & Zinatizadeh, A. A. A critical review on recent proton exchange membranes applied in microbial fuel cells for renewable energy recovery. J Cleaner Prod 2020;264:121446

[2] International Energy Agency. Electricity generation by source, Mexico 1990-2018. https://www.iea.org/data-and statistics?country=MEXICO&fuel=Electricity%20and%20heat&indicator=Electricity%20generation%20by%20source; 2018 [accessed 10.07.2020]

[3] Góngora Molina, A. C., Ochoa Mancilla, J., Sosa Assi, M. E., & Vázquez Borges, E. Energía: celdas de combustible microbianas. Ingeniería: Revista Académica, 2020; 21:54-62.

[4] Secretaría de Medio Ambiente y Recursos Naturales. http://dsiappsdev.semarnat.gob.mx/datos/residuos/padron/ [accessed 10.07.2020]

[5] Base de Datos Estadísticos del Sistema Nacional de Información Ambiental y de Recursos Naturales. Consulta temática: Residuos Peligrosos, http://dgeiawf.semarnat.gob.mx:8080/approot/dgeia_mce/html/mce_index.html?De=BADESNIARN; (2018) [accessed 10.07.2020].
[6] Flores López, J. Lubricantes Usados. Instituto Nacional de Ecología y Cambio Climático. http://www2.inecc.gob.mx/publicaciones2/libros/35/lubricantes.html; 2007 [accessed 11.07.2020]
[7] Kumar, S. S., Kumar, V., Kumar, R., Malyan, S. K., & Pugazhendhi., A. Microbial fuel cells as a sustainable platform technology for bioenergy, biosensing, environmental monitoring, and other low power device applications, Fuel 2019; 255, 115682.
[8] Gajda, I., Greenman, J. y Leropoulos, L.A. Recent advancements in real-world Microbial Fuel Cells applications. Curr Opin Electrochem 2018,78-83.
[9] Enciso Hernández, E.A. Caracterización de una celda de combustible microbiana (CCM) para el tratamiento de glicerina residual de la producción de biodiésel [Tesis de título de Ingeniería, Instituto Politécnico Nacional]; 2018.
[10] Zhao, L., Deng, J., Hou, H., Li, J., & Yang, Y, Investigation of PAH and oil degradation along with electricity generation in soil using an enhanced plant-microbial fuel cell. J Cleaner Prod 2019; 221:678-683.
[11] Jianga, M., Xu, T., & Chen, S. A mechanical rechargeable small-size microbial fuel cell with long-term and stable power output. Applied Energy 2020; 260:114336.
[12] Madigan, M. T., Martinko, J. M., Bender, K. S., Buckley, D. H., y Stahl, D. A. Biología de los microorganismos. 14ª ed. Madrid, España: Pearson Educación S.A.; 2015.
[13] Microbial Growth. Growth curve of bacterial growth in phases. https://microbialgrowth101.weebly.com/growth-curve-of-bacterial-growth-in-phases.html [accessed 11.07.2020]
[14] Kashyap, D., Dwivedi, P. K ., Pandey, J. K., Kim, Y. H., Sharma, A. y Goel, S. Application of electrochemical impedance spectroscopy in bio-fuel cell characterization: A review. Int J Hydrogen Energy 2014; 39:20159-20170.

ID 035

Human Urine Role as Water, Nutrients, and Energy Source in Bioelectrochemical Systems Based on the Circular Economy Concept: A Review

M. Martínez-Castrejón[a], J.A. López-Díaz[b], Z.S. Galarza-Brito[c], J. Ramirez-Nava[d], J.M. Bravo-Ramos[a], O. Solorza-Feria[e], O. Talavera-Mendoza[b], A.L. Rodríguez-Herrera[a], O. Alcaraz-Morales[f], G. Hernández-Flores[g,*]

[a] Centro de Ciencias de Desarrollo Regional, Universidad Autónoma de Guerrero, Privada de Laurel No. 13, Col. El Roble, Acapulco, Guerrero. C.P. 39640, Mexico
[b] Universidad Autónoma de Guerrero, Escuela Superior de Ciencias de la Tierra, Ex Hacienda San Juan Bautista S/n,
Taxco el Viejo, Guerrero, C.P. 40323, Mexico
[c] Ingeniería en Tecnología Ambiental, Universidad Politécnica del Estado de Guerrero. Carretera Federal Iguala-Taxco, km 105, Puente Campuzano, Taxco de Alarcón, Guerrero, C.P. 40321, Mexico.
[d] Facultad de Ecología Marina, Universidad Autónoma de Guerrero, Gran vía tropical No 20, Fracc. Las playas, C.P. 39390, Acapulco, Guerrero, Mexico
[e] Centro de Investigación y de Estudios Avanzados del Instituto Politécnico Nacional, Dept. of Chemistry, Av. Instituto Politécnico Nacional 2508, Col. San Pedro Zacatenco, Delegación, Gustavo A. Madero, C. P. 07360, Mexico
[f] Facultad de Arquitectura y Urbanismo, Universidad Autónoma de Guerrero, Av. Juárez No.38 interior. C.U. Zona Norte, Chilpancingo, Guerrero, C.P. 39000, Mexico
[g] CONACyT - Universidad Autónoma de Guerrero, Escuela Superior de Ciencias de la Tierra, Ex Hacienda San Juan Bautista S/n, Taxco el Viejo, Guerrero, C.P. 40323, Mexico
* Corresponding author: ghernandez@conacyt.mx

ABSTRACT

The uncontrolled population growth increases the challenge of meeting human necessities. The consumption habits have compromised natural resources to unsustainable levels. Water and energy represent two basic requirements for each human being, and both are limited resources. Nowadays, sustainable practices for effluents treatment such as decentralized systems focused on recovering energy, nutrients, and water have drawn attention. Human urine (*HU*) is a physiological liquid waste where the principal component is water (~95%) and 5% are dissolved solids. The main components in this low percentage are nitrogen, phosphorous, and potassium. Also, a relatively high organic matter content is part of this effluent. From these characteristics, the *HU* is an effluent with the potential to recover nutrients, water, and energy from, through bioelectrochemical systems (*BS*). Thus, the aim of this work was to review the *HU* potential as water, nutrients, and energy source when used in bioelectrochemical devices based on the circular economy concept.

In *BS*, the *HU* is an organic matter source that can be used as a substrate and converted to electrical energy by bacteria. Some anaerobic bacteria use the chemical energy of organic and inorganic compounds to grow and to deliver as electricity through a biochemical oxidation process. On the other hand, the microbial electrolysis cells (*MEC*s) need an external electrical current to convert the organic compounds into other products, *e.g*., nitrogen to ammonia sulfate or bicarbonate.

The *HU* is an effluent that typically does not contain fecal coliforms. A person (age>15) produces *ca*. 2 L per day, *i.e*., this effluent can be used in sustainable practices to harvest energy and produce water. The proposal to use *HU* in electrochemical or *BS* is a novel way to treat and to take advantage of this physiological effluents. All the efforts done and developed in this field must be discussed and analyzed to improve the efficiency of systems.

Keywords: bioelectrochemical systems; circular economy; electrochemical systems; human urine

1. Introduction

Water is a key and finite natural resource for life. Quality freshwater is essential for the proper functioning of the human metabolism. Furthermore, water is a fundamental part of innumerable production processes, *i.e.,* water is an indispensable resource for the existence of humanity and its socio-economic development [1]. Unfortunately, due to its excessive and irrational use in productive and consumptive processes, water quality has been alarmingly deteriorated [2]. The water limitations in arid regions, the increasing demand in urban areas due to the rapid population growth, and the deterioration of water quality from supply sources (rivers, lakes, and springs), has caused society to seek different strategies to stock up on the vital fluid. One of the strategies has been to make society aware of making efficient use of water. This results in using only the necessary water or its reuse in different processes depending on its quality. On the other hand, to recover the quality of the contaminated water and reinsert it into the productive sector, specific treatments focused on removing contaminants have been developed [1].

Anthropogenic activities produce a big number of polluted effluents of varied and complex compositions typically called wastewater. Fortunately, most polluted effluents can be subjected to treatments to recover their quality. The human urine (*HU*), unlike other contaminated and complex effluents, is a physiological effluent that in the last decade has shown potential not only as a source of recovered water but as a source of energy and nutrients using biolectrochemical systems (*BS*) [3-6]. The *HU* is a metabolic waste generated from the use of freshwater in its different physiological processes [7,8]. Its composition is relatively complex but generally is free of enteropathogenic bacteria such as *Escherichia coli*. Their composition reflects the state of health and eating habits. The

composition of the *HU* can be divided into water and dissolved solids (*DS*), *ca*. 95 and 5%, respectively. Within the *DS*, the highest concentration is due to the presence of urea, inorganic salts, organic compounds, and organic ammonium salts [9]. Its composition is a problem for wastewater treatment plants due to the high content of N and P [10]. Nevertheless, N and P are two essential elements for plant nutrition that can be recovered by bioelectrochemical systems and reused as fertilizers. Additionally, using *BS* is possible to use the organic compounds present in the *HU* as fuel within these devices and generate electrical energy [6,10]. Once components such as N, P, and K have been removed from the urine, considered as plant nutrients, and organic matter has converted into an energy source, *HU* can be subjected to additional treatments to extract water. This type of bioelectrochemical process allows converting a problem effluent into a solution. They allow adding value to waste and reinserting it within different consumptive and productive uses, increasing the efficiency of the use of the water resource. These types of actions are within the philosophy considered by a relatively new concept: "circular economy" [11].

2. Circular economy

The accelerated environmental detriment has demonstrated the need to implement or modify processes that allow us to think about a sustainable future [12]. The circular economy *(CE)* model has gained interest in recent years despite being a concept still under theoretical construction [13-16]. It is emerging as the appropriate paradigm to achieve the transition to models compatible with sustainable development [17]. Stahel [18] proposes "*the performance economy*". The concept prioritizes the activities of reuse, repair, reconditioning, restoration, etc. intending to minimize the use of virgin natural resources, energy flow, and environmental detriment. On the other hand, Frosch and Gallopulos [19] propose the "*industrial ecology*" concept and criticize the traditional industrial model. The traditional industrial model prioritizes the maximization of immediate economic benefits for producers and consumers without considering the sustainability aspects. The holistic approach "industrial ecology" establishes a balance between economic benefits and environmental needs. From this, a new philosophy emerges for waste: "*waste equals food*", *i.e.*, wastes represent a source of raw material for other processes, thus reducing the impact of the industry on the environment. Lyle [20] proposes the "*regenerative design*" in which the linear flow model of performance is displaced by that of flow cycles. In these cycles, the use of renewable energy sources is proposed, maximizing materials by reusing them and maintaining the generation of waste within nature's capacity for regeneration.

The *CE* concept has been based in biomimetics. The biomimetics concept was proposed by Benyus [21] and focused on imitating the natural processes of ecosystems and their components to solve problems of anthropic origin. The key principles of biomimetics are nature as a model for solving human problems; nature as a measure to judge human innovations; and nature as a mentor [22].

One of the most recent concepts that have contributed to the *CE* is "from cradle to cradle" [23]. The economic model is considered from the design stage of the products or services

offered, focusing on effectiveness over efficiency. It is explained that the objective is to achieve a positive effect instead of a "less bad" or less harmful effect on the ecological system. The authors indicate that the *CE* "must be dynamic and adaptive". In the case of water, it is an indispensable resource for human survival and economic development. Furthermore, water is essential to guarantee ecosystem services [24]. Currently, two-thirds of the world's population experience water shortages for at least one month a year. This means that around 500 million people live in areas where consumption is 200% greater than the recharge capacity of the ecosystems present [25]. The global water shortage, its lack of availability, and the cost of its purification and treatment have driven the restoration and reuse of the water resource. Reuse manifests itself as an alternative supply for the satisfaction of human needs at a global level [1]. The ability to reuse water, regardless of whether the intention is to increase the water supply or manage nutrients in treated effluents (also a factor leading to water reuse), has positive benefits that are also key reasons for implementing programs of reuse [26]. These benefits include better agricultural production; reduced energy consumption associated with the production, treatment, and distribution of water; and significant environmental benefits, such as the reduction of the nutrient load in the receiving waters due to the reuse of the treated wastewater [27].

The circular economy offers a new way of looking at the relationships between markets, customers, and natural resources, promoting sustainable and efficient policies and practices in the use of resources. This model discourages the extraction of virgin resources, prioritizing waste treatment, and reincorporating them into the production and consumption chain. It moves away from the linear economy by breaking the waste chain. This transition encourages efficient water use, combined with strong incentives for innovation, can improve an economy's ability to handle the demands of the growing imbalance between water supply and demand [28]. From a *CE* perspective, reusing water is a beneficial option for both humans and the biosphere. The complete cycle of wastewater management is a critical component for the *CE* since its generation, collection (on-site sanitation systems and sewers), and treatment for its disposal and reuse. In this process: water, nutrients, and energy recovery intervene [29]. The *CE* initiative aims to close resource flows and extend their useful life through use, reuse, and recovery processes [30]. Addressing the increasing demand for humanity's resources, water, energy, and food will require a combination of approaches including water conservation, recycling, and wastewater treatment focusing on conventional sources or non-traditional such as *HU* [31].

3. Human urine

Urine is a waste from the human body and mammals in general [32]. The *HU* is a liquid waste produced by the kidneys action [7,8]. It is composed of water, urea, electrolytes (inorganic salts), organic acids, toxins, compounds resulting from the breakdown of blood, heavy metals and metabolites in general, from what a person ingests through food, water or exposure to the environment [7,33]. This physiological effluent is the result of the metabolism of the body and since the ancient inhabitants of Egypt, Babylon, and India, it has been used to evaluate the health condition of people.

HU has certain physical-chemical characteristics that make it a potential effluent to revalue it based on its composition. Typically, adults excrete between 1,500 and 1,600 mL/d. However, it is normal if an adult person generates between 600 and 2,000 mL in a 24 h period. However, the excreted volume may be higher in those people who increase the regular consumption of water by the application of intravenous medical solutions, as well as by the alcohol intake or caffeine [32]. It has a color range (depending on the degree of hydration or health problems) from slightly yellow to brown or reddish [7]. Fresh *HU* is odorless. However, the presence or absence of odor depends on the type of food consumed and medications taken [32]. Furthermore, it is relevant to note that *HU* begins to give off a characteristic odor as its emitted from the body. This is mainly due to the decomposition of urea to ammonia. In people with poorly treated diabetes, the almond odor can be sensed due to the presence of ketone bodies [7]. A normal fresh *HU* is transparent and has a pH ranging from 5.5-7.0 with high electrical conductivity (160-270 mS/cm) due to a high content of salts [9]. However, the decomposition of urea into ammonia by the effect of bacterial growth at room temperature modifies the pH from acid to alkaline [32]. The physicochemical characteristics of urine are due to the composition of this physiological effluent. In general, two major components can be observed at the *HU*: water and *DS*. Water is the component with the highest concentration. The water content is in an average range of 91-95% and the rest represents the content of *DS*. The highest concentration of *DS* is due to the presence of N (14-18%), C (13%), P (3.7%), and K (3.7%). Nitrogen is the main component of *DS* and its concentration reaches 8.12 g/L. Table 1 shows the main solutes representing *DS* [9].

Table 1. Principal solutes in human urine.

Solutes	Concentration (g/L)
Urea	9.30-23.30
Inorganic salts	14.16
Organic ammonium salts	4.13
Organic compounds	5.36
Chemical oxygen demand	6.30-17.50
Total nitrogen	4.00-13.90
Total phosphorus	0.20-2500
Potassium	0.45-1.44

The composition of the *HU* depends on factors such as physical activity, environmental conditions, type of diet, and the amount of salt and water ingested [9].

Urea is the predominant solute and represents *ca*. 50% of the total dissolved organic solids and represents an important source of nitrogen. The high concentration of N, P, and K found in the urine are part of the main nutrients that can be used for plants. From urine, it is possible to obtain between 60-90% of the N, P, and K in solution, which the plants require for their correct development [34]. From these characteristics, the perception of urine has changed. Its composition can provide the equivalent of 37% N, 20% P, and 15% K of commercial fertilizers used in agriculture as fertilizer [35]. On the other hand, due to the content of chemical oxygen demand (*COD*), the chemical energy stored in oxidizable compounds can be converted to bioelectricity by bioelectrochemical systems [4,6]. Finally, through additional processes, once the content of N, P, K, and *COD* has been removed, the water can be subjected to additional treatments for recovery or used in water that does not require a higher quality, *e.g.*, garden irrigation.

3.1. Microorganisms in human urine

Urine produced by the kidneys is sterile. In general, the urinary system is free of microorganisms, except for the distal zones of the ureter [36,37]. For this reason, a human urine sample may contain a diversity of harmless bacterial species potentially responsible for urinary tract infection (*UTI*) [38]. *Escherichia coli* is the causal agent of 80% of all *UTI* in humans [36]. However, other species cause infections such as *Staphylococcus aureus, Streptococcus pyogens*, and the enterococci species, all of them are gram-positive. Gram-negative species also cause *UTI* (*Pseudomonas aeruginosa, Klebsiella pneumonie*). Fungi *(Candida albicans)* and protozoa *(Trichomonas vaginalis)* are other causal agents of *UTI* [38]. Low counts ($<10^4$) are a sign of normal microbial in the urinary system, and, unlike an infective process, the cells belong to more than one species. Recently, it has become evident that urine in healthy people is not sterile. In other words, the bacterial counts do not just come from the distal zone of the urinary system; there is evidence that microorganisms can live in the urine. In the human body, these bacteria can perform reactions that precipitate calcium, and this can produce stones in the kidney [36]. Besides, there is evidence of tens of microorganism's species are forming part of the microbiota´s bladder, but their role in human health is still unknown [39]. It has been mentioned urea is the second principal component of urine, and this molecule is quite common in nature. One of the first species to be reported as urea consumer was *Ureaplasma urealyticum* [40] which causes urethritis in males. But this is not an isolated case. It has been estimated that ~50% of heterotrophic soil bacteria are ureolytic [41]. Why is quite common this metabolic ability? Urease, the enzyme found in that species, performs the reaction that converts urea in ammonia + carbon dioxide. This is a branch of the nitrogen cycle.

Overall, compared to feces the *HU* poses a lower risk to human health. However, it may contain some pathogenic bacteria and even helminth eggs. Other examples of bacteria that can grown in *HU* are *Salmonella typhi, Salmonella paratyphi, Schistosoma haematobium,* and *Leptospira interrogans* [9].

4. Human urine as fuel in bioelectrochemical systems

The *HU* has unique physicochemical characteristics that make it an ideal electrolyte to use in *BS*. Its high content of inorganic salts translates into a high value of electrical conductivity (160-270 mS/m), a property of electrolytes that considerably decreases ohmic losses and, consequently, reduces the internal resistance of *BS*, favoring power generation. On the other hand, the content of organic compounds or organic matter present in the *HU* expressed in terms of *COD* represents the potential of chemical energy that can be converted into electrical energy (Table 1). The *COD* content in *HU* is 7 to 20 times higher than the *COD* content found in domestic wastewater (160 to 850 mg/L), another waste effluent used in *BS*. Furthermore, the low conductivity value of household's wastewater (~1 mS/cm) is reflected in terms of low power densities. Other effluents that have been used in *BS* and have a lower *COD* content than *HU* are brewery wastewater and animal wastewater with 2,250 and 8,320 mg/L, respectively [5,9,42]. Recently, *HU* has generated considerable interest in the field of wastewater treatment using microbial fuel cells (*MFC´*s), especially in the past 20 years. The separation of urine from feces from the source has been possible by implementing divergent or "no-mix" toilets [6]. Separating urine from municipal wastewater *(MWW)* reduces the contaminant load of *MWW* by 10, 75, and 50% of *COD*, N, and P [43]. Furthermore, this makes it possible to treat *HU* by itself and increase the efficiency of N, P recovery, or oxidation of the *COD* by decreasing the complexity of the effluent [44-46].

4.1. Microbial fuel cells and human urine

In the early second decade of the 21st century, the use of *HU* in *MFC*'s as an energy source was reported [4]. From this study, the number of publications in this novel proposal began to grow significantly [6]. The proposal has leaped in a short time, going from prototypes at the laboratory level to prototypes on a pilot scale in real scenarios.

The University of KwaZulu-Natal, Durban, South Africa, implemented a small scale 66 *BS* configuration. The devices were batch fed for approximately 780 h with fresh *HU*. This design produced an average power density of 1.46 W/m^3, which gradually decreased over time. Besides, the University of West of England *(UWE)* Frenchay campus in 2015 implemented a *BS* system. The *BS* configuration consisted of 288 *MFC's*. This configuration objective, commercially known as the Pee Power® urinal, was to evaluate the technological parameters of the system and identify the limitations in a real-life scenario. The results showed that with 5 d of biofilm developed, the *BS* generated enough energy to light four domestic LED luminaires connected to a motion sensor also powered by *HU*-operated *MFC's*. The power accumulates in supercapacitors keeping it available. This trial implementation was executed in collaboration between *UWE* and Oxfam. The participation of the international confederation was motivated by the interest of applying the Pee Power® urinal in refugee camps [47]. On the other hand, in 2015, a new study with the Pee Power® urinal was developed using *ca.* 250,000 people. The configuration, similar to that implemented at the *UWE*, was complemented by 4 more packages of *MFC's* connected to a larger urine flow system. The complete system contained 330 L of urine and fed 6 LED modules at night for 6 h. An average *COD* removal of 30% was reported. One year later,

another trial was carried out with some changes to the device configuration. The modification consisted of reducing the urinal stands, as well as in the installation of a passive feeding mechanism that controlled the hydraulic retention time. Taking advantage of the laboratory experience reported by Walter *et al.* [48], membrane-less, single-chamber *MFC's* operating in a self-straightening column were implemented. This system consisted of 12-cell modules, an energy harvesting and distribution system, and a passive power mechanism. This configuration powered 6 commercial LED tubular lamps with a modified voltage at 2,650 V DC for 9.5 h/d placed inside the urinal cubicles. This new configuration achieved a *COD* removal 37% higher than that reported in the 2015 study [6].

Undoubtedly, this type of study shows the potential that *HU* poses to be considered as a raw material to generate energy, *i.e*., from this, the concept of *HU* as waste will change. Now it can be seen as an energy source and can be reincorporated into the production cycle. Furthermore, during this energy conversion, the content of organic matter is reduced and, this is reflected in a lower pollution load of the *HU*, giving a secondary treatment to recover water.

5. Human urine oxidation by electrolysis systems

Unlike bioelectrochemical systems, specifically *MFC's*, an electrolysis device requires an external source of electrical current. Its operation depends on external energy consumption. Electrolysis has been a method used to remove nitrogen from the urine [49]. In recent years the electrochemical oxidation of ammonia and urea has gained attention [50]. On the other hand, electrolysis has also functioned as an ammonia sensor in effluents and for the recovery of hydrogen and urea [51,52]. In the treatment of *MWW*, the most common mechanism for electrochemical oxidation of ammonia is indirect oxidation with chlorine [53]. The above means that it is possible to harvest hydrogen through electrolysis, which is considered as the fuel of the future because it does not generate CO_2 as a product of its combustion [54].

The type of treatment required depends on the specific nutrients to extract, *e.g.*, the decrease in pH by an electrochemical method in combination with a magnesium-titanium corrosion cell allows the separation of nitrogen and phosphorus by variation of voltages.

6. Human urine a source rich in nitrogen, phosphorous, and potasium

The *HU* is a physiological residue that contains N, P, K, Mg, Na, S, Ca in ionic form, and to a lesser extent, minor elements such as Cu, Zn, Mn, Bo, and Fe. The above means that *HU* is a potential source of N, P, and K, considered some of the main macronutrients needed by plants for their correct growth. [35,55,56]. Its availability to plants is comparable to that of chemical fertilizers [34,57]. From this perspective, its composition allows adding value to this physiological residue. Recent research suggests the recovery of each of these components and water from the constantly increasing world volume of *MWW* [58]. Physiologically, human beings can excrete ~500 L of urine annually. It is estimated that from this volume of *HU* a

person can produce between 2.5-4.3 kg of N, ~1 kg of P, and ~1 kg of K. These values are higher than those registered for fecal matter (~0.7 kg N, ~0.5 kg P and ~0.2 kg K). These macronutrients represent between 60-90% of the intake of N, P, and K that plants require for their functions [34, 59-61]. In the current conventional agriculture sector, there is a dependence on industrialized technologies based on high monetary investments [56]. This aspect of the sector is unidirectional and makes it impossible to control recycling, favoring the generation of pollution, environmental degradation and hinders economic development, *i.e.,* highlights an unsustainable industrial and environmental panorama [62]. The use and implementation of organic products is an attractive alternative. *HU* has been proposed to be a residue with the potential to substitute for conventional artificial fertilizers or inorganic nutrients [56,63]. It has been used in different crops such as cabbage, tomato, cereals, corn, sweet pepper, amaranth, red beet, banana, coconut, potato, cucumber, spinach, among others [55-57,59,61,64]. Nutrient recovery from *HU* reduces the need to produce, acquire, and import chemical fertilizers and prevents high nutrient loading *MWW* discharges from coming into contact with natural bodies and streams, avoiding eutrophication problems [56,61,64].

The phosphorus recovery through the precipitation of struvite is one of the most developed issues in this aspect of waste recovery [65,66]. In addition to the recovery of macronutrients, due to the high percentage of water reported in its composition, the recovery and purification of water from urine are fields developed parallelly [67]. Amongst the technologies implemented for the treatment of urine, electrochemical, and bioelectrochemical treatment devices stand out, being *MFC*s the most scientifically developed. This type of device allows for duality in the treatment by producing clean energy such as bioelectricity while remediating residual discharges simultaneously [4].

Despite the different revaluation approaches that the scientific community has reported for *HU*, its use remains a subject associated with prejudice. However, today *HU* is challenging for science and society to become an unconventional resource. The popularity of this residue attributes increasing recognition to it, associating it with great economic-environmental benefits [58].

7. Water from human urine

The largest component of *HU* is water (*ca.* 95%). Considering a person produces a volume of 2 L of water per day, the amount of water that can be recovered from that volume is 1.9 L daily per person. Average per capita *HU* production per day is estimated to be 1.5 L and 300 to 550 L per year [68]. Considering a world population of 7.7 billion, it is calculated that *ca.* 19,250 million L of *HU* per day, *i.e*., 18,288 million L of water per day could be recovered [69]. This effluent is part of the sanitary discharges mixed with urban effluents, which in turn are conducted in the best of cases to wastewater treatment plants *(WWTP).* Larsen *et al*. [43] have estimated an average of 184 L of wastewater *(WW)* produced daily per person. From this parameter, it is inferred that the world population generates a total of 1,416,800 million L of *WW* per day. Taking into account the amount of urine produced per capita daily,

the percentage of urine present in the *WW* is 1.36%. Today, the recovery of water from *WW* poses a challenge for *WWTP* due to the complexity of the *WW* matrix; where different sorts of *WW* effluents combine, including fecal matter. The recovery of water from the *HU* would be easier if this excreta was directly treated. In other words, avoiding mixing the *HU* with other effluents would facilitate the task and reduce the risk of contamination by other contaminants.

8. Outlook

The world demand for freshwater (an essential resource for life but limited by its abundance and quality on the planet) has increased directly due to the demographic explosion. This has been the trigger for the scientific community to seek unconventional resources to renew, recover, or reuse water to increase its efficiency of use. Residual effluents are a problem depending on the adopted perspective. This vision can be modified depending on *WW* composition and the possibility to recover byproducts of socio-environmental interest. For society, the *HU* is an unconventional resource due to its advantageous composition. It is considered one of the principal sources of macronutrients for plants. Furthermore, its organic matter content can be converted into energy using *BS*. Additionally, it represents an unconventional water source through *WWTP* or *BS* directly or indirectly from the transpiration of plants (Fig. 1).

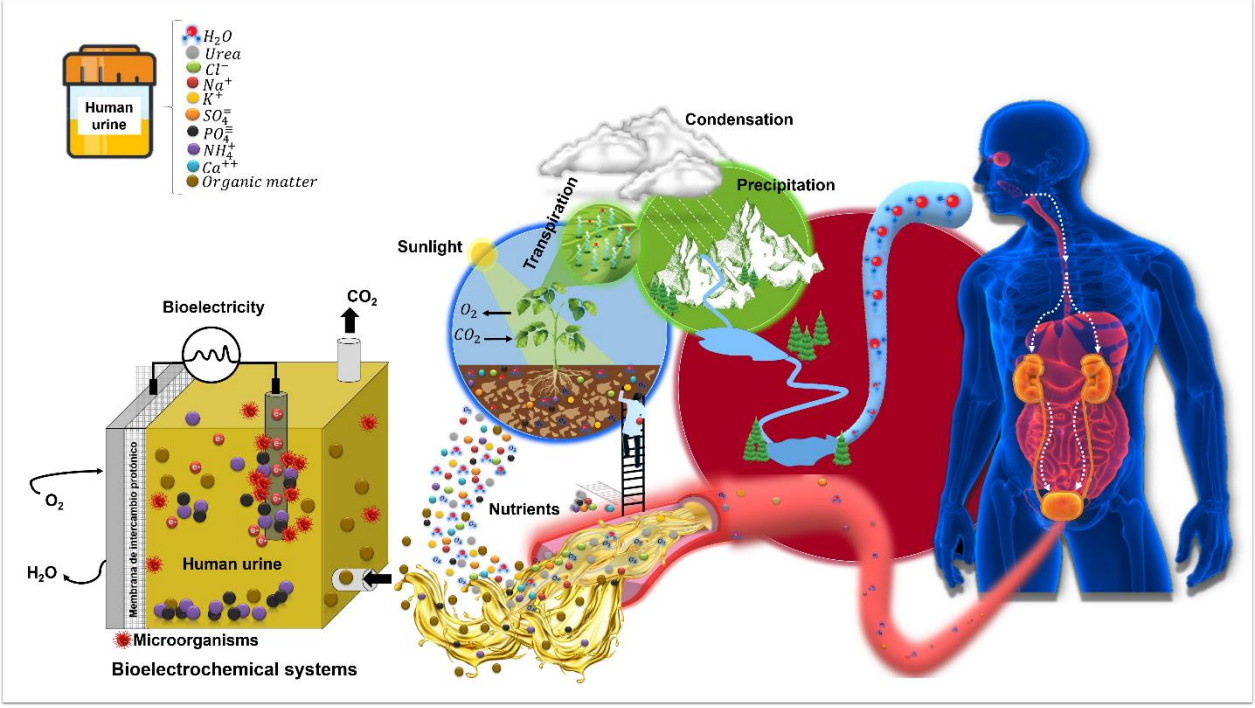

Figure 1. Human urine and the circular economy concept.

From the concept of *CE, WW* or *HU*, could be the raw material for other processes to obtain products such as hydrogen, methane, fertilizers, electricity, and, of course, water.

BS's are an interesting technology that would contribute to the reintegration of *HU* as a source of nutrients, energy, and water within the productive sector, *i.e.,* through this technology the valorization of *HU* will change. It will no longer be a waste without value. It will become a product of social interest. Even that *MFC's* operated with urine as anolyte do not generate attractive potential outputs or produce considerable amounts of bioelectricity, the results are promising. Electro and bioelectrochemical systems are a technology that allows urine to be pretreated for secondary processes that can be coupled to recover water. According to Sadin *et al.* (1988) [70], the commercial suitability of a technology is determined by a classification system according to its level of technological readiness *(TRL).* This classification, ranks *MFC's* in the *TRL*1-*TRL*3 region, meaning that their scientific development is ongoing at the laboratory level. However, scientific evidence shows the potential of this technology to revalue *HU*. In recent years it has been widely demonstrated that *MFC's* perform useful functions without requiring external energy to operate using *HU* as fuel [47].

On the other hand, nutrients recovery as N, P, and K is easier from source-separated *HU* than from *WW.* Retrofitting hydrosanitary facilities to separate *UH* from *WW*, contributes to urine recovery for different treatments to obtain byproducts such as water, bioelectricity, and nutrients like N, P, and K from a less complex matrix more efficiently. Today, unconventional water and energy sources are needed; *HU* is one of them.

Acknowledgements

Mariana Martínez-Castrejón, Jonathan Ramirez-Nava & Jesús Manuel Bravo-Ramos received a graduate scholarship from CONACyT, Mexico; registration numbers 733907, 744493, and 758791, respectively. Mariana Martínez-Castrejón wishes to thank the Mexican Hydrogen Society and XX International Congress of the Mexican Hydrogen Society Organizing Committee for the received registration fee fellowship.

References

[1] Voulvoulis N. Water reuse from a circular economy perspective and potential risks from an unregulated approach. Curr Opin Environ Sci Health 2018;2:32-45. doi: https://doi.org/10.1016/j.coesh.2018.01.005

[2] Sánchez-Montoya G, Talavera-Mendoza O, Hernández-Flores G, Díaz-Villaseñor E, Ramírez-Guzmán AH, Galarza-Brito Z. Potentially toxic elements determination and chemical-microbiological analysis of potable water in Taxco de Alarcón, Guerrero. Rev Mex de Cienc Geol 2019;36:147-158. doi: https://doi.org/10.22201/cgeo.20072902e.2019.2.927.

[3] He L, Du P, Chen Y, Lu H, Cheng X, Chang B, Wang Z. Advances in microbial fuel cells for wastewater treatment. Renew Sustain Energy Rev 2017;71:388-403. doi: http://dx.doi.org/10.1016/j.rser.2016.12.069

[4] Ieropoulos I, Greenman J, Melhuish C. Urine utilisation by microbial fuel cells; energy fuel for the future. Phys Chem Chem Phys 2012;14(1):94-98. doi: 10.1039/c1cp23213d

[5] Santoro C, Ieropoulos I, Greenman J, Cristiani P, Vadas T, Mackay A, Li B. Power generation and contaminant removal in single chamber microbial fuel cells (SCMFCs)

treating human urine. Int J Hydrogen Energy 2013;38(26):11543-11551. doi: 10.1016/j.ijhydene.2013.02.070
[6] Santoro C, Salar Garcia MJ, Walter XA, You J, Theodosiou P, Gajda I, Obata O, Winfield J, Greenman J, Ieropoulos I. Urine in bioelectrochemical systems: an overall review. ChemElectroChem 2020;7:1312-1331. doi: https://doi.org/10.1002/celc.201901995
[7] Cook JD, Caplan YH, LoDico CP, Bush DM. The characterization of human urine for specimen validity determination in workplace drug testing: A review. J Anal Toxicol 2000;24:579-88. doi: https://doi.org/10.1093/jat/24.7.579.
[8] Robberecht HJ, Deelstra HA. Selenium in human urine: concentration levels and medical implications. Clin Chim Acta 1984;136:107-120. doi: https://doi.org/10.1016/0009-8981(84)90282-1.
[9] Rose C, Parker A, Jefferson B, Cartmellthe E. characterization of feces and urine: a review of the literature to inform advanced treatment technology. Crit Rev Env Sci Tec 2015;45:1827-1879. doi: 10.1080/10643389.2014.1000761
[10] Sharma P, Mutnuri S. Nutrient recovery and microbial diversity in human urine fed microbial fuel cell. Water Sci Technol 2019;79(4):718-730. doi: 10.2166/wst.2019.089
[11] Ghisellini P, Cialani C, Ulgiati S. A review on circular economy: the expected transition to a balanced interplay of environmental and economic systems. J Clean Prod 2016;114:11-32. doi: http://dx.doi.org/10.1016/j.jclepro.2015.09.007
[12] Geissdoerfer M, Savaget P, Bocken N, Hultink E. The Circular Economy – A new sustainability paradigm?. J Clean Prod 2017;143:757-768. doi: https://doi.org/10.1016/j.jclepro.2016.12.048
[13] Gregson N, Crang M, Fuller S, Holmes H. the circular economy: the moral economy of resource recovery in the EU. Econ Soc 2015;44:218-243. doi: 10.1080/03085147.2015.1013353
[14] Hobson K, Lynch N. Diversifying and de-growing the circular economy: Radical social transformation in a resource-scarce world. Futures 2016;82:15-25. doi: 10.1016/j.futures.2016.05.012
[15] Kirchherr J, Reike D, Hekkert M. Conceptualizing the Circular Economy: An Analysis of 114 Definitions. Resour Conserv Recycl 2017;127:221-232. doi: 10.2139/ssrn.3037579
[16] Lazarevic D, Valve H. Narrating expectations for the circular economy: Towards a common and contested European transition. Energy Res Soc Sci 2017;31:60-69. doi: 10.1016/j.erss.2017.05.006
[17] Pomponi F, Moncaster A. Circular economy for the built environment: A research framework. J Clean Prod 2016;143:710-718. doi: https://doi.org/10.1016/j.jclepro.2016.12.055
[18] Stahel WR. The product life factor. An inquiry into the nature of sustainable societies: the role of the private sector, Series: 1982 Mitchell Prize Papers, NARC, available at: https://p2infohouse.org/ref/33/32217.pdf. 1982 [accessed 13.07.20]
[19] Frosch RA, Gallopoulos NE. Strategies for Manufacturing. Sci Am 1989;261:144-152. doi: https://doi.org/10.1038/scientificamerican0989-144
[20] Lyle JT. Regenerative Design for Sustainable Development, John Wiley & Sons, California: 1996. ISBN-13: 978-0471178439
[21] Benyus JM. Biomimicry: Innovation Inspired by Nature. New York: HarperCollins;1997.
[22] Webster K. The Circular Economy: A Wealth of Flows. 2nd ed., Ellen MacArthur Foundation; 2017.

[23] Braungart M, McDonough W, Bollinger A. Cradle-to-cradle design: creating healthy emissions-a strategy for eco-effective product and system design. J Clean Prod 2007;15:1337-1348. doi: 10.1016/j.jclepro.2006.08.003
[24] UNEP. Water security and ecosystem services the critical connection. WWAP, UNESCO, Nairobi, Kenya; 2009.
[25] UN. Wastewater: the untapped resource. WWDR 2017. UNESCO, Nairobi, Kenya; 2017.
[26] EPA. Guidelines for Water Reuse. USEPA, Washington, D.C., 2012.
[27] Fatta-Kassinos D, Dionysiou DD, Kümmerer K. Advanced treatment technologies for urban wastewater reuse (the handbook of environmentalchemistry). Springer; 2016.
[28] Kearney MS, Harris BH, Hershbein B, Jácome E, Nantz G. In times of drought: nine economic facts about water in the United States. 2014. Available at: https://www.brookings.edu/wp-content/uploads/2016/06/nineeconomicfactsaboutuswaterkearneyharris.pdf [Accessed 02.07.20].
[29] SIWI. Water and waste: reduce and reuse. Overarching conclusions. Stockholm International Water Institute. 2017. Available at: https://www.siwi.org/wp-content/uploads/2017/10/OC-final.pdf [accessed 21.07.20]
[30] Busch J, Dawson D, Roelich K. Closing the low-carbon material loop using a dynamic whole system approach. J Clean Prod 2017;149:751-761. doi: https://doi.org/10.1016/j.jclepro.2017.02.166
[31] Hinkebein T. Desalination: limitations and challenges. National Research Council (US). In Water and sustainable development: opportunities for the chemical sciences: a workshop Report to the chemical sciences roundtable. Washington (DC): National Academies Press (US); 2004.
[32] Echeverry G., Hortin G.L. RAJ. Introduction to Urinalysis: Historical Perspectives and Clinical Application. In: Rai AJ, editor. Urin. Proteome. 1st ed., Humana Press;2010:1–12. doi: https://doi.org/https://doi.org/10.1007/978-1-60761-711-2_1.
[33] Silva MJ, Samandar E, Preau JL, Reidy JA, Needham LL, Calafat AM. Quantification of 22 phthalate metabolites in human urine. J Chromatogr B Anal Technol Biomed Life Sci 2007;860:106–112. doi: https://doi.org/10.1016/j.jchromb.2007.10.023.
[34] Kirchmann H, Pettersson S. Human urine - Chemical composition and fertilizer use efficiency. Fertil Res 1995;40(2):149-154. doi: https://doi.org/10.1007/BF00750100
[35] Pradhan SK, Nerg AM, Sjöblom A, Holopainen JK, Heinonen-Tanski H. Use of Human Urine Fertilizer in Cultivation of Cabbage (Brassica oleracea)-Impacts on Chemical, Microbial, and Flavor Quality. J Agric Food Chem 2007;55:8657-8663. doi: 10.1021/jf0717891
[36] Black JG, Black LJ. Microbiology. Principles and explorations. 9th ed. USA. John Wiley & Sons, Inc.; 2015.
[37] Ridley JW. Fundamentals of the Study of Urine and Body Fluids. 1st ed. Cham: Springer International Publishing; 2018. doi: https://doi.org/10.1007/978-3-319-78417-5.
[38] Cappuchino JG, Welsh C. Microbiology. A laboratory manual. 12th ed. Nueva York: Pearson; 2020.
[39] Hilt EE, McKinley K, Pearce MM, Rosenfeld AB, Zilliox MJ, Mueller ER,… Schreckenberge PC. Urine is not sterile: Use of enhanced urine culture techniques to detect resident bacterial flora in the adult female bladder. J Clin Microbiol 2014;52:871–876. doi: https://doi.org/10.1128/JCM.02876-13

[40] Smith DGE, Russell WC, Ingledew WJ, Thirkell D. Hydrolysis of urea by Ureaplasma urealyticum generates a transmembrane potential with resultant ATP synthesis. J Bacteriol 1993;175(11):3253-3258. doi: https://doi.org/10.1128/jb.175.11.3253-3258.1993
[41] Killham K, Prosser JI. The bacteria and archaea. In: Paul E A, editor. Soil microbiology, ecology, and biochemistry. 4th ed. Academic Press, USA; 2015, p. 41-76
[42] Ahn Y, Logan BE. Domestic wastewater treatment using multi-electrode continuous flow MFCs with a separator electrode assembly design. Appl Microbiol Biotechnol 2013;97:409-416. doi: https://doi.org/10.1007/s00253-012-4455-8.
[43] Larsen TA, Hoffmann S, Luthi C, Truffer B, Maurer M. Emerging solutions to the water challenges of an urbanizing world. Science 2016;352: 928-933. doi:10.1126/science.aad8641
[44] Maurer M, Schwegler P, Larsen TA. Nutrients in urine: energetic aspects of removal and recovery. Water Sci Technol 2003;48:37-46. doi: 10.2166/wst.2003.0011
[45] Maurer M, Pronk W, Larsen TA. Treatment processes for source-separated urine. Water Res 2006;40:3151–3166. doi: 10.1016/j.watres.2006.07.012
[46] Udert KM, Larsen TA, Gujer W. Fate of major compounds in source-separated urine. Water Sci Technol 2006;54:413-420. doi: 10.2166/wst.2006.921
[47] Ieropoulos IA, Stinchcombe A, Gajda I, Forbes S, Merino-Jimenez I, Pasternak G, Sanchez-Herranz D, Greenman J. Pee power urinal-microbial fuel cell technology field trials in the context of sanitation. Environ Sci Water Res Technol 2016;2:336-343. doi: 10.1039/c5ew00270b
[48] Walter XA, Greenman J, Ieropoulos I. Binder materials for the cathodes applied to self-stratifying membraneless microbial fuel cell. Bioelectrochem 2018;123:119-124. doi: 10.1016/j.bioelechem.2018.04.011
[49] Anglada A, Urtiaga A, Ortiz I. Contributions of electrochemical oxidation to waste-water treatment: fundamentals and review of applications. J Chem Technol Biot 2009;84:1747-1755. doi:10.1002/jctb.2214
[50] Amstutz V, Katsaounis A, Kapalka A, Comninellis C, Udert KM. Effects of carbonate on the electrolytic removal of ammonia and urea from urine with thermally prepared IrO2 electrodes. J Appl Electrochem 2012;42:787-795. doi:10.1007/s10800-012-0444-y
[51] Boggs BK, King RL, Botte GG. Urea electrolysis: direct hydrogen production from urine. ChemComm 2009;32:4859. doi:10.1039/b905974a
[52] Rosca V, Duca M, de Groot MT, Koper MTM. Nitrogen Cycle Electrocatalysis. Chem Rev 2009;109:2209-2244. doi:10.1021/cr8003696
[53] Díaz V, Ibáñez R, Gómez P, Urtiaga AM, Ortiz I. Kinetics of electro-oxidation of ammonia-N, nitrites and COD from a recirculating aquaculture saline water system using BDD anodes. Water Res 2011;45:125-134. doi:10.1016/j.watres.2010.08.020
[54] Murcio-Hernández S, Rueda-Solorio AV, Banda-Alemán JA, González-Nava C, Rodríguez FJ, Bustos E, … Manríquez J. Electrocatalytic urea mineralization in aqueous alkaline medium using Ni II cyclam-modified nanoparticulate TiO 2 anodes and its relationship with the simultaneous electrogeneration of H 2 on Pt counterelectrodes. Arab J Chem 2018;13(1): 1641-1660. doi:10.1016/j.arabjc.2017.12.029
[55] Heinonen-Tanski H, Sjöblom A, Fabritius H, Karinen P. Pure human urine is a good fertiliser for cucumbers. Bioresource Technol 2007;98:214-217. doi: 10.1016/j.biortech.2005.11.024

[56] Shrestha D, Srivastava A, Shakya SM, Khadka J, Acharya BS. Use of compost supplemented human urine in sweet pepper (Capsicum annuum L.) production. Sci Hortic-Amsterdam 2013;153:8-12.doi: 10.1016/j.scienta.2013.01.022
[57] Mnkeni PNS, Kutu FR, Muchaonyerwa P, Austin LM. Evaluation of human urine as a source of nutrients for selected vegetables and maize under tunnel house conditions in the Eastern Cape, South Africa. Waste Manage Res 2008;26:132-139. doi: 10.1177/0734242X07079179
[58] Qadir M, Drechsel P, Jiménez Cisneros B, Kim Y, Pramanik A, Mehta P, Olaniyan O. Global and regional potential of wastewater as a water, nutrient and energy source. Nat Resour Forum 2020;44:40-51. doi: 10.1111/1477-8947.12187
[59] Heinonen-Tanski H, Wijk-Sijbesma CV. Human excreta for plant production. Bioresource Technol 2005;96:403-411. doi: 10.1016/j.biortech.2003.10.036
[60] AdeOluwa OO, Cofie O. Urine as an alternative fertilizer in agriculture: Effects in amaranths (Amaranthus caudatus) production. Renew Agr Food Syst 2012;27(4):287-294. doi: 10.1017/S1742170511000512
[61] Karak T, Bhattacharyya P. Human urine as a source of alternative natural fertilizer in agriculture: A flight of fancy or an achievable reality. Resour Conserv Recy 2011;55:400-408. doi: 10.1016/j.resconrec.2010.12.008
[62] FAO. La seguridad alimentaria mundial y la función de la fertilización sostenible. Departamento de Agricultura de la FAO, Roma, Italia., 2003
[63] Tidåker P, Mattsson B, Jönsson H. Environmental impact of wheat production using human urine and mineral fertilisers e a scenario study. J Clean Prod 2007;15:52-62.
[64] Pradhan SK, Holopainen JK, Heinonen-Tanski H. Stored Human Urine Supplemented with WoodAsh as Fertilizer in Tomato (Solanum lycopersicum) Cultivation and Its Impacts on Fruit Yield and Quality. J Agric Food Chem 2009;57:7612-7617. doi: 10.1021/jf9018917
[65] Liu Z, Zhao Q, Wang K, Lee D, Qiu W, Wang J. Urea hydrolysis and recovery of nitrogen and phosphorous as MAP from stale human urine. J Environ Sci 2008;20(8):1018-1024. doi: 10.1016/s1001-0742(08)62202-0
[66] Liu B, Giannis A, Zhang J, Chang VWC, Wang JY. Characterization of induced struvite formation from source-separated urine using seawater and brine as magnesium sources. Chemosphere 2013;93(11):2738-2747. doi: 10.1016/j.chemosphere.2013.09.025
[67] Khumalo N, Nthunya L, Derese S, Motsa M, Verliefde A, Kuvarega A, Mamba BB, Mhlanga S, Dlamini DS. Water recovery from hydrolysed human urine samples via direct contact membrane distillation using PVDF/PTFE membrane. Sep Purif Technol 2018. doi: 10.1016/j.seppur.2018.10.035
[68] Tilley E, Ulrich L, Lüthi C, Reymond P, Schertenleib R, Zurbrügg C. Compendium of Sanitation Systems and Technologies. Eawag: Swiss Federal Institute of Aquatic Science and Technology, Dübendorf, Switzerland: 2014. ISBN: 978-3-906484-57-0
[69] Merino Jimenez I, Greenman J, Ieropoulos I. Electricity and catholyte production from ceramic MFCs treating urine. Int J Hydrogen Energy 2017;42:1791-1799. doi: 10.1016/j.ijhydene.2016.09.163
[70] Sadin SR, Povinelli FP, Rosen R. The NASA technology push towards future space mission systems, presented at the IAF. In: International Astronautical Congress, 39th, Bangalore, India, October 8-15, 1988.

ID 069

Stem of faba bean as potential source for fermentative biohydrogen production

J. C. Gómora-Hernández[1,2], M. del C. Carreño-de-León[1], S. M. Fernández-Valverde[2*]

[1]División de Estudios de Posgrado e Investigación, Tecnológico Nacional de México/Instituto Tecnológico de Toluca, Av. Tecnológico s/n. Colonia Agrícola Bellavista, Metepec, Estado de México, C.P. 52149, México.
[2]bDepartamento de Química, Gerencia de Ciencias Básicas, Instituto Nacional de Investigaciones Nucleares, Carretera México-Toluca S/N, La Marquesa, Ocoyoacac, Estado de México, 52750, México.

ABSTRACT

Faba bean is a legume cultivated and consumed worldwide with a high content of proteins, carbohydrates, fiber and other trace elements such as calcium, iron and phosphorus. At the end of the faba bean harvest different residues are produced being stems the most rigid and recalcitrant fraction, which due to their high polysaccharides content are possible sources for value-add products production. Acid hydrolysis is a chemical method capable to disrupt the complex lignocellulosic matrix of stems and to produce monomeric sugars from cellulose and hemicellulose; these sugars are used for fermentative purposes. In this work, biohydrogen production was evaluated in mesophilic regime using 2 pure strains; *Clostridium butyricum* and *Enterobacter cloacae,* and stem of faba bean acid hydrolysates as the only carbon source. The concentration of the total reducing sugars and furfural obtained by hydrolysis with phosphoric acid were 11.82 g/L and 0.36 g/L respectively. Fermentation tests were performed in 20 mL vials prepared inside an anaerobic box, in which acid hydrolysate and minimum culture medium were mixed at different ratios. Microbial growth, biohydrogen production and pH were monitored throughout the experiment, while temperature and incubation time were set at 37 ± 1 ºC and 20 hours respectively. Microbial growth does not reached the stability phase since an increase in sugar loading rise the bacteria concentration, similar behavior was observed for volumetric biohydrogen production reaching a maximum of 3 mL with an initial sugar mass of 0.030 g. With 0.02 g of sugars, the volume of biohydrogen produced was lower; 2.23 mL, however at this sugar loading the maximum biohydrogen yield as function of either initial sugar mass or metabolized sugars was achieved; 111.05 mL H_2 / g initial sugar and 138.16 mL H_2 / g metabolized sugar respectively. Experimental results suggest that hydrogen yield can improve in a biorreactor increasing initial sugar loading since sugar bacterial degradation efficiency was around 80% in all experiments Stem of faba bean acid hydrolysates is a substrate with high potential to produce biohydrogen by dark fermentation. ***Keywords:*** biohydrogen; stem of faba bean; lignocelluloses; dark fermentation

1. Introduction

Hydrogen is well known to be the most promising energy source among all fuels due to its high calorific power (142 kJ / g), ability to produce water as the main combustion by-product in the form of steam and its high abundance. From these characteristic properties, hydrogen has been considered as a suitable option to replace fossil fuels, however, the most employed methods to produce this fuel; methane reforming, gasification and electrolysis are expensive, energy intensive and contribute to the carbon footprint of hydrogen by CO_2 emissions to the atmosphere. Hydrogen can also be produced by biological routes which are environmental friendly, cheaper than conventional methods and usually employ residues and wastes with high organic content as raw materials [1]. The main biological methods are fermentation and bio-photolysis, among this dark fermentation has several advantages such as high hydrogen rate and production, low reaction times, feasibility to use a wide range of materials from simple sugars to complex carbohydrates.

In the last years, lignocellulosic materials have been evaluated to produce biohydrogen; however, direct fermentation of lignocelluloses is difficult mainly caused by their recalcitrance and their complex physicochemical structure impeding the transformation of carbohydrates into clean hydrogen. The main idea of use lignocelluloses is to convert the most abundant natural source around the world into valuable products diminishing the cost of the processes since lignocelluloses are cheap and valorising waste agricultural residues [2]. Prior to dark fermentation, lignocelluloses are chemically or enzymatically treated in order to transform the cellulose and hemicellulose into their corresponding monomeric sugars which are easily fermentable by hydrogenic microorganisms. Different lignocellulosic materials have been employed for biohydrogen production in an acid hydrolysis – dark fermentation sequential process; *Agave tequilana* bagasse [3], corn stover [4], soybean straw [5], sugarcane bagasse [6] and wheat straw [7].

In Mexico, the major contributor of faba bean is Mexico State; after harvesting this agricultural crop generates a wide kind of lignocellulosic materials such as husks, leaves, branches and stems, being this last one not easily metabolized by cattle and usually disposed at open dumps generating atmospheric pollutants and plagues. Moreover, stem of faba bean is a natural source that has been scarcely studied for biotechnological purposes. The aim of this work is to evaluate the potential of stem of faba bean to produce monomeric sugars by acid hydrolysis and their subsequent feasibility in dark fermentative hydrogen production. The characterization of acid hydrolysate was reported and the effect of initial sugar concentration on hydrogen production is also discussed.

2. Materials and Methods

2.1 Raw material

Stem of faba bean samples employed in this study were collected from crops located at Xalatlaco, Mexico State. The samples were air dried and mechanically milled, sieved and particles with a diameter fewer than 250 µm were recovered and characterized as reported in previous work [8]. The composition of raw stem of faba bean was: 61.48 % holocellulose, 12.16 % lignin, 92.18 % total volatile solids and 7.82 % ashes. These less than 250 µm particles were also used in acid hydrolysis experiments.

2.2 Acid hydrolysis

For acid hydrolysis, 15 g of dried stem of faba bean particles were mixed with 225 mL of phosphoric acid solution in a 500 mL GL55 vial and homogenized. The vial was sealed and heated in a furnace without agitation. The hydrolysis temperature, acid concentration and reaction time were selected in basis of a previous experience [9], they were: 110 ºC, 1.34 M phosphoric acid and 300 minutes respectively. After hydrolysis, vial was cooled at room temperature during 15 minutes and the phases were separated by filtration. The experiment was carried out by duplicate. Liquid phase also known as hydrolysate was used to determine the concentration of both reducing sugars and furfural. The total concentration of reducing sugars was determined by 3-5 dinitrosalicylic acid method [10] in a *Perkin Elmer Lambda XLS* UV-Vis spectrometer using a wavelength of 540 nm and glucose as reference sugar, while furfural was quantified in the same instrument at 277 nm. Glucose and furfural employed for calibration curves were analytical grade. The identification of individual sugars present in hydrolysates was performed by High Performance Anionic Exchange Chromatography coupled to Pulsed Amperometric Detector (HPAEC-PAD) [11].

2.3 Fermentative hydrogen production

Fermentation tests were carried out by duplicate. The media solution was composed of (g/L): K_2HPO_4, 10.5; KH_2PO_4, 4.5; $(NH_4)SO_4$, 1; and 1 mL L^{-1} of pre-sterilized 1M $MgSO_4*7H_2O$ solution. Acid hydrolysates were neutralized with magnesium hydroxide (Eq. 1) and the precipitated magnesium phosphate was separated by filtration. The remaining hydrolysate was autoclaved at 121 ºC during 15 minutes and used in fermentation tests as the only carbon source.

$$2H_3PO_4 + 3Mg(OH)_2 \rightarrow Mg_3(PO_4)_2 + 6H_2O \qquad \text{(Eq. 1)}$$

To evaluate the effect of initial sugar loading on biohydrogen production, 9 mL of the media solution (was mixed in 20 mL vials with the following volumes of hydrolysate: 0.5, 1.0, 1.5, 2.0, 2.5, 3.0 and 4.0 mL. Vials were prepared inside an anaerobic box in nitrogen atmosphere maintaining the aseptic conditions with a UV lamp. After that, vials were sealed with butyl rubber stoppers and aluminum crimp seals, inoculated with 100 µL of both *Clostridium butyricum* and *Enterobacter cloacae,* and incubated at 37 °C ± 1 °C during 20 hours. The produced hydrogen was quantified in a *Varian 3600* chromatograph equipped with Thermal Conductivity Detector (TDC) and Porapak Q40 packed column using Argon as carrier gas. The pH of the leachates and the concentration of reducing sugars were determined in a potentiometer and by 3-5 dinitro salicylic acid method respectively, while microbial growth was studied in a Petroff-Hausser counting chamber as described in a previous work [8].

3. Results and Discussion

3.1 Composition of stem of faba bean hydrolysate

The reducing sugars and furfural concentrations determined in acid hydrolysate were: 10.05 ± 0.4 g L^{-1} and 399.14 ± 23.63 mg L^{-1} respectively. This sugar concentration corresponds to a sugar yield of 15.07 g / 100 g raw stem of faba bean which was slightly lower than the 16.6 g / 100 g raw stem of faba bean achieved in a previous work at 130 °C, 1.34 M phosphoric acid and 120 minutes reaction time [8]. After neutralization with magnesium hydroxide, the concentration of reducing sugars not only increased but also the amount of furfural diminished reaching the respectively following values; 11.82 ± 0.03 g L^{-1} and 359.08 ± 8.33 mg L^{-1}. The sugar yield obtained after hydrolysate neutralization was 17.73 g / 100 g raw stem of faba bean, this value is in the range described by our research team in a previous work [9]. The low sugar yield obtained with stem of faba bean is attributed to its rigid and mechanical resistance which is higher than other lignocellulosic materials such as leaves, husks, stover, peels and straw. The increase in reducing sugars concentration after hydrolysate neutralization can be attributed to a partial evaporation of both water and furfural during neutralization stage, this fact is supported by the diminishing in furfural concentration in neutralized hydrolysate.

The identification of individual sugars performed by HPAEC-PAD showed that glucose was the most abundant monomeric sugar in stem of faba bean acid hydrolysate. As seen in Fig. 1, arabinose and trehalose were also detected in hydrolysate; this last one is a disaccharide composed by 2 molecules of glucose cross-linked by α1-1 glycosidic bond, is naturally found in bacteria, algae and fungus and even it can be located in some legume nodules such as faba bean and bean [12]. In addition, according to Akobi *et al.* [13], metabolic activity of hydrogen producing microorganisms is inhibit at furfural concentrations

higher than 1 g L^{-1}, this concentration is much higher to that determined in this study. The presence of glucose as the major sugar and the low concentration of furfural suggest that stem of faba hydrolysate is a suitable substrate for fermentative biohydrogen production without detoxification stage.

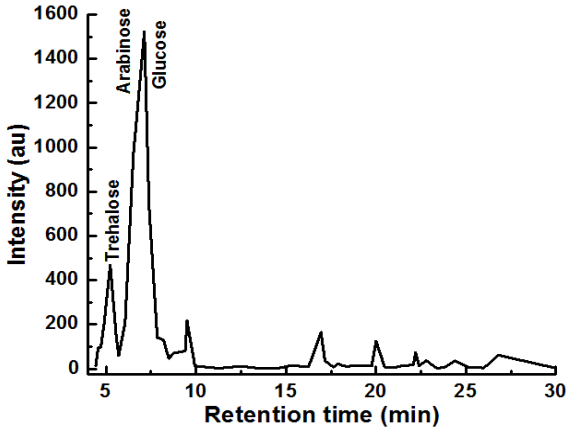

Fig. 1. Chromatogram of stem of faba bean hydrolysate obtained by HPAEC-PAD

3.1 Hydrogen production from stem of faba bean hydrolysate

The maximum hydrogen production was 3.1 mL obtained in the experiment performed with 3 mL of hydrolysate. In Fig. 2 can be appreciated that an increase in initial sugar loading is associated with a raise in biohydrogen production, an opposite behavior was observed for pH reaching the minimum value of 6.2 with 3 mL of hydrolysate.

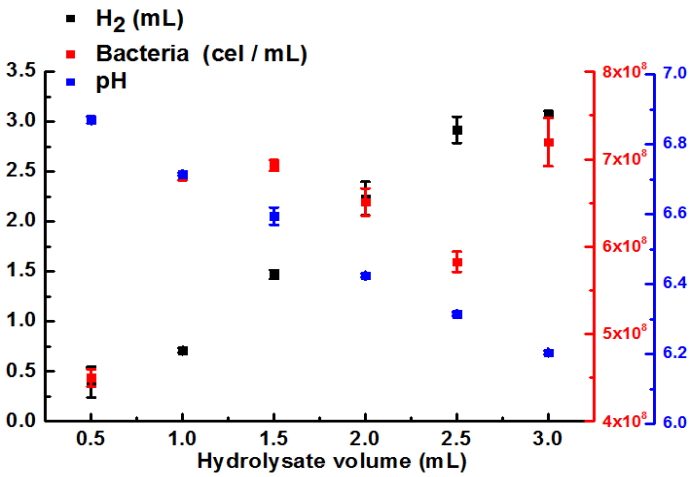

Fig. 2. Hydrogen production, microbial growth and pH obtained during hydrolysates fermentation

In all experiments, bacteria grew well but the stability phase was not observed, this behavior suggest that stem of faba bean hydrolysate is a suitable carbon source for microorganism's development, and thus the ratio between hydrolysate and minimum media could increase in order to produce a major amount of hydrogen.

Table1 summarizes experimental data obtained during fermentation of hydrolysates. As can be seen in this table, the sugar degradation efficiency was around 80% for each test and the maximum hydrogen production (3.07 mL) was associated to the minimum pH value (6.21) which can be due to a better acidogenic activity of hydrogen producing bacteria. Despite this, the highest sugar degradation efficiency was 85.12 % observed in the experiment performed with 2.5 mL of hydrolysate and the highest hydrogen yield given in mL H_2 per g of degraded sugar was 138.16 determined with 2.0 mL of hydrolysate and 0.020 g of sugar as initial amount of substrate. This hydrogen yield was similar to that reported previously by López-Hidalgo *et al.* [7], who determined a maximum of 140.1 mL H_2 / g sugar during fermentation of wheat straw hydrolysates with *Escherichia coli*.

Since glucose was the major sugar in hydrolysate, the hydrogen yield can also be approximately calculated in terms of mol H_2 / mol glucose. At hydrolysate volumes higher than 1.5 mL the hydrogen yield was raise to 1.0 being 1.12 mol H_2 / mol glucose the highest yield determined with 2.0 mL of hydrolysate and 0.73 mol H_2 / mol glucose the lowest value obtained with 1 mL of hydrolysate. These yields are higher to that reported in other works [14], and show the feasibility of stem of faba bean to produce reducing sugars and biohydrogen with low furfural concentration.

Table1. Hydrogen production by fermentation of Stem of faba bean hydrolysates

Hydrolysate (mL)	pH_{in}	pH_{end}	H_2 (mL)	$Sugar_{in}$ (g)	$Sugar_{end}$ (g)	$Sugar_{deg}$ (%)	mL H_2 / g $sugar_{deg}$
0.5	6.95	6.87	0.39	0.005	0.0013	74.65	104.46
1.0	6.94	6.72	0.71	0.010	0.0022	78.11	90.47
1.5	6.94	6.59	1.47	0.015	0.0034	77.54	125.82
2.0	6.94	6.43	2.23	0.020	0.0039	80.38	138.16
2.5	6.93	6.31	2.92	0.025	0.0037	85.12	136.49
3.0	6.93	6.21	3.07	0.030	0.0063	79.03	129.01

4. Conclusion

Stem of faba bean is a suitable material to produce reducing sugars by phosphoric acid hydrolysis. Experimental conditions promote sugars production avoiding their decomposition into inhibitory bacterial compound such as furfural. The identification of individual sugars revealed that glucose was the main monomeric sugar in hydrolysate. Stem of faba bean hydrolysate is suitable substrate for both microbial growth and biohydrogen production.

Acknowledgements

J.C. Gómora-Hernández thanks CONACYT for Doctoral scholarship and also ININ. Authors thank Dr. Mercedes G. López from CINVESTAV-Irapuato for the HPAEC-PAC analysis, technicians of the chemistry department of ININ and also TNM-ITT and ININ.

References

[1] Srivastava N., Srivastava M., Malhotra B.D., Gupta V.K., Ramteke P.W., Silva R.N., Shukla P., Dubey K.K., Mishra P.K. Nanoengineered cellulosic biohydrogen production via dark fermentation: A novel approach. Biotechnol Adv. 2019;37:107384.

[2] Nagarajan D., Lee D.J., Chang J.S. Recent insights into consolidated bioprocessing for lignocellulosic biohydrogen production. Int J Hydrogen Energ. 2019;44:14362-14379.

[3] Valdez-Guzmán B.E., Ríos-Del-Toro E.E., Cardenas-López R.L., Méndez-Acosta H.O., González-Álvarez V., Arreola-Vargas J. Enhancing biohydrogen production from Agave tequilana bagasse: Detoxified vs. undetoxified acid hydrolysates. Bioresour Technol. 2019;276:74-80.

[4] Rodríguez-Valderrama S., Escamilla-Alvarado C., Magnin J.P., Rivas-García P., Valdez-Vazquez I., Ríos-Leal E. Batch biohydrogen production from dilute acid hydrolyzates of fruits and vegetables wastes and corn stover as co-substrates. Biomass Bioenerg. 2020;140:105666.

[5] Han H., Wei L., Liu B., Yang H., Shen J. Optimization of biohydrogen production from soybean straw using anaerobic mixed bacteria. Int J Hydrogen Energ. 2012;37:13200-13208.

[6] Hu B.B., Li M.Y., Wang Y.T., Zhu M.J. Enhanced biohydrogen production from dilute acid pretreated sugarcane bagasse by detoxification and fermentation strategy. Int J Hydrogen Energ. 2018;43:19366-19374.

[7] Lopez-Hidalgo A.M., Sánchez A., De León-Rodríguez A. Simultaneous production of bioethanol and biohydrogen by Escherichia coli WDHL using wheat straw hydrolysate as substrate. Fuel. 2017;188:19-27.

[8] Gómora-Hernández J.C., Alcántara-Díaz D., Fernández-Valverde S.M., Hernández-Berriel M.C. Biohydrogen production by anaerobic digestion of corn cob and stem of faba hydrolysates. 2016. XVI International Congress of the Mexican Hydrogen Society. 2017: 1-6. Doi: 10.1109/CSMH.2016.7947659.

[9] Gómora-Hernández J.C., Carreño-De-León M.C., Fernández-Valverde S.M. Dilute phosphoric acid hydrolysis of stem of faba for reducing sugars production. Proceedings of the XVIII International Congress of the Mexican Hydrogen Society. 2018;5: 526-536.
[10] Miller G.L. Use of dinitrosalicylic reagent for determination of reducing sugars. Anal Chem. 1959;31:426-428.
[11] Mellado-Mojica E., Seeram N.P., López M.G. Comparative analysis of maple syrups and natural sweeteners: Carbohydrates composition and classification (differentiation) by HPAEC-PAD and FTIR spectroscopy-chemometrics. J Food Compos Anal. 2016;52:1-8.
[12] Müller J., Xie Z.P., Staebeliln C., Mellor R.B., Boller T., Wiemken A. Trehalose and trehalase in root nodules from various legumes. Physiol Plant. 1994;90:86-92.
[13] Akobi C., Hafez H., Nakhla G. Impact of furfural on biological hydrogen production kinetics from synthetic lignocellulosic hydrolysate using mesophilic and thermophilic mixed cultures. Int J Hydrogen Energ. 2017;42:12159-12172.
[14] Chun-Min L., Chen-Yeon C., Wan-Yu L., Ya-Chieh L., Shu-Yii W., Yen-Ping C. Biohydrogen production evaluation from rice straw hydrolysate by concentrated acid pretreatment in both batch and continuous systems. Int J Hydrogen Energ. 2013;38:15823-15829.

Renewable energy systems

ID 007

Electrolyte flow influence analysis in the behaviour of 15 kW alkaline water electrolysis stack

Valeria Juárez Casildo[1,2], Mónica Sánchez Delgado[2*], Rosa de Guadalupe González Huerta[1*]

[1]ESIQIE-IPN, Lab. Electroquímica y Corrosión, UPALM, CP 07738, Ciudad de México
*rosgonzalez_h@yahoo.com.mx
[2]Centro Nacional del Hidrogeno (CNH2), Prolongación Fernando El Santo s/n, 13500 Puertollano, Ciudad Real, España
*monica.sanchez@cnh2.es

ABSTRACT

It is well known that a really important problem in electrochemical proceses is the bifasic mixtures generation; when a electric potenitial is induced to an alkaline electrolyzer, the water molecule is broken producing H_2 and O_2, in consequense the electrolyte (KOH) starts moving by natural convection (NC) [1],[2] to a separator vessels where the electrolyte is desgasified.

The gas bubbles act as electrical insulatings, therfore the electrolyte conductivity becomes low and the ohmic resistances increases and a high electric consum. There are diferent ways to eliminate gas bubbles between electrodes, the easier one is pumping the electrolyte. Many estudies has been done in laboratory scale, they found that increasing de recycling flow (forced convection (FC)) improve the electrical eficiency by reducing the voltage consumption. On the other hand, diferent studies has been indicated that increasing flow has a negative efect in the gases purity [3],[4].

In this work, two flow profiles (NC and FC) has been evaluated in a 15 kW alkaline electrolyzer, wich has an active area of 1000 cm^2. In this complex system the CN is equal to 1.7 L/min and it was found that a low current densities becomes unestable increasing the void fraction. Also it has been demostrated that diferent flow values do not has influence in the V-i curve, but it has an impact in the gases difusion wich is stronger at low current densities; HTO (Hydrogen to oxygen) increased from 2.3% to 2.6 % vol and OTH (oxygen to hydrogen) from 0.14% to 0.34%vol. In addition, it has been found that system thermal management was improved by increasing the reciclying flow.

Keywords: Electrolyte flow rate; Energy consumption; Gas purity.

1. Introduction

An important problem in electrochemical processes is the convection induced by bubbles, when electric current is applied to an alkaline electrolyser (AEL), the consequent gases production (H_2 and O_2) generates biphasic mixtures as a result of the water molecule breakdown, that initiates the solution movement in natural convection, which arises from heterogeneous reactions (electrolyte-electrode interaction) and significantly, due to the densities difference between phases. Gas bubbles act as electrical insulators, so their presence between electrodes promote electrolyte conductivity decrease considerably, increasing the electrolyser ohmic resistance, resulting in a higher voltage demand.

Different researchers [1,2] have found, high voltage demand is more significant at high currents when gas generation is higher and more relevant at small distances between electrodes. Therefore, there will be a significant increase in the energy consumption to carry out the electrolysis, which implies a less efficient process. Furthermore, the presence of many gas bubbles inside an electrolysis cell could drive different problems such as instantaneous pressure drops and damage on cell components.

Studies made at the cell level affirm that using forced convection (FC) reduces the limitations due to mass transfer and favours bubbles transport, so that they can be removed from the system easily, avoiding the gases mixing through the diaphragm. According literature, the use of FC has the following effects in an alkaline electrolyser [5]:

1. The ohmic overpotentials reduction, increase the alkaline electrolyser overall efficiency, reduce the residence time of the bubbles, and allow to renew the electrolyte inside the cell at greater speed, decreasing the void fraction between electrodes.
2. Using a pump to drive the electrolyte increases the energy consumption of the entire process affecting the system overall efficiency, therefore, the key criterion in the implementation of FC in an electrolysis system is: the pump energy consumption have to be less than the energy quantity could be reduced in the electrolyser.
3. According to Oviedo J. [6], a fraction of gas dissolved in the electrolyte could return to electrolysis circuit due to pump suction, although the introduction of gas traps or baffles in the separators could reduce this effect.

Several researches has focused on studying the effect of electrolyte flow in an alkaline electrolysis system, they can be classified according to their objectives; On one hand, there are studies whose goal is to determine the flow impact on the voltage demand taking into account the distribution and size bubbles. On the other hand, there are those whose main objective is to analyse how the recirculation flow variation influences the gases purity, where issues such as diffusion, gas solubility and “crossover” effect are involved.

Zhang et al [6], found that bubbles diameter that come off the electrode surface was drastically reduced when forced convection applied due to the drag and buoyancy forces created by the electrolyte flow.

Haug [4], demonstrated that gas quality decreases significantly with high recirculation flow rates at the cell level, the amount of hydrogen going to the oxygen side (HTO) increases with high flow values. Therefore, the author recommends that optimal electrolyte flow in the system must minimize the gases mixing and allowing good process thermal management.

Applying forced convection at stack level decreases the pressure drops and eliminates hot spots in electrolysis cells. Therefore, it can be affirmed that large scale FC improves the process thermal management.

2. Materials and Methods

2.1. Alkaline electrolysis 15-kW test bench

Centro Nacional del Hidrogeno (CNH2) developed an alkaline electrolysis test bench, which allows characterizing and validating alkaline electrolysers up to 15 kW (Error! Reference source not found.).

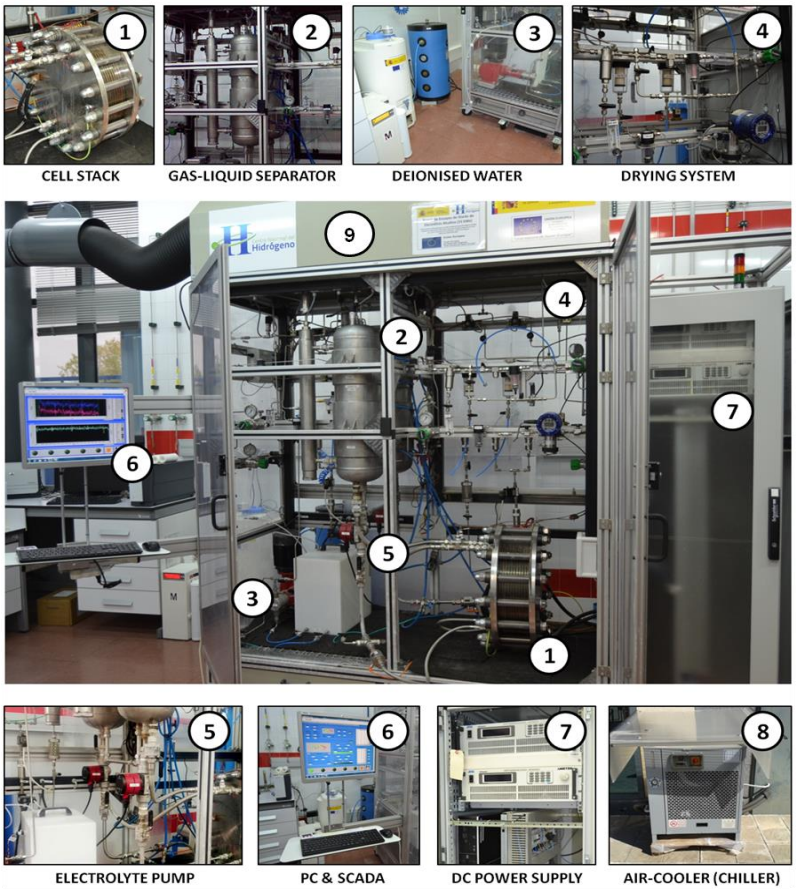

Fig. 1. 15-kW alkaline water electrolysis test-bench developed by CNH2

The test bench consists of the following modules:

i. *Balance of Plant (BoP):* includes the process equipment and instrumentation as electrolyser (1), liquid-gas separation system (2), gas purification stages (4), and electrolyte pumping system (5).
ii. *Power supply (7):* two direct current sources (250 A) in serial connection.
iii. *Monitoring, process control and data acquisition (6):* collects all the information on electrical signals, both analog and digital, from the test bench.
iv. *Auxiliary services*: involves external systems that are highly necessary for the control of process variables and safety issues as deionized water supply (3), cooling water supply (8) and air hood (9).

The test bench has a maximum hydrogen production capacity of 3Nm^3/h and works with pressures of up to 30 bar. It is a facility designed with wide operating intervals, as flexible as possible, to have the ability to evaluate prototypes of different stacks configurations.

2.2. Experimental sample

The experimental sample of this work is an alkaline electrolyser stack (S10) with area of 1000 cm^2, it has 12 cells (zero-gap) in serial connection. Its maximum working pressure is 10 bars and its operating range goes from 100 to 600 A (Error! Reference source not found.**).**

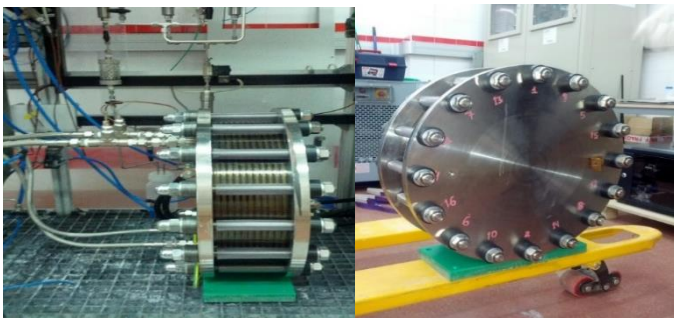

Fig. 2. Experimental sample S10, alkaline electrolysis stack (zero-gap cell).

2.3. Evaluation tests Curve i-V

The electrolyser characterization was carried out using the standardized CNH2 protocol for construction of the i-V curve, that is, the voltage response for each current applied to the stack is measured. This procedure begins with a starting stage (250 A) for 5 min, followed by the stabilization stage (400 A, constant pressure and temperature) for 30 min and finally, the i-V curve stage where a current sweep is made from 500 to 100 A in steps of 100 A; each current step is evaluated for 30 min.

The construction of V-i curve was performed using the protocol for regulated flows (natural convection, 0.5, 1, 2, 4 and 6 L), this experiment had as goal to study the influence of the flow of recirculated electrolyte (KOH 35%) on demanded voltage by the electrolyser. The test plan is presented in Error! Reference source not found.

Table. 1 Test plan for i-V curve under forced convection conditions.

TEST	OPERATION PARAMETERS			
	Pressure (bar)	**T (ºC)**	**[KOH] (%)**	Electrolyte flow rate
E00	**7 bar**	**75 ºC**	**35%**	**Natural Convection (NC)**
E01	7 bar	75 ºC	35%	0,5 L/min
E02				1 L/min
E03				2 L/min
E04				4 L/min
E05				6 L/min

In order to study the effect of electrolyte flow rate on the process thermal management, constant current (400 A) studies were carried out by modifying the recirculation flow rate. The experiments were made according to the operation conditions described in Error! Reference source not found.

Table. 2. Tests plan at forced convection and constant current

Test	OPERATION PARAMETERS				
	Current (A)	**T (ºC)**	**[KOH] (%)**	**Pressure (bar)**	**Electrolyte flow rate**
E08	400	60 ºC	35%	7 bar	1-10 L/min
E09	400	60ºC	35%	7 bar	Natural convection$_{@400\ A}$-12 L/min

3. Results and Discussion

Error! Reference source not found. shows the effect of the recirculation flow rate on the characteristic curve of the 15kW alkaline electrolyser.

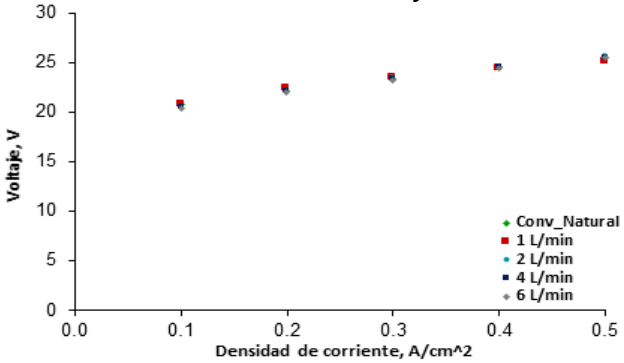

Fig. 3. Electrolyte recirculation flow rate impact on the i-V curve.

In the previous figure, the curves made at different flow conditions overlap each other and it is not possible to see significant differences between the one corresponding to natural convection and the one that belongs to the maximum flow rate evaluated (6 L / min); therefore, for this system at conditions of 7 Bar, 75ºC, in the range of current density and recirculation flow rates studied, **no influence of forced convection was found on the potential demanded by the 15 kW stack.**

In Error! Reference source not found., the i-V curve was zoomed and compared with the temperature behaviour for each flow rate evaluated. Small differences are detected between curves, which are not due to the change in flow directly but correspond to changes in temperature, which is highly influenced by forced convection.

The curve of 1 L/min shows relatively greater differences; with 0.5 A / cm2 it can be observed a voltage decrease because at this point, the system temperature is 80ºC, that is, 5 ° C above the setpoint (75°C) promoting the demanded potential decreasing. While at low current densities the potential is higher because temperature falls 10 ºC below setpoint. Taking into account that flow in natural convection oscillate between 1.4-2 L/min, at 1 L/min the system operates below its natural conditions, due to this, at high current densities the temperature rises too high because the flow rate it is not enough to eliminate heat.

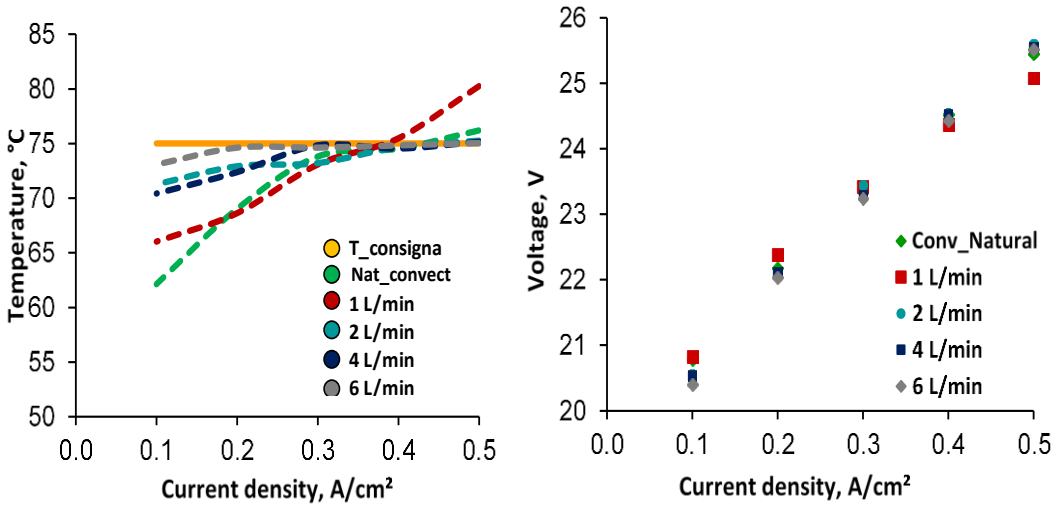

Fig. 4. Relationship between temperature and voltage for each recirculation flow point

Error! Reference source not found. shows that high electrolyte flow rate promote hydrogen diffusion to the oxygen side (HTO), for example, at 0.2 A / cm2 in natural convection, there is a concentration of 1.6% vol, while with 6 L / min (FC) is 2.12% vol. With high densities, there is no great difference in the data obtained due to the high rate of gas production that leads to short residence times in the electrolyser.

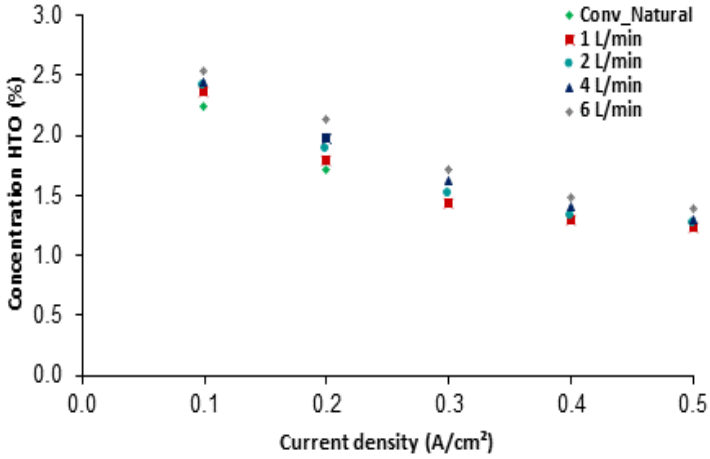

Fig. 5. Electrolyte flow Influence on the hydrogen amount that goes to oxygen side (HTO)

Regarding the amount of oxygen that goes to the side of hydrogen (OTH), it was found that high electrolyte flows lead to a significant increase in OTH concentration (Error! Reference source not found.). This effect may be since higher electrolyte flow rates promote a greater amount of dissolved oxygen, therefore increasing the amount of gas that is transferred through the separator. It is interesting to note that these results obtained for the 15-kW stack are comparable with those reported by Haug [4], who at the cell level studied the effect of flow on the gases purity.

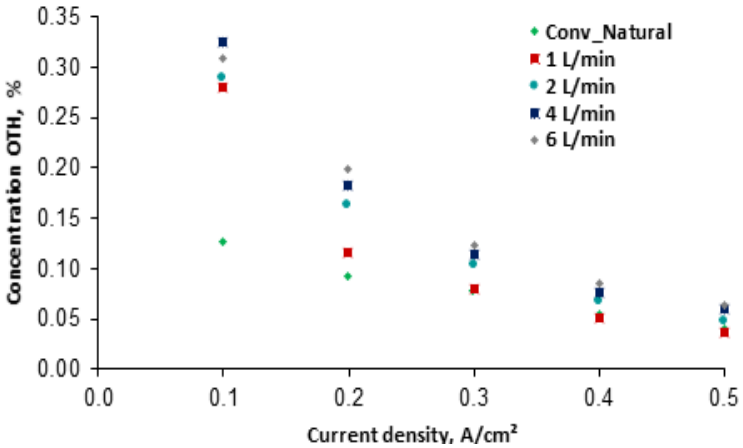

Fig. 6. Electrolyte flow Influence on the oxygen amount that goes to hydrogen side (OTH)

Error! Reference source not found. shows the results of the experiments carried out at 400 A y 60ºC at different flow values; in the first one it was evaluated from 1 L /min to 12 L/min and in the second one, natural convection 10 and 12 L/min were analyzed.

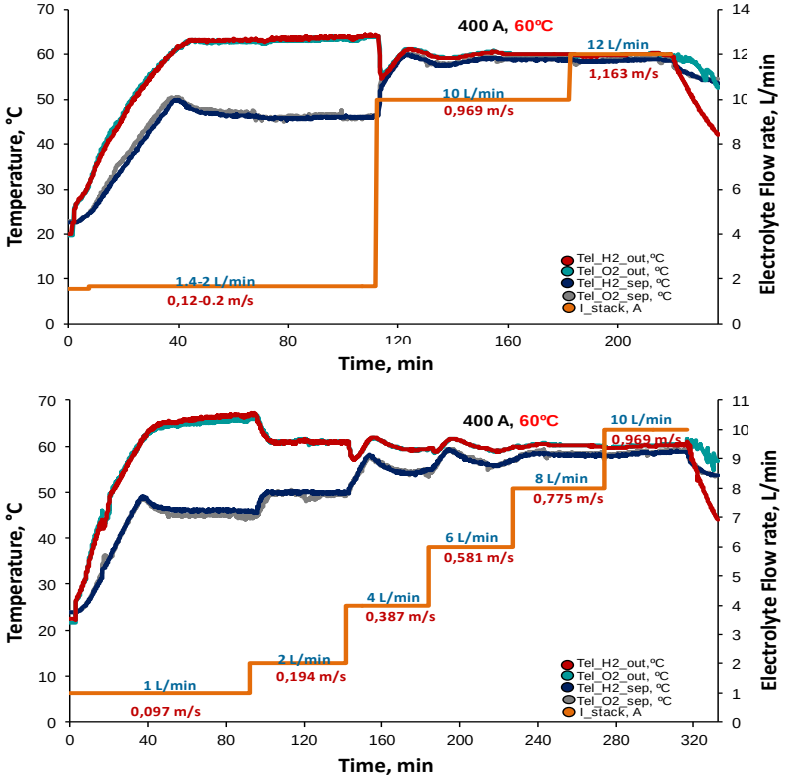

Fig. 7. Temperature evolution over time as a function of the recirculation flow.

In the previous figure it is observed that temperature response to the flow change is immediate, in addition to the fact that stack output currents and the separator output become similar with the increase electrolyte flow, on the other hand, the oscillations are reduced until you have a stable system. It is also possible to appreciate the drastic change that exists when going from natural convection to forced circulation with high flow rates, where the flow is not enough to remove heat from the stack, causing the outlet temperatures of the separators to become very cold and the electrolyser outlet get too hot causing big differences.

4. Conclusions

It was determined that in the studied flow rate interval, there is no influence of the recirculated flow on the potential demanded by the stack. It was shown that the conclusions obtained in the bibliography where at the cell level and small dimensions the voltage decreases with the increase in the flow, are not fulfilled in medium-scale systems.

It was shown that any variation in voltage present in the i-V curve is due to changes in the temperature of the system, which is strongly influenced by the amount of electrolyte that enters and leaves the electrolyser per unit time.

The implementation of forced convection has great benefits in thermal management: higher recirculation flow rates 4-6 L / min allow to maintain constant temperature in a curve i-V test in almost entire range of current densities studied. In the experiments carried out at constant current, it was found that large recirculation flow rates (10-12 L / min) allow reaching a stable regime

Acknowledgements

Authors thank the financial support from Instituto Politecnico Nacional, received through the multidisciplinary project 2024 and innovation project 20200935, the CONACYT project CEMIEOcean-249795: Transversal Line I-LT1 and project CB A1-S-15770.

References

[1] K. N. Javor y R. G. Comptom, «Review Article Natural convection effects in electrochemical systmes,» Current Opinion in Electrochemistry, vol. 7, pp. 118-129, 2018.

[2] R. Hreinz, L. Abdelouahed y e. al., «Electrogenerated bubbles induced convection innarrow vertical cells: A review,» Chemical Engineering Research and Design, vol. 100, pp. 268-281, 2015.

[3] H. Philipp, M. Koj y T. Thomas, «Influence of process conditions on gas purity in alkaline water electrolysis,» Int. Journal of Hydrogen Energy, pp. 1-13, 2016.

[4] P. Haug, K. Bejarne y K. Mattias, «Process modelling of an alkaline water electrolizer,» Int. Journal of Hydrogen energy, vol. 42, pp. 15689-15707, 2017.

[5]J. Oviedo, Optimización Fluidodinámica de una celda de eectrólisis alcalina para la producción de hidrógeno, Ciudad Real, España, 2015.

[6] Z. Houcheng, S. Shanhe, L. Guoxing y C. Jincan, «Configuration Designs and Parametric Optimum Criteria of an Alkaline Water Electrolyzer System for Hydrogen Production,» Int. Journal of electrochemical science, vol. 6, pp. 2566-2580, 2011.

ID 033

Dye-Sensitized Solar Cells - Comparative Study of Sensitizers and Co-Sensitizer Effects of a New Tetrazole Derivative

L. da Silva[1*], R. Benavides[1], D. Morales-Acosta[1], H. S. Freeman[2]

[1]Centro de Investigacion en Quımica Aplicada, Blvd. Enrique Reyna H. 140, Saltillo, 25294, Mexico.
[2]Fiber and Polymer Science Program, North Carolina State University, USA
[*]E-mail: luciano.dasilva@ciqa.edu.mx

ABSTRACT

Dye-sensitized solar cell (DSSC) is a semiconductor photovoltaic device that directly converts solar radiation into electric current. A typical DSSC consists of a mesoporous photoanode with a dye-sensitized titanium dioxide (TiO_2) film, an electrolyte containing iodide/triiodide (I^{-1}/I_3^{-1}) redox couple, and a counter electrode with platinum (Pt) catalyst. Upon the absorption of light energy, a photo-excited electron is injected from the excited state of the dye (Dye*) into the conduction band of the TiO_2. However, the immobilization of the adsorbing dye molecules onto the surface of semiconducting metal oxide nanoparticles is crucial for initiating an electrical current, via the injection of electrons, which collectively act as the working electrode of a DSSC. Herein we report the synthesis, characterization and evaluation of the compound N,N-diethyl-4-{[(4'-nitro-2'-tetrazoyl)phenyl] diazenyl}aniline (**SD-1**). This dye was incorporated into DSSCs as sensitizer and a co-sensitizer with **HD-2** dye, to prepare the photoanode for a dye-sensitized solar cell (DSSC). **HD-2** is a dye described by H. Chemma et al. and is considered as an efficient sensitizer based on benzodioxan-stilbazole ancillary ligand. The photovoltaic performance was evaluated and compared with the co-sensitizer deoxycholic acid (**DCA**). The energy conversion efficiency of the DSSC was 8.38 % from **HD-2 – DCA**, 7.81% from **HD-2 – SD-1**, and 1.32% from **SD-1 – DCA**. The latter results suggest that steric effects restrict the anchoring ability of the tetrazole groups, by hindering their approach to TiO_2 surface and by restricting the coplanarity of the system. However, this effect is not significantly important when the **SD-1** is used as co-sensitizer for **HD-2**, which showed similar conversion efficiency as the **DCA**.

Keywords: *Tetrazole; solid electrolytes; sensitizers; co-sensitizer; dye-sensitized solar cell.*

1. INTRODUCTION

Dye-sensitized solar cells (DSSCs) based on nanocrystalline oxide semiconductors are a type of solar cells that convert the sun's energy to electric energy using a sensitizing dye [1]. Among the fundamental concepts for the development of the dye-sensitive solar cell is the preparation of a highly porous nanocrystalline TiO_2 film (which provides a large area of inherent adsorptive surface), containing a dye with a high molar extinction coefficient anchored chemically to the surface, to form the working electrode of the solar cell [2]. In this concept, a typical DSSC consists of a nanoparticle TiO_2 photoelectrode sensitized by a ruthenium bipyridine complex and a platinum counter-electrode separated by an iodide-triiodide (I-1/I3-1) liquid electrolyte [3]. In DSSCs, the photosensitizer and its interactions with nanocrystalline TiO_2 film are the key point to obtain high photoconversion efficiency, this is, high efficiency to harvest light and inject electrons. Until now, hundreds of photosensitizers have been designed and synthesized for improving the photovoltaic performance and exploring the relationship of structure and performance of DSSCs. Among them, the ruthenium complex dyes, such as N719, N3, C101 and HD-14, have dominated the highly efficient DSSCs for many years [4]. For example, the efficiency of DSSC based on N719 has exceeded 12% [5]. However, the scarcity of ruthenium metal is a big problem for the future commercial development and applications. Compared with the metal complex dyes, the metal-free organic dyes have some advantages, such as the relative simplicity of synthesis and purification, convenient structural modification and high molar extinction coefficient. Thus, searching new metal-free organic dyes with excellent photovoltaic performance has attracted considerable attention. Many organic dyes, which exhibit comparably excellent photovoltaic performances to ruthenium complexes, have been designed and obtained [6]. However, designing the new organic dyes via simple and convenient synthetic routes is still a challenge in DSSCs. In last decade, various kinds of functional groups and their derivatives have been combined to generate D-π-A organic dyes. Among them, an arylamine group, thiophene derivatives and cyanoacrylic acid moiety are the most common subunits that act as an electron donor, p-linker, and an electron acceptor/anchoring group, respectively. Especially, the p-linker as a bridge that connects the donor and acceptor exerts a significant influence on the transmission and recombination of electron during the photoelectric conversion process in DSSCs [7]. The introduction of 1,2,3-triazole group as an electron deficient unit in the linear D-π-A organic dyes can effectively enhance the open-circuit voltage of the DSSCs with good efficiency [15]. The introduction of tetrazole group as an anchoring group has been pursued. The photovoltaic results further obtained with the tetrazole derivative outperformed those of the carboxylic analogue showing a significant increase in photovoltage for a device using the tetrazole dye [8].

Much effort has been paid to widen to the light absorption efficiency of the dyes and the charge transfer efficiency for the crystalline structure of TiO_2. Unfortunately, their photovoltaic performances are still not significantly improved due to their aggregation during the photoelectrode fabrication process. Thus, co-sensitization using two or more sensitizers is an effective approach to achieve panchromatic harvest [9]. Co-sensitization also termed as “dye-cocktail” method to DSSCs, is a widely followed strategy. Due to the complexity associated with the system formed by only one dye, like charge recombination, dye aggregation, and semiconductor surface protonation, that are important and unwanted

processes, co-sensitization is employed [10]. The key criteria for a potential dye co-sensitizer includes (a) a lowest unoccupied molecular orbital (LUMO) energy level that lies above the semiconductor conduction band, (b) a highest occupied molecular orbital (HOMO) energy level that lie below the electrolyte redox potential, (c) presence of an anchor group to provide coupling between dye and semiconductor, (d) directed intramolecular charge transfer on photoexcitation from donor to semiconductor through the anchor, (e) good chemical compatibility between dye sensitizers, (f) reduced the charge recombination and (g) should be suitable for the competitive adsorption without aggregation on the working electrode (nanocrystalline TiO_2 film) surface [11].

The co-sensitizations of organic dyes have been extensively investigated, which exhibit an effective and promising photovoltaic performance [11]. Here we report the photovoltaic performance of DSSCs derived from dye of **HD-2**, dye **SD-1** and co-adsorbent **DCA** (Fig. 1).

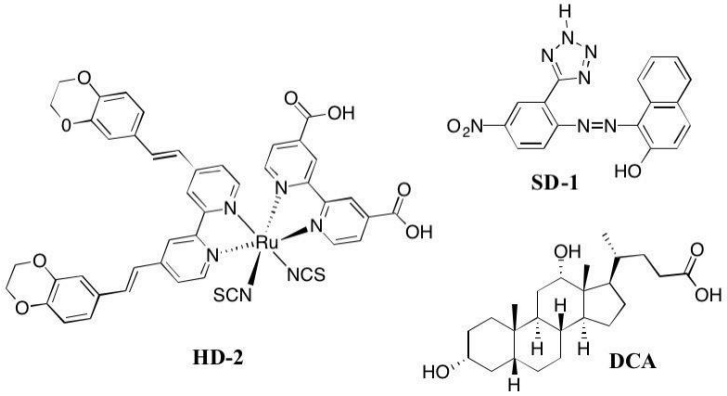

Fig. 1. Molecular structures of dye **HD-2**, dye **SD-1** and co-adsorbent **DCA**.

2. MATERIALS AND METHODS

2.1. General Information

The solvents and chemicals were purchased from Sigma-Aldrich, Fisher Scientific or TCI-America and used as received. The mass spectrometry analysis was carried out on a high-resolution mass spectrometer – Thermo Fisher Scientific Exactive Plus MS, a benchtop full-scan OrbitrapTM mass spectrometer using Heated Electrospray Ionization (HESI). Samples were dissolved in methanol and sonicated for 15 min. They were then diluted 1:1 with 20 mM ammonium acetate and analyzed via syringe injection into the mass spectrometer at a flow rate of 10 mL/min. The mass spectrometer was operated in negative ion mode. FT-IR (ATR) spectra were recorded on a Nicolet Nexus 470 FT-IR spectrometer (Thermo Scientific, USA) and UV-Visible spectra were measured by using Cary 300 spectrophotometer. Fluorescence, recorded at room temperature on a Fluorolog-3 spectrofluorometer (HORIBA Jobin Yvon Inc.). ^{1}HNMR (Hydrogen Nuclear Magnetic Resonance) and ^{13}CNMR (Carbon Nuclear Magnetic Resonance) spectra were recorded in a Bruker 500 MHz spectrometer.

2.2. Synthesis

2.2.1. 5-(2'-Amino-5'-nitrophenyl)tetrazole (1)

The synthesis of the tetrazole system was carried out as depicted in the literature [11]. To a solution of 2-amino-5-nitrobenzonitrile (1) (7.0 g, 0.043 mol) in 28 mL N,N-dimethyl formamide (DMF) was added sodium azide (11.0 g, 0.17 mol) and ammonium chloride (9.0 g, 0.17 mol). The mixture was stirred for 24 h maintaining the temperature at 120 °C. The reaction mixture was cooled to room temperature and was poured into 50 mL of ice cold water. The mixture was acidified with concentrated HCl to pH 2. The precipitate formed was filtered off and the product was recrystallized from ethanol giving yellow crystals. Yield 65%; mp 264-266 ºC; $mp_{Lit.}$ 268-270 ºC [28]. FTIR-ATR v_{max} = 3420, 2710–2630 (br), 1613, 1597, 1504, 1292, 842. ^{1}HNMR (500MHz, $CDCl_3$) δ = 7.45 (s, 1H, C_6H_3), 7.05 (d, J=8.4 Hz, 1H, C6H3), 6.62 (d, J=8.4 Hz, 1H, C_6H_3) 3.38 (br s, 1H, CN4H). ^{13}CNMR (100 MHz, DMSO-d_6): 155.8 (1C), 137.3 (1C), 134.5 (1C), 117.1 (1C), 114.3 (1C), 112.6 (2C), 111.1(1C).

2.2.2. Synthesis of **1-{[(4'-nitro-2'-tetrazoyl)phenyl]diazenyl}naphtha-lene-2-ol** (**SD-1**)

5-(2-Amino-5-nitrophenyl)tetrazole (2.06 g, 0.01 mol) was dissolved in hydrochloric acid (20 mL) with stirring, then, the solution was cooled to 0 ºC in an ice-bath. A solution of sodium nitrite (0.69 g, 0.01 mol) in 5mL water, cooled to 0 ºC was added. The mixture was stirred for 30 min at 0 ºC to get the clear diazonium salt solution. The coupling component (2-naphthol, 6-benzoylamido-1-naphthol-3-sulfonic acid or N,N-diethylaniline) was dissolved in NaOH (15 mL, 1N) and then solution cooled down to 0 ºC. To this well stirred solution, the above diazonium salt solution was added slowly so that temperature did not rise above 4 ºC while maintaining the pH 4-5 by the action of a sodium acetate solution (10% w/v). The mixture was stirred for 3 h at 0 ºC. Finally, the solid obtained was collected by filtration, washed three times with cold water and dried. The crude product was recrystallized from hexane:ethylacetate (1:1), giving red crystals, 2,60 g, yield 72%; mp >300 ºC. FTIR-ATR: 1489.9 cm^{-1} and 1333.1 cm^{-1} (N-O stretch), 3546.8 cm^{-1} (N-H stretch of tetrazole). ^{1}HNMR, (500 MHz, DMSO-d_6): 9.02 (s, 1H), 8.43 (d, J=10 Hz, 1H), 8.42 (d, J=10 Hz, 1H), 8.23 (d, J=5 Hz, 1H), 7.86 (d, J=10 Hz, 1H), 7.68 (d, J=10 Hz, 1H), 7.58 (t, J=10 Hz, 1H), 7.46 (t, J=10 Hz, 1H) 6.64 (d, J=10 Hz, 1H). ^{13}CNMR (100 MHz, DMSO-d_6): 145.1 (1C), 143.1 (1C), 142.7 (1C), 133.3 (1C), 131.6 (1C), 129.6 (2C), 129.3(1C), 128.7 (1C), 127.6 (1C), 126.9 (2C), 123.4 (1C), 123.2 (1C), 122.6 (1C), 119.6 (1C), 116.7 (1C). HRMS (ESI Full) m/z: calcd for $C_{17}H_{12}O_3N_7$ $[M+H]^+$, 362.0996; Found, 362.0992.

2.2.4 Synthesis of **HD-2**. **HD-2** was synthesized according to the procedures reported by Cheema et al. [12].

2.3. Measurements of ground state oxidation potential (GSOP) by cyclic voltammetry

The experimental HOMO and E_{0-0} energy values for SD-1 was measured using a cyclic voltammetry (CV) whereas E_{0-0} was determined from the absorption onset of the relevant compound. The CV was carried in DMF with 0.1 M [TBA][PF_6] as an electrolyte at a scan rate of 50 mV s^{-1}. Glassy carbon was used as the working electrode (WE), Pt wire as counter electrode and Ag/Ag^+ in ACN was used as the reference electrode. Fc/Fc^+ was used as internal references, voltage measured was converted to NHE by addition of 0.63 V.

2.4. TiO_2 electrode preparation and device fabrication

The photo-anodes composed of nanocrystalline TiO_2 and counter electrodes were prepared using a known procedure [5]. Fluorine-doped tin oxide (FTO) coated glasses (2.2 mm thickness, sheet resistance of 8 U/cm^2, TEC 8, Pilkington) were washed with detergent, water, acetone and ethanol, sequentially. After this FTO glass plates were immersed into a 40 mM aqueous $TiCl_4$ solution at 70 ºC for 30 min and washed with water and ethanol. Thin layer (8-12 mm thick) of TiO_2 (Solaronix, Ti-Nanoxide D/SP) was deposited (active area,

0.18 cm^2) on transparent conducting glass by squeegee printing. After drying the electrodes at 120 °C for 6 min, scattering layer (5 mm thick) TiO_2 particles (Solaronix, Ti- Nanoxide R/SP) were printed. The TiO_2 electrodes were heated under an airflow at 350 °C for 10 min, followed by heating at 500 °C for 30 min. After cooling to room temperature, the TiO_2 electrodes were treated with 40 mM aqueous solution of $TiCl_4$ at 70 °C for 30 min and then washed with water and ethanol. The electrodes were heated again at 500 °C for 30 min and left to cool to 80 °C before dipping into the dye solution. The dye solutions (**HD-2** or **SD-1**) (0.3 mM) were prepared in 1:1:1 acetonitrile/t-butyl alcohol/DMSO. Deoxycholic acid (**DCA**), or **SD-1** was added to the dye solution as a coadsorbent at a concentration of 20 mM. The electrodes were immersed in the dye solutions with active area facing up and then kept at 25 °C for 20 h to adsorb the dye onto the TiO_2 surface.

For preparing the counter electrode, pre-cut FTO glasses were washed with water followed by 0.1 M HCl in EtOH, and sonication in acetone bath for 10 min. These washed FTO were then dried at 400 °C for 15 min. Thin layer of Pt-paste (Solaronix, Platisol T/SP) on FTO was printed and the printed electrodes were then cured at 450 °C for 10 min. The dye sensitized TiO_2 electrodes were sandwiched with Pt counter electrodes and were sealed using a 40 µm Syrlyn spacer through heating of the polymer frame. The electrolyte (Solaronix, Iodolyte AN-50) was then injected into the cell, while the two electrodes were held together with the clips.

2.5. Photo-electrochemical measurements

Photocurrent-voltage characteristics of DSSCSs were measured using a Keithley 2400 source meter under illumination of AM 1.5 G solar light from solar simulator (SOL3A, Oriel) equipped with a 450 W xenon lamp (91160, Oriel). The incident light intensity was calibrated using a reference Si solar cell (Newport Oriel, 91150V) to set 1 Sun (100 mW cm^{-2}). The measurement was fully controlled by Oriel IV Test Station software. IPCE (incident monochromatic photon to current conversion efficiency) experiments were carried out using a system (QEX10, PV Measurements, USA) equipped with a 75 W short arc xenon lamp (UXL-75XE, USHIO, Japan) as a light source connected to a monochromator. Calibration of incident light was performed before measurements using a silicone photodiode (IF035, PV Measurements). All the measurements were carried out without the use of anti-reflecting film.

3. RESULTS AND DISCUSSION

3.1. Synthesis of Dye

The synthetic routes used for preparation of compound **SD-1** is shown in Scheme 1. The 2-amino-5-nitrobenzonitrile was converted to the tetrazole heterocyclic by a Huisgen 1,3-dipolar cycloaddition with sodium azide [11]. Diazotization and coupling were carried out at 0-5 °C. All the compounds were fully characterized by mass spectroscopy, NMR and IR spectroscopy.

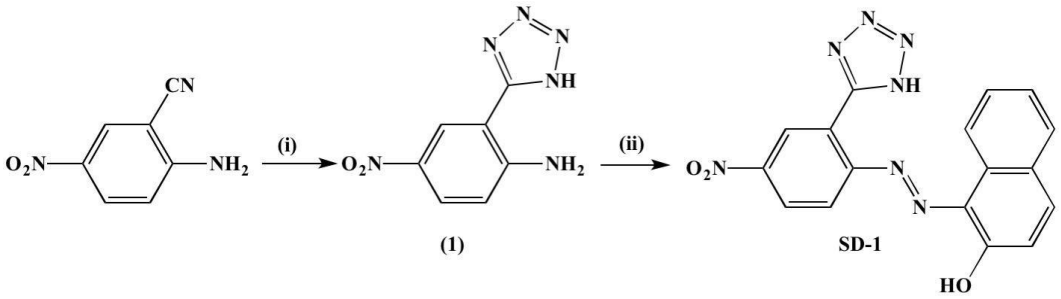

Scheme 1. Synthetic route to target dyes. Reaction conditions: (i) NaN_3 /NH_4Cl/DMF, yield 65%; (ii) $NaNO_2$, HCl, 5 °C, 2-naphthol.

3.2. Photophysical measurements

The UV−Vis absorption and photoluminescence spectra of the organic dye **SD-1** in DMF (concentration of 1,8 x 10^{-5} M) is depicted in Fig. 2, and the corresponding photophysical data are summarized in Table 1. In the electronic absorption spectra, the dye exhibited a prominent band with the absorption maximum in 513 nm and an extinction coefficient higher than 1.8 × 10^4 $M^{-1}cm^{-1}$. Such absorption characteristic can be ascribed to the π−π* transition of the whole D−π−A conjugation backbone. The charge transfer emission maximum shifts from 580 nm for **SD-1**.

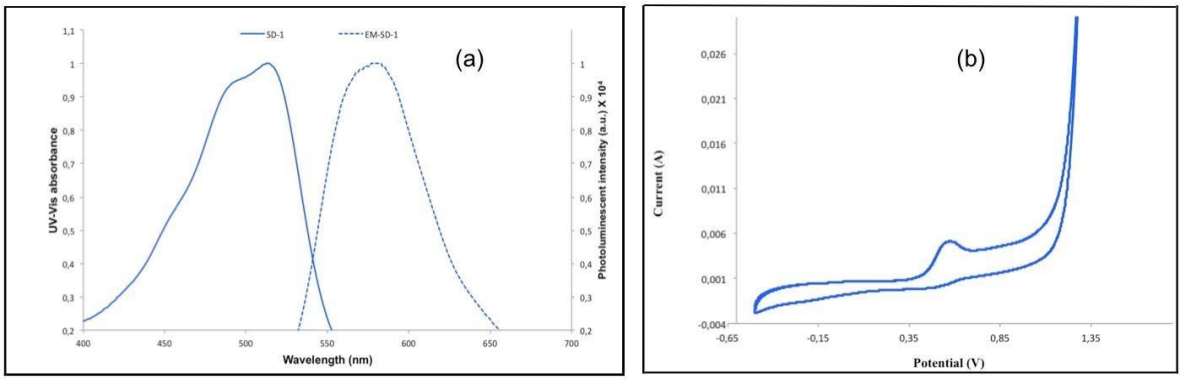

Fig. 2. Photophysical and electrochemical measurements of organic dye **SD-**. (a) UV-Vis absorption (solid-lines) and emission spectra (dashed-lines) measured in DMF (2 x10^{-2} M); (b) Cyclic voltammograms in DMF with 0.1 M [TBA][PF_6] as an electrolyte at a scan rate of 50 mVs^{-1}.

Table 1. Physical properties of organic dye **SD-1**.

Compound	Absorption λmax (nm)	ε (M^{-1} cm^{-1})	Emission λmax (nm)	Stokes shift (nm)
SD-1	513	17,400	580	67

3.3. Electrochemical measurements

To fabricate an efficient DSSC, besides the light-harvesting yield of a dye-adsorbed TiO_2, it is also of importance that there are favorable energy-offsets of the dye molecules with respect to the TiO_2 nanocrystals and redox electrolytes. Here, the electrochemical behaviors of these dyes were measured by cyclic voltammetry (CV) CV graphs (Figure 2) were used to calculate the oxidation onset, which are equivalent to the GSOP (ground state oxidation potential) or HOMO level. The values of $E_{0\text{-}0}$ and GSOP were used to calculate the ESOP (excited state oxidation potential), the values in volts (V) against NHE were converted to electron volt (eV) according to Equation (1) [29].

$$ESOP = [(GSOP\ (V) + 4.7) - E_{0\text{-}0}]\ eV \quad (1)$$

The HOMO level of **SD-1** is more negative than that of the iodide/triiodide coupled electrolyte (- 5.2 eV), thus providing ample driving force for efficient dye regeneration. This difference between iodide/tri-iodide potential and the HOMO level is favorable for the dye regeneration. Furthermore, based on the band gap (E_{00}) estimated from the onset of the UV-visible absorption spectra, the lowest unoccupied molecular orbital (LUMO) was obtained (table 2). The LUMO levels (ESOP) of the dyes is less negative than the conduction band edge (CB) nanocrystalline TiO_2 (- 4.2 eV), indicating that electron can be energetically injected into the TiO2 conduction band from the excited dyes, thus providing ample driving force for efficient dye regeneration (Table 2).

Table 2. Excited state oxidation potential – ESOP (E*), ground state oxidation potential (GSOP) and the lowest electronic transitions ($E_{0\text{-}0}$) for **SD-1**.

Sensitizer	Experimental (eV)		
	[a]$E_{0\text{-}0}$ (eV)	[b,c]GSOP (E_{HOMO})	ESOP (E^*_{LUMO})
SD-1	2.26	-5.72	-3.46

[a] $E_{0\text{-}0}$ = calculated from the onset of absorption spectra (DMF).
[b] GSOP = ground state oxidation potential = E_{HOMO}.
[c] GSOP was measured in DMF with 0.1 M [TBA] [PF6] and with a scan rate of 50 mV s^{-1}. It was calibrated with Fc/Fc^+ as internal reference and converted to NHE by addition of 0.63 V; Excited-state oxidation potential ESOP (E*) was calculated from: **E* = GSOP + [a]E0-0**

3.4. Photovoltaic device characterizations

In order to determine the practical utility of the synthesized molecule (**SD-1**) as dye and/or co-adsorbent in DSSCs, *deoxycholic acid (**DCA**)* was used as standard co-adsorbent and **HD-2** was used as standard dye and photovoltaic characterizations were carried out. Three prototypes of each dye-co-adsorbent system were prepared (**SD-1 - DCA**, **HD-2 - DCA** and **HD-2 - SD-1**). Nanocrystalline TiO_2 electrodes were prepared according to the procedure reported previously [30]. Sandwich types DSSCs were prepared from the stained photodiodes and Pt coated cathode. Photovoltaic measurements were carried out after introducing the electrolyte between the glass electrodes. There are two widely used techniques for photovoltaic characterization: current–voltage measurements under

simulated sunlight (producing J–V curves) and monochromatic light generated current measurements (producing incident photon-to-current conversion efficiency (IPCE) spectra (Fig. 4). The photocurrentvoltage (IV) characteristics were measured under a simulated solar light (AM 1.5 G, 100 mW cm^{-2}) (Fig 5). The incident photon-to-current conversion efficiency (IPCE) spectra were measured under with a 75 W short arc xenon lamp and a monochromator. The photovoltaic parameters including short-circuit photocurrent density (J_{sc}), open- circuit voltage (V_{oc}), fill factor (FF) and overall power conversion efficiency (PCE) can be obtained by the current–voltage measurements (Table 3) [13].

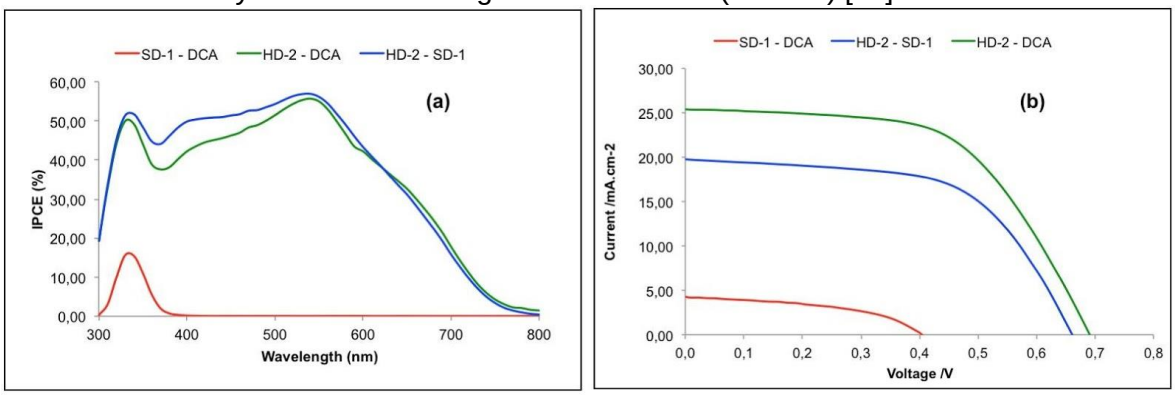

Fig. 4. Photo-electrochemical measurements from dyes **SD-1 -DCA**, **HD-2 – DCA** and **HD-2 – SD-1** anchored on nanocrystalline TiO_2 film. (a) IPCE spectra; (b) Photocurrent−voltage characteristics. The concentration of the co-adsorbent used was 20 mM for all dyes.

The IPCE value corresponds to the photocurrent density that is produced in the external circuit under monochromatic illumination of the cell divided by the photon flux that strikes the cell. The IPCE is determined by the light harvesting ability, the amount of adsorbed dyes on the TiO_2 surface, the overall charge collective efficiency and the overall electron injection efficiency. It is noted that the maximum IPCEs for DSSCs generally should be smaller than 90% because of the reflection and absorption loss due to the FTO glass. For the prototype prepared **with SD-1 – DCA,** the IPCE response of higher than 10% from 320 nm to 380 nm was exhibited by the dyes. Such spectral responses are not consistent with the trend in the absorption spectra, implying their poor light harvesting ability on visible region. For the prototype prepared with **HD-2 - SD-1**, from 330 nm to 640 nm, the IPCE response is higher than for prototypes prepared with **HD-2 – DCA**.

These results indicate that there is a direct relationship between geometry and the anchoring group effect for DSSCs. The tetrazole group is in ortho position in relation to the AZO bridge, by steric effects the efficiency is very low to work as anchoring group. The Nitro group is in the *para* position relative to the AZO bridge, however, the results also demonstrate the poor efficiency of the nitro group, to be used as an anchoring group in DSSC.

The photovoltaic parameters including the short-circuit photocurrent density (J_{SC}), open-circuit voltage (V_{OC}), fill factors (ff) and overall cell efficiencies (%η) are summarized in Table 3 and I-V results are shown in Figure 5. The use of **SD-1 – DCA** resulted in J_{SC} of 16.52 $mA.cm^{-2}$, **HD-2 – DCA** resulted in J_{SC} of 21.15 $mA.cm^{-2}$ and **HD-2 – SD-1** resulted in J_{SC} 16.46 $mA.cm^{-2}$, respectively. The fact that SD-1 dyes present poor values of photocurrent density, even with co-adsorbent **DCA**, shows the difficulty of anchoring the

TiO_2 surface and, consequently, the difficulty of injecting electrons. The dye **SD-1 - DCA** resulted in V_{oc} of 0.40 V, and total conversion efficiency (%η) of 1.30%, while **HD-2 - DCA** resulted in V_{oc} of 0.69 V, and total conversion efficiency (%η) of 8.38% and **HD-2 – SD-1** resulted in V_{oc} of 0.66 V, and total conversion efficiency (%η) of 7.81%.

Table 3. Photovoltaic characteristics of **SD-1** – DCA, HD-2 – DCA and HD-2 – SD-1.

Photosensitizer	J_{sc} (mA.cm^{-2})	V_{oc}(V)	FF	η (%)
HD-2 – DCA	21.15	0.69	0.57	8.38
SD-1 – DCA	16.52	0.40	0.44	1.30
HD-2 – SD-1	16.46	0.66	0.59	7.81

4. CONCLUSIONS

Experimental work has been carried out on three metal-free organic dyes containing tetrazole and arylazo groups, to study the effects of structural modifications on dye uptake on TiO_2 in DSSCs. The solution phase absorption spectra revealed that dyes are capable of harvesting sunlight with λ_{max} in the order of 513 nm for 1-{[(4'-nitro-2'-tetrazoyl)-phenyl]-diazenyl} naphthalene-2-ol (**SD-1**). The absorption spectrum confirmed the charge transference from donor to acceptor. CV graphs were used to calculate the ground state oxidation potential (HOMO) and excited state oxidation potential (LUMO). The HOMO energy level of the dye **SD-1** was below the redox energy level of I^-/I_3^- and the LUMO level was above the CB of TiO_2. This scenario is suitable for fabricating nanocrystalline TiO_2 based solar cells. In order to determine the practical utility of **SD-1** as a dye and/or co-adsorbent for solar cells, photovoltaic measurements were carried out. Incident photon to current conversion efficiency (IPCE) responses of higher than 10% was observed only from 320 nm to 380 nm for the dye **SD-1 – DCA. SD-1** as co-adsorbent proved to be better than DCA however, the results of conversion efficiency were below the observed to **DCA** co-adsorbent.

References

[1] Hagfeldt, A., Boschloo, G., Sun, L., Kloo, L., Pettersson, H., *Dye-Sensitized Solar Cells*. Chem. Rev. 2010, 110, 6595-6663.

[2] ITO, S., Murakami, T. N., Comte, P., Liska, P., Grätzel, C., Nazeeruddin, M. K., Grätzel, M., *Fabrication of thin film dye sensitized solar cells with solar to electric power conversion efficiency over 10%*, Thin Solid Films 2008, 516, 4613–4619.

[3] Magne, C., Dufour, F., Labat, F., Lancel, G., Durupthy, O., Cassaignon, S., Pauporte, T., *Effects of TiO_2 nanoparticle polymorphism on dye-sensitized solar cell photovoltaic properties*. J Photochem Photobiol A 2012; 232:22-31.

[4] Nazeeruddin, M. K., et al. *Engineering of efficient panchromatic sensitizers for nanocrystalline TiO2-based solar cells*. J. Am. Chem. Soc. 2001, 123, 1613-1624.

[5] Ito, S., et al., *Photovoltaic characterization of dye-sensitized solar cells: effect of device masking on conversion efficiency*. Prog. Photovolt., 2006,14, 589-601.
[6] Zhang, G., et al., *High efficiency and stable dye-sensitized solar cells with an organic chromophore featuring a binary pconjugated spacer.* Chem. Commun., 2009, 2198-200.
[7] Zeng, W., et al. *Efficient dye-sensitized solar cells with an organic photosensitizer featuring orderly conjugated ethylenedioxythiophene and dithienosilole blocks*. Chem. Mater., 2010, 22, 1915-1925.
[8] Massin, J., Ducasse, L., Toupance, T., Olivier, C., *Tetrazole as a New Anchoring Group for the Functionalization of TiO2 Nanoparticles: A Joint Experimental and Theoretical Study*, J. Phys. Chem. C, 2014, 118, 10677−10685.
[9] Nguyen, L. H., et al., *A selective co-sensitization approach to increase photonconversion efficiency and electron lifetime in dye-sensitized solar cells*. Phys. Chem. Chem. Phys., 2012, 14, 16182-16186.
[10] Lee, C. L., Lee, W. H., Yang, C. H., *The effects of co-sensitization in dye-sensitized solar cells.* J. Mater. Sci., 2013, 48, 3448-3453.
[11] Da Silva, L., Freeman, H. S., *Variation in hydrophobic chain length of co-adsorbents to improve dye-sensitized solar cell performance*, Phys. Chem. Chem. Phys*.,* 2019, 21, 16771-16778.
[12] Cheema, H., Islam, A., Han, L., El-Shafei, A.,Benzodioxan-Stilbazole-based Ancillary Ligands on Dye Packing, Photovoltage and Photocurrent in Dye-Sensitized Solar Cells, ACS Appl. Mater. Interfaces 2014, 6, 11617−11624.
[13] Zhang, M., et al., *Design of high-efficiency organic dyes for titania solar cells based on the chromophoric core of cyclopentadithiophene-benzothiadiazole.* Energy Environ. Sci., 2013, 6, 2944-2949.

ID 080

Sustainability Criteria for Systems with Hydrogen Energy Storage Devices located in Mexico

Paola Andrea Urbano Arcila[1]*, Orlando Lastres Danguillecourt[2], Geovanni Hernández Galvez[3], Guillermo Rogelio Ibáñez Duharte[2], Jesús Antonio Enríquez Santiago[1]

[1]PhD. Candidate in the Universidad de Ciencias y Artes de Chiapas (UNICACH). Libramiento Norte Poniente 1150, Colonia Lajas Maciel C.P. 29039 Tuxtla Gutiérrez, Chiapas, México.
[2] PhD. Professor and researcher in the Universidad de Ciencias y Artes de Chiapas (UNICACH). Libramiento Norte Poniente 1150, Colonia Lajas Maciel C.P. 29039 Tuxtla Gutiérrez, Chiapas, México.
[3]PhD. Professor and researcher in the Universidad Popular de la Chontalpa. Carretera Cárdenas-Huimanguillo. Ranchería Paso y Playa, C. P. 86500 Heroica Cárdenas, Tabasco, México.

*Corresponding author: paolaurbano@hotmail.com

ABSTRACT

Sustainable development is one of the common objectives of almost all Nations, as well as the energy security and the access to this basic service for everyone. Renewable energy systems have different characteristics which put them closer to the sustainability objectives than the traditional energy generation systems, mainly in remote areas far from the national electric energy network. Isolated systems require a storage component. Battery banks have been mainly used, and less frequently the hydrogen storage systems (HSS). Most of the literature and researches have been developed in Europe, Asia, and North America. Every single location has different social, economic, and environmental characteristics, among others. That is why it is important to analyze those conditions for a Latin-American project site. Taking in account the criteria used in similar studies in other latitudes as well as the sustainable development criteria formulated for Latin America, particularly in Mexico; the analysis, selection and estimation of the sustainable criteria was carried out; This in order to include sustainability criteria in the traditional economic optimizations of isolated systems with a HSS.

This paper presents a comparison between the most common used values for some sustainable criteria for both energy storage technologies: Battery banks and HSS; which would be used later for a multicriteria analysis process to design and optimize a sustainable and renewable energy system with a storage component, principally for the electrification of remote communities. The obtained results allow to obtain solid and sufficient arguments to promote the hydrogen storage technologies application, highlighting its economic, operational and environmental advantages, mainly for the isolated systems.

Keywords: Hydrogen storage, sustainability criteria, renewable energy systems.

1. Introduction

Currently the great challenges that humanity faces are related to energy security, sustainability and climate change. The use of renewable energies for the electrification of rural or remote areas, as well as their application for the transition towards the exploitation of clean energies, opens a promising panorama for the design of renewable hybrid energy systems (HRES) with a sustainability focus; through techniques to aid decision-making, such as multicriteria analysis. In this way, technical, economic, environmental, social and institutional criteria can be taken into account, which add value to the different electrification alternatives for a particular case.

Around the world, for more than 40 years, HRES have been implemented, mainly for the electrification of remote areas, for example islands in Italy and Germany. For its part in Latin America, different projects and investigations have been carried out with very little dissemination. On the one hand, the publications on the multicriteria design of hybrid systems is limited according to an extensive bibliographic review; and on the other hand, the investigation of installed systems, for example in the case of Mexico, is poorly reported. The most complete and recognized compendium of which is known, was published in the year 2000 [1] and as of that date, these systems have hardly been mentioned, due in part to the fact that several have been dismantled. It is of great importance to breathe new life into sustainable hybrid systems, especially for developing countries where a large number of rural communities lack this basic service.

From the single parameter design using a commercial software tool, (HOMER), the alternatives of renewable systems are obtained, whose characteristics allow the transformation of the available energy resources, into sufficient energy to supply the required energy demand, in a given location. These alternatives are subsequently compared under sustainability criteria. The criteria selected and weighted according to each particular case and by means of different techniques such as paired comparison, order of importance or direct allocation. By applying the multi-criteria analysis tools, a list of the alternatives is obtained in order of punctuation, which indicates which system is closest to the sustainable ideal.

In particular, HSS have not been taken into consideration in Mexico and other Latin American countries. However, these countries have some of the most abundant and cost-competitive renewable energy resources in the world, including hydropower, W/PV; The elements that make the region a world leader in renewable energy can facilitate a similar rise for clean hydrogen production in this decade. But it is important to keep in mind that to stimulate investment, economies of scale must be supported and improved through market incentive policies and programs [2]. In this way, when considering other sustainability criteria (in addition to the economic aspect), this rising hydrogen market can be promoted from renewable energies, due to its favorable characteristics in environmental issues, with the institutional support of government policies that support them. according to studies that have been carried out in other countries in Asia and Europe [3,4,5].

2. Background

The findings of a literature review related to the multicriteria analysis for group decision making, to obtain a sustainable HRES, considering hydrogen storage, are:

Baños et al. [6] analyzed the MODM (Multiobjective decision making) based on the vital importance of the energy to the integral development of emerging countries, whose rapid economic growth leads to an accelerated increase in the generation of greenhouse gas emissions, and the increase in the gasoline price, which encourages the use of sustainable RES (renewable energy systems). The increase in the number of publications that use MODM to solve RES problems is evident, especially in the area of solar and wind energy. Some of the most used methods were mixed integer linear programming (MILP), Lagrangian relaxation, quadratic programming (MIQP) and simplex search. As well as heuristic techniques, such as genetic algorithms (GA) and Particle Swarm Optimization (PSO). They present a bibliographic review of investigations that seek to optimize hybrid systems with hydrogen storage, but do not mention the sustainability criteria used or their values.

Distributed energy planning (DEP) is another of the research topics, where Manfren [7] used optimization software to take advantage of different energy sources. They comment on the applicability of the HYDROGems software, for the simulation of systems with HSS. They do not provide information on sustainability criteria. For their part, Mallikarjun and Lewis [8] used MODM tools to determine the optimal location of a system with distributed resources for commercial buildings in the United States. Hydrogen storage is analyzed, however it is outside the main ranking. Kim et al. [9] applied the AHP (Analytic Hierarchy Process), MAVT (Multi-attribute value theory) methodology, PROMETHEE (Preference Ranking Organization Method for Enrichment Evaluations), ELECTRE (Elimination and Choice Expressing Reality), to compare the results obtained, emphasizing in the storage system. Fuel cells are different from batteries which store electrical energy chemically in a closed system, whereas fuel cells consume reactants, which must be replenished. Electrodes of a fuel cell are catalytic and relatively stable while a battery react and change when a battery is charged or discharged. The utilization of a water electrolysis unit is a typical approach to deliver hydrogen which can be put away in high pressure compartments and / or transmitted by pipelines for later utilize. When using the stored hydrogen for electricity generation, the fuel cell (otherwise called regenerative energy unit) is embraced, which is the key innovation in hydrogen EES (electrical energy storage). The world's first utility-scale test of a stand-alone RES integrated with hydrogen storage and fuel cells was introduced in Norway, which conveyed power with required quality and high unwavering quality. One of the world's largest biogas fuel cell power plants, which converts biogas into electricity and usable high-quality heat is reported to have been launched in 2012 in California (2.8 MW). They present a summary table of the storage technologies in different types of batteries and, in the case of hydrogen storage, they present such criteria: technological maturity, energy density, application at different scales, cost ($ 6-20 / kWh) and efficiency (30-60%).

In the field of the hybrid systems design (HSD), Theodosius et al. [10] used the Life Cycle Analysis (LCA) and the MCDM methodologies to design a HRES with conventional and renewable sources. Suggest criteria such as: Carcinogenic effects humans Respiratory effects (inorganics) on humans, Respiratory effects (organics) on humans, Human Health

Damages due to Climate Change, Human Health effects by Ionizing Radiation, Human Health effects Ozone Layer Depletion, Damage Ecosystem Quality by Ecotoxic Emissions, Damage Ecosystem Quality by Acidification / Eutrophication, Damage Ecosystem Quality Land Occupation & Conversion, Damage Resources by extraction of Minerals, Damage Resources by extraction of Fossil Fuels, Human Health, Ecosystem Quality Resources. They analyze different alternatives but perform the calculations using global criteria by system, but not by component. Hernández et al. [11], applied the VIKOR (Multicriteria Optimization and Compromise Solution, Serbian) methodology to perform the optimal selection of two HES; one of these interconnected to the grid, using wind and solar resources, and to supply the demand of the laboratories at a university in the Tehuantepec Isthmus. And another system, also wind/photovoltaic (W/PV) with HSS, for a rural area electrification in Cuba; for which they took into account sustainability criteria such as the equivalent emissions in the system life cycle (Fuel cell (H_2 by electrolysis) 20 gCO_2eq./kWh, and Electrolyzer and H_2 tank 11 gCO_2eq./kWh), the capital cost and the social acceptance.

On another hand, Bakhtiari & Naghizadeh [3] proposed the multicriteria Shuffled frog leaping) / ε-constrain (SFLA), for a HRES design including a W/PV, fuel cells, electrolyzer, hydrogen tank and a battery bank , with an intermittent load profile. They also include comparative parameters such as LPSP (loss of power supply probability), TEL (total energy loss) and TELSUB (the power difference between generation and storing capacity)) and the equations to estimate them for each of the alternatives to take into account. account within the analysis. Meanwhile, Malekpoor et al. [5] suggested increasing the energy technologies with low CO_2 emissions and reducing the use of coal and gasoline. The approach Gray Relational Analysis- Multi-objective Gray Linear Programming (GRA-MOGLP) provides an effective tool for the evaluation and optimization of the planning of sustainable electricity generation. They also conclude that the market maturity for various energy storage technologies is growing fast and brings renewables and storage hybrid solutions off their small-scale past. They set criteria such as: Heavy metal emissions, Water consumption, Effect on global Warming, Land use, Disturbance of ecologic al balance, Particulate matter PM10 and Particulate matter PM25, Job creation, Social acceptability, Mortality rate, External cost associated with health; and the way of estimating them for the generated alternatives, given a particular case.

The RES source selection is another field where MCDM has been applied, as in the Sengül et al., Research in 2015 [12], where they stated as the main objective of their research, to develop a support framework to prioritize the energy supply systems in Turkey. Selecting a set of energy supply systems involves many conflicting criteria, for which multicriteria decision (MCDM) methods have been used for their analysis. The Shanon interval entropy methodology (fuzzy TOPSIS) was used to determine the value of the criteria weights. For three alpha cutoff levels, the same sequential order of the alternatives was obtained. According to the results, the first criterion in the ranking is the amount of energy produced, followed by the extension of the impacted land, the cost of operation and maintenance, the installed capacity, the efficiency, the period of recovery of the investment, the cost of investment, job creation, and CO_2 emissions. Therefore, the AMC showed that a hydroelectric station is the best renewable energy supply system for Turkey. They analyze hydrogen as a fuel and report that it is 33% more efficient than gasoline.

Arce et al. [13], argued that the European energy systems are characterized by high dependency on fossil fuels and energy imports, while describing the energy transition from conventional to renewable energy area; which improves the situation. Therefore, the

analysis of the energy systems is required, thus becoming a multi-attribute decision-making problem that challenges developers. This situation makes necessary to implement MCDM methodologies, using gray ratio methods (such as criteria selection and weighting methods). It is observed that the technical parameters are more frequently evaluated, followed by the environmental. AHP is used for the weighting process, because it is the most popular to evaluate the experts panel opinion. They do not present relevant information regarding sustainability criteria and their values. They explain the AHP method for weighting by paired comparison.

In 2017, Ioannou et al. [14], in 2017, they published a bibliographic review of risk-based methods for sustainable energy planning. They found that in quantitative methods, risk is measured primarily with variance or with probability density distributions of technical and economic parameters; while semi-quantitative methods such as multicriteria decision-making analysis (MCDA) scenarios may also include non-statistical parameters such as socioeconomic factors. Also in 2017, Sahabmanesh & Saboohi [15], applied the AHP tool, for the assessment of the sustainability of RES, from various sources. They compare the different alternatives using 29 different criteria. SESM (sustainable energy system model) software allows simulating systems and generating electrification alternatives, with innumerable elements of energy transformation, adaptation, storage, control and distribution. Due to the wide range of elements and components, it does not report criteria or values thereof for systems with hydrogen energy storage.

Finnally, Chen et al. [4] implemented proposals that included a hybrid NSGA (non sorting GA) II/Pareto/MOEA (Multi-Objective Evolutionary Algorithm)/DA (differential algorithm), for the transformation of energy into a W/cell/PEMFC (Proton Excechance Membrane Fuel Cell) system incorporated into the architecture of the site. They ensure that hydrogen technologies represent high efficiency, and low levels of noise and pollution.

Later, the specific analysis of the HSS is developed in the aforementioned investigations and the evaluations that its sustainability indicators receive by different authors and research groups. The methodology used to obtain, classify, and analyze the information found on the sustainability of HRES with a hydrogen component, compared to other energy storage technologies, is explained below..

2. Materials and Methods

The researches analyzed were found using the Web of Science platform, in which the analysis of the references was carried out in chronological order, taking from each one the important data for the present analysis, such as the multicriteria analysis tools used, the components of the hybrid system with hydrogen storage, and the sustainability indicators directly related to the storage system, and the way to estimate its qualitative or numerical values. Finally, a comparative analysis is carried out between the sustainability criteria found and the differences between the values used between the different sources of information. In order to complement the list of criteria, other items are suggested that may have a relationship or impact with the sustainability of the HRES in the particular case of Mexico, as a representative country of Latin America.

3. Results and Discussion

From what is stated in section 1, it can be seen that the specific information on the sustainability criteria for hybrid systems with hydrogen storage technology is limited and poorly detailed by the reviewed authors. The following specific data can be outlined:

Authors in [9] refer to criteria such as technological maturity, energy density, versatility of application at different scales, cost (which provides a range of values of $ 6 - 20 / kWh), and efficiency (30 - 60%). Reference [4] presents advantages of hydrogen technologies as high efficiency, low noise and pollution levels. Also, the use of 29 sustainability criteria for choosing the system closest to the ideal optimum is rescued from the [15] research, although the criteria used for HSS are not specifically mentioned. Finally, the contributions of [10] and [5] who mention the following sustainability criteria to be taken into account in systems with hydrogen storage: Carcinogenic effects humans, Respiratory effects (inorganics) on humans, Respiratory effects (organics) on humans, Human Health Damages due to Climate Change, Human Health effects by Ionizing Radiation, Human Health effects Ozone Layer Depletion, Damage Ecosystem Quality by Ecotoxic Emissions, Damage Ecosystem Quality by Acidification / Eutrophication, Damage Ecosystem Quality Land Occupation & Conversion, Damage Resources by extraction of Minerals, Damage Resources by extraction of Fossil Fuels, Human Health, Ecosystem Quality Resources. And, Heavy metal emissions, Water consumption, Effect on global Warming, Land use, Disturbance of ecological balance, Particulate matter PM10 and Particulate matter PM25, Job creation, Social acceptability, Mortality rate, External cost associated with health.

A new search for information allowed finding Report prepared by the Institute for Sustainable Futures for the Australian Council of Learned Academies [16], called Sustainability Evaluation of Energy Storage Technologies, which contains information gathered from different sources. They clearly present various environmental and social sustainability criteria, as well as their qualitative assessments for different storage technologies. From the information found there, table 1 is constructed comparatively between conventional battery systems and HSS:

Table 1. Sustainability criteria for systems with hydrogen storage and other conventional technologies.

Sustainability criteria	Hydrogen	Lithium-ion NMC	Lithium-ion LPF	Lead-acid	Flow	Sodium-based
Round trip efficiency	Low	High	High (but lower than NMC)	Medium	Low	Medium
Cycle life	Greater than on conventional batteries. [11]	Long	Long	Short	Long	Medium
Lifespan	Under research 18, 30 and 50 years [17,18]	Long (~10 years)	Long (~10 years)	Med (~5-10 years)	Long (>10 years)	Med (~8 years)

Life cycle GHG emissions	Medium	Low	Low	Medium	Medium	Medium
Supplay chain criticaly	Medium	High	Medium	Low	Medium	Low
Material intensity	Low	Medium	Medium	Low	Medium	Low
Recyclability	Low	Medium	Medium	Low	Medium	Medium
Environmental healt damage	Low	Medium	Medium	Medium	Low	Medium
Human rights vulneration	Low	High	Medium	Low	Low	Low
Health and safety risk	Medium	High	Medium	Medium	Low	Low

*NMC: Nickel Manganese Cobalt
*LPF: lithium phosphate ferrite

According to table 1, it is observed that the lifespan of hydrogen storage systems is one of its main strengths; on the other hand round trip efficiency may be its main weakness. To improve efficiency, an R&D agenda improving energy efficiency electrolysis, process intensification (upstream) for ammonia pathway is being developed [16].

Based on numerous sustainability indicators found in a 2000 INEGI (National Institute of Statistic and Geography, Spanish) report [19], some sustainability criteria were found for developing countries that can be used for multi-criteria analysis of hybrid systems with storage in hydrogen. Some of which are mentioned below: Future grid compatibility, number of electrified households generating income, business development, implementation of public lighting, better conditions for working children, visual and auditory impact, ease of operation and system administration. On the other hand, the current Mexican legislation has promoted some policies in support of hybrid systems. In August 2019, the Ministry of Economy released in the DOF (Official Gazette of the Federation, Spanish), the Declaration of Validity of the Mexican Standard NMX-J-657-3-ANCE-2018 that came into force 60 days later of his publication, which deals with Hybrid Systems and Renewable Energy, as a guide for the electrification of non-urban areas of difficult access [20].

4. Conclusions

The prospects for hydrogen storage systems (HSS) have very good development prospects in Mexico, as well as in other Latin American countries. At the same time, the uptake of these new technologies by the academic sector of the different institutions of the country and the continent, allow research and development efforts to be applied in the short and medium term, thanks to the government and private incentives they seek sustainable energy development. A compendium of different sustainability criteria applicable to the design and planning of HRES with hydrogen storage was achieved, which may be used in the future in

different multi-criteria analysis studies, where this storage technology is contemplated, providing specific values and references to carry out the calculation or estimation thereof according to each particular case. The multi-criteria analysis is expected to give greater importance to the environmental and social aspects that would tip the balance towards clean technologies that include hydrogen.

Acknowledgements

Authors would like to express their sincere gratitude to the CONACYT (National Council for Science and Technology, acronym in Spanish) for its continuous support during this study.

References

[1] Agredano J. Sistemas híbridos. Lecciones aprendidas. San Miguel Regla. Hidalgo. Noviembre del 2000.
[2] Aguillón C. La economía potencial de hidrógeno verde en América Latina, http://www.ipsnoticias.net/2020/06/la-economia-potencial-hidrogeno-verde-america-latina/; 2020 [accessed 27.07.20]
[3] Bakhtiari H, Naghizadeh R A. Multi-criteria optimal sizing of hybrid renewable energy systems including wind, photovoltaic, battery, and hydrogen storage with ε-constraint method. Ren. Power Gen. 2018; 12 (8): 883 - 892. DOI: 10.1371/journal.pone.0211642
[4] Chen X, Zhou H, Li W, Yu Z, Gong G, Yan Y, Luo L, Wan Z, Ding Y. Multi-criteria assessment and optimization study on 5 kW PEMFC based residential CCHP system. Ener. Conversion and Management 2018; 160: 384–395. DOI: 10.1016/j.enconman.2018.01.050
[5] Malekpoor H, Chalvatzis K, Mishra N, Kumar M, Zafirakis D, Song M. Integrated grey relational analysis and multi objective grey linear programming for sustainable electricity generation planning. Ann Oper. Research 2018; 269: 475–503. DOI: 10.1007/s10479-017-2566-4
[6] Baños R, Manzano-Agugliaro F, Montoya G, Gila C, Alcayde A, Gomez J. Optimization methods applied to renewable and sustainable energy: A review. Renewable and Sustainable Energy Reviews 2011; 15: 1753–1766. DOI: 10.1016/j.rser.2010.12.008
[7] Manfren M, Caputo P, Costa G. Paradigm shift in urban energy systems through distributed generation: Methods and models. Applied Energy 2011; 88: 1032–1048. DOI: 0.1016/j.apenergy.2010.10.018
[8] Mallikarjun S, Lewis H F. Energy technology allocation for distributed energy resources: A strategic technology-policy framework. Energy 2014; 72: 783-799. DOI: 10.1016/j.energy.2014.05.113
[9] Kim J, Suharto Y, Daim T U. Evaluation of Electrical Energy Storage (EES) technologies for renewable energy: A case from the US Pacific Northwest. Journal of Energy Storage 2017; 11: 25–54. DOI: 10.1016/j.est.2017.01.003
[10] Theodosiou G, Stylos N, Koroneos C. Integration of the environmental management aspect in the optimization of the design and planning of energy systems. Journal of Cleaner Production 2015; 106: 576-593. DOI: 10.1016/j.jclepro.2014.05.096

[11] Hernández G, Dorrego J R, Núñez A, Lastres O, Ixtlilco L, Juantorena A, Sarracino O, Sebastian P J. Selection of hybrid systems with hydrogen storage based on multiple criteria: application to autonomous systems and connected to the electrical grid. Int. J. Energy Res. 2014; 38: 702–713. DOI: 10.1002/er.3074

[12] Sengül Ü, Eren M, Shiraz S E, Gezder V, Sengül A B. Fuzzy TOPSIS method for ranking renewable energy supply systems in Turkey. Renewable Energy 2015; 75: 617-625. DOI: 10.1016/j.renene.2014.10.045

[13] Arce M E, Saavedra A, Míguez J L, Granada E. The use of grey-based methods in multi-criteria decision analysis for the evaluation of sustainable energy systems: A review. Renewable and Sustainable Energy Reviews 2015; 47: 924–932. DOI: 10.1016/j.rser.2015.03.010

[14] Ioannou A, Angus A, Brennan F. Risk-based methods for sustainable energy system planning: A review. Renewable and Sustainable Energy Reviews 2017; 74: 602–615. DOI: 10.1016/j.rser.2017.02.082

[15] Sahabmanesh A, Saboohi Y. Model of sustainable development of energy system, case of Hamedan. Energy Policy 2017; 104: 66–79. DOI: 10.1016/j.enpol.2017.01.039

[16] Sustainability Evaluation of Energy Storage Technologies. Institute for Sustainable Futures for the Australian Council of Learned Academies, 2017. In: https://acola.org/wp-content/uploads/2018/08/wp3-sustainability-evaluation-energy-storage-full-report.pdf [accessed 28.07.20]

[17] University reveals hydrogen storage with triple the lifespan of Li-ON. Smart energy, 2019, https://www.smart-energy.com/industry-sectors/electric-vehicles/university-reveals-der-hydrogen-storage-with-triple-the-lifespan-of-li-on/ [accessed 28.07.20]

[18] Answer to energy storage problem could be hydrogen, NREL, Techxplore, 2020 https://www.nrel.gov/news/program/2020/answer-to-energy-storage-problem-could-be-hydrogen.html [accessed 28.07.20]

[19] Indicadores de desarrollo sustentable en México. Instituto Nacional de Ecología-INEGI, 2000, http://centro.paot.org.mx/documentos/inegi/indicadores_desarrollo_sustentable.pdf [accessed 28.07.20]

[20] Zarco J. Sistemas Híbridos y de Energía Renovable. PV Magazine, 2019, https://www.pv-magazine-mexico.com/2019/08/07/sistemas-hibridos-y-de-energia-renovable/ [accessed 28.07.20]

Influence on the Performance of the Counter Electrode by Varying the Deposit Materials in the Application of Sensitized Solar Cells

J.R. Ramos Nava[1]*; W.J. Pech Rodríguez[1]; E.N. Armendáriz Mireles[1].

[1]1 Universidad Politécnica de Victoria, Parque Científico y Tecnológico de Tamaulipas, Ciudad Victoria, Tamaulipas 87138, México.
*831-113-9630 1430543@upv.edu.mx

ABSTRACT

In the present research work, the optimization of the counter electrode of the solar cell sensitized by dye was carried out by varying the electrocatalyst by depositing it by the screen-printing method. The electrodes obtained were characterized by means of electrochemical tests. Electrochemical studies showed that the electrodes composed of carbon and silver have a favorable reaction mechanism to carry out the ion collection and ion reduction processes of Iodo. From the V.I curves, it was possible to demonstrate that the current density and the open circuit potential depend to a great extent on the material deposited on the conductive glasses. It is concluded that carbon and silver composite counter electrodes are a viable option since the production cost of the cell can be reduced without compromising its efficiency.

Keywords: *DSSC, Curve V-I, screen-printing.*

1. Introduction

To reduce the current energy crisis, intensive research is carried out on new or alternative technologies. One of the most driven lately has been the solar cells which produce electrical energy through sunlight. However, previous generations (inorganic solar cells) have shown great development, the disadvantage of these is the high cost of production which has limited their use. Today, the creation of dye-sensitized solar cells (DSSC) has increased, but their low efficiency makes them not yet suitable enough to replace conventional energy production.

In order for solar cells to improve their cost-efficiency ratio, it is necessary to create anodes and cathodes with different materials and techniques, trying to control variables. For this, an analysis was carried out varying the materials used in the cathode by means of the silk-screen deposition technique in DSSC cells. This technique is used in the industry to adhere or engrave material on a homogeneous surface.

This deposition allows a controlled and precise adherence on the material to be deposited. That is why it is intended to create cathodes by means of this technique, which needs a thermal treatment once the material is deposited since the evaporation of organic compounds is required. The materials to be analyzed are silver, platinum and carbon. These materials provide some improvement in the cathode, thus increasing the efficiency of the DSSCs, however, they have different characteristics, which create variable efficiency.

2. Materials and Methods

If the counter electrode is involved, platinum is the material par excellence because it makes an excellent dumbbell with the iodide / triiodide pair. That is why we opted to make a material variation on the counter electrode (Silver and Carbon). the dye used is N719 in company with the Idolyte HI-30 electrolyte [1].

The use of the screen-printing technique for the deposition of our materials to be studied, is very common in the manufacture of DSSC cells, it consists of a screen-printing mesh that is mounted on a box used as a base.

This technique allows completing a printed pattern on the mesh, which can be small molds or holes that are the means of entry of the paste or mixture to be used towards the object where it is desired to be deposited. On the other hand, the rest of the mesh has a kind of varnish so that the mixture does not leak through any other source than the design that is printed on the mesh.

The deposition of the material layers is carried out as follows, it should be mentioned that the process is carried out according to the number of material layers required. The first part is cleaning the holes in the mesh, placing the material in which it is going to be deposited by the part below it, lowering the mesh and placing the paste on one side of the holes to later be carried to these, the expansion of the material along the holes is carried out at a constant speed and pressure by means of the rubber squeegee. When carrying out the deposition, a heat treatment is carried out depending on the material deposited on the base.

In case of requiring more layers of material, the same screen-printing procedure is carried out, it is worth mentioning that between the deposition of each layer, the temperature of the

object used as the basis for the deposition, together with the deposited material layer, decreases to room temperature. Variants that can influence poor deposition are: the force with which the squeegee is pushed into the screen (mesh), the complement of the distance, the speed of the squeegee and the viscosity of the solution [2,3].

When carrying out the appropriate deposition, the anode and cathode are joined to form our DSSC cell, which can be seen in the following figure. The union is carried out by means of a thermal treatment on a thermal plate. At the end of the electrolyte it will be injected through a hole into the cell and subsequently sealed to prevent the rapid evaporation of this component.

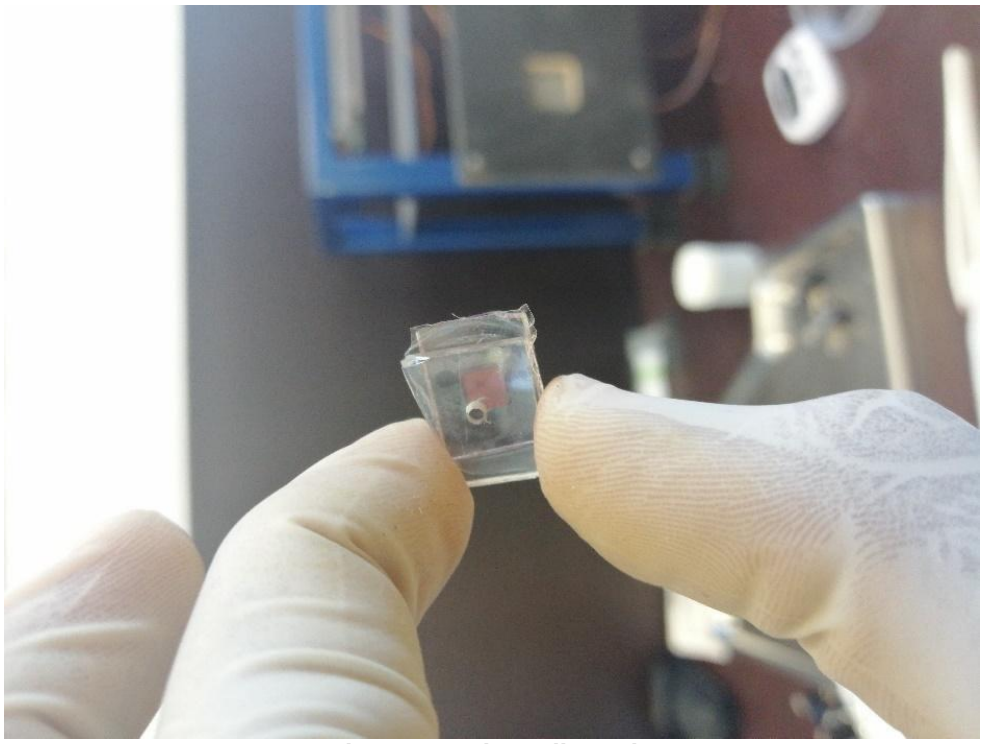

Figure 1: Solar cell result.

3. Results and Discussion

As a result, visual images of the deposition on the counter electrode were obtained by means of the Nikon ECLIPSE MA200 microscope using visual amplification x20 (100 µm). The images of the resulting deposition are shown below.

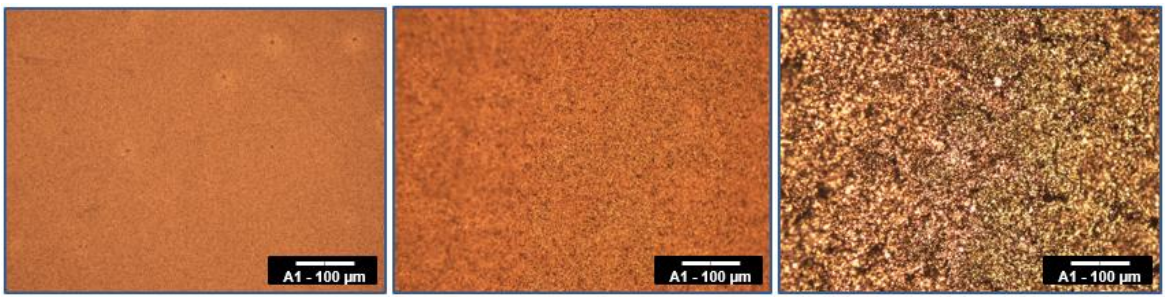

figure 2: Visual analysis result under a microscope.

As you can see in the figures the deposition is homogeneous, however, in the different materials we can see a different roughness. Figure A) (Platinum) shows a low roughness compared to B) and C) (Silver and Carbon) where it is more pronounced. This is due to the particle size, and the presentation of the solutions where the materials used come from.

In the following table you can see the best cell obtained by each material, we can see that the silver and carbon cells increase the efficiency of the cells. The form factor is considered good in the literature since it is mentioned that the expected range is between 40.00 and 70.00, since reaching 100.00 is too complex.

Tabla 1: Best cells by Material

Mejores Celdas por Material					
Material	Stream (I_{sc})(mA/cm^{-2})	Voltage (V_{ocp})(mV/cm^{-2})	Form factor (FF)	Power (P_{max}) (mW/cm^{-2})	Efiiciency (η) (%)
Platinum	4.599	0.763	62.353	2.188	2.188
Silver	4.909	0.765	64.227	2.412	2.412
Carbon	5.502	0.771	57.024	2.419	2.419

4. Conclusion

The change of materials is only one more variable in solar cells. There are hundreds of variables to control from cleaning substrates to sealing cells for electrolyte injection. In this case, the selected variable gave us a positive result, increasing the efficiency of the solar cells without compromising the manufacturing technique or the cost.

The form factor acquired by the cells is relatively good. Due to the characteristics of the materials, it was possible to effectively replace platinum with silver and carbon, even improving the performance of the cells from an average of 2.1% efficiency to an average of 2.4%, which represents a significant advance. As can be seen in the previous table, the improvement was remarkable, however, even more variables can be controlled which directly affect the performance of the cells, the type of electrolyte, the material in the anode, among others.

This topic of solar cells is applicable in the decomposition of water by means of electrolysis. It is known that this technique needs a means that generates electric current, be it a battery or a cell, the implementation of solar cells in the process helps to acquire, through sunlight, the charge necessary to keep the process running without consuming conventional electrical energy.

Acknowledgements

We thank the National Council for Science and Technology (CONACYT) for awarded master's scholarships and the postgraduate academic body at the Universidad Politécnica de Victoria.

References

[1] G. Z. G. Nora Aydeé Sánchez Bojorge, Luz María Rodríguez Valdez, “CELDAS SOLARES SENSIBILIZADAS POR COLORANTES (CSSC),” Quim. No 1., vol. 1, no. 1, pp. 1–10.

[2] C. S. T. L. DANIELA CAROLINA AGUAS ITURRALDE, “Estudio del uso de diferentes tipos de pastas de dióxido de titanio para la elavoración de celdas solares sensibilizadas con pigmentos,” Tesis, 2016. [Online]. Available: http://dspace.ups.edu.ec/bitstream/123456789/5081/1/UPS-CYT00109.pdf

[3] F. C. Krebs, “Fabrication and processing of polymer solar cells : A review of printing and coating techniques,” SSolar Energy Mater. Sol. Cells, vol. 93, pp. 394–412, 2009, doi: 10.1016/j.solmat.2008.10.004.